universität wien

DISSERTATION / DOCTORAL THESIS

Titel der Dissertation /Title of the Doctoral Thesis

„Petrography, geochemistry, and shock metamorphism of the impactites from the Chicxulub impact structure peak ring (Yucatán peninsula, Mexico) recovered by the IODP-ICDP Expedition 364 drilling"

verfasst von / submitted by

Jean-Guillaume Feignon, Lic. master

angestrebter akademischer Grad / in partial fulfilment of the requirements for the degree of

Doktor der Naturwissenschaften (Dr. rer. nat.)

Wien, 2022 / Vienna, 2022

<u>Preface</u>

This thesis presents and discusses the results of research conducted mainly at the Department of Lithospheric Research of the University of Vienna (Austria), based on the investigation of the impactite samples recovered within the Chicxulub impact structure peak ring (Yucatán peninsula, Mexico) during the joint International Ocean Discovery Program-International Continental Scientific Drilling Program (IODP-ICDP) Expedition 364 drilling (M0077A drill core), which took place in May 2016. A ~829 m continuous core was recovered. The main objective of this thesis was to characterize in detail the petrography, the geochemistry, and the shock metamorphism of the peak ring rocks, including granitic basement, pre-impact volcanic dikes, impact melt rocks, and suevites. Part of the work was made and shared in the framework of a collaboration launched in 2018 with the Analytical, Environmental, and Geochemistry Research Group (AMGC) of the Vrije Universiteit Brussels (VUB) in Belgium, which resulted in several joint publications. Petrographic investigations included general macroscopic and microscopic observations, using, e.g., optical microscopy, in order to identify the different minerals, textures, and clast types composing the different recovered lithologies within the drill core. Other techniques, such as scanning electron microscopy (SEM) and universal stage (U-stage) were used for the identification of accessory phases, and the characterization of shock-induced deformation features in quartz (i.e., planar fractures [PFs], feather features [FFs], and planar deformation features [PDFs]), and in other minerals (such as plagioclase, apatite, titanite, zircon), providing constraints on shock pressures experienced by the granitic basement. Geochemical (major, trace, and highly siderophile element [HSE] contents) and isotopic data (Sr–Nd and Re–Os isotope ratios) were obtained using micro X-ray fluorescence (µXRF) chemical mapping, X-ray fluorescence spectrometry (XRF), instrumental neutron activation analysis (INAA), thermal ionization mass spectrometry (TIMS), and inductively coupled mass spectrometry (ICP-MS). The geochemical data obtained allowed to: identify the contribution of pre-impact target lithologies to the suevite and impact melt rock lithologies; characterize the granitic basement rocks and their possible sources, and identify a hydrothermal alteration event; and search for a possible meteoritic signature within the impact melt rocks of the Chicxulub peak ring. The whole rock, powdered, and thin section samples are stored at the Natural History Museum Vienna and at the University of Vienna.

This thesis is divided into eight chapters. Chapter 1 is a general introduction of impact cratering processes. Chapter 2 presents a review of the typical features of meteorite impact structures, including the main impactite types that can form during an impact event, the shock-induced metamorphic features that can be observed in rocks and minerals, as well as the possible preservation of the meteoritic material that can be identified within an impact structure. Chapter 3 provides an overview of the Chicxulub impact structure, including an introduction to the IODP-ICDP Expedition 364 drilling. Chapter 4 consists of an extended section describing the different methods used for the completion of this thesis. Chapters 5–7 are published manuscripts in refereed journals, while chapter 8, called "Potpourri", presents further detailed investigations conducted on impactite samples that were not included in chapters 5, 6, and 7, but mostly integrated into other co-authored publications. Finally, in the Appendices are

reported detailed petrographic descriptions of the investigated samples from the M0077A drill core, as well as, all the associated geochemical data. In the next sections, the main conclusions of chapters 5–8 are summarized.

Chapter 5 is an article published in the journal *Meteoritics & Planetary Science* (Vol. 55, 2206–2223, doi:10.1111/maps.13570) in 2020, presenting and discussing 963 measurements of PDF set orientations in 352 quartz grains in 11 granite samples from the basement unit of the M0077A drill core. Measurements were made on thin sections, using the U-stage, and have shown that almost all quartz grains are shocked (99.8% are shocked), with an average of 2.8 PDF sets per grain, which is significantly higher than previously investigated shocked quartz grains from other drill cores within the Chicxulub impact structure and also in most K–Pg boundary samples. Shock pressure estimates yield values between ~16 and 18 GPa, with a slight shock attenuation with increasing depth within the drill core, and suggest that the granitic basement of the Chicxulub peak ring could be one of the sources of the shocked quartz grains found in the most distal K–Pg boundary sites.

Chapter 6 is an article published in the journal *Meteoritics & Planetary Science* (Vol. 56, 1243–1273, doi:10.1111/maps.13705) in 2021. This paper presents and discusses petrographic and geochemical (major and trace elements, Sr–Nd isotopes) composition of the granitic basement unit of the M0077A drill core (~600 m thick from the core bottom), based on the investigation of 41 samples. The granite samples (as well as granite clasts in impact melt rock, granite breccias, and aplites) display relatively homogeneous compositions, both in term of major and trace element compositions, but are unique compared to other granite and gneiss compositions measured in other Chicxulub drill cores. The granite can be defined as a high-K, calc-alkaline granite, composed of K-feldspar, plagioclase, quartz, and minor (commonly chloritized) biotite as main mineral phases. The Sr and Nd isotopic data indicate that a minor Grenville-aged basement component may have been involved in the granite genesis. The results are consistent with previous studies, indicating that the granite intruded the Maya block of the Yucatán peninsula during the Carboniferous, in an arc setting (crustal melting related to the closure of the Rheic ocean associated with the Pangea assembly). Moreover, the Sr isotopic data, coupled with fluid-mobile trace element compositions, suggest that two distinct hydrothermal alteration events affected the granite: (1) a hydrothermal metasomatic event has occurred approximately 50 Myr after the granite formation, during the Pangea breakup, and (2) post-impact hydrothermal alteration related to the onset of a long live hydrothermal system within the Chicxulub impact structure.

Chapter 7 is an article published in the journal *Geochimica et Cosmochimica Acta* (Vol. 323, 74–101, doi:10.1016/j.gca.2022.02.006) in 2022, reporting moderately siderophile (Cr, Co, Ni), HSE concentrations, and Re–Os isotopic compositions in impact melt rock, suevite, and pre-impact lithology samples from the M0077A core, in order to constrain the degree of preservation of meteoritic material within the Chicxulub peak ring. Similar to major and other trace elements, moderately siderophile element contents of the impact melt rocks reflect primarily mixing between a felsic (granite) and a mafic (dolerite) component, with the incorporation of carbonate material in the impact melt rocks located above the granite basement unit, while no unambiguous chondritic contribution was identified. The HSE contents of the impact melt rock samples are generally similar to upper continental crust, while Re–Os isotopic compositions probably reflect a heterogeneous target rock contribution to the impact melt rocks,

and were probably affected by post-impact hydrothermal alteration, remobilizing, e.g., Re and/or Os. Moreover, the identification of an unambiguous meteoritic component within the impact melt rocks is hindered by the presence of a significant (~20–60 and up to 80–90%) mafic component (dolerite), which can yield $^{187}Os/^{188}Os$ ratios similar to a minor (~0.1%) chondritic component. Only one of the investigated impact melt rock samples was interpreted as having a possible minor (~0.01–0.05%) meteoritic component. These results are consistent with most of the previous studies from within the Chicxulub impact structure, indicating a very low and heterogeneous incorporation of a meteoritic material within the structure, while distal ejecta are enriched (up to ~5%) in meteoritic material. This may result from a combination of the assumed steeply-inclined trajectory of the Chicxulub impactor (enhanced vaporization, and incorporation of projectile material within the expansion plume), the impact velocity, and the volatile-rich target lithologies.

Chapter 8 presents and discusses additional investigations performed on M0077A drill core samples. The first section of the chapter presents observations, using optical microscopy and SEM, of shock-induced microstructures in mineral other than quartz (i.e., plagioclase, biotite, titanite, apatite, and zircon grains). Observations in plagioclase were integrated into the Pittarello et al. (2020) paper, published in *Meteoritics & Planetary Science* (Vol. 55, 1082–1092, doi:10.1111/maps.13490). The second section consists of detailed petrographic and geochemical (major and trace element) investigations of suevite samples, with a discussion proposing a reclassification of the suevite sequence of the M0077A drill core, and a possible scenario explaining the suevite unit formation. The data from this section were integrated into a publication by Kaskes et al. (2022), in *Geological Society of America Bulletin* (Vol. 134, 895–927, doi:10.1130/B36020.1). The third section of the chapter presents and discusses Sr and Nd isotopic composition of pre-impact dike lithologies, with this data being part of a paper by de Graaff et al. submitted to the journal *Lithos*. The last section of the chapter is a summary of the Yucatán peninsula basement geological history and a refined scenario for the Chicxulub impact event following the investigations made in this thesis and in associated publications following the IODP-ICDP Expedition 364 drilling.

<u>Acknowledgements</u>

I would like to thank my colleagues and friends at the Laboratoire Magmas et Volcans in Clermont Ferrand (France), especially Patrick Bachèlery, Olivier Roche, Nicolas Cluzel, and Séverine Moune, who put me on the path of science research during two Master's projects in volcanology/petrology/geochemistry and without whom I would not be where I am today. I was happy to be able to continue working with them on a publication during the completion of my PhD and I thank them for their support, advice, and interesting discussions.

I thank the European Volcanological Association (L.A.V.E.) and its members who allowed me to keep in touch with the world of volcanoes and volcanology, and also to allow me to share my knowledge on volcanoes and impact craters to the general public at the occasion of public lectures.

A huge thank you to my longtime friends and my family members, who have been present all the time, in both good and bad times. I dedicate this thesis to all of you. Thanks to Madebene, Valentin Gueugneau, Alyson Sicard, Aude Hansmetzger, Alexis Menard, Ludovic Aumeunier, Anais Igonin, Julie Noël, and Solène Daignot. We met at the University in Clermont-Ferrand, and the field works, the different trips, and the years have united us. I do not forget also Jean-Baptiste Desille and Keny Martinet, my "road trips" companions since high school (time passed now since we were in the room 112 at the boarding school!). I am also very happy to have been able to make you discover the beauties of Austria for some of you. I can't wait for the next road trips, travels, and good moments together. Finally, I would like to warmly thank my family, in particular my parents, Françoise and Michel Feignon, who have always helped and supported me in my choices and my different projects and, allowed me to live my passion and to discover a number of volcanoes around the world in the last almost two decades, my grandmother Marie Feignon and my great aunt Jacqueline Feignon. I also have a thought for Jeannot and Josette Guichard, as well as René Feignon, who are unfortunately no longer with us to see the accomplishment of this work, but who I am sure have seen it from where they are now.

Finally, I would like to end these acknowledgements with a distinct paragraph to thank Pauline Rio, who has shared my life for more than 10 years now, from the bottom of my heart. A huge huge thank you for putting up with me and to cope with the distance between us during these last few years. Thank you for all your support, your patience during the long periods and sleepless nights of work in Vienna, for being with me in the good and bad times, and for motivating me when I needed it. I owe you all my love.

<u>Abstract</u>

From April to May 2016, in IODP-ICDP Expedition 364, the peak ring of the ~200-km diameter, and ~66.05 Ma Chicxulub impact structure (Yucatán peninsula, Mexico) was drilled and led to the recovery of a continuous 829 m core (M0077A). This provided a unique opportunity to investigate the nature, properties, and composition of the peak-ring rocks and the mechanism of their formation. The core was divided into four main lithological units, from top to bottom: (1) a ~112 m-thick post-impact Paleogene, carbonate-rich sedimentary rock section (from 505.7 to 617.3 mbsf [meters below sea floor]), with the bottom of unit (1) defined as a ~75 cm-thick, fine-grained and carbonate-rich transitional unit (from 616.58 to 617.33 mbsf), marking the uppermost part of the Chicxulub peak ring; (2) a ~98 m impact melt-bearing polymict impact breccia (defined as suevite) unit (from 617.3 to 715.6 mbsf); (3) a ~31 m thick impact melt rock sequence (from 715.6 to 747.0 mbsf), also termed as the upper impact melt rock (UIM) unit; and (4) a crystalline basement rock unit (from 747.0 to 1334.7 mbsf) mainly made of shocked, fractured, and deformed, coarse-grained granite, which is cross-cut by different types of pre-impact volcanic dikes (dolerite, felsite, and dacite) and intercalations of impact melt rock-bearing units (LIMB). This thesis presents detailed investigations on the petrography, geochemistry, and shock metamorphism of 219 samples from the Chicxulub peak ring, in order to characterize suevite, impact melt rock, granitic basement, and pre-impact dike or clast (dolerite, amphibolite, felsite, and dacite) lithologies. The data obtained give important insights on how the peak ring rocks emplaced, refining the scenario of the impact event, the nature of the Yucatán peninsula basement, and the fate of the Chicxulub impactor.

The ~600 m-thick granitic basement is characterized as a high-K, calc-alkaline and metaluminous granite, with K-feldspar, plagioclase, quartz, and biotite (commonly chloritized) as main mineral components. The major and trace element compositions of granite samples are relatively homogenous throughout the drill core, which is consistent with previous studies showing that the granite intruded the Maya block of the Yucatán peninsula in a volcanic arc context (during the Carboniferous). The Sr–Nd isotope data indicate that a fluid metasomatic event occurred ~50 Myr after granite formation (possibly related to the first stages of Pangea breakup), and that a minor Grenville-aged basement component has been involved in the granite source. In addition, the granite was further altered by the onset of a long-lived post-impact hydrothermal system, with fluid circulation enhanced by the presence of fractures, preferentially affecting fluid-mobile element contents. Universal stage investigations of shocked quartz grains within the granite unit indicate a relatively high shock level, with the presence of multiple planar fracture (PF) sets, associated feather features (FFs), and an average of 2.8 planar deformation feature (PDF) sets per grain, which is higher than in all previously investigated drill cores from Chicxulub and most K–Pg boundary sites for which detailed reports are available. Based on PDF orientations, shock pressures experienced by the granite were estimated between ~16 and ~18 GPa, with a slight shock attenuation with increasing depth within the core. Further optical microscope and scanning electron microscope observations have shown the presence of shock-induced planar microstructures in feldspar, apatite, and

titanite, while fracturing was observed in zircon grains. Additionally, kinkbanding is commonly observed in micas.

The impact melt rocks are distinct between the UIM and the LIMB. The UIM is mainly composed of two intermingled, and chemically distinct, impact melt rock phases, i.e., a SiO_2-rich and trachyandesitic, clast-poor black impact melt, and a CaO-rich green phase, composed mainly of secondary clay minerals and sparitic calcite, while the LIMB is similar to the black impact melt rock (but is clast-poor to clast-rich), with an absence of carbonate material. Major and trace element compositions of the impact melt rocks primarily reflect mixing between mafic (dolerite) and felsic (granite) components, with the incorporation of carbonate material in the UIM unit. Measurements of highly siderophile element contents and Re–Os isotopic compositions did not reveal any unambiguous or detectable meteoritic component, excepted one UIM sample having a possible (~0.01–0.05%) chondritic component. This is similar to most of the previous studies that have shown that impactites within the Chicxulub impact structure contain less than 0.1% of a meteoritic contribution. This may be explained by the presence of a significant mafic component (dolerite) within the impact melt rocks, and post-impact hydrothermal alteration processes that have probably remobilized Re and Os in impact melt rocks and pre-impact lithologies. However, the low amount of meteoritic material preserved within impactites of the Chicxulub impact structure is consistent with the assumed steeply-inclined trajectory of the Chicxulub impactor, leading to enhanced vaporization, and incorporation of projectile material within the expansion plume (up to 5% of meteoritic material identified in some distal K–Pg boundary sites), the impact velocity, and the volatile-rich target lithologies.

The suevite unit is mainly made of angular to sub-rounded clasts in a fine-grained, micritic carbonate matrix, with a general trend of increasing clast size with increasing depth within the core (from <1 cm at 620 mbsf to more than ~10 cm at 710–720 mbsf). Clast types are mainly altered vitric (glassy) melts, carbonates, impact melt rocks, shocked and unshocked minerals (quartz, and feldspar, generally derived from the crystalline basement), and pre-impact lithologies (e.g., granite, gneiss, dolerite, amphibolite). Fossils (mainly foraminifera) are also preserved within the matrix of the suevite unit. Quartz grains are shocked (PFs and PDFs), and some are toasted. Ballen silica is also present. In general, major element contents of the suevite show a decrease in CaO and an increase in SiO_2 contents with increasing depth, due to the felsic basement clasts being more abundant in the lower part of the suevite over carbonates than in the upper part of the core. The suevite sequence was divided into three subunits, from top to bottom: (a) ~3.5 m-thick bedded suevite, (b) ~89 m-thick graded suevite, and (c) ~5.6 m-thick non-graded suevite. A possible scenario of the suevite sequence emplacement suggests that debris-poor ocean water entered the Chicxulub crater from a gap in the N-NE outer rim and reached the peak ring site ~30 minutes after the impact, interacting with the hot impact melt rock, and causing quench fragmentation (phreatomagmatic-like processes), leading to non-graded suevite emplacement. The following hours, the impact structure was flooded by debris-rich ocean resurge, leading to the deposition of the graded suevite. With the ocean resurge energy decreasing, seiche waves then dominated the deposition processes and formed the bedded suevite. Finally, less than twenty years after the impact, slow deposition of atmospheric fallout of very fine dust enriched in meteoritic material (~0.1% of chondritic component and positive iridium anomaly) lead to the formation of the transitional unit.

Zusammenfassung

Von April bis Mai 2016 wurde in der IODP-ICDP-Expedition 364 der innere Ring der Chicxulub-Einschlagstruktur (Halbinsel Yucatán, Mexiko, Durchmesser ca. 200 km; Alter 66.05 Ma) erbohrt und ein durchgehender, 829-m-langer Bohrkern (M0077A) gewonnen. Dies bot die Gelegenheit, Natur, Eigenschaften, Zusammensetzung und Bildungsmechanismus des inneren Rings zu untersuchen. Der Kern wurde, von oben nach unten, in vier lithologische Haupteinheiten unterteilt: (1) ein ~112 m starker karbonatreicher Sedimentgesteinsabschnitt aus dem Paläogen (direkt nach dem Einschlag, von 505.7 bis 617.3 mbsf [Meter unter dem Meeresboden]), wobei der untere Teil der Einheit (1) als ~75 cm dicke, feinkörnige und karbonatreiche Übergangseinheit (von 616.58 bis 617.33 mbsf) definiert ist, die den obersten Teil des inneren Ringes von Chicxulub markiert; (2) eine ~98 m mächtige, polymiktische Impaktbrekzie (Suevit), mit etwas Impaktschmelze (von 617.3 bis 715.6 mbsf); (3) eine ~31 m mächtige Impaktschmelzgestein-Sequenz (von 715.6 bis 747.0 mbsf), die auch als obere Impaktschmelzgestein-Einheit (UIM) bezeichnet wird; und (4) eine kristalline Grundgebirgseinheit (von 747,0 bis 1334. 7 mbsf), die hauptsächlich aus geschocktem, zerklüftetem und deformiertem, grobkörnigem Granit besteht, der von vulkanischen Gängen (Dolerit, Felssit und Dazit; alle-prä-Impakt) und Einlagerungen von Einschlagschmelzgesteinen (LIMB) durchzogen ist. Diese Arbeit enthält detaillierte Untersuchungen zu Petrographie, Geochemie und Schockmetamorphose von 219 Proben aus dem Bohrkern, zur Charakterisierung der diversen Grund- und Impaktgesteine. Die Daten liefern wichtige Erkenntnisse über die Bildung des inneren Ringes, die Beschaffenheit des Grundgebirges der Halbinsel Yucatán und das Schicksal des Chicxulub-Impaktors.

Das ca. 600 m mächtige Grundgebirge ist ein Granit mit K-Feldspat, Plagioklas, Quarz und Biotit (häufig chloritiert). Die homogene Verteilung der Haupt- und Spurenelemente der Granitproben stimmt mit früheren Studien überein, die zeigen, dass der Granit im Maya-Block von Yucatán im Kontext eines Vulkanbogens (während des Karbon) intrudiert ist. Die Sr-Nd-Isotopendaten deuten darauf hin, dass ~50 Myr nach der Granitbildung ein metasomatisches Ereignis stattgefunden hat (möglicherweise in den ersten Phasen des Auseinanderbrechens von Pangea) und dass eine geringe Grenville-Grundgebirgskomponente beteiligt war. Darüber hinaus wurde der Granit durch den Beginn eines impaktinduzierten langlebigen hydrothermalen Systems verändert, wobei die Flüssigkeitszirkulation durch das Vorhandensein von Brüchen verstärkt wurde. Untersuchungen von geschockten Quarzkörnern des Granits mit Hilfe desUniversaldrehtisches deuten auf ein hohes Schockniveau hin, mit dem Vorhandensein mehrerer planarer Brüche (PF), oft mit sogenannten „feather –features" (FF) und durchschnittlich 2.8 planaren Deformationsstrukturen (PDF) pro Korn, was höher ist als in allen zuvor untersuchten Bohrkernen von Chicxulub und den meisten K-Pg-Grenzen, an denen geschockter Quarz vorhanden ist. Daraus wurden die Schockdrücke in der Graniteinheit auf ~16 bis ~18 GPa geschätzt, wobei mit zunehmender Tiefe im Kern eine leichte Schockabschwächung zu verzeichnen ist. Weitere lichtmikroskopische und rasterelektronenmikroskopische Beobachtungen haben schockinduzierte planare

Mikrostrukturen in Feldspat, Apatit und Titanit gezeigt, während in Zirkonkörnern Brüche beobachtet wurden. Außerdem sind in Glimmern häufig Knicke vorhanden.

Bei den Impaktschmelzgesteine gibt es obere (UIM) uns untere (LIMB) Enheiten. Die Zusammensetzung der Haupt- und Spurenelemente in den Impaktschmelzgesteinen spiegelt in erster Linie die Vermischung zwischen mafischen (Dolerit) und felsischen (Granit) Komponenten wider. Die Gehalte an hoch siderophilen Elementen und die Re-Os-Isotopenzusammensetzung haben keine eindeutige oder nachweisbare meteoritische Komponente ergeben, mit Ausnahme einer UIM-Probe, die möglicherweise ~0.01-0.05 % einer chondritischen Komponente enthält. Dies lässt sich durch das Vorhandensein einer bedeutenden mafischen Komponente (Dolerit) in der Impaktschmelze und die hydrothermalen Alterationsprozesse nach dem Impakt erklären, die wahrscheinlich Re und Os in der Impaktschmelze und den Lithologien vor dem Impakt remobilisiert haben.

Die Suevit-Einheit besteht hauptsächlich aus kantigen bis unrunden Klasten in einer feinkörnigen, mikritischen Karbonatmatrix. Bei den Klasten handelt es sich hauptsächlich um alterierte glasartige Schmelzen, Karbonate, Impaktschmelzen, geschockte und nicht geschockte Minerale (Quarz und Feldspat, die im Allgemeinen aus dem kristallinen Grundgebirge stammen) und Lithologien aus der Zeit vor dem Impakt (z. B. Granit, Gneis, Dolerit, Amphibolit). Quarzkörner sind geschockt. Im Allgemeinen zeigen die Hauptelementgehalte des Suevits eine Abnahme des CaO- und eine Zunahme des SiO_2-Gehalts mit zunehmender Tiefe, was darauf zurückzuführen ist, dass die felsischen Grundgebirgsschollen im unteren Teil des Suevits über den Karbonaten häufiger vorkommen als im oberen Teil. Die Suevitsequenz wurde auf der Grundlage petrographischer und geochemischer Daten von oben nach unten in drei Untereinheiten unterteilt: (a) ~3.5 m dicker geschichteter Suevit, (b) ~89 m dicker abgestufter Suevit und (c) ~5.6 m dicker nicht abgestufter Suevit. Ein mögliches Szenario für die Einlagerung der Suevitsequenz deutet darauf hin, dass trümmerarmes Ozeanwasser aus einer Lücke im N-NE-Außenrand in den Chicxulub-Krater eindrang und ~30 Minuten nach dem Einschlag den inneren Ring erreichte, wo es durch Wechselwirkung mit dem heißen Einschlagschmelzgestein zu phreatomagmatischen Prozessen kam. In den darauffolgenden Stunden wurde die Einschlagstruktur von trümmerreichem Ozean überflutet, was zur Ablagerung des gradierten Suevits führte. Mit abnehmender Energie der Meeresaufwallung dominierten dann Seichenwellen die Ablagerungsprozesse und bildeten den geschichteten Suevit. Schließlich, weniger als zwanzig Jahre nach dem Einschlag, führte die langsame Ablagerung von atmosphärischem Fallout aus sehr feinem Staub, der mit meteoritischem Material angereichert war (~0.1 % chondritische Komponente und positive Iridiumanomalie), zur Bildung der Übergangseinheit.

Table of contents

CHAPTER 1: Impact cratering process

1.1. Introduction

Impact cratering is now recognized as an important and ubiquitous geological process in the Solar System, affecting all planetary objects, and having played an important role in the formation and evolution of planets and satellites. With the notable exception of Earth, meteorite impact structures are one of the most common geological landforms on all the solid planetary bodies, including rocky, terrestrial planets, rocky and icy moons (with just few exceptions) of the giant planets (Jupiter, Saturn, Uranus, and Neptune), asteroids, and comets. A unique feature of the impact cratering process is to bring material from depth (back) to the surface in the form of impact ejecta deposits and, whenever the case, central uplifts, providing insights into the subsurface composition of planetary bodies (Osinski and Pierazzo, 2012).

The more common interest for the study of impact cratering did not start until the 1960s and 1970s, with the Apollo landings on the Moon and the space probes launched to explore the Solar System. However, serious discussions of the importance of hypervelocity impacts as a geological process of importance for Earth evolution began only in the 1980s with the discovery of evidence for a large impact event in sediments from the Cretaceous-Paleogene (K-Pg) boundary 66 Myr ago that was suggested as the cause for the mass extinction event that occurred during this period (Alvarez et al., 1980). The impact site was subsequently identified in 1991 (e.g., Hildebrand et al., 1991): the ca. 200-km diameter (e.g., Gulick et al., 2013) Chicxulub impact structure, buried beneath approximately 1 km of sediments in the Yucatán peninsula, Mexico (Hildebrand et al., 1991). A detailed description and geological history of the Chicxulub impact structure is provided in Chapter 3. Additionally, the impact of fragments of the comet Shoemaker-Levy 9 on Jupiter in July 1994 and, more recently, the explosion in the Earth atmosphere of a ca. 20-m-sized meteoroid near Chelyabinsk (Russia) on 15th February 2013, damaging buildings and injuring more than one thousand people (Popova et al., 2013), were reminders that impact events are a process still occurring to the present day, and even a threat we are facing. There are significative differences between impact cratering and other geological processes (e.g., volcanism, crustal metamorphism, subduction, etc.) mainly due to: (1) the extreme pressure and temperature conditions, (2) the high strain rates involved (~10^4 to 10^6 s^{-1} for impact versus 10^{-6} to 10^{-3} s^{-1} for tectonic and metamorphic processes), (3) the high energy released at a single point on Earth's surface, and (4) the timescale which is virtually instantaneous (e.g., seconds to minutes) compared to other geological processes that require generally several thousands to millions of years, only volcanic eruptions having a nearly comparable timescale, going from hours to years (e.g., French, 1998; Kenkmann et al., 2014).

Unlike most bodies in the Solar System, Earth's surface is constantly renewed by active geological processes such as plate tectonics, volcanic eruptions, and erosion. In addition, the deposition of sediments, and ocean and forest cover, makes the identification of impact structures even more difficult. Currently, about 200 impact structures are definitely recognized on Earth (see Fig. 1.1, modified from Ferrière, 2021; See also Schmieder and Kring, 2020; Kenkmann et al., 2021; Osinski et al., 2022), with a few 'new' impact structures being

confirmed each year, but many other ones have not yet been discovered (or have been destroyed by erosion). The recognition and confirmation of a 'new' meteorite impact structure need to be supported by the presence of unambiguous shock metamorphic features and/or traces of extraterrestrial matter (e.g., French and Koeberl, 2010; and see Chapter 2 for details).
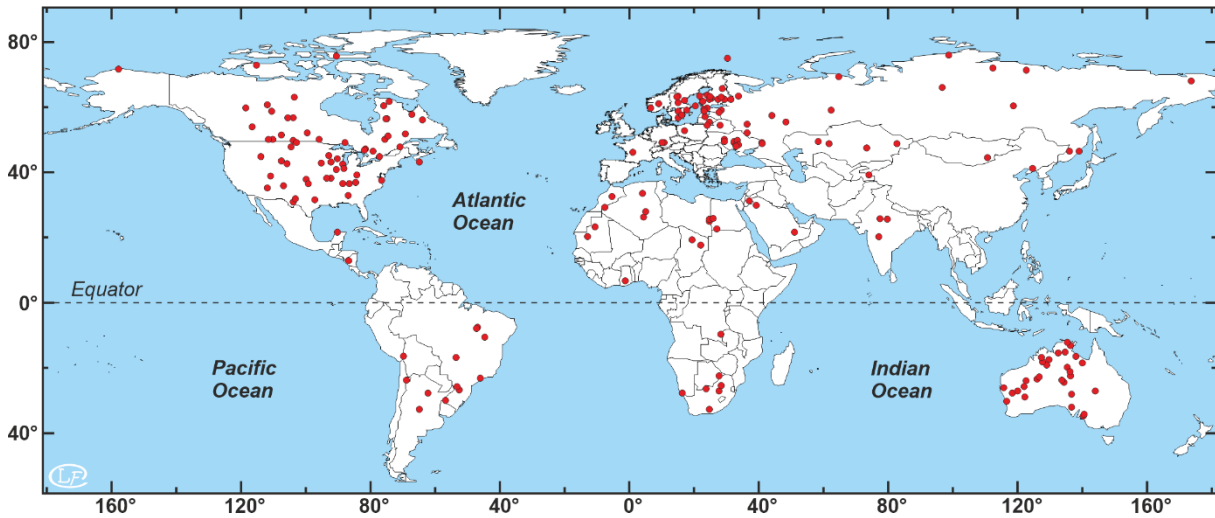
Figure 1.1. *Earth map showing the distribution of the 200 confirmed meteorite impact structures. Modified from Ferrière (2021, http://www.meteorimpactonearth.com/meteorite.html), and references therein, with data modified from the Earth Impact Database (2021).*

However, because of the continuous crustal recycling and alteration processes, young and large terrestrial impact structures are preferentially recorded. Also, some countries of the world are not well investigated because of ongoing armed conflicts and/or difficult access (Ferrière, 2008). As of today, the oldest impact structures known on Earth with a precise dating are the ~70 km-diameter Yarrabubba impact structure located in Western Australia, with an age of 2.229 ± 0.005 Ga (Erickson et al., 2020), the 2.023 ± 0.004 Ga, >250 km diameter Vredefort Dome in South Africa (Kamo et al., 1996), and the 1.850 ± 0.001 Ga, >200 km Sudbury structure in Canada (Krogh et al., 1984). Other proposed Paleoproterozoic-age impact structures have either poorly constrained ages, such as the ~16 km-diameter Suavjärvi structure (Russia) with an estimated stratigraphic age of ~2.4 Ga (Mashchak and Naumov, 1996) and the Dhala structure (India) with a formation age ranging from ~1.7 to 2.5 Ga (Pati et al., 2008), or are not definitely confirmed with unambiguous evidence as impact structure (e.g., Reimold et al., 2014). On the other hand, only "small" impact craters (i.e., some of which cannot be considered as hypervelocity impact craters due to the lack of evidence for shock metamorphism, see also Osinski et al., 2022, and references therein) formed relatively recently are known, such as the Wabar craters (Saudi Arabia), ~110 m-diameter (for the largest crater) and supposedly formed in AD 1714 ± 38, according to luminescence dating (Prescott et al., 2004), with a possible formation on 1st September, 1704, according to two poems (Basurah, 2003; Gnos et al., 2013); the Sikhote Alin craters (Russia), ~27 m-diameter (for the largest crater) formed in 1947 (Earth Impact Database, 2021) and the ~15 m impact crater of Carancas (Peru), formed on September 15th 2007 (Kenkmann et al., 2009), which is, until today, the youngest recorded impact crater. However, no hypervelocity impact events, leading to the formation of large impact craters, were

recorded in historical times on Earth (Osinski et al., 2022). Thus, only numerical modeling, explosion experiments, and detailed investigations of impact structures on Earth and on other planetary surfaces can be used to understand the impact cratering processes. The different levels of erosion from an impact structure to another allow in-depth view of the whole structure. In addition, samples from several impact structures were recovered during drilling campaigns.

1.2. Impact crater morphologies

The study of a large number of impact structures on the Moon, as well as on other planetary rocky bodies, i.e., Mercury, Venus, and Mars, has permitted to characterize different morphological aspects and types of impact craters. The impact crater morphologies vary as a function of size. Two main impact structure types are defined: simple and complex craters (Melosh, 1989; French, 1998). The latter category is generally further divided into central peak, peak ring, and multi-ring basins with increasing crater size (see, e.g., Kenkmann et al., 2014; Kenkmann 2021; and references therein). Multi-ring basins have also been considered as a third distinct category from simple and complex crater morphologies (see, e.g., French, 1998). This classification is true for all bodies in the Solar System. However, the transition between simple and complex crater occurs at different crater diameters on different planetary bodies, as the threshold is depending mainly on the gravitational attraction (i.e., decreasing threshold with increasing gravitational acceleration) and also on the target rock nature (French, 1998). The following subsections are describing the different impact structure morphologies in more detail.

1.2.1. Simple craters

Simple craters are the most abundant impact structures in the Solar System. They consist of a bowl-shaped depression. On Earth, the maximal diameter of simple impact structures ranges from 2 to 4 km, depending on the nature of the target rocks, i.e., the transition between simple and complex crater occurs at lower diameter in sedimentary target rocks (from ~2 km) than in non-porous crystalline rocks (from ~4 km) (Grieve, 1987). Simple craters, when not too eroded, have uplifted rim and have their floor generally filled with impact breccia, also called "allochthonous breccia lens" or "crater-fill breccia" that comprises relatively low shocked target material, possibly mixed with impact melt-bearing lithologies (Shoemaker, 1960; Grieve et al., 1977; French, 1998; Dence, 2017). The crater depth, defined as the distance between crater rim and crater floor, is ~1/3 to ~1/5 of the crater diameter, depending on the filling of the cavity with impact breccia (Grieve and Pilkington, 1996; Kenkmann et al., 2014), while rim height relative to the target rock level is about four percent of the crater diameter (Melosh, 1989). The 1.2-km diameter, ~49–50 ka Barringer Crater (or Meteor Crater), located in Arizona, USA (Sutton, 1985; Phillips et al., 1991), represents the best example of a relatively young, well-preserved and documented simple impact crater on Earth (Fig. 1.2).

Figure 1.2. *Two examples of well-preserved, terrestrial, simple impact structures. A) Aerial view of the 1.2-km-diameter Barringer Crater (or Meteor Crater), located in Arizona (USA). This represents the typical example of a small, bowl-shaped, simple impact crater, with near-circular shape, uplifted rim, and hummocky deposits of ejecta beyond the rim. The crater formed ca. 50 ka following the impact of a ~50 m iron meteorite on Paleozoic-Mesozoic sedimentary rocks of the Arizona's Colorado Plateau. The impact origin of the crater was confirmed by the presence of preserved iron meteorite fragments and shock metamorphic features in its rocks (see French, 1998). The north is on the upper part of the photograph. (Author: Steve Jurvetson, Creative Commons license, https://commons.wikimedia.org/wiki/File:Meteor_Crater_%28crop-tight%29.jpg). B) The New Quebec (or Pingualuit) crater, located in Quebec, Canada. The impact crater formed around 1.4 Ma and has a diameter of 3.4 km (Grieve et al., 1989). The target material consists of old, strongly deformed gneisses of the Precambrian shield. Evidence of shock metamorphism was discovered in minerals from gneiss samples recovered within the crater. The impact crater was later filled with a 250-meter-deep lake. North is on the bottom of the photograph (Author: Lkovac, Creative Commons license, https://www.britannica.com/place/Ungava-Quebec-Crater#/media/1/614437/165615).*

1.2.2. Complex craters

1.2.2.1. Central uplift and peak ring crater

As noted above, terrestrial complex craters form at diameters larger than 2 or 4 km, depending on the target rock nature (Grieve, 1987; French, 1998). On the Moon, the transition occurs at diameters between 15 and 20 km (e.g., Howard, 1974). Complex craters display different and more complicated forms than simple craters. These craters are typically characterized by a central uplift, a flat floor, and a faulted rim (Fig. 1.3). These features form following gravitational adjustments during the modification stage of impact crater formation (see section 1.3.3.2). Complex crater depth is lower than for simple crater, being approximately 1/10 to 1/20 of the crater diameter (Melosh, 1989). The central uplift was determined to be approximately 1/10 of the crater rim diameter on terrestrial impact structures (see also, Melosh, 1989; Grieve and Pilkington, 1996). An important and unique feature of complex crater formation is that material from depth is brought to the surface. This provides important information on the deep crust composition (and structure) both on Earth and other planetary bodies (Osinski and Pierazzo, 2012). Similar to simple craters, complex craters are filled by impact melt rocks, brecciated material containing both unshocked and shocked rock and mineral clasts, and material slumped into the crater from the walls and crater rim.
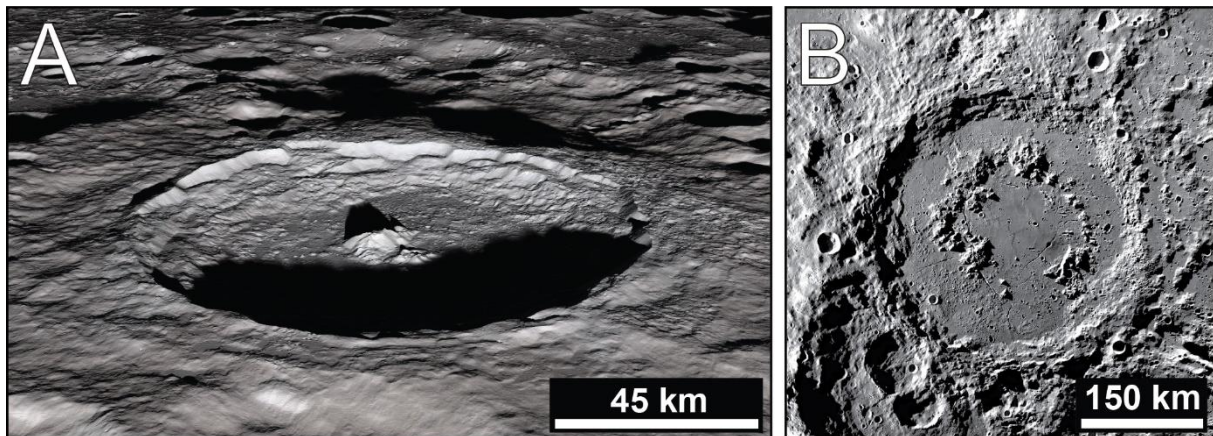
Figure 1.3. *Examples of complex craters on the Moon with well-preserved central peak (A) and peak ring (B). Slumped and faulted terraces are also visible on the rims of these impact structures. A) The 86-km-diameter Tycho crater, which possess a central peak (https://www.flickr.com/photos/gsfc/26560950357). B) The Schrödinger crater, 316-km-diameter, displays a peak ring above its central flat floor (https://commons.wikimedia.org/wiki/File:Schr%C3%B6dinger_(LRO)_500_km.png; NASA, Images acquired by the Lunar Reconnaissance Orbiter).*

With increasing size of the impact crater, the central uplift evolves from a central peak to a peak ring, i.e., a well-developed ring of peaks but with no central peak (Stöffler et al., 2006). On Earth, post-impact processes, such as erosion and tectonics, modify the initial morphology of the impact structure, thus, it is difficult to distinguish between a central peak and a peak ring, even for relatively young complex impact structures such as Haughton, Canada, or the Ries, Germany (Grieve and Therriault, 2004). Consequently, peak ring craters are known mainly from planetary bodies other than Earth, preventing detailed study of their main features. Typical examples of peak ring craters in the Solar System are the 316-km-diameter Schrödinger

crater on the Moon (Fig. 1.3), or the 290-km-diameter Rachmaninoff basin on Mercury. The complex crater diameter threshold corresponding to the onset of a peak ring instead of a central peak cannot be estimated using terrestrial data. Observations and calculations performed by Baker et al. (2011) for the other terrestrial planets yield peak ring crater onset diameters of 227 km (Moon), 116 km (Mercury), 56 km (Mars), and 33 km (Venus). As Venus has a relatively similar, albeit lower gravitational acceleration (8.87 m/s^{-2}) compared to Earth (9.81 m/s^{-2}), a similar, or slightly lower, diameter threshold (i.e., ~30 km) can be assumed for the onset of a peak ring crater as on Earth. The Chicxulub (Mexico) structure is the only known example of a terrestrial impact structure with an unequivocal, well-preserved peak ring due to its burial by sedimentary deposits that prevented erosion (e.g., Morgan et al., 1997; Gulick et al., 2013, and references therein).

1.2.2.2. Multi-ring impact basins

The multi-ring basins correspond to the largest impact structures observed in the Solar System; their main characteristic is to be surrounded by one or more concentric fractures or scarps. Two types of multi-ring impact basins were described based on their morphology (e.g., Melosh and McKinnon, 1978). The first type is characterized by several inward-facing scarps with gentle outward slopes. A classic example is the 930-km-diameter Orientale basin on the Moon. The second type shows tens to hundreds of spaced rings forming a graben surrounding a central, flat basin, such as Valhalla (~3,000 km diameter) on Jupiter's moon Callisto. So far, multi-ring impact basins were not unequivocally identified on terrestrial planets (Melosh, 1989). As this work is focused on a terrestrial impact structure, multi-ring impact basins will not be discussed further in this chapter.

1.3. Impact crater formation

Impact cratering is a process occurring on a very short timescale, from few seconds to some minutes, depending on the magnitude of the impact event (e.g., Melosh, 1989; Ivanov and Artemieva, 2002). The projectile, either an asteroid or a comet, strikes the Earth's surface at hypervelocity, from ~10 to ~72 km/s (e.g., Melosh, 1989). Therefore, in the case of hypervelocity impact, the projectile must be large enough (typically >20 m for an iron object and >50 m for a stony body) to pass through the atmosphere with little or no deceleration (French, 1998). Smaller projectiles generally disintegrate in the atmosphere, with only some fragments reaching the surface at relatively low speed. These fragments, which may excavate and form small 'penetration craters', not much larger than the rock itself, are called meteorites (French, 1998; Osinski and Pierazzo, 2012).

Formation of impact craters is generally divided into three distinct stages: (1) contact and compression, (2) excavation, and (3) modification (for a detailed review, see, e.g., Gault et al., 1968; Grieve, 1987; Melosh, 1989; French, 1998; Osinski and Pierazzo, 2012; Kenkmann et al., 2014; Ivanov, 2020). The post-impact chemical and hydrothermal alteration is sometimes considered as a separate, final stage of the cratering process (Kieffer and Simonds, 1980).

1.3.1. Contact and compression stage

The contact and compression stage of an impact event starts when the projectile contacts the surface of the target. At that moment, the projectile is stopped and, if the target is solid, does not penetrate into the ground for more than one to two times its diameter (see Fig. 1.4; Kieffer and Simonds, 1980; O'Keefe and Ahrens, 1982). The kinetic energy of the projectile is then transferred to the target rocks in the form of shock waves (compressing and accelerating the material) travelling at speeds faster than sound (Melosh, 1989). The resulting pressures experienced by the projectile and target material at the point of contact are on the order of hundreds of gigapascals (GPa) and the duration of the 'contact' is between ~0.05 and ~0.1 s (Ivanov, 2020). These shock waves are also simultaneously reflected and propagate into the projectile itself. When the reflected shock waves reach the upper surface of the projectile, they are reflected back into the projectile in the form of rarefaction or tensional waves (Ahrens and O'Keefe, 1972). Therefore, the passage of a rarefaction wave through the projectile leads to a release, or unloading, from high shock pressures, resulting in vaporization/melting of most (if not all) of the projectile material (Gault et al., 1968; Melosh, 1989). In rare cases (usually at small craters), fragments of the projectile may be recovered within or around the impact crater. The propagation of the shock wave and subsequent rarefaction wave through the target rocks also leads to vaporization and melting of a significant volume of target material, especially close to the point of impact. With increasing distance in the target rocks from the impact point, shock waves decrease in energy density, causing shock metamorphism in the autochthonous rocks, i.e., basement rocks (Fig. 1.4; Ahrens and O'Keefe, 1972; Grieve et al., 1977). The study of shock effects in rock-forming minerals (e.g., transformations, deformations, spatial distribution) can be used to estimate shock pressures and, thus, the rate of shock attenuation within the target rock (for details, see Chapter 5). In the case of large impact structures, shock pressures of ~10 to ~50 GPa can be reached even at several kilometers' depth within the basement rocks (Ferrière, 2008). At greater distances from the impact point, shock waves have lost so much energy that they become seismic or elastic waves, with pressures of ~1-2 GPa, which are not enough to form any diagnostic shock metamorphic features, but instead rock brecciation and faulting (Kieffer and Simonds 1980; French, 1998).

The end of the contact and compression stage occurs after the projectile has completely unloaded from high pressure, with, as a consequence, the transfer of most of the projectile kinetic energy to the target. This stage is extremely brief, ending within no more than a second, even for large impact events (e.g., Melosh, 1989). The impact crater forms during the next stage: the excavation stage.

1.3.2. Excavation stage

The excavation stage occurs in the continuity of the contact and compression stage. As the projectile was already unloaded from high shock pressures, vaporized and/or melted during the contact and compression stage, it plays no role in the excavation of the crater. During this stage, the impact crater is opened up by complex interactions between the expanding shock waves, and subsequent rarefaction waves, with, as a main consequence, an acceleration of the target material (Fig. 1.4; Melosh, 1989).
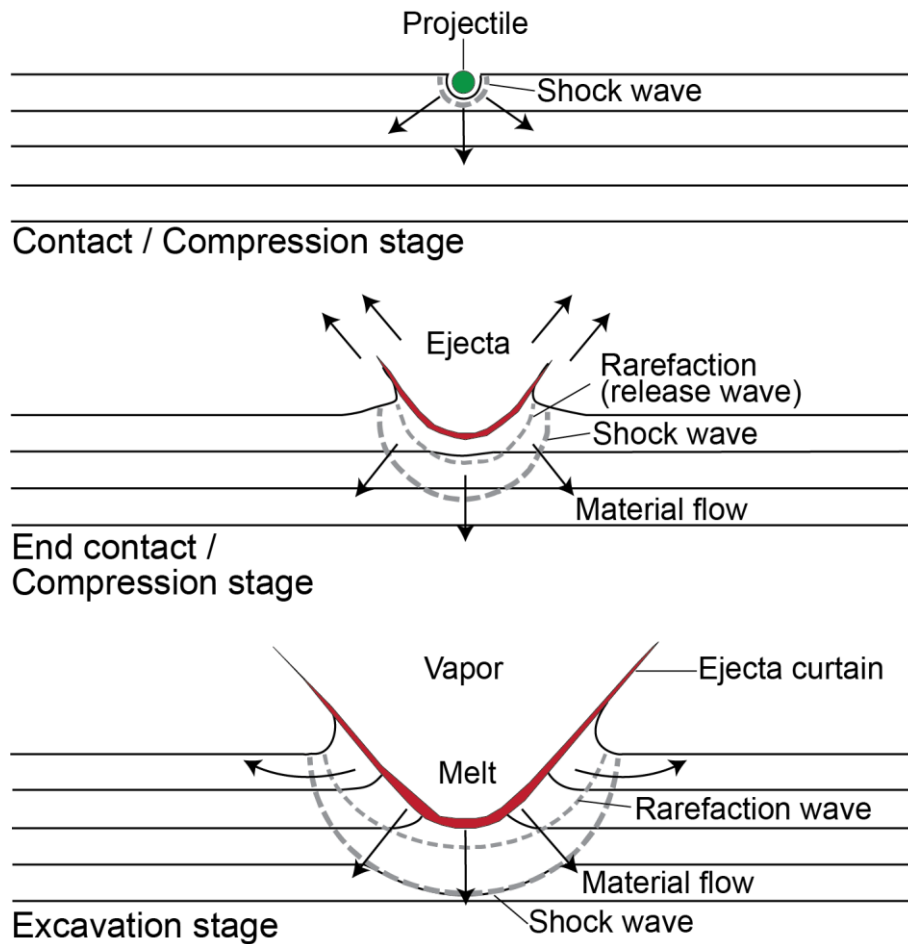
Figure 1.4. *Cross-section diagrams showing the two first stages of an impact crater formation, i.e., the contact/compression stage, and the excavation stage. The stages depicted here are almost identical for both simple and complex impact craters. See text for details of impact crater formation (modified after French, 1998; Ferrière, 2021).*

When the tensional stress exceeds the mechanical strength of the target rocks, the excavation starts, forming a so-called 'transient cavity' (Dence, 1968; Grieve and Cintala, 1982). Target rocks are fractured and shattered, and displaced in various directions, i.e., mainly out and upwards in the upper, 'excavated zone', and mainly outwards and down in the lower part of the transient cavity, also called the 'displaced zone' (Fig. 1.5; Ferrière, 2008; Osinski and Pierazzo, 2012). In the upper 'excavated zone', the material is ejected ballistically beyond the transient cavity rim, forming an impact ejecta blanket (Fig. 1.5; Oberbeck, 1975). Generally, the material within the 'displaced zone' remains within the transient cavity (Stöffler et al., 1975), forming crater-fill impactites (Fig. 1.5, and, see Chapter 2 for an overview of the different types of impactites). The excavation of the transient cavity stops when shock and rarefaction waves have lost enough energy to not be able to eject material beyond the transient cavity rim. The duration of the excavation stage is comprised from few seconds to few minutes, depending on the crater size, e.g., ~6 seconds to excavate a 1-km-diameter crater, and roughly one minute and thirty seconds for a 200-km-diameter crater (Melosh, 1989; French, 1998).

1.3.3. Modification stage

1.3.3.1. Simple craters

When the transient cavity reaches its maximum size and stops its growth, the modification stage starts. The extent of the modifications experienced by the transient cavity is mainly a function of the transient cavity size, the properties of the target rock lithologies, and also the gravitational acceleration of the impacted body (Melosh and Ivanov, 1999). In the case of small, simple craters (i.e., <2–4 km-diameter on Earth), only minor modification occurs to the bowl-shaped transient cavity, such as debris flows sliding down the inner rim, and filling the transient cavity, as well as redeposition of falling ejecta (Fig. 1.5; French, 1998). Consequently, the final crater diameter may increase by as much as 20% (Melosh, 1989).

1.3.3.2. Complex craters

In contrast to simple craters, the modifications are much more significant in the case of large, complex craters. Above the diameter of 2–4 km for terrestrial impact structures, the transient cavity becomes unstable and undergoes modification driven by gravitational forces, forming a subsequent complex impact crater (Dence, 1965). Two processes occur during the modification stage of a complex crater: the gravitational collapse of the inner rim, and the uplift of the transient cavity floor, leading to the formation of a central uplift (Fig. 1.5). The steep walls of the transient cavity collapse under gravitational forces, implying inward and downward movement of large (from ~100 m to kilometer-sized) fault-bounded blocks that form characteristic terraces (Osinski and Pierazzo, 2012). Also, some processes occur in order to reduce (at least temporarily) the strength of rocks (weakening) during complex crater formation (Melosh and Ivanov, 1999). In the case of moderately sized complex impact structures (e.g., the 10.5-km diameter Bosumtwi structure, Ghana), it is suggested that the central uplift develops by displacements along faults as a brittle component (Ferrière et al., 2008). For larger impact structures, complex crater formation is generally successfully reproduced using acoustic fluidization models, with the rocks behaving as a Coulomb material (see also Melosh, 1979; Melosh, 1989; Melosh and Ivanov, 1999). Recent observations and numerical modelling at the Chicxulub impact structure supports the role of acoustic fluidization of rocks, particularly during the earliest phases of transient cavity collapse (see also Riller et al., 2018, Rae et al., 2019, Chapter 3). According to Ivanov (2020), terrestrial impact craters with diameters from 10 to 100 km are formed from within 60 to 200 s, respectively.
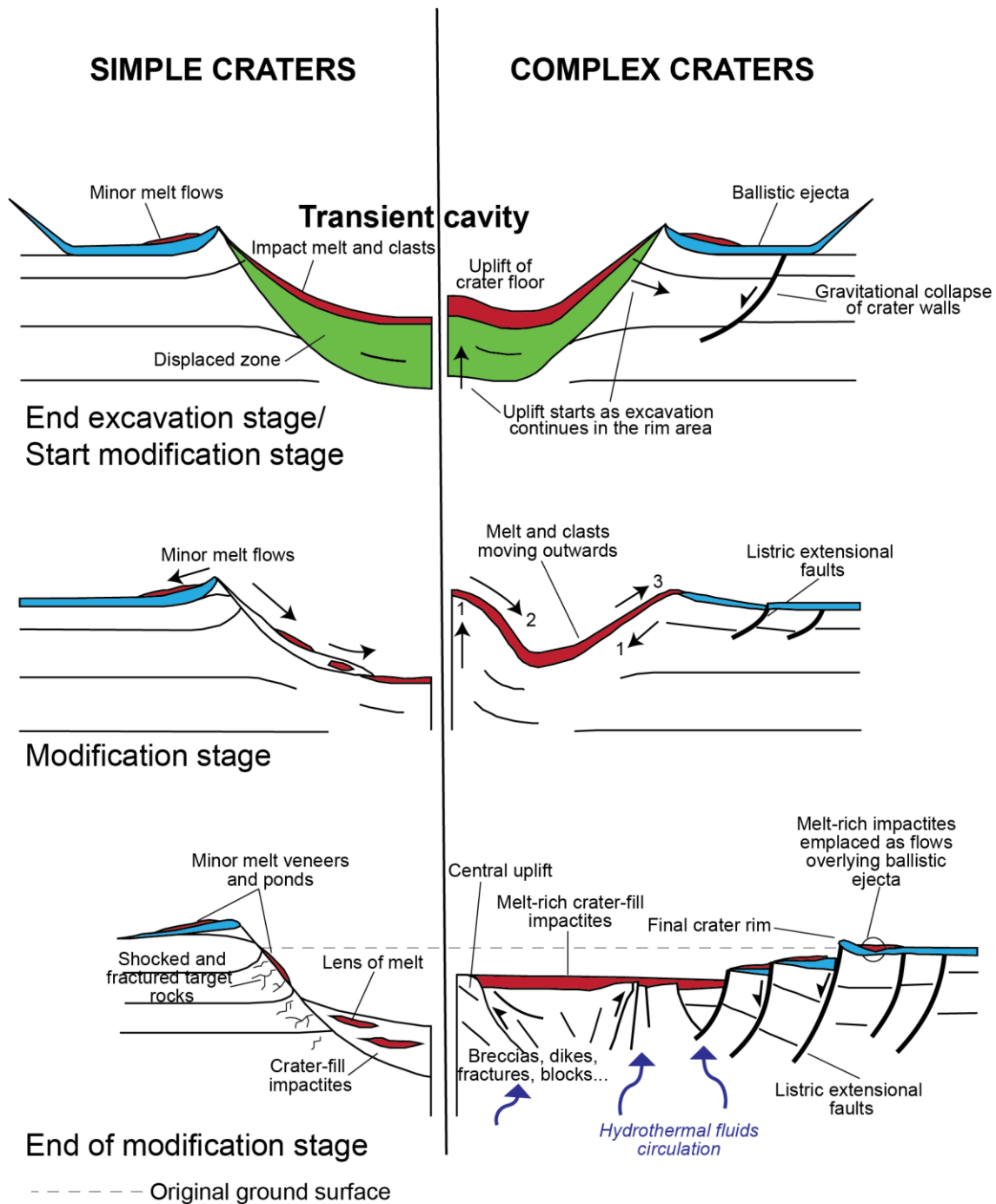
Figure 1.5. *Cross-section diagrams, showing the end of the excavation and modification stages for simple (left, i.e., diameter <2–4 km) and complex (right, i.e., diameter >2–4 km) impact craters. In the modification stage, labelled arrows represent different time steps with (1) the gravitational collapse of crater walls and central uplift as a result of inwards movement of material. Then, (2) melt and clasts flow off the central uplift. Finally, (3) after the crater wall collapse is over, there is still some movement of melt and clasts outwards of the crater. Modified from Osinski and Pierazzo (2012).*

For the largest impact structures (i.e., larger than ~30 km on Earth), a peak ring will form, instead of a central peak. Two major models have been proposed to explain the formation of a peak ring crater: (1) the dynamic collapse and (2) the nested melt-cavity models (see

detailed description of both models in Baker and Head, 2013; Baker et al., 2016, and references therein). The dynamic collapse model explains peak ring formation as a consequence of the gravitational collapse of an over-heightened central peak, which was first suggested following studies of impact basins on the Moon, Mars, and Mercury (Murray, 1980), and terrestrial impact structures (Grieve, 1981). Further quantitative assessments were made on the basis of theory (Melosh, 1989), and based on numerical modeling combined with geological and geophysical observations (e.g., Morgan et al., 2000; Collins et al., 2002, 2008; Ivanov, 2005; Riller et al., 2018). In the dynamic collapse model, the rocks are behaving like a fluid, moving downward and outward from the unstable central peak (which can reach a height of ~10 to 20 km above the crater rim), then meet and/or overlay the collapsed transient cavity wall, to finally form a peak ring after the completion of the central peak collapse (Murray, 1980; Collins et al., 2002, 2008; Ivanov, 2005; Baker and Head, 2013). Observations on Venus have shown that the ratio between the peak ring diameter and the crater rim diameter does not exceed ~0.5 (Murray, 1980). The alternative hypothesis explaining the formation of peak ring crater is the nested melt-cavity, a conceptual model established following observations of peak ring craters on the Moon and Mercury (Cintala and Grieve, 1998; Head, 2010; Baker et al., 2016). In this case, the peak ring is the result of a non-proportional growth of the impact melt volume produced with increasing crater size, in addition to an increase in the depth of melting relative to the depth of the transient crater (Osinski and Pierazzo, 2012; Baker and Head, 2013). The upper part of the central uplift is melted during the impact, which attenuate the uplifting below the impact melt sheet. The uplifted region within the crater is limited to the periphery around the periphery of the melt zone to form peak ring (Osinski and Pierazzo, 2012). The formation of peak ring is further described in Chapter 3, following the recent observations made on the Chicxulub impact structure peak ring.
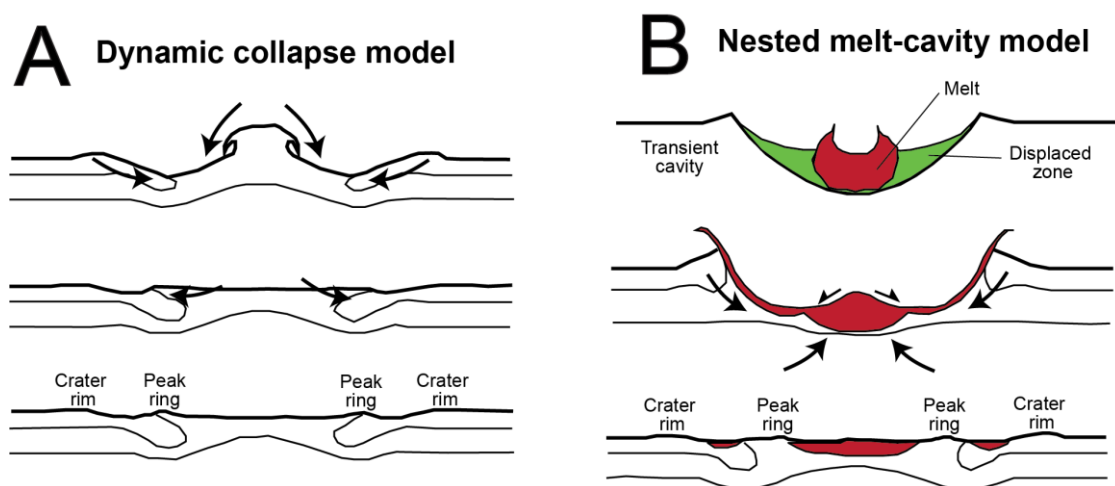
Figure 1.6. *Schematic representations of peak ring crater formation models. A) The 'dynamic collapse' model corresponding to the complete collapse of a gravitationally unstable overheightened central peak. The material collapses in a fluid-like behavior, downward and outward, and folds over the collapsed rim material, forming a peak ring. B) The 'nested melt-cavity' conceptual model where a significant volume of melt is produced, the melt will prevent the formation of a central peak. The uplift is not sufficient to compete with the depth of melting, or, the column of material that would eventually form a central peak is fully melted. In this case, only the uplifted periphery of the melt zone remains, forming a peak ring. Modified after Baker and Head (2013).*

Further modifications to the impact crater take place, generally on longer timescale (from years to millions of years), such as seismic readjustments, sedimentation within the crater, onset of an hydrothermal system, and/or erosion processes. Evidence for impact-related hydrothermal systems has been recognized to date at over 70 impact structures on Earth, with the rocks and minerals being (sometimes heavily) altered (e.g., Naumov, 2005; Osinski et al., 2013). The heat which leads to the onset of an hydrothermal system at an impact crater may originate from: (1) cooling impact melt rocks and impact melt-bearing breccias, (2) elevated geothermal gradients in central uplifts, and (3) thermal energy deposited in central uplifts due to the passage of the shock wave (e.g., Osinski et al., 2005).

References

Ahrens T. J. and O'Keefe J. D. 1972. Shock melting and vaporization of Lunar rocks and minerals. *Moon* 4:214–249. https://doi.org/10.1007/BF00562927.

Alvarez L. W., Alvarez W., Asaro F., and Michel H. V. 1980. Extraterrestrial cause for the Cretaceous-Tertiary extinction. *Science* 208:1095–1108. https://doi.org/10.1126/science.208.4448.1095.

Baker D. M. H. and Head J. W. 2013. New morphometric measurements of craters and basins on Mercury and the Moon from MESSENGER and LRO altimetry and image data: An observational framework for evaluating models of peak-ring basin formation. *Planetary and Space Science* 86:91–116. https://doi.org/10.1016/j.pss.2013.07.003.

Baker D. M. H., Head J. W., Fassett C. I., Kadish S. J., Smith D. E., Zuber M. T., and Neumann G. A. 2011. The transition from complex crater to peak-ring basin on the Moon: New observations from the Lunar Orbiter Laser Altimeter (LOLA) instrument. *Icarus* 214:377–393. https://doi.org/10.1016/j.icarus.2011.05.030.

Baker D. M. H., Head J. W., Collins G. S., and Potter R. W. K. 2016. The formation of peak-ring basins: Working hypotheses and path forward in using observations to constrain models of impact-basin formation. *Icarus* 273:146–163. https://doi.org/10.1016/j.icarus.2015.11.033.

Basurah H. M. 2003. Estimating a new date for the Wabar meteorite impact. *Meteoritics and Planetary Science* 38:A155–A156. https://doi.org/10.1111/j.1945-5100.2003.tb00324.x.

Cintala M. J. and Grieve R. A. F. 1998. Scaling impact-melt and crater dimensions: implications for the lunar cratering record. *Meteoritics and Planetary Science* 33:889–912. https://doi.org/10.1111/j.1945-5100.1998.tb01695.x.

Collins G. S., Melosh H. J., Morgan J. V., and Warner M. R. 2002. Hydrocode simulations of Chicxulub crater collapse and peak-ring formation. *Icarus* 157:24–33. https://doi.org/10.1006/icar.2002.6822.

Collins G. S., Morgan J., Barton P., Christeson G. L., Gulick S., Urrutia J., Warner M., and Wünnemann K. 2008. Dynamic modeling suggests terrace zone asymmetry in the Chicxulub crater is caused by target heterogeneity. *Earth and Planetary Science Letters* 270:221–230. https://doi.org/10.1016/j.epsl.2008.03.032.

Dence M. R. 1965. The extraterrestrial origin of Canadian craters. *Annals of the New York Academy of Science* 123:941–969.

Dence M. R. 1968. Shock zoning at Canadian craters: petrography and structural implications. In *Shock Metamorphism of Natural Materials*, edited by B. M. French and N. M. Short. Baltimore: Mono Book Corporation. pp. 169–184.

Dence M. R. 2017. On critical observations that constrain models of terrestrial hypervelocity impact craters. *Meteoritics and Planetary Science* 52:1285–1299. https://doi.org/10.1111/maps.12822.

Earth Impact Database 2021. http://passc.net/EarthImpactDatabase/New%20website_05-2018/Index.html (accessed 30th November 2021).

Erickson T. M., Kirkland C. L., Timms N. E., Cavosie A. J., and Davison T. M. 2020. Precise radiometric age establishes Yarrabubba, Western Australia, as Earth's oldest recognised meteorite impact structure. *Nature Communications* 11:Article No. 300. https://doi.org/10.1038/s41467-019-13985-7.

Ferrière L. 2008. *Shock metamorphism and geochemistry of impactites from the Bosumtwi impact structure: A case study of shock-induced deformations and transformations in quartz and associated methodology*. PhD thesis, University of Vienna, Austria. 279 p.

Ferrière L. 2021. World map with confirmed meteorite impact structures. http://www.meteorimpactonearth.com/meteorite.html (accessed 12th August 2022).

Ferrière L., Koeberl C., Ivanov B. A., and Reimold W. U. 2008. Shock metamorphism of Bosumtwi impact crater rocks, shock attenuation, and uplift formation. *Science* 322:1678–1681. https://doi.org/10.1126/science.1166283.

French B. M. 1998. *Traces of catastrophe: A handbook of shock-metamorphic effects in terrestrial meteorite impact structures*. LPI Contribution #954. Houston, Texas: Lunar and Planetary Institute. 120 p. https://www.lpi.usra.edu/publications/books/CB-954/CB-954.intro.html.

French B. M. and Koeberl C. 2010. The convincing identification of terrestrial meteorite impact structures: What works, what doesn't, and why. *Earth-Science Reviews* 98:123–170.

Gault D. E., Quaide W. L., and Oberbeck V. R. 1968. Experimental and analytical studies of crystalline damage useful for the recognition of impact structures. In *Shock metamorphism of natural materials*, edited by B. M. French and N. M. Short. Baltimore: Mono Book Corporation. pp. 87–99.

Gnos E., Hofmann B. A., Halawani M. A., Tarabulsi Y., Hakeem M., Shanti M. A., Greber N. D., Holm S., Alwmark C., Greenwood R. C., and Ramseyer K. 2013. The Wabar impact craters, Saudi Arabia, revisited. *Meteoritics and Planetary Science* 48:2000–2014. https://doi.org/10.1111/maps.12218.

Grieve R. A. F. 1981. Constraints on the formation of ring impact structures, based on terrestrial data. In *Multi-ring basins: formation and evolution*, edited by P. H. Schultz and R. B. Merrill. Proceedings of the Lunar and Planetary Science 12A. New York and Oxford: Pergamon Press. pp. 37–57.

Grieve R. A. F. 1987. Terrestrial impact structures. *Annual Reviews of Earth Planetary Science* 15:245–270. https://doi.org/10.1146/annurev.ea.15.050187.001333.

Grieve R. A. F. and Cintala M. J. 1982. A method for estimating the initial impact conditions of terrestrial cratering events, exemplified by its application to Brent crater, Ontario. *Proceedings of the Lunar and Planetary Science Conference* 12B:1607–1621.

Grieve R. A. F. and Pilkington M. 1996. The signature of terrestrial impacts. *Journal of Australian Geology and Geophysics* 16:399–420. https://ecat.ga.gov.au/geonetwork/srv/api/records/fae9173a-718b-71e4-e044-00144fdd4fa6.

Grieve R. A. F. and Therriault A. 2004. Observations at terrestrial impact structures: their utility in constraining crater formation. *Meteoritics and Planetary Science* 39:199–216. https://doi.org/10.1111/j.1945-5100.2004.tb00336.x.

Grieve R. A. F., Dence M. R., and Robertson P. B. 1977. Cratering processes: as interpreted from the occurrences of impact melts. In *Impact and Explosion Cratering*, edited by D. J. Roddy, R. O. Pepin, and R. B. Merrill, Pergamon Press, New York, NY, pp. 791–814.

Grieve R. A. F., Robertson P. B., and Bouchard M. A. 1989. Origin and age of the Cratère du Nouveau-Québec. In *L'histoire naturelle du Cratère du Nouveau Québec*, edited by M. A. Bouchard and S. Peloquin, Collection Environnement et Géologie Vol. 7., Université de Montréal, Montréal, Canada, pp. 59–72.

Gulick S. P. S., Christeson G. L., Barton P. J., Grieve R. A. F., Morgan J. V., and Urrutia-Fucugauchi J. 2013. Geophysical characterization of the Chicxulub impact crater. *Reviews of Geophysics* 51:31–52. https://doi.org/10.1002/rog.20007.

Head J. W. 2010. Transition from complex craters to multi-ringed basins on terrestrial planetary bodies: scale-dependent role of the expanding melt cavity and progressive interaction with the displaced zone. *Geophysical Research Letters* 37:L02203. https://doi.org/10.1029/2009GL041790.

Hildebrand A. R., Penfield G. T., Kring D. A., Pilkington M., Camargo Z. A., Jacobsen S. B., and Boynton W. V. 1991. Chicxulub crater: A possible Cretaceous/Tertiary boundary impact crater on the Yucatán Peninsula, Mexico. *Geology* 19:867–871. https://doi.org/10.1130/0091-7613(1991)019<0867:CCAPCT>2.3.CO;2.

Howard K. A. 1974. Fresh lunar impact craters: Review of variations with size. In: *Lunar Science Conference, 5th, Houston, Tex., March 18-22, 1974, Proceedings, Volume 1,* Pergamon Press Inc., New York, United States, pp. 61–69.

Ivanov B. A. 2005. Numerical modeling of the largest terrestrial meteorite craters. *Solar System Research* 39:381–409. https://doi.org/10.1007/s11208-005-0051-0.

Ivanov B. A. 2020. Cratering. *Oxford Research Encyclopedia of Planetary Science.* https://oxfordre.com (Accessed 30th November 2020). https://doi.org/10.1093/acrefore/9780190647926.013.7.

Ivanov B. A. and Artemieva N. A. 2002. Numerical modeling of the formation of large impact craters. In *Catastrophic events and mass extinctions: Impacts and beyond*, edited by C. Koeberl and K. G. MacLeod. GSA Special Paper #356. Boulder, Colorado: Geological Society of America. pp. 619–630.

Kamo S. L., Reimold W. U., Krogh T. E., and Colliston W. P. 1996. A 2.023 Ga age for the Vredefort impact event and a first report of shock metamorphosed zircons in pseudotachylitic breccias and Granophyre. *Earth and Planetary Science Letters* 144:369–387. https://doi.org/10.1016/S0012-821X(96)00180-X.

Kenkmann T. 2021. The terrestrial impact crater record: A statistical analysis of morphologies, structures, ages, lithologies, and more. *Meteoritics & Planetary Science* 56:1024–1070. https://doi.org/10.1111/maps.13657.

Kenkmann T., Artemieva N. A., Wünnemann K., Poelchau M. H., Elbeshausen D., and Núñez del Prado H. 2009. The Carancas meteorite impact crater, Peru: Geologic surveying and modeling of crater formation and atmospheric passage. *Meteoritics and Planetary Science* 44:985–1000. https://doi.org/10.1111/j.1945-5100.2009.tb00783.x.

Kenkmann T., Poelchau M. H., and Wulf G. 2014. Structural geology of impact craters. *Journal of Structural Geology* 62:156–182. https://doi.org/10.1016/j.jsg.2014.01.015.

Kieffer S. W. and Simonds C. H. 1980. The role of volatiles and lithology in the impact cratering process. *Reviews of Geophysics and Space Physics* 18:143–181. https://doi.org/10.1029/RG018i001p00143.

Krogh T. E., Davis D. W., and Corfu F. 1984. Precise U–Pb zircon and baddeleyite ages for the Sudbury area. In *The geology and ore deposits of the Sudbury structure, vol. 1*, edited by E. G. Pye, A. J. Naldrett, and P. E. Giblin. Toronto: Ontario Geological Survey Special Publication. pp. 431– 446.

Mashchak M. S. and Naumov M. V. 1996. The Suavjärvi structure: An early Proterozoic impact site on the Fennoscandian shield (abstract). 27th Lunar and Planetary Science Conference. pp. 825–826. http://adsabs.harvard.edu/full/1996LPI....27..825M.

Melosh H. J. 1979. Acoustic fluidization: A new geologic process? *Journal of Geophysical Research* 84:7513–7520. https://doi.org/10.1029/jb084ib13p07513.

Melosh H. J. 1989. *Impact cratering–A geological process*. New York: Oxford University Press. 245 p.

Melosh H. J. and Ivanov B. A. 1999. Impact crater collapse. *Annual Review of Earth and Planetary Science* 27:385–415. https://doi.org/10.1146/annurev.earth.27.1.385.

Melosh H. J. and McKinnon W. 1978. The mechanics of ringed basin formation. *Geophysical Research Letters* 5:985–988. https://doi.org/10.1029/GL005i011p00985.

Morgan J., Warner M., the Chicxulub Working Group, Brittan J., Buffler R., Camargo A., Christeson G., Denton P., Hildebrand A., Hobbs R., Macintyre H., Mackenzie G., Maguire P., Marin L., Nakamura Y., Pilkington M., Sharpton V., Snyder D., Suarez G., and Trejo A. 1997. Size and morphology of the Chicxulub impact crater. *Nature* 390:472–476. https://doi.org/10.1038/37291.

Morgan J. V., Warner M. R., Collins G. S., Melosh H. J., and Christeson G. L. 2000. Peak-ring formation in large impact craters: geophysical constraints from Chicxulub. *Earth and Planetary Science Letters* 183:347–354. https://doi.org/10.1016/S0012-821X(00)00307-1.

Murray J. B. 1980. Oscillating peak model of basin and crater formation. *Earth Moon Planets* 22:269–291. https://doi.org/10.1007/BF01259285.

Naumov M. V. 2005. Principal features of impact-generated hydrothermal circulation systems: mineralogical and geochemical evidence. *Geofluids* 5:165–184. https://doi.org/10.1111/j.1468-8123.2005.00092.x.

O'Keefe J. D. and Ahrens T. J. 1982. Cometary and meteorite swarm impact on planetary surfaces. *Journal of Geophysical Research* 87:6668–6680. https://doi.org/10.1029/JB087iB08p06668.

Oberbeck V. R. 1975. The role of ballistic erosion and sedimentation in lunar stratigraphy. *Reviews of Geophysics and Space Physics* 13:337–362. https://doi.org/10.1029/RG013i002p00337.

Osinski G. R. and Pierazzo E. 2012. Impact Cratering: Processes and Products. In *Impact Cratering: Processes and Products*, edited by G. R. Osinski and E. Pierazzo. Chichester, UK: Blackwell Publishing Ltd. pp. 1–20. https://doi.org/10.1002/9781118447307.ch1.

Osinski G. R., Lee P., Parnell J., Spray J. G., and Baron M. 2005. A case study of impact-induced hydrothermal activity: The Haughton impact structure, Devon Island, Canadian High Arctic. *Meteoritics and Planetary Science* 40:1859–1877. https://doi.org/10.1111/j.1945-5100.2005.tb00150.x.

Osinski G. R., Tornabene L. L., Banerjee N. R., Cockell C. S., Flemming R., Izawa M. R. M., McCutcheon J., Parnell J., Preston L. J., Pickersgill A. E., Pontefract A., Sapers H. M., and Southam G. 2013. Impact-generated hydrothermal systems on Earth and Mars. *Icarus* 224:347–363. https://doi.org/10.1016/j.icarus.2012.08.030.

Osinski G. R., Grieve R. A. F., Ferrière L., Losiak A., Pickersgill A., Cavosie A. J., Hibbard S. M., Hill P., Bermudez J. J., Marion C. L., Newman J. D., and Simpson S. L. 2022. Impact Earth: A review of the terrestrial impact record. *Earth-Science Reviews* 232:104112. https://doi.org/10.1016/j.earscirev.2022.104112.

Pati J. K., Reimold W. U., Koeberl C., and Pati P. 2008. The Dhala structure, Bundelkhand craton, Central India – Eroded remnant of a large Paleoproterozoic impact structure. *Meteoritics and Planetary Science* 43:1383-1398. https://doi.org/10.1111/j.1945-5100.2008.tb00704.x.

Phillips F. M., Zreda M. G., Smith S. S., Elmore D., Kubik P. W., Dorn R. I., and Roddy D. J. 1991. Age and geomorphic history of Meteor Crater, Arizona, from cosmogenic ^{36}Cl and ^{14}C in rock varnish. *Geochimica et Cosmochimica Acta* 55:2695–2698. https://doi.org/10.1016/0016-7037(91)90387-K.

Popova O. P., Jenniskens P., Emelyanenko V., Kartashova A., Biryukov E., Khaibrakhmanov S., Shuvalov V., Rybnov Y., Dudorov A., Grokhovsky V. I., Badyukov D. D., Yin Q.-Z., Gural P. S., Albers J., Granvik M., Evers L. G., Kuiper J., Kharlamov V., Solovyov A., Rusakov Y. S., Korotkiy S., Serdyuk I., Korochantsev A. V., Larionov M. Y., Glazachev D., Mayer A. E., Gisler G., Gladkovsky S. V., Wimpenny J., Sanborn M. E., Yamakawa A., Verosub K. L., Rowland D. J., Roeske S., Botto N. W., Friedrich J. M., Zolensky M. E., Le L., Ross D., Ziegler K., Nakamura T., Ahn I., Lee J. I., Zhou Q., Li X.-H., Li Q.-L., Liu Y., Tang G.-Q., Hiroi T., Sears D., Weinstein I. A., Vokhmintsev A. S., Ishchenko A. V., Schmitt-Kopplin P., Hertkorn

N., Nagao K., Haba M. K., Komatsu M., Mikouchi T., and The Chelyabinsk Airburst Consortium. 2013. Chelyabinsk Airburst, Damage Assessment, Meteorite Recovery, and Characterization. *Science* 342:1069–1073. https://doi.org/10.1126/science.1242642.

Prescott J. R., Robertson G. B., Shoemaker C., Shoemaker E. M., and Wynn J. 2004. Luminescence dating of the Wabar meteorite craters, Saudi Arabia. *Journal of Geophysical Research* 109:1–8. https://doi.org/10.1029/2003JE002136.

Rae A. S. P., Collins G. S., Poelchau M., Riller U., Davison T. M., Grieve R. A. F., Osinski G. R., Morgan J. V., and IODP-ICDP Expedition 364 Scientists. 2019. Stress-Strain Evolution During Peak-Ring Formation: A Case Study of the Chicxulub Impact Structure. *JGR Planets* 124:396–417. https://doi.org/10.1029/2018JE005821.

Reimold W. U., Ferrière L., Deutsch A., and Koeberl C. 2014. Impact controversies: Impact recognition criteria and related issues. *Meteoritics and Planetary Science* 49:723–731. https://doi.org/10.1111/maps.12284.

Riller U., Poelchau M. H., Rae A. S. P., Schulte F. M., Collins G. S., Melosh H. J., Grieve R. A. F., Morgan J. V., Gulick S. P. S., Lofi J., Diaw A., McCall N., Kring D. A., and the IODP–ICDP Expedition 364 Science Party. Rock fluidization during peak-ring formation of large impact structures. *Nature* 562:511–518. https://doi.org/10.1038/s41586-018-0607-z.

Schmieder M. and Kring D.A. 2020. Earth's Impact Events Through Geologic Time: A List of Recommended Ages for Terrestrial Impact Structures and Deposits. *Astrobiology* 20:91–141. http://doi.org/10.1089/ast.2019.2085.

Shoemaker E. M. 1960. Penetration mechanics of high velocity meteorites, illustrated by Meteor Crater, Arizona. *Report of the International Geological Congress, XXI Session, Norden*. Part XVIII, International Geological Congress, Copenhagen, pp. 418–434.

Stöffler D., Gault D. E., Wedekind J., and Polkowski G. 1975. Experimental hypervelocity impact into quartz sand: distribution and shock metamorphism of ejecta. *Journal of Geophysical Research* 80:4062–4077. https://doi.org/10.1029/JB080i029p04062.

Stöffler D., Ryder G., Ivanov B. A., Artemieva N. A., Cintala M. J., and Grieve R. A. F. 2006. Cratering history and lunar chronology. *Reviews in Mineralogy and Geochemistry* 60:519–596. https://doi.org/10.2138/rmg.2006.60.05.

Sutton S. R. 1985. Thermoluminescence measurements on shock-metamorphosed sandstone and dolomite from Meteor Crater, Arizona: 2. Thermoluminescence age of Meteor Crater. *Journal of Geophysical Research: Solid Earth* 90:3690–3700. https://doi.org/10.1029/JB090iB05p03690.

CHAPTER 2: Typical features of meteorite impact structures

During an impact event, almost all of the impacting projectile is destroyed (Melosh, 1989), with only in rare cases fragments of the projectile preserved. Consequently, diagnostic features of a meteorite impact are usually found in the rocks and minerals that have experienced extreme pressure and temperature following the passage of the shock waves generated by the impact (Melosh, 1989). Several geological features are not restricted to impact structures, including, e.g., a broadly circular form, circular gravity and/or magnetic anomalies, or the presence of large units of igneous rocks exposed at the surface. Commonly, this variety of circular features forms as a result of conventional geological processes, such as volcanism, salt diapirism, or internal igneous activity. The confirmation of a meteorite impact structure is based on the identification and characterization of features which are unique products of impact events, including macroscopic (e.g., shatter cones) or microscopic (e.g., planar deformation features in minerals) shock-metamorphic features, the occurrence of high-pressure mineral polymorphs (e.g., coesite and stishovite in a specific assemblage), and/or moderately-to-highly siderophile element (e.g., Ir, Pt) or isotopic (e.g., Os) anomalies compared to the target rock lithologies (e.g., French and Short, 1968; French, 1998, and references therein; Koeberl, 2002; Langenhorst, 2002; French and Koeberl, 2010).

The "shock-metamorphic" effects include all types of shock-induced changes, such as the formation of planar microstructures and phase transformation, whereas impact metamorphism includes target rock melting, decomposition, and vaporization (e.g., Stöffler and Grieve, 2007). These irreversible changes occur when the rocks are subjected to shock pressures higher than their Hugoniot elastic limit (HEL). Stöffler (1972) defines this limit as "the critical shock pressure at which a solid yields under the uniaxial strain of a plane shock wave". For example, the HEL of quartz is comprised between 5–8 GPa, while the HEL of most geological materials is between 1–10 GPa (e.g., Stöffler, 1972; Stöffler and Langenhorst, 1994). During the passage of the shock waves, the target rocks are exposed to conditions that are unlike those observed during any other geological deformation and metamorphism (Fig. 2.1). An hypervelocity impact event exposes a large volume of target rocks to transient shock pressures between ~5 and more than 60 GPa (>100 GPa near the point of impact, Melosh, 1989), in contrast with the up to ~1–3 GPa observed for metamorphism within Earth's crust, and associated with strain rates on the order of ~10^4–10^6 s^{-1}, several orders of magnitude higher than in terrestrial tectonic processes (i.e., ~10^{-6}–10^{-3} s^{-1}; Carter, 1965, 1968; French and Short, 1968; Stöffler, 1971; Grieve, 1991). The heating occurring after the passage of the shock waves through the target rocks may be on the order of ~2000 °C or even more, which is higher than the temperatures generated by igneous processes on Earth, and will produce distinct melting and/or transformation reactions (Stöffler, 1984). The impact cratering process is also nearly instantaneous (i.e., with shock waves passing through 1 cm of target rock in ~10^{-6} s, and less than one hour is needed to produce a 100 km-diameter impact structure) allowing the preservation of disequilibrium features, generally following rapid cooling (French and Koeberl,

2010). In contrast, tectonic, metamorphic, and igneous processes generally occur during timescales on the order of hundreds of thousands to several million years (e.g., Philpotts, 1990; Vernon, 2004).
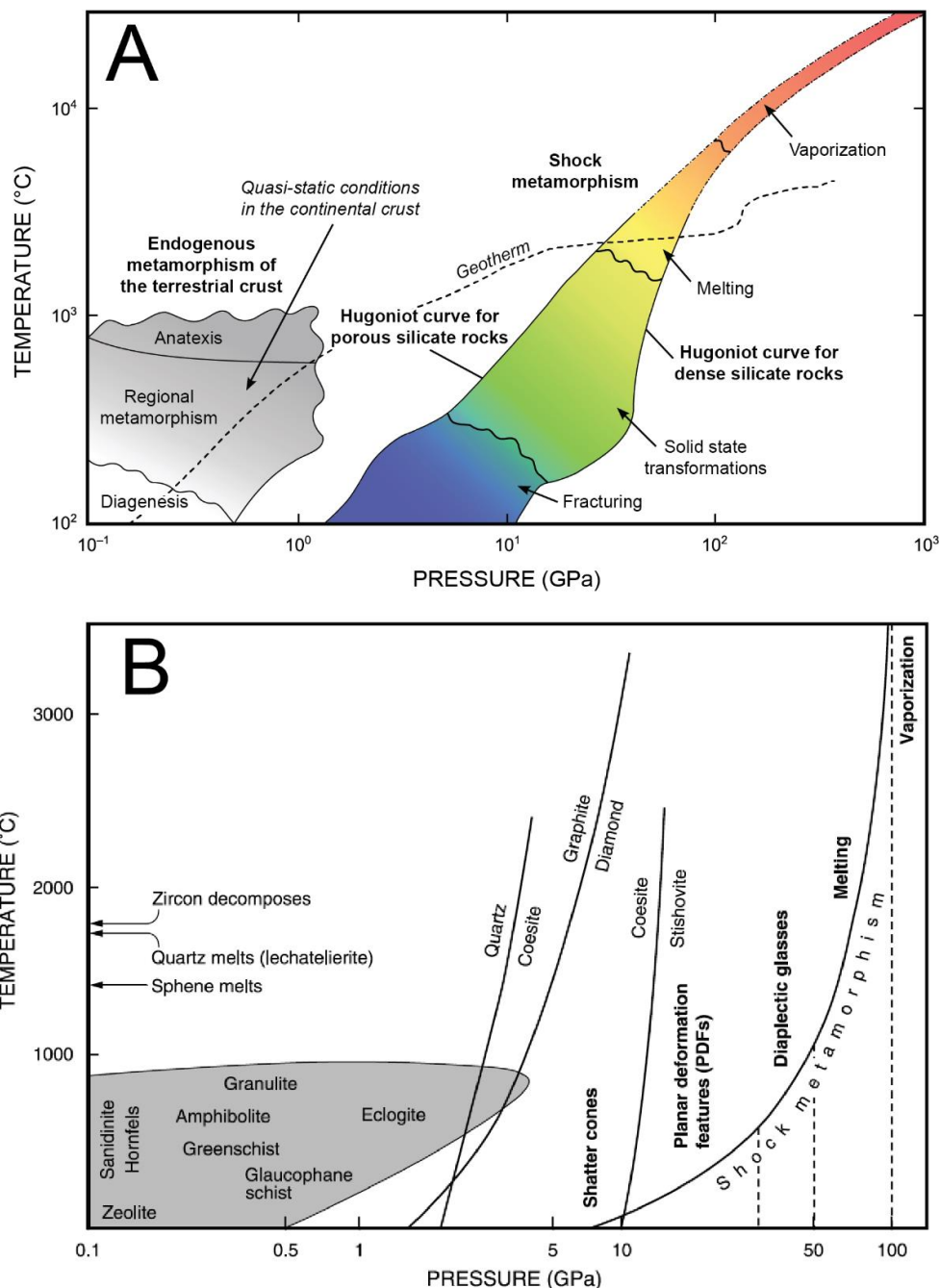
Figure 2.1. *A) Pressure-temperature diagram comparing shock metamorphism conditions for silicate rocks with endogenous metamorphism of the terrestrial crust. Modified from Stöffler et al. (2018). References for Hugoniot curves, geotherm, and pressure-temperature estimates for upper melting and vaporization fields can be found in Stöffler et al. (2018). B) Similar diagram as A) showing the pressure-temperature conditions for the onset of specific shock effects in rocks and minerals (indicated by the dashed lines). The exponential "Shock metamorphism" curve shows the relation between pressure and post-shock temperature for granitic rocks (from French, 1998).*

With increasing distance from the point of impact, the shock pressure associated with the shock wave decreases (Kieffer and Simonds, 1980; Melosh, 1989). This will produce distinctive shock effects within the target rocks: rock melting (~≥ 60 GPa); selective mineral melting (~40–60 GPa); diaplectic glass phases (~30–45 GPa; in the case of non-porous rocks); high-pressure polymorph minerals (~12–30 GPa), planar deformation features (PDFs) in quartz (~8–25 GPa); shatter cones formation (~2–5 GPa); for details, see Stöffler (1984), Melosh (1989), Stöffler and Langenhorst (1994), French and Koeberl (2010), and the description of these features in the following sections of this chapter.

Shock effects in minerals are very diverse, and have been extensively investigated and discussed during the last decades mainly for quartz (e.g., French and Short, 1968; Engelhardt and Bertsch, 1969; Stöffler, 1972; Stöffler and Langenhorst, 1994; Grieve et al., 1996; French, 1998; Montanari and Koeberl, 2000; Langenhorst, 2002; Trepmann, 2008; French and Koeberl, 2010; Ferrière and Osinski, 2013, and references therein), and also for feldspar (e.g., Stöffler, 1967; Robertson, 1975; Ostertag, 1983; Dressler, 1990; Bischoff and Stöffler, 1992; Pittarello et al., 2020, Pickersgill et al., 2021, and references therein), olivine (e.g., Reimold and Stöffler, 1978; Bauer, 1979; Stöffler et al., 1991; Bischoff and Stöffler, 1992; Schmitt, 2000; and references therein), and pyroxene (e.g., Rubin et al., 1997). However, a large number of recent works are focused on the detailed characterization of shock metamorphism effects in accessory phases, such as in apatite (e.g., Cavosie and Centeno, 2014; Cox et al., 2020; Darling et al., 2021), in titanite (e.g., Timms et al., 2019, 2020), and in zircon grains (e.g., Wittmann et al, 2006; Kenny et al., 2017; Cavosie et al., 2018). A review of shock effects in rocks and minerals, including a brief presentation of two examples of post-shock, thermal effects (i.e., toasted quartz and ballen silica) is provided in the following sections, mainly based on Ferrière (2008), and Ferrière and Osinski (2013). The investigation of shock effects in minerals is essential to constrain the pressure-temperature conditions experienced by the target rocks in response to an hypervelocity impact, and the associated processes occurring.

2.1. Impactites

Minerals experiencing shock metamorphism occur in different rock types and petrographic assemblages. The full spectrum of shock-diagnostic features is not necessary present in all impact structures, as it depends on the lithology and properties of the target rock(s), the extent of erosion/alteration of the impact structure, the magnitude of the impact event, etc. The different rocks produced or affected by an hypervelocity impact event, including shocked rocks, impact breccias, impact melt rocks, (micro)tektites, and impactoclastic airfall beds, are defined as "impactites" (see extensive reviews by French, 1998; Stöffler and Grieve, 2007; Stöffler et al., 2018). Given the various types of impactites, their classification and definition are complex, and still strongly discussed. The main types of impactites are described and classified in Stöffler and Grieve (2007), using criteria such as, their location in relation to the impact structure, the occurrence of microstructure(s), the lithological nature or components, the degree of shock metamorphism, and their geological or structural setting. This classification was recommended by the International Union of Geological Sciences (IUGS). Impactites range from fractured target rocks to completely new lithologies formed during the impact event, such as impact melt rocks. Generally, they contain evidence of shock metamorphism. When it is not

the case, the classification as impactite is made according to their geological setting being associated with the presence of a confirmed impact structure (Grieve and Therriault, 2013). Terrestrial impactites are usually divided in two main types (Fig. 2.2): (1) the proximal impactites, located within and around the final impact structure, and (2) the distal impactites, which are ejecta material deposits (Stöffler and Grieve, 2007; Stöffler et al., 2018). Further subdivision is made between parautochthonous (moved but appear to be in place), and allochthonous (formed elsewhere, and moved to their current location, such as crater-fill impactites, ejecta, or dikes within parautochthonous) impactites (Stöffler and Grieve, 2007; Grieve and Therriault, 2013). The impactite types described and used in this thesis follow the IUGS recommendations on the nomenclature and classification of terrestrial impactites by Stöffler and Grieve (2007), but take into account the proposed updated classification of Stöffler et al. (2018), as presented in Figure 2.2.
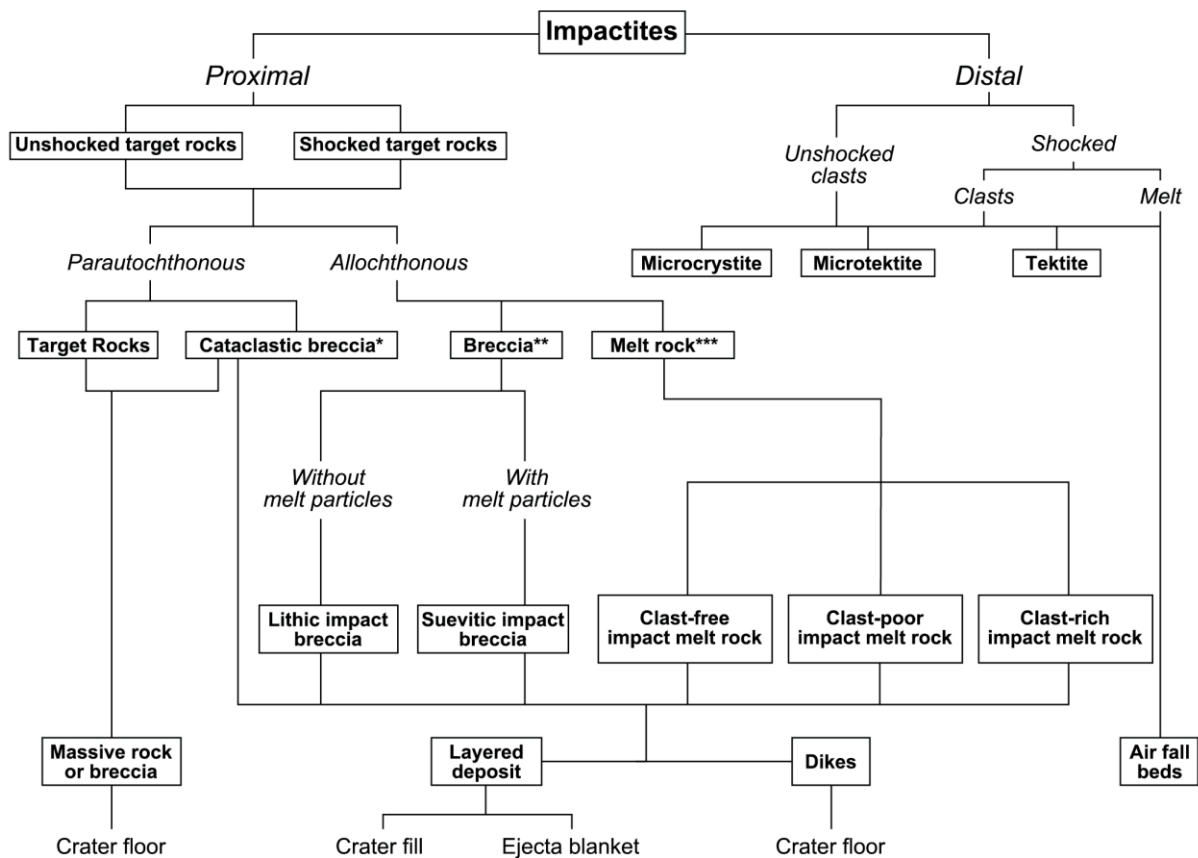
*Typically monomict
**Generally polymict, but can be monomict, e.g., in a single target lithology
***Includes hyaline (glassy), hypocrystalline, and holocrystalline varieties

Figure 2.2. *Impactites classification based on geological setting, texture, and degree of shock metamorphism in the case of terrestrial impact structures (from Stöffler et al., 2018).*

2.1.1. Proximal impactites

Proximal impactites are classified into three major groups, independently of their geological setting: (1) shocked target rocks, (2) impact breccias, and (3) impact melt rocks (Stöffler and Grieve, 2007).

2.1.1.1. Shocked target rocks

Shocked target rocks are defined as "non-brecciated rocks, which show unequivocal effects of shock metamorphism, exclusive of whole rock melting" (Stöffler and Grieve, 2007). Further subclassification is made according to the degree of shock metamorphism, i.e., 5 to 7 stages of progressively increasing shock metamorphism, depending on the lithology, e.g., ultramafic, mafic, felsic crystalline rocks, consolidated and unconsolidated sedimentary rocks, as at a given shock pressure, each rock type will be modified differently (see detailed descriptions and tables in Stöffler et al., 2018). Shocked target rocks occur mainly within the impact structure basement but also as clasts within impact breccias and impact melt rocks (Stöffler et al., 2018).

2.1.1.2. Impact breccias

Impact breccias are generally divided in three subgroups: (1) cataclastic impact breccia, (2) lithic impact breccia, and (3) suevitic breccia, according to the updated classification of Stöffler et al. (2018). These subgroups are based on the degree of mixing of different target lithologies, and on the occurrence of impact melt particles (Stöffler and Grieve, 2007). Pseudotachylitic breccia does not belong to the original classification, however, it is also included here, as another specific type of impact breccia.

2.1.1.2.1. Cataclastic (monomict) impact breccia

Cataclastic impact breccia (Stöffler et al., 2018), previously termed as "monomict impact breccia" is defined by Stöffler and Grieve (2007) as "a cataclasite produced by impact and displaying weak or no shock metamorphism". It corresponds to a breccia containing only a single lithology of lithic clasts (Fig. 2.3). The cataclastic impact breccia occurs generally in the "parautochthonous floor of an impact crater", or as clasts "within polymict impact breccia" (Stöffler and Grieve, 2007). However, in the case where no evidence of shock metamorphism is observed, it is impossible to distinguish a cataclastic impact breccia from a cataclasite formed by e.g., tectonic processes. In this thesis, the term cataclasite is used to describe microbrecciated veins which generally crosscut the basement rocks; these cataclasites display unequivocal shock metamorphic features (such as quartz grains with PDFs).
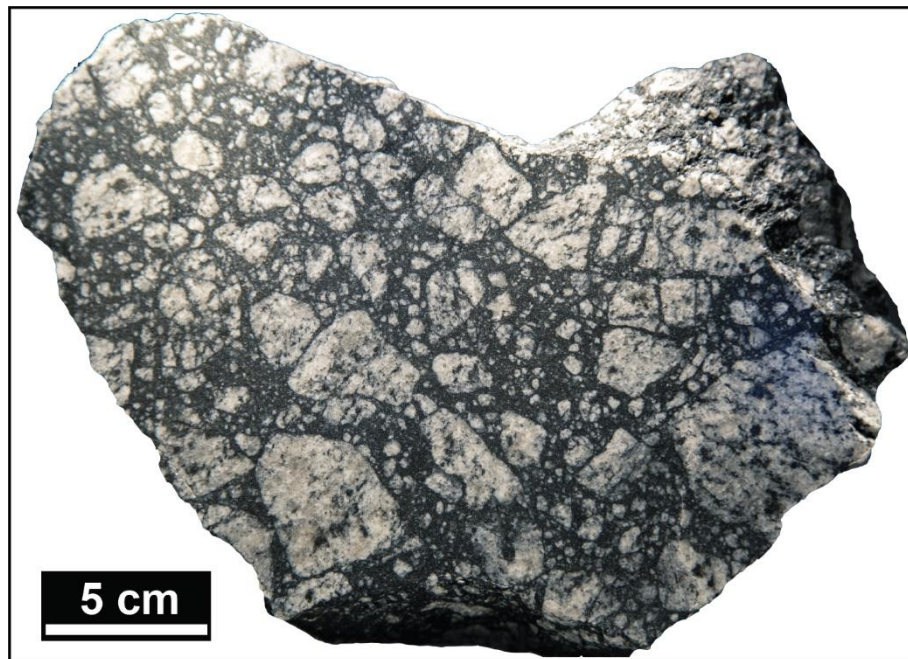
Figure 2.3. *Cataclastic (monomict) impact breccia from the 4.5 km-diameter Gardnos impact structure, Norway, composed uniquely of granite clasts embedded in a black matrix. Sample on display at the Natural History Museum Vienna (NHMV), Austria.*

2.1.1.2.2. Lithic impact breccia

Lithic impact breccia is defined as a polymict impact breccia, i.e., containing clasts of different lithologies and mineral clasts included in a clastic matrix, without impact melt particles (Fig. 2.4A; Stöffler and Grieve, 2007). The clasts are excavated from different areas of the target rock, transported, mixed together, and deposited inside or around the impact structure, and/or injected as dikes into the target rocks (Stöffler and Grieve, 2007). Lithic impact breccia can be (rarely) monomict in the case of a target consisting of only one lithology.

2.1.1.2.3. Suevitic breccia (Suevite)

The suevitic breccia (or suevite breccia, or suevite) is a polymict impact breccia containing lithic and mineral clasts in all stages of shock metamorphism included in a particulate matrix, with the presence of cogenetic impact melt particles which are (if not altered) in a glassy or in a crystallized state (Stöffler and Grieve, 2007; Figs. 2.4B–D). According to their formation processes, suevitic breccia on Earth can occur as "primary suevite" and "secondary suevite". The "primary suevite" corresponds to the fallback material from the ejecta plume formed during an impact event, while the "secondary suevite" is thought to have formed following the interaction of hot impact melt with water (or other volatiles), also known as fuel-coolant interaction (Artemieva et al., 2013; Stöffler et al., 2013). In this work, for clarity, suevitic breccia is termed either as melt-bearing polymict impact breccia, or also as "suevite". Suevite dikes have also been reported, such as in the central uplift of the Bosumtwi impact structure, Ghana (Ferrière et al., 2007).
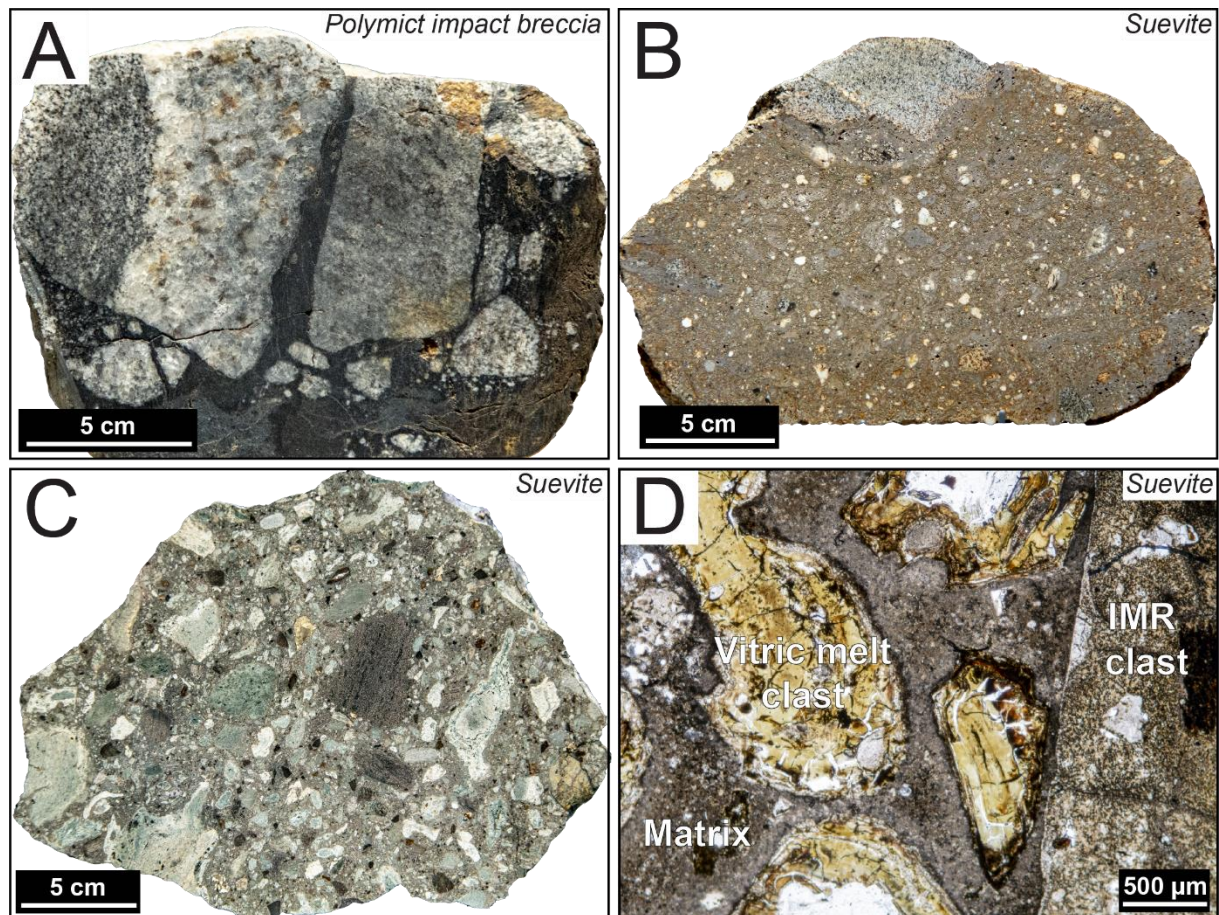
Figure 2.4. *Macrophotographs (A–C) and microphotograph (D, plane-polarized light [PPL]) of different impact breccia samples. A) Polymict impact breccia with angular clasts in a dark matrix. Sample from the 2.7-km-diameter Ritland impact structure, Norway. B) Suevite sample from the Lappajärvi impact structure (~24-km-diameter), Finland, containing various clasts (including impact melt (rock) fragments) generally less than 1 cm in size. C) Suevite sample from the Rochechouart impact structure (~18–25-km-diameter), France. D) Thin section microphotograph of a suevite sample from the Chicxulub impact structure peak ring, recovered by the Expedition 364 drilling (see chapter 3; sample 58R3_8–10.5, depth: 673.68 meters below seafloor). The suevite is mainly composed of altered vitric melt clasts embedded in a clastic matrix. Mineral clasts, such as quartz and calcite, are also present within the matrix. A large impact melt rock (IMR) clast is located on the right side of the photograph. Samples A–C are on display at the NHMV, Austria.*

2.1.1.2.4. Impact pseudotachylite

Impact pseudotachylite (or pseudotachylite, or pseudotachylitic breccia, or pseudotachylite-like breccia) typically occurs as irregular dike-like bodies, in the basement of large impact structures, such as at Vredefort (South Africa) and Sudbury (Canada). They were recognized for the first time by Shand (1916), and, since then, have been the subject of numerous debate and controversies regarding their characteristics, their origin, and their use as a diagnostic feature for impact structures (see review by, e.g., French and Koeberl, 2010). Impact pseudotachylite consists of a breccia containing both unshocked and shocked minerals,

as well as lithic clasts, in a glassy, or very fine-grained (aphanitic) crystalline matrix (Stöffler and Grieve, 2007). Clasts are both rounded and angular, with sizes ranging from microscopic to several meters (Fig. 2.5). The formation process of impact pseudotachylite is still discussed, either frictional melting, shock melting, or decompression melting. Additionally, pseudotachylites are not restricted to impact craters and can also be formed by other geological processes (e.g., large landslides, or seismic faulting) and thus they do not constitute a diagnostic criterion for confirming an impact structure (for more information and discussions, see, e.g., Reimold, 1995; French, 1998; Melosh, 2005; Reimold and Gibson, 2005; French and Koeberl, 2010).
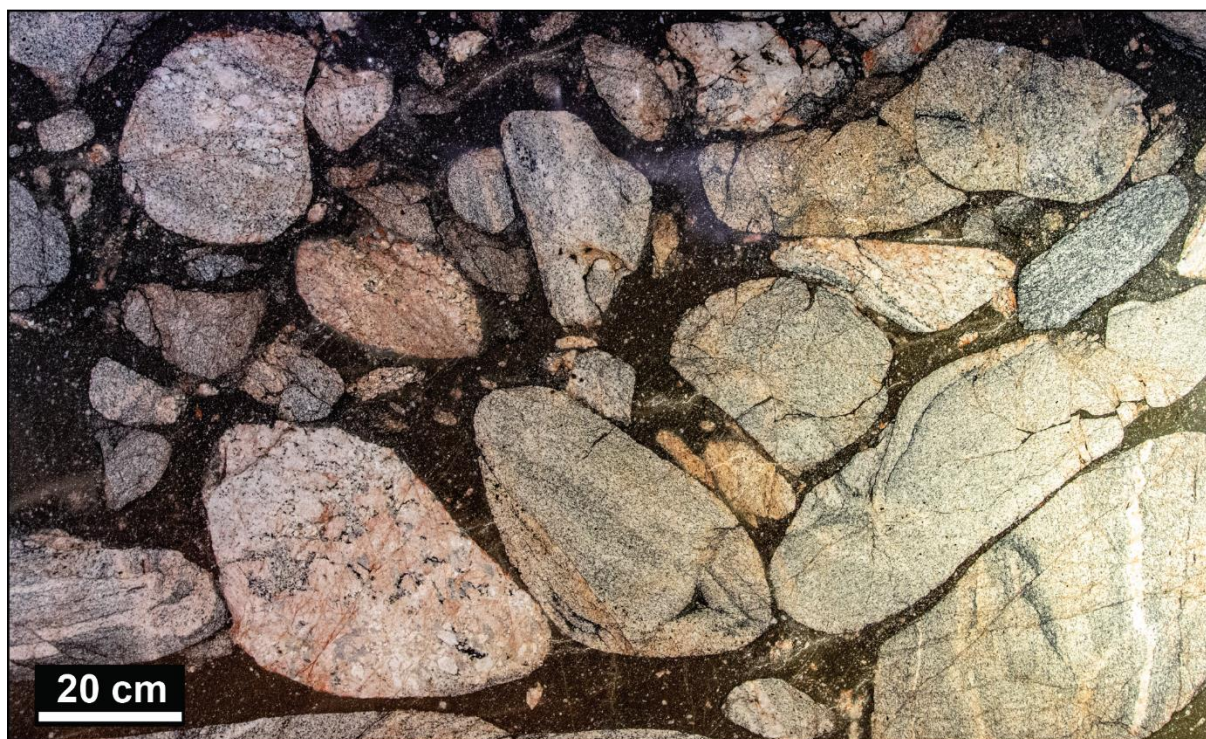
Figure 2.5. *Impact pseudotachylite (or pseudotachylitic breccia), from the Vredefort impact structure (~300-km-diameter), South Africa. It contains large rounded gneiss clasts in a dark, glassy matrix possibly formed by frictional melting within the basement of the impact structure. Large polished plate on display at the NHMV, Austria.*

2.1.1.3. Impact melt rocks

Impact melt rocks (Fig. 2.6) represent the highest degree of shock metamorphism, as they are the product of shock-induced ($\geq$60 GPa) whole target rock melting (French, 1998; Osinski et al., 2013; Stöffler et al., 2018). Impact melt rocks are defined, according to Stöffler and Grieve (2007) as "crystalline, semihyaline, or hyaline rock solidified from impact melt and containing variable amounts of clastic debris of different degree of shock metamorphism". Impact melt rocks are classified according to their clast content (Stöffler and Grieve, 2007), i.e., clast-free, clast-poor (>0–25 vol%), and clast-rich (>25 vol%). A subclassification is possible according to the degree of crystallinity of the impact melt rocks (French, 1998; Stöffler et al., 2018), i.e., holohyaline (glassy), hypocrystalline (mixture of glass and crystals), and

holocrystalline (completely crystalline). A common feature of crystalline impact melt rocks is the presence of quench microlites or crystallites (commonly plagioclase, pyroxene, and/or olivine), indicating a fast cooling and rapid crystallization of the impact melt (Bryan, 1972; Lofgren, 1974; Donaldson, 1976). Vesicularity, as well as flow structures can also be observed in impact melt rocks (Fig. 2.6). Generally, in large impact structures, impact melt rocks derived from crystalline target rocks have a relatively homogenous composition when compared to the original target material (Dressler and Reimold, 2001). Impact melt rocks can occur in a variety of settings within and around impact structures: (1) as large kilometer-sized impact melt rock layers or "sheets", or as isolated bodies inside the impact structure and/or at the rim, (2) as centimeter- to meter-sized clasts within in impact breccias (e.g., in suevite), and (3) as centimeter- to tens of meter-sized injections (sill or dike bodies) penetrating the basement rocks (e.g., French, 1998; Osinski et al., 2013). As an example, the impact melt rock sheet preserved within the Manicouagan impact structure (100-km-diameter, Quebec) is ~55 km in diameter with an average thickness of 230 m (Floran et al., 1978; Simonds et al., 1978). In some cases, impact melt rocks may record an admixture of impactor material (see section 2.3, and publication chapter 7).
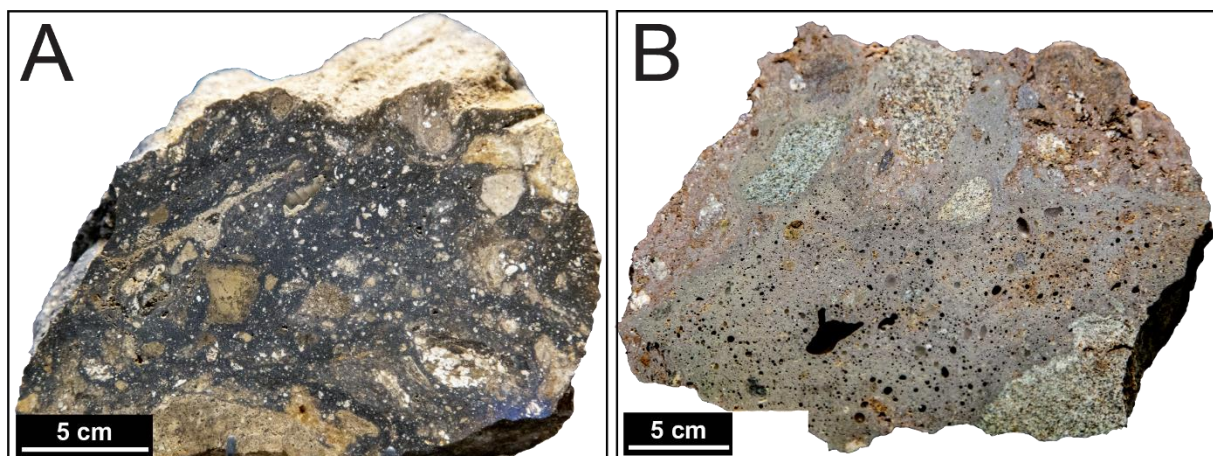
Figure 2.6. *Macrophotographs of impact melt rock samples displaying different textures. A) Clast-rich impact melt rock from the ~19-km-diameter Dellen impact structure, Sweden. B) Vesicular impact melt rock from the ~24-km-diameter Ries impact structure, Germany. Samples on display at the NHMV, Austria.*

2.1.2. Distal impactites

Distal impactites are defined as ejecta located outside the outer limit of the continuous ejecta blanket of an impact structure, i.e., located within some distance (i.e., more than 5 crater radii) from the final impact structure (Stöffler and Grieve, 2007). The distal impactites are divided into two categories: (1) consolidated (including tektites, microtektites, and microkrystites), and (2) unconsolidated (the air fall beds).

2.1.2.1. Tektites, microtektites, and microkrystites

The definition of tektites, according to Stöffler and Grieve (2007), is "an impact glass formed at terrestrial impact craters from melt ejected ballistically and deposited sometimes as aerodynamically shaped bodies in a strewn field outside the continuous ejecta blanket". The tektites range from 1 mm and up to decimeter-size, while microtektites are smaller than 1 mm in size and are usually found well-preserved in deep-sea sediments (Glass, 1990; Stöffler and Grieve, 2007). Tektites appear mostly glassy, green to black in color, but also brown and grey, and display various shapes (e.g., O'Keefe, 1963; Koeberl, 1994; Osinski et al., 2013, and references therein). According to their shape, tektites have been divided into three distinct groups: (1) splash form, i.e., teardrop, sphere, dumbbell or bar shapes, resulting from the solidification of rotating liquid in the air, (2) aerodynamically shaped tektites, i.e., splash form tektites showing evidence of atmospheric ablation (pits, grooves, flanged button) shapes corresponding to a partial melting as they were ejected outside Earth's atmosphere (e.g., Koeberl, 1994), and (3) Muong Nong (or layered) tektites, mainly found in Asia and displaying a blocky shape and layered vesicular texture (Glass, 1990; Koeberl, 1992). The impact origin of tektites has been confirmed following detailed geochemical and petrographic investigations (e.g., Koeberl and Shirey, 1993). One of the main characteristics of tektites is their very low abundance of water (<300 ppm) and more generally volatiles (Osinski et al., 2013, and references therein). These investigations allow to discriminate between volcanic (e.g., obsidian) and impact glass, such as, for example, the Cali glass (found in Colombia), which was confirmed to be of volcanic origin (rhyolitic obsidian with at least 0.4 wt.% H_2O), rather than formed in an impact event (see details in Ferrière et al., 2021). In some cases, tektites may also contain relict mineral clasts (shocked and unshocked, e.g., quartz, zircon, rutile, chromite, etc.), spherules, as well as lechatelierite inclusions, coesite, baddeleyite (a high temperature breakdown product from zircon), etc. (e.g., Chao, 1963; Glass 1990, and references therein).

A microkrystite is defined as a "microtektite-like spherule containing quenched crystals usually of clinopyroxene and spinel; probably derived from condensation of impact rock vapour" (Stöffler and Grieve, 2007). They have been found in marine sediments and are associated with iridium and other siderophile element anomalies (e.g., Glass, 1990; Stöffler and Grieve, 2007).
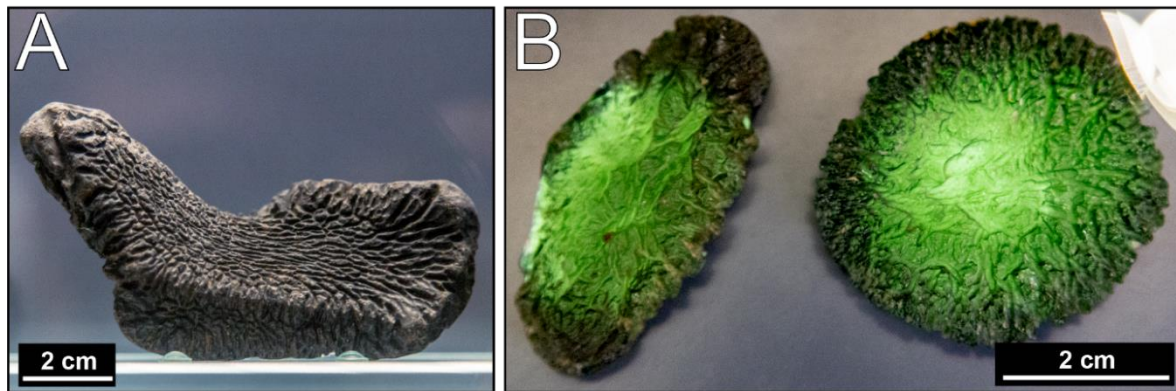
Figure 2.7. *Macrophotographs of tektites. A) Black tektite from the Australasian tektite strewn field. B) Greenish tektites from the Central European tektite strewn field, also known as "moldavites". Samples on display at the NHMV, Austria.*

Currently, four tektite strewn fields have been identified around the globe (for details, see, e.g., O'Keefe, 1963; Glass, 1990, and references therein): (1) the Australasian strewn field, with an age of ~0.79–0.80 Ma and for which still no source impact structure is known for sure (Glass and Koeberl, 2006), (2) the Central European tektites associated with the Ries impact structure (Germany), (3) the Ivory Coast tektites, which are associated with the Bosumtwi impact crater (Ghana), and (4) the North American tektites associated with the Cheseapeake Bay impact structure (USA) (e.g., Koeberl, 1994). Two new possible tektites strewn field have been recently proposed, in Uruguay and in Belize, respectively. The Uruguaite tektites, named after their place of occurrence (i.e., Uruguay), are found within a strewn field of at least 230 km in the longest dimension (Ferrière et al., 2017, 2019). No source impact structure is known at present (Ferrière et al., 2019). The glass field in Belize have a limited extension (<30 km). Detailed petrographic and geochemical investigations of recovered Belize glasses provided several lines of evidence for an impact origin, sharing similarities with known tektites (e.g., (Koeberl and Schulz, 2016; Koeberl et al., 2022). The recovered glasses share some characteristics with known tektites, e.g., presence of lechatelierite (see section 2.2.5), low water contents of ~82–133 ppm, reduced iron oxidation states (Koeberl and Schulz, 2016; Koeberl et al. 2022). Geochemical and isotopic data suggest a close relationship between Belize glasses and arc lavas from Guatemala and Honduras, with a different source from the Australasian tektites (according to Cr, Co, and Ni abundances, Sr–Nd isotope signatures, and also ^{10}Be concentrations), with the admixture of a minor, meteoritic component in some samples (indicated by elevated Ir contents up to 145 ppt, and near-chondritic Pt/Ir and ^{187}Os/^{188}Os ratios), and may indicate that the glasses were not transported far from their source (Koeberl et al., 2022). Chromium isotope data also show a contamination of the glass by ordinary chondrite material (Rochette et al., 2021). It has been suggested that the source is the 14 km-diameter Pantasma structure of proposed impact origin located in Nicaragua (Rochette et al., 2021). However, further investigations are needed to investigate any relation between the Pantasma structure and the glass field in Belize.

2.1.2.2. Air fall beds

An air fall bed, also termed "impactoclastic air fall bed" to make the distinction with the air fall beds describing the pyroclastic debris or ash layers, is defined as a "pelitic sedimentary layer containing a certain fraction of shock-metamorphosed material, e.g., shocked minerals and melt particles (e.g., spherules), which has been ejected from an impact crater and deposited by interaction with the atmosphere over large regions of a planet or globally" (Stöffler and Grieve, 2007). Impactoclastic air fall beds can be found in marine and in terrestrial environments (Stöffler et al., 2018). The Cretaceous–Paleogene (K–Pg) boundary, associated with the Chicxulub impact event, represents one of the best examples of impactoclastic air fall bed (see, e.g., Kring, 2007; and Chapter 3 for details).

2.2. Shock metamorphism features

2.2.1. Shatter cones

Shatter cones constitute the only macroscopic shock-metamorphic feature (i.e., diagnostic evidence of an hypervelocity impact event) that is visible directly with the naked eye at the hand specimen or outcrop scale (e.g., Dietz, 1960, 1968; French, 1998; French and Koeberl, 2010; Baratoux and Reimold, 2016). Shatter cones consist of conical to curviplanar striated fractures, forming partial to (more rarely) complete cones (see Fig. 2.8; French, 1998). They are best-developed in fine-grained lithologies (e.g., limestone, Fig. 2.8A), and generally more poorly developed in coarse-grained, crystalline, lithologies, e.g., granite, gneiss (Ferrière and Osinski, 2013). At the microscopic scale, planar fractures (PFs) and planar deformation features (PDFs) may be observed in minerals (e.g., Wieland et al., 2006; Ferrière and Osinski, 2010).

Shatter cones are generally found within the central uplifts, or below the floor of complex impact structures, and more rarely as clasts in impact breccias (e.g., Haughton impact structure, Canada; Osinski and Spray, 2006). Studying the distribution of (in situ) shatter cones at an impact site has been used as a parameter to estimate the minimal original size of the structure, especially in the case of old and eroded impact structures (Ferrière and Osinski, 2013; Osinski and Ferrière, 2016). Recent field mapping work by Osinski and Ferrière (2016) at Haughton and Tunnunik impact structures (Canada), combined with literature data for other impact structures, have allowed them to determine a relationship, $D_{SC} = 0.4\ D_a$ (where D_{SC} is the maximum spatial extent of shatter cones, and D_a the apparent crater diameter), which can be used to estimate the apparent (minimum) diameter of eroded complex impact structures on Earth.
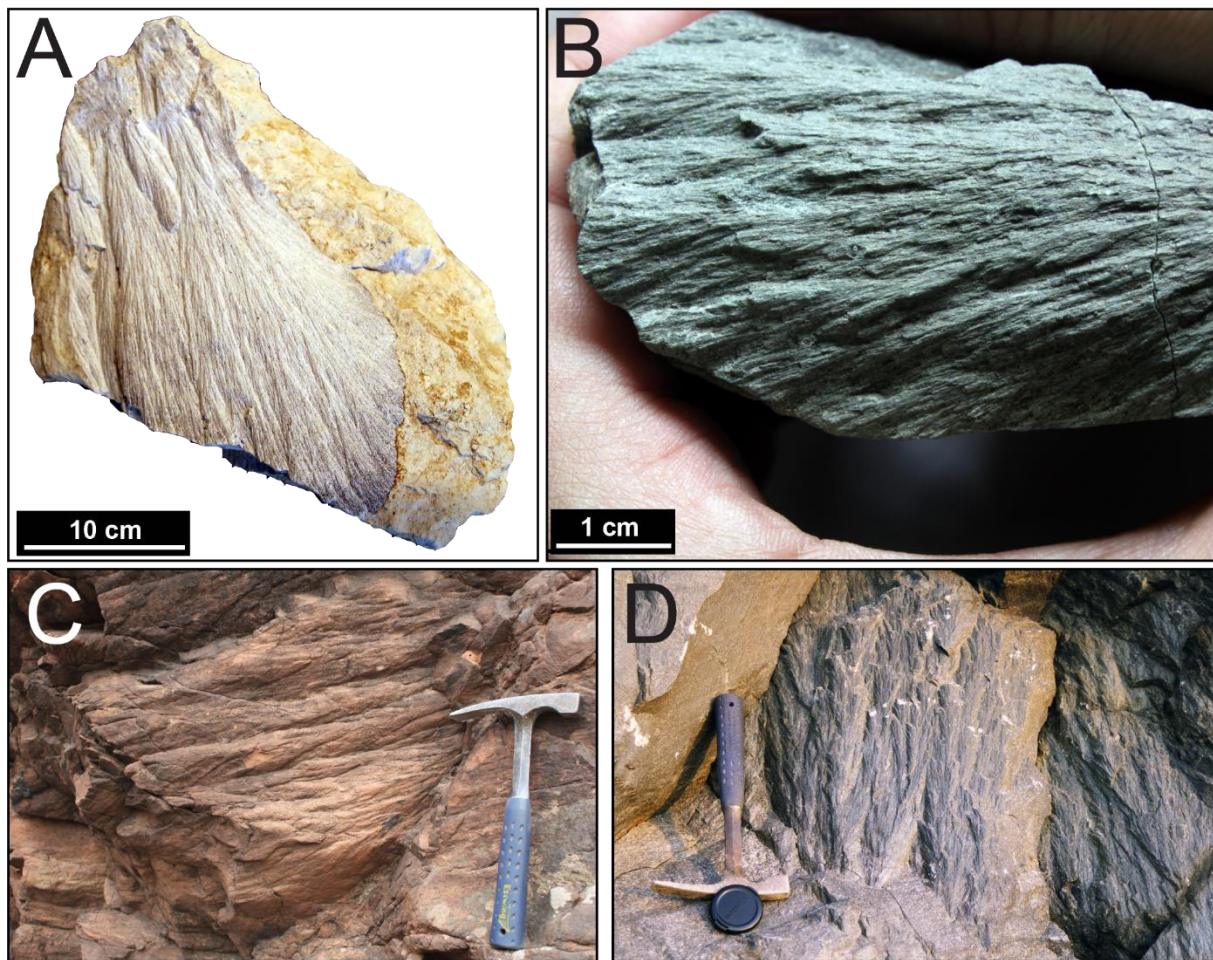
Figure 2.8. *Macrophotographs of shatter cones. A) Typical shatter cone formed in limestone from the Steinheim impact structure, Germany. Sample on display at the Ries Crater Museum, Nördlingen, Germany. B) Shatter cone in an amphibolite clast embedded within suevite from the Chicxulub impact structure peak ring (M0077A drill core, 708.5 meters below seafloor; photograph courtesy of L. Ferrière). C) Outcrop showing shatter cones in arkosic sandstone from the Luizi impact structure, Democratic Republic of the Congo. Hammer is 27 cm in length (photograph courtesy of L. Ferrière). D) Shatter cones in sandstone outcrop from the Sudbury impact structure, Canada. Hammer is 27 cm in length (photograph courtesy of L. Ferrière).*

The formation process of shatter cones has been extensively discussed, and several models were proposed (see, e.g., Dietz, 1960; Johnson and Talbot, 1964; Gash, 1971; Milton, 1977; Sagy et al., 2002, 2004; Baratoux and Melosh, 2003; Wieland et al., 2006; Osinski and Ferrière, 2016; Kenkmann et al., 2016). The most recent hypotheses, which are broadly consistent with observations, suggest that shatter cones formed due to tensional stresses generated by the scattering of the shock wave when it passes through heterogeneities within the target rocks (Johnson and Talbot, 1964). These heterogeneities may constitute the initiation point of shatter cones formation (Baratoux and Melosh, 2003). Additionally, these tensional stresses seem to occur during the decay of the shock wave, but before the passage of the subsequent rarefaction wave initiating the transient crater excavation (Osinski and Ferrière, 2016). Finally, it was suggested that shatter cones may reduce the target rocks strength, enhancing the crater collapse (Osinski and Ferrière, 2016).

It is generally accepted that shatter cones start to form at relatively low shock pressures, i.e., at least ~2 GPa, but can also form at pressures up to ~30 GPa (Dietz, 1968; Milton, 1977). Thus, they can form in a large volume of target rocks, explaining that they played a significant role in the identification and confirmation of impact structures (French and Koeberl, 2010, and references therein). However, shatter cones may be confused with non-impact features such as cone-in-cone structures, ventifacts, or even slickenslides (see detailed discussion in French and Koeberl, 2010; Baratoux and Reimold, 2016).

2.2.2. Deformation features in quartz

Quartz is the most commonly investigated mineral used to confirm an impact structure or an impact ejecta, mainly due to its abundance (occurring in both crystalline and sedimentary rocks), its resistance to weathering/alteration, and its capacity to develop unique deformation features over a large range of shock pressures (Stöffler and Langenhorst, 1994; Grieve et al., 1996; French and Koeberl, 2010, and references therein). During shock compression, quartz develops irregular fractures (which are not diagnostic shock effects) and, at higher pressures, several types of planar microstructures (Fig. 2.9; Ferrière and Osinski, 2013). Mosaicism and changes in optical properties and density of quartz also occur. Two main types of planar microstructures can be identified in quartz: planar fractures (PFs), and planar deformation features (PDFs; e.g., French and Short, 1968; Engelhardt and Bertsch, 1969; Stöffler and Langenhorst, 1994; Grieve et al., 1996; French, 1998; Trepmann, 2008; French and Koeberl, 2010; Ferrière and Osinski, 2013). Because planar microstructures are controlled by crystallography, PFs and PDFs are oriented parallel to specific crystallographic planes. The Miller-Bravais indices are used to identify the planes within the crystal. In the case of quartz, which belongs to the hexagonal system, four numbers (*hkil*) are used, which represent the inverse plane intercepts along the a_1, a_2, a_3, and c axis, respectively (e.g., Bloss, 1971).
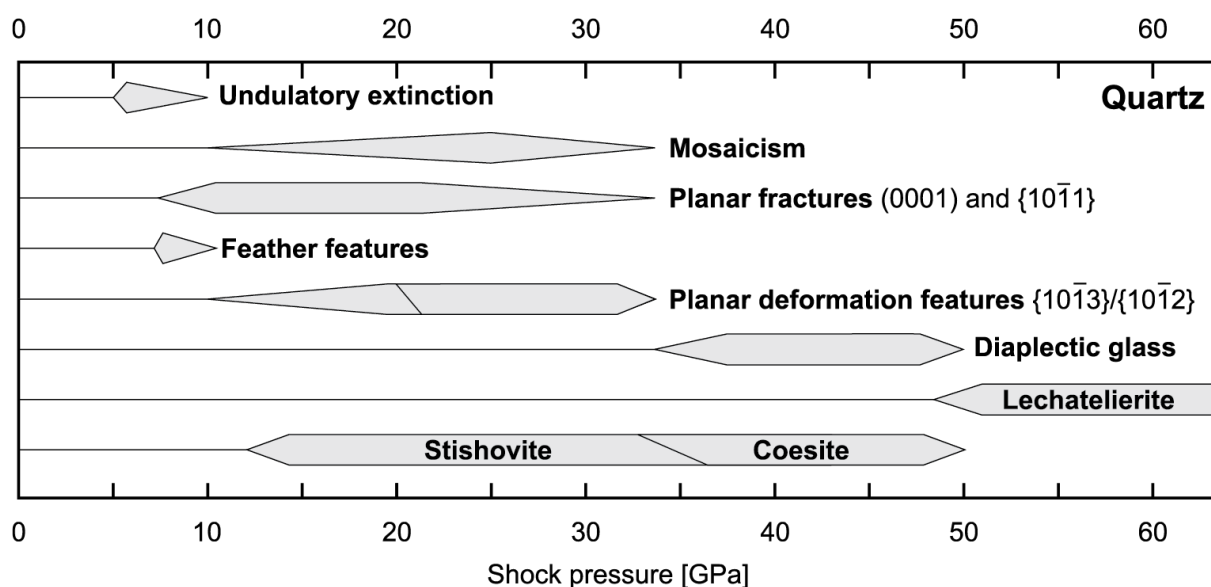
Figure 2.9. *The different shock effects occurring in quartz relative to the shock pressure (from Stöffler et al., 2018, and references therein).*

2.2.2.1. Planar fractures (PFs) and feather features (FFs)

Planar fractures are thin (typically ~3–10 µm wide) open fissures, generally with a spacing of ~15–20 µm or more from each other, and generally filled with secondary minerals (Fig. 2.10; e.g., Stöffler and Langenhorst, 1994; Grieve et al., 1996; French, 1998; French and Koeberl, 2010, and references therein). The PFs occur generally as multiple (2–3) sets (Stöffler and Langenhorst, 1994; French et al., 2004), and have been observed in both sedimentary and crystalline rocks from various impact structures (Ferrière and Osinski, 2013). Planar fractures are generally oriented parallel to planes with low Miller-Bravais indices, e.g., (0001) and $\{10\bar{1}1\}$, and more rarely to $\{10\bar{1}3\}$. It is suggested that PFs formation occur before the PDFs formation in quartz grain, as the occurrence of PFs controls/limits the development of adjacent PDF sets (e.g., Engelhardt and Bertsch, 1969; Stöffler and Langenhorst, 1994). As PFs form at relatively low shock pressures, between ~5–8 GPa, there are ongoing discussions over whether the presence of PFs can be considered as a unique impact structure diagnostic criteria (see discussions in French and Koeberl, 2010, and references therein), as they rarely occur in quartz grains from non-impact contexts (French, 1998).

In a number of impact structures, within both sedimentary and crystalline target rocks, it has been observed that narrowly spaced, short, parallel to subparallel lamellae branch off of PFs (Poelchau and Kenkmann, 2011; Fig. 2.10;). These planar microstructures are called "feather features" (FFs) and seem to be shock related (i.e., they have so far been found only in impactites), even their formation process is still poorly understood. The FFs are crystallographically controlled to a certain degree (Poelchau and Kenkmann, 2011). It has been suggested that they represent the development of incipient PDFs at low shock pressures (<10 GPa; French et al., 2004), while Poelchau and Kenkmann (2011) suggest that FFs are formed by the shearing of PFs during shock deformation, at assumed shock pressures of ~7 GPa.
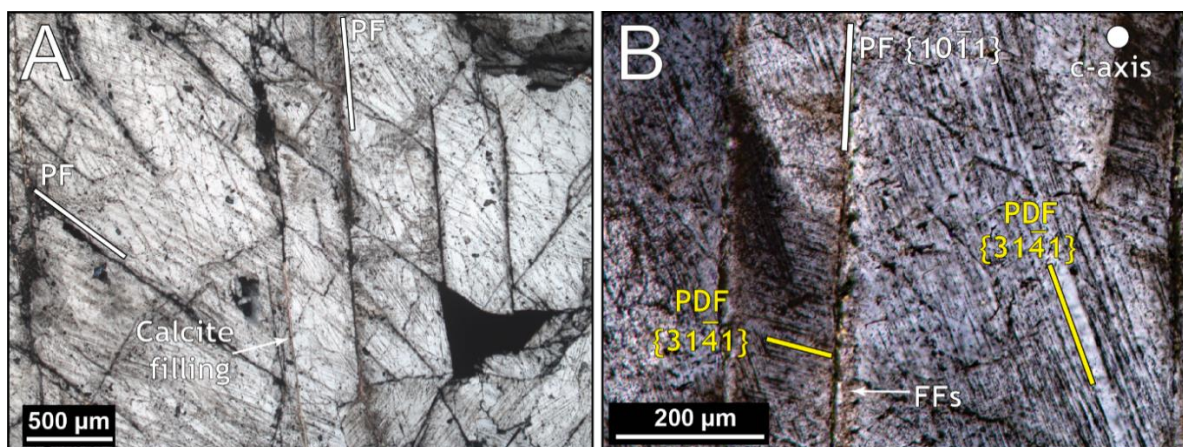
Figure 2.10. *Microphotographs (cross-polarized light [XPL]) of shocked quartz grains with planar fractures (PFs) from the Chicxulub impact structure peak ring, Mexico. Quartz grains are from granite rocks. A) Shocked quartz grain displaying two sets of PFs. On the bottom part the PFs are filled with secondary, post-impact calcite. Planar deformation features (PDFs) are also abundant. Sample 142R2_105–109, depth: 861.89 meters below seafloor. B) Detailed view of a shocked quartz grain having one set of PF associated with feather features (FFs). Two sets of PDFs are also visible with their crystallographic orientation relative to the quartz c-axis provided. Sample 97R3_10–12.5, depth: 752.54 meters below seafloor.*

2.2.2.2. Planar deformation features (PDFs)

Planar deformation features in quartz grains are largely accepted as one of the best criteria indicating the occurrence of high shock pressures, and, therefore, of a meteorite impact structure (French and Koeberl, 2010). Planar deformation features develop in quartz grains over a pressure range of ~8–10 to ~35 GPa (Stöffler and Langenhorst, 1994; French, 1998, and references therein), which is far higher than present in any other terrestrial processes occurring in crustal rocks. Compared to PFs, PDFs are not open fractures, but composed of narrow, straight, individual planar lamellae (usually less than 200 nm thick) of amorphous material, forming parallel sets spaced ~2–10 µm from each other (Fig. 2.11; e.g., Engelhardt and Bertsch, 1969; Stöffler, 1972; Stöffler and Langenhorst, 1994). Planar deformation features are generally observed as multiple sets per grain, parallel to more than one crystallographic orientation. Most commonly, PDFs are oriented parallel to planes with low Miller-Bravais indices, such as $\{10\bar{1}3\}$, $\{10\bar{1}2\}$, (0001), and $\{10\bar{1}4\}$ (e.g., Engelhardt and Bertsch, 1969; Stöffler and Langenhorst, 1994; Grieve et al., 1996; Ferrière et al., 2008, 2009a; French and Koeberl, 2010, Ferrière and Osinski, 2013, and references therein). In crystals showing a (strong) undulose extinction (under the optical microscope in cross-polarized light), due to a plastic deformation of the crystal lattice (e.g., Trepmann and Spray, 2005), the PDFs can look curved. In some rare cases, PDFs are associated with kinkbanding. The PDFs are in many cases more or less recrystallized, but they are still optically visible due to decoration of arrays of small fluid inclusions, usually less than 2 µm in diameter (Goltrant et al. 1992; Trepmann and Spray, 2006), easing their identification by means of optical microscopy. The decorations are formed following post-shock annealing and aqueous alteration of non-decorated, amorphous PDFs (e.g., Stöffler and Langenhorst, 1994; Grieve et al., 1996; Leroux, 2005).
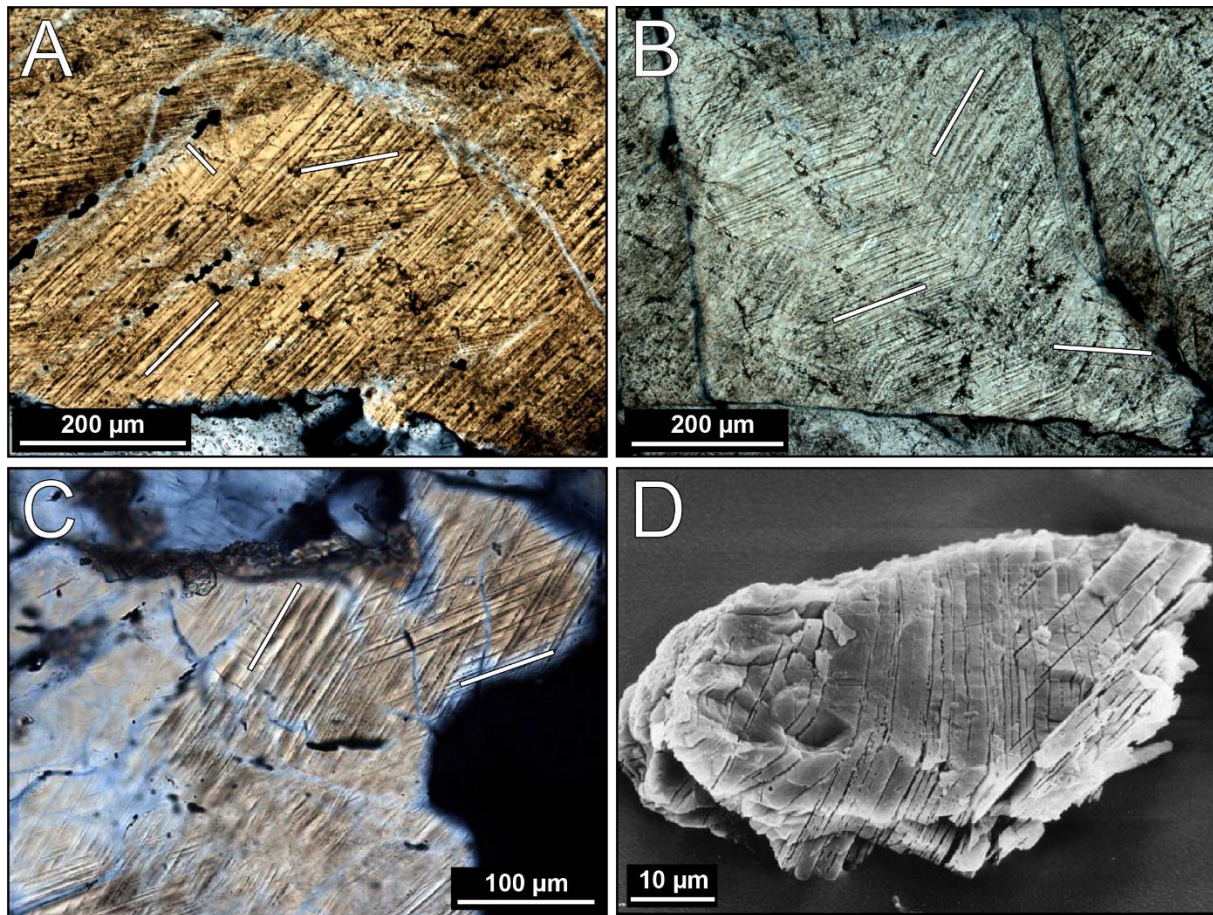
Figure 2.11. *Microphotographs (XPL) of shocked quartz grains with PDFs (A–C), and secondary electron microscope image (D). PDF orientations are highlighted by white bars. A) Shocked quartz grain with two prominent decorated PDF sets and a third set of PDFs that is barely visible. Granite from the Chicxulub impact structure peak ring (sample 201R1_70–74, depth: 1022.19 meters below seafloor [mbsf]). B) Shocked quartz grain from the Chicxulub peak ring granite having three sets of decorated PDFs (sample 300R1_78–79.5, depth: 1323.07 mbsf). C) Shocked quartz grain with two PDF sets, relatively non-decorated, from a quartzite clast within suevite from the Bosumtwi impact structure (~10.5 km diameter), Ghana (microphotograph courtesy of L. Ferrière). D) Acid-etched shocked quartz grain showing two PDF sets. The acid dissolved the amorphous material constituting the PDFs, making the PDFs visible. Sample from a K–Pg boundary layer (Deep Sea Drilling Project site 596) from the South Pacific (from French and Koeberl, 2010).*

Characterization of PDFs and measurement of their orientations can be performed using transmission electron microscopy (TEM) technique (e.g., Goltrant et al., 1991), or also the spindle stage (e.g., Bohor et al., 1987), when dealing with single quartz grains. Orientation of PDFs in a large number of grains in a given sample can only be done efficiently and easily, using routine universal stage measurements (see, e.g., Ferrière et al., 2009a). As specific PDF orientations in quartz form at given shock pressures (e.g., Hörz, 1968; Müller and Défourneaux, 1968; Huffman and Reimold, 1996), it is possible to estimate the shock pressure of a sample by assigning fixed values of pressures to each PDF orientation, then, to each quartz grain before making the average of all the grains (e.g., Robertson and Grieve, 1977; Grieve et al., 1990;

Dressler et al., 1998). The pressure range associated to specific PDF orientations was determined following experimental shock studies. For details and recommendations on the universal stage technique, as well as the limitation of this technique, see the universal stage method description in chapter 4, and investigation of shocked quartz grains from the Chicxulub peak ring granites in the publication in chapter 5, and also Ferrière et al. (2009a) and Holm-Alwmark et al. (2018).

The mechanism leading to PDFs formation is still discussed. It seems that their formation involves interactions between the shock wave and specific directions in the quartz crystal lattice (Brannon et al., 1983; Stöffler and Langenhorst, 1994; Trepmann, 2008). Additionally, the development of PDFs seems also constrained by several parameters, such as, the lithology, the porosity, the grain size, with, e.g., a PDF development favored in large quartz grains in sedimentary rocks (Grieve et al., 1996).

2.2.2.3. Mosaicism

A quartz grain displaying mosaicism, or mosaic structure, is characterized by an irregular, or "mottled" extinction pattern, distinct from the undulatory extinction (which is common in tectonically deformed quartz; Ferrière and Osinski, 2013). The mosaicism is caused by a plastic deformation (i.e., distortion) of the lattice into small domains that are rotated by low angles from each other (Ferrière and Osinski, 2013). Thus, the quartz grain is composed of several small sub-domains (also called subgrains) with slightly to significantly different orientation of the optical axis (e.g., Dachille et al., 1968 ; Stöffler, 1972 ; Stöffler and Langenhorst, 1994 ; French and Koeberl, 2010). Generally, mosaicism is associated with kinkbands (i.e., deformation bands ~<20 µm wide showing extinction directions different from the host mineral; e.g., French and Koeberl, 2010) and/or PFs and PDFs (e.g., Stöffler, 1972). Semi-quantitative characterization of mosaicism can be performed using X-ray diffraction study of the degree of asterism (i.e., the extent of elongation of initially sharp diffraction spots of lattice planes) in a single grain, and can further be used as an indicator of the shock pressure recorded by the quartz grain (e.g., Hörz and Quaide, 1973). However, this correlation cannot be correct if the investigated minerals where subjected to secondary thermal metamorphism (Stöffler, 1972). Mosaic textures can also be produced by endogenic processes (e.g., Spry, 1969), even if it is suggested that high shock pressures (≥10 GPa) mosaicism is generally more pronounced (Dachille et al., 1968). Therefore, it cannot be recognized as a definitive diagnostic feature of shock metamorphism.

2.2.2.4. Change in optical properties and density

Extensive investigations were made on the optical properties of quartz, e.g., refractivity and birefringence (e.g., Stöffler, 1974; Stöffler and Langenhorst, 1994). These studies have shown that, with increasing shock pressure, both the refractive index and birefringence decrease, until reaching the amorphous state (i.e., diaplectic glass, see section 2.2.4). Similarly, when shock pressures reach 25 to 35 GPa, and depending on the pre-shock temperature, and also depending of the shock wave direction relative to the c-axis, the density of quartz decreases

from the normal value of 2.650±0.002 to values as low as 2.280±0.002 g.cm^{-3} (Langenhorst and Deutsch, 1994).

2.2.3. Deformation features in other minerals

Shock-induced deformation not only occur in quartz, but also in all minerals, with a high dependence on the crystal structure and on the mineral composition (e.g., Stöffler, 1972; Langenhorst, 2002). Commonly, two main categories of shock-induced microstructures are identified (Fig. 2.12), i.e., planar microstructures (PFs and PDFs) and deformation bands (kinkbands and mechanical twins). Mosaicism was also documented in minerals other than quartz, such as olivine and pyroxene (e.g., Reimold and Stöffler, 1978; Bauer, 1979; Rubin et al., 1997). Compared to quartz in terrestrial impactites, and olivine in meteorites (Reimold and Stöffler, 1978; Bauer, 1979; Stöffler et al., 1991; Bischoff and Stöffler, 1992; Schmitt, 2000, and references therein), shock features in other minerals have been relatively less investigated (but this is changing, see below). This is mainly due to the relative complexity of the shock features in other minerals, which are also less obvious and more challenging to characterize under the optical microscope, and/or because of the effects of post-impact (hydrothermal) alteration which may modify or erase these features (e.g., Ferrière and Osinski, 2013). Detailed review of shock pressure ranges of shock effects in different minerals is provided in Stöffler et al. (2018), and references therein.

In the case of terrestrial impactites, after quartz, shock features in feldspar represent probably the most often investigated object in the literature, with descriptions of fracturing, plastic deformations, PFs, and PDFs (sometimes decorated), in both alkali-feldspar and plagioclase (e.g., Chao, 1967; Stöffler, 1972; French, 1998; Stöffler et al., 2018, and references therein; Pittarello et al., 2020; Pickersgill et al., 2021). Planar deformation features have also been documented in olivine, pyroxene, amphibole, sillimanite, apatite, garnet, and zircon (e.g., Stöffler, 1972; French, 1998; Langenhorst, 2002; Wittmann et al., 2006; Stöffler et al., 2018, and references therein). As for quartz, PDFs in those minerals are oriented parallel to the main crystallographic planes of rock-forming minerals, but detailed investigations are scarce in the literature (Ferrière and Osinski, 2013). Planar fractures and PDFs have yet to be documented in carbonate or sulfate minerals (Ferrière and Osinski, 2013).

Shock metamorphic features in olivine have been largely investigated within shocked meteorite samples, where they are abundant (e.g., Stöffler et al., 1991). In contrast to quartz, the occurrence of PFs in olivine is considered as a criteria indicative of shock metamorphism, as they are oriented parallel to crystallographic planes different of the normal cleavage planes of olivine (Langenhorst, 2002).
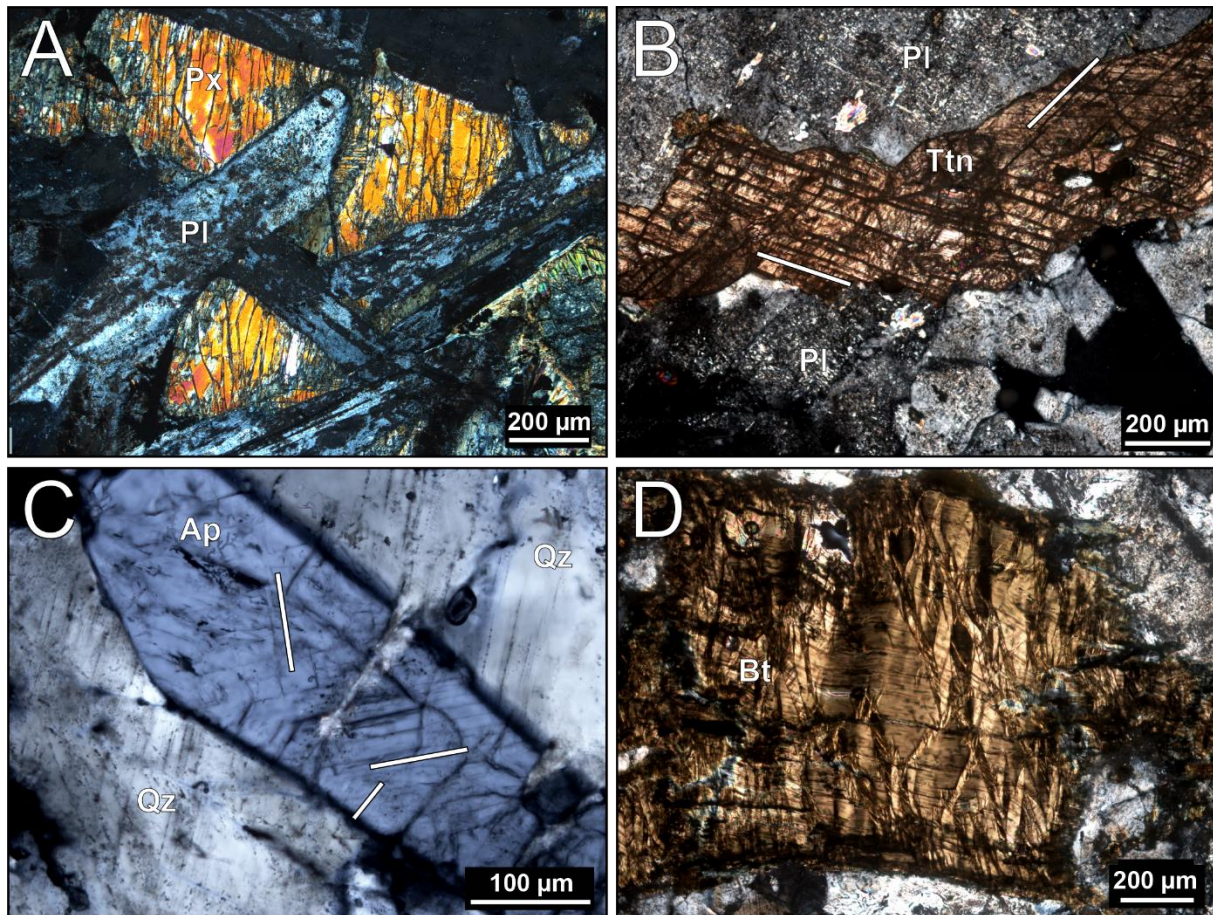
Figure 2.12. *Microphotographs (XPL) showing planar microstructures and deformation features in some minerals observed in shocked target rocks recovered during the drilling of the Chicxulub impact structure peak ring. A) Highly fractured pyroxenes (Px) showing one set of planar fractures, from a dolerite clast in impact melt rock. Plagioclase (Pl) crystals are strongly altered (sample 290R1_66–68, depth: 1291.95 mbsf). B) Titanite (Ttn) with well-developed shock-induced planar microstructures (at least two sets visible) next to strongly altered (sericitized) plagioclases (Pl; dacite sample 164R2_110–115, depth: 920.15 mbsf). C) Shocked apatite (Ap) showing two sets of planar microstructures, with a third one barely visible at the crystal rim. Quartz (Qz) is also shocked with one set of PDFs visible (granite sample 212R1_129–131.5, depth: 1056.01 mbsf). D) Large, well-developed kinkbands in biotite (Bt) (granite sample 183R1_20–23, depth: 969.84 mbsf).*

In the case of zircon grains, unique shock metamorphic effects only occur at pressures above 20 GPa (e.g., Bohor et al., 1993; Kamo et al., 1996; Wittmann et al., 2006; Timms et al., 2017). They include planar microdeformation features, e.g., pervasive micro-cleavage, dislocation patterns (Leroux et al., 1999), granular textures (e.g., Bohor et al., 1993; Gucsik et al., 2004; Wittmann et al., 2006), and "former reidite in granular neoblastic" (FRIGN) zircons (Cavosie et al., 2018; see section 2.2.6). For apatite, recent studies have described deformation bands and PFs with specific crystallographic orientations (Cox et al., 2020; Kenny et al., 2020).

Within mica minerals, e.g., muscovite and biotite, kinkbands are frequently observed (Fig. 2.12), but also in other minerals, such as graphite (Stöffler, 1972). Kinkbanding occurs preferentially in sheet silicates, without any specific orientation relative to the main

crystallographic planes (Ferrière and Osinski, 2013). Kinkbands are also commonly observed in non-shocked metamorphic rocks formed by tectonic processes (e.g., Spry, 1969; Vernon, 2004), and it is not possible to distinguish between shock-induced kinkbands, and those formed by endogenic processes. Therefore, kinkbanding in mica minerals cannot be considered as a diagnostic shock feature.

During shock metamorphism, mechanical twins can form and are observed in a large variety of minerals, e.g., pyroxene, amphibole, ilmenite, titanite, and also in plagioclase (but rarer). They occur as sets of parallel bands having width ranging from submicroscopic to ~10 µm (Stöffler, 1972). The mechanical twins are one of the few shock effects known to form in calcite (e.g., Langenhorst et al., 2002, and references therein). Although, low shear stresses of ~10 MPa is required to develop mechanical twins in calcite (Schedl, 2006), a high density of twins can be indicative of high differential stresses of several hundred MPa to 1 GPa (Seybold et al., 2022). Therefore, twinning may be used as shock indicator for low-shocked carbonate material but not as a diagnostic shock feature (Ferrière and Osinski, 2013).

2.2.4. Diaplectic mineral glasses

When shock pressures as high as about 35–50 GPa are reached in the case of non-porous crystalline rocks, minerals, especially quartz and feldspar, are converted into an amorphous, glassy phase without melting (i.e., by solid-state transformation), forming diaplectic glass (e.g., Stöffler, 1972; Stöffler and Langenhorst, 1994; French, 1998, and references therein). In the case of porous rocks (e.g., sandstones), diaplectic glass can start to form at pressures as low as ~5.5 GPa (Kieffer et al., 1976; see also Kowitz et al., 2013), and the complete conversion of quartz into diaplectic glass occurs at pressures between ~10 and 20 GPa, with the pressure limit for complete conversion decreasing with increasing pre-shock temperature (see Ferrière and Osinski, and references therein). Other minerals such as pyroxene or biotite, are generally oxidized and decomposed due to the high shock pressures, and do not form diaplectic glass (Ferrière and Osinski, 2013). Even after the formation of diaplectic glass, the original, pre-shock morphology and texture of the mineral is preserved, while flow structures or vesicles are absent (Stöffler and Langenhorst, 1994). Literature reports two types of diaplectic glasses, diaplectic quartz glass and diaplectic plagioclase glass (e.g., Milton and De Carli, 1963; Ferrière and Brandstaetter, 2015). Diaplectic glasses constitute another diagnostic criteria for shock metamorphism, however, as they are forming at relatively high pressures, which affected a smaller volume of target rocks, they are less abundant than shatter cones or PDFs in quartz grains (French and Koeberl, 2010). They occur either as shocked clasts in crater-fill impact breccias, or within the central uplift of large impact structure where the shock pressure was sufficient (French and Koeberl, 2010; and references therein). According to thermal annealing experiments, at temperatures above 1200 °C, diaplectic quartz glass starts to recrystallize, being replaced by ballen α-cristobalite (see section 2.2.6.2; Ferrière et al., 2009b).

2.2.5. Mineral and whole-rock melting

Shock pressures higher than 50 GPa will produce very high residual temperature after the passage of shock waves through target rock material, generally >1500 °C (Melosh, 1989).

Consequently, at 50 GPa, melting starts for individual minerals (Stöffler, 1972), while when shock pressures reach 60 GPa, the post-shock temperature is high enough to melt the whole rock, in the case of non-porous crystalline rocks (Osinski et al., 2013). In contrast, for sandstones, melting of quartz grains can start at pressures of ~20 GPa, and whole rock melting at ~30–35 GPa (Kieffer et al., 1976). The melts formed display a relatively similar composition compared to the original material. Impact melt can occur in various forms and settings (see Fig. 2.13, and details in sections 2.1.1.3, and 2.1.2.1; Dressler and Reimold, 2001; French and Koeberl, 2010; Osinski et al., 2013; Stöffler et al., 2018). Generally, alteration of impact glasses to secondary minerals, such as clay minerals, zeolites, and chalcedony, is common (e.g., Grieve and Therriault, 2013).
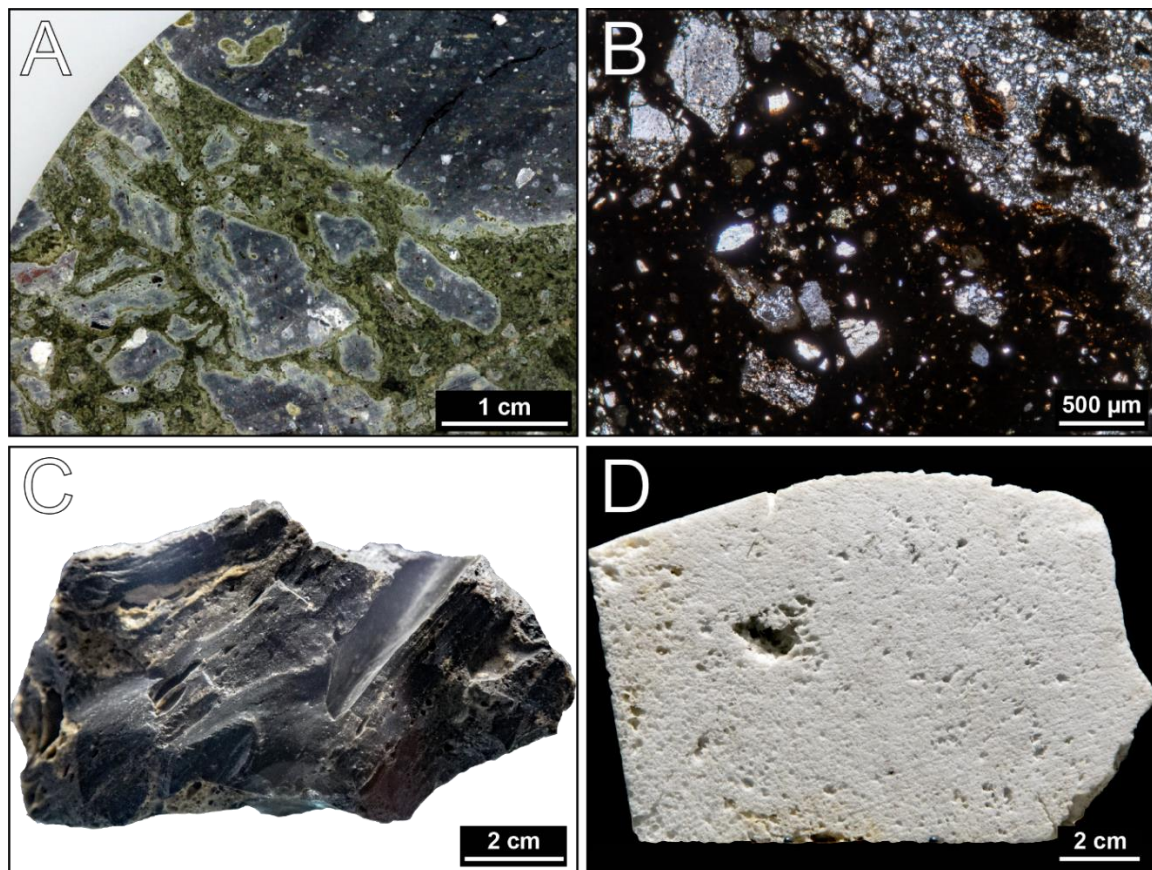
Figure 2.13. *Macrophotographs (A, C–D) and microphotograph (B, XPL) of impact melting products. A) Impact melt rock sample from the Chicxulub impact structure peak ring, representing a mingling (schlieren) between a relatively clast-poor, black impact melt rock and a green, Ca-rich and altered phase (sample 92R2_89–91.5, depth: 737.10 mbsf). B) Thin section of an impact melt rock from the Chicxulub, in contact with finely brecciated basement material (sample 303R3_22.5–25, depth: 1334.38 mbsf). C) Impact glass fragment from the ~14-km-diameter Zhamanshin impact structure, Kazakhstan. D) Lechatelierite (melted quartz sandstone) from Meteor Crater, United States. Samples C and D are on display at the NHMV, Austria.*

When the temperature is higher than 1750 °C, without necessarily requiring high shock pressures, a silica (SiO_2) melt is formed, the so-called lechatelierite (Fig. 2.13D), which can occur in glassy bodies as bands or schlieren. Lechatelierite is a common indicator of impact-

produced high temperatures, and occurs in impactites but also in fulgurites (Stöffler and Langenhorst, 1994; French and Koeberl, 2010). Other indicators of the occurrence of high temperature at the impact site are, e.g., baddeleyite (ZrO_2), which forms at ~1850 °C and is a decomposition product of zircon ($ZrSiO_4$; Wittmann et al., 2006), or the melting of titanite at ~1450 °C (French and Short, 1968).

2.2.6. High-pressure mineral phases (polymorphs)

In addition to the formation of shock microstructures in minerals, the passage of high pressure shock waves through the target rocks can transform minerals into phases that are normally stable in high static pressure domains which correspond to the lower crust or mantle. The presence of these high-pressure mineral phases (or polymorphs) at the surface, or near-surface of a circular structure can be used as a diagnostic criteria to confirm its impact origin, but with some care as they are not unique to shock metamorphism (French and Koeberl, 2010). High pressure mineral phases are commonly found in impactites (e.g., Stöffler, 1972), such as coesite and stishovite (from quartz), reidite (from zircon), diamond (from graphite), TiO_2-II and akaogiite (from rutile; El Goresy et al., 2001a; El Goresy et al., 2010). In general, high pressure polymorphs of minerals described in thin or thick sections cannot be directly identified with certainty by using uniquely optical microscopy (e.g., unlike the identification of PDFs in quartz). To verify the exact nature of the mineral, several techniques can be used, such as, X-ray diffraction, TEM, electron backscatter diffraction (EBSD), and/or Raman spectroscopy (Fig. 2.14; French and Koeberl, 2010, and references therein).
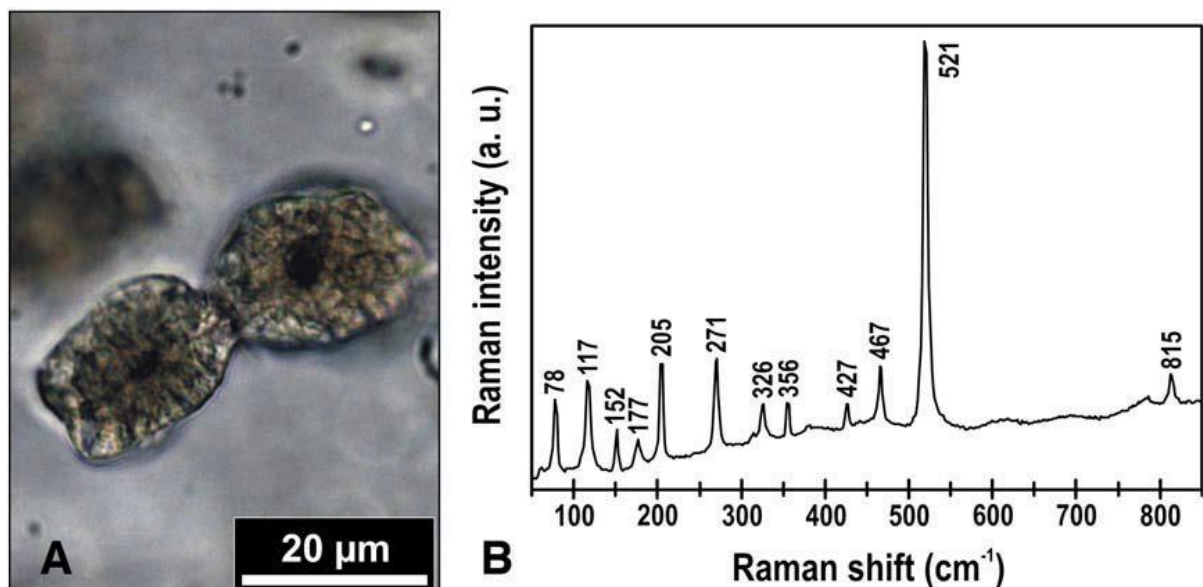
Figure 2.14. *A) Microphotograph (PPL) of two coesite aggregates within diaplectic quartz glass from suevite sampled outside the crater rim of the Bosumtwi impact structure (Ghana). B) MicroRaman spectrum of (A), typical of coesite. (microphotograph and spectrum courtesy of L. Ferrière).*

Coesite and stishovite, the high-pressure polymorphs of quartz, form and are metastably preserved in non-porous crystalline target rocks that experienced shock pressure ranges

between 30–60 GPa, and 12–45 GPa, respectively (e.g., Stöffler and Langenhorst, 1994). In sedimentary rocks, coesite can start to form at shock pressures of ~5.5 GPa, and is common above 10 GPa (Kieffer et al., 1976). The two polymorphs generally form within diaplectic glass found in impactites (Fig. 2.14), along grain boundaries, or associated with PDFs (Stöffler, 1971; Kieffer et al., 1976; Stähle et al., 2008). Coesite has been identified in the form of small aggregates (up to 200 µm in size) in several impact structures, such as at Meteor Crater, United States (Chao et al., 1960), the Ries, Germany (Shoemaker and Chao, 1961), Bosumtwi, Ghana (Littler et al., 1961), and Haughton, Canada (Osinski, 2007). Stishovite was identified at Meteor Crater, Vredefort, and the Ries, with its occurrence used (coupled with coesite) to confirm the impact origin of the Ries crater (Shoemaker and Chao, 1961).

Some care should be taken in the use of high pressure polymorphs of quartz (and also impact diamonds) in order to confirm the impact origin of a structure, especially by considering the geological context of the investigated samples (French and Koeberl, 2010). Under static high pressures, coesite starts to form at ~2 GPa, and stishovite at ~7–8 GPa (Heaney et al., 1994, and references therein). Coesite has been commonly observed in non-impact environments, e.g., within kimberlites or ultra-high-pressure metamorphic rocks (French and Koeberl, 2010, and references therein), while post-stishovite phases are found within the basaltic layer of subducting slabs (Liu et al., 2007). Excepted in very specific contexts, such as in diamonds (Wirth et al., 2007), stishovite have only been found in meteorites and impactite rocks (e.g., Gillet et al., 2007). Therefore, by looking at the rock paragenesis and the geological context, coesite formed in an impact event can easily be identified (e.g., French and Koeberl, 2010; Ferrière and Osinski, 2013, and references therein).

Upon shock compression (shock pressures of ~30–40 GPa; El Goresy et al., 2001b), graphite occurring in target rocks can be transformed into diamonds. Terrestrial impact diamonds were discovered for the first time at the Popigai impact structure, Russia (Masaitis et al., 1972) and later at the Ries, Germany (Rost et al., 1978), and then at some other impact structures (El Goresy et al., 2001b, and references therein). These diamonds inherited some features of the former graphite and are defect-rich (e.g., Koeberl et al., 1997). Further discussion regarding impact diamond formation can be found in e.g., Ferrière and Osinski (2013).

When zircon is exposed to shock pressures of ~20 GPa, it starts to be transformed to the high pressure polymorph reidite, by solid-state transformation (Reid and Ringwood, 1969; Fiske et al., 1994). The first identification of reidite in impactites was in zircon from the upper Eocene impact ejecta layer (Glass et al., 2002). Reidite was then found in impactites from the Ries impact structure (Gucsik et al., 2004) and then in a dozen of other impact structures (see, e.g., Plan et al., 2021). As reidite is refractory, it can survive temperatures of up to ~1000 °C (Fiske et al., 1994), and it is also resistant to alteration, thus, it can be used to estimate shock pressures experienced by a given impactite sample (Glass et al., 2002). When temperature reaches more than ~1100 °C, reidite is reverted back to granular-textured zircon (Wittmann et al., 2006, and references therein). These granular zircons, also termed as neoblasts, were recently investigated and classified as FRIGN zircons (see Cavosie et al., 2018, and references therein). Cavosie et al. (2018) investigated FRIGN zircons found within impact melt rocks from Luizi (Democratic Republic of the Congo), and in glass from the Pantasma (Nicaragua) impact structures. The measured crystallographic orientations of the neoblasts relative to the adjacent domains allowed Cavosie et al. (2018) to conclude that these orientations can only be produced

by the transformation of reidite back to neoblastic zircon, under high pressure (≥ 30 GPa) and temperature (≥ 1673 °C) conditions. Therefore, FRIGN zircon is considered a unique diagnostic shock metamorphism indicator. It was found in the last few years in a number of other impact structures, including Meteor Crater, Acraman (Australia), Chicxulub, Rochechouart (France), Mien (Sweden), Mistastin Lake (Canada), etc.

2.2.6. Post-shock features

2.2.6.1. Toasted quartz

Toasted quartz is a term which describe quartz grains showing an aspect similar to "toasted bread", with an orange-brown to grayish-reddish brown appearance (Fig. 2.15). Detailed investigations were made on toasted quartz grains by Short and Gold (1996), and Whitehead et al. (2002), and have been commonly observed in many impact structures in both crystalline and sedimentary target rocks.
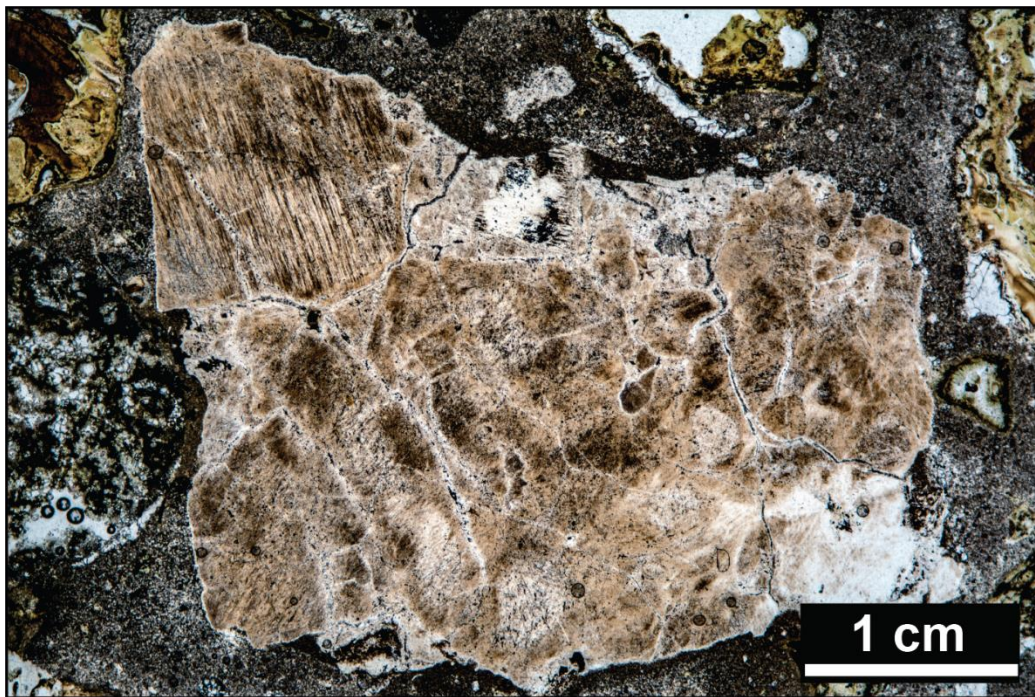
Figure 2.15. *Microphotograph (XPL) of a relatively large toasted polycrystalline quartz grain within suevite from the Chicxulub impact structure peak ring (sample 49R1_64–66.5, depth: 644.33 mbsf). One decorated set of PDFs if visible on the upper left of the crystal.*

Toasted quartz is described as a post-shock feature (Short and Gold, 1996). Two main mechanisms have been proposed to explain the formation of toasted quartz grains, i.e., (1) by "hydrothermal and other post-shock modifications" according to Short and Gold (1996), and (2) by the "exsolution of water from glass, primarily along PDFs, during heat-driven recrystallization" (Whitehead et al., 2002). The browning occurring in toasted quartz grains does not seem to be related to modifications of the chemical composition, but rather due to the presence of a high amount of tiny fluid inclusions, mainly located along decorated PDFs (Whitehead et al., 2002). A subsequent study by Ferrière et al. (2009c) confirmed the high

abundance of small fluid inclusions. However, Ferrière et al. (2009c) suggested that rather than being related to the recrystallization of PDF glass, toasted quartz grains more likely formed by vesiculation after pressure release, at high post-shock temperatures, representing the beginning of quartz breakdown due to heating. More investigations would be needed in order to better constrain the formation processes of toasted quartz grains in impactites.

2.2.6.2. Ballen quartz and cristobalite

Ballen silica is observed in impactites, as independent clasts mostly within impact melt rocks and, rarely, suevite, within diaplectic quartz glass or lechatelierite inclusions, and displays either an α-quartz or α-cristobalite structure (Ferrière et al., 2009b). It is worth noting that ballen silica has only been observed within impactites formed in completely crystalline target rocks (e.g., Carstens, 1975; Grieve, 1975; Bischoff and Stöffler, 1984; Ferrière et al., 2009c; Ferrière et al., 2010); or in impactites derived from crystalline lithologies in crystalline-sedimentary target rocks (e.g., the Ries impact structure; Ferrière et al., 2010; Trepmann et al., 2020). Ballen are described as more or less spheroidal bodies of ~8–215 µm in diameter, intersecting or penetrating each other (Fig. 2.16; Ferrière et al., 2009b, 2010). Ballen silica textures were described in several studies (Carstens, 1975; Bischoff and Stöffler, 1984) and then, classified (Ferrière et al., 2009b), i.e., from type I (α-cristobalite ballen with homogeneous extinction) to type V (chert-like recrystallized ballen quartz). Two processes have been proposed to explain the formation of ballen silica (Ferrière et al., 2009b): (1) solid state transformation of α-quartz into diaplectic quartz glass during the passage of high pressure shock waves, then, formation of ballen of β-cristobalite and/or β-quartz at high temperature, and back transformation to α-cristobalite and/or α-quartz; or (2) high temperature melting transforming quartz into lechatelierite, followed by nucleation and crystal growth. As ballen silica results from back-transformation from shock-induced states, it is only an indirect evidence of shock metamorphism, and, thus, cannot be used as a diagnostic criterion. More information and discussions on ballen silica can be found in Ferrière et al. (2009b, 2010).
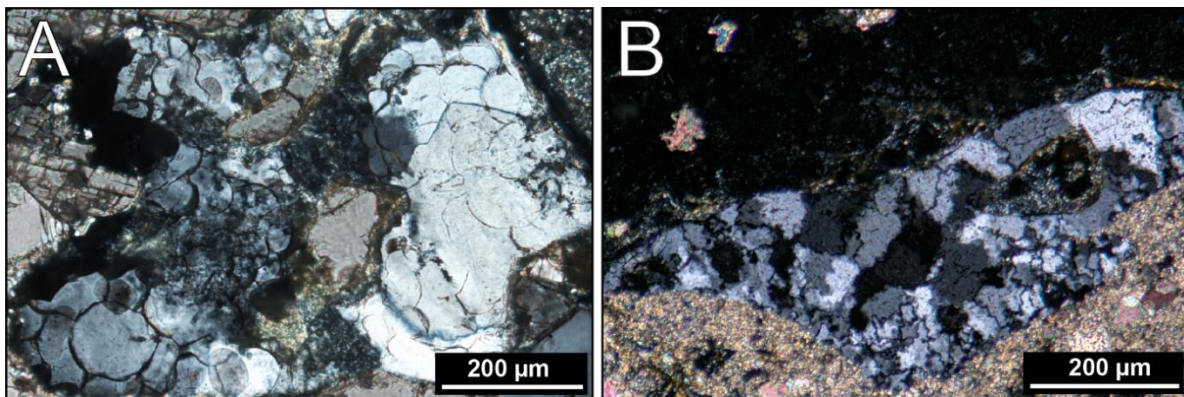
Figure 2.16. *Microphotographs (XPL) of ballen silica in suevite samples from the Chicxulub impact structure peak ring. A) Relatively spherical ballen silica either of type I (α-cristobalite) or II (α-quartz), displaying homogeneous extinction (sample 81R1_67–69, depth: 708.01 mbsf). B) Ballen quartz of type V, recognizable by its chert-like texture, completely recrystallized (sample 41R1_106–108, depth: 620.35 mbsf).*

2.3. Preservation of the impactor

2.3.1. Chemical and isotopic signatures from a meteoritic component

In most cases, the projectile does not survive to the impact event and is completely melted and/or vaporized (see Chapter 1). However, a fraction of this melted/vaporized projectile material can be incorporated within impactites during the impact crater formation, mostly into impact melt rocks (French and Koeberl, 2010; Goderis et al., 2013a). This projectile (meteoritic) component can be detected and in some cases its relative abundance quantified, even after geological periods of time, by searching for distinct geochemical and/or isotopic signatures in impactites. This provides a reliable evidence for the occurrence of an impact event (e.g., see reviews in Koeberl, 1998; Tagle and Hecht, 2006; Koeberl, 2014). Similarly, incorporation of meteoritic material can occur within distal ejecta, and the same geochemical and isotopic signatures can be used to confirm the impact origin of glassy bodies, and more broadly, of an impact ejecta layer deposited at significant distance from the source crater. The best example accounting for this process, are the well-known distal ejecta distributed worldwide at K–Pg boundary sites (for details, see Chapter 3; Alvarez et al., 1980; Smit and Hertogen, 1980; Claeys et al., 2002; Goderis et al., 2013b). During an impact event, dilution of the projectile material occurs, following mixing with a large volume of target rocks that is orders of magnitude higher than the projectile. Consequently, the meteoritic contribution within the crater impactites is relatively small, generally much less than 1 wt.% (Koeberl, 1998; French and Koeberl, 2010; Goderis et al., 2013a). Additionally, due to this high dilution of the projectile material, its distribution within the impact melt rocks is often heterogeneous compared to the relative homogeneous composition in major (and some trace) elements (Grieve et al., 1977; Koeberl, 2014, and references therein). However, higher values can rarely be recorded, with, for example, meteoritic contributions in impact melt rocks of up to ~5 wt.% within Morokweng, South Africa (McDonald et al., 2001; Koeberl and Reimold, 2003), and up to ~8 wt.% within East Clearwater, Canada (Grieve et al., 1980).

	Cr	Co	Ni	Re	Os	Ir	Ru	Pt	Pd	$^{187}Os/^{188}Os$
Chondrites	2575–3810	452–2360	9581–51750	-	364–2850	336–2635	522–4120	707–1596	500–964	-
CI-chondrites	2796	521	10863	36.6	450	418	627	872	567	0.1260
Primitive upper mantle	2645	105	1985	0.35	3.90	3.50	7.00	7.60	7.10	0.1296
Continental crust	126–185	24–29	56–105	0.20	0.03	0.02	0.21	0.51	0.52	1.4

Table 2.1. *Average moderately and highly siderophile element abundances (in ppm for Cr, Co, and Ni; in ppb for Re, Os, Ir, Ru, Pt, and Pd), and Os isotopic signatures of chondritic meteorites, CI-chondrites meteorites, primitive upper mantle, and continental crust. Importantly, the continental crust is strongly depleted in siderophile elements and has more radiogenic $^{187}Os/^{188}Os$ ratio relative to chondritic meteorites, and also to the upper mantle. Data for chondrites are from Tagle and Berlin (2008), and Fischer-Gödde et al. (2010); for primitive upper mantle from Meisel et al. (2001), Becker et al. (2006), and Lubetskaya and Korenaga (2007); for continental crust from Taylor and McLennan (1985), and Peucker-Ehrenbrink and Jahn (2001).*

In order to detect these rather low amount of projectile material, two main approaches are use, i.e., to detect elevated concentrations of moderately (e.g., Cr, Co, and Ni) and highly siderophile elements (Ru, Rh, Pd, Re, Os, Ir, Pt, and Au; HSEs), and to identify atypical isotopic ratios compared to the target rocks (see Figs. 2.17, 2.18; French and Koeberl, 2010; Goderis et al., 2013a). Those elements are typically enriched in several classes of meteorites relative to the typical terrestrial crustal rocks (Table 2.1; Taylor and McLennan, 1985). In particular, analysis of Ir concentrations is used as a first approach in order to identify a possible meteoritic component in impactite samples in a number of impact structures, as Ir can be relatively easily measured using instrumental neutron activation analysis (INAA) method (details on the method provided in chapter 4), compared to other HSEs (e.g., Morgan et al., 1975; Palme et al., 1978, 1979; Schmidt et al., 1997). The Ir content analyses have also established the impact origin (by detecting a "positive Ir anomaly") of the K–Pg boundary layer (Alvarez et al., 1980). Then, the development of inductively coupled plasma mass spectrometry (ICP-MS) have made possible the simultaneous measurement of all HSE abundances (e.g., McDonald et al., 2001; Norman et al., 2002; Tagle and Claeys, 2005; Lee et al., 2006). However, these elements have very low concentrations (generally on the order of ppb, or even ppt, with 1 ppb = 10^{-9} g.g^{-1}, and 1 ppt = 10^{-12} g.g^{-1}) in typical crustal rock samples (Fig. 2.17 and Table 2.1), thus, careful sample selection, preparation, and analysis are essential to obtain reliable results (see details in chapter 4; also, French and Koeberl, 2010). Generally, Ir contents of 1–2 ppb in impactites strongly support the incorporation of meteoritic material. The confirmation can be made if the other HSE abundances show a meteoritic (e.g., chondritic) distribution pattern, rather than a terrestrial (crustal) one (Fig. 2.17; French and Koeberl, 2010; Koeberl, 1998, 2014).
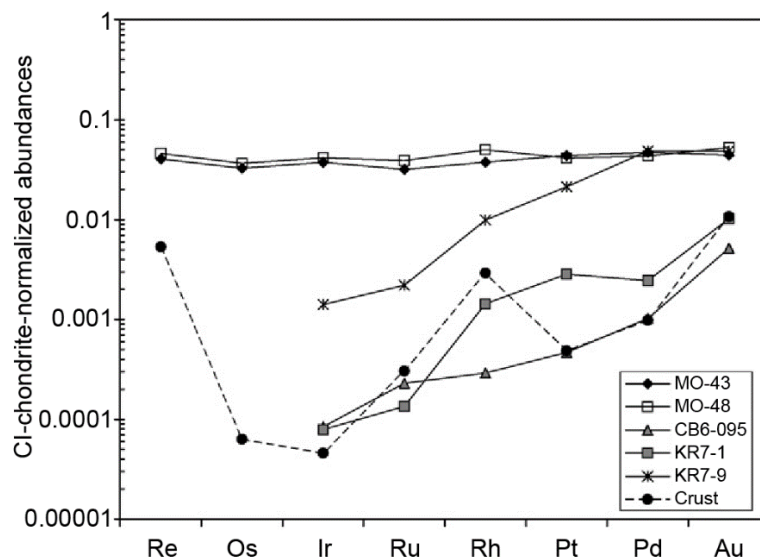
Figure 2.17. *CI-chondrite-normalized HSE abundances in some impactites samples, i.e., impact melt rocks from the Morokweng impact structure, South Africa (MO-43 and MO-48), suevite from the Chesapeake Bay impact structure, United States (CB6-095), and a lithic breccia and a suevite from the Bosumtwi impact structure, Ghana (KR7-1 and KR7-9, respectively). The average composition of the continental crust is also reported. The Morokweng impact melt rocks, which show flat abundance patterns, are clearly enriched in HSEs compared to the continental crust, indicating the presence of a significant (several percent) meteoritic component (from French and Koeberl, 2010, and references therein).*
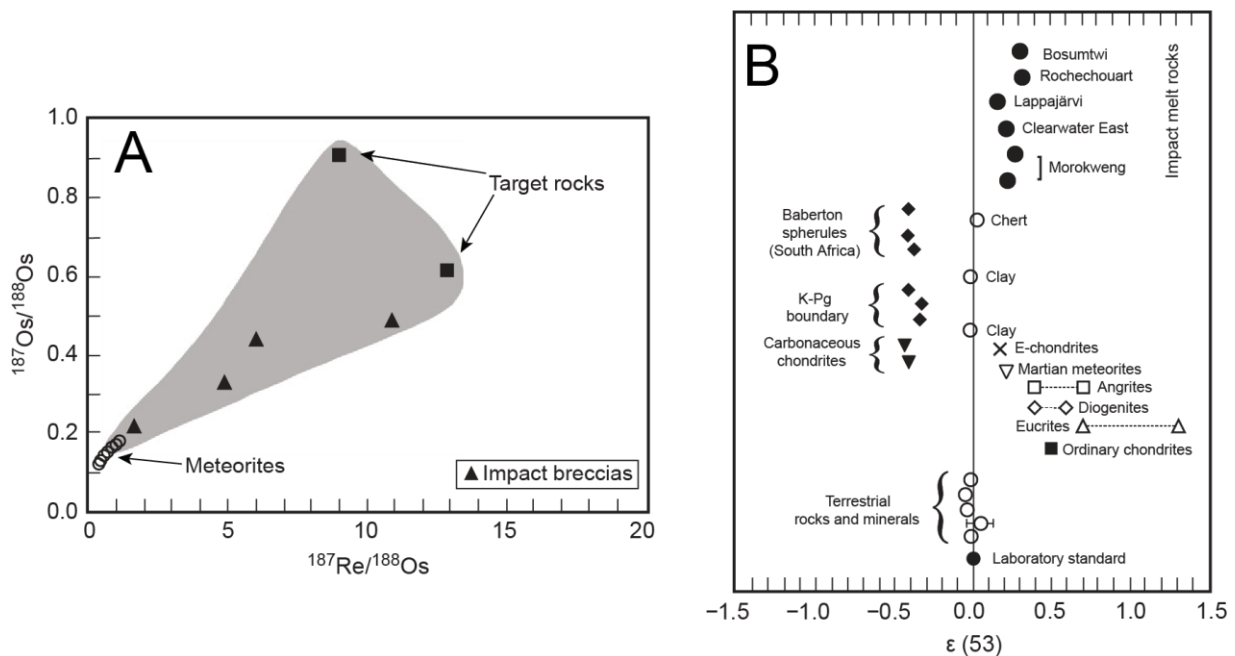
Figure 2.18. *A) Rhenium–Os isotopic diagram with the compositions of target rocks (squares) and impact breccias (triangles) from the Kalkkop impact structure (South Africa) (see Koeberl, 2014, for references). The meteorite Os isotopic compositions are also given (open circles), and highlight a mixing which occurred in the impact breccias between the target rock and a meteoritic component. B) Diagram showing the Cr isotopic composition of samples from various origins, including K–Pg boundary ejecta, and impact melt rocks from different impact structures (references in Koeberl, 2014). Meteoritic admixture is indicated when the sample composition plots outside the terrestrial line. The impactor type can, therefore, be identified, e.g., for the K–Pg boundary and the Archean spherules of Barberton (a carbonaceous chondrite impactor) and for the impact melts rocks (in most cases an ordinary chondrite impactor). Additional investigations using other systematics can still be necessary to confirm the impactor type. Modified from Koeberl (2014).*

Meteoritic material shows also isotopic signatures distinct from terrestrial crustal values (Fig. 2.18). Isotopic measurements performed by thermal ionization mass spectrometry (TIMS) or multi-collector (MC)-ICP-MS allow to quantify, even in the case of very minor admixture of meteoritic material to the impactites (see chapter 4 for a review of sample preparation, and method description). The Os (Koeberl and Shirey, 1993; Koeberl et al., 1996; Lee et al., 2006: Koeberl, 2014, and references therein), and Cr isotopes (Shukolyukov and Lugmair, 1998; Shukolyukov et al., 1999; Koeberl et al., 2007; Koeberl, 2014, and references therein) are the most common isotope systematic used for the determination of an impactor component (Fig. 2.18). Determining $^{187}Os/^{188}Os$ isotope ratios offers a sensitive and powerful tool which allows to detect very low (e.g., ~0.01%) amounts of meteoritic contribution to continental-crustal lithologies. In order to identify the impactor type, $^{53}Cr/^{52}Cr$, and $^{54}Cr/^{52}Cr$ isotope ratios can be measured, allowing to discriminate between carbonaceous and other chondrites, and, in some cases, whenever possible, even between different types of chondrites (see also, e.g., Goderis et al., 2013a; Koeberl, 2014, and references therein). Further discrimination of the projectile type can be made using HSE elemental ratios (e.g., Palme et al., 1981; Koeberl, 1998, 2014; Goderis

et al., 2013b). However, the large variety of possible impactors, with numerous subtypes, makes their type determination not straightforward, with important variations in HSE compositions. For example, achondritic projectiles have lower abundances of the HSEs compared to chondritic and iron meteoritic composition, and generally requires additional analysis (Goderis et al., 2013a).

Investigating the HSE abundances, as well as Os and Cr isotopic signatures in impactites is not sufficient to confirm the presence of a meteoritic component. A representative suite of the target rocks (i.e., if possible not affected by the impact) contributing to the impactites have to be analyzed in order to exclude any terrestrial-derived HSE or isotopic contributions. Several terrestrial rocks, especially when mantle-derived, may contain significant amount of HSEs, e.g., ≤10 ppb for ultramafic rocks, and, if present and involved during the impact cratering process, may imitate (or mask) a meteoritic component in the resulting impact melt rocks (e.g., Palme et al., 1981; Koeberl, 1998, 2014; French and Koeberl, 2010).

2.3.2. Preserved meteorite fragments

As previously stated, almost all the projectile is melted/vaporized during an impact event. The occurrence of preserved, solid meteorite fragments associated with an impact structure is extremely rare (French and Koeberl, 2010). Additionally, even if meteorite fragments survive the impact, it is not likely that they survive over long geological timescales, as they are rather quickly affected by weathering. Estimates of survival ages for meteorites exposed to the terrestrial environment do not exceed few million years (Zolensky, 1998; Bland, 2001), and are often below 50 ka (e.g., Jull, 2001).
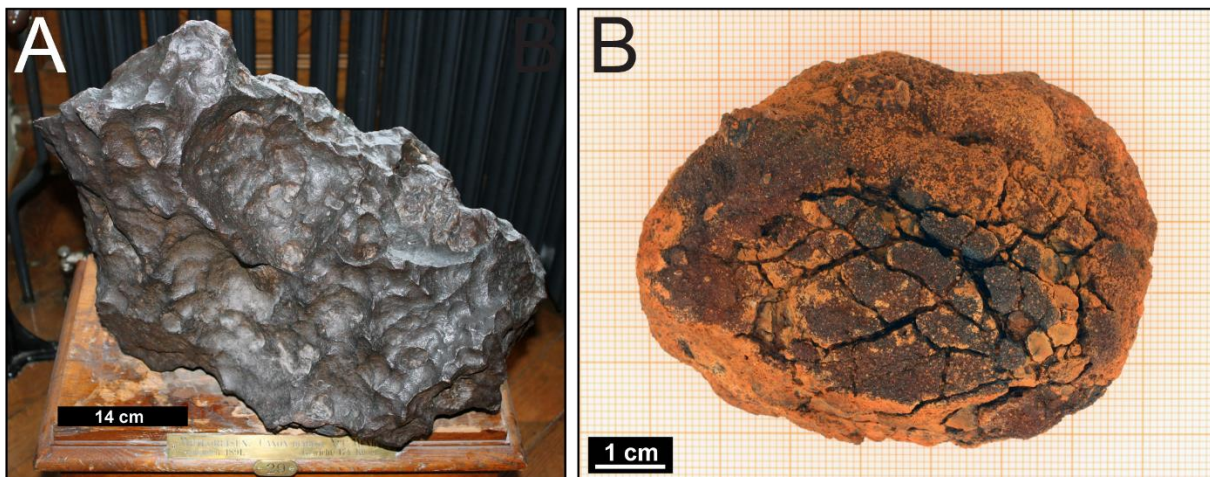
Figure 2.19. *Preserved iron meteorite fragments found in the ejecta blanket of impact structures. A) Canyon Diablo iron (IAB-MG) meteorite fragment (174 kg), found at the Meteor Crater, Arizona, United States, on display at the NHMV (photograph courtesy of L. Ferrière). B) Fragment of the Wolf Creek iron (IIIAB) meteorite (167.5 g) found in the Wolfe Creek crater, Australia (photograph courtesy of L. Ferrière).*

Projectile fragments tend to be found at the youngest impact structures, which are also the smallest ones (i.e., less than 1.5 km in diameter). Small iron meteoroids are more likely to

survive the passage through the atmosphere and collide the terrestrial crust with enough kinetic energy to create a hypervelocity impact structure (Melosh, 1989). Indeed, iron meteorite fragments have been found in several young impact structures (Fig. 2.19) such as at the Meteor Crater in Arizona, United States (49.2 ± 1.7 ka; Nishiizumi et al., 1991), Henbury, Australia (4.2 ± 1.9 ka; Storzer and Wagner, 1977), and Wolfe Creek, Australia (120 ± 9 ka; Barrows et al., 2019), indicating that these iron meteorite fragments can be recovered up to hundreds of thousands of years after the impact. Thus, confirming the impact origin of a structure using the association with preserved meteorite fragment(s) can only be made in the case of relatively recent impact structures, and is not suitable for old, deeply eroded impact structures (see discussions in French and Koeberl, 2010; Goderis et al., 2013a).

In case projectile fragments are protected from alteration, they can survive for extended periods of time within the impactites. For example, a 2.5 mm-diameter (fossil) carbonaceous chondritic meteorite was recovered within K–Pg boundary marine sediments recovered in the Pacific Ocean, and is most likely a fragment of the Chicxulub impactor (Kyte, 1998). Similarly, a large (25 cm), unaltered, chondritic meteorite fragment and several smaller fragments (Maier et al., 2006) were recovered in impact melt rocks from a drill core sampling within the Morokweng impact structure (South Africa, 146.06 ± 0.16 Ma; Kenny et al., 2021). However, this kind of discovery does not constitute a rule, and the aforementioned geochemical tools need to be used to characterize the meteorite type.

References

Alvarez L. W., Alvarez W., Asaro F., and Michel H. V. 1980. Extraterrestrial cause for the Cretaceous-Tertiary extinction. *Science* 208:1095–1108. https://doi.org/10.1126/science.208.4448.1095.

Artemieva N., Wünnemann K., Krien F., Reimold W. U., and Stöffler D. 2013. Ries crater and suevite revisited—Observations and modeling, Part II: Modeling. *Meteoritics & Planetary Science* 48:590–627. https://doi.org/10.1111/maps.12085.

Baratoux D. and Melosh H. J. 2003. The formation of shatter cones by shock wave interference during impacting. *Earth and Planetary Science Letters* 216:43–54. https://doi.org/10.1016/S0012-821X(03)00474-6.

Baratoux D. and Reimold W. U. 2016. The current state of knowledge about shatter cones: Introduction to the special issue. *Meteoritics & Planetary Science* 51:1389–1434. https://doi.org/10.1111/maps.12678.

Barrows T. T., Magee J., Miller G., and Fifield L. K. 2019. The age of Wolfe Creek meteorite crater (*Kandimalal*), Western Australia. *Meteoritics & Planetary Science* 54:2686–2697. https://doi.org/10.1111/maps.13378.

Bauer J. F. 1979 Experimental shock metamorphism of mono and polycrystalline olivine: a comparative study. In *Proceedings of the 10th Lunar and Planetary Science Conference, Houston, Texas, March 19–23, 1979, Volume 3*. Pergamon Press Inc., New York, New York. pp. 2573–2596. https://adsabs.harvard.edu/full/1979LPSC...10.2573B.

Becker H., Horan M. F., Walker R. J., Gao S., Lorand J.-P., and Rudnick R. L. 2006. Highly siderophile element composition of the Earth's primitive upper mantle: Constraints from new data on peridotite massifs and xenoliths. *Geochimica et Cosmochimica Acta 70:4528–4550.* https://doi.org/10.1016/j.gca.2006.06.004.

Bischoff A. and Stöffler D. 1984. Chemical and structural changes induced by thermal annealing of shocked feldspar inclusions in impact melt rocks from Lappajärvi crater, Finland. *Proceedings of the 14th Lunar and Planetary Science Conference, Houston, Texas, March 14– 18, 1983, Journal of Geophysical Research, Supplement* 89:B645–B656. https://adsabs.harvard.edu/full/1984LPSC...14..645B.

Bischoff A. and Stöffler D. 1992. Shock metamorphism as a fundamental process in the evolution of planetary bodies: information from meteorites. *European Journal of Mineralogy* 4:707–755.

Bland P. A. 2001. Quantification of meteorite infall rates from accumulations in deserts, and meteorite accumulations on Mars. In *Accretion of Extraterrestrial Matter throughout Earth's History*, edited by B. Peucker-Ehrenbrink and B. Schmitz, and B. Kluwer. Academic/Plenum Publishers, New York, New York. pp. 267–303. https://doi.org/10.1007/978-1-4419-8694-8_15.

Bloss F. D. 1971. *Crystallography and crystal chemistry: an introduction*. Holt, Rinehart, and Winston, New York, New York. 545 p.

Bohor B. F., Modreski P. J., and Foord E.E. 1987. Shocked quartz in the Cretaceous–Tertiary boundary clays: evidence for a global distribution. *Science* 236:705–708. https://doi.org/10.1126/science.236.4802.705.

Bohor B. F., Betterton W. J., and Krogh T. E. 1993. Impact-shocked zircons: discovery of shock-induced textures reflecting increasing degrees of shock metamorphism. *Earth and Planetary Science Letters* 119:419–424. https://doi.org/10.1016/0012-821X(93)90149-4.

Brannon P. J., Konrad C., Morris R. W., Jones E. D., and Asay J. R. 1983. Studies of the spectral and spatial characteristics of shock-induced luminescence from X-cut quartz. *Journal of Applied Physics* 54:6374–6381. https://doi.org/10.1063/1.331913.

Bryan W. B. 1972. Morphology of quench crystals in submarine basalts. *Journal of Geophysical Research* 77:5812–5819. https://doi.org/10.1029/JB077i029p05812.

Carstens H. 1975. Thermal history of impact melt rocks in the Fennoscandian Shield. *Contributions to Mineralogy and Petrology* 50:145–155.

Carter N. L. 1965. Basal quartz deformation lamellae — a criterion for recognition of impactites. *American Journal of Science* 263:786–806. https://doi.org/10.2475/ajs.263.9.786.

Carter N. L. 1968. Meteoritic impact and deformation of quartz. *Science* 160:526–528. https://doi.org/10.1126/science.160.3827.526.

Cavosie A. J. and Centeno L. 2014. Shocked Apatite from the Santa Fe Impact Structure (USA): a New Accessory Mineral for Studies of Shock Metamorphism (abstract). 45th Lunar and Planetary Science Conference, Abstract #1691. https://www.hou.usra.edu/meetings/lpsc2014/pdf/1691.pdf.

Cavosie A. J., Timms N. E., Ferrière L., and Rochette P. 2018. FRIGN zircon—The only terrestrial mineral diagnostic of high-pressure and high-temperature shock deformation. *Geology* 46:891–894. https://doi.org/10.1130/G45079.1.

Chao E. C. T. 1963. The petrographic and chemical characteristics of tektites. In *Tektites*, edited by J. A. O'Keefe. University of Chicago Press, Chicago, Illinois. pp. 51–94.

Chao E. C. T. 1967. Shock effects in certain rock-forming minerals. *Science* 156:192–202. https://doi.org/10.1126/science.156.3772.192.

Chao E. C. T., Shoemaker E. M, and Madsen B. M. 1960. First natural occurrence of coesite. *Science* 132:220–222. https://doi.org/10.1126/science.132.3421.220.

Claeys P., Kiessling W., and Alvarez W. 2002. Distribution of Chicxulub ejecta at the Cretaceous–Tertiary boundary. In *Catastrophic events and mass extinctions: impacts and beyond*, edited by C. Koeberl and K. G. MacLeod. Geological Society of America Special Paper #356. Geological Society of America, Boulder, Colorado. pp. 55–68. https://doi.org/10.1130/0-8137-2356-6.55.

Cox M. A., Erickson T. M., Schmieder M., Christoffersen R., Ross D. K., Cavosie A. J., Bland P. A., Kring D. A., and IODP–ICDP Expedition 364 Scientists. 2020. High-resolution microstructural and compositional analyses of shock deformed apatite from the peak ring of the Chicxulub impact crater. *Meteoritics & Planetary Science* 55:1715–1733. https://doi.org/10.1111/maps.13541.

Dachille F., Gigl P., and Simons P.Y. 1968. Experimental and analytical studies of crystalline damage useful for the recognition of impact structures. In *Shock metamorphism of natural materials*, edited by B. M. French and N. M. Short. Mono Book Corporation, Baltimore, Maryland. pp. 555–569.

Darling J. R., White L. F., Kizovski T., Černok A., Moser D. E., Tait K. T., Dunlop J., Langelier B., Douglas J. O., Zhao X., Franchi I. A., and Anand M. 2021. The shocking state of apatite and merrillite in shergottite Northwest Africa 5298 and extreme nanoscale chlorine isotope variability revealed by atom probe tomography. *Geochimica et Cosmochimica Acta* 293:422–437. https://doi.org/10.1016/j.gca.2020.11.007.

Dietz R. S. 1960. Meteorite impact suggested by shatter cones in rock. *Science* 131:1781–1784. https://www.jstor.org/stable/1705208.

Dietz R. S. 1968. Shatter cones in cryptoexplosion structures. In *Shock metamorphism of natural materials*, edited by B. M. French and N. M. Short. Mono Book Corporation, Baltimore, Maryland. pp. 267–285.

Donaldson C. H. 1976. An experimental investigation of olivine morphology. *Contributions to Mineralogy and Petrology* 57:187–213. https://doi.org/10.1007/BF00405225.

Dressler B. 1990. Shock metamorphic features and their zoning and orientation in the Precambrian rocks of the Manicouagan structure, Quebec, Canada. *Tectonophysics* 171:229–245. https://doi.org/10.1016/0040-1951(90)90101-D.

Dressler B. O. and Reimold W. U. 2001. Terrestrial impact melt rocks and glasses. *Earth Science Reviews* 56:205–284. https://doi.org/10.1016/S0012-8252(01)00064-2.

Dressler B. O., Sharpton V. L., and Schuraytz B. C. 1998. Shock metamorphism and shock barometry at a complex impact structure: State Islands, Canada. *Contributions to Mineralogy and Petrology* 130:275–287. https://doi.org/10.1007/s004100050365.

El Goresy A., Chen M., Dubrovinsky L., Gillet P., and Graup G. 2001a. An ultradense polymorph of rutile with seven-coordinated titanium from the Ries crater. *Science* 293:1467–1470. https://doi.org/10.1126/science.1062342.

El Goresy A., Gillet P., Chen M., Künstler F., Graup G., and Stähle V. 2001b. In situ discovery of shock-induced graphite–diamond phase transition in gneisses from the Ries crater, Germany. *American Mineralogist* 86:611–621. https://doi.org/10.2138/am-2001-5-603.

El Goresy A., Dubrovinsky L., Gillet P., Graup G., and Chen M. 2010. Akaogiite: an ultra-dense polymorph of TiO_2 with the baddeleyite-type structure, in shocked garnet gneiss from the Ries crater, Germany. *American Mineralogist* 95:892–895. https://doi.org/10.2138/am.2010.3425.

Engelhardt W. v. and Bertsch W. 1969. Shock induced planar deformation features in quartz from the Ries Crater, Germany. *Contributions to Mineralogy and Petrology* 20:203–234. https://doi.org/10.1007/BF00377477.

Ferrière L. 2008. *Shock metamorphism and geochemistry of impactites from the Bosumtwi impact structure: A case study of shock-induced deformations and transformations in quartz and associated methodology*. PhD thesis, University of Vienna, Austria. 279 p.

Ferrière L. and Brandstaetter F. 2015. What is maskelynite? Back to the original description and thin sections in which it was first described. 78th Annual Meeting of the Meteoritical Society, Abstract #5184. https://www.hou.usra.edu/meetings/metsoc2015/pdf/5184.pdf.

Ferrière L. and Osinski G. R. 2010. Occurrence and characterization of shocked quartz in shatter cones. *Meteoritics & Planetary Science* 45:A53. Abstract #5273. https://doi.org/10.1111/j.1945-5100.2010.01051.x.

Ferrière L. and Osinski G. R. 2013. Shock metamorphism. In *Impact Cratering: Processes and Products*, edited by G. R. Osinski and E. Pierazzo. Wiley-Blackwell, Hoboken, New Jersey. pp. 106–124.

Ferrière L., Koeberl C., and Reimold W. U. 2007. Drill core LB-08A, Bosumtwi impact structure, Ghana: petrographic and shock metamorphic studies of material from the central uplift. *Meteoritics & Planetary Science* 42:611–633. https://doi.org/10.1111/j.1945-5100.2007.tb01064.x.

Ferrière L., Koeberl C., Ivanov B. A., and Reimold W. U. 2008. Shock Metamorphism of Bosumtwi Impact Crater Rocks, Shock Attenuation, and Uplift Formation. *Science* 322:1678–1681. https://doi.org/10.1126/science.1166283.

Ferrière L., Morrow J. R., Amgaa T., and Koeberl C. 2009a. Systematic study of universal-stage measurements of planar deformation features in shocked quartz: implications for statistical significance and representation of results. *Meteoritics & Planetary Science* 44:925–940. https://doi.org/10.1111/j.1945-5100.2009.tb00778.x.

Ferrière L., Koeberl C., and Reimold W. U. 2009b. Characterization of ballen quartz and cristobalite in impact breccias: new observations and constraints on ballen formation. *European Journal of Mineralogy* 21:203–217. https://doi.org/10.1127/0935-1221/2009/0021-1898.

Ferrière L., Koeberl C., Reimold W.U, Hecht L., and Bartosova K. 2009c. The origin of 'toasted' quartz in impactites revisited. 40th Lunar and Planetary Science Conference, Abstract #1751. https://www.lpi.usra.edu/meetings/lpsc2009/pdf/1751.pdf.

Ferrière L., Koeberl C., Libowitzky E., Reimold W. U., Greshake A., and Brandstätter F. 2010. Ballen quartz and cristobalite in impactites: New investigations. In *Large Meteorite Impacts and Planetary Evolution IV*, edited by R. L. Gibson and W. U. Reimold. Geological Society of America Special Paper #465. Geological Society of America, Boulder, Colorado. pp. 609–618. https://doi.org/10.1130/2010.2465(29).

Ferrière L., Barrat J.-A., Giuli G., Koeberl C., Schulz T., Topa D., and Wegner W. 2017. A New Tektite Strewn Field Discovered in Uruguay. 80th Annual Meeting of the Meteoritical Society, Abstract #6195. https://www.hou.usra.edu/meetings/metsoc2017/pdf/6195.pdf.

Ferrière L., Meier M. M. M., Busemann H., Maden C., and Koeberl C. 2019. Investigation of the Noble Gas Content of the Uruguaite Tektites (abstract). Large Meteorite Impacts VI, Abstract #5115. https://www.hou.usra.edu/meetings/lmi2019/pdf/5115.pdf.

Ferrière L., Crósta A. P., Wegner W., Libowitzky E., Iwashita F., and Koeberl C. 2021. Distinguishing volcanic from impact glasses—The case of the Cali glass (Colombia). *Geology* 49:1421–1425. https://doi.org/10.1130/G48925.1.

Fischer-Gödde M., Becker H., and Wombacher F. 2010. Rhodium, gold and other highly siderophile element abundances in chondritic meteorites. *Geochimica et Cosmochimica Acta* 74:356–379. https://doi.org/10.1016/j.gca.2009.09.024.

Fiske P. S., Nellis W. J., and Sinha A. K. 1994. Shock-induced phase transitions of $ZrSiO_4$, reversion kinetics, and implications for terrestrial impact craters (abstract). *EOS, Transactions, American Geophysical Union* 75:416–417.

Floran R. J., Grieve R. A. F., Phinney W. C., Warner J. L., Simonds C. H., Blanchard D. P., and Dence M. R. 1978. Manicouagan impact melt, Quebec, 1, stratigraphy, petrology, and chemistry. *Journal of Geophysical Research: Solid Earth* 83:2737–2759. https://doi.org/10.1029/JB083iB06p02737.

French B. M. 1998. *Traces of catastrophe: A handbook of shock-metamorphic effects in terrestrial meteorite impact structures*. LPI Contribution #954. Houston, Texas: Lunar and Planetary Institute. 120 p. https://www.lpi.usra.edu/publications/books/CB-954/CB-954.intro.html.

French B. M. and Koeberl C. 2010. The convincing identification of terrestrial meteorite impact structures: What works, what doesn't, and why. *Earth-Science Reviews* 98:123–170. https://doi.org/10.1016/j.earscirev.2009.10.009.

French B. M. and Short N. M. 1968. *Shock Metamorphism of Natural Materials*. Baltimore: Mono Book Corporation. 644 p.

French B. M., Cordua W. S., and Plescia J. B. 2004. The Rock Elm meteorite impact structure, Wisconsin: geology and shock-metamorphic effects in quartz. *Geological Society of America Bulletin* 116:200–218. https://doi.org/10.1130/B25207.1

Gash P. J. S. 1971. Dynamic mechanism for the formation of shatter cones. *Nature* 230:32–35. https://doi.org/10.1038/physci230032a0.

Gillet P., El Goresy A., Beck P., and Chen M. 2007. High-pressure mineral assemblages in shocked meteorites and shocked terrestrial rocks: Mechanisms of phase transformations and constraints to pressure and temperature histories. In *Advances in High-Pressure Mineralogy*, edited by E. Ohtani. Geological Society of America Special Paper #421. Geological Society of America, Boulder, Colorado. pp. 57–82.

Glass B. P. 1990. Tektites and microtektites: key facts and inferences. *Tectonophysics* 171:393–404. https://doi.org/10.1016/0040-1951(90)90112-L.

Glass B. P. and Koeberl C. 2006. Australasian microtektites and associated impact ejecta in the South China Sea and the Middle Pleistocene supereruption of Toba. *Meteoritics & Planetary Science* 41:305–326. https://doi.org/10.1111/j.1945-5100.2006.tb00211.x.

Glass B. P., Liu S., and Leavens P. B. 2002. Reidite: an impact produced high-pressure polymorph of zircon found in marine sediments. *American Mineralogist* 87:562–565. https://doi.org/10.2138/am-2002-0420.

Goderis S., Paquay F., and Claeys P. 2013a. Projectile identification in terrestrial impact structures and ejecta material. In *Impact Cratering: Processes and Products*, edited by G. R. Osinski and E. Pierazzo. Wiley-Blackwell, Hoboken, New Jersey. pp. 223–239.

Goderis S., Tagle R., Belza J., Smit J., Montanari A., Vanhaecke F., Erzinger J., and Claeys P. 2013. Reevaluation of siderophile element abundances and across the Cretaceous–Paleogene (K–Pg) boundary: Implications for the nature of the projectile. *Geochimica et Cosmochimica Acta* 120:417–446. https://doi.org/10.1016/j.gca.2013.06.010.

Goltrant O., Cordier P., and Doukhan J.-C. 1991. Planar deformation features in shocked quartz: a transmission electron microscopy investigation. *Earth and Planetary Science Letters* 106:103–115. https://doi.org/10.1016/0012-821X(91)90066-Q.

Goltrant O., Leroux H., Doukhan J.-C., and Cordier P. 1992. Formation mechanisms of planar deformation features in naturally shocked quartz. *Physics of the Earth and Planetary Interiors* 74:219–240. https://doi.org/10.1016/0031-9201(92)90012-K.

Grieve R. A. F. 1975. Petrology and chemistry of the impact melt at Mistastin Lake crater, Labrador. *Geological Society of America Bulletin* 86:1617–1629. https://doi.org/10.1130/0016-7606(1975)86<1617:PACOTI>2.0.CO;2.

Grieve R. A. F. 1991. Terrestrial impact: the record in the rocks. *Meteoritics* 26:175–194. https://doi.org/10.1111/j.1945-5100.1991.tb01038.x.

Grieve R. A. F. and Therriault M. 2013. Impactites: their characteristics and spatial distribution. In *Impact Cratering: Processes and Products*, edited by G. R. Osinski and E. Pierazzo. Wiley-Blackwell, Hoboken, New Jersey. pp. 90–105.

Grieve R. A. F., Dence M. R., and Robertson P. B. 1977. Cratering process: as interpreted from the occurrence of impact melts. In *Impact and Explosion Cratering: Planetary and Terrestrial Implications*, edited by D. J. Roddy, R. O. Pepin, and R. B. Merrill, Pergamon Press, New York, New York. pp. 791–814. https://adsabs.harvard.edu/full/1977iecp.symp..791G.

Grieve R. A. F., Palme H., and Plant A. G. 1980. Siderophile-rich particles in the melt rocks at the E. Clearwater impact structure, Quebec: their characteristics and relationship to the impacting body. *Contributions to Mineralogy and Petrology* 75:187–198. https://doi.org/10.1007/BF01166759.

Grieve R. A. F., Coderre J. M., Robertson P. B., and Alexopoulos J. 1990. Microscopic planar deformation features in quartz of the Vredefort structure: anomalous but still suggestive of an impact origin. *Tectonophysics* 171:185–200. https://doi.org/10.1016/0040-1951(90)90098-S.

Grieve R. A. F., Langenhorst F., and Stöffler D. 1996. Shock metamorphism of quartz in nature and experiment: II. Significance in geoscience. *Meteoritics & Planetary Science* 31:6–35. https://doi.org/10.1111/j.1945-5100.1996.tb02049.x.

Gucsik A., Koeberl C., Brandstätter F., Libowitzky E., and Reimold W. U. 2004. Cathodoluminescence, electron microscopy, and Raman spectroscopy of experimentally shock metamorphosed zircon crystals and naturally shocked zircon from the Ries impact crater. In *Cratering in Marine Environments and on Ice*, edited by H. Dypvik, P. Claeys, and M. Burchell. Springer, Berlin, Germany. pp. 281–322. https://doi.org/10.1007/978-3-662-06423-8_15.

Heaney P. J., Prewitt C. T., and Gibbs G. V. 1994. *Silica: Physical Behavior, Geochemistry and Materials Applications.* Reviews in Mineralogy 29. Mineralogical Society of America, Washington, District Columbia. 606 p.

Holm-Alwmark S., Ferrière L., Alwmark C., and Poelchau M. H. 2018. Estimating average shock pressures recorded by impactite samples based on universal stage investigations of planar deformation features in quartz–Sources of error and recommendations. *Meteoritics & Planetary Science* 53:110–130. https://doi.org/10.1111/maps.13029.

Hörz F. 1968. Statistical measurements of deformation structures and refractive indices in experimentally shock loaded quartz. In *Shock metamorphism of natural materials*, edited by B. M. French and N. M. Short. Mono Book Corporation, Baltimore, Maryland. pp. 243–253.

Hörz F. and Quaide W. L. 1973 Debye–Scherrer investigations of experimentally shocked silicates. *The Moon* 6:45–82. https://doi.org/10.1007/BF02630652.

Huffman A. R. and Reimold W. U. 1996. Experimental constraints on shock-induced microstructures in naturally deformed silicates. *Tectonophysics* 256:165–217. https://doi.org/10.1016/0040-1951(95)00162-X.

Johnson G. P. and Talbot R. J. 1964. *A Theoretical Study of the Shock Wave Origin of Shatter Cones*, Thesis, Air Force Institute of Technology, Dayton, Ohio. 170 pp.

Jull A. J. T. 2001. Terrestrial ages of meteorites. In *Accretion of Extraterrestrial Matter throughout Earth's History*, edited by B. Peucker-Ehrenbrink and B. Schmitz, Kluwer Academic/Plenum Publishers, New York, New York. pp. 241–266. https://doi.org/10.1007/978-1-4419-8694-8_14

Kamo S. L., Reimold W. U., Krogh T. E., and Colliston W. P. 1996. A 2.023 Ga age for the Vredefort impact event and a first report of shock metamorphosed zircons in pseudotachylitic breccias and granophyre. *Earth and Planetary Science Letters* 144:369–387. https://doi.org/10.1016/S0012-821X(96)00180-X.

Kenkmann T., Hergarten S., Kuhn T., and Wilk J. 2016. Formation of shatter cones by symmetric fracture bifurcation: Phenomenological modeling and validation. *Meteoritics & Planetary Science* 51:1519–1533. https://doi.org/10.1111/maps.12677.

Kenny G. G., Morales L. F., Whitehouse M. J., Petrus J. A., and Kamber B. S. 2017. The formation of large neoblasts in shocked zircon and their utility in dating impacts. *Geology* 45:1003–1006. https://doi.org/10.1130/G39328.1.

Kenny G. G., Karlsson A., Schmieder M., Whitehouse M. J., Nemchin A. A., and Bellucci J. J. 2020. Recrystallization and chemical changes in apatite in response to hypervelocity impact. *Geology* 48:19–23. https://doi.org/10.1130/G46575.1.

Kenny G. G., Harrigan C. O., Schmitz M. D., Crowley J. L., Wall C. J., Andreoli M. A. G., Gibson R. L., and Maier W. D. 2021. Timescales of impact melt sheet crystallization and the precise age of the Morokweng impact structure, South Africa. *Earth and Planetary Science Letters* 567:117013. https://doi.org/10.1016/j.epsl.2021.117013.

Kieffer S. W. and Simonds C. H. 1980. The role of volatiles and lithology in the impact cratering process. *Reviews of Geophysics and Space Physics* 18:143–181. https://doi.org/10.1029/RG018i001p00143.

Kieffer S. W., Phakey P. P., and Christie J. M. 1976. Shock processes in porous quartzite: transmission electron microscope observations and theory. *Contributions to Mineralogy and Petrology* 59:41–93. https://doi.org/10.1007/BF00375110.

Koeberl C. 1992. Geochemistry and origin of Muong Nong-type tektites. *Geochimica et Cosmochimica Acta* 56:1033–1064. https://doi.org/10.1016/0016-7037(92)90046-L.

Koeberl C. 1994. Tektite origin by hypervelocity asteroidal or cometary impact: Target rocks, source craters, and mechanisms. In *Large Meteorite Impacts and Planetary Evolution*, edited by B. O. Dressler, R. A. F. Grieve, and V. L. Sharpton. Geological Society of America Special Paper #293. Geological Society of America, Boulder, Colorado. pp. 133–151.

Koeberl C. 1998. Identification of meteoritic component in impactites. In *Meteorites: Flux with Time and Impact Effects*, edited by M. M. Grady, R. Hutchison, G. J. H. McCall, and D. Rothery. Geological Society of London Special Publications #140. Geological Society, London, United Kingdom. pp. 133–153.

Koeberl C. 2002. Mineralogical and geochemical aspects of impact craters. *Mineralogical Magazine* 66:745–768. https://doi.org/10.1180/0026461026650059.

Koeberl C. 2014. The Geochemistry and Cosmochemistry of Impacts. In *Treatise on Geochemistry (Second Edition), Volume 2*, edited by H. D. Holland and K. K. Turekian. Elsevier, Amsterdam, Netherlands. pp. 73–118. https://doi.org/10.1016/B978-0-08-095975-7.00130-3.

Koeberl C. and Reimold W. U. 2003. Geochemistry and petrography of impact breccias and target rocks from the 145 Ma Morokweng impact structure, South Africa. *Geochimica et Cosmochimica Acta* 67:1837–1862. https://doi.org/10.1016/S0016-7037(02)00994-8.

Koeberl C. and Schulz T. 2016. Osmium isotopic investigation of tektite-like glasses from Belize (abstract). 47th Lunar and Planetary Science Conference, Abstract #1654. https://www.hou.usra.edu/meetings/lpsc2016/pdf/1654.pdf.

Koeberl C. and Shirey S. B. 1993. Detection of a meteoritic component in Ivory Coast tektites with rhenium-osmium isotopes. *Science* 261:595–598. https://doi.org/10.1126/science.261.5121.595.

Koeberl C., Reimold W. U., Shirey S. B. 1996. A Re–Os isotope and geochemical study of the Vredefort Granophyre: clues to the origin of the Vredefort structure, South Africa. *Geology* 24:913–916. https://doi.org/10.1130/0091-7613(1996)024<0913:ROIAGS>2.3.CO;2.

Koeberl C., Masaitis V. L., Shafranovsky G. I., Gilmour I., Langenhorst F., and Schrauder M. 1997. Diamonds from the Popigai impact structure, Russia. *Geology* 25:967–970. https://doi.org/10.1130/0091-7613(1997)025<0967:DFTPIS>2.3.CO;2.

Koeberl C., Shukolyukov A., and Lugmair G. W. 2007. Chromium isotopic studies of terrestrial impact craters: Identification of meteoritic components at Bosumtwi, Clearwater East, Lappajärvi, and Rochechouart. *Earth and Planetary Science Letters* 256:534–546. https://doi.org/10.1016/j.epsl.2007.02.008.

Koeberl C., Glass B. P., Schulz T., Wegner W., Giuli G., Cicconi M. R., Trapananti A., Stabile P., Cestelli-Guidi M., Park J., Herzog G. F., and Caffee M. W. 2022. Tektite glasses from Belize, Central America: Petrography, geochemistry, and search for a possible meteoritic component. *Geochimica et Cosmochimica Acta* 325:232–257. https://doi.org/10.1016/j.gca.2022.02.021.

Kowitz A., Schmitt R. T., Reimold W. U., and Hornemann U. 2013. The first MEMIN shock recovery experiments at low shock pressure (5–12.5 GPa) with dry, porous sandstone. *Meteoritics & Planetary Science* 48:99–114. https://doi.org/10.1111/maps.12030.

Kring D. A. 2007. The Chicxulub impact event and its environmental consequences at the Cretaceous–Tertiary boundary. *Palaeogeography, Palaeoclimatology, Palaeoecology* 255:4–21. https://doi.org/10.1016/j.palaeo.2007.02.037.

Kyte F. T. 1998. A meteorite from the Cretaceous/Tertiary boundary. *Nature* 396:237–239. https://doi.org/10.1038/24322.

Langenhorst F. 2002. Shock metamorphism of some minerals: basic introduction and microstructural observations. *Bulletin of the Czech Geological Survey* 77:265–282. http://www.geology.cz/bulletin/contents/art2002.04.265.

Langenhorst F. and Deutsch A. 1994. Shock experiments on preheated α- and β-quartz: I. Optical and density data. *Earth and Planetary Science Letters* 125:407–420. https://doi.org/10.1016/0012-821X(94)90229-1.

Lee S. R., Horton Jr J. W., and Walker R. J. 2006. Confirmation of a meteoritic component in impact melt rocks of the Chesapeake Bay impact structure, Virginia, USA – evidence from osmium isotopic and PGE systematics. *Meteoritics & Planetary Science* 41:819–833. https://doi.org/10.1111/j.1945-5100.2006.tb00488.x.

Leroux H. 2005. Weathering features in shocked quartz from the Ries impact crater, Germany. *Meteoritics & Planetary Science* 40:1347–1352. https://doi.org/10.1111/j.1945-5100.2005.tb00405.x.

Littler J., Fahey J. J., Dietz R. S., and Chao E. C. T. 1961. Coesite from the Lake Bosumtwi crater, Ashanti, Ghana. In *Abstracts for 1961*. Geological Society of America Special Paper #68. Geological Society of America, Boulder, Colorado. p. 218.

Liu L., Zhang J., Green II H. W., Jin Z., and Bozhilov K. N. 2007. Evidence of former stishovite in metamorphosed sediments, implying subduction to >350 km. *Earth and Planetary Science Letters* 263:180–191. https://doi.org/10.1016/j.epsl.2007.08.010.

Lofgren G. 1974. An experimental study of plagioclase crystal morphology: isothermal crystallization. *American Journal of Science* 274:243–273. https://doi.org/10.2475/ajs.274.3.243.

Lyubetskaya T. and Korenaga J. 2007. Chemical composition of Earth's primitive mantle and its variance: 1. Method and results. *Journal of Geophysical Research: Solid Earth* 112:B03211. https://doi.org/10.1029/2005JB004223.

Maier W. D., Andreoli M. A., McDonald I., Higgins M. D., Boyce A. J., Shukolyukov A., Lugmair G. W., Ashwal L. D., Gräser P., Ripley E. M., and Hart R. J. 2006. Discovery of a 25-cm asteroid clast in the giant Morokweng impact crater, South Africa. *Nature* 441:203–206. https://doi.org/10.1038/nature04751.

Masaitis V. L., Futergendler S. I., and Gnevushev M. A. 1972. Diamonds in impactites of the Popigai meteorite crater. *Zapiski Vsesoyuznoge Mineralogicheskogo Obshchestva* 101:108–112 (in Russian).

McDonald I., Andreoli M. A. G., Hart R. J., and Tredoux M. 2001. Platinum-group elements in the Morokweng impact structure, South Africa: evidence for the impact of a large ordinary chondrite projectile at the Jurassic–Cretaceous boundary. *Geochimica et Cosmochimica Acta* 65:299–309. https://doi.org/10.1016/S0016-7037(00)00527-5.

Melosh H. J. 1989. *Impact cratering–A geological process*. New York: Oxford University Press. 245 p.

Melosh H. J. 2005. The mechanics of pseudotachylite formation in large impact events. In *Impact Tectonics*, edited by C. Koeberl and H. Henkel. Springer, Berlin, Heidelberg. pp. 55–80. https://doi.org/10.1007/3-540-27548-7_2.

Milton D. J. 1977. Shatter cones – an outstanding problem in shock mechanics. In *Impact and Explosion Cratering*, edited by D. J. Roddy, R. O. Pepin, and R. B. Merrill. Pergamon Press, New York, New York. pp. 703–714. https://adsabs.harvard.edu/full/1977iecp.symp..703M.

Milton D. J. and De Carli P. S. 1963. Maskelynite: formation by explosive shock. *Science* 140:670–671. https://doi.org/10.1126/science.140.3567.670.

Montanari A. and Koeberl C. 2000. *Impact Stratigraphy: The Italian Record*. Lecture Notes in Earth Sciences, vol. 93. Springer Verlag, New York, New York. 364 pp.

Morgan J. W., Ganapathy R., and Anders E. 1975. Meteoritic material in four terrestrial meteorite craters. In *Proceedings of the 6th Lunar Science Conference, Houston, Texas, March 17–21, 1975, Volume 2*. Pergamon Press Inc., New York, New York. pp. 1609–1623. https://adsabs.harvard.edu/full/1975LPSC....6.1609M.

Müller W. F. and Défourneaux M. 1968. Deformationsstrukturen im Quarz als Indikator für Stosswellen: Eine experimentelle Untersuchung an Quartz-Einkristallen. *Zeitschrift für Geophysik* 34:483–504.

Nishiizumi K., Kohl C. P., Shoemaker E. M., Arnold J. R., Klein J., Fink D., and Middleton R. 1991. *In situ* ^{10}Be-^{26}Al exposure ages at Meteor Crater, Arizona. *Geochimica et Cosmochimica Acta* 55:2699–2703. https://doi.org/10.1016/0016-7037(91)90388-L.

Norman M. D., Bennett V. C., and Ryder G. 2002. Targeting the impactors: siderophile element signatures of lunar impact melts from Serenitatis. *Earth and Planetary Science Letters* 202:217–228. https://doi.org/10.1016/S0012-821X(02)00780-X.

O'Keefe J. A., ed., 1963. *Tektites*. University of Chicago Press, Chicago, Illinois. 228 p.

Osinski G. R. 2007. Impact metamorphism of $CaCO_3$-bearing sandstones at the Haughton structure, Canada. *Meteoritics & Planetary Science* 42:1945–1960. https://doi.org/10.1111/j.1945-5100.2007.tb00552.x.

Osinski G. R. and Ferrière L. 2016. Shatter cones: (Mis)understood? *Science Advances* 2:e1600616. https://doi.org/10.1126/sciadv.1600616.

Osinski G.R. and Spray J. G. 2006. Shatter cones of the Haughton impact structure, Canada. *Proceedings of the 1st International Conference on Impact Cratering in the Solar System*, European Space Agency Special Publication SP-612. https://sci.esa.int/documents/33321/35974/1567255426117-ESLAB40-Proc_296362-Osinski.pdf.

Osinski G. R., Grieve R. A. F., Marion C., and Chanou A. 2013. Impact melting. In *Impact Cratering: Processes and Products*, edited by G. R. Osinski and E. Pierazzo. Wiley-Blackwell, Hoboken, New Jersey. pp. 125–145.

Ostertag R. 1983. Shock experiments on feldspar crystals. *Journal of Geophysical Research* 88:B364–B376. https://doi.org/10.1029/JB088iS01p0B364.

Palme H., Janssens M. J., Takahashi, H., Anders E., and Hertogen J. 1978. Meteoritic material at five large impact craters. *Geochimica et Cosmochimica Acta* 42:313–323. https://doi.org/10.1016/0016-7037(78)90184-9.

Palme H., Göbel E., and Grieve R. A. F. 1979. The distribution of volatile and siderophile elements in the impact melt of East Clearwater (Quebec). In *Proceedings of the 10th Lunar and Planetary Science Conference, Houston, Texas, March 19–23, 1979*. Pergamon Press Inc., New York, New York. pp. 2465–2492. https://adsabs.harvard.edu/full/1979LPSC...10.2465P.

Palme H., Grieve R. A. F., and Wolf R. 1981. Identification of the projectile at the Brent crater, and further considerations of projectile types at terrestrial craters. *Geochimica et Cosmochimica Acta* 45:2417–2424. https://doi.org/10.1016/0016-7037(81)90095-8.

Peucker-Ehrenbrink B. and Jahn B. 2001. Rhenium-osmium isotope systematics and platinum group element concentrations: Loess and the upper continental crust. *Geochemistry, Geophysics, Geosystems* 2:2001GC000172. https://doi.org/10.1029/2001GC000172.

Philpotts A. R. 1990. *Principles of Igneous and Metamorphic Petrology*. Prentice-Hall, Englewood Cliffs, New Jersey. 498 pp.

Pickersgill, A. E., Jaret, S., Pittarello, L., Fritz, J., and Harris, R. 2021. Shock effects in feldspars: An overview. In *Large Meteorite Impacts and Planetary Evolution VI*, edited by W. U. Reimold and C. Koeberl. Geological Society of America Special Paper #550. Geological Society of America, Boulder, Colorado. pp. 537–549. https://doi.org/10.1130/2021.2550(23).

Pittarello L., Ferrière L., Feignon J.-G., Osinski G. R., and Koeberl C. 2020. Preferred orientation distribution of shock-induced planar microstructures in quartz and feldspar. *Meteoritics & Planetary Science* 55:1082–1092. https://doi.org/10.1111/maps.13490.

Plan A., Kenny G. G., Erickson T. M., Lindgren P., Alwmark C., Holm-Alwmark S., Lambert P., Scherstén A., and Söderlund U. 2021. Exceptional preservation of reidite in the Rochechouart impact structure, France: New insights into shock deformation and phase transition of zircon. *Meteoritics & Planetary Science* 56:1795–1828. https://doi.org/10.1111/maps.13723.

Poelchau M. H. and Kenkmann T. 2011. Feather features: a low-shock-pressure indicator in quartz. *Journal of Geophysical Research: Solid Earth* 116:B02201. https://doi.org/10.1029/2010JB007803.

Reid A. F. and Ringwood A. E. 1969. Newly observed high pressure transformations in Mn_3O_4, $CaAl_2O_4$, and $ZrSiO_4$. *Earth and Planetary Science Letters* 6:205–208. https://doi.org/10.1016/0012-821X(69)90091-0.

Reimold W. U. 1995. Pseudotachylite in impact structures – Generation by friction melting and shock brecciation?: A review and discussion. *Earth-Science Reviews* 39:247–264. https://doi.org/10.1016/0012-8252(95)00033-X.

Reimold W. U. and Gibson R. L. 2005. "Pseudotachylites" in large impact structures. *In Impact Tectonics*, edited by C. Koeberl and H. Henkel, Springer, Berlin, Heidelberg. pp. 1–53. https://doi.org/10.1007/3-540-27548-7_1.

Reimold W. U. and Stöffler D. 1978. Experimental shock metamorphism of dunite. *Proceedings of the 9th Lunar and Planetary Science Conference, Houston, Texas, March 13–17, 1978, Volume 2.* Pergamon Press Inc., New York, New York. pp. 2805–2824. https://adsabs.harvard.edu/full/1978LPSC....9.2805R.

Robertson P. B. 1975. Experimental shock metamorphism of maximum microcline. *Journal of Geophysical Research* 80:1903–1910. https://doi.org/10.1029/JB080i014p01903.

Robertson P. B. and Grieve R. A. F. 1977. Shock attenuation at terrestrial impact structures. In *Impact and Explosion Cratering*, edited by D. J. Roddy, R. O. Pepin, and R. B. Merrill. Pergamon Press, New York, New York. pp. 687–702.

Rochette P., Beck P., Bizzarro M., Braucher R., Cornec J., Debaille V., Devouard B., Gattacceca J., Jourdan F., Moustard F., Moynier F., Nomade S., and Reynard B. 2021. Impact glasses from Belize represent tektites from the Pleistocene Pantasma impact crater in Nicaragua. *Communications Earth & Environment* 2:94. https://doi.org/10.1038/s43247-021-00155-1.

Rost R., Dolgov Y. A., and Vishnevsky S. A. 1978. Gases in inclusions of impact glass in the Ries crater, West Germany and finds of high pressure carbon polymorphs. *Doklady Akademia Nauk SSSR* 241:695–698 (in Russian).

Rubin A. E., Scott E. R. D., and Keil K. 1997. Shock metamorphism of enstatite chondrites. *Geochimica et Cosmochimica Acta* 61:847–858. https://doi.org/10.1016/S0016-7037(96)00364-X.

Sagy A., Reches Z., and Fineberg J. 2002. Dynamic fracture by large extraterrestrial impacts as the origin of shatter cones. *Nature* 418:310–313. https://doi.org/10.1038/nature00903.

Sagy A., Fineberg J., and Reches Z. 2004. Shatter cones: Branched, rapid fractures formed by shock impact. *Journal of Geophysical Research: Solid Earth* 109:B10209. https://doi.org/10.1029/2004JB003016.

Schedl A. 2006. Applications of twin analysis to studying meteorite impact structures. *Earth and Planetary Science Letters* 244:530–540. https://doi.org/10.1016/j.epsl.2006.02.018.

Schmidt G., Palme H., and Kratz K. L. 1997. Highly siderophile elements (Re Os, Ir, Ru, Rh, Pd, Au) in impact melts from three European impact craters (Sääksjärvi, Mien and Dellen): clues to the nature of the impacting bodies. *Geochimica et Cosmochimica Acta* 61:2977–2987. https://doi.org/10.1016/S0016-7037(97)00129-4.

Schmitt R. T. 2000. Shock experiments with the H6 chondrite Kernouvé: pressure calibration of microscopic shock effects. *Meteoritics & Planetary Science* 35:545–560. https://doi.org/10.1111/j.1945-5100.2000.tb01435.x.

Seybold L., Trepmann C. A., Kaliwoda M., Dellefant F., and Hölzl S. 2022. Twinned calcite in polymict breccias from the Ries impact structure – Brecciation and mixing of target rocks. 80th Annual Meeting of the Meteoritical Society, Abstract #6287. https://www.hou.usra.edu/meetings/metsoc2022/pdf/6287.pdf.

Shand S. J. 1916. The pseudotachylyte of Parijs (Orange Free State) and its relation to "trap-shotten gneiss" and "flinty crush-rock". *Quarterly Journal Geological Society of London* 72:198–221. https://doi.org/10.1144/GSL.JGS.1916.072.01-04.12.

Shoemaker E. M. and Chao E. C. T. 1961. New evidence for the impact origin of the Ries Basin, Bavaria, Germany. *Journal of Geophysical Research* 66:3371–3378. https://doi.org/10.1029/JZ066i010p03371.

Short N. M. and Gold D. P. 1996. Petrography of shocked rocks from the central peak at the Manson impact structure. In *The Manson Impact Structure, Iowa: Anatomy of an Impact Crater*, edited by C. Koeberl and R. R. Anderson. Geological Society of America Special Paper #302. Geological Society of America, Boulder, Colorado. pp. 245–265. https://doi.org/10.1130/0-8137-2302-7.245.

Shukolyukov A. and Lugmair G. W. 1998. Isotopic evidence for the Cretaceous–Tertiary impactor and its type. *Science* 282:927–929. https://doi.org/10.1126/science.282.5390.927.

Shukolyukov A., Lugmair G. W., Koeberl C., and Reimold W. U. 1999. Chromium in the Morokweng impact melt: evidence for extraterrestrial components and type of impactor (abstract). *Meteoritics and Planetary Science* 34:A107–A108. https://adsabs.harvard.edu/full/1999M%26PSA..34S.107S.

Simonds C. H., Floran R. J., McGee P. E., Phinney W. C., and Warner J. L. 1978. Petrogenesis of melt rocks, Manicouagan impact structure, Quebec. *Journal of Geophysical Research: Solid Earth* 83:2773–2778.

Smit J. and Hertogen J. 1980. An extraterrestrial event at the Cretaceous–Tertiary boundary. *Nature* 285:198–200. https://doi.org/10.1038/285198a0.

Spry A. 1969. *Metamorphic Textures*. Pergamon Press, New York, New York. 350 pp. https://doi.org/10.1016/C2013-0-02201-3.

Stähle V., Altherr R., Koch M., and Nasdala L. 2008. Shock-induced growth and metastability of stishovite and coesite in lithic clasts from suevite of the Ries impact crater (Germany). *Contributions to Mineralogy and Petrology* 155:457–472. https://doi.org/10.1007/s00410-007-0252-2.

Stöffler D. 1967. Deformation und Umwandlung von Plagioklas durch Stoßwellen in den Gesteinen des Nördlinger Ries. *Contributions to Mineralogy and Petrology* 16:51–83. https://doi.org/10.1007/BF00371608.

Stöffler D. 1971. Progressive metamorphism and classification of shocked and brecciated crystalline rocks at impact craters. *Journal of Geophysical Research* 76:5541–5551. https://doi.org/10.1029/JB076i023p05541.

Stöffler D. 1972. Deformation and transformation of rock-forming minerals by natural and experimental shock processes: I. Behavior of minerals under shock compression. *Fortschritte der Mineralogie* 49:50–113.

Stöffler D. 1984. Glasses formed by hypervelocity impact. *Journal of Non-Crystalline Solids* 67:465–502. https://doi.org/10.1016/0022-3093(84)90171-6.

Stöffler D. and Grieve R. A. F. 2007. Impactites, Chapter 2.11. In *Metamorphic Rocks: A Classification and Glossary of Terms, Recommendations of the International Union of Geological Sciences*, edited by D. Fettes and J. Desmons. Cambridge University Press, Cambridge, United Kingdom. pp.82–92, 111–125, and 126–242.

Stöffler D. and Langenhorst F. 1994. Shock metamorphism of quartz in nature and experiment: I. Basic observation and theory. *Meteoritics* 29:155–181. https://doi.org/10.1111/j.1945-5100.1994.tb00670.x.

Stöffler D., Keil K., and Scott E. R. D. 1991. Shock metamorphism of ordinary chondrites. *Geochimica et Cosmochimica Acta* 55:3845–3867. https://doi.org/10.1016/0016-7037(91)90078-J.

Stöffler D., Artemieva N., Wünnemann K., Reimold W. U., Jacob J., Hansen B. K., and Summerson I. A. T. 2013. Ries crater and suevite revisited—Observations and modeling. Part I: Observations. *Meteoritics & Planetary Science* 48:515–589. https://doi.org/10.1111/maps.12086.

Stöffler D., Hamann C., and Metzler K. 2018. Shock metamorphism of planetary silicate rocks and sediments: Proposal for an updated classification system. *Meteoritics & Planetary Science* 53:5–49. https://doi.org/10.1111/maps.12912.

Storzer D. and Wagner G. A. 1980. Australites older than Indochinites. *Naturwissenschaften* 67:90. https://adsabs.harvard.edu/pdf/1977Metic..12..368S.

Tagle R. and Berlin J. 2008. A database of chondrite analyses including platinum group elements, Ni, Co, Au, and Cr: Implications for the identification of chondritic projectiles. *Meteoritics & Planetary Science* 43:541–559. https://doi.org/10.1111/j.1945-5100.2008.tb00671.x.

Tagle R. and Claeys P. 2005. An ordinary chondrite impactor for the Popigai crater, Siberia. *Geochimica et Cosmochimica Acta* 69:2877–2889. https://doi.org/10.1016/j.gca.2004.11.024.

Tagle R. and Hecht L. 2006. Geochemical identification of projectiles in impact rocks. *Meteoritics & Planetary Science* 41:1721–1735. https://doi.org/10.1111/j.1945-5100.2006.tb00448.x.

Taylor S. R. and McLennan S. M. 1985. *The Continental Crust: Its Composition and Evolution*. Blackwell, Oxford, United Kingdom. 328 p.

Timms N. E., Erickson T. M., Pearce M. A., Cavosie A. J., Schmieder M., Tohver E., Reddy S. M., Zanetti M. R., Nemchin A. A., and Wittmann A. 2017. A pressure-temperature phase diagram for zircon at extreme conditions. *Earth-Science Reviews* 165:185–202. https://doi.org/10.1016/j.earscirev.2016.12.008.

Timms N. E., Pearce M. A., Erickson T. M., Cavosie A. J., Rae A. S. P., Wheeler J., Wittman A., Ferrière L., Poelchau M. H., Tomioka N., Collins G. S., Gulick S. P. S., Rasmussen C., Morgan J. V., and IODP-ICDP Expedition 364 Scientists. 2019. New shock microstructures in titanite ($CaTiSiO_5$) from the peak ring of the Chicxulub impact structure, Mexico. *Contributions to Mineralogy and Petrology* 174:38. https://doi.org/10.1007/s00410-019-1565-7.

Timms N. E., Kirkland C. L., Cavosie A. J., Rae A. S. P., Rickard W. D. A., Evans N. J., Erickson T. M., Wittmann A., Ferrière L., Collins G. S., and Gulick S. P. S. 2020. Shocked titanite records Chicxulub hydrothermal alteration and impact age. *Geochimica et Cosmochimica Acta* 281:12–30. https://doi.org/10.1016/j.gca.2020.04.031.

Trepmann C. A. 2008. Shock effects in quartz: compression versus shear deformation — an example from the Rochechouart impact structure, France. *Earth and Planetary Science Letters* 267:322–332. https://doi.org/10.1016/j.epsl.2007.11.035.

Trepmann C. A. and Spray J. G. 2005. Planar microstructures and Dauphine twins in shocked quartz from the Charlevoix impact structure, Canada. In *Large Meteorite Impacts III*, edited by T. Kenkmann, F. Hörz, and A. Deutsch. Geological Society of America Special Paper #384. Geological Society of America, Boulder, Colorado. pp. 315–328. https://doi.org/10.1130/0-8137-2384-1.315.

Trepmann C. A. and Spray J. G. 2006. Shock-induced crystal-plastic deformation and post-shock annealing of quartz from crystalline target rocks of the Charlevoix Structure, Canada. *European Journal of Mineralogy* 18:161–173. https://doi.org/10.1127/0935-1221/2006/0018-0161.

Trepmann C. A., Dellefant F., Kaliwoda M., Hess K.-U., Schmahl W. W., and Hölzl S. 2020. Quartz and cristobalite ballen in impact melt rocks from the Ries impact structure, Germany, formed by dehydration of shock-generated amorphous phases. *Meteoritics & Planetary Science* 55:2360–2374. https://doi.org/10.1111/maps.13590.

Vernon R. H. 2004. *A Practical Guide to Rock Microstructure*. Cambridge University Press, New York, New York. 594 pp. https://doi.org/10.1017/9781108654609.

Whitehead J., Spray J. G., and Grieve R. A. F. 2002. Origin of 'toasted' quartz in terrestrial impact structures. *Geology* 30:431–434. https://doi.org/10.1130/0091-7613(2002)030<0431:OOTQIT>2.0.CO;2.

Wieland F., Reimold W. U., and Gibson R. L. 2006. New observations on shatter cones in the Vredefort impact structure, South Africa, and evaluation of current hypotheses for shatter cone formation. *Meteoritics & Planetary Science* 41:1737–1759. https://doi.org/10.1111/j.1945-5100.2006.tb00449.x.

Wirth R., Vollmer C., Brenker F., Matsyuk S., and Kaminsky F. 2007. Inclusions of nanocrystalline hydrous aluminum silicate "Phase Egg" in superdeep diamonds from Juina (Mato Grosso State, Brazil). *Earth and Planetary Science Letters* 259:384–399. https://doi.org/10.1016/j.epsl.2007.04.041.

Wittmann A., Kenkmann T., Schmitt R. T., and Stöffler D. 2006. Shock-metamorphosed zircon in terrestrial impact craters. *Meteoritics & Planetary Science* 41:433–454. https://doi.org/10.1111/j.1945-5100.2006.tb00472.x.

Zolensky M. 1998. The flux of meteorites to Antarctica. In *Meteorites: Flux with Time and Impact Effects*, edited by M. M. Grady, R. Hutchison, G. J. H. McCall, and D. Rothery. Geological Society of London Special Publications #140. Geological Society, London, United Kingdom. pp. 93–104.

CHAPTER 3: The Chicxulub impact structure, Mexico, and the IODP-ICDP Expedition 364

The Chicxulub impact structure is located in the northwestern part of the Yucatán peninsula, Mexico, and centered at 21.29° N, 89.53° W (Hildebrand et al., 1995). It is a ~200 km diameter impact structure (e.g., Gulick et al., 2013), with an estimated age of 66.05 Ma (Sprain et al., 2018 and reference therein). It is the only known terrestrial impact structure with a nearly intact, well-preserved peak ring (see Morgan et al., 1997, 2016). The Chicxulub impact event is now widely recognized as the cause of the major mass extinction which occurred at the Cretaceous-Paleogene (K–Pg) boundary (formerly known as the Cretaceous-Tertiary (K–T) boundary), and responsible of the demise of the non-avian dinosaurs (e.g., Alvarez et al., 1980; Smit and Hertogen, 1980; Hildebrand et al., 1991; Swisher et al., 1992; Smit, 1999; Molina et al., 2009; Schulte et al., 2010; Renne et al., 2013; Chiarenza et al., 2020). More broadly, apart from the non-avian dinosaurs, it has been estimated that ~76% of the species then living on Earth became extinct during the K–Pg mass extinction (e.g., Jablonski, 2004; Schulte et al., 2010 and references therein). Of the four other major extinction events that occurred throughout the Phanerozoic (i.e., the Late Ordovician (~445 Ma), the Late Devonian (~380–360 Ma), the Permian-Triassic boundary (~250 Ma), and the Triassic-Jurassic boundary (~201 Ma) events), only the K–Pg mass extinction can be related to the impact of a large asteroid (see, e.g., Keller, 2005; Martín-Peinado and Rodríguez-Tovar, 2010; Schulte et al., 2010). Additionally, studies allowed to correlate the Chicxulub impact structure with K–Pg boundary layer sites across the world, which were (earlier) interpreted as impact ejecta layers (see sections 3.1 and 3.2).

Figure 3.1. *Artistic representations of the Chicxulub impact event. A) "The extinction of dinosaurs". Credit: Shigemi Numazawa. B) "K/T impact painting". Credit: Dona Jalufka.*

3.1. The K-Pg boundary and discovery of impact-induced features

The impact hypothesis at the K–Pg boundary dates back more than forty years, in the late 1970s. At that time, a geologist, Walter Alvarez, was investigating sedimentary rocks in Italy, specifically in the Umbria-Marche Appenines, near the town of Gubbio. The sedimentary rocks around Gubbio consist of pelagic limestones, mainly composed of calcareous

nannofossils and planktonic foraminifera, which can be used as a tool for dating and make long-distance correlation. These rocks record the Late Cretaceous and Paleogene, without any disturbance by erosional gaps (Alvarez, 2009). The purpose of the study undertaken by W. Alvarez was to estimate the sedimentation rate, and, thus, the deposition time needed to form a specific layer. He discussed the problem with his father, L. Alvarez, physicist and Nobel-prize winner, who had the idea to use the cosmic dust flux (which falls onto the Earth's surface at a relatively constant rate), as recorded in sedimentary rocks as proxy for the variations of the sedimentation rate. Following this, Alvarez and colleagues measured the Ir content of the sedimentary rocks from Gubbio, in order to determine the sedimentation rate, i.e., the higher the Ir content of a layer, the longer it took to deposit (see details in Alvarez, 1997). The K–Pg boundary, between the Cretaceous and Paleogene limestone layers, is marked by a thin, ~1-cm dark clay layer, marking also the mass extinction event (Fig. 3.2). Below the clay layer, the Cretaceous limestones were composed of large, abundant foraminifera (*Globotruncana* species), while above the clay layer, the Paleogene foraminifera were smaller, less abundant, and of different species (*Globigerina*) with the disappearance of the Cretaceous foraminifera (Fig. 3.2).
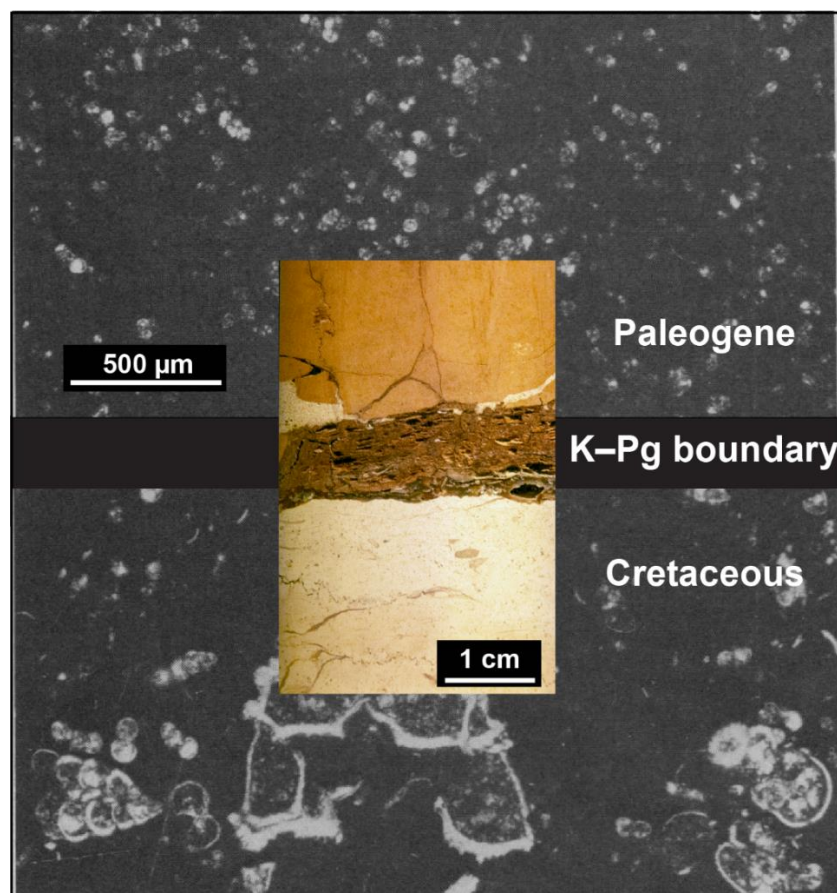
Figure 3.2. *Thin-section microphotographs (same scale for both) of the Cretaceous and Paleogene limestones from Gubbio (Italy), showing the biotic turnover in foraminifera species (i.e., Globotruncana contusa in the Cretaceous unit, and Globigerina eugubina in the Paleogene unit). Macrophotograph of the K–Pg clay layer as it is occurring at Gubbio is shown in the foreground (this section is displayed at the NHM Vienna). Microphotographs from Alvarez et al. (1980).*
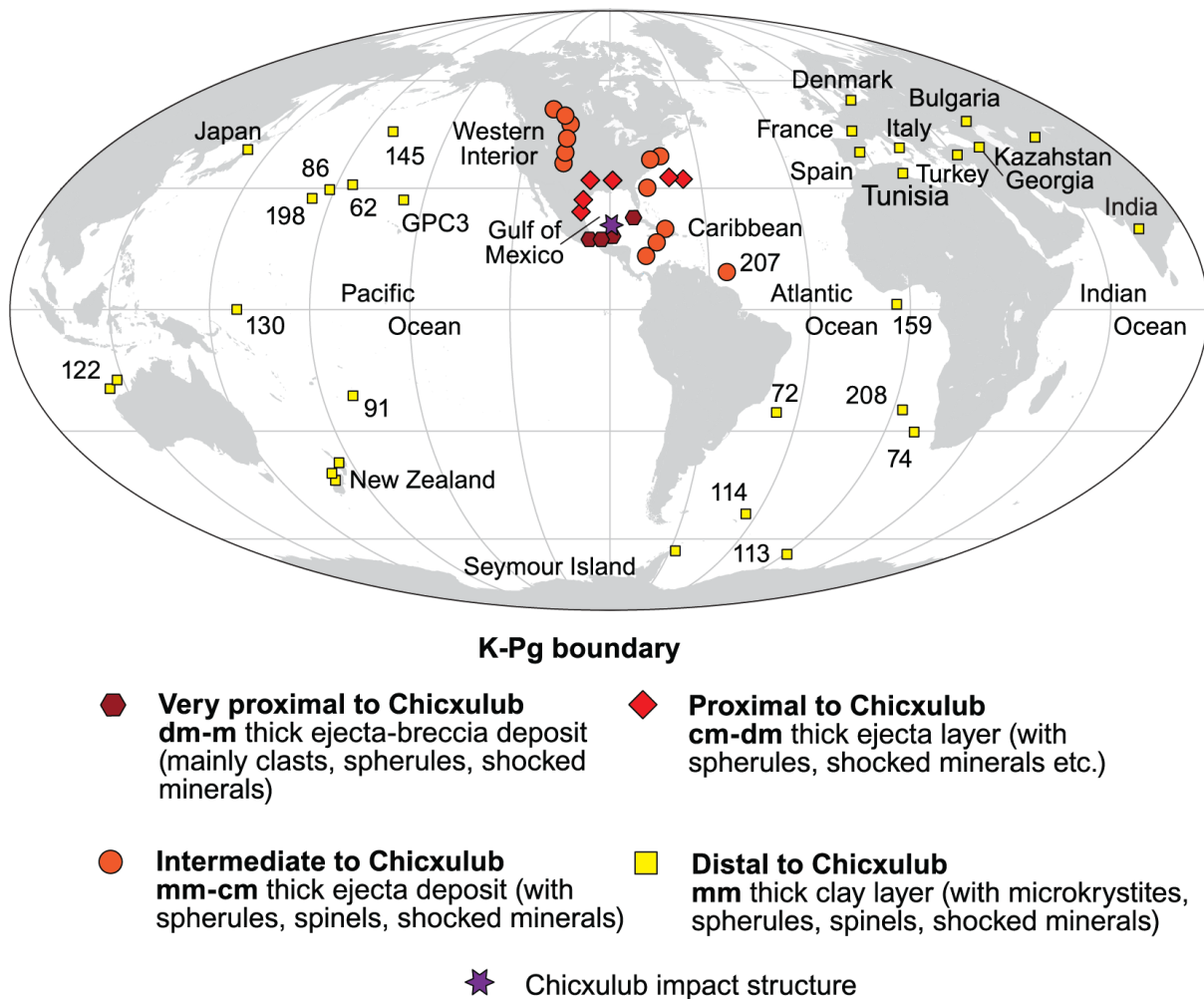
Figure 3.3. *Distribution map of K–Pg boundary deposit locations. Deep-sea drill sites are referred to the corresponding Deep Sea Drilling Project (DSDP) and ODP Leg numbers. The K–Pg boundary deposit sites are classified according to their distance relative to the Chicxulub impact structure (purple star). The very proximal sites are up to 500 km from Chicxulub, proximal sites up to 1,000 km, intermediate sites between 1,000 and 5,000 km, and distal sites are more than 5,000 km away from Chicxulub. Modified from Goderis et al. (2013).*

Surprisingly, while the Ir contents measured in the Cretaceous and Paleogene limestones at Gubbio were similar to expected values in deep-sea clay sediments (~0.3 ppb), the K–Pg boundary clay displayed Ir contents up to 30 times higher (~9.1 ppb) than the neighboring limestones (Alvarez et al., 1980). Similar measurements were performed within another K–Pg boundary site (i.e., at Stevns Klint, Denmark) revealing the same Ir enrichment (later known as "Ir positive anomaly"), up to 160 times higher in the K–Pg boundary layer than in the Cretaceous and Paleogene rocks. These results were published by Alvarez et al. (1980), and they suggested that the Ir enrichment in the K–Pg boundary clay may have been caused by a sudden cosmic event, namely the impact of a large asteroid (~10 km-diameter), and that this impact event may have been responsible for the mass extinction. Subsequently, the Ir anomaly was confirmed in more than 120 marine and continental K–Pg boundary sites worldwide (e.g., Smit and Hertogen, 1980; Evans et al., 1993, 1995; Claeys et al., 2002; Schulte et al., 2010; Goderis et al., 2013, and references therein), and the K–Pg clay layer has been found, so far, in

more than 350 terrestrial and marine sites around the world (Fig. 3.3; e.g., Smit, 1999; Claeys et al., 2002; Schulte et al., 2010). The measurements of the abundances of other highly siderophile elements (HSEs, see Chapter 2) revealed also elevated concentrations relative to the upper continental crustal values and flat, "chondritic" signatures (Fig. 3.4; Goderis et al., 2013).
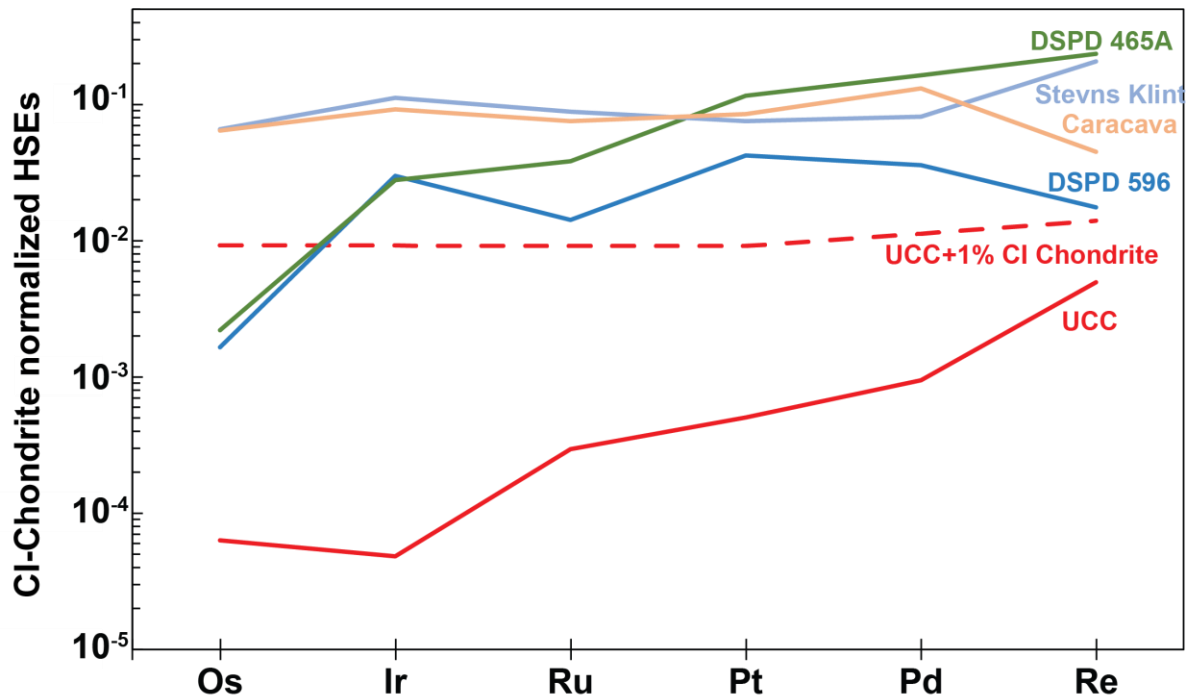
Figure 3.4. *CI-chondrite normalized HSE abundance patterns of several terrestrial (Caracava, Spain, and Stevns Klint, Denmark) and marine (DSPD 465A and 596) K–Pg boundary sites. The enrichment in HSEs relative to the upper continental crust (UCC) is clearly visible, indicative of the presence of a meteoritic component. For comparison, the admixture of 1% of carbonaceous chondrite (CI) to the UCC was calculated (dashed red line). The normalizing values are from McDonough and Sun (1995), while HSE contents of UCC and CI-Chondrite are from Peucker-Ehrenbrink and Jahn (2001), and Fischer-Gödde et al. (2010).*

After the publication of Alvarez et al. (1980), there was still some debate regarding the origin of the Ir anomaly, with opponents of the impact hypothesis suggesting a terrestrial origin (e.g., intense volcanism) for the Ir anomaly (e.g., Rampino, 1982, and references therein). Other convincing evidence (i.e., impact-induced features, such as shocked quartz grains; Bohor et al., 1984, 1987) of an impact origin of the K–Pg boundary layer were discovered later, ruling out a terrestrial origin. The hypothesis that volcanism (i.e., the Deccan Traps flood basalts in India) caused the mass extinction by releasing dust, carbon dioxide, and sulfur aerosols into the atmosphere, provoking global climate change, was still supported by some studies back then (Duncan and Pyle, 1988; Courtillot, 1990; Keller et al., 2008). The Deccan flood basalts emplaced from a series of short (~100 kyr), intermittent eruption pulses, in two main phases, at ~67.4 Ma, and ~66.1 Ma, the latter lasting ~710 kyr and erupting $>10^6$ km^3 of magma (Schoene et al., 2019; Sprain et al., 2019; Hull et al., 2020). However, the Deccan lavas, which erupted over a relatively long period of time, seem not to have been the primary cause of the extinction. Importantly, there is a temporal match between the K–Pg boundary layer and the onset of the extinctions, suggesting a mass extinction over a short period of time, following a global

darkening and "impact winter" after the impact (Schulte et al., 2010, and references therein). Moreover, the Deccan volcanism may have increased habitat suitability by mitigating the extreme effects of the asteroid impact, with the carbon dioxide emission inducing climate warming (e.g., Chiarenza et al., 2020, and references therein). Other hypotheses suggested for the mass extinction either including both, effects of the impact event, and volcanism and other causes (Archibald and Fastovsky, 2004), or that the impact triggered more intense eruptions (Renne et al., 2015), or that the impact gave the final blow to the biosphere which was already stressed by the intense volcanism (White and Saunders, 2005; Arens and West, 2008; Renne et al., 2013).

A few years after the publication of Alvarez et al. (1980), shocked quartz grains with planar deformation features (PDFs), an unequivocal shock metamorphic feature (see Chapter 2), were first described within K–Pg boundary clays in the USA by Bohor et al. (1984). Shocked quartz grains were then found in more than 50 K–Pg boundary sites worldwide, as well as shock-induced planar microstructures in other minerals, such as in feldspar and zircon grains (e.g., Bohor et al., 1987; Alvarez et al., 1995; Claeys et al., 2002). Impact diamonds (nanometer- to micrometer-sized, see Chapter 2), have been found and investigated at a few K–Pg boundary sites, and constitute another marker of a large impact event with high shock pressures (Carlisle and Braman, 1991; Hough et al., 1997, 1999). Altered microkrystite spherules (see Chapter 2) were also found within the K–Pg boundary clay layer, with a significant volume (~200 spherules/cm^3; see e.g., Montanari et al., 1983; Smit and Romein, 1985). The K–Pg microkrystites were interpreted as a product of the condensation of silicate melt droplets from the expanding vapor plume rising above the crater (Smit et al., 1992; Ebel and Grossman, 2005). Associated with these spherules, Ni-rich, oxidized magnesioferrite spinels were identified in K–Pg clay, generally displaying a dendritic quench texture (e.g., Kyte and Smit, 1986; Robin et al., 1991, 1992; Smit, 1999). Such spinel minerals cannot be derived from terrestrial magmas, which are strongly depleted in Ni, and evolve under extremely low oxygen fugacity (Gayraud et al., 1996). Consequently, as there is no terrestrial analogue, they are likely products of the impact event. Finally, charcoal and soot, indicative of large-scale wildfires following the impact, were observed at some K–Pg boundary sites (e.g., Wolbach et al., 1985; Kruge et al., 1994). Consequently, the K–Pg boundary clay layer is now widely accepted to be a global impact ejecta layer, resulting from the deposition of fractured, shocked, and/or melted minerals from the impact crater target rocks and meteoritic material that were ejected during the formation of a large impact structure (e.g., Alvarez et al., 1995; Artemieva and Morgan, 2009; Glass and Simonson, 2012a, 2012b; Goderis et al., 2013).

3.2. Identification and characterization of the Chicxulub impact structure

3.2.1. Identification of the Chicxulub impact structure and its relation to the K-Pg boundary

Considering all the evidence indicating that a major impact event occurred approximately 66 Ma, i.e., the age of the K–Pg boundary, there was still the problem to find the corresponding impact structure. According to Alvarez et al. (1980), the impacting projectile

would have had an assumed diameter of 10 ± 4 km, resulting in an impact structure diameter estimated to be ~200 km in diameter. At that time, the three impact structures known to have a diameter of 100 km or larger, i.e., Vredefort (South Africa), Sudbury (Canada), and Popigai (Russia), were excluded as possible candidates due to their formation ages. Alvarez et al. (1980) suggested that the impact occurred most likely within an ocean basin, and that it may have been partially or totally destroyed by subduction, explaining the obstacles for a straightforward recognition. Nevertheless, the search for the impact structure continued over the years, in parallel to investigations to characterize K–Pg boundary sites and identify the impactor signature and target lithologies. Interestingly, one year after the publication of Alvarez et al. (1980), the results of a geophysical survey, which took place in the framework of oil exploration conducted by the Mexican state-owned oil company Petroleos Mexicanos (PEMEX), were presented in an abstract at the 51st Annual International Meeting of the Society of Exploration Geophysicists in Los Angeles. This abstract describes a buried circular structure of ~200 km in diameter, highlighted by gravity and magnetic anomalies, in the Yucatán peninsula carbonate platform (Penfield and Camargo, 1981). The report also interpreted the structure as a possible large impact crater, even making the association between the structure and the K–Pg boundary extinction (Penfield and Camargo, 1981). However, this presentation was not followed by a proper publication and the abstract was "forgotten". Thus, only a decade later, after additional studies, was the location of the source impact structure confirmed. Some evidence already pointed towards the Gulf of Mexico area, where thick K–Pg proximal ejecta deposits of the impact were identified, e.g., a 50-cm-thick K–Pg boundary layer in Haiti, as well as a cross-bedded sandstone layer with glass spherules at the base, fining upward into a clay layer containing Ir anomaly and shocked quartz in northeastern Mexico, the latter K–Pg deposit is interpreted as the result of tsunami waves triggered by the Chicxulub impact event (Hildebrand and Boynton, 1990a, 1990b; Smit et al., 1996). Following this, the Bouguer gravity anomalies were mapped again more precisely at the Chicxulub structure area (see Fig. 3.5), providing evidence in support of an impact origin and an estimated diameter of ~180 km, according to the negative gravity anomalies (Hildebrand et al., 1991). The structure is buried under ~1 km of Cenozoic limestones, preventing the direct study of the crater forming and filling lithologies. The only surface expression of the impact structure is the presence of a semicircular ring of cenotes (i.e., water-filled sinkholes) in the Cenozoic limestones, overlying the onshore portion of the impact structure (Pope et al., 1991). Several PEMEX drill cores that were recovered during petroleum exploration campaigns within the crater structure were later investigated, revealing the presence of impact metamorphic features (e.g., shocked quartz grains, impact melt rocks and other breccias), further confirming the Chicxulub as an impact structure (e.g., Hildebrand et al., 1991; Sharpton et al., 1992; Camargo-Zanoguera and Suarez-Reynoso, 1994; Pope et al., 1996; Sharpton et al., 1996).

After the confirmation of Chicxulub as an impact structure, it was necessary to test if Chicxulub was indeed the source impact structure of the K–Pg boundary ejecta layer. Therefore, a variety of geochemistry methods were used to compare impactites from within the structure and K–Pg boundary ejecta samples. Similarities were identified in the geochemistry (i.e., major and trace element compositions, isotopic signatures, and overlapping of the $^{40}Ar/^{39}Ar$ ages with the K–Pg boundary) between the microtektites found at the Haiti K–Pg boundary site and the melt particles and impact melt rocks recovered in some of the Chicxulub drill cores (e.g.,

Sigurdsson et al., 1991; Sharpton et al., 1992; Swisher et al., 1992; Blum et al., 1993). Additionally, it was observed that the ejected (e.g., shocked quartz grains) particle sizes increased with decreasing distance from Chicxulub (e.g., Hildebrand et al., 1991; Claeys et al., 2002; Croskell et al., 2002; Morgan et al., 2006), and also the U–Pg ages estimated for ejected shocked zircon grains from K–Pg boundary sites in North America are identical to those found in Chicxulub impact breccias (Krogh et al., 1993a, 1993b; Kamo and Krogh, 1995). Therefore, the geochemical and geochronological data confirmed that Chicxulub corresponds to the K–Pg impact event.
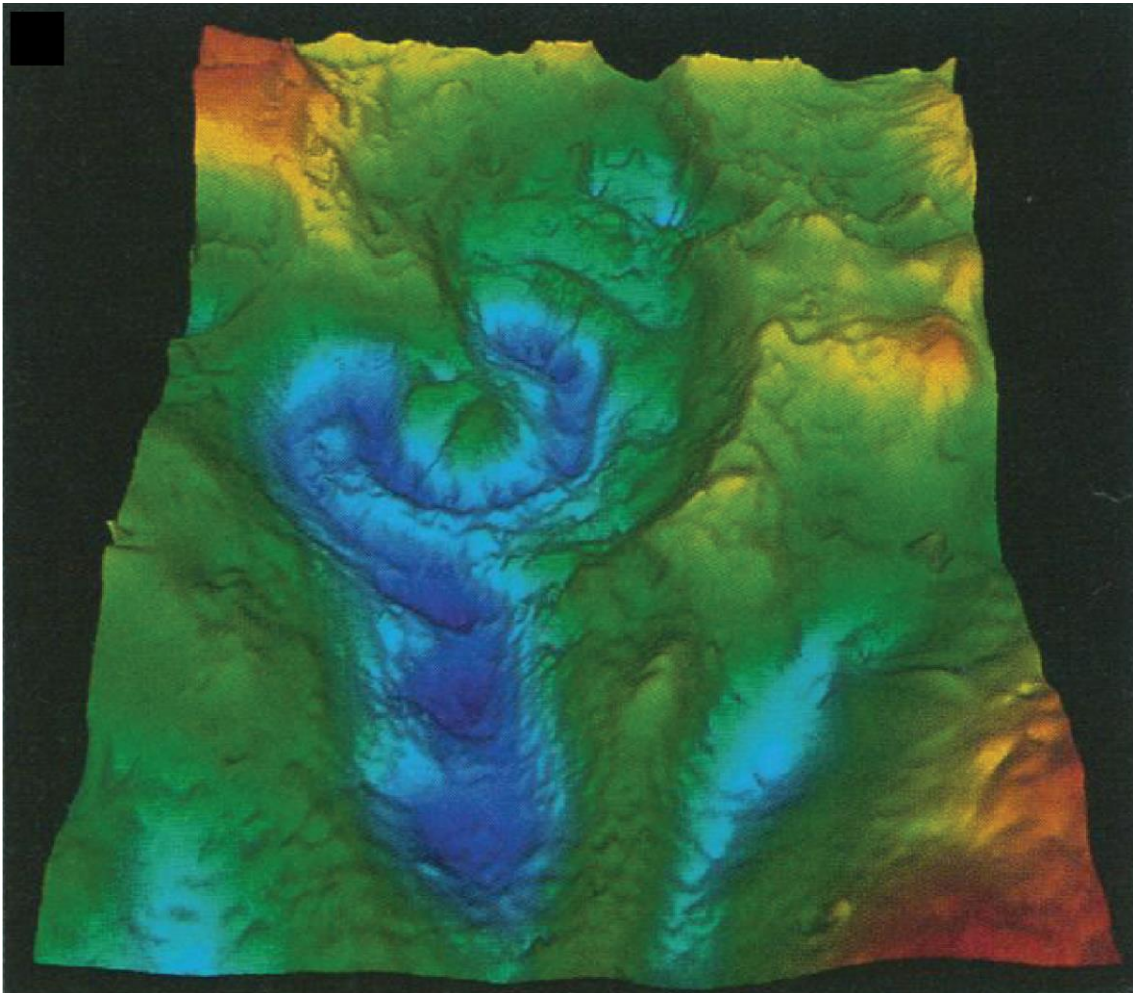
Figure 3.5. *Relief-shaded, 3D Bouguer gravity anomaly map of the Chicxulub area, revealing the circular features of the impact structure (from Sharpton et al., 1993).*

3.2.2. Main characteristics of the Chicxulub impact structure

Following the discovery of the impact structure, several geophysical studies, as well as new drillings, were performed in order to better constrain the size, detailed structure, and geology of Chicxulub (see reviews in Urrutia-Fucugauchi et al., 2011; Gulick et al., 2013; and following sections). The most recent estimates, based on geophysical data, give an impact structure diameter of ~200 km (Gulick et al., 2013). The subsurface structure was resolved following seismic reflection and refraction survey campaigns (Morgan et al., 1997; Gulick et

al., 2008). These survey campaigns revealed an inner rim of ~140–170 km in diameter, with outer ring faults beyond, a floor ~1 km beneath the surface, and a 80–90 km diameter peak ring, rising up to 400 m above the impact structure floor (see also, Gulick et al., 2013, and references therein). Moreover, below the impact structure, mantle uplifting of 1.5–2 km was observed (Christeson et al., 2009). According to the seismic velocities (>5.8 km/s), the pre-impact crust, below the sedimentary cover, consists of high-density, non-porous rocks (Christeson et al., 2001). The maximal negative Bouguer gravity anomaly is ring-shaped, with within the structure an inward dipping, suggesting that the peak ring rocks have the lowest density of the rocks composing the impact structure (Gulick et al., 2013).

3.2.3. The Chicxulub impact event and its consequences

The size of the Chicxulub projectile is generally estimated between ~10–14 km, with a commonly given ~12 km diameter (Morgan et al., 1997), and impacted, according to numerical modeling, at a steep angle of 45–60° from the northeast (Pierazzo and Melosh, 1999; Collins et al., 2020). Also, several studies using available geophysical, drilling, and K–Pg boundary site data, have reconstructed the course of the impact event (which will be further discussed and developed after the summary on the Expedition 364 drilling, see section 3.6). The impactor strokes the Earth surface and formed a transient cavity of ~100 km diameter and ~30 km depth, only tens of seconds after the impact (Collins et al., 2002; Ivanov, 2005). At a local scale, the impact led to a significant collapse of the Yucatán shelf, landslides, mass wasting, gravity flows, earthquakes and aftershocks, multiple tsunamis, which produced the thick K–Pg sequences observed in the Gulf of Mexico surroundings (e.g., Smit, 1999; Schulte et al., 2010). The spherules found around Chicxulub and in North America are thought to have been ejected ballistically at relatively low velocities (e.g., Artemieva and Morgan, 2009), while the thin, distal K–Pg layers are thought to be the product of vaporized and melted projectile and target rocks, ejected at high velocity in the expanding vapor plume (e.g., Alvarez et al., 1980; Melosh and Vickery, 1991; Smit, 1999). At the time of the impact, the target area consisted of a ~600 m depth shallow sea (Gulick et al., 2008), covering a ~3 km thick Mesozoic carbonate and evaporite platform overlying a Paleozoic and Precambrian crystalline and metamorphic basement (López-Ramos, 1975; Zhao et al., 2020, and references therein). The vaporization of the carbonate and sulfate-rich sedimentary rocks lead to the ejection and global dispersal of a large volume of dust, ashes, sulfur, carbon dioxide, and other aerosols into the atmosphere (e.g., Pierazzo et al., 1998, 2003; Schulte et al., 2010; Vellekoop et al., 2014; Kaiho et al., 2016; Artemieva et al., 2017). Consequently, the injection of such large volumes of volatiles and material in the atmosphere has provoked a prolonged global darkening and cooling, i.e., an "impact winter", which had severe effects on the living species (e.g., Alvarez et al., 1980; Pope et al., 1997; Pierazzo et al., 2003; Schulte et al., 2010; Vellekoop et al., 2014; Brugger et al., 2017). Moreover, the ejected particles, when reentering into the atmosphere, were heated and have potentially ignited extensive wildfires (Wolbach et al., 1985; Melosh et al., 1990; Kring and Durda, 2002; Durda and Kring, 2004; Morgan et al., 2013). Details on the global environmental effects of the impact are provided in section 3.6.

3.3. Geological setting of the Yucatán peninsula

Due to the burial of the Chicxulub impact structure and the surrounding area by up to ~1 km of nearly horizontal strata of Cenozoic carbonates and evaporites (López-Ramos, 1975), the Yucatán peninsula pre-impact target rocks (both sedimentary and crystalline basement) stratigraphy is not directly accessible to investigation, with an absence of exposures. Moreover, a relatively limited amount of basement material has been recovered from drilling within and around the impact structure (Hildebrand et al., 1991; Dressler et al., 2003; Kring et al., 2017). Large sedimentary units are preserved within the ring structure, as kilometer-sized slump blocks within the impact structure terrace area, and as clasts in the Chicxulub suevite (Claeys et al., 2003; Belza et al., 2012). In the suevite are also preserved clasts of mica schist, gneiss, metasediments, granite, and dolerite from the crystalline basement (Claeys et al., 2003; Kettrup and Deutsch, 2003; Tuchscherer et al., 2005; Morgan et al., 2017). Outcrops of pre-impact lithologies are only found at proximal K–Pg ejecta deposits located ~350 km southeast from the Chicxulub impact structure center, at the border of the Mexican province of Quintana Roo and northern Belize (Ocampo et al., 1996). In-place crystalline basement outcrops which may represent the Maya block located underneath the Yucatán peninsula, are located even further away, in the Chiapas Massif Complex, in proximity of the México-Guatemala border, ~700 km from the Chicxulub structure (Ortega-Gutiérrez et al., 2018, and references therein).
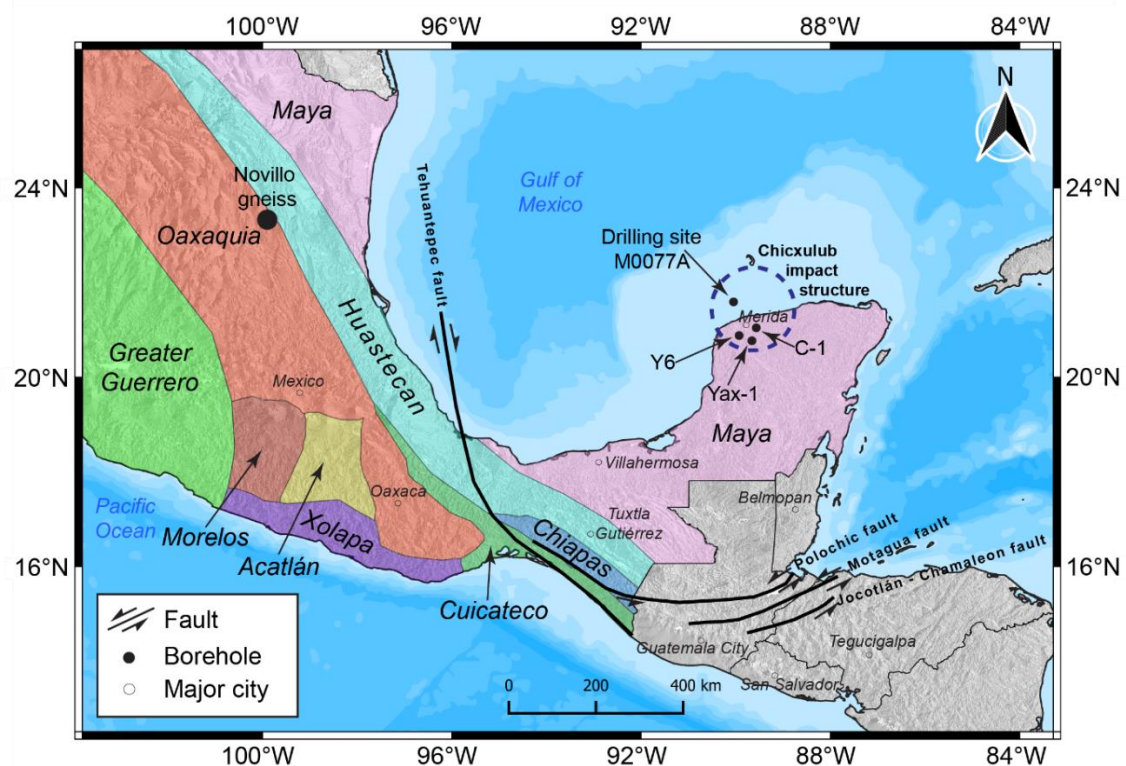
Figure 3.6. *Map of southeast Mexico with the main tectonostratigraphic domains proposed by Ortega-Gutiérrez et al. (2018), major faults, and the Chicxulub impact structure (dashed circle; 200 km-in-diameter) with the IODP-ICDP Expedition 364 (M0077A) and previous drilling (Y6, Yax-1, and C-1) locations (from Feignon et al., 2021; modified from Weber et al., 2012, 2018; Ortega-Gutiérrez et al., 2018). SRTM data can be found online at: https://www2.jpl.nasa.gov/srtm/cbanddataproducts.html.*

The Maya block is described as encompassing the Yucatán peninsula, the northeast of Mexico, the coastal plains of the western and northern Gulf of Mexico, and the Chiapas massif complex (Keppie et al., 2011; Weber et al., 2012, 2018), with its north and northeastern boundaries bordered by continental shelves and oceanic lithosphere (Alaniz-Álvarez et al., 1996; Keppie et al., 2011). The Maya block was thought to be bordered in the northwest by the Oaxaquia block (Grenvillian-aged); in the southwest by the Cuicateco complex; and in the south by the Polochic, Motagua, and Jocotlán-Chamaleón fault systems (Fig. 3.6), making the separation with the Caribbean plate (Dengo, 1969; Donnelly et al., 1990; Weber et al., 2012, 2018). However, recent work by Ortega-Gutiérrez et al. (2018) suggests that the Chiapas massif (or Southern Maya massif) forms a distinct lithotectonic domain (Fig. 3.6), characterized by the presence of medium- to high-grade metamorphic rock outcrops that were not observed in the Maya block (Weber et al., 2008; Ortega-Gutiérrez et al., 2018). The Chiapas massif would be separated from the Maya block by the Paleozoic-aged Huastecan orogenic belt. This orogenic system is mostly buried and extends from the Ouachita suture belt in Northwest Mexico to the Polochic, Motagua, and Jocotlán-Chamaleón fault systems in Guatemala. Consequently, the Huastecan orogenic belt separates the Maya block from the Oaxaquia and Cuicateco terranes in the west and southwest, respectively (Fig. 3.6).

Dating, using the $^{40}Ar/^{39}Ar$ dating method, yields an age of 546 ± 5 Ma (Pan-African) for a tholeiitic dolerite intruded in the Grenvillian Novillo gneiss in the Ciudad Victoria area (Keppie et al., 2011). Similarly, the dating of ejected zircon grains found at various K–Pg boundary sites range mainly between 550 and 545 Ma, just after the Cambrian-Precambrian boundary (Krogh et al., 1993a, 1993b; Kettrup and Deutsch, 2003, and references therein; Kamo et al., 2011; Keppie et al., 2011). This suggests that the northern part of the Yucatán peninsula, where the Chicxulub impact structure is located, is composed of predominantly Late Ediacaran basement (Ortega-Gutiérrez et al., 2018). The Sm–Nd T_{DM} model ages reported from orthogneiss, impact melt rock, impact glass, and amphibolite samples from drill cores recovered within the Chicxulub impact structure display a wide range between 1.4 and 0.7 Ga, suggesting the involvement of a Grenvillian component during the formation of the Yucatán crystalline basement (Kettrup and Deutsch, 2003; Keppie et al., 2011). Granites and zircon grains with younger ages (i.e., late Paleozoic in age, ~320–345 Ma) are also reported (Kamo and Krogh, 1995; Kamo et al., 2011; Keppie et al., 2011), with the granite basement unit found in the peak ring (see section 3.6, and publication chapter 6) yielding zircon ages of 326 ± 5 (Zhao et al., 2020) and 334 ± 2.3 Ma (Ross et al., 2022).
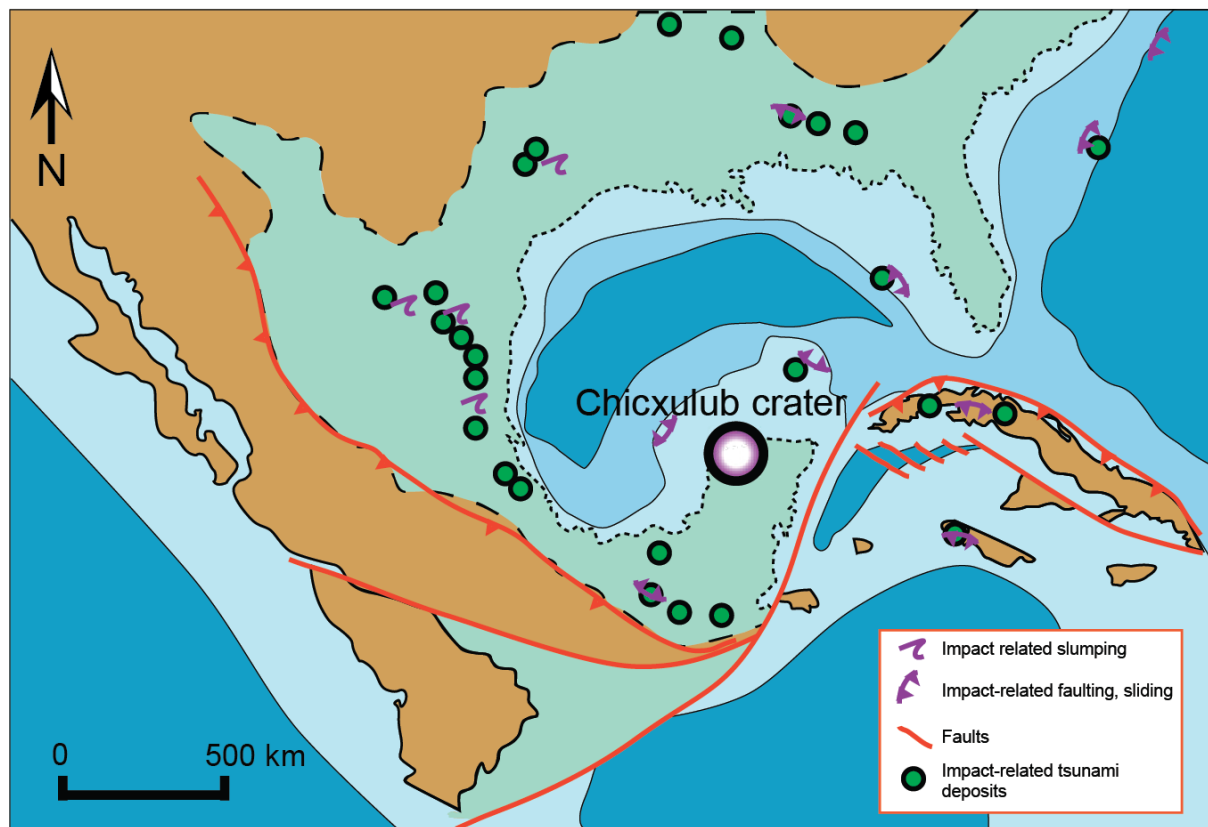
Figure 3.7. *Paleogeographic map of the Gulf of Mexico at the end of the Cretaceous, with the location of the Chicxulub impact event. The Yucatán peninsula consisted of a stable carbonate platform covered by a shallow sea. Cretaceous lands are in orange, while current geography is highlighted in light green. The green dots show the locations of K–Pg-age impact-related tsunami deposits. Modified from Vellekoop et al. (2014), and references therein.*

At the time of the Chicxulub impact event, at ~66.05 Ma (Sprain et al., 2018), the Yucatán basement was covered by an approximately 3 km thick, stable carbonate platform composed of limestone, dolomite, marl, and anhydrite (Fig. 3.7; López Ramos, 1975; Kring, 2005). Additionally, the platform was covered by seawater, deepening to the north and northeast with an average water depth of ~600 m (Gulick et al., 2008). As the region was and remained tectonically and magmatically inactive since ~150 Ma (Molina-Garza et al., 1992), the overall structure of the Chicxulub remained relatively pristine, offering an ideal case study to understand the formation processes of a peak ring complex crater. The Yucatán peninsula pre-impact basement rocks and geologic history are presented and discussed in details in publication Chapter 6 (Feignon et al., 2021), as well as in Chapter 8, in Zhao et al. (2020) and references therein, and in de Graaff et al. (2022).

3.4. Chicxulub drill cores (before IODP-ICDP Expedition 364)

Drilling within and outside the Chicxulub impact structure provided an incredible amount of information on the subsurface stratigraphy, the structure, the physical properties, the geochemistry, the shock metamorphic features and associated shock levels, the type of impactites, and pre-impact lithologies. Several drilling programs have been conducted, the first

being the PEMEX oil exploration surveys that have started in the mid-1950s, and that were completed in the mid-1970s, within and around Chicxulub (nine boreholes in the Chicxulub area in total), and being extensively re-investigated after the confirmation of the impact origin of the crater structure (López-Ramos, 1975; Hildebrand et al., 1991; Sharpton et al., 1992; Urrutia-Fucugauchi et al., 2011, and references therein).
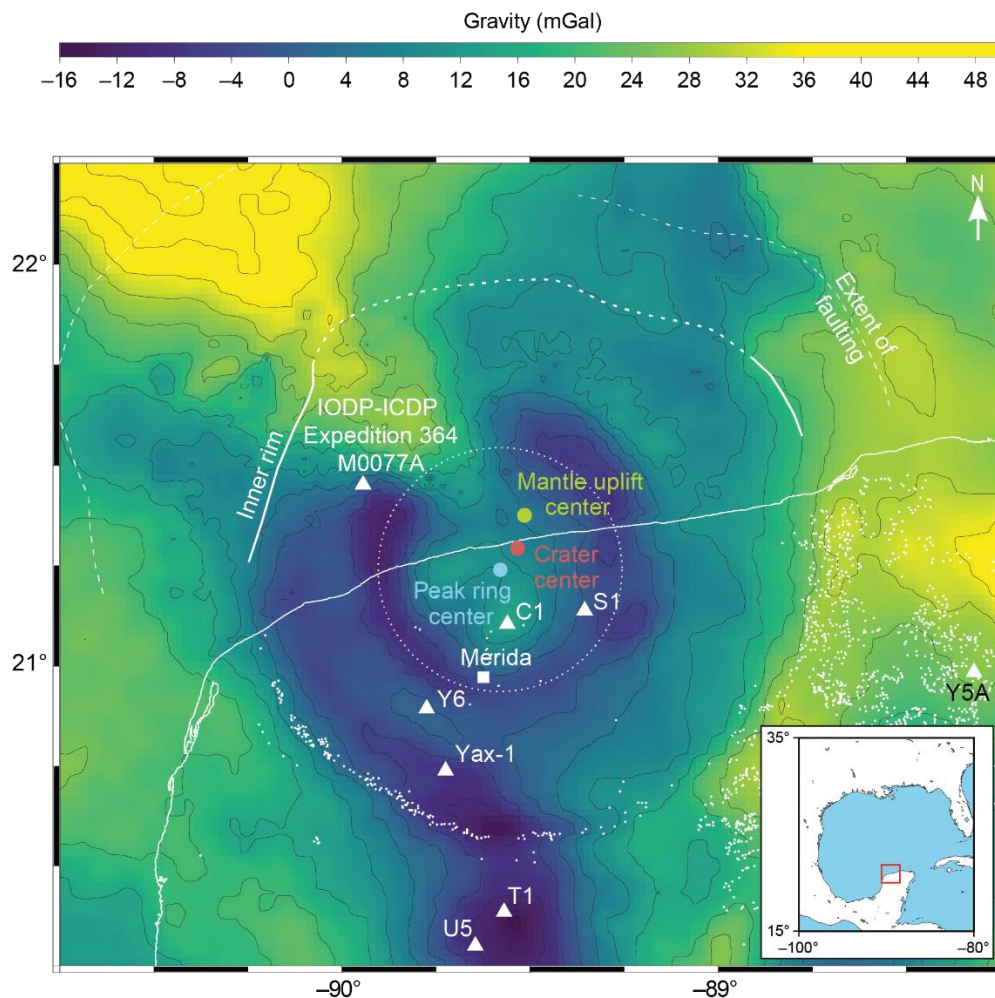
Figure 3.8. *Map of the northeast Yucatán peninsula, centered on the Chicxulub impact structure, showing the Bouguer gravity anomaly and the locations of the main drilling sites within and in proximity of Chicxulub. Red circle: nominal position of the impact structure center; green circle: center of maximum mantle uplift; blue circle: peak ring center; square: location of Mérida, the main city in the area; white triangles: locations of drilling sites, including the 2016 IODP-ICDP Expedition 364 drilling site. The cenotes and sinkholes are represented by white dots. Lines offshore mark the approximate location of the impact structure inner rim and the extent of faulting according to seismic data (modified from Collins et al., 2020, and references therein).*

A second shallow-drilling campaign was conducted by the Universidad Nacional Autónoma de México (UNAM), in the mid-1990s, and recovered a total of eight drill cores (Urrutia-Fucugauchi et al., 1996; Rebolledo-Vieyra et al., 2000; Urrutia-Fucugauchi et al., 2011). The third drilling campaign, was conducted by the International Continental Scientific Drilling

Program (ICDP), in the winter months of 2001/2002 at the Yaxcopoil-1 (Yax-1) drilling site, located ~62 km south from the impact structure center (Dressler et al., 2003, 2004; Stöffler et al., 2004; Urrutia-Fucugauchi et al., 2004; Urrutia-Fucugauchi et al., 2011, and references therein; see Fig. 3.8). The most recent drilling, to date, was performed in 2016, for the first time, offshore, and right above the Chicxulub peak ring, by the joint International Ocean Discovery Program (IODP) and ICDP, as Expedition 364, at site M0077A (Fig. 3.8; see details in section 3.6).

3.4.1. The PEMEX drill cores

During the drilling program carried out by PEMEX, the amount of coring was rather limited, and their interest in the area waned after reaching Paleozoic basement and impactites without any sign of hydrocarbons. Only limited samples are now available for investigation. The stratigraphy of these drill cores is presented in Figure 3.9. Three drill cores were recovered within the Chicxulub impact structure, at boreholes Chicxulub-1 (C1, 1581 m total depth), Sacapuc-1 (S1, 1530 m), and Yucatán-6 (Y6, 1645 m). The C1, S1, and Y6 drill cores penetrated a sequence of Mesozoic and Cenozoic carbonate platform sedimentary rocks, and reached impactite lithologies, i.e., impact melt rocks and impact breccias (suevite), at depths of ~1.0–1.1 km. The suevite unit in these drill cores is ~250–400 m thick, and the impact melt rock has a minimum thickness of 250 m (i.e., the drilling ended in this unit; see details in Urrutia-Fucugauchi et al., 2011, and references therein).

The C1 drill core was recovered near the center of the structure, penetrating the innermost central melt sheet. Unfortunately, only two impact melt rock samples have been preserved (C1-N9, and C1-N10 at ~1400 m depth). The impact melt rock is composed of abundant millimeter-sized melt fragments embedded in a cryptocrystalline to microcrystalline matrix made of pyroxene (augite) and lath-shaped plagioclase grains (~0.5 mm in size) (Sharpton et al., 1992, Koeberl et al., 1994; Claeys, 2006; Urrutia-Fucugauchi et al., 2011). The majority of the clasts are digested in the matrix, only some subhedral to euhedral pyroxene and feldspar grains remaining, indicating a relatively slow cooling of the central melt sheet after the impact, also supported by the crystallization age of 65.2 ± 0.4 Ma obtained from $^{40}Ar/^{39}Ar$ radiometric dating (Sharpton et al., 1992; Swisher et al., 1992; Schuraytz et al., 1994). Alteration seems to have been rather limited in these samples, compared to Y6 or Yax-1 core samples, as calcite, anhydrite, and albite rims around plagioclases are rarely observed (Koeberl et al., 1994; Claeys, 2006).
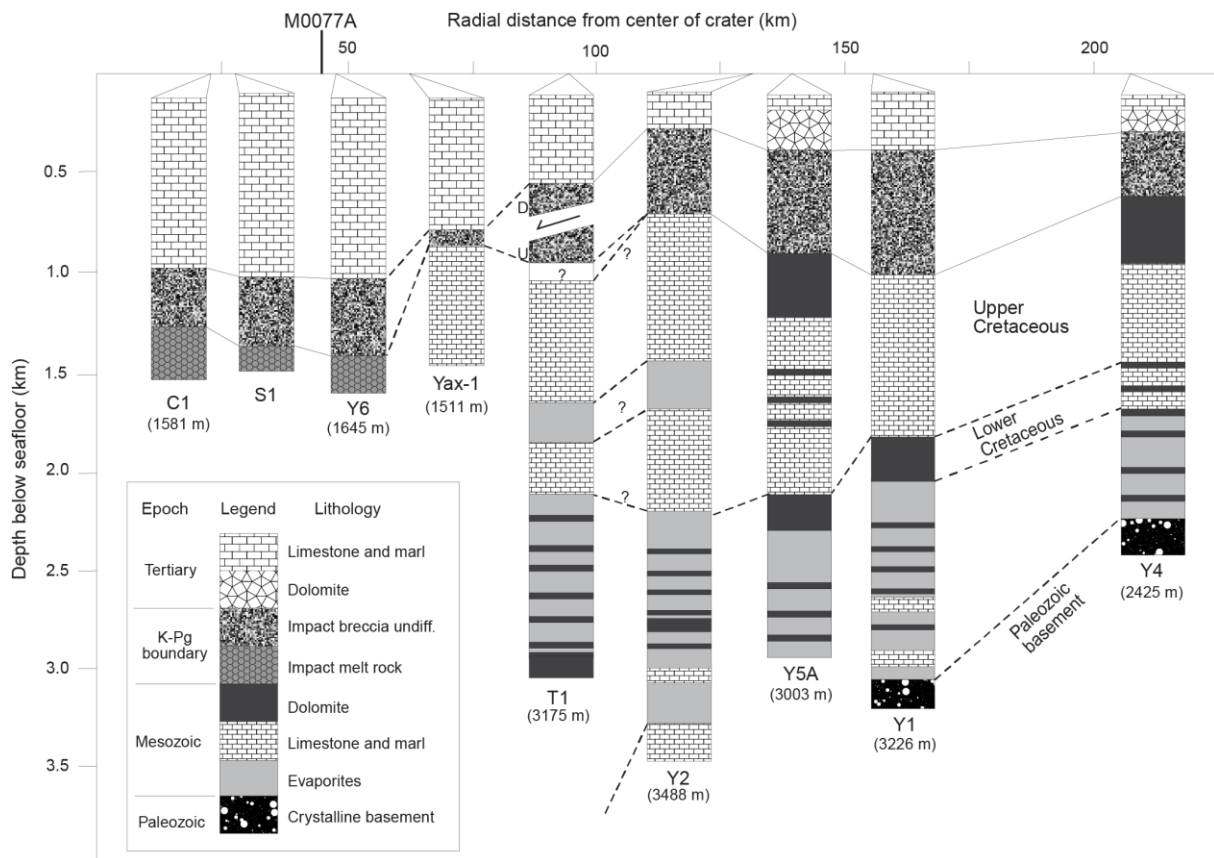
Figure 3.9. *Stratigraphic log with lithologies of Yax-1 and PEMEX boreholes. The classification is made according to the distance of the drilling site from the center of the Chicxulub impact structure. For comparison, the location of the Expedition 364 drilling (site M0077A) is indicated (modified from Urrutia-Fucugauchi et al., 2011).*

The Y6 drill core was recovered in proximity of the peak ring area, ~50 km southwest from the center of the Chicxulub impact structure. In comparison to C1, more samples are available from Y6, allowing to reconstruct the impactites sequence, which consists of ~250 m thick suevite (Sharpton et al., 1996) starting at ~1100 m depth, below Cenozoic sedimentary layers and overlying ~330 m of brecciated impact melt rock (starting from ~1260–1270 m; Claeys et al., 2003; Claeys, 2006). The bottom of Y6 drill core (from ~1641 m) is made, according to PEMEX reports, of dolomite-anhydrite breccia (Claeys, 2006). Claeys et al. (2003) described in detail the suevite lithology of Y6 core, which was divided in three units (the thickness of these units is difficult to constrain due to the non-continuous availability of samples), from top to bottom: (1) the upper suevite (or carbonate-rich suevite), dominated by small (~0.5 mm), densely packed, carbonate clasts, while melted basement clasts altered to phyllosilicates are also present. The porous matrix is composed of microcrystalline (~10–30 µm) calcite, feldspar, and quartz; (2) the middle suevite (or clast-rich suevite) is composed mainly of millimeter- to centimeter-sized silicate basement (shocked quartzite and gneiss) and impact melt clasts, while the proportion of carbonate clasts decreases compared to the upper suevite. Rare anhydrite clasts are also present. The matrix is calcite-rich (~40 wt.%). This unit is described as a "typical" fall-back suevite similar to the one described at the Ries structure in Germany; and (3) the lower suevite (or melt-rich, thermometamorphic suevite) is composed of abundant impact melt fragments, as well as shocked crystalline basement clasts, with rare

carbonate clasts. The matrix is recrystallized with euhedral feldspar and pyroxene grains. The emplacement of the suevite sequence was interpreted as: the lower suevite represents an early fall-back material (mainly excavated from the basement) or ground-surged material formed during the collapse of the transient cavity, and the matrix was probably thermometamorphosed and recrystallized at the contact of the hot, underlying melt rock, then, a typical fall-back suevite (middle suevite) emplaced, followed by the settlement of the fall-back material (mainly sedimentary material) through the water column or by reworking after the impact structure inundation (Claeys et al., 2003). The Y6 impact melt rock, according to available samples, has a similar andesitic-to-dacitic composition than C1 impact melt rock, which can be explained by a mixture of sedimentary and crystalline basement rocks known to occur in the Yucatán crust (Hildebrand et al., 1991; Kring and Boynton, 1992; Sharpton et al., 1992; Warren et al., 1996). However, petrographically, Y6 impact melt rock is richer in carbonate, and undigested clasts, and more finely crystallized compared to C1 impact melt rock, indicating a possible faster cooling (e.g., Koeberl, 1993; Schuraytz et al., 1994; Claeys et al., 2003).

Regarding the S1 drill core, located ~30 km southeast from the Chicxulub impact structure center, only one suevite sample has been described in the literature (S1-N18 at 1365–1368 m depth). It was described as being similar to the "middle suevite" of Y6 (Sharpton et al., 1996; Claeys et al., 2003).

Outside the Chicxulub impact structure, some drill cores were recovered, with increasing distance from the center of the impact structure, at boreholes Ticul-1 (T1, 3175 m), Yucatán-2 (Y2, 3488 m), Yucatán-5A (Y5A, 3003 m), Yucatán-1 (Y1, 3226 m), and Yucatán-4 (Y4, 2425 m) (Urrutia-Fucugauchi et al., 2011). In the drill cores T1, Y2, Y5A, Y1, and Y4 were recovered thick (up to ~2.0–2.5 km) sequences of Cretaceous rocks, comprising limestones, marls, dolomites, carbonates, and sections of evaporites and anhydrites of the Lower Cretaceous. The Paleozoic basement was sampled in Y1 and Y2 cores, at ~3.3 km depth. Impactites, in the form of polymict impact breccia sections of ~400–600 m in thickness, overly the Cretaceous sedimentary rocks (see details in Hildebrand et al., 1991; Sharpton et al., 1996; Urrutia-Fucugauchi et al., 2011, and references therein). A study by Ward et al. (1995) estimated the pre-impact sedimentary rock stratigraphy of the area to be composed of ~35–40 vol% dolomite, ~25–30 vol% limestone, ~25–30 vol% anhydrite, and ~3–4 vol% sandstone and shale.

3.4.2. The UNAM drill cores

The scientific drilling program conducted by UNAM investigated eight boreholes (from U1 to U8, see Fig. 3.10) located in the southern sector of the Chicxulub impact structure, distributed within and outside the impact structure rim, and recovered (average recovery rate of 87%) drill cores from 60 to 702 m depth (Urrutia-Fucugauchi et al., 1996; Rebolledo-Vieyra et al., 2000; Urrutia-Fucugauchi et al., 2011). Of the eight available drill cores, three (U5, U6, and U7) were located outside of the Chicxulub impact structure (105, 150, and 125 km from the impact structure center, respectively) and sampled impactite material (belonging to the proximal ejecta blanket) in contact with the Paleogene carbonates (Urrutia-Fucugauchi et al., 1996; Rebolledo-Vieyra et al., 2000). The depth of the contact between the Paleogene carbonates and the impactites is 332 m in U5, 283 m in U6, and 222 m in U7, and marks the

K–Pg boundary (Urrutia-Fucugauchi et al., 1996; Rebolledo-Vieyra et al., 2000). The impactites were divided into distinct units, i.e., a suevite unit overlying a polymict impact breccia. The suevite, also termed as "fall-out suevite", is composed of various proportions of crystalline basement, impact glass, impact melt rock, carbonate, and anhydrite clasts embedded in a clastic carbonate-rich matrix, whereas the polymict impact breccia unit contains no or very few impact melt rock fragments, and is mainly composed of carbonate (limestone and dolomite) and evaporite clasts (Urrutia-Fucugauchi et al., 1996; Rebolledo-Vieyra et al., 2000; Urrutia-Fucugauchi et al., 2008, 2011).
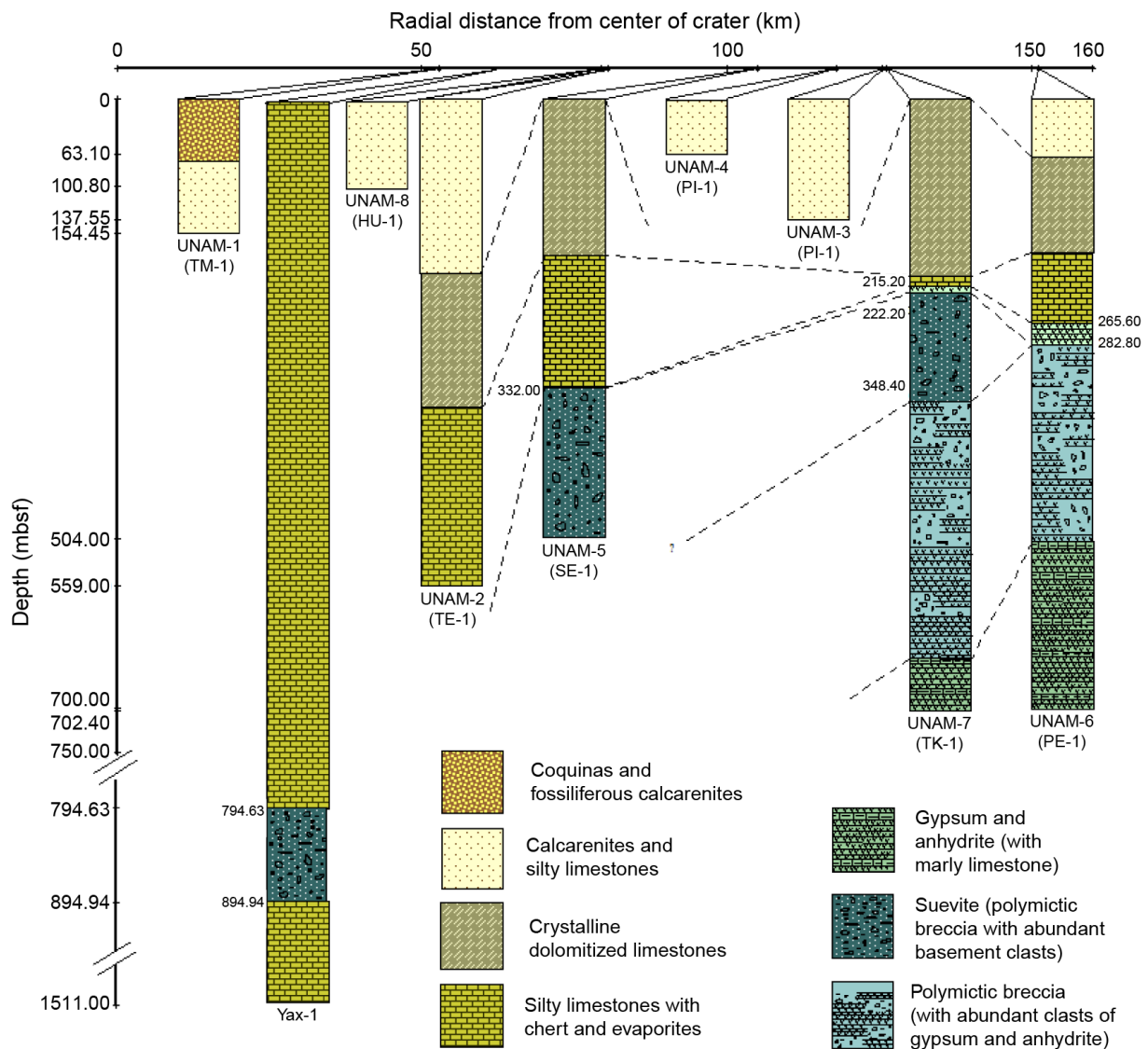
Figure 3.10. *Stratigraphic and lithologic columns of the UNAM drill cores, with Yax-1 for comparison (from Urrutia-Fucugauchi et al., 2011).*

In the U5 drill core, only the suevite occurs from the contact with the Paleogene carbonates to the core bottom at 504 m (Urrutia-Fucugauchi et al., 1996). In U7 drill core, the suevite occurs at depths from 222 to 348 m and the polymict impact breccia occurs below. Finally, in UNAM 6, which is further away from the Chicxulub, there is no suevite unit, with only the polymict impact breccia being present. The succession of polymict impact breccia

topped by suevite is similar to the Bunte breccia (fall-out suevite) units seen outside the Ries impact structure, Germany (Rebolledo-Vieyra et al., 2000). The thickness of the suevite is decreasing with increasing distance from the impact structure, whereas the thickness of the polymict impact breccia increases. Additionally, the reverse stratigraphy of the impactites (i.e., suevite with basement and melt clasts overlying on carbonate breccias) is the result of the outward excavation flow forming an "overturned flap" of ejecta, depositing the first material (i.e., Mesozoic sedimentary target rocks) ejected, and then, the deep, basement material is excavated and deposited out of the ejecta plume above the "Bunte-Breccia", rich in carbonate and evaporite clasts (Rebolledo-Vieyra et al., 2000; Urrutia-Fucugauchi et al., 2008). The polymict impact breccia unit may be related to the impact breccias observed in PEMEX drill cores Y1, Y2, Y4, Y5A, and T1, but this is still to be confirmed (Morgan et al., 2017).

In the remaining drill cores (U1–U4, and U8), only the Paleogene carbonate layers (~200 m thick) were sampled. They are composed mainly of limestones, dolomitized limestones, calcarenites, and fossiliferous horizons (Rebolledo-Vieyra et al., 2000).

3.4.3. The Yax-1 drill core

Between December 2001 and March 2002, a scientific drilling was carried out by ICDP at the Hacienda Yaxcopoil, recovering continuous cores from 404 to 1511 m depth (see Fig. 3.11). The drilling site of Yax-1 is located ~62 km south from the center of the Chicxulub impact structure, and ~15 km south of the previously described Y6 drilling site, and corresponds to the annular through located between the peak ring and the impact structure rim (Fig. 3.8; Dressler et al., 2003; Urrutia-Fucugauchi et al., 2004). For the first time, a full sequence of, from top to bottom, post-impact, crater-filling, Cenozoic sedimentary rock layers (interlayered carbonaceous siltstones and calcarenites, 795 m thick, cored only between 495 and 795 m), impactites (suevite-like lithology, ~100 m thick, from 795 to 895 m), and Cretaceous pre-impact sedimentary target rocks (dolomite, limestone, and anhydrite layers, 616 m thick, from 895 to core bottom at 1511 m), were recovered, and, in contrast to the PEMEX drill cores, Yax-1 borehole was fully cored (Dressler et al., 2003; Stöffler et al., 2004; Urrutia-Fucugauchi et al., 2004). The impactite sequence has been extensively described and investigated and was subdivided into 6 units (Fig. 3.11; see details in Dressler et al., 2003, 2004; Kring et al., 2004; Kenkmann et al., 2004; Schmitt et al., 2004; Stöffler et al., 2004; Wittmann et al., 2004; and more broadly in special volume 39, issues 6 and 7 (June and July 2004), of the journal *Meteoritics & Planetary Science,* which were dedicated to results from the Yaxcopoil-1 drilling). Only Tuchscherer et al. (2004a, 2004b, 2005, 2006) grouped the two upper units, based on macro- and microscopic observations, considering that they form a continuous, fining upward sequence (Tuchscherer et al., 2004a). In general, the impactites of Yax-1 are rich in impact melt and glass clasts, mostly derived from the crystalline silicate basement, while the matrix shows a major carbonate component (Dressler et al., 2004; Stöffler et al., 2004; Tuchscherer et al., 2004a). The Yax-1 drill core impactites are pervasively hydrothermally altered, to a higher degree than for Y6, with the former impact melt and glass clasts generally altered to phyllosilicates or replaced by secondary K-feldspars (Ames et al., 2004; Hecht et al., 2004; Zürcher and Kring, 2004). The hydrothermal alteration of Yax-1 impactites is thought to

have been caused by the combined effects of a saline brine and heat coming from adjacent areas where the impact melt sheet was thicker (Zürcher and Kring, 2004).

Unit 1 (upper sorted suevite, 795–808 m depth), is a homogenous, fine-grained (~1–2 mm), partly laminated, and clast-supported suevite composed mainly of greenish-to-brownish impact melt, carbonate, and rare crystalline basement (granitic) clasts. The matrix is composed of fine calcite crystals, with silicates only occurring locally in the form of patches between clasts. The Unit 2 (lower sorted suevite, 808–823 m) displays the same components (both clast types and matrix) than the upper sorted suevite, but is coarser grained, with clasts reaching sizes up to several centimeters. Both Units 1 and 2 are sorted, with an increase in clast size with increasing depth in the core, and were interpreted as a reworked fallout deposit, the grains sorting occurring during continuous deposition through the air or water (Stöffler et al., 2004; Tuchscherer et al., 2004a). The Units 1 and 2 have also been described as very similar to the "upper suevite" unit defined in Y6 drill core (Claeys et al., 2003; Tuchscherer et al., 2004a). Unit 3 (upper suevite, also termed as "chocolate-brown melt breccia" by Dressler et al. (2003), 823–846 m) is distinct from the two overlying units. If impact melt clasts are still the most abundant (shard-like shaped), crystalline basement clasts dominate over carbonate clasts. The clast size is ~2 cm on average. The impact melt rock fragments display a green fluidal texture (schlieren), with abundant microlites aligned following the direction of the flow, and are in some cases vesiculated. The matrix, representing more than 50% of the rock, is fine-grained, brown in color, and thought to be mainly composed of carbonate and altered melt (Dressler et al., 2004; Tuchscherer et al., 2004a). Unit 4 (middle suevite, 846–861 m) is composed of impact melt clasts displaying various range of colors (brown, gray, and green, with brown clasts proportion increasing with depth) with reaction rims, the average clast size is similar to Unit 3 (~2 cm) but larger clasts are more abundant. The amount of matrix is also less abundant (~30%) than in Unit 3. Units 3 and 4 have been correlated with the "middle suevite" of Y6, sharing similarities, and interpreted as formed following a fall-back process as the vapor plume was rising above the impact structure (Claeys et al., 2003; Tuchscherer et al., 2004; Claeys, 2006). Unit 5 (brecciated impact melt rock, 861–885 m), is considered as an impact melt rock breccia, green in color. Impact melt rock clasts are abundant, representing ~75–80 vol% of the rock, and display a banding texture, highlighted by compositional and alteration heterogeneities (Ames et al., 2004). Crystalline basement (mainly) and carbonate clasts also occur, with a lower abundance compared to impact melt rock clasts. Some of the clasts have relatively large size (>20 cm). The matrix, representing less than 10 vol% of the rock, is mainly composed of recrystallized plagioclase and pyroxene. Possibly, this unit may be an equivalent to the impact melt rock unit occurring in the bottom part of the Y6 drill core (Claeys, 2006). Finally, Unit 6 (lower suevite, 885–895 m) consists of dispersed impact melt rock clasts embedded in a carbonate-rich, microcrystalline to fine-grained (<0.05–2 mm) matrix. Unit 6 has the highest carbonate content of all the impactite units (Tuchscherer et al., 2004a). Pre-impact lithology clasts include mainly limestone and dolomite, and rare crystalline basement. No equivalents of this unit are known in the Y6 drill core (Tuchscherer et al., 2004a; Claeys, 2006). Units 5 and 6 were likely formed following a ground surge deposit, when the impact melt sheet flowed into the annular basin, from the collapsing central peak (Stöffler et al., 2004).
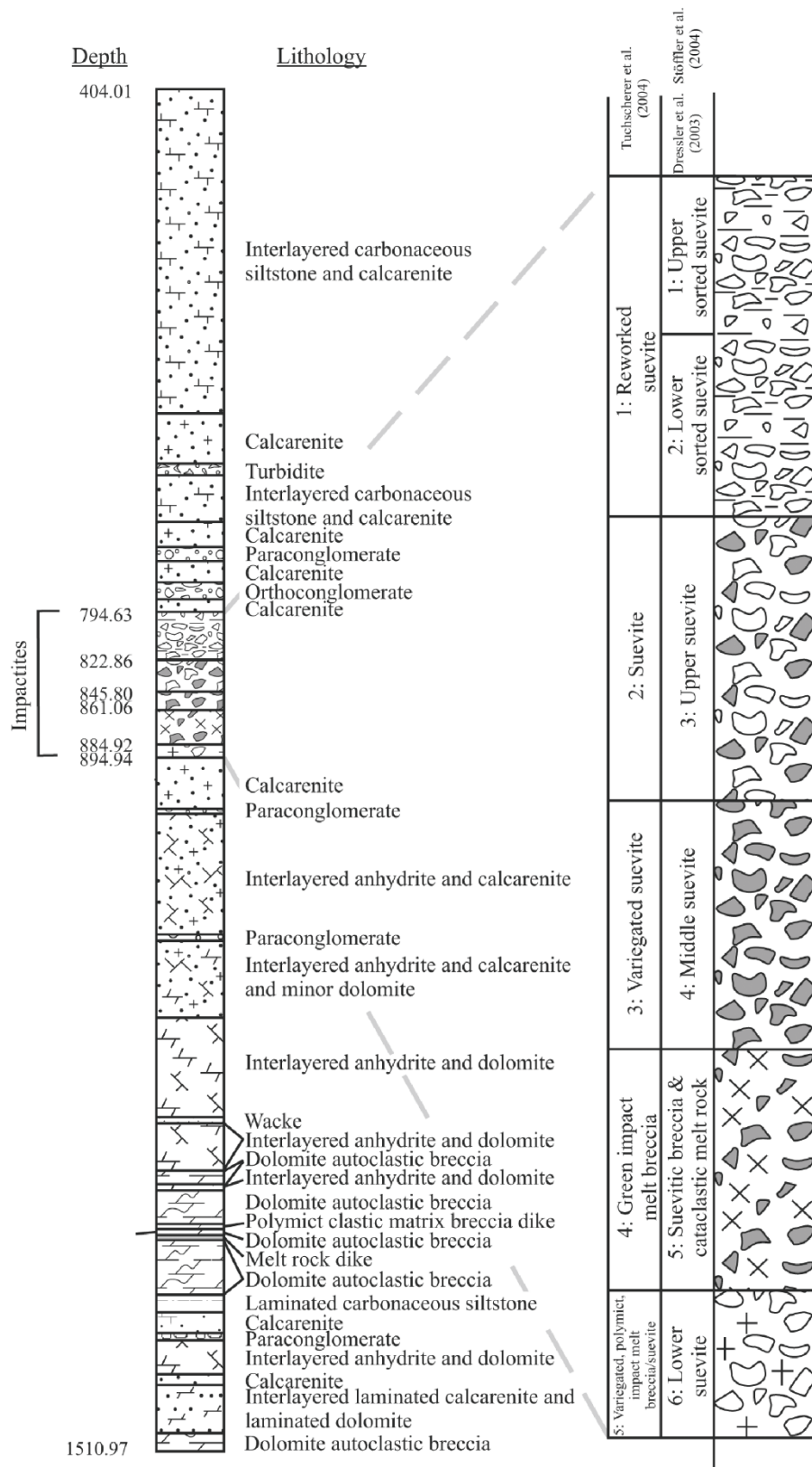
Figure 3.11. *Stratigraphic column of the Yax-1 drill core, with enlarged impactite sequence. The original unit classification of Dressler et al. (2003), and Stöffler et al. (2004) is shown, as well as the classification of Tuchscherer et al. (2004a). Modified from Tuchscherer et al. (2004b), and references therein.*

The generally accepted formation model for the entire impactite sequence of Yax-1 suggests that ground surging at the base of the ejecta curtain was followed by continued collapse of the ejecta plume, and reworking in presence of water at the top (Dressler et al., 2004; Goto et al., 2004; Kring et al., 2004; Stöffler et al., 2004; Tuchscherer et al., 2004a; Wittmann et al., 2007).

In terms of geochemistry, the impactites from Yax-1 have heterogeneous compositions (both in major and trace element contents) at the sample scale (8–16 cm^3), mainly due to variations in the mixing between carbonate and silicate components, and the effects of post-impact hydrothermal alteration (Hecht et al., 2004; Tuchscherer et al., 2004b, 2005). The Units 1 to 4 have similar major and trace element compositions, while the Unit 5 indicates that impact melt rocks formed from melted Yucatán crystalline basement, with the involvement of a mafic component (Tuchscherer et al., 2004b, 2005). The Unit 6 displays high variations in composition from a sample to another, and represents a mixing between carbonate and siliceous impact melt particles that underwent secondary hydrothermal alteration (Tuchscherer et al., 2004b).

Below the impactites sequence, the lower part of the Yax-1 core consists of >70% carbonate (i.e., limestone and dolomite), and ~27% anhydrite Cretaceous megablocks, that appear to have been rotated relative to each other, possibly indicative of slumping (i.e., displacement) from the inner rim of the Chicxulub into the annular through, to form a terraced rim zone during the modification stage of the crater (Dressler et al., 2003, 2004; Kenkmann et al., 2004; Belza et al., 2012). Therefore, this slumping prevents the understanding of the true thickness of the impactites sequence, its nature, and its formation dynamics within the Chicxulub impact structure (Kring et al., 2017). The megablocks are also intruded by suevite, impact melt rock, cataclastic, and polymict dikes (Wittmann et al., 2004).

The bottom part of the post-impact, Cenozoic sedimentary rock sequence reveals gravity flows and resurge deposits that formed as part of the initial crater fill (Goto et al., 2004; Whalen et al., 2008, 2013) and shows geochemical evidence (high concentrations of Mn, Fe, P, Ti, and Al at the bottom part of the Cenozoic sequence relative to the upper part) indicative of the injection of hydrothermal fluids (i.e., hydrothermal venting) into the Cenozoic seawater (Rowe et al., 2004; Zürcher and Kring, 2004).

3.5. Identification of the Chicxulub impactor

As discussed in Chapter 2, the identification of the impactor type is generally made difficult by the complete vaporization of the projectile, especially in the case of large impact events, and only a fraction of meteoritic material may be incorporated within impactites (Tagle and Hecht, 2006). Details on the search for a meteoritic component within the impact melt rocks of the Chicxulub peak ring and its implications are presented in publication Chapter 7 (Feignon et al., 2022).

Within the Chicxulub impact structure, several studies have tried to identify and/or to quantify the presence of a meteoritic component within the impactites recovered in C1, Y6, and Yax-1 drill cores, and came up with mostly a low and/or heterogeneously distributed meteoritic component (Koeberl et al., 1994, Gelinas et al., 2004, Tagle et al., 2004; Tuchscherer et al., 2004b). Most of the investigated impact melt rock and suevite samples in the Yax-1 drill core

have low Ir contents, generally below 100 ppt, and highly siderophile element (HSE) abundance patterns similar to those of the UCC (Tagle et al., 2004, Tuchscherer et al., 2004b). Clast-rich (with quartz, feldspar, anhydrite, and carbonate clasts) impact melt rock sample Y6-N19 from the Y6 drill core shows similar upper crustal HSE composition (Tagle et al., 2004). In these impactites, the meteoritic component, if present, corresponds to the equivalent of less than 0.05% chondrite (Tagle et al., 2004). Minor enrichments were measured in three samples from Yax-1, i.e., (1) a clast-supported, reworked suevite, with limestone, fossil, and melt clast at 800.4 m depth in the core, (2) a fine-grained, carbonate groundmass supported suevite containing melt particles at 844.8 m depth, and (3), a polymict impact melt breccia with a fine-grained carbonate groundmass at 890.5 m depth (Tuchscherer et al., 2004b). The Ir contents of these samples are up to ~400 ppt, which is higher by a factor of 50 compared to other impactites from Yax–1 and upper crustal values (Tuchscherer et al., 2004b). These Ir enrichments were thought to be indicative of a minor, heterogeneously distributed, meteoritic signature within the impactites (Tuchscherer et al., 2004b). Other impact melt rock samples from Yax-1 were investigated by Gelinas et al. (2004), using Re–Os isotope systematics (as was already done by Koeberl et al., 1994, for C1 and Y6 samples), and have revealed variable Os contents, ranging from 11 to 368 ppt, and corresponding ^{187}Os/^{188}Os ratios, which range from ~0.19 to ~2.31. These data were interpreted to indicate the presence of a minor and heterogeneously distributed chondritic component, equivalent to less than 0.1% of a chondritic admixture in four samples but less than 0.01% of such a component in nine samples (Fig. 3.12). Only two studies reported elevated Ir contents, potentially indicative of a meteoritic component in C1 and Y6 impact melt rocks. Iridium concentrations of ~6 and ~13.8 ppb, respectively were measured in powder splits (i.e., aliquot from the same prepared powder) from C1 and Y6 impact melt rocks (Koeberl et al., 1994, Schuraytz et al., 1996). The powder split from one sample of the C1 core, showing a high Ir content (~6 ppb), also had a high Os concentration of ~25 ppb, associated with a subchondritic ^{187}Os/^{188}Os ratio of ~0.11 (Fig. 3.12). This was explained as representing an admixture of ~3% of meteoritic material (Koeberl et al., 1994). However, other studies failed to reproduce these anomalies in Y6 and C1 (see also Tagle et al., 2004, and references therein).

The most compelling evidence of a chemical contamination from the projectile is found in distal K–Pg impact ejecta, including Ir and other HSEs enrichments in the K–Pg clay layer at different sites worldwide (Schulte et al., 2010, Goderis et al., 2013, and references therein). At several K–Pg boundary sites, the HSE abundances and ^{187}Os/^{188}Os isotopic signatures have revealed the presence of up to ~5% of a chondritic component (Fig. 3.12; Quitté et al., 2007; Goderis et al., 2013). Chromium isotopes were also used in order to identify the impactor type of the Chicxulub impact event. Results of Cr isotope ratios by Shukolyukov and Lugmair (1998), and Quitté et al. (2007) were consistent with a carbonaceous chondritic projectile (Fig. 3.12). The calculation, using linear regression analysis, of HSE inter-element abundance ratios in meteorites and in a large database of K–Pg deposits suggested that the Chicxulub impactor was a carbonaceous chondrite either of the CM or CO group (Goderis et al., 2013). This identification was also refined by Trinquier et al. (2006), using high-precision measurement of $\varepsilon(^{54}$Cr), and proposed that the projectile was a CM2 chondrite (i.e., of the CM group and petrologic type 2).
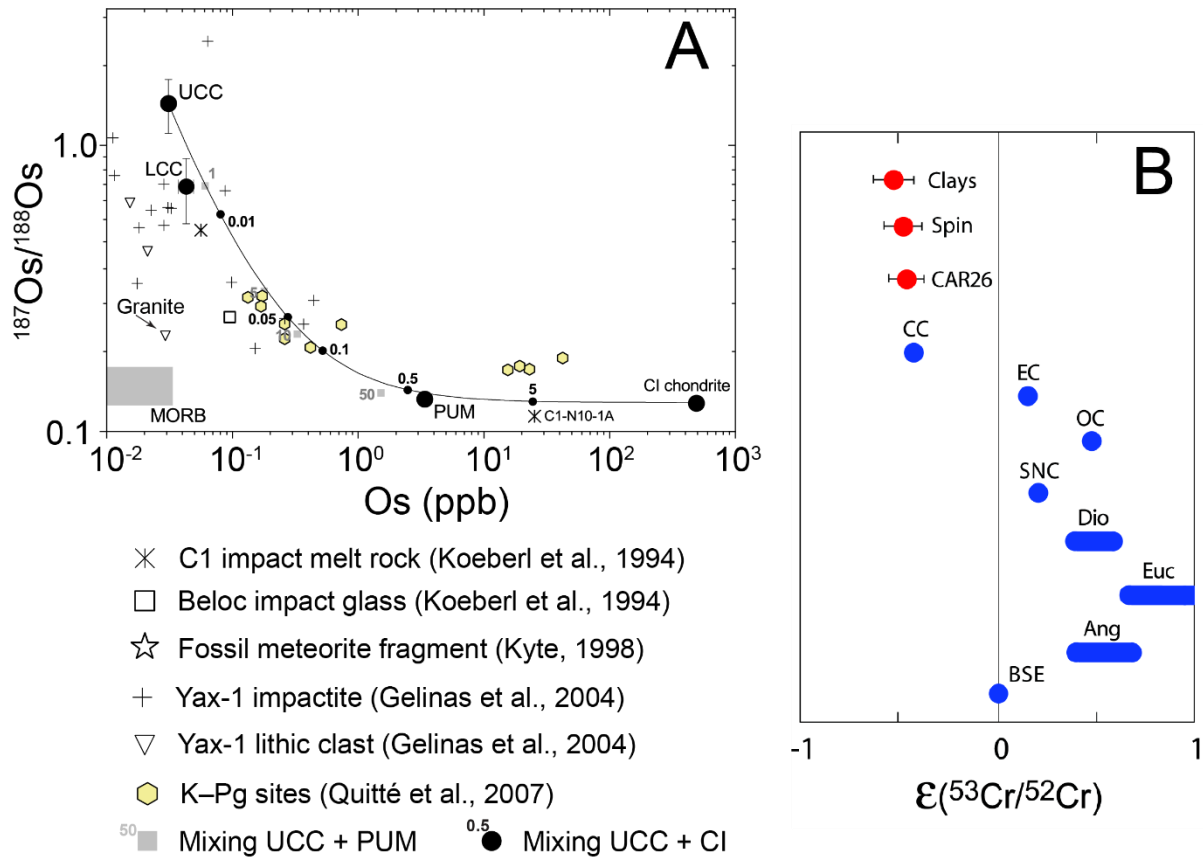
Figure 3.12. *A) Osmium isotopic ratio versus Os concentration (based on Tagle and Hecht (2006), and references therein). Here are shown the measured $^{187}Os/^{188}Os$ versus Os concentration of impactite and lithic clasts samples from Yax-1 drill core (Gelinas et al., 2004), C1 drill core and Beloc (Haiti) impact glass (Koeberl et al., 1994; details on Haiti glass geochemistry can be found in Koeberl and Sigurdsson, 1992), and several K–Pg boundary sites (Quitté et al., 2007). The curve represents a mixing line between upper continental crust (UCC) and CI-chondrite composition. Gray numbers follow a mixing line between the UCC and the primitive upper mantle (PUM). LCC: lower continental crust; MORB: mid-ocean ridge basalt. With the exception of one C1 impact melt rock (~5% of chondritic admixture), the investigated impactites in Yax-1 have no more than 0.1% meteoritic component, with the majority of the samples plotting on or below 0.01%, indicating a low meteoritic component within the Chicxulub impact structure. In contrast, the K–Pg boundary compositions range between ~0.1 and 5% of chondritic admixture. B) Chromium isotopic compositions of K–Pg boundary sites samples (red) compared with a variety of meteorites (blue). The K–Pg samples are consistent with a carbonaceous chondritic impactor for the Chicxulub impact event. Clays and Spin (= spinel crystals): Bidart site, France; CAR26: Caravaca, Spain; CC: carbonaceous chondrites; OC: ordinary chondrites; SNC: Martian meteorites; Dio: diogenites; Euc: eucrites; Ang: angrites; BSE: bulk silicate Earth. From Quitté et al. (2007), and references therein.*

These results were consistent with the recovery of a 2.5 mm diameter altered fossil meteorite (included as a clast in a ~4-mm-sized-light-brown clay inclusion), which was classified (according to its petrographic and geochemical characteristics) as a CV, CO, or CR group carbonaceous chondrite (Kyte, 1998). This fossil meteorite fragment was found in a drill

core from Deep Sea Drilling Project (DSDP) Hole 576, which sampled marine K–Pg sediments from the North Pacific Ocean, and is considered to represent material from the Chicxulub projectile (Fig. 3.13; Kyte, 1998). In contrast, the proximal K–Pg ejecta deposits found around the Gulf of México, which are thicker than distal ejecta (i.e., from a few centimeters to tens of meters of clastic beds) and were formed following high-energy sediment transport (tsunami or gravity flows), show a more moderate Ir anomaly due to dilution processes, with an Ir content generally below 1.5 ppb (e.g., Smit, 1999, Claeys et al., 2002, Schulte et al., 2010, Goderis et al., 2013, Sanford et al., 2016). Therefore, the main fraction of the projectile seems to have been ejected within and beyond the stratosphere, distributed globally, before being deposited in the K–Pg ejecta deposits. Only a minor fraction of the projectile remained within the newly formed Chicxulub impact structure, which was interpreted as possibly reflecting an oblique impact (Pierazzo and Melosh, 1999, 2000; Goderis et al., 2013).
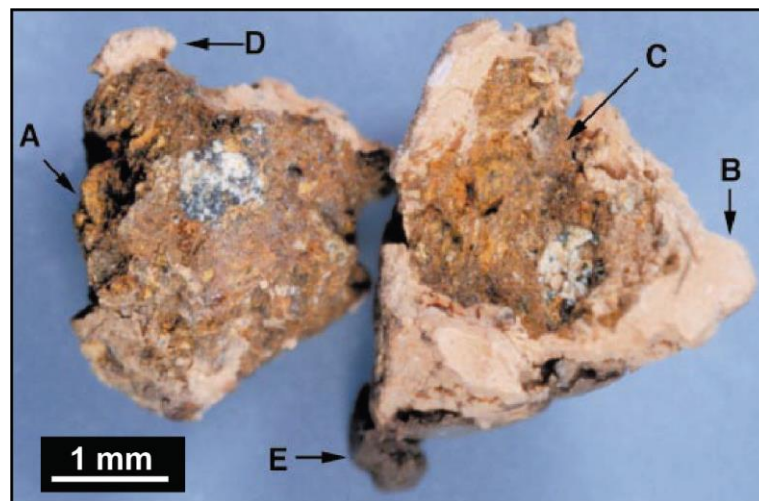
Figure 3.13. *Photograph from Kyte (1998) of the separated fossil meteorite fragment (A) surrounded by light-brown clay (B). The interior cavity of the light-brown clay is highlighted by (C), while the white spot is a portion of a black and white inclusion occurring at the center of the meteorite surface. Some light-brown clay remains on the meteorite surface (D), and the typical K–Pg sediments of DSDP site 576 are dark brown and can be seen on the bottom part of the light-brown rim (E). The largest dimension of the meteorite is ~2.5 mm.*

3.6. The IODP-ICDP Expedition 364 drill core

Of the large (> 100 km diameter) impact structures identified on Earth, only Chicxulub seems to have preserved an intact peak ring, due to its burial by Cenozoic sedimentary rocks (Fig. 3.14; Morgan et al., 2000; Gulick et al., 2013, and references therein). The geophysical data indicate that the peak ring is composed of low density rocks, possibly porous and highly fractured (Morgan et al., 2000, 2011; Gulick et al., 2013). However, there was still debate on the geologic nature of the peak rings, or their mode of formation (see details in Chapter 1; Grieve et al., 2008; Baker et al., 2016). In general, numerical modeling suggested that peak rings formed during the initial stages of impact cratering, following the collapse of the overheightened and unstable central uplift, also known as the "dynamic collapse model" (see also Chapter 1; Morgan et al., 2000; Collins et al., 2002; Ivanov, 2005; Senft and Stewart, 2009;

Morgan et al., 2011). However, the precise kinematics, and mechanics occurring during peak ring formation were still unclear, requiring weakening of the target rocks (Melosh, 1979; O'Keefe and Ahrens, 1993). Also, of the previous drill cores recovered within the Chicxulub impact structure, none have penetrated the peak ring, and no offshore drilling was performed (Morgan et al., 2017).
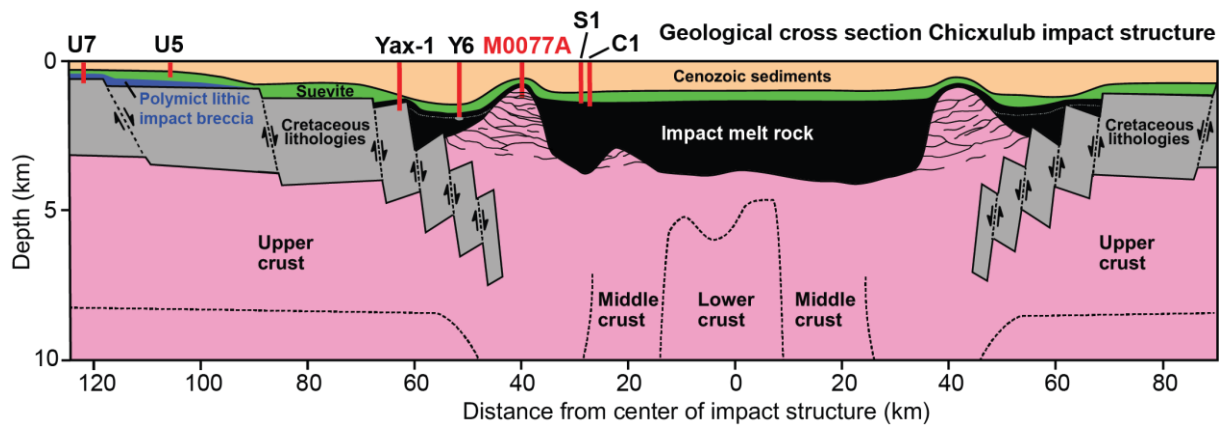
Figure 3.14. *Schematic cross section through the Chicxulub impact structure, showing the main lithological units identified following geophysical investigations and drilling surveys. Previous drillings and the 2016 Expedition 364 (site M0077A) are also shown. The peak ring lithologic sequence recovered from Expedition 364 drilling is, from bottom to top, crystalline basement, impact melt rock, suevite, and post-impact Cenozoic sediments. From Kaskes et al. (2022), and references therein.*

Consequently, the joint IODP-ICDP Expedition 364 was designed, and, after the proposals were approved by both IODP and ICDP, planned in order to address the following scientific objectives through drilling at site M0077A, located offshore (shallow sea of 19.8 m depth) at 21.45°N, 89.95°W, 40 km northwest from the center of the impact structure (Figs. 3.8 and 3.14; according to Expedition 364 Proceedings, see details in Morgan et al., 2017):
- The nature and formation of a topographic peak ring;
- How rocks are weakened during large impacts to allow them to collapse and form relatively wide, flat craters;
- The nature and extent of post-impact hydrothermal circulation;
- The habitability of the peak ring and effect of this impact on the modern and ancient deep biosphere;
- The recovery of life in a sterile zone;
- The nature of the Eocene and Paleocene hyperthermals and the Paleocene-Eocene Thermal Maximum transition;
- The nature and composition of the suevite, impact melt rock, and basement rocks forming the peak ring;
- The volume of dust and climatically active gases released into the stratosphere by this impact;
- The climatic effects of this impact;
- The sedimentology and stratigraphy of the Paleocene–Eocene Chicxulub impact basin infill;
- The geo- and thermochronology of the rocks forming the peak ring;

- Petrophysical properties measured on cores and downhole to calibrate geophysical models and integrate with seismic velocity data; and
- Integration of all data to calibrate impact crater models for crater formation and environmental effects.

The drilling took place between the 5th April and the 31st May 2016, and recovered a total of 303 core segments, from 505.70 to 1334.69 meters below seafloor (mbsf), with an average core recovery of ~99% (Morgan et al., 2017). Offshore, the cores were cut in sections of up to 1.5 m length, and labelled with marks giving their orientation. Initial descriptions were made on the recovered cores, as well as physical measurements of bulk density, P-wave velocity, electrical resistivity, magnetic susceptibility, and natural gamma radiation, before storing (Morgan et al., 2017).

The core sections, with a diameter of 8.3 cm, were then imaged using three-dimensional (3D) dual energy X-ray computed tomography (CT) at 0.3 mm resolution at the Weatherford Laboratories in Houston, Texas. Finally, they were sent to the Bremen Core Repository (Germany), where they were split lengthwise into working and archive halves. After splitting, scanning, preliminary petrographic and geochemical documenting, and sample selection for the research groups involved in the project, were done during the Onshore Science Party, between 21st September and 15th October 2016. The cores are now permanently archived at the Gulf Coast Repository, College Station, Texas (USA).
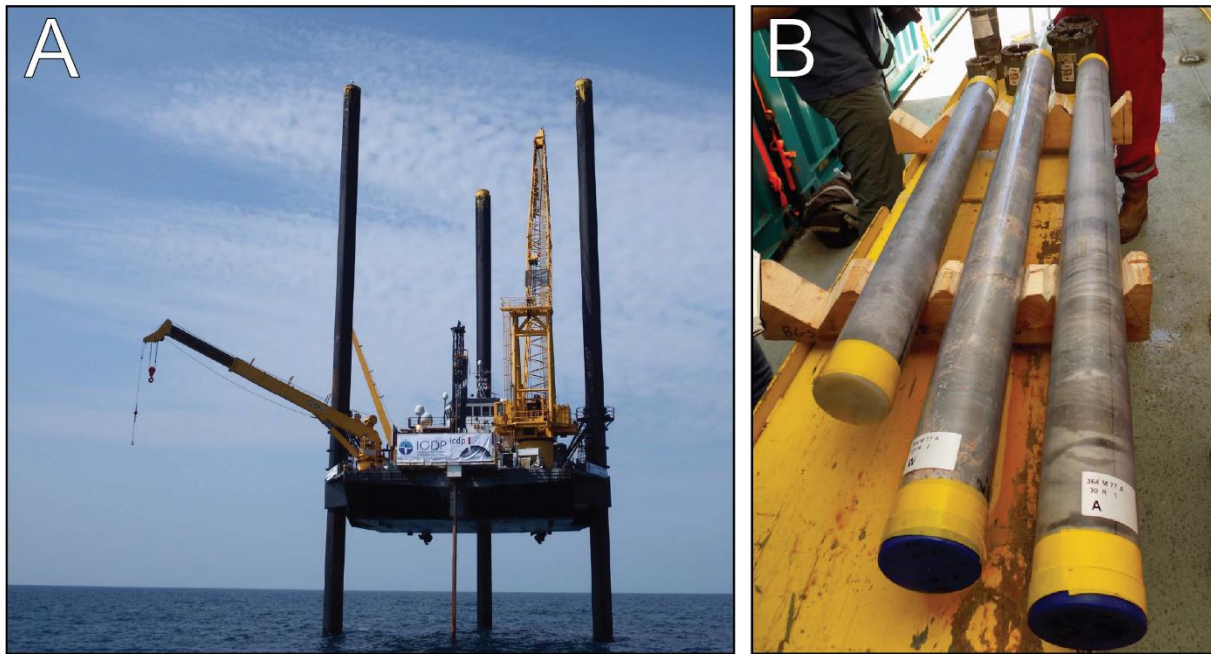
Figure 3.15. *A) The liftboat L/B Myrtle at drilling site M0077A. The drilling rig is visible in red, cantilevered off the bow (image by L. Perez-Cruz, in Morgan et al., 2017). B) The recovered drill cores on the L/B Myrtle, being prepared for storage (image by Kevin Kurtz, available at: https://joidesresolution.org/chicxulub-crater-cores-are-not-what-jr-fans-are-used-to/).*

The following sections describe succinctly the main lithological units identified within the IODP-ICDP Expedition 364 drill core (site M0077A), and the main results of the drilling

that are outside the scope of this thesis. All information concerning the drilling operations, organization, conditions, preliminary petrographic and geochemical results, etc. is reported in detail in the IODP-ICDP Expedition 364 Proceedings (Morgan et al., 2017).

3.6.1. Stratigraphy of the drill core M0077A

The lithostratigraphy (see also Fig. 3.16) presented below follows and summarizes the preliminary descriptions made in the Expedition 364 Proceedings (Morgan et al., 2017). Subsequent detailed investigations are presented in the following chapters of the thesis and related publications.
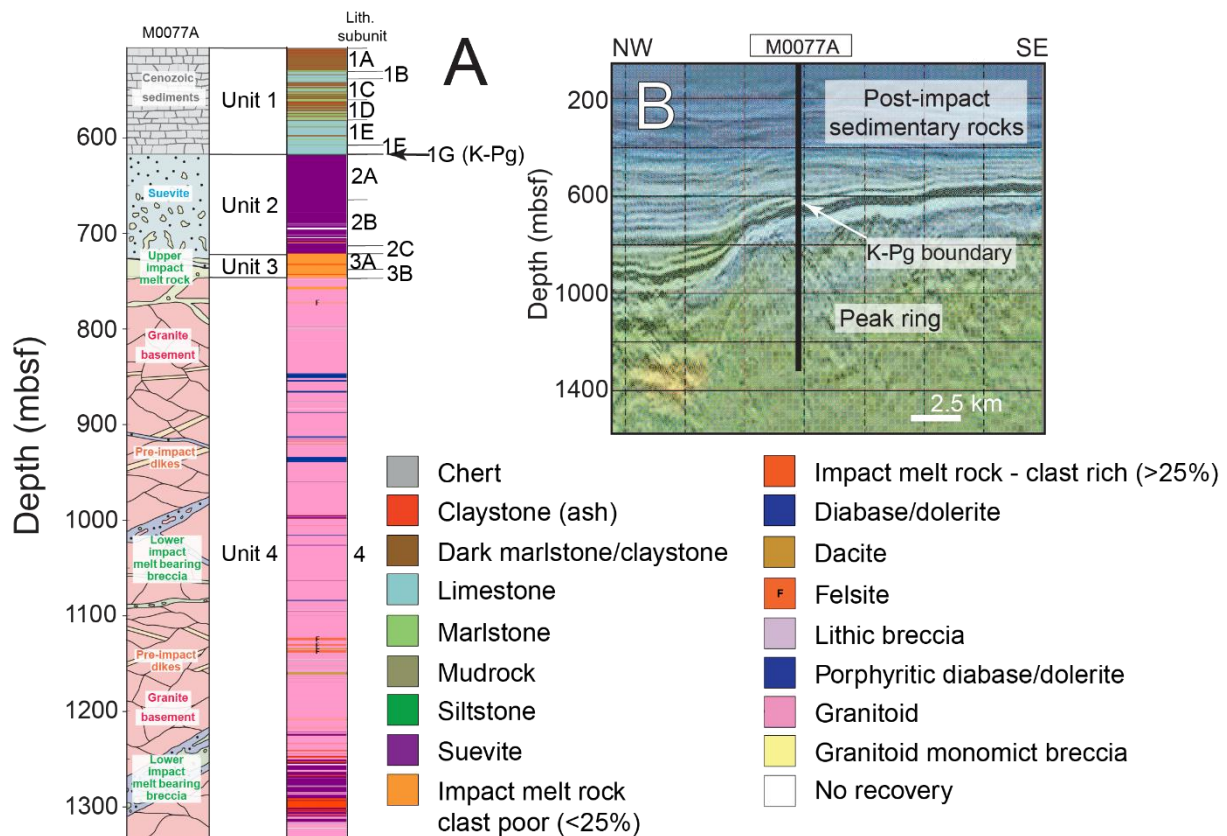
Figure 3.16. *A) Simplified representation (left) of the lithostratigraphic column of M0077A drill core with the main units (modified from Morgan et al., 2016). Detailed lithostratigraphic column (right) with the different lithologies identified during the Onshore Science Party and the subunits (modified from Morgan et al., 2017). B) Radial seismic profile of the peak ring at the drilling site and borehole location (from Morgan et al., 2016).*

3.6.1.1. Unit 1: post-impact Cenozoic sedimentary rocks

Following the preliminary investigations made at the Onshore Science Party in Bremen, the drill core was divided into four main lithological units (Morgan et al., 2017). The uppermost part of the drill core corresponds to a succession of post-impact (i.e., Cenozoic), pelagic sedimentary rocks, which were recovered between 505.70 and 617.33 mbsf (~112 m, from core 1R to core section 40R1). This unit was further subdivided in seven subunits, from 1A to 1G

(top to bottom, see Fig. 3.17), depending on the distribution of the lithologies, as well as the occurrence of erosional truncations or abrupt change in lithology. Subunits 1A to 1E are of Eocene ages, while the subunits 1F and 1G have Paleocene ages.
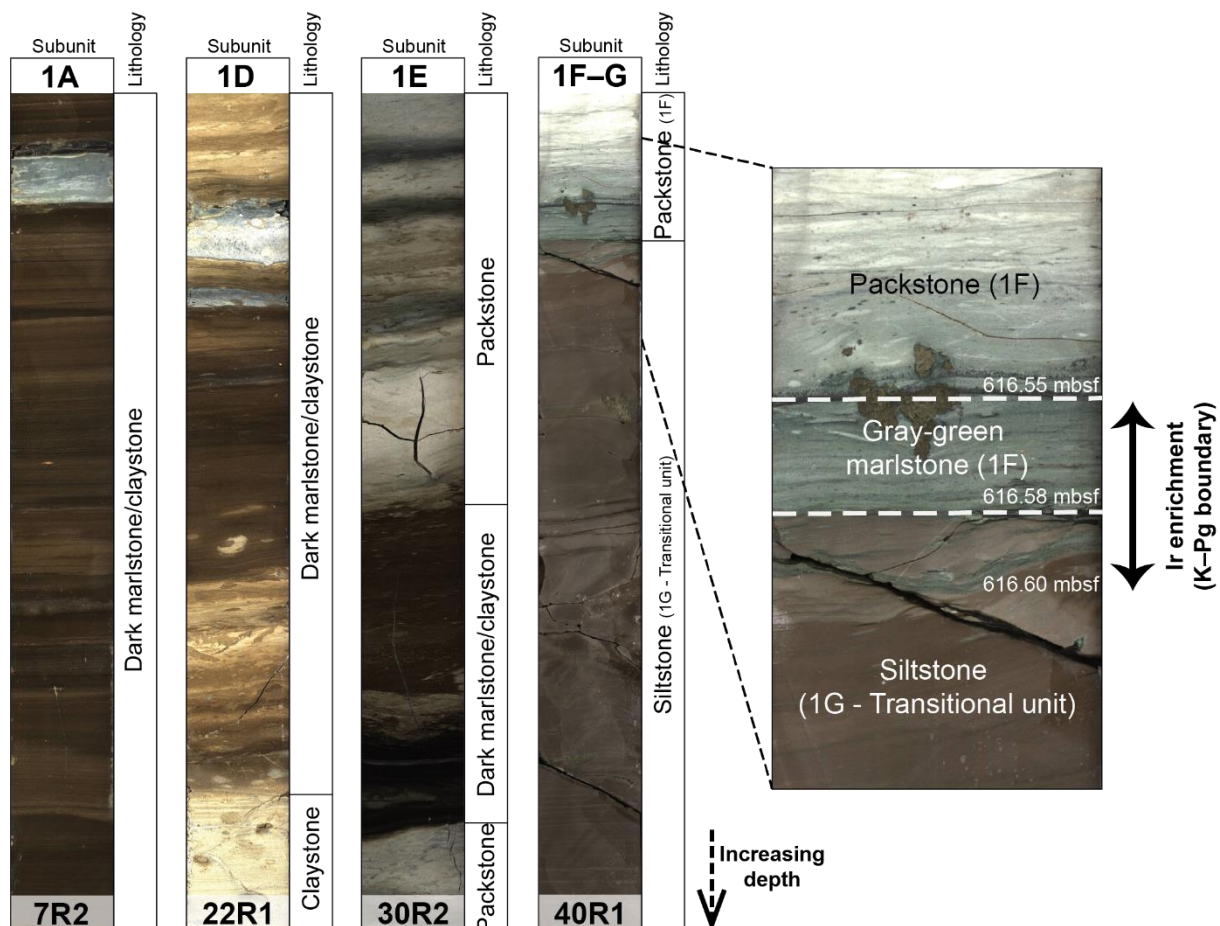
Figure 3.17. *Examples of core sections (scans) encountered in the post-impact Cenozoic sediments unit (unit 1), showing the variations of lithologies (see also, Morgan et al., 2017). The core sections are oriented with increasing depth from top to bottom. The core depths are: 517 mbsf (7R2), 561 mbsf (22R1), 587 mbsf (30R2), and 616 mbsf (40R1). Core width is consistently 83 mm. The core 40R1 marks the contact between the Danian pelagic limestone (packstone, subunit 1F) and the ~75 cm thick transitional unit (subunit 1G), composed of laminated, fining-upward, carbonate-rich siltstone, which was deposited by the final settling of suspended and transported sediments by tsunami and seiche waves (see details in Gulick et al., 2019; Whalen et al., 2020). The subunit 1G is overlain by a ~3 cm thick gray green marlstone layer (see enlarged section on the right). The gray-green marlstone layer and the uppermost 2 cm of subunit 1G show an Ir enrichment, marking the K–Pg boundary within the Chicxulub impact structure (see details in Goderis et al., 2021).*

The subunit 1A (505.70–530.18 mbsf) is composed of millimeter- to decimeter-scale laminated dark marlstone/claystone. The subunit 1B (530.18–537.80 mbsf) consists of bedded intervals (millimeter- to decimeter-scale) of dark marlstone/claystone, marlstone, wackestone, and packstone with local claystone intervals. Subunit 1C (537.80–559.75 mbsf) is composed of intercalations of dark marlstone/claystone, marlstone, wackestone, packstone, and local

claystone. Soft-sediment deformation also occurs locally. The subunit 1D (559.75–580.89 mbsf) contains intercalated centimeter- to decimeter-scale dark/marlstone, claystone, marlstone, wackestone, and packstone. Wackestones and packstones show high levels of bioturbation. Subunit 1E (580.89–607.27 mbsf) is composed of interbedded dark marlstone/claystone, light brown marlstone, light brown to bluish wackestone and packstone, and black shale. Stylolites are observed in lithologies other than black shale. Subunit 1F (607.27–616.58 mbsf) contains interbedded light gray to light bluish gray wackestone and packstone, and light to dark bluish gray marlstone at the centimeter to decimeter scale. All lithologies display stylolites. The bottom part of the subunit 1F is marked by the occurrence of a ~3 cm-thick gray-green marlstone layer (Fig. 3.17, 616.55 to 616.58 mbsf), which have Ni, Cr, Ir, and other HSE enrichments (e.g., Ir content of ~1.0 ppb on average, one order of magnitude higher than the over- and underlying rocks; Goderis et al., 2021).

Finally, subunit 1G (616.58–617.33 mbsf), also known as the "transitional unit" (Fig. 3.17; Gulick et al., 2019; Whalen et al., 2020), is composed of generally fining-upward, laminated dark brown to dark grayish brown carbonate-rich silty claystone to micrite. Post-depositional sulfides nodules (e.g., pyrites) disrupt the bedding. The uppermost part of subunit 1G (Fig. 3.17; 616.58–616.60 mbsf) is composed of greenish marlstone interbedded with gray mud/wackestone, and also present the same enrichment in moderately and highly siderophile elements than in the overlying gray-green marlstone (subunit 1F). The bottom part of the transitional unit is composed of two graded beds of packstone (each <1 cm thick) containing impact glass shards and a variety of carbonate grains, and stylolitized at the base, overlying the upper suevite of unit 2A. These two beds also present enrichment in Cr and Ni, but not in Ir abundances, relative to the neighboring rocks (Goderis et al., 2021). With the exception of the transitional unit and the gray-green marlstone, the post-impact, Cenozoic sedimentary rocks will not be discussed further in this thesis.

3.6.1.2. Unit 2: suevite

The unit 2 marks the entry within the peak ring itself, which was formed during the impact. The units 2 and 3 are also termed the "upper peak ring section" (Morgan et al., 2017). Unit 2 consists of a ~104 m thick impact melt-bearing polymict breccia which is, therefore, referred to as suevite (617.33–721.62 mbsf, from core section 40R1 to 87R2), further divided into three subunits (2A–2C; Fig. 3.18). In general, the suevite is composed of a variety of impact melt rock clasts (green to black in colors, and also altered impact glass), as well as, to a lesser extent, lithic fragments, such as Mesozoic sedimentary rocks and crystalline basement clasts. Clast size varies from ~0.2 to more than 25 cm, with a fining-upward trend. Subsequent observations have highlighted that the suevite unit has a high porosity (19–22%), and underwent a high degree of hydrothermal alteration (Christeson et al., 2018; Kring et al., 2020).

Subunit 2A (617.33–664.52 mbsf) consists of a suevite that is relatively well-sorted in the upper part, and poorly-sorted in the lower part. In the uppermost part of the unit, laminations can be observed. The suevite is matrix supported, and gray in color, and is composed mainly of micritic carbonate. Clast types include limestone, isolated fossils (e.g., foraminifers), and altered impact melt rock with glassy to microcrystalline textures. The suevite of subunit 2B (664.52–712.83 mbsf) has similar matrix and composition than the suevite in 2A, but only

shows a fining-upward trend and no other sedimentary features. The clast sizes increase to up to ~10 cm in the bottom part of the subunit. Two large, clast-poor, black impact melt rock clasts also occur in sections 80R2 (~706 mbsf) and 81R2 (~709 mbsf), reaching sizes of 60 and 90 cm, respectively. Clast population is dominated by altered impact melt rock, while mineral (quartz and feldspar, generally shocked) and lithic clasts also occur. The lithic clasts consist generally of shocked crystalline basement rocks, and also limestone, locally with fossils. The matrix is composed of very fine-grained, microcrystalline carbonate. The subunit 2C (712.83–721.62 mbsf), is a ~9 m thick suevite. The transition from suevite subunit 2B is marked by a change in the matrix (from dark brown to green) and in the clast shape (angular to subrounded). The suevite is mainly matrix-supported, but locally also clast-supported. Impact melt rock clasts display sizes from a few millimeters to more than 10 cm, and are black, gray, or green. Apart from impact melt rock, carbonate and granite also occur as clasts, as well as minor amounts of gneiss, granodiorite, amphibolite, siltstone, and shale. Detailed petrographic and geochemical investigations of the suevite unit are presented and discussed in Chapter 8, and in Kaskes et al. (2022), with also a revision of the classification of the suevite unit.
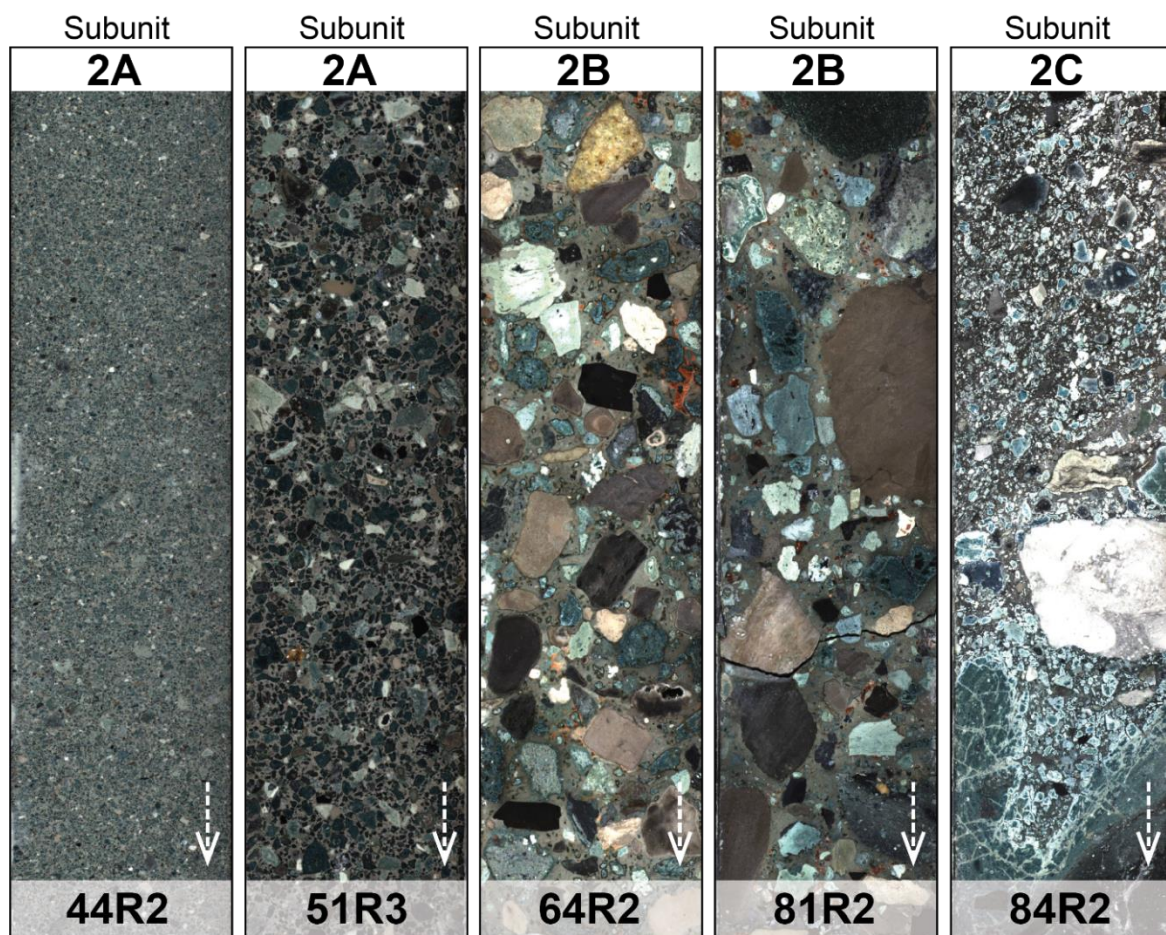
Figure 3.18. *Representative core sections showing the texture variations of the suevite unit (unit 2, according to the lithological classification of Morgan et al., 2017). The arrow is oriented according to increasing depth. Core width is 83 mm. The increase in grain size from the top (subunit 2A) to the bottom (subunit 2C) of the suevite can be seen. Depths of the core sections are: 630 mbsf (44R2), 652 mbsf (51R3), 687 mbsf (64R2), 708 mbsf (81R2), and 714 mbsf (84R2).*

3.6.1.3. Unit 3: impact melt rocks

The second lithology occurring in the "upper peak ring section", and forming the unit 3, is a ~25 m thick, mainly clast-poor, impact melt rock sequence (721.62–747.02 mbsf, from core section 87R2 to 95R3). This unit is also termed the "upper impact melt rock" (UIM) by de Graaff et al. (2022), and in publication Chapter 7 (Feignon et al., 2022). Two subunits (3A–B) were defined for the UIM (Fig. 3.19). The upper boundary of the subunit 3A with subunit 2C was defined by the first occurrence of massive, black impact melt rock. However, the transition is relatively gradual, from coarse-grained, poorly sorted suevite, to impact melt rock.
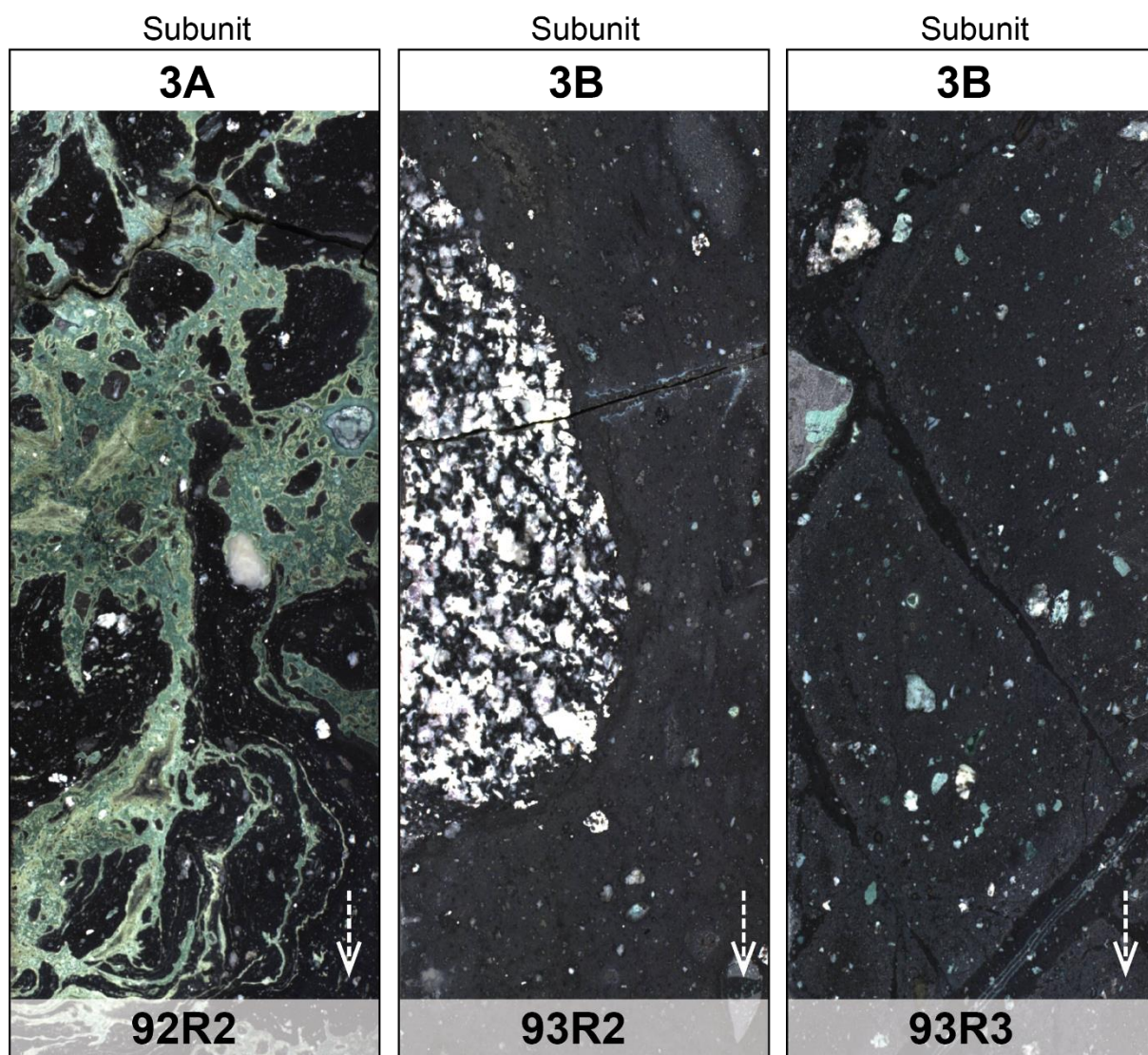
Figure 3.19. *Representative core sections of the upper impact melt rock (UIM) unit (unit 3, according to the lithological classification of Morgan et al., 2017). The arrow is oriented according to increasing depth. Core width is 83 mm. While subunit 3A is composed of black impact melt rock with green schlieren (left), subunit 3B is composed of black impact melt rock (middle and right). In the middle scan, a ~14 cm-sized granite clast can be seen. Depths of the core sections are: 736 mbsf (92R2), 739 mbsf (93R2), and 740 mbsf (93R3).*

Subunit 3A (721.62–737.56 mbsf) represents a ~16-m-thick mixture between a clast-poor, SiO_2-rich black impact melt rock and a CaO-rich green phase, initially identified as an impact melt rock (Morgan et al., 2017), but subsequently termed as a "green phase" (Schulte et al., 2021) or "green schlieren" (de Graaff et al., 2022; Kaskes et al., 2022), according to the texture formed by millimeter- to centimeter-sized greenish veins occurring in the black impact melt rock (Fig. 3.19). Locally, centimeter- to decimeter-sized clasts of shocked crystalline basement occur in black impact melt rock areas, and undigested minerals (such as quartz or feldspar) are also observed. The black impact melt rock groundmass is generally aphanitic, while the green phase is mainly composed of clay minerals (sheet silicates) and calcite. Subunit 3B (737.56–747.02 mbsf, ~9 m thick) is composed only of clast-poor, black impact melt rock. The contact with subunit 3A is defined where the green schlieren does not occur anymore. Granitic clasts are dominating, and increase in abundance and in size with increasing depth (a ~42 cm granite clast occurs at the base of the unit, see also Fig. 3.19), while sedimentary clasts are lacking. The matrix is fine-grained, composed of plagioclase laths and opaque minerals and melt altered to clay minerals. Mineral clasts include quartz, K-feldspar, and plagioclase, and are undigested to partially digested. Importantly, in both units 2 and 3, anhydrite was not observed as clast lithology, in contrast to previous Chicxulub drill cores (Morgan et al., 2017). Detailed characterization and discussion of the UIM is provided in publication Chapter 7, in Schulte et al. (2021), and in de Graaff et al. (2022).

3.6.1.4. Unit 4: crystalline basement

The lower unit of the M0077A drill core (also known as the "lower peak ring section") consists of a single unit of granitic rocks intruded by a variety of pre-impact, subvolcanic dikes, as well as impactites (suevite-like breccia and impact melt rock) dikes (Fig. 3.20). Unit 4 extends from 747.02 (core section 95R3) to 1334.69 (core 303R) mbsf, and is not further divided in subunits. In contrast to previous drillings where only granite clasts were found, unit 4 represents the first continuous section of uplifted crystalline basement from the Chicxulub impact structure (Feignon et al., 2020, 2021). The boundary of unit 4 to subunit 3B corresponds to the first occurrence of granite exceeding 1 m in length, albeit impact melt rock bodies are observed down to ~12 m below the boundary (Morgan et al., 2017). Petrophysical observations have shown that the density of the granitic basement is 2.10–2.55 g.cm^{-3} (average 2.41 g.cm^{-3}), and the P-wave velocities are 3.5–4.5 km.s^{-1} (average 4.1 km.s^{-1}), which are lower than the typical values for granite (>2.60 g.cm^{-3} and >5.5 km.s^{-1}; Morgan et al., 2016). The porosity is also extremely high (8–13%) compared to typical granite (Christeson et al., 2018). This confirmed the previous geophysical observations and modeling (Pilkington et al., 1994; Morgan et al., 2011). The main lithology of the "lower peak ring section" is a coarse-grained, shocked, and fractured, granite (composed of K-feldspar, plagioclase, quartz, and biotite as main phases; Fig. 3.20) with locally centimeter- to decimeter-sized aplite and pegmatite facies areas. The granite is intruded by centimeter- to several-meter-sized pre-impact, subvolcanic dikes (e.g., dacite, felsite, and dolerite), and by impact melt rock (clast-poor to clast-rich) and impact melt rock-bearing breccia dikes (suevite-like).
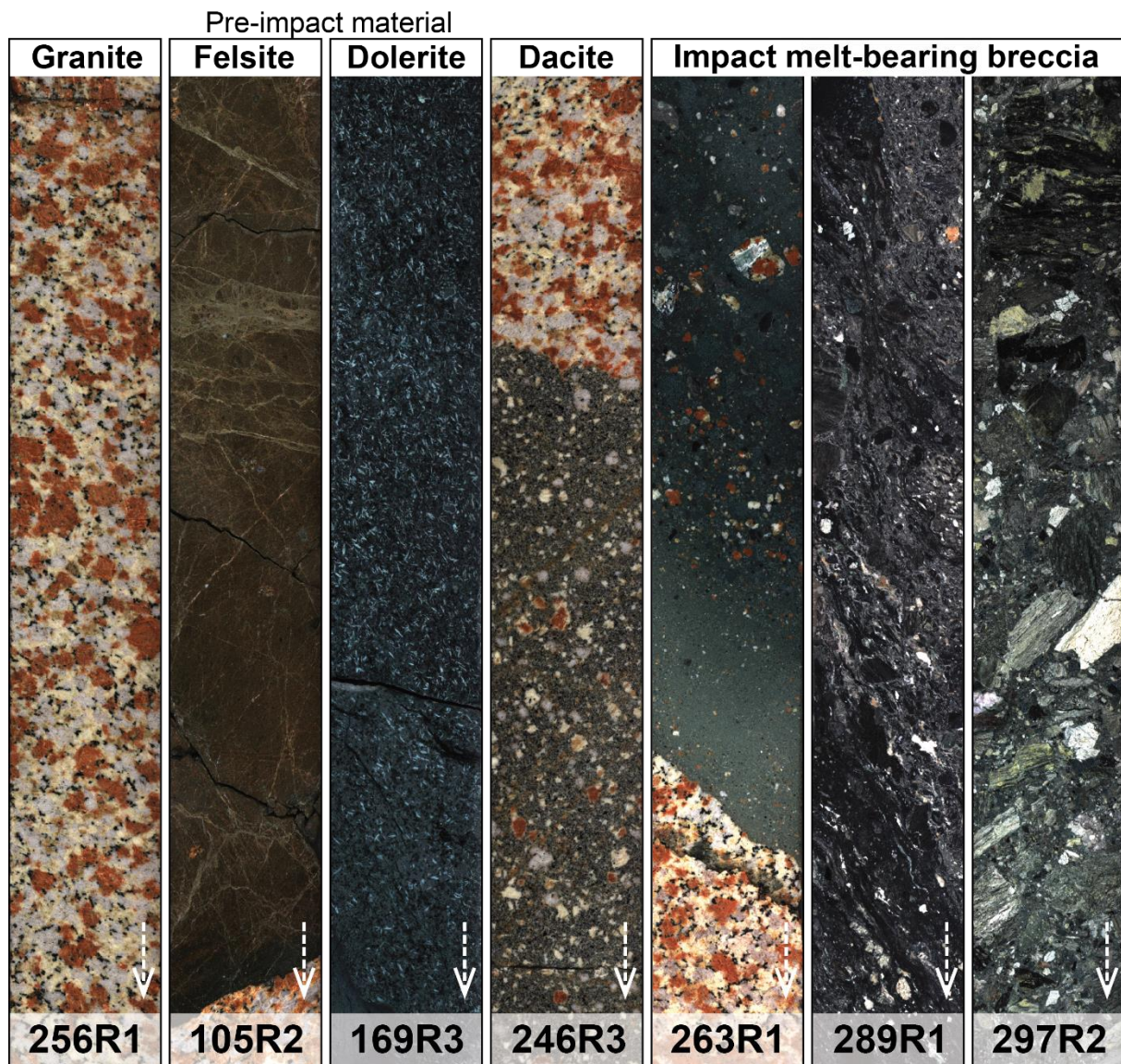
Figure 3.20. *Representative core sections of the crystalline basement unit 4 (according to the lithological classification of Morgan et al., 2017). The arrow is oriented according to increasing depth. Core width is 83 mm. Unit 4 is dominated by granite (256R1, left) crosscut by different types of pre-impact subvolcanic dikes such as felsite (105R2), dolerite (with a porphyritic texture here, 169R3), and dacite (246R3). The three section scans on the right side of the figure show the different textures (i.e., relatively clast-poor (263R1), with flow texture (289R1), and clast-rich (297R2)) of the impact melt-bearing breccia dikes cutting the granite, also termed the "lower impact melt-bearing breccia" (de Graaff et al., 2022). Depths of the core sections are (from left to right): 1188 mbsf (256R1), 772 mbsf (105R2), 935 mbsf (169R3), 1160 mbsf (246R3), 1209 mbsf (263R1), 1290 mbsf (289R1), and 1315 mbsf (297R2).*

For the first time at Chicxulub, well-developed shatter cones were observed in felsite dikes, and also in an amphibolite clast from unit 2 (Fig. 3.21; Morgan et al., 2017). A ~100 m thick suevite and impact melt rock unit occurs from 1215 to 1316 mbsf, separated by decimeter- to meter-sized granite areas. The impactite dikes crosscutting the granite unit are also known as the "lower impact melt-bearing breccia" (LIMB; de Graaff et al., 2022) to distinguish from

the UIM (Unit 3). Flow-banding textures are observed in the impact melt rocks (Fig. 3.20), and clasts consist mainly of basement material (mainly granite, felsite, dolerite, amphibolite, gneiss, and quartzite). Other areas of the impact melt rock display a high abundance of brecciated material (mainly granite, see Fig. 3.20). Unlike the "upper peak ring section", no sedimentary (e.g., carbonate) clasts are visible. Clast size is below 5 cm, but 10–20 cm clasts are also common. They are undigested to partially digested in the impact melt rock. Post-impact calcite veins occur throughout the whole unit. The petrography and geochemistry of the granitic basement, pre-impact subvolcanic dikes, and LIMB are presented and discussed in details in the publications in chapters 5–7 (Feignon et al., 2020, 2021, 2022) and in de Graaff et al. (2022).
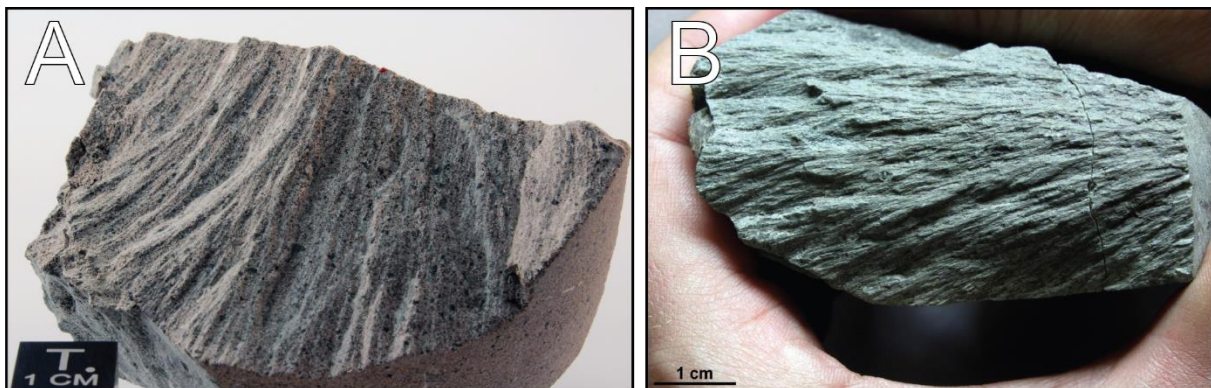
Figure 3.21. *Shatter cones recovered from the M0077A drill core, for the first time at the Chicxulub impact structure. A) Shatter cone in a felsite dike (sample 239R1_121–124, 1138.3 mbsf). B) Shatter cone in an amphibolite clast (suevite unit, sample 81R1_110–116, 708.4 mbsf). Both photographs by L. Ferrière, NHM Vienna.*

3.6.2. Main outcomes of the drilling

The IODP-ICDP Expedition 364 brought new insights allowing to understand more accurately the course of the events regarding the peak ring formation processes, the shock-effects in rock-forming minerals, the impact-induced hydrothermal system, and more broadly, the K–Pg mass extinction and the global climatic effects of the impact. In the following text, the main outcomes of the drilling are summarized, excluding those aspects that are presented and discussed in the next chapters of this thesis (i.e., the petrography and geochemistry of the suevite, impact melt rock, granite, and pre-impact dike lithologies, the shock metamorphic effects in quartz and in other minerals, and the search for a meteoritic component within the impact melt rocks of the peak ring).

3.6.2.1. Implications for Chicxulub peak ring formation

The first main outcome of the drilling project was the confirmation of the dynamic collapse model (see Chapter 1) as a mechanism to explain the formation of peak ring in large impact structures (Morgan et al., 2016). The juxtaposition of the units in the peak ring, i.e., the granitic basement occurring above Mesozoic sedimentary rocks, is consistent with the dynamic collapse model for peak ring formation, as this was not predicted by, e.g., the nested melt-cavity

model (Head, 2010; Baker et al., 2016). Moreover, the broadly estimated shocked pressures experienced by peak ring rocks recovered were 10–35 GPa, also consistent with the dynamic collapse model, whereas the nested melt-cavity model predict lower (Baker et al., 2016), or higher (Head, 2010) shock pressures. Therefore, the dynamic collapse model may be of use in simulations for large impact crater formation on other planetary bodies (Morgan et al., 2016). Subsequent work on drill core samples has shown that the dominant process occurring during peak ring formation is acoustic fluidization of rocks, where extremely weakened rocks behave like a flow (Riller et al., 2018). Then the rocks regain sufficient strength as the fluidization becomes less important and is replaced by shear faulting, allowing the peak ring topography to be sustained (Riller et al., 2018). Additionally, Riller et al. (2018) suggested that, at the end of the peak ring formation, melt bodies were entrained and trapped in target rock thrust zones, leading to the formation of the LIMB observed in unit 4. Modeling and observations suggest that the crystalline basement rocks of unit 4 were displaced, and uplifted from pre-impact depth of 8–10 km (Morgan et al., 2016; Riller et al., 2018). Moreover, models of Chicxulub peak ring formation become better constrained and allow to estimate several parameters such as, the orientation of rocks relative to their pre-impact orientation, the total strain, strain rates and type of shear occurring during each stage of cratering, the orientation and magnitude of principal stresses, further supporting that the dynamic collapse model for the formation of the Chicxulub impact structure is accurate (see details in Rae et al., 2019). For example, it probably took 5–10 minutes to form the peak ring (Rae et al., 2019; Collins et al., 2020). These results, coupled with previous geophysical observations, have permitted to model that the Chicxulub impact structure was most likely formed following a steeply-inclined (45–60°) impact from the northeast, making a low angle (<30°) impact (Collins et al., 2020, and references therein) less likely.

3.6.2.2. Refining the scenario of the Chicxulub impact event

Apart from the peak ring formation mechanisms, the continuous impactite sequence recovered in the M0077A drill core provides a record that allows to reconstruct a series of events occurring in days/years after the impact (Fig. 3.22; see details in Gulick et al., 2019; Whalen et al., 2020; Goderis et al., 2021). Few minutes after the collapse of the overheightened central uplift and the associated crystalline basement to form the peak ring, it was covered of melt rocks (Gulick et al., 2019). Within tens of minutes, possibly ocean water and rock mixture entered the newly formed crater (ocean resurge) and formed the lower part of the suevite (~40 m thick) by melt-water interactions, similar to explosive phreatomagmatic eruptions (Gulick et al., 2019; Osinski et al., 2020). At the boundary between the suevite and the impact melt, possible shearing occurred and mixed both phases, i.e., the black impact melt rock and the green carbonate-rich phase (Schulte et al., 2021). Within hours, the resurge was completed, depositing, through settling and seiches, the fining-upward suevite deposit (Gulick et al., 2019). Finally, within a day, the upper part of the suevite subunit 2A was deposited (cross-bedded interval), corresponding to the reflected rim-wave tsunami (Gulick et al., 2019). Then, the deposition of the transitional unit (subunit 1G) recorded the final impact-related deposition processes, operating for weeks to potentially years after the impact, and indicate that the wave energy was significantly reduced compared with subunit 2A, as the grain size was strongly

reduced and cross-bedding occurs commonly (Gulick et al., 2019; Whalen et al., 2020). The formation processes of suevite and impact melt rock units are further discussed in de Graaff et al. (2022), and Kaskes et al. (2022).

For the first time, the positive iridium anomaly associated with the K–Pg boundary deposits, was discovered within the Chicxulub impact structure, in the uppermost part of the transitional unit and at the base of subunit 1F (gray-green marlstone) of core M0077A (Goderis et al., 2021). This layer was interpreted as corresponding to the deposition of the fine-grained impact ejecta that circulated in the atmosphere, and which was recorded by the low-energy depositional environment of the Chicxulub impact structure at this time (Whalen et al., 2020; Goderis et al., 2021). It was suggested that the Ir-rich dust deposition took less than 20 years (Goderis et al., 2021), and, therefore, making the transitional unit an unique record of the Chicxulub impact event timeline.
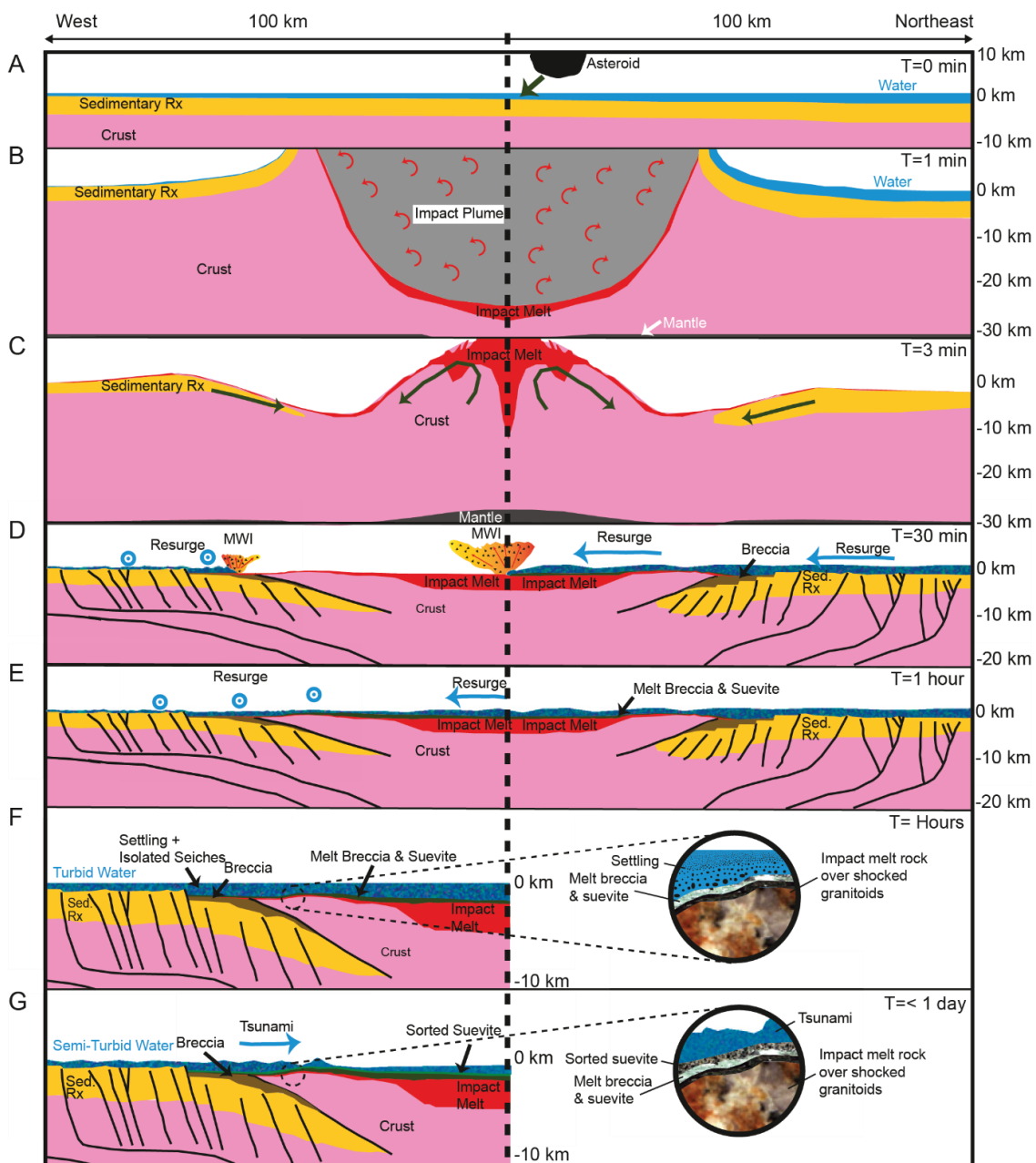
Figure 3.22. *Schematic representation by Gulick et al. (2019), proposing a reconstruction of the Chicxulub impact event based on numerical modeling, geophysical data, and results from the IODP-ICDP Expedition 364 drilling, with two perspectives (from the west and northeast). A) A ~12 km diameter impactor comes from the northeast before striking the Yucatán peninsula platform. B) Formation of a 100 km diameter transient cavity and ejection of an impact plume composed of vaporized/melted/fragmented target rocks (limestones, evaporites, and mainly granitic crystalline basement). C) Formation of a central uplift, which starts to undergo dynamic collapse. D) Crater morphology after the dynamic collapse of the central uplift and peak ring formation. The ocean resurge starts and melt-water explosive interaction occurs. E) The ocean resurge covered the whole structure, reaching the M0077A drilling site. F) The bulk suevite deposit forms by settling of the debris within the flooded crater and covering the peak ring. G) Tsunamis with lower energy occur, leading to the deposition of the sorted suevite, before the deposition of the transitional unit with decreasing wave energy, possibly going on for weeks to years after the impact. For details, see Gulick et al. (2019), and references therein.*

3.6.2.3. Re-estimation of the gas/dust volume injected into the atmosphere

The calculations of the quantities of gases released into the atmosphere from the vaporization of sedimentary rocks have been improved following the IODP-ICDP Expedition 364 drilling. New estimations by Artemieva et al. (2017) of the amounts of sulfur (S) and carbon dioxide (CO_2) released yield values of 325 ± 130 Gt (gigatons) S, larger than the previous estimate (~100 Gt) of Brugger et al. (2017), and 425 ± 160 Gt CO_2, which is lower than the previous estimate (~1400 Gt) of Brugger et al. (2017). These values also refined the intervals estimated by Pierazzo et al. (1998) of 40–560 Gt S, 350–3,500 Gt CO_2 released into the atmosphere. For comparison, the explosive eruption of Pinatubo, in 1991, released ~0.02 Gt of SO_2 into the atmosphere, leading to a decrease in global temperatures of ~0.3 °C for nearly two years (McCormick et al., 1995; Soden et al., 2002). In addition to the gases, dust has also been released, and investigations of the Chicxulub impact structure sedimentary rocks have estimated that between 0.75 and 2.50 Gt of black carbon (i.e., soot) have been released from the crater (Lyons et al., 2020). Such high volumes of gases and dust released on a very short time scale (few hours needed to travel around the globe) initiated an "impact winter" and global darkening, which significantly reduced surface and ocean temperatures for up to hundreds of years after the Chicxulub impact event, playing a major role in the mass extinction event (Artemieva et al., 2017; Chiarenza et al., 2020; Lyons et al., 2020).

3.6.2.4. The Chicxulub hydrothermal system

In addition to the identification of the lithological units composing the M0077A drill core, preliminary observations have shown that hydrothermal alteration is pervasive throughout the whole core, especially the suevite in unit 2 (Morgan et al., 2017). Detailed investigations were performed on the hydrothermal alteration features in order to better constrain the duration and extent of the post-impact hydrothermal system within the Chicxulub impact structure (see details in Kring et al., 2020; Simpson et al., 2020, 2022). The main alteration phases identified

are Fe-Mg clay minerals, zeolites, alkali feldspars, calcites, minor sulfides, sulfates, opal, and Fe-Ti oxides (Simpson et al., 2020). This was consistent with previous studies, suggesting an alteration of rock by alkaline-saline water (Simpson et al., 2020, and references therein). The circulation of fluids was enhanced by the high levels of fracturing, shearing, and porosity of the impactites and target lithologies (Christeson et al., 2018; Kring et al., 2020). Further investigations have shown that the hydrothermal system at Chicxulub impact structure modified $\sim 1.4 \times 10^5$ km^3 of Earth's crust, nine time that of the Yellowstone caldera system (Kring et al., 2020, and references therein). Additionally, Kring et al. (2020) have shown that the hydrothermal system was long lived, with initially high temperatures of 300–400°C, which required ~2 million years to cool down to 90°C at 1 km depth. This was further supported by an enrichment in Mn observed in the carbonate sediments overlying the suevite unit, with similar enrichment observed in the Yax-1 drill core (Rowe et al., 2004; Kring et al., 2020). After several million years, at ~56 Ma (?), when the hydrothermal system became cooler (~20–50°C), clay minerals formed throughout the "upper peak ring section" by interaction of the impactites with fluids mainly composed of meteoric water (Simpson et al., 2022). .

3.6.2.5. The recovery of life after the impact

Several studies have estimated the time needed for life to recover from the impact event, and to return to similar levels as those of the Late Cretaceous period (see details in Smit, 2022; Alegret et al., 2022; Arz et al., 2022). It was proposed that the recovery (of the global marine ecosystem) was geographically heterogeneous (Hull and Norris, 2011; Alegret et al., 2022), with on the order of 300,000 years needed for life to recover in the Gulf of Mexico and North Atlantic-western Thetys area (Alegret et al., 2001, 2004; Alegret and Thomas, 2005; Hull and Norris, 2011; Alegret et al., 2022). This delay may have been caused by the proximity of the impact site, where the environment was probably less favorable for life, possible due to the presence of toxic metal poisoning (Jiang et al., 2010). However, the study of foraminifers, nannoplankton, trace fossils, and elemental abundance in samples from the M0077A drill core have shown that the life within the impact structure re-appeared only a few years after the impact, and that a high-productive ecosystem was in place about 30 thousand years after the impact event (Lowery et al., 2018). Also, there was no impact-related environmental control on the life recovery, and the proximity of the impact, paleo-water depth, and paleolatitude do not seem to be related to the severity of the extinction of benthic foraminifera (Lowery et al., 2018; Alegret et al., 2022). Also, Alegret et al. (2022) suggested that oceans were heterogeneous in term of life recovery, with geographical and time variability from one place to another.

References

Alaniz-Álvarez S. A., van der Heyden P., Nieto-Samaniego A. F., and Ortega-Gutiérrez F. 1996. Radiometric and kinematic evidence for Middle Jurassic strike-slip faulting in southern Mexico related to the opening of the Gulf of Mexico. *Geology* 24:443–446. https://doi.org/10.1130/0091-7613(1996)024<0443:RAKEFM>2.3.CO;2.

Alegret L. and Thomas E. 2005. Cretaceous/Paleogene boundary bathyal paleo-environments in the central North Pacific (DSDP site 465), the northwestern Atlantic (ODP site 1049), the Gulf of Mexico, and the Tethys: the benthic foraminiferal record. *Palaeogeography Palaeoclimatology, Palaeoecology* 224:53–82. https://doi.org/10.1016/j.palaeo.2005.03.031.

Alegret L., Molina E., and Thomas E. 2001. Benthic foraminifera at the Cretaceous–Tertiary boundary around the Gulf of Mexico. *Geology* 29:891–894. https://doi.org/10.1130/0091-7613(2001)029<0891:BFATCT>2.0.CO;2.

Alegret L., Arenillas I., Arz J. A., and Molina E. 2004. Foraminiferal event-stratigraphy across the Cretaceous/Paleogene boundary. *Neues Jahrbuch für Geologie und Paläontologie Abhandlungen* 231:25–50. https://doi.org/10.1127/njgpa/234/2004/25.

Alegret L., Arreguín-Rodríguez G. J., and Thomas E. 2022. Oceanic productivity after the Cretaceous/Paleogene impact: Where do we stand? The view from the deep. In *From the Guajira Desert to the Apennines, and from Mediterranean Microplates to the Mexican Killer Asteroid: Honoring the Career of Walter Alvarez,* edited by C. Koeberl, P. Claeys, and A. Montanari. Geological Society of America Special Paper #557, Geological Society of America, Boulder, Colorado, pp. 449–470. https://doi.org/10.1130/2022.2557(21).

Alvarez W. 1997. *T. rex and the crater of doom.* Princeton University Press, Princeton, New Jersey, 185 pp.

Alvarez W. 2009. The historical record in the Scaglia limestone at Gubbio: magnetic reversals and the Cretaceous-Tertiary mass extinction. *Sedimentology* 56:137–148. https://doi.org/10.1016/j.gca.2010.05.009.

Alvarez L. W., Alvarez W., Asaro F., and Michel H. V. 1980. Extraterrestrial cause for the Cretaceous-Tertiary extinction. *Science* 208:1095–1108. https://doi.org/10.1126/science.208.4448.1095.

Alvarez W., Claeys P., and Kieffer S. W. 1995. Emplacement of K/T boundary shocked quartz from Chicxulub crater. *Science* 269:930–935. https//doi.org/10.1126/science.269.5226.930.

Ames D. E., Kjarsgaard I., Pope K. O., Dressler B., and Pilkington M. 2004. Secondary alteration of the impactite and mineralization in the basal Tertiary sequence, Yaxcopoil-1, Chicxulub impact crater, Mexico. *Meteoritics & Planetary Science* 39:1145–1167. https://doi.org/10.1111/j.1945-5100.2004.tb01134.x.

Archibald J. D. and Fastovsky D. E. 2004. Dinosaur extinction. In *The Dinosauria*, 2nd edition, edited by D. B. Weishampel, P. Dodson, and H. Osmólska. University of California Press, Berkeley, California, pp. 672–684. https://doi.org/10.1525/california/9780520242098.003.0033.

Arens N. C. and West I. D. 2008. Press-pulse: a general theory of mass extinction? *Paleobiology* 34:456–471. https://doi.org/10.1666/07034.1.

Artemieva N. and Morgan J. V. 2009. Modeling the formation of the K–Pg boundary layer. *Icarus* 201:768–780. https://doi.org/10.1016/j.icarus.2009.01.021.

Artemieva N., Morgan J., and Expedition 364 Science Party 2017. Quantifying the release of climate-active gases by large meteorite impacts with a case study of Chicxulub. *Geophysical Research Letters* 44:10,180–10,188. https://doi.org/10.1002/2017GL074879.

Arz J. A., Arenillas I., Grajales-Nishimura J. M., Liesa C. L., Soria A. R., Rojas R., Calmus T., and Gilabert V. 2022. No evidence of multiple impact scenario across the Cretaceous/Paleogene boundary based on planktic foraminiferal biochronology. In *From the Guajira Desert to the Apennines, and from Mediterranean Microplates to the Mexican Killer Asteroid: Honoring the Career of Walter Alvarez,* edited by C. Koeberl, P. Claeys, and A. Montanari. Geological Society of America Special Paper #557, Geological Society of America, Boulder, Colorado, pp. 415–448. https://doi.org/10.1130/2022.2557(20).

Baker D. M. H., Head J. W., Collins G. S., and Potter R. W. K. 2016. The formation of peak-ring basins: Working hypotheses and path forward in using observations to constrain models of impact-basin formation. *Icarus* 273:146–163. https://doi.org/10.1016/j.icarus.2015.11.033.

Belza J., Goderis S., Keppens E., Vanhaecke F., and Claeys P. 2012. An emplacement mechanism for the mega-block zone within the Chicxulub crater, (Yucatán, Mexico) based on chemostratigraphy. *Meteoritics & Planetary Science* 47:400–413. https://doi.org/10.1111/j.1945-5100.2012.01345.x.

Blum J. D., Chamberlain C. P., Hingston M. P., Koeberl C., Marin L. E., Schuraytz B. C., and Sharpton V. L. 1993. Isotopic comparison of K/T boundary impact glasses with melt rock from the Chicxulub and Manson impact structures. *Nature* 364:325–327. https://doi.org/10.1038/364325a0.

Bohor B. F., Foord E. E., Modreski P. J., and Triplehorn D. M. 1984. Mineralogic evidence for an impact event at the Cretaceous-Tertiary boundary. *Science* 224:867–869. https://doi.org/10.1126/science.224.4651.867.

Bohor B. F., Modreski P. J., and Foord E. E. 1987. Shocked quartz in the Cretaceous-Tertiary boundary clays: Evidence for a global distribution. *Science* 236:705–708. https://doi.org/10.1126/science.236.4802.705.

Brugger J., Feulner G., and Petri S. 2017. Baby, it's cold outside: Climate model simulations of the effects of the asteroid impact at the end of the Cretaceous. *Geophysical Research Letters* 44:419–427. https://doi.org/10.1002/2016GL072241.

Camargo-Zanoguera A. and Suárez-Reynoso G. 1994. Evidencia sísmica del cráter de impacto de Chicxulub. *Boletín de la Asociación Mexicana de Geólogos Petroleros* 34:1–28.

Carlisle D. B. and Braman D. R. 1991. Nanometre-size diamonds in the Cretaceous/Tertiary boundary clay of Alberta. *Nature* 352:708–709. https://doi.org/10.1038/352708a0.

Chiarenza A. A., Farnsworth A., Mannion P. D., Lunt D. J., Valdes P. J., Morgan J. V., and Allison P. A. 2020. Asteroid impact, not volcanism, caused the end-Cretaceous dinosaur extinction. *Proceedings of the National Academy of Sciences of the United States of America* 117:17084–17093. https://doi.org/10.1073/pnas.2006087117.

Christeson G. L., Nakamura Y., Buffler R. T., Morgan J., and Warner M. 2001. Deep crustal structure of the Chicxulub impact crater. *Journal of Geophysical Research: Solid Earth* 106:21751–21769. https://doi.org/10.1029/2001JB000337.

Christeson G. L., Collins G. S., Morgan J. V., Gulick S. P. S., Barton P. J., and Warner M. R. 2009. Mantle deformation beneath the Chicxulub impact crater. *Earth and Planetary Science Letters* 284:249–257. https://doi.org/10.1016/j.epsl.2009.04.033.

Christeson G. L., Gulick S. P. S., Morgan J. V., Gebhardt C., Kring D. A., Le Ber E., Lofi J., Nixon C., Poelchau M., Rae A. S. P., Rebolledo-Vieyra M., Riller U., Schmitt D. R., Wittmann A., Bralower T. J., Chenot E., Claeys P., Cockell C. S., Coolen M. J. L., Ferrière L., Green S., Goto K., Jones H., Lowery C. M., Mellett C., Ocampo-Torres R., Perez-Cruz L., Pickersgill A. E., Rasmussen C., Sato H., Smit J., Tikoo S. M., Tomioka N., Urrutia-Fucugauchi J., Whalen M. T., Xiao L., and Yamaguchi K. E. 2018. Extraordinary rocks from the peak ring of the Chicxulub impact crater: P-wave velocity, density, and porosity measurements from IODP/ICDP Expedition 364. *Earth and Planetary Science Letters* 495:1–11. https://doi.org/10.1016/j.epsl.2018.05.013.

Claeys P. 2006. Chicxulub, anatomy of a large impact structure: from impactite to ejecta distribution (abstract). 40th ESLAB-ESA First International Conference on Cratering in the Solar System, pp. 1–12. https://sci.esa.int/documents/33321/35974/1567255424998-ESLAB40-Proc_368081-Claeys.pdf.

Claeys P., Kiessling W., and Alvarez W. 2002. Distribution of Chicxulub ejecta at the Cretaceous-Tertiary boundary. In *Catastrophic events and mass extinctions: impacts and beyond*, edited by C. Koeberl and K. G. MacLeod. Geological Society of America Special Paper #356. Geological Society of America, Boulder, Colorado. pp. 55–68. https://doi.org/10.1130/0-8137-2356-6.55.

Claeys P., Heuschkel S., Lounejeva-Baturina E., Sanchez-Rubio G., and Stöffler D. 2003. The suevite of drill hole Yucatàn 6 in the Chicxulub impact crater. *Meteoritics & Planetary Science* 38:1299–1317. https://doi.org/10.1111/j.1945-5100.2003.tb00315.x.

Collins G. S., Melosh H. J., Morgan J. V., and Warner M. R. 2002. Hydrocode simulations of Chicxulub crater collapse and peak-ring formation. *Icarus* 157:24–33. https://doi.org/10.1006/icar.2002.6822.

Collins G. S., Patel N., Davison T. M., Rae A. S. P., Morgan J. V., Gulick S. P. S., IODP-ICDP Expedition 364 Science Party, and Third-Party Scientists 2020. A steeply-inclined trajectory for the Chicxulub impact. *Nature Communications* 11:1480. https://doi.org/10.1038/s41467-020-15269-x.

Courtillot V. 1990. Deccan volcanism at the Cretaceous-Tertiary boundary: past climatic crises as a key to the future? *Palaeography, Palaeoclimatology, Palaeoecology* 89:291–299. https://doi.org/10.1016/0031-0182(90)90070-N.

Croskell M., Warner M., and Morgan J. 2002. Annealing of shocked quartz during atmospheric reentry. *Geophysical Research Letters* 29:1940–1944. https://doi.org/10.1029/2001GL014382.

de Graaff S. J., Kaskes P., Déhais T., Goderis S., Debaille V., Ross C. H., Gulick S. P. S., Feignon J.-G., Ferrière L., Koeberl C., Smit J., Mattielli N., and Claeys P. 2022. New insights into the formation and emplacement of impact melt rocks within the Chicxulub impact structure, following the 2016 IODP-ICDP Expedition 364. *Geological Society of America Bulletin* 134:293–315. https://doi.org/10.1130/B35795.1.

Dengo G. 1969. Problems of tectonic relations between Central America and the Caribbean. *Gulf Coast Association of Geological Societies Transactions* 19:311–320.

Donnelly T. W., Horne G. S., Finch R. C., and López-Ramos E. 1990. Northern Central America; the Maya and Chortis blocks. In *The Caribbean region; The Geology of North America*, edited by G. Dengo and J. E. Case. Geological Society of America, Boulder, Colorado, pp. 371– 396. https://doi.org/10.1130/DNAG-GNA-H.37.

Dressler B. O., Sharpton V. L., Morgan J., Buffler R., Moran D., Smit J., Stöffler D., and Urrutia J. 2003. Investigating a 65-Ma-old smoking gun: Deep drilling of the Chicxulub Impact Structure. *EOS, Transactions, American Geophysical Union* 84:125–136. https://doi.org/10.1029/2003EO140001.

Dressler B. O., Sharpton V. L., Schwandt C. S., and Ames D. 2004. Impactites of the Yaxcopoil-1 drilling site, Chicxulub impact structure: Petrography, geochemistry, and depositional environment. *Meteoritics & Planetary Science* 39:857–878. https://doi.org/10.1111/j.1945-5100.2004.tb00935.x.

Duncan R. A. and Pyle D. G. 1988. Rapid eruption of the Deccan flood basalts at the Cretaceous/Tertiary boundary. *Nature* 333:841–843. https://doi.org/10.1038/333841a0.

Durda D. D. and Kring D. A. 2004. Ignition threshold for impact-generated fires. *Journal of Geophysical Research: Planets* 109:E08004. https://doi.org/10.1029/2004JE002279.

Ebel D. S. and Grossman L. 2005. Spinel-bearing spherules condensed from the Chicxulub impact-vapor plume. *Geology* 33:293–296. https://doi.org/10.1130/G21136.1.

Evans N. J., Gregoire D. C., Grieve R. A. F., Goodfellow W. D., and Veizer J. 1993. Use of platinum-group elements for impactor identification: terrestrial impact craters and Cretaceous–Tertiary boundary. *Geochimica et Cosmochimica Acta* 57:3737–3748. https://doi.org/10.1016/0016-7037(93)90152-M.

Evans N. J., Ahrens T. J., and Gregoire D. C. 1995. Fractionation of ruthenium from iridium at the Cretaceous–Tertiary boundary. *Earth and Planetary Science Letters* 134:141–153. https://doi.org/10.1016/0012-821X(95)00117-U.

Feignon J.-G., Ferrière L., Leroux H., and Koeberl C. 2020. Characterization of shocked quartz grains from Chicxulub peak ring granites and shock pressure estimates. *Meteoritics & Planetary Science* 55:2206–2223. https://doi.org/10.1111/maps.13570.

Feignon J.-G., de Graaff S. J., Ferrière L., Kaskes P., Déhais T., Goderis S., Claeys P., and Koeberl C. 2021. Chicxulub impact structure, IODP-ICDP Expedition 364 drill core: Geochemistry of the granite basement. *Meteoritics & Planetary Science* 56:1243–1273. https://doi.org/10.1111/maps.13705.

Feignon J.-G., Schulz T., Ferrière L., Goderis S., de Graaff S. J., Kaskes K., Déhais T., Claeys P., and Koeberl C. 2022. Search for a meteoritic component within the impact melt rocks of the Chicxulub impact structure peak ring, Mexico. *Geochimica et Cosmochimica Acta* 323:74–101. https://doi.org/10.1016/j.gca.2022.02.006.

Fischer-Gödde M., Becker H., and Wombacher F. 2010. Rhodium, gold and other highly siderophile element abundances in chondritic meteorites. *Geochimica et Cosmochimica Acta* 74:356–379. https://doi.org/10.1016/j.gca.2009.09.024.

Gayraud J., Robin E., Rocchia R., and Froget L. 1996. Formation conditions of oxidized Ni-rich spinel and their relevance to the K/T boundary event. In *The Cretaceous-Tertiary Event and Other Catastrophes in Earth History*, edited by G. Ryder, D. E. Fastovsky, and S. Gartner. Geological Society of America Special Paper #307, Geological Society of America, Boulder, Colorado, pp. 425–444. https://doi.org/10.1130/0-8137-2307-8.425.

Gelinas A., Kring D. A., Zurcher L., Urrutia-Fucugauchi J., Morton O., and Walker R. J. 2004. Osmium isotope constraints on the proportion of bolide component in Chicxulub impact melt rocks. *Meteoritics & Planetary Science* 39:1003–1008. https://doi.org/10.1111/j.1945-5100.2004.tb00941.x.

Glass B. P. and Simonson B. M. 2012a. Distal impact ejecta layers: spherules and more. *Elements* 8:43–48. https://doi.org/10.2113/gselements.8.1.43.

Glass B. P. and Simonson B. M. 2012b. *Distal impact ejecta layers: A record of large impacts in sedimentary deposits.* Springer-Verlag, Berlin Heidelberg, Germany, 731 p. https://doi.org/10.1007/978-3-540-88262-6.

Goderis S., Tagle R., Belza J., Smit J., Montanari A., Vanhaecke F., Erzinger J., and Claeys P. 2013. Reevaluation of siderophile element abundances and across the Cretaceous–Paleogene (K–Pg) boundary: Implications for the nature of the projectile. *Geochimica et Cosmochimica Acta* 120:417–446. https://doi.org/10.1016/j.gca.2013.06.010.

Goderis S., Sato H., Ferrière L., Schmitz B., Burney D., Kaskes P., Vellekoop J., Wittmann A., Schulz T., Chernonozhkin S. M., Claeys P., de Graaff S. J., Déhais T., de Winter N. J., Elfman M., Feignon J.-G., Ishikawa A., Koeberl C., Kristiansson P., Neal C. R., Owens J. D., Schmieder M., Sinnesael M., Vanhaecke F., Van Malderen S. J. M., Bralower T. J., Gulick S. P. S., Kring D. A., Lowery C. M., Morgan J. V., Smit J., Whalen M. T., and IODP-ICDP Expedition 364 Scientists. 2021. Globally distributed iridium layer preserved within the Chicxulub impact structure. *Science Advances* 7:eabe3647. https://doi.org/10.1126/sciadv.abe3647.

Goto K., Tada R., Tajika E., Bralower T. J., Hasegawa T., and Matsui T. 2004. Evidence for ocean water invasion into the Chicxulub crater at the Cretaceous/Tertiary boundary. *Meteoritics & Planetary Science* 39:1233–1247. https://doi.org/10.1111/j.1945-5100.2004.tb00943.x.

Grieve R. A. F., Reimold W. U., Morgan J., Riller U., and Pilkington M. 2008. Observations and interpretations at Vredefort, Sudbury, and Chicxulub: towards an empirical model of terrestrial impact basin formation. *Meteoritics & Planetary Science* 43:855–882. https://doi.org/10.1111/j.1945-5100.2008.tb01086.x.

Gulick S. P. S., Barton P. J., Christeson G. L., Morgan J. V., McDonald M., Mendoza-Cervantes K., Pearson Z. F., Surendra A., Urrutia-Fucugauchi J., Vermeesch P. M., and Warner M. R. 2008. Importance of pre-impact crustal structure for the asymmetry of the Chicxulub impact crater. *Nature Geoscience* 1:131–135. https://doi.org/10.1038/ngeo103.

Gulick S. P. S., Christeson G. L., Barton P. J., Grieve R. A. F., Morgan J. V., and Urrutia-Fucugauchi J. 2013. Geophysical characterization of the Chicxulub impact crater. *Reviews of Geophysics* 51:31–52. https://doi.org/10.1002/rog.20007.

Gulick S. P. S., Bralower T. J., Ormö J., Hall B., Grice K., Schaefer B., Lyons S., Freeman K. H., Morgan J. V., Artemieva N., Kaskes P., de Graaff S. J., Whalen M. T., Collins G. S., Tikoo S. M., Verhagen C., Christeson G. L., Claeys P., Coolen M. J. L., Goderis S., Goto K., Grieve R. A. F., McCall N., Osinski G. R., Rae A. S. P., Riller U., Smit J., Vajda V., Wittmann A., and the Expedition 364 Scientists 2019. The first day of the Cenozoic. *Proceedings of the National*

Academy of Sciences of the United States of America 116:19342–19351. https://doi.org/10.1073/pnas.1909479116.

Head J. W. 2010. Transition from complex craters to multi-ringed basins on terrestrial planetary bodies: scale-dependent role of the expanding melt cavity and progressive interaction with the displaced zone. *Geophysical Research Letters* 37:L02203. https://doi.org/10.1029/2009GL041790.

Hecht L., Wittmann A., Schmitt R. T., and Stöffler D. 2004. Composition of impact melt particles and the effects of postimpact alteration in suevitic rocks at the Yaxcopoil-1 drill core, Chicxulub crater, Mexico. *Meteoritics & Planetary Science* 39:1169–1186. https://doi.org/10.1111/j.1945-5100.2004.tb01135.x.

Hildebrand A. R. and Boynton W. V. 1990a. Locating the Cretaceous/Tertiary boundary impact crater(s). *EOS, Transactions, American Geophysical Union* 71:1424–1425.

Hildebrand A. R. and Boynton W. V. 1990b. Proximal Cretaceous-Tertiary boundary impact deposits in the Caribbean. *Science* 248:843–847. https://doi.org/10.1126/science.248.4957.843.

Hildebrand A. R., Penfield G. T., Kring D. A., Pilkington M., Camargo Z. A., Jacobsen S. B., and Boynton W. V. 1991. Chicxulub crater: A possible Cretaceous/Tertiary boundary impact crater on the Yucatán Peninsula, Mexico. *Geology* 19:867–871. https://doi.org/10.1130/0091-7613(1991)019<0867:CCAPCT>2.3.CO;2.

Hildebrand A. R., Pilkington M., Connors M., Ortiz-Aleman C., and Chavez R. E. 1995. Size and structure of the Chicxulub crater revealed by horizontal gravity gradients and cenotes. *Nature* 376:415–417. https://doi.org/10.1038/376415a0.

Hough R. M., Gilmour I., Pillinger C. T., Langenhorst F., and Montanari A. 1997. Diamonds from the iridium-rich K-T boundary layer at Arroyo el Mimbral, Tamaulipas, Mexico. *Geology* 25:1019–1022. https://doi.org/10.1130/0091-7613(1997)025<1019:DFTIRK>2.3.CO;2.

Hough R. M., Gilmour I., and Pillinger C. T. 1999. Carbon isotope study of impact diamonds in Chicxulub ejecta at Cretaceous-Tertiary boundary sites in Mexico and the Western Interior of the United States. In *Large meteorite impacts and planetary evolution; II,* edited by B. O. Dressler and V. L. Sharpton. Geological Society of America Special Paper #339, Geological Society of America, Boulder, Colorado. pp. 215–222. https://doi.org/10.1130/0-8137-2339-6.215.

Hull P. M. and Norris R. D. 2011. Diverse patterns of ocean export productivity change across the Cretaceous–Paleogene boundary: New insights from biogenic barium. *Paleoceanography and Paleoclimatology* 26:PA3205. https://doi.org/10.1029/2010PA002082.

Hull P. M., Bornemann A., Penman D. E., Henehan M. J., Norris R. D., Wilson P. A., Blum P., Alegret L., Batenburg S. J., Brown P. R., Bralower T. J., Cournede C., Deutsch A., Donner B., Friedrich O., Jehle S., Kim H., Kroon D., Lippert P. C., Loroch D., Moebius I., Moriya K., Peppe D. J., Ravizza G. E., Röhl U., Schueth J. D., Sepúlveda J., Sexton P. F., Sibert E. C., Śliwińska K. K., Summons R. E., Thomas E., Westerhold T., Whiteside J. H., Yamaguchi T., and Zachos J. C. 2020. On impact and volcanism across the Cretaceous-Paleogene boundary. *Science* 367:266–272. https://doi.org/10.1126/science.aay5055.

Ivanov B. A. 2005. Numerical modeling of the largest terrestrial meteorite craters. *Solar System Research* 39:381–409. https://doi.org/10.1007/s11208-005-0051-0.

Jablonski J. 2004. Extinction: past and present. *Nature* 427:589. https://doi.org/10.1038/427589a.

Jiang S., Bralower T. J., Patzkowsky M. E., Kump L. R., and Schueth J. D. 2010. Geographic controls on nannoplankton extinction across the Cretaceous/Palaeogene boundary. *Nature Geoscience* 3:280–285. https://doi.org/10.1038/ngeo775.

Kaiho K., Oshima N., Adachi K., Adachi Y., Mizukami T., Fujibayashi M., and Saito R. 2016. Global climate change driven by soot at the K-Pg boundary as the cause of the mass extinction. *Scientific Reports* 6:28427. https://doi.org/10.1038/srep28427.

Kamo S. L. and Krogh T. E. 1995. Chicxulub crater source for shocked zircon crystals from the Cretaceous-Tertiary boundary layer, Saskatchewan: evidence from new U-Pb data. *Geology* 23:281–284. https://doi.org/10.1130/0091-7613(1995)023<0281:CCSFSZ>2.3.CO;2.

Kamo S. L., Lana C., and Morgan J. V. 2011. U-Pb ages of shocked zircon grains link distal K–Pg boundary sites in Spain and Italy with the Chicxulub impact. *Earth and Planetary Science Letters* 310:401–408. https://doi.org/10.1016/j.epsl.2011.08.031.

Kaskes P., de Graaff S. J., Feignon J.-G., Déhais T., Goderis S., Ferrière L., Koeberl C., Smit J., Wittmann A., Gulick S. P. S., Debaille V., Matielli N., and Claeys P. 2022. Formation of the Crater Suevite Sequence from the Chicxulub Peak Ring: a Petrographic, Geochemical, and Sedimentological Characterization. *Geological Society of America Bulletin* 134:895–927. https://doi.org/10.1130/B36020.1.

Keller G. 2005. Impacts, volcanism and mass extinction: random coincidence or cause and effect? *Australian Journal of Earth Sciences* 52:725–757. https://doi.org/10.1080/08120090500170393.

Keller G., Adatte T., Gardin S., Bartolini A., and Bajpai S. 2008. Main Deccan volcanism phase ends near the K–T boundary: Evidence from the Krishna–Godavari Basin, SE India. *Earth and Planetary Science Letters* 268:293–311. https://doi.org/10.1016/j.epsl.2008.01.015.

Kenkmann T., Wittmann A., and Scherler D. 2004. Structure and impact indicators of the Cretaceous sequence of the ICDP drill core Yaxcopoil-1, Chicxulub impact crater, Mexico. *Meteoritics & Planetary Science* 39:1069–1088. https://doi.org/10.1111/j.1945-5100.2004.tb01129.x.

Keppie J. D., Dostal J., Norman M., Urrutia-Fucugauchi J., and Grajales-Nishimura M. 2011. Study of melt and a clast of 546 Ma magmatic arc rocks in the 65 Ma Chicxulub bolide breccia, northern Maya block, Mexico: Western limit of Ediacaran arc peripheral to northern Gondwana. *International Geology Review* 53: 1180–1193. https://doi.org/10.1080/00206810903545527.

Kettrup B. and Deutsch A. 2003. Geochemical variability of the Yucatán basement: Constraints from crystalline clasts in Chicxulub impactites. *Meteoritics & Planetary Science* 38:1079–1092. https://doi.org/10.1111/j.1945-5100.2003.tb00299.x.

Koeberl C. 1993. Chicxulub crater, Yucatan: Tektites, impact glasses, and the geochemistry of target rocks and breccias. *Geology* 21:211–214. https://doi.org/10.1130/0091-7613(1993)021<0211:CCYTIG>2.3.CO;2.

Koeberl C. and Sigurdsson H. 1992. Geochemistry of impact glasses from the K/T boundary in Haiti: Relation to smectites, and a new type of glass. *Geochimica et Cosmochimica Acta* 56:2113–2129. https://doi.org/10.1016/0016-7037(92)90333-E.

Koeberl C., Sharpton V. L., Schuraytz B. C., Shirey S. B., Blum J. D., and Marin L. E. 1994. Evidence for a meteoritic component in impact melt rock from the Chicxulub structure. *Geochimica et Cosmochimica Acta* 58:1679–1684. https://doi.org/10.1016/0016-7037(94)90567-3.

Kring D. A. 2005. Hypervelocity collisions into continental crust composed of sediments and an underlying crystalline basement: Comparing the Ries (~24 km) and Chicxulub (~180 km) impact craters. *Geochemistry* 65:1–46. https://doi.org/10.1016/j.chemer.2004.10.003.

Kring D. A. and Boynton W. V. 1992. Petrogenesis of an augite-bearing melt rock in the Chicxulub structure and its relationship to K/T impact spherules in Haiti. *Nature* 358:141–144. https://doi.org/10.1038/358141a0.

Kring D. A. and Durda D. D. 2002. Trajectories and distribution of material ejected from the Chicxulub impact crater: Implications for postimpact wildfires. *Journal of Geophysical Research: Planets* 107:6-1–6-22. https://doi.org/10.1029/2001JE001532.

Kring D. A., Hörz F., Zurcher L., and Urrutia Fucugauchi J. 2004. Impact lithologies and their emplacement in the Chicxulub impact crater: Initial results from the Chicxulub Scientific Drilling Project, Yaxcopoil-1, Mexico. *Meteoritics & Planetary Science* 39:879–897. https://doi.org/10.1111/j.1945-5100.2004.tb00936.x.

Kring D. A., Claeys P., Gulick S. P. S., Morgan J. V., Collins G. S., and the IODP-ICDP Expedition 364 Science Party 2017. Chicxulub and the Exploration of Large Peak-Ring Impact Craters through Scientific Drilling. *GSA Today* 27:4–8. https://doi.org/10.1130/GSATG352A.1.

Kring D. A., Tikoo S. M., Schmieder M., Riller U., Rebolledo-Vieyra M., Simpson S. L., Osinski G. R., Gattacceca J., Wittmann A., Verhagen C. M., Cockell C. S., Coolen M. J. L., Longstaffe F. J., Gulick S. P. S., Morgan J. V., Bralower T. J., Chenot E., Christeson G. L., Claeys P., Ferrière L., Gebhardt C., Goto K., Green S. L., Jones H., Lofi J., Lowery C. M., Ocampo-Torres R., Perez-Cruz L., Pickersgill A. E., Poelchau M. H., Rae A. S. P., Rasmussen C., Sato H., Smit J., Tomioka N., Urrutia-Fucugauchi J., Whalen M. T., Xiao L., and Yamaguchi K. E. 2020. Probing the hydrothermal system of the Chicxulub impact crater. *Science Advances* 6:eaaz3053. https://doi.org/10.1126/sciadv.aaz3053.

Krogh T. E., Kamo S. L., and Bohor B. F. 1993a. Fingerprinting the K/T impact site and determining the time of impact by U Pb dating of single shocked zircons from distal ejecta. *Earth and Planetary Science Letters* 119:425–429. https://doi.org/10.1016/0012-821X(93)90150-8.

Krogh T. E., Kamo S. L., Sharpton V. L., Marin L. E., and Hildebrand A. R. 1993b. U/Pb ages of single shocked zircons linking distal K/T ejecta to the Chicxulub crater. *Nature* 366:731–734. https://doi.org/10.1038/366731a0.

Kruge M. A., Stankiewicz A., Crelling J. C., and Montanari A. 1994. Fossil charcoal in Cretaceous–Tertiary boundary strata: evidence for catastrophic firestorm and megawave. *Geochimica et Cosmochimica Acta* 58:1393–1397. https://doi.org/10.1016/0016-7037(94)90394-8.

Kyte F. T. 1998. A meteorite from the Cretaceous/Tertiary boundary. *Nature* 396:237–239. https://doi.org/10.1038/24322.

Kyte F. T. and Smit J. 1986. Regional variations in spinel compositions: An important key to the Cretaceous/Tertiary event. *Geology* 14:485–487. https://doi.org/10.1130/0091-7613(1986)14<485:RVISCA>2.0.CO;2.

López-Ramos E. 1975. Geological summary of the Yucatan peninsula. In *The Gulf of Mexico and the Caribbean*, edited by A. E. M. Nairn and F. G. Stehli. Springer, Boston, Massachusetts, pp. 257–282. https://doi.org/10.1007/978-1-4684-8535-6_7.

Lowery C. M., Bralower T. J., Owens J. D., Rodríguez-Tovar F., Jones H., Smit J., Whalen M. T., Claeys P., Farley K., Gulick S. P. S., Morgan J. V., Green S., Chenot E., Christeson G. L., Cockell C. S., Coolen M. J. L., Ferrière L., Gebhardt C., Goto K., Kring D. A., Lofi J., Ocampo-Torres R., Perez-Cruz L., Pickersgill A. E., Poelchau M. H., Rae A. S. P., Rasmussen C., Rebolledo-Vieyra M., Riller U., Sato H., Tikoo S. M., Tomioka N., Urrutia-Fucugauchi J.,

Vellekoop J., Wittmann A., Xiao L., Yamaguchi K. E., and Zylberman W. 2018. Rapid recovery of life at ground zero of the end-Cretaceous mass extinction. *Nature* 558:288–291. https://doi.org/10.1038/s41586-018-0163-6.

Lyons S. L., Karp A. T., Bralower T. J., Grice K., Schaefer B., Gulick S. P. S., Morgan J. V., and Freeman K. H. 2020. Organic matter from the Chicxulub crater exacerbated the K–Pg impact winter. *Proceedings of the National Academy of Sciences of the United States of America* 117:25327–25334. https://doi.org/10.1073/pnas.2004596117.

Martín-Peinado F. J. and Rodríguez-Tovar F. J. 2010. Mobility of iridium in terrestrial environments: implications for the interpretation of impact-related mass-extinctions. *Geochimica et Cosmochimica Acta* 74:4531–4542. https://doi.org/10.1016/j.gca.2010.05.009.

McCormick M. P., Thomason L. W., and Trepte C. R. 1995. Atmospheric effects of the Mt Pinatubo eruption. *Nature* 373:399–404. https://doi.org/10.1038/373399a0.

McDonough W. F. and Sun S. 1995. The composition of the Earth. *Chemical Geology* 120:223–253. https://doi.org/10.1016/0009-2541(94)00140-4.

Melosh H. J. 1979. Acoustic fluidization: a new geologic process? *Journal of Geophysical Research: Solid Earth* 84:7513–7520. https://doi.org/10.1029/JB084iB13p07513.

Melosh H. J. and Vickery A. M. 1991. Melt droplet formation in energetic impact events. *Nature* 350:494–497. https://doi.org/10.1038/350494a0.

Melosh H. J., Schneider N. M., Zahnle K. J., and Latham D. 1990. Ignition of global wildfires at the Cretaceous/Tertiary boundary. *Nature* 343:251–254. https://doi.org/10.1038/343251a0.

Molina E., Alegret L., Arenillas I., Arz J. A., Gallala N., Grajales-Nishimura J. M., Murillo-Muñetón G., and Zaghbib-Turki D. 2009. The Global Boundary Stratotype Section and Point for the Base of the Danian Stage (Paleocene, Paleogene, 'Tertiary', Cenozoic): auxiliary sections and correlation. *Episodes* 32:84–95. https://doi.org/10.18814/epiiugs/2009/v32i2/002.

Molina-Garza R. S., Van der Voo R., and Urrutia-Fucugauchi J. 1992. Paleomagnetism of the Chiapas Massif, southern Mexico: Evidence for rotation of the Maya Block and implications for the opening of the Gulf of Mexico. *Geological Society of America Bulletin* 104:1156–1168. https://doi.org/10.1130/0016-7606(1992)104<1156:POTCMS>2.3.CO;2.

Montanari A., Hay R. L., Alvarez W., Asaro F., Michel H. V., Alvarez L. W., and Smit J. 1983. Spheroids at the Cretaceous-Tertiary boundary are altered impact droplets of basaltic composition. *Geology* 11:668–671. https://doi.org/10.1130/0091-7613(1983)11<668:SATCBA>2.0.CO;2.

Morgan J., Warner M., the Chicxulub Working Group, Brittan J., Buffler R., Camargo A., Christeson G., Denton P., Hildebrand A., Hobbs R., Macintyre H., Mackenzie G., Maguire P., Marin L., Nakamura Y., Pilkington M., Sharpton V., Snyder D., Suarez G., and Trejo A. 1997. Size and morphology of the Chicxulub impact crater. *Nature* 390:472–476. https://doi.org/10.1038/3729.

Morgan J., Lana C., Kearsley A., Coles B., Belcher C., Montanari S., Diaz-Martinez E., Barbosa A., and Neumann V. 2006. Analyses of shocked quartz at the global K–Pg boundary indicate an origin from a single, high-angle, oblique impact at Chicxulub. *Earth and Planetary Science Letters* 251:264–279. https://doi.org/10.1016/j.epsl.2006.09.009.

Morgan J., Artemieva N., and Goldin T. 2013. Revisiting wildfires at the K-Pg boundary. *Journal of Geophysical Research: Biogeosciences* 118:1508–1520. https://doi.org/10.1002/2013JG002428.

Morgan J. V., Warner M. R., Collins G. S., Melosh H. J., and Christeson G. L. 2000. Peak-ring formation in large impact craters: geophysical constraints from Chicxulub. *Earth and Planetary Science Letters* 183:347–354. https://doi.org/10.1016/S0012-821X(00)00307-1.

Morgan J. V., Warner M. R., Collins G. S., Grieve R. A. F., Christeson G. L., Gulick S. P. S., and Barton P. J. 2011. Full waveform tomographic images of the peak ring at the Chicxulub impact crater. *Journal of Geophysical Research: Solid Earth* 116:B06303. https://doi.org/10.1029/2010JB008015.

Morgan J. V., Gulick S. P. S., Bralower T., Chenot E., Christeson G., Claeys P., Cockell C., Collins G. S., Coolen M. J. L., Ferrière L., Gebhardt C., Goto K., Jones H., Kring D. A., Le Ber E., Lofi J., Long X., Lowery C., Mellett C., Ocampo-Torres R., Osinski G. R., Perez-Cruz L., Pickersgill A., Poelchau M., Rae A., Rasmussen C., Rebolledo-Vieyra M., Riller U., Sato H., Schmitt D. R., Smit J., Tikoo S., Tomioka N., Urrutia-Fucugauchi J., Whalen M., Wittmann A., Yamaguchi K. E., and Zylberman W. 2016. The formation of peak rings in large impact craters. *Science* 354:878–882. https://doi.org/10.1126/science.aah6561.

Morgan J. V., Gulick S., Mellet C. L., Green S. L., and Expedition 364 Scientists 2017. *Chicxulub: Drilling the K-Pg impact crater*. Proceedings of the International Ocean Discovery Program, 364. International Ocean Discovery Program, College Station, Texas. https://doi.org/10.14379/iodp.proc.364.2017. [176 p. (+ 352 p. of SM + Maps + Tables)].

O'Keefe J. D. and Ahrens T. J. 1993. Planetary cratering mechanics. *Journal of Geophysical Research: Planets* 98:17011–17028. https://doi.org/10.1029/93JE01330.

Ocampo A. C., Pope K. O., and Fischer A. G. 1996. Ejecta blanket deposits of the Chicxulub crater from Albion Island, Belize. In *The Cretaceous-Tertiary Event and Other Catastrophes in Earth History*, edited by G. Ryder, D. E. Fastovsky, and S. Gartner. Geological Society of

America Special Paper #307, Geological Society of America, Boulder, Colorado, pp. 75–88. https://doi.org/10.1130/0-8137-2307-8.75.

Ortega-Gutiérrez F., Elías-Herrera M., Morán-Zenteno D. J., Solari L., Weber B., and Luna-González L. 2018. The pre-Mesozoic metamorphic basement of Mexico, 1.5 billion years of crustal evolution. *Earth-Science Reviews* 183:2–37. https://doi.org/10.1016/j.earscirev.2018.03.006.

Osinski G. R., Grieve R. A. F., Hill P. J. A., Simpson S. L., Cockell C., Christeson G. L., Ebert M., Gulick S., Melosh H. J., Riller U., Tikoo S. M., and Wittmann A. 2020. Explosive interaction of impact melt and seawater following the Chicxulub impact event. *Geology* 48:108–112. https://doi.org/10.1130/G46783.1.

Penfield G. T. and Camargo-Zanoguera A. 1981. Definition of a major igneous zone in the central Yucatan platform with aeromagnetics and gravity. Technical Program, Abstracts and Bibliographies, 51st Annual Meeting, Society of Exploration Geophysicists, Tulsa, Oklahoma, p. 37.

Peucker-Ehrenbrink B. and Jahn B.-M. 2001. Rhenium-osmium isotope systematics and platinum group element concentrations: Loess and the upper continental crust. *Geochemistry, Geophysics, Geosystems* 2:1061. https://doi.org/10.1029/2001GC000172.

Pierazzo E. and Melosh H. J. 1999. Hydrocode modeling of Chicxulub as an oblique impact event. *Earth and Planetary Science Letters* 165:163–176. https://doi.org/10.1016/S0012-821X(98)00263-5. https://doi.org/10.1111/j.1945-5100.2000.tb01979.x.

Pierazzo E. and Melosh H. J. 2000 Hydrocode modeling of oblique impacts: The fate of the projectile. *Meteoritics & Planetary Science* 35:117–130.

Pierazzo E., Kring D. A., and Melosh H. J. 1998. Hydrocode simulation of the Chicxulub impact event and the production of climatically active gases. *Journal of Geophysical Research* 103:28,607–28,625. https://doi.org/10.1029/98JE02496.

Pierazzo E., Hahmann A. N., and Sloan L. C. 2003. Chicxulub and climate: Radiative perturbations of impact-produced S-bearing gases. *Astrobiology* 3:99–118. https://doi.org/10.1089/153110703321632453.

Pilkington M., Hildebrand A. R., and Ortiz-Aleman C. 1994. Gravity and magnetic field modeling and structure of the Chicxulub crater, Mexico. *Journal of Geophysical Research: Planets* 99:13147–13162. https://doi.org/10.1029/94JE01089.

Pope K. O., Ocampo A. C., and Duller C. E. 1991. Mexican site for K/T impact crater? *Nature* 351:105. https://doi.org/10.1038/351105a0.

Pope K. O., Ocampo A. C., Kinsland G. L., and Smith R. 1996. Surface expression of the Chicxulub Crater. *Geology* 24:527–530. https://doi.org/10.1130/0091-7613(1996)024<0527:SEOTCC>2.3.CO;2.

Pope K. O., Baines K. H., Ocampo A. C., and Ivanov B. A. 1997. Energy, volatile production, and climatic effects of the Chicxulub Cretaceous/Tertiary impact. *Journal of Geophysical Research: Planets* 102:21645–21664. https://doi.org/10.1029/97JE01743.

Quitté G., Levasseur S., Capmas F., Rocchia R., Birck J. L., and Allègre C. J. 2007. Osmium, tungsten, and chromium isotopes in sediments and in Ni-rich spinel at the K-T boundary: signature of a chondritic impactor. *Meteoritics & Planetary Science* 42:1567–1580. https://doi.org/10.1111/j.1945-5100.2007.tb00591.x.

Rae A. S. P., Collins G. S., Poelchau M., Riller U., Davison T. M., Grieve R. A. F., Osinski G. R., Morgan J. V., and IODP-ICDP Expedition 364 Scientists 2019. Stress-Strain Evolution During Peak-Ring Formation: A Case Study of the Chicxulub Impact Structure. *Journal of Geophysical Research: Planets* 124:396–417. https://doi.org/10.1029/2018JE005821.

Rampino M. R. 1982. A non-catastrophist explanation for the iridium anomaly at the Cretaceous/Tertiary boundary. In *Geological Implications of Impacts of Large Asteroids and Comets on the Earth*, edited by L. T. Silver and P. H. Schultz. Geological Society of America Special Paper #190. Geological Society of America, Boulder, Colorado. pp. 455–460. https://doi.org/10.1130/SPE190-p455.

Rebolledo-Vieyra M., Urrutia-Fucugauchi J., Marin L. E., Trejo-Garcia A., Sharpton V. L., and Soler-Arechalde A. M. 2000. UNAM scientific shallow-drilling program of the Chicxulub impact crater. *International Geology Review* 42:928–940. https://doi.org/10.1080/00206810009465118.

Renne P. R., Deino A. L., Hilgen F. J., Kuiper K. F., Mark D. F., Mitchell W. S., III, Morgan L. E., Mundil R., and Smit J. 2013. Time scales of critical events around the Cretaceous-Paleogene boundary. *Science* 339:684–687. https://doi.org/10.1126/science.1230492.

Renne P. R., Sprain C. J., Richards M. A., Self S., Vanderkluysen L., and Pande K. 2015. State shift in Deccan volcanism at the Cretaceous-Paleogene boundary, possibly induced by impact. *Science* 350:76–78. https://doi.org/10.1126/science.aac7549.

Riller U., Poelchau M. H., Rae A. S. P., Schulte F. M., Collins G. S., Melosh H. J., Grieve R. A. F., Morgan J. V., Gulick S. P. S., Lofi J., Diaw A., McCall N., Kring D. A., and IODP-ICDP Expedition 364 Science Party 2018. Rock fluidization during peak-ring formation of large impact structures. *Nature* 562:511–518. https://doi.org/10.1038/s41586-018-0607-z.

Robin E., Boclet D., Bonte P., Froget L., and Jéhanno C. 1991. The stratigraphic distribution of Ni-rich spinels in Cretaceous– Tertiary boundary rocks at El Kef (Tunisia), Caravaca (Spain)

and Hole 761C (Leg 122). *Earth and Planetary Science Letters* 107:715–721. https://doi.org/10.1016/0012-821X(91)90113-V.

Robin E., Bonté Ph., Froget L., Jéhanno C., and Rocchia R. 1992. Formation of spinels in cosmic objects during atmospheric entry: a clue to the Cretaceous-Tertiary boundary event. *Earth and Planetary Science Letters* 108:181–190. https://doi.org/10.1016/0012-821X(92)90021-M.

Ross C. H., Stockli D. F., Rasmussen C., Gulick S. P. S., de Graaff S. J., Claeys P., Zhao J., Xiao L., Pickersgill A. E., Schmieder M., Kring D. A., Wittmann A., and Morgan J. 2022. Evidence of Carboniferous arc magmatism preserved in the Chicxulub impact structure. *Geological Society of America Bulletin* 134:241–260. https://doi.org/10.1130/B35831.1.

Rowe A. J., Wilkinson J. J, Coles B. J., and Morgan J. V. 2004. Chicxulub: testing for post-impact hydrothermal inputs into the Tertiary ocean. *Meteoritics & Planetary Science* 39:1223–1231. https://doi.org/10.1111/j.1945-5100.2004.tb01138.x.

Sanford J. C., Snedden J. W., and Gulick S. P. S. 2016. The Cretaceous-Paleogene boundary deposit in the Gulf of Mexico: Large-scale oceanic basin response to the Chicxulub impact. *Journal of Geophysical Research: Solid Earth* 121:1240–1261. https://doi.org/10.1002/2015JB012615.

Schmitt R. T., Wittmann A., and Stöffler D. 2004. Geochemistry of drill core samples from Yaxcopoil-1, Chicxulub impact crater, Mexico. *Meteoritics & Planetary Science* 39:979–1001. https://doi.org/10.1111/j.1945-5100.2004.tb00940.x.

Schoene B., Eddy M. P., Samperton K. M., Keller C. B., Keller G., Adatte T., and Khadri S. F. R. 2019. U-Pb constraints on pulsed eruption of the Deccan Traps across the end-Cretaceous mass extinction. *Science* 363:862–866. https:/:doi.org/10.1126/science.aau2422.

Schulte F. M., Wittmann A., Jung S., Morgan J. V., Gulick S. P. S., Kring D. A., Grieve R. A. F., Osinski G. R., Riller U., and IODP-ICDP Expedition 364 Science Party 2021. Ocean resurge-induced impact melt dynamics on the peak-ring of the Chicxulub impact structure, Mexico. *International Journal of Earth Sciences* 110: 2619–2636. https://doi.org/10.1007/s00531-021-02008-w.

Schulte P., Alegret L., Arenillas I., Arz J. A., Barton P. J., Bown P. R., Bralower T. J., Christeson G. L., Claeys P., Cockell C. S., Collins G. S., Deutsch A., Goldin T. J., Goto K., Grajales-Nishimura J. M., Grieve R. A. F., Gulick S. P. S., Johnson K. R., Kiessling W., Koeberl C., Kring D. A., MacLeod K. G., Matsui T., Melosh J., Montanari A., Morgan J. V., Neal C. R., Nichols D. J., Norris R. D., Pierazzo E., Ravizza G., Rebolledo-Vieyra M., Reimold W. U., Robin E., Salge T., Speijer R. P., Sweet A. R., Urrutia-Fucugauchi J., Vajda V., Whalen M. T., and Willumsen P. S. 2010. The Chicxulub asteroid impact and mass extinction at the

Cretaceous-Paleogene boundary. *Science* 327:1214–1218. https://doi.org/10.1126/science.1177265.

Schuraytz B. C., Sharpton V. L., and Marín L. E. 1994. Petrology of impact-melt rocks at the Chicxulub multiring basin, Yucatán, Mexico. *Geology* 22:868–872. https://doi.org/10.1130/0091-7613(1994)022<0868:POIMRA>2.3.CO;2.

Schuraytz B. C., Lindstrom D. J., Marín L. E., Martinez R. R., Mittlefehldt D. W., Sharpton V. L., and Wentworth S. J. 1996. Iridium metal in Chicxulub impact melt: forensic chemistry on the K-T smoking gun. *Science* 271:1573–1576. https://doi.org/10.1126/science.271.5255.1573.

Senft L. E. and Stewart S. T. 2009. Dynamic fault weakening and the formation of large impact craters. *Earth and Planetary Science Letters* 287:471–482. https://doi.org/10.1016/j.epsl.2009.08.033.

Sharpton V. L., Dalrymple G., Marin L., Ryder G., Schuraytz B., and Urrutia-Fucugauchi J. 1992. New links between the Chicxulub impact structure and the Cretaceous/Tertiary boundary. *Nature* 359:819–821. https://doi.org/10.1038/359819a0.

Sharpton V. L., Burke K., Camargo-Zanoguera A., Hall S. A., Lee D. S., Marín L. E., Suárez-Reynoso G., Quezada-Muñeton J. M., Spudis P. D., and Urrutia-Fucugauchi J. 1993. Chicxulub Multiring Impact Basin: Size and Other Characteristics Derived from Gravity Analysis. *Science* 261:1564–1567. https://doi..org/10.1126/science.261.5128.1564.

Sharpton V. L., Marin E. L., Carney J. L., Lee S., Ryder G., Schuraytz B. C., Sikora P., and Spudis P. D. 1996. A model of the Chicxulub impact basin based on evaluation of geophysical data, well logs, and drill core samples. In *The Cretaceous-Tertiary Event and Other Catastrophes in Earth History*, edited by G. Ryder, D. E. Fastovsky, and S. Gartner. Geological Society of America Special Paper #307, Geological Society of America, Boulder, Colorado, pp. 55–74. https://doi.org/10.1130/0-8137-2307-8.55.

Shukolyukov A. and Lugmair G. W. 1998. Isotopic evidence for the Cretaceous-Tertiary impactor and its type. *Science* 282:927–930. https:/:doi.org/10.1126/science.282.5390.927.

Sigurdsson H., D'Hondt S., Arthur M. A., Bralower T. J., Zachos J. C., van Fossen M., and Channel J. E. T. 1991. Glass from the Cretaceous/Tertiary boundary in Haiti. *Nature* 349:482–487. https://doi.org/10.1038/349482a0.

Simpson S. L., Osinski G. R., Longstaffe F. J., Schmieder M., and Kring D. A. 2020. Hydrothermal alteration associated with the Chicxulub impact crater upper peak-ring breccias. *Earth and Planetary Science Letters* 547:116425. https://doi.org/10.1016/j.epsl.2020.116425.

Simpson S. L., Longstaffe F. J., Osinski G. R., Caudill C. M., and Kring D. A. 2022. A low-temperature, meteoric water-dominated origin for smectitic clay minerals in the Chicxulub impact crater upper peak ring, as inferred from their oxygen and hydrogen isotope compositions. *Chemical Geology* 588:120639. https://doi.org/10.1016/j.chemgeo.2021.120639.

Smit J. 1999. The global stratigraphy of the Cretaceous-Tertiary boundary impact ejecta. *Annual Review of Earth and Planetary Sciences* 27:75–113. https://doi.org/10.1146/annurev.earth.27.1.75.

Smit J. 2022. The KPg boundary Chicxulub impact-extinction hypothesis: The winding road towards a solid theory. In *From the Guajira Desert to the Apennines, and from Mediterranean Microplates to the Mexican Killer Asteroid: Honoring the Career of Walter Alvarez,* edited by C. Koeberl, P. Claeys, and A. Montanari. Geological Society of America Special Paper #557, Geological Society of America, Boulder, Colorado, pp. 391–414. https://doi.org/10.1130/2022.2557(19).

Smit J. and Hertogen J. 1980. An extraterrestrial event at the Cretaceous-Tertiary boundary. *Nature* 285:198–200. https://doi.org/10.1038/285198a0.

Smit J. and Romein A. J. T. 1985. A sequence of events across the Cretaceous–Tertiary boundary. *Earth and Planetary Science Letters* 74:155–170. https://doi.org/10.1016/0012-821X(85)90019-6.

Smit J., Alvarez W., Montanari A., Swinburne N., van Kempen T. M., Klaver G. T., and Lustenhouwer W. J. 1992. ''Tektites'' and microkrystites at the Cretaceous-Tertiary boundary: Two strewn fields, one crater? *Proceedings of the 22nd Lunar and Planetary Science Conference* 22:87–100. https://adsabs.harvard.edu/full/1992LPSC...22...87S.

Smit J., Roep T. B., Alvarez W., Montanari A., Claeys P., Grajales-Nishimura J. M., and Bermudez J. 1996. Coarse-grained, clastic sandstone complex at the K/T boundary around the Gulf of Mexico : Deposition by tsunami waves induced by the Chicxulub impact? In *The Cretaceous-Tertiary Event and Other Catastrophes in Earth History*, edited by G. Ryder, D. E. Fastovsky, and S. Gartner. Geological Society of America Special Paper #307, Geological Society of America, Boulder, Colorado, pp. 151–182. https://doi.org/10.1130/0-8137-2307-8.151.

Soden B. J., Wetherald R. T., Stenchikov G. L., and Robock A. 2002. Global Cooling After the Eruption of Mount Pinatubo: A Test of Climate Feedback by Water Vapor. *Science* 296:727–730. https://doi.org/10.1126/science.296.5568.727.

Sprain C. J., Renne P. R., Clemens W. A., and Wilson G. P. 2018. Calibration of chron C29r: New high-precision geochronologic and paleomagnetic constraints from the Hell Creek region, Montana. *Geological Society of America Bulletin* 130:1615–1644. https://doi.org/10.1130/B31890.1.

Sprain C. J., Renne P. R., Vanderkluysen L., Pande K., Self S., and Mittal T. 2019. The eruptive tempo of Deccan volcanism in relation to the Cretaceous-Paleogene boundary. *Science* 363:866–870. https://doi.org/10.1126/science.aav1446.

Stöffler D., Artemieva N. A., Ivanov B. A., Hecht L., Kenkmann T., Schmitt R. T., Tagle R. A., and Wittmann A. 2004. Origin and emplacement of the impact formations at Chicxulub, Mexico, as revealed by the ICDP deep drilling Yaxcopoil-1 and by numerical modeling. *Meteoritics & Planetary Science* 39:1035–1067. https://doi.org/10.1111/j.1945-5100.2004.tb01128.x.

Swisher C. C., Grajales-Nishimura J. M., Montanari A., Margolis S. V., Claeys P., Alvarez W., Renne P., Cedillo-Pardoa E., Maurrasse F. J.-M. R., Curtis G. H., Smit J., and McWilliams M. O. 1992. Coeval ^{40}Ar/^{39}Ar ages of 65.0 million years ago from Chicxulub crater melt rock and Cretaceous-Tertiary boundary tektites. *Science* 257:954–958. https://doi.org/10.1126/science.257.5072.954.

Tagle R. and Hecht L. 2006. Geochemical identification of projectiles in impact rocks. *Meteoritics & Planetary Science* 41:1721–1735. https://doi.org/10.1111/j.1945-5100.2006.tb00448.x.

Tagle R., Erzinger J., Hecht L., Schmitt R. T., Stöffler D., and Claeys P. 2004. Platinum group elements in impactites of the ICDP Chicxulub drill core Yaxcopoil-1: Are there traces of the projectile? *Meteoritics & Planetary Science* 39:1009–1016. https://doi.org/10.1111/j.1945-5100.2004.tb00942.x.

Trinquier A., Birck J. L., and Allègre C. J. 2006. The nature of the KT impactor. A ^{54}Cr reappraisal. *Earth and Planetary Science Letters* 241:780–788. https://doi.org/10.1016/j.epsl.2005.11.006.

Tuchscherer M. G., Reimold W. U., Koeberl C., and Gibson R. L. 2004a. Major and trace element characteristics of impactites from the Yaxcopoil-1 borehole, Chicxulub structure, Mexico. *Meteoritics & Planetary Science* 39:955–978. https://doi.org/10.1111/j.1945-5100.2004.tb00939.x.

Tuchscherer M. G., Reimold W. U., Koeberl C., Gibson R. L., and de Bruin D. 2004b. First petrographic results on impactites from the Yaxcopoil-1 borehole, Chicxulub structure, Mexico. *Meteoritics & Planetary Science* 39:899–930. https://doi.org/10.1111/j.1945-5100.2004.tb00937.x.

Tuchscherer M. G., Reimold W. U., Koeberl C., and Gibson R. L. 2005. Geochemical and petrographic characteristics of impactites and Cretaceous target rocks from the Yaxcopoil-1 borehole, Chicxulub impact structure, Mexico: Implications for target composition. *Meteoritics & Planetary* Science 40:1513–1536. https://doi.org/10.1111/j.1945-5100.2005.tb00415.x.

Tuchscherer M. G., Reimold W. U., Gibson R. L., de Bruin D., and Späth A. 2006. Major and trace element compositions of melt particles and associated phases from the Yaxcopoil-1 drill core, Chicxulub impact structure, Mexico. *Meteoritics & Planetary Science* 41:1361–1379. https://doi.org/10.1111/j.1945-5100.2006.tb00527.x.

Urrutia-Fucugauchi J., Marin L., and Trejo-Garcia A. 1996. UNAM scientific drilling program of Chicxulub impact structure – Evidence for a 300 kilometer crater diameter. *Geophysical Research Letters* 23:1565–1568. https://doi.org/10.1029/96GL01566.

Urrutia-Fucugauchi J., Morgan J., Stöffler D., and Claeys P. 2004. The Chicxulub Scientific Drilling Project (CSDP). *Meteoritics & Planetary Science* 39:787–790. https://doi.org/10.1111/j.1945-5100.2004.tb00928.x.

Urrutia-Fucugauchi J., Chavez-Aguirre J. M., Pérez-Cruz L., and De la Rosa J. L. 2008. Impact ejecta and carbonate sequence in the eastern sector of the Chicxulub crater. *Comptes Rendus Geoscience* 340:801–810. https://doi.org/10.1016/j.crte.2008.09.001.

Urrutia-Fucugauchi J., Camargo-Zanoguera A., Pérez-Cruz L., and Pérez-Cruz G. 2011. The Chicxulub multi-ring impact crater, Yucatan carbonate platform, Gulf of Mexico. *Geofísica Internacional* 50:99–127. http://www.scielo.org.mx/scielo.php?script=sci_arttext&pid=S0016-71692011000100009.

Vellekoop J., Sluijs A., Smit J., Schouten S., Weijers J. W. H., Damsté J. S. S., and Brinkhuis H. 2014. Rapid short-term cooling following the Chicxulub impact at the Cretaceous-Paleogene boundary. *Proceedings of the National Academy of Sciences of the United States of America* 111:7537–7541. https://doi.org/10.1073/pnas.1319253111.

Ward W. C., Keller G., Stinnesbeck W., and Adatte T. 1995. Yucatán subsurface stratigraphy: Implications and constraints for the Chicxulub impact. *Geology* 23:873–876. https://doi.org/10.1130/0091-7613(1995)023<0873:YNSSIA>2.3.CO;2.

Warren P. H., Claeys P., and Cedillo-Pardo E. 1996. Mega-impact melt petrology (Chicxulub, Sudbury, and the Moon): Effects of scale and other factors on potential for fractional crystallization and development of cumulates. In *The Cretaceous-Tertiary Event and Other Catastrophes in Earth History*, edited by G. Ryder, D. E. Fastovsky, and S. Gartner. Geological Society of America Special Paper #307, Geological Society of America, Boulder, Colorado, pp. 105–124. https://doi.org/10.1130/0-8137-2307-8.105.

Weber B., Valencia V. A., Schaaf P., Pompa-Mera V., and Ruiz J. 2008. Significance of provenance ages from the Chiapas Massif Complex (Southeastern Mexico): Redefining the Paleozoic basement of the Maya Block and its evolution in a Peri-Gondwanan realm. *The Journal of Geology* 116: 619– 639. https://doi.org/10.1086/591994.

Weber B., Scherer E. E., Martens U. K., and Mezger K. 2012. Where did the lower Paleozoic rocks of Yucatan come from? A U-Pb, Lu–Hf, and Sm–Nd isotope study. *Chemical Geology* 312–313:1–17. https://doi.org/10.1016/j.chemgeo.2012.04.010.

Weber B., González-Guzmán R., Manjarrez-Juárez R., de León A. C., Martens U., Solari L., Hecht L., and Valencia V. 2018. Late Mesoproterozoic to Early Paleozoic history of metamorphic basement from the southeastern Chiapas Massif Complex, Mexico, and implications for the evolution of NW Gondwana. *Lithos* 300–301:177–199. https://doi.org/10.1016/j.lithos.2017.12.009.

Whalen M. T., Gulick S. P. S., Lowery C. M., Bralower T. J., Morgan J. V., Grice K., Schaefer B., Smit J., Ormö J., Wittmann A., Kring D. A., Lyons S., Goderis S., and IODP-ICDP Expedition 364 Scientists 2020. Winding down the Chicxulub impact: The transition between impact and normal marine sedimentation near ground zero. *Marine Geology* 430:106368. https://doi.org/10.1016/j.margeo.2020.106368.

White R. V. and Saunders A. D. 2005. Volcanism, impact and mass extinctions: incredible or credible coincidences? *Lithos* 79:299–316. https://doi.org/10.1016/j.lithos.2004.09.016.

Wittmann A., Kenkmann T., Schmitt R. T., Hecht L., and Stöffler D. 2004. Impact-related dike breccia lithologies in the ICDP drill core Yaxcopoil-1, Chicxulub impact structure, Mexico. *Meteoritics & Planetary Science* 39:931–954. https://doi.org/10.1111/j.1945-5100.2004.tb00938.x.

Wittmann A., Kenkmann T., Hecht L., and Stöffler D. 2007. Reconstruction of the Chicxulub ejecta plume form its deposits in drill core Yaxcopoil-1. *Geological Society of America Bulletin* 119:1151–1167. https://doi.org/10.1130/B26116.1.

Wolbach W. S., Lewis R. S., and Anders E. 1985. Cretaceous Extinctions: Evidence for Wildfires and Search for Meteoritic Material. *Science* 230:167–170. https://doi.org/10.1126/science.230.4722.167.

Zhao J., Xiao L., Gulick S. P. S., Morgan J. V., Kring D. A., Urrutia-Fucugauchi J., Schmieder M., de Graaff S. J., Wittmann A., Ross C. H., Claeys P., Pickersgill A., Kaskes P., Goderis S., Rasmussen C., Vajda V., Ferrière L., Feignon J.-G., Chenot E., Perez-Cruz L., Sato H., Yamaguchi K., and IODP-ICDP Expedition 364 Scientists 2020. Geochemistry, geochronology and petrogenesis of Maya Block granitoids and dykes from the Chicxulub impact crater, Gulf of Mexico: Implications for the assembly of Pangea. *Gondwana Research* 82:128–150. https://doi.org/10.1016/j.gr.2019.12.003.

Zürcher L. and Kring D. A. 2004. Hydrothermal alteration in the core of the Yaxcopoil-1 borehole, Chicxulub impact structure, Mexico. *Meteoritics & Planetary Science* 39:1199–1221. https://doi.org/10.1111/j.1945-5100.2004.tb01137.x.

CHAPTER 4: Methodology

The selected samples were investigated using a large variety of techniques, including methods for petrography (including optical microscopy, universal stage (U-stage), and scanning electron microscopy (SEM)), and also high precision methods for geochemical analysis (including X-ray fluorescence (XRF), elemental mapping using micro-X-ray fluorescence (µXRF), instrumental neutron activation analysis (INAA), and mass spectrometry). A review of the different analytical techniques used is provided in the following sections.

4.1. Samples

4.1.1. Sample selection

As presented in Chapter 3 (section on the IODP-ICDP Expedition 364 drilling), the investigated samples were obtained following the drilling of the Chicxulub impact structure peak ring in May 2016 (drilling site M0077A), offshore the Yucatán peninsula. Following the drilling, the core sections were scanned using 3D X-ray computed tomography at Weatherford Laboratories, in Houston, Texas (see chapter 2 of Morgan et al., 2017). Then, they were sent to the Bremen Core Repository (Germany), and were split (Fig. 4.1), scanned, and investigated for preliminary petrographic and geochemical documenting. Additionally, paleomagnetic measurement, and a variety of physical properties (e.g., density, porosity) were also obtained (Morgan et al., 2017). A total of 368 core samples, with masses ranging from ~20 to ~120 g, were selected (by Ludovic Ferrière and the other Expedition 364 scientists) during the Onshore Science Party at the Bremen Core Repository (between 21st September and 15th October 2016), and then were cut and mailed to the Natural History Museum Vienna (NHMV). The sample labeling used in this study is defined as Core#Section#_Top(cm)–Bottom(cm), and indicates the exact sampling interval as defined in Morgan et al. (2017), while the centimeters indicate the position of the core section from the top. The core and sections numbers increase with increasing depth within the core. Among the 368 samples available, 206 were selected to prepare polished thin sections, while 114 were powdered for geochemical investigations (101 samples having both polished thin section and powder available). Macrophotographs of all the samples were taken at the NHMV before any further preparation. The full list of selected and investigated samples is provided in Appendix A.

Figure 4.1. *Perspective macrophotograph of a split core (granite lithology) from the IODP-ICDP Expedition 364. Core sections similar to this one were further cut at selected intervals, and the obtained samples were sent to the NHMV for investigations. The core width is 86 mm. From Morgan et al. (2017).*

4.1.2. Sample preparation

Representative samples of the different lithologies occurring within the drill core, with masses ranging from ~20 to ~70 g, were selected and crushed in polyethylene wrappers, and then powdered in a clean agate bowl using a Retsch RS200 vibratory disc mill at the Department of Lithospheric Research, University of Vienna (Fig. 4.2). The powdered samples were then stored in clean, hermetically sealed, polyethylene vials, before being used for bulk geochemical investigations. Due to the relatively small size of the samples, half or quarter of cores (i.e., 83 mm in diameter), special care was taken to obtain representative compositions. As such, for suevite and impact melt rock lithologies, samples with large clasts, several centimeters in size, were excluded. Similarly, granite samples having porphyritic texture (with large K-feldspar minerals up to 7 cm in size), were excluded as their chemistry would be biased by K-feldspar accumulation rather than representing whole rock composition. The full geochemical results obtained by XRF, INAA, and mass spectrometry are presented in Appendices B, C, D, and E. Results of geochemical investigations are also presented and discussed in the publications in Chapters 6, 7, and Chapter 8.
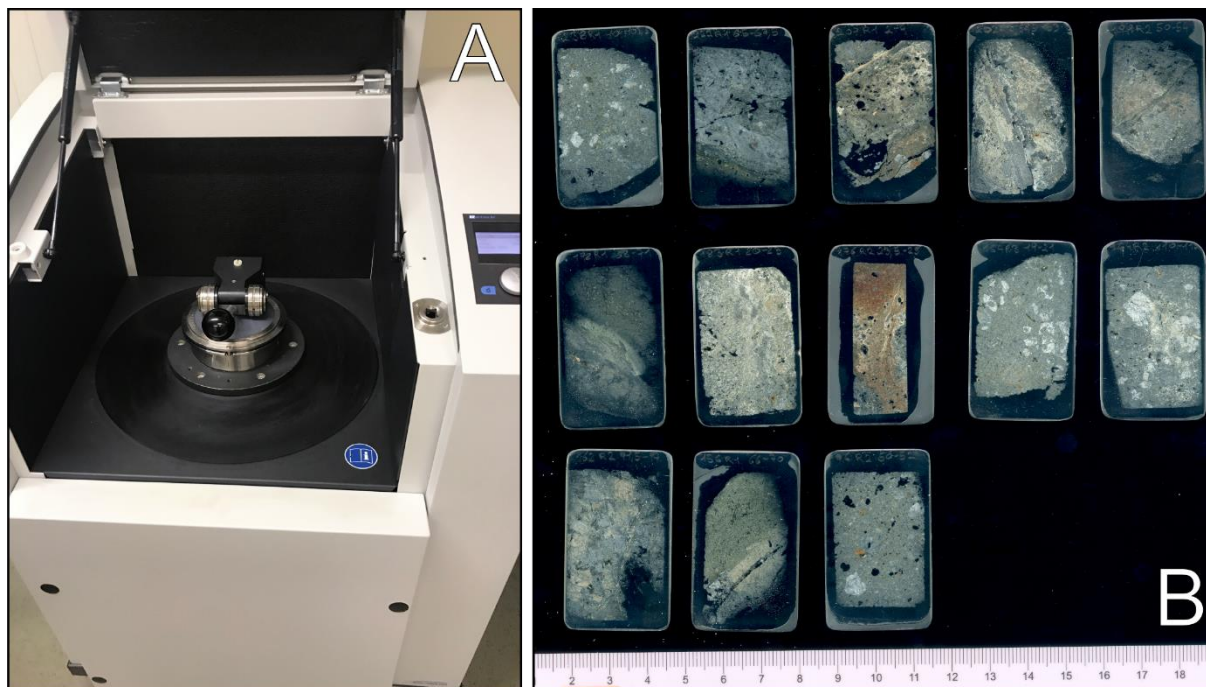
Figure 4.2. *A) Retsch RS200 vibratory disc mill at the Department of Lithospheric Research, University of Vienna, Austria, with the agate bowl mounted in it, ready for whole rock sample powdering. B) Scan of some polished thin sections from the IODP-ICDP Expedition 364 drill core. Scale in centimeters.*

For petrographic investigations (i.e., optical microscopy, universal stage, SEM, and µXRF), polished thin sections (and associated thick sections, i.e., the part left from thin section preparation, usually embedded in epoxy resin) were prepared at the NHMV and at the University of Vienna (Fig. 4.2). Detailed petrographic descriptions of the samples are reported in Appendix A.

4.2. Analytical methods

4.2.1. Optical microscope and universal stage (U-stage)

An optical microscope was used to observe the thin sections in both transmitted and reflected light. Modal compositions were obtained on several thin sections by image analysis using ImageJ software. Some thin sections were also selected for SEM and µXRF mapping.

Eleven thin sections from granite samples were selected for additional investigation using a U-stage mounted on a Leitz optical microscope at the Department of Lithospheric Research of the University of Vienna (Fig. 4.3; see publication Chapter 5; for details on the U-stage, see also, e.g., Reinhard, 1931; Emmons, 1943). The U-stage was used in order to determine the orientations of planar fractures (PFs) and planar deformation features (PDFs) in quartz grains (see also Chapter 2). It allows to describe and measure mineral grains in three dimensions (i.e., in the limit of the thickness, about 30 micrometers, of the thin section), and constitute a quick, and inexpensive method to investigate PF and PDF set orientations in a large number of quartz grains in a thin section, but it is also time-consuming to obtain statistically robust, significant, and precise results (see Ferrière et al. 2009; Holm-Alwmark et al. 2018).

Measurements of the crystallographic orientations of PFs and PDFs were made following the methods described in Stöffler and Langenhorst (1994), and Ferrière et al. (2009). The main steps for the use of the U-stage are described in the following sections, from the notes provided at the Department of Lithospheric Research (French, 2005; Ferrière, 2008). These thin sections were obtained from samples taken at regular intervals between 747.0 and 1334.7 mbsf, in the "lower peak ring" section, and selected due to their relative abundance in quartz grains (at least 20 grains per thin section). Also, the U-stage method allows to investigate only about 3/5 of a rectangular thin section, thus, the quartz grains should be preferentially located in the central part of the thin section. Finally, to obtain reliable statistics on the PDF orientations, at least 75 PDF sets were measured for each thin section (following recommendations by Ferrière et al., 2009).

4.2.1.1. Installation of the U-stage

The Leitz microscope is prepared for U-stage use with specific objectives of 10x and 30x magnifications, while the microscope stage is locked at 0°/360°. The U-stage is fixed by two screws onto the microscope stage with the outer horizontal stage at right (the large wheel on Fig. 4.3). Moreover, the outer vertical stage (Fig. 4.3) is locked with index 10°/10° by using the two screws located inside the outer horizontal stage.

Four components form the assembly U-stage, namely, from bottom to top (Fig. 4.3):
- The lower hemisphere (circular shape); index n = 1.554.
- The circular glass plate and inner disk.
- The thin section.
- The upper hemisphere (rectangular shape); index n = 1.554.
The index (or refractive index) of the lower and upper hemispheres is selected to match index of quartz (n = 1.554). Hemispheres with other index are available for U-stage investigation of minerals other than quartz (e.g., index n = 1.516 for K-feldspar).
The mounting of the assembly U-stage is made following these steps:
1) Add a drop of glycerin at the top of the lower hemisphere and put the circular glass plate on it.
2) Insert the attached assemblage into the inner disk and adjust.
3) Add a drop of glycerin on the glass plate and place the thin section (with top side up) on it.
4) Add a drop of glycerin and put the upper hemisphere on the thin section.
5) Lock carefully the assembly to the inner vertical (Fig. 4.3) stage using the two screws located on each side of the upper hemisphere.

4.2.1.2. Calibration of the U-stage

After the assemblage of the U-stage is completed, calibration is needed in order to minimize measurement errors. The calibration is made following these steps:
1) Center U-stage objectives.
2) Center U-stage on the microscope stage using the two screws located at the base of the U-stage (see Fig. 4.3). Following stages 1) and 2), when rotating the inner vertical stage and looking at the microscope, the thin section should turn around the center of the crosshairs

without deviating. The best way to check for centering is to select a small mineral grain on the thin section, and move it at the center of crosshairs, rotate the inner stage, and adjust the centering if necessary.

3) Adjust the vertical elevation of the stage using the rotating ring in the inner disk. When tilting the inner horizontal stage, the thin section should move around an axis (if not, the movement would be like "a rocking boat"). After the calibration is done, the measurements can begin.

4.2.1.3. Measurement of the c-axis orientation in quartz grains

In order to obtain the best possible measurements, the 30x magnification objective is used. It is recommended to start the search for shocked quartz grains at one corner of the thin section area available for measurement. At first, it is necessary to measure the c-axis orientation of the selected shocked quartz grain following this procedure:

1) Move the thin section until the selected shocked quartz grain is under crosshairs.

2) Check that all settings are set to 0°.

3) Turn the inner vertical stage until extinction of the grain. In the case of any quartz grain that shows undulose extinction (due to a change in c-axis orientation within the grain), it is important to measure the c-axis related to the PDF that will be measured. Two orientations of extinction are possible: N-S or E-W. For PDF orientation measurement, the c-axis should be oriented E-W.

4) Check the c-axis orientation using the gypsum plate (Fig. 4.3). With the grain at extinction, rotate the microscope stage clockwise ~30°. Then, insert the gypsum plate; in case the grain becomes gray/yellow, the orientation is correct (E-W orientation). Otherwise, if the grain becomes blue/green, the orientation is not correct (N-S orientation), and the inner vertical stage should be rotated until the next extinction.

5) Remove the gypsum plate and put back the microscope stage to initial (0°/360°) position.

6) Rotate the outer horizontal stage (Fig. 4.3) ~20–40° until the grain comes out of extinction and as bright as possible.

7) Rotate the inner horizontal stage (Fig. 4.3) until the quartz grain is again at extinction, or at the maximum extinction position.

8) Make a final check by rotating again the outer horizontal stage before putting it back to 0°.

9) Check if the c-axis is horizontal or vertical by rotating clockwise the microscope stage ~45°. If the grain goes out of extinction, the c-axis is horizontal (most of the cases), whereas, if the grain remains extinct, the c-axis is vertical (rare).

10) Record the c-axis orientation (azimuth and inclination). In the case of a vertical c-axis, it is necessary to "subtract" 90° from the inclination, and to correct the azimuth by 180° (the easiest way is to change W to E (or E to W), and to "subtract" 90° from the inclination. As an example, a vertical c-axis with a measured azimuth/inclination of 240°/15°E is corrected to 60°/75°E.

11) Repeat the c-axis measurement by rotating the inner vertical stage 180°. This was done in the investigated samples in order to prevent measurement errors, and due to the common undulose extinction of the shocked quartz grains in Chicxulub granites. For some c-axis orientations, a difference of 2–3° was common between the first and the second measurement (see details in the publication in Chapter 5, Feignon et al., 2020).
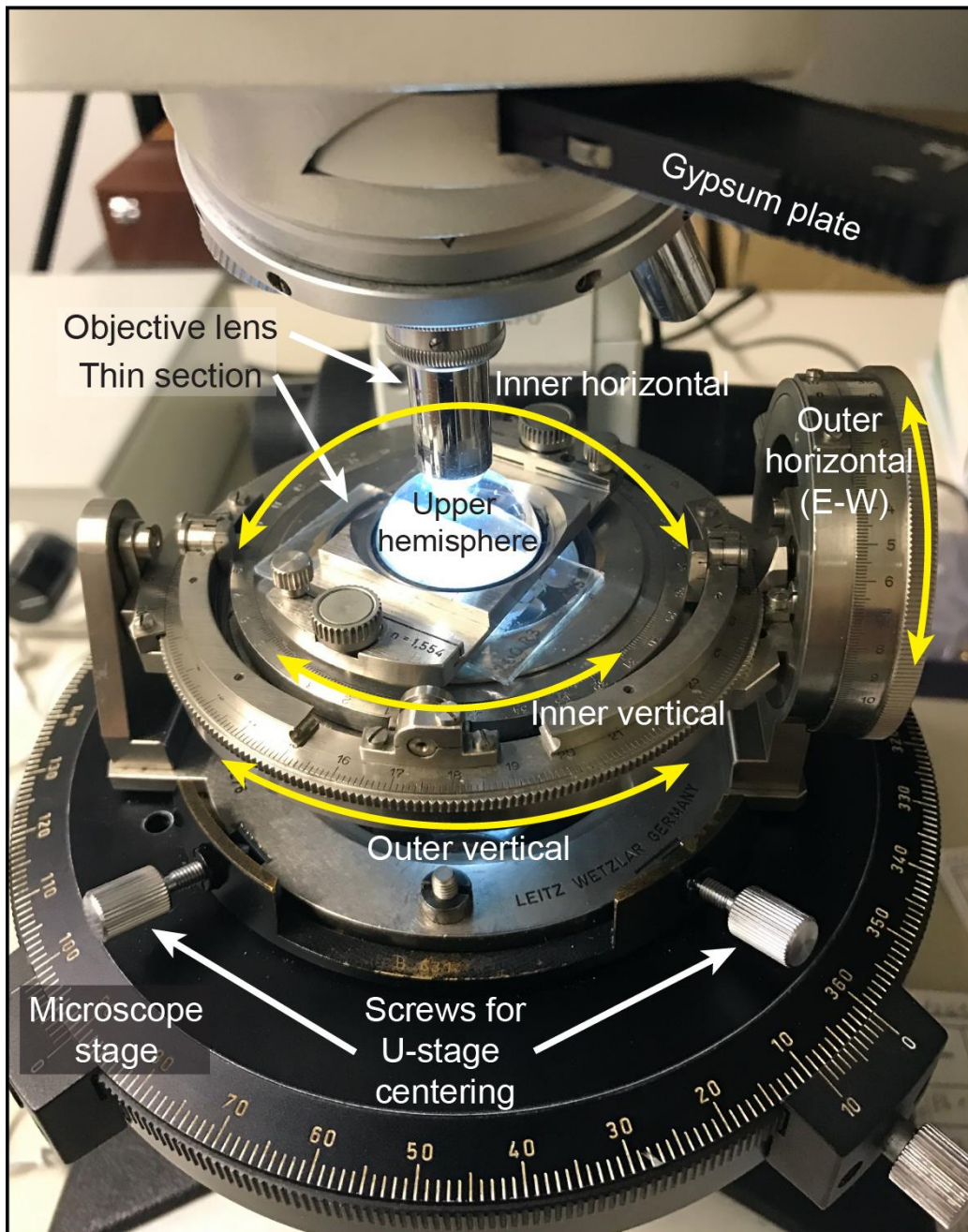
Figure 4.3. *Photograph of the four axis universal stage mounted on the Leitz optical microscope at the Department of Lithospheric Research (University of Vienna), showing the different components.*

4.2.1.4. Measurement of the PDF sets orientations in quartz grains

After the c-axis orientation measurements are done, the orientations of PDF sets can be determined following these steps (the procedure is similar for PF orientation measurements):
1) Rotate the inner vertical stage until the selected PDF set is oriented parallel to N-S crosshairs.
2) Tilt the inner horizontal stage until the PDF set appears at maximum sharpness. For better visibility, both plane- and cross-polarized light can be used.
3) Record the PDF orientation (azimuth and inclination).

4) Repeat the measurement by rotating 180° the inner vertical stage. As for the c-axis measurements, this step was done in the investigated samples to prevent measurement errors, resulting, in some cases, in a difference of up to 2–3° between the two measurements of a PDF set orientation.

5) Move to the next PDF set to measure (if present) in the shocked quartz grain.

4.2.1.5. Plotting of measurements and indexing of PF and PDF sets orientations

When the measurements of the c-axis and of the poles perpendicular to planes of all PFs and PDFs are completed, data are plotted on a stereographic Wulff net. Finally, the planes measured are indexed using the updated stereographic projection template (USPT; see Fig. 4.4) of Ferrière et al. (2009). The USPT allows the indexing of fifteen typical PDF crystallographic orientations in quartz, within a 5° envelop of measurement error (e.g., Engelhardt and Bertsch, 1969; Stöffler and Langenhorst, 1994; Ferrière et al., 2009). The 2–3° c-axis and PDF orientations measurement error recorded in some grains (see sections 4.2.1.3 and 4.2.1.4) induce a slightly higher error than the previously stated 5°. When a set of PDF (or PF) does not plot inside the envelope of typical PDF orientations provided by the USPT, the set is considered as unindexed.

The measurements were indexed using both manual and automated methods, the latter using the web-based indexing program (WIP; Losiak et al., 2016). At first, manual indexing was done, which was followed by the automated indexing using WIP in order to verify the results obtained with the manual indexing method and check the reliability of the automated indexing. For example, the manual indexing allows to correct the artificially higher proportion of $\{10\bar{1}4\}$ orientations found using WIP due to the program failing to consider $\{10\bar{1}4\}$ as a minor orientation, subordinate to the $\{10\bar{1}3\}$ orientation. If the pole perpendicular to PDF plane plots in the overlapping area between $\{10\bar{1}4\}$ and $\{10\bar{1}3\}$ orientations, the orientation is recorded as $\{10\bar{1}3\}$ orientation (Ferrière et al., 2009; Holm-Alwmark et al., 2018). Additionally, in the case of quartz grains displaying strong undulose extinction, the c-axis has to be measured in several areas of the grain, and only the manual indexing allows to index the PDFs relative to each other, whereas each measurement has to be considered as a separate grain in WIP.

The results are then compiled to establish statistics in order to show the frequency of a given PDF orientation in a thin section, and the average number of PDF set(s) per grain. The calculated frequencies presented in the publication Chapter 5 (Feignon et al., 2020) are absolute frequencies, as described by Engelhardt and Bertsch (1969). They are calculated as the number of symmetrically equivalent planes measured in *n* quartz grains, divided by the total number of measured PDF sets in *n* quartz grains.

Plane	Pole angle to c-axis				
1 (0001) 0.00°	**6 {11$\bar{2}$2}** 47.73°	**11 {22$\bar{4}$1}** 77.20°
2 {10$\bar{1}$3} 22.95°	**7 {11$\bar{2}$1}** 65.56°	**12 {31$\bar{4}$1}** 77.91°
3 {10$\bar{1}$2} 32.42°	**8 {21$\bar{3}$1}** 73.71°	**13 {40$\bar{4}$1}** 78.87°
4 {10$\bar{1}$1} 51.79°	**9 {51$\bar{6}$1}** 82.07°	**14 {51$\bar{6}$0}** 90.00°
5 {10$\bar{1}$0} 90.00°	**10 {11$\bar{2}$0}** 90.00°	**a {10$\bar{1}$4}** 17.62°
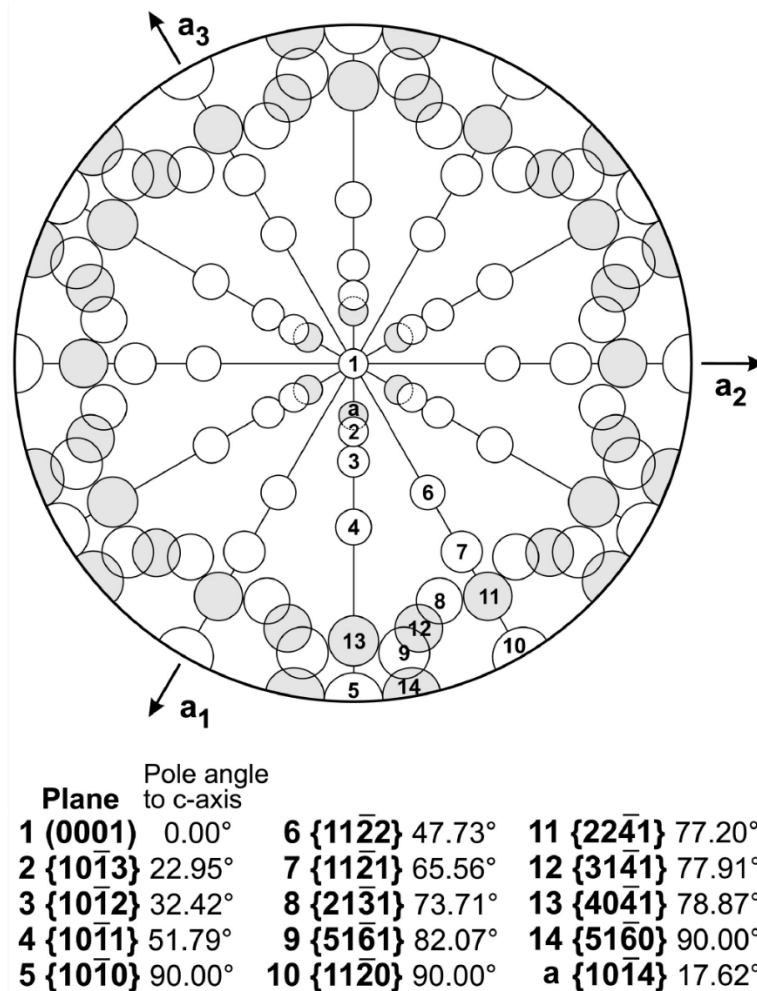
Figure 4.4. *Updated stereographic projection template (USPT), from Ferrière et al. (2009), which is used for the investigation of shock features in quartz grains. The c-axis is plotted in the center, and each circle (5° radius) shows the position of the most common poles to PDF planes.*

4.2.1.6. Shock pressure assignation

Following the indexing of PF and PDF sets, the shock pressure experienced by a sample can be estimated. Experimental works on quartz have shown that specific orientations of PDFs in quartz form at different shock pressures (e.g., Hörz, 1968; Müller and Défourneaux, 1968; Huffman and Reimold, 1996). Several studies have then derived average shock pressures for a given sample, using a classification of each quartz grain depending on the measured PDF orientations (e.g., Grieve and Robertson, 1976; Feldman, 1992; Fel'dman et al., 1996; Dressler et al., 1998; Ferrière et al., 2008; Rae et al., 2017; Holm-Alwmark et al., 2018). A specific shock pressure is assigned to each quartz grain; then a mean value is calculated, giving an average shock pressure for the sample.

The method described in Holm-Alwmark et al. (2018) was used in this study to estimate shock pressures in a given sample, as it is adapted for non-porous crystalline rocks. Shocked quartz grains were classified in six different categories, i.e., from quartz grains with no PDFs to type D. Quartz grains with no PDFs were assigned a shock pressure of 5 GPa, corresponding

to the mean pressure between the onset of shatter cones (2 GPa; e.g., French, 1998) and the formation of type A quartz grains. Type A quartz grains contain exclusively basal PDFs (parallel to [0001]), and were assigned a shock pressure of 7.5 GPa. Type B grains contain PDFs that are parallel to one or more $\{10\bar{1}3\}$- or $\{10\bar{1}4\}$-equivalent plane(s), and were assigned a shock pressure of 15 GPa. Type B2 grains contain three or more PDFs oriented parallel to $\{10\bar{1}3\}$- and $\{10\bar{1}4\}$-equivalent planes, and were assigned a shock pressure of 16.5 GPa. Type C grains contain PDFs with high index orientation(s), such as $\{11\bar{2}2\}$ and/or $\{22\bar{4}1\}$, and were assigned a shock pressure of 17 GPa. Type D quartz grains contain PDFs parallel to one or more $\{10\bar{1}2\}$-equivalent orientation(s), and have a corresponding shock pressure of 20 GPa. Feldman (1992) added an additional type (type E), corresponding to quartz grains transformed into diaplectic glass. However, no type E grains were identified in any of the here investigated samples.

4.2.2. Scanning electron microscopy (SEM)

Scanning electron microscopy (SEM) is a routine technique that uses a beam of high-energy electron bombarding the surface of the sample, resulting in an electron image. High magnification images, particularly secondary electron (SE) and back-scattered electron (BSE) images, are typically acquired using this method. Semi-quantitative chemical analysis can also be obtained using a SEM equipped with an X-ray analyzer. The main components of a SEM consist, from top to bottom, of an electron gun, a column (composed of condenser lenses, scanning foils, and objective lens) to focus the electron beam, a sample chamber, and a X-ray analyzer (see Fig. 4.5). Detailed information on SEM can be found in, e.g., Potts (1987), Potts et al. (1995), Gill (1997), Watt (1997); these references, as well as the review by Ferrière (2008) were used for the preparation of the following summary.

4.2.2.1. Principle

The electron beam is emitted from an electron source (i.e., either a tungsten filament [as illustrated on Fig. 4.5.], a LaB_6 / CeB_6 crystal, or a field emission gun) located at the top of the column. The kinetic energy of the electron beam is typically within the range of 10–30 keV. The electron beam emerges from an anode (which has a positive charge), passes through condenser lenses (that focus the beam), pairs of scanning coils (used to deflect the beam over the sample surface), and an objective lens (controlling the focus). Finally, the electron beam interacts with the sample (Fig. 4.5). The interaction volume, which has a hemispherical or elliptical shape, is determined by the kinetic energy of the electron beam, the atomic number, and the density of the sample. The electrons interact with the sample by elastic and inelastic scattering, i.e., a part of the incident electrons is absorbed, whereas others are scattered. As a result, radiation such as X-rays, cathodoluminescence, Auger electrons, secondary electrons, and backscattered electrons are created (Fig. 4.5). To distinguish between SE, BSE, and diffracted back-scattered electrons, several detectors are used.

Secondary electrons (SE) are low energy electrons ($< 50eV$) produced by inelastic interaction and ejected in an ionized state from the k-orbitals of the surface sample atoms. These

electrons are used to produce SE images, giving details mainly on the sample surface and topography. The contrast is given by, e.g., topographic irregularities, and/or roughness of the sample surface. The images are digitally captured and displayed on a computer monitor.
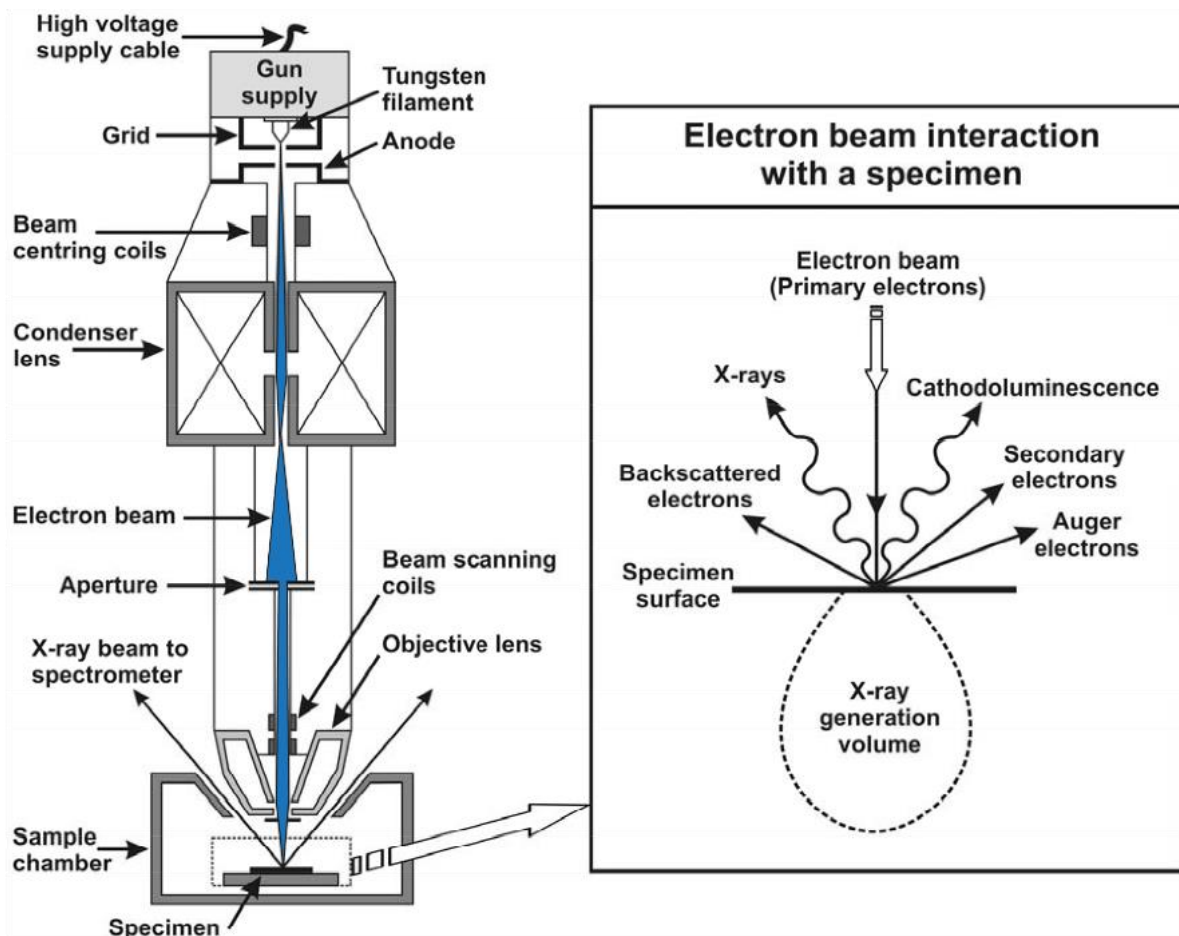
Figure 4.5. *Schematic cross section of a typical electron column of a scanning electron microscope (modified from Potts, 1987). On the right side are represented the different photons and particles emitted following the interaction of the incident electron beam with the specimen surface (modified from Watt, 1997).*

Back-scattered electrons are produced following elastic interaction of the electron beam with the sample. The amount of BSE increases with the mean atomic number (Z) of the sample, and, thus, information on the sample composition, and the distribution of the different elements within the sample is provided by BSE images. On BSE images, areas where mean atomic number is high will be bright, while where the mean atomic number is low, the areas will be dark. As the backscattering of electrons is also influenced by the sample topography, polished (thin or thick) sections are usually used.

Additionally, the interaction between the electron beam and the sample produces characteristic X-rays, having wavelengths and energies specific to the elements from which they are emitted. These X-rays can be used to analyze the sample's chemical composition. The

chemical composition is determined by comparing the intensities of the X-rays emitted by the sample to the intensities of reference standard materials. An X-ray analyzer selects and counts specific wavelengths of X-rays. To distinguish the different components of the X-ray spectrum, two types of X-ray analyzers are generally used, either based on photon energy (energy dispersive X-ray spectrometer; EDS) or by separating wavelengths (wavelength dispersive spectrometer; WDS). These spectrometers have advantages and disadvantages, as well as differences in resolution and efficiency.

The EDS detector is made up of a solid-state semi-conductor that electronically sorts and measures X-rays based on their energies. Its main function is to obtain qualitative data, as the EDS provides full spectra very quickly. However, the sensitivity of EDS detector is insufficient to reveal X-ray peaks from elements present in low concentrations (generally <0.1–0.5 wt.%), as the energy dispersive element peaks are broader than those obtained with a WDS. The WDS sorts X-rays based on their wavelengths using Bragg diffraction. Only one wavelength of the incoming X-rays is selected and reaches the detector, allowing better measurement accuracy than for EDS. The detection limit is also better when using WDS than with EDS.

4.2.2.2. Scanning electron microscope investigations

The polished thin sections selected for SEM investigations were at first carbon-coated. Then, they were examined on a JEOL JSM-6610 variable pressure (VP) or low-vacuum (LV) SEM at the Natural History Museum Vienna, Austria (Fig. 4.6). The electron source is a tungsten cathode. The LV mode allows to realize high resolution imaging and chemical analysis of uncoated samples. The SEM is equipped with several detectors, i.e., a BRUKER EDS, a BRUKER EBSD unit, and a GATAN cathodoluminescence system MonoCL4. The resolution is 3 nm (high vacuum mode), and the magnification range from x5 to x300,000. The thin sections were examined in SE and BSE modes, at a working distance of about 15 mm. Semi-quantitative chemical analyses were performed for the identification and to obtain the composition of some minerals. The analyses were done using the BRUKER EDS. A 15 kV accelerating voltage was used during investigations, as well as a ~1.2 nA beam current. The EDS results were automatically normalized to 100 wt.%. For EDS analysis, the detection limits are ~0.1–0.2 wt.%, depending on the element, while the associated measurement error is generally <10 rel.%.

Figure 4.6. *The JEOL JSM-6610 LV at the Natural History Museum Vienna, Austria.*

4.2.3. X-Ray fluorescence (XRF) spectrometry

The X-ray fluorescence spectrometry is a common technique used in Earth Sciences to determine the bulk chemical composition of geological material. The high accuracy and reproducibility of this technique allow to determine the bulk concentrations of major and minor elements, as well as of some trace elements, of a given sample. Detailed information on XRF spectrometry is provided in the reviews of, e.g., Potts (1987), Gill (1997), Ferrière (2008), which were used for preparation of the following summary. More details on the XRF measurements and instrumentation at the Department of Lithospheric Research (University of Vienna, Austria) can be found in Nagl and Mader (2019) and Duboc et al. (2019).
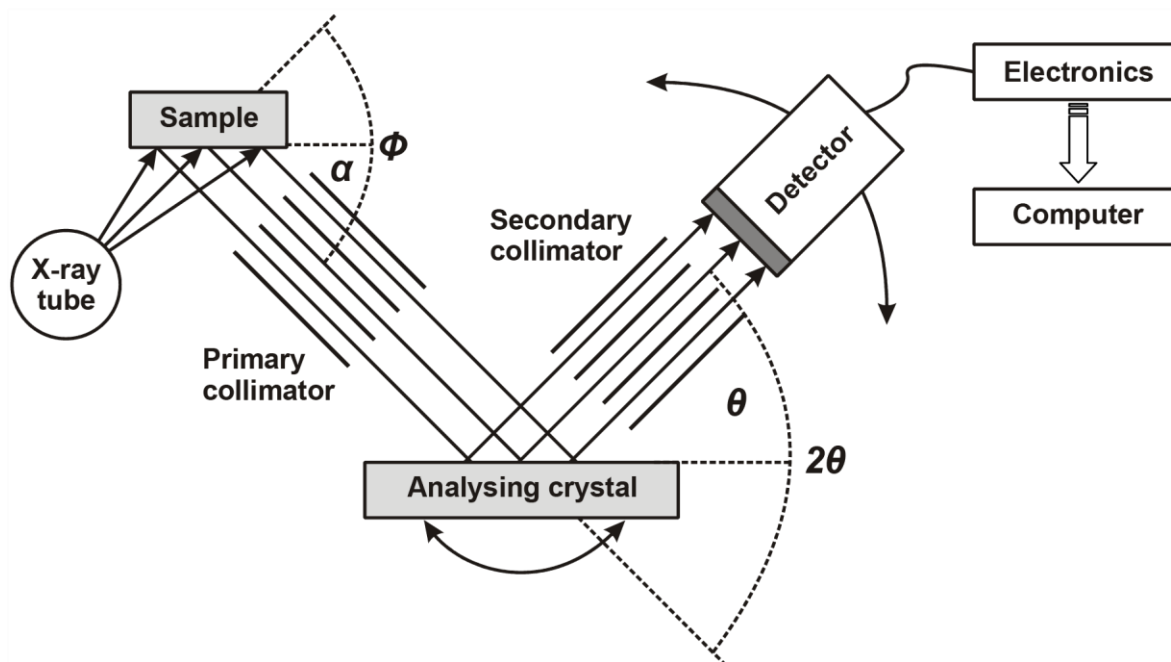
Figure 4.7. *Schematic diagram of a typical XRF spectrometer (from Gill, 1997).*

4.2.3.1. Principle

The XRF technique is based on the excitation of the atoms contained in a sample. An XRF spectrometer is composed of an X-ray tube (source of the primary X-ray), a sample holder, a primary collimator (which parallelizes the emitted photons), an analyzing crystal, a second collimator, and a detector (see Fig. 4.7). The high-energy X-ray photons produced by the X-ray tube irradiate the atoms of the sample. The X-rays hit the inner shell electrons (at the strongest bound electron orbitals), near of the atom nucleus, and these electrons are ejected. The open positions are then filled by an electron from the outer shell (to restore the atoms to a more stable state), resulting in the emission of secondary X-rays (also known as fluorescent X-rays, or fluorescence radiation). The energy of the secondary X-rays is equal to the energy difference between the two electron shells, and, because each element has a unique set of energy levels, the secondary X-rays produced have a unique set of energies. Therefore, it is possible to identify which element is present in the sample. The fluorescent X-rays are then collimated to form a

parallel beam before being spectrally divided using a synthetic analyzing crystal. Then, the diffracted X-rays pass through a secondary collimator, before reaching, as a parallel beam, a detector (Fig. 4.7). The detector and the secondary detector can move around the rotation axis of the analyzing crystal (i.e., Rowland circle). This mechanism, allowing the measurement of the rotation angle, is called a goniometer. Only secondary X-rays which have a wavelength (λ) satisfying the Bragg equation ($n\lambda = 2d \sin\theta$) are reflected from the analyzing crystal into the detector. In the Bragg equation, n is an integer, d is the lattice spacing of the analyzing crystal, and θ is the Bragg angle. This process handles each X-ray one by one, but with a very high speed. Current XRF spectrometer detectors can handle one million counts per second, resulting in a quasi-simultaneous measurement. The longer the measurement time is, the better the statistics are, providing improved precision, peak-to-background, and detection limits. Thus, to obtain a highly precise analysis of an element present in a given sample, a few million counts should be collected. Finally, the quantification of a given major or trace element is made by comparing the wavelength and intensities of the emitted X-rays with standard reference materials (see section 4.2.3.3).

4.2.3.2. Sample preparation for XRF analysis

For XRF analysis, the powdered samples were prepared in two different forms: (1) as glass beads for major element analysis (contents generally >0.1 wt.%), and (2) as pressed powder pellets for trace element analysis (see Fig. 4.8). The samples were prepared at the Department of Lithospheric Research at the University of Vienna, Austria. Approximately 15 g of sample powder are required for the whole XRF analysis.
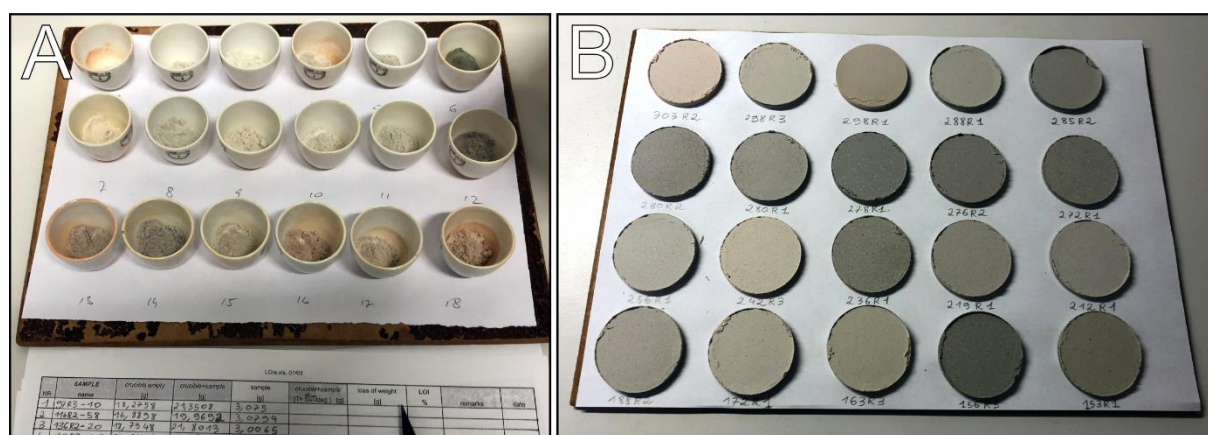
Figure 4.8. *Preparation of powdered samples for bulk XRF analysis. A) Porcelain crucibles filled with sample powders after being weighed and before being placed in an oven for drying. The powders will be used to prepare glass beads in order to measure bulk XRF major element abundances. B) Pressed powder pellets that will be used for bulk XRF trace element abundances analysis.*

Before preparing the glass bead, the loss on ignition (LOI) of the sample, expressed in weight-percent, was determined. The LOI corresponds to the mass loss experienced by a sample after it was heated at a specified high temperature. This mass loss is due to the escape of volatile

components (e.g., H_2O, organic content) from the sample. A clean porcelain crucible was heated at 1050 °C for at least three hours and then cooled to room temperature in a desiccator. The empty crucible was weighed and the balance was tared. Approximately 3 g of rock powder were added into the crucible and the rock powder weight was recorded. The rock powder was dried overnight in an oven at 110 °C, and weighed again, providing the loss on drying (LOD), which corresponds to the sample mass loss following the drying. Afterwards, the crucible (with the sample powder in it) was placed into a muffle furnace and ignited at 850 °C for three hours. Then, the furnace temperature was progressively decreased, and the sample was stored in an oven at a temperature of 110 °C until the weighing could take place. After taking out the crucible out of the oven, it was cooled for >30 minutes in a desiccator, and weighed one last time. In the case of rock samples containing a significant amount of carbonates (e.g., suevite samples from the M0077A drill core), a second heating was performed, at 1050 °C for three hours, before the sample being weighed again. The LOI was calculated using the following equation, where *M* is the mass in grams:

$$LOI = \frac{\left[\left(M_{pre-ignited}^{crucible+sample} - M_{ignited}^{crucible+sample}\right) \times 100\right]}{M^{sample}}$$

Of the investigated lithologies, the suevite and some impact melt rock samples show a high LOI (>10% and up to 24%). In this case, the major element data were recalculated on a LOI-free basis, in order to better identify impact melt rock and suevite components (see publication in Chapter 7, Feignon et al., 2022; and Chapter 8).

For the glass beads (also termed as fused beads) preparation, 0.8 g of the previously calcined sample powder (see previous section on LOI), were weighed into a small porcelain mould. Then, 8.0 g of dehydrated di-lithium tetraborate and di-lithium metaborate (Fluxana FX-X65-2) mixture (2:1 ratio) were added. Both powders were homogenized within the porcelain mould using a thin glass rod. Then, the mixture was put into a platinum crucible. The crucible and the casting dish (a 40-mm diameter mould) is composed of an 95% platinum and 5% gold alloy, permitting the complete detachment of the melt or glass bead from the crucible, and from the mould. The fused bead was done automatically using a fusion furnace PANalytical EAGON 2, designed to produce fused beads for XRF spectrometry analysis. The heating, casting, and cooling cycle of the sample are controlled by the microprocessor of the furnace. Finally, the platinum crucible and casting dish were cleaned by immersion in hot, diluted citric acid, while glass and porcelain tools were cleaned with acetone.

The pressed powder pellets were prepared by adding 0.5 mL of an aqueous polyvinyl alcohol solution (MERCK Mowiol) to approximately 10 g of non-ignited rock powder. The mixing was done in a 100 mL glass beaker by manual stirring with a glass rod for ~10 minutes. The mixture was then placed into a hydraulic press tool with of 40 mm in diameter. Before inserting a steel die, the powder was smoothed and gently tapped down using a glass rod with a flat tip. The pressure applied was ~16 tons per square centimeter during few minutes. The pressed powder pellet was then produced, being strong enough to resist sample handling, rotation, and vacuum in the XRF spectrometer during the measurement. The pellet was also dried overnight in an oven at 70 °C. All tools were cleaned using acetone.

4.2.3.3. X-ray fluorescence analysis

The XRF analyses were performed using a sequential PHILIPS PW2404 X-ray spectrometer at the Department of Lithospheric Research of the University of Vienna (Austria), using a super-sharp end-window X-ray tube with a Rh-anode. Several analyzing crystals (LiF200, LiF220, PE002, Ge111, polysynthetic monochromator PX1), collimators (coarse 550 µm, fine 150 µm), filters (750 µm and 200 µm Al, 400 µm, 100 µm brass), and channel masks are available, and used in order to get optimal analytical conditions. The element analysis conditions are fully software controlled. The accompanying software is PANalytical "SuperQ" version 5.1B (5.2822.3) with the options "Pro-Trace" and "Omnian".

Analysis of the fused beads provided the contents of major element oxides (SiO_2, TiO_2, Al_2O_3, Fe_2O_3, MnO, MgO, CaO, Na_2O, K_2O, and P_2O_5), given in wt.%. A calibration curve for each element was established using the intensities of geologic international reference materials, i.e., SG1-A (granite), TDB-1 (diabase), BHVO-2 (ocean island basalt), and JH-1 (hornblendite). Inter-element effects, such as enhancement and absorption, tend to alter the linearity of the calibration curve. These effects are called "matrix effects", and were corrected by applying a matrix correction model in the SuperQ software. The major element oxide contents were recalculated afterwards, using the MAJORS program (Petrakakis and Nagl, 1993), taking into account the LOI, in order to obtain the "raw" major element contents. Accuracy and precision values (in wt.%) are about 0.6 for SiO_2, 0.5 for Fe_2O_3, 0.3 for Al_2O_3, 0.2 for Na_2O, 0.05 for CaO, 0.04 for MgO, 0.02 for TiO_2, K_2O, and P_2O_5, and 0.01 for MnO.

The trace element contents were determined on the pressed powder pellets using the "ProTrace" module of SuperQ software, using, e.g., intensities at peak and background positions, which were measured on blank specimens for interpolating background intensity at the peak position; prepared interference standards for calculation of spectral overlap factors on net peak intensities; overlap corrections for tube lines; correction of "matrix effects" mainly due to absorption using mass absorption coefficients (see details in Nisbet et al., 1979). Thus, the use of ProTrace allows to produce accurate trace element data even at low concentrations in geological samples. The international reference material used for bulk XRF trace element concentration calibration was GSR 1–6 (Xie et al., 1989). The following trace element contents were measured using bulk XRF analysis: As, Ba, Ce, Co, Cr, Cu, Ga, La, Mo, Nb, Nd, Ni, Pb, Rb, Sc, Sn, Sr, Ta, Th, U, V, W, Y, Zn, and Zr (concentrations of underlined elements were preferentially used in the following chapters because they are not measured by instrumental neutron activation analysis (INAA), or because their precisions and accuracies are better than for the INAA data).

To prevent instrumental drift during both major and trace element analysis, the samples were measured in groups and the count rates were ratioed to monitor samples. Also, a batch of so-called in-house (or quality) control samples was measured together with each group. Table 4.1 provides typical example of replicate analysis precision values on in-house control samples (mafic and felsic, see also Nagl and Mader, 2019).

Table 4.1. *Example of precision values for mafic (basalt) and felsic (gneiss) in-house control sample replicate analysis performed at the Department of Lithospheric Research, University of Vienna, Austria. Standard deviation is given in wt.% for major elements and in ppm for trace elements. rel.%: relative %; n.d.: not determined. Data from Nagl and Mader (2019).*

Element	Basalt BAS1 (n=14)		Gneiss ZGN1 (n=10)	
	Standard deviation	rel.%	Standard deviation	rel.%
[wt.%]				
SiO_2	0.17	0.4	0.43	0.6
TiO_2	0.01	0.5	0.01	3.0
Al_2O_3	0.06	0.4	0.09	0.6
Fe_2O_3	0.02	0.2	0.03	1.4
MnO	0.003	1.9	n.d.	n.d.
MgO	0.03	0.3	0.03	2.4
CaO	0.03	0.3	0.01	0.5
Na_2O	0.02	0.5	0.05	1.2
K_2O	0.01	0.7	0.05	1.4
P_2O_5	0.004	0.6	0.01	6.7
[ppm]				
Sc	1.2	21	0.8	28
V	1.3	0.6	1.0	3.2
Cr	4.4	3.4	1.2	8.1
Co	1.0	2.5	0.4	5.6
Ni	1.8	1.4	0.4	10
Cu	1.0	2.1	0.5	7.0
Zn	0.7	0.9	1.0	2.5
Ga	0.3	1.5	0.2	1.1
As	1.1	31	1.0	77
Rb	0.5	0.7	2.2	1.4
Sr	4.1	0.4	2.2	0.5
Y	0.2	0.8	0.4	2.6
Zr	1.1	0.4	4.1	2.7
Nb	0.5	0.5	0.3	1.8
Mo	0.2	6.5	1.0	100
Sn	0.9	11	0.6	6.3
Ba	9.2	0.8	19	2.5
La	3.3	4.3	2.8	8.9
Ce	5.2	4.4	3.9	7.2
Nd	3.7	7.9	2.8	14
Hf	0.7	23.3	0.9	41
Ta	0.8	16	0.4	36
W	1.2	40	0.3	1.2
Pb	0.6	16	0.6	2.1
Th	0.5	4.2	1.3	5.8
U	0.5	7.2	0.8	7.0

4.2.4. *Micro-X-Ray fluorescence (µXRF) analysis*

4.2.4.1. General principle

As indicated by its name, the micro-X-ray fluorescence (µXRF) technique uses a similar principle as XRF (see section 4.2.3). The sample atoms are excited after interaction with an X-ray beam, resulting in fluorescence allowing the characterization of element abundances in the sample (Norris and Chappell, 1967). However, the µXRF technique combines both the advantages of the spectral resolution offered by a high-energy X-ray source, and of an automated microscope-guided high precision movable stage system. This allows to perform fast, non-destructive, and high resolution (25 µm) elemental analysis (Beckhoff et al., 2006; Gauglitz and Moore, 2014). The µXRF apparatus (see Fig. 4.9) is typically composed of an X-ray source composed of rhodium or tungsten. The produced X-ray beam is focused using a polycapillary lens, in order to reach the small spot size needed for high-resolution measurements. The X-ray beam is focused with a minimal energy loss, producing well-resolved X-ray spectra of small surfaces of the sample. The moving stage with the sample on top is able to make displacement in the *xyz* directions, allowing to produce either spot analysis, line scans, or two-dimensional chemical maps of the sample surface. Spot (spot size of 25 or 200 µm) and line scan analysis (generally densely spaced spot analysis) are useful for in-depth characterization, and quantification of micrometer- to millimeter-sized chemical changes within an homogeneous phase. However, these analysis necessitate a long measurement time (60–300 s) to obtain an accurate and representative spectrum (de Winter and Claeys, 2017), and are not adapted for geochemical characterization of large, heterogeneous (and possibly unknown) samples, such as the Chicxulub peak ring suevites and impact melt rocks (see publication in Chapter 7, Feignon et al., 2022; Chapter 8). The µXRF chemical mapping can cover areas significantly larger than those investigated by spot and line analysis, with a very short integration time. The large dimension of the vacuum chamber of the µXRF device offers the possibility to analyze sample surfaces with a size up to 19 x16 cm. For example, up to 14 thin/thick sections can be analyzed in a single measuring session. The resulting µXRF chemical maps can either be qualitative, showing the distribution of different elements, or semi-quantitative, using a color scale related to the intensities (number of counts) of the peaks recorded for a given element, providing a first idea of the chemical composition of the sample. In contrast to methods like SEM, where carbon coating of the section is necessary, or like XRF where bulk chemical analysis is done on powdered samples, the µXRF analysis is non-destructive (however, the sample should be rather flat and, thus, cut (/polished) surfaces are preferred), and no sample coating is necessary. More details on the µXRF instrument, analysis, and applications can be found in the publications by, e.g., de Winter and Claeys (2017) and Kaskes et al. (2021), which were used for the present summary.
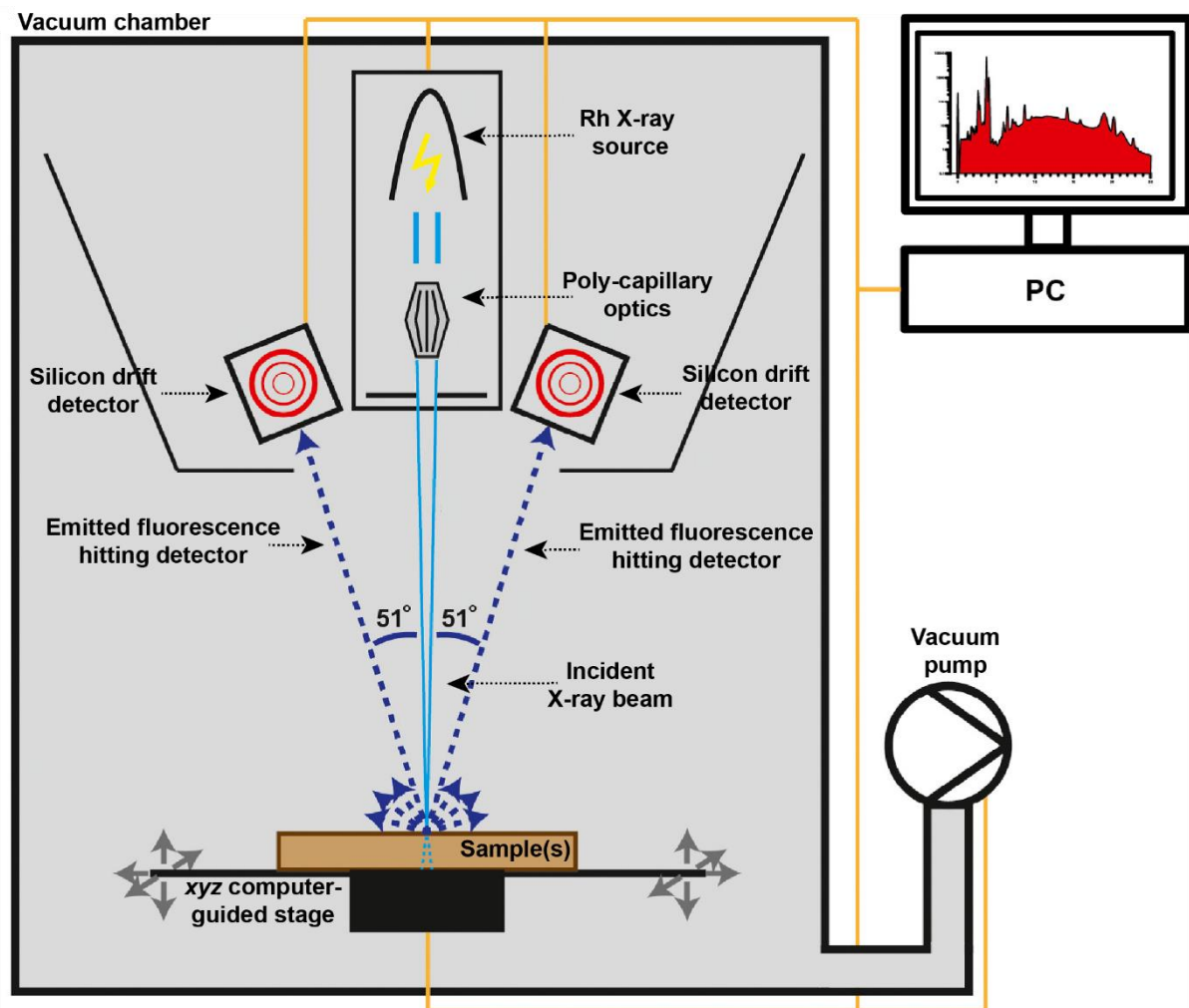
Figure 4.9. *Schematic representation of the Bruker M4 Tornado µXRF instrument used at the Vrije Universiteit Brussels, Brussels, Belgium. Modified from de Winter and Claeys (2017).*

4.2.4.2. Micro-X-ray fluorescence investigations

The µXRF analysis presented here were made using a Bruker M4 Tornado benchtop energy-dispersive µXRF scanner (Bruker Nano GmbH, Berlin, Germany; see Figs. 4.9–4.10), at the Vrije Universiteit Brussels (VUB), Brussels, Belgium. Both polished thin and related polished thick sections from the M0077A drill core (suevite, impact melt rock, and pre-impact lithologies samples) were selected for µXRF analysis. Thick sections were used as the measured surface not only needs to be as flat as possible, but also because a total sample thickness of at least 1 mm is required to account for the maximum attenuation depth of the X-rays, which is equivalent to ~800 µm (Beckhoff et al., 2006). Polished thick sections are placed in a plastic (e.g., polypropylene) holder filled with kinetic sand, and adjusted in the same horizontal plane prior being inserted inside the vacuum chamber for measurement (Fig. 4.10). In the case of polished thin section (~30 µm thick), X-rays are not fully attenuated within the sample, and the material located below the thin section can affect the analysis. Therefore, the sample holder is only made of plastic, which is composed of light elements that cannot be measured with the µXRF technique (Fig. 4.10). The sample holder is then placed on a motorized *xyz* stage composed of Plexiglas (poly(methyl methacrylate)) material. In the case of the Bruker M4

Tornado, the maximal dimensions and weight of the sample holder are 20 cm length, 16 cm width, 12 cm height, and 5 kg, respectively (see details in de Winter and Claeys, 2017; Kaskes et al., 2021).
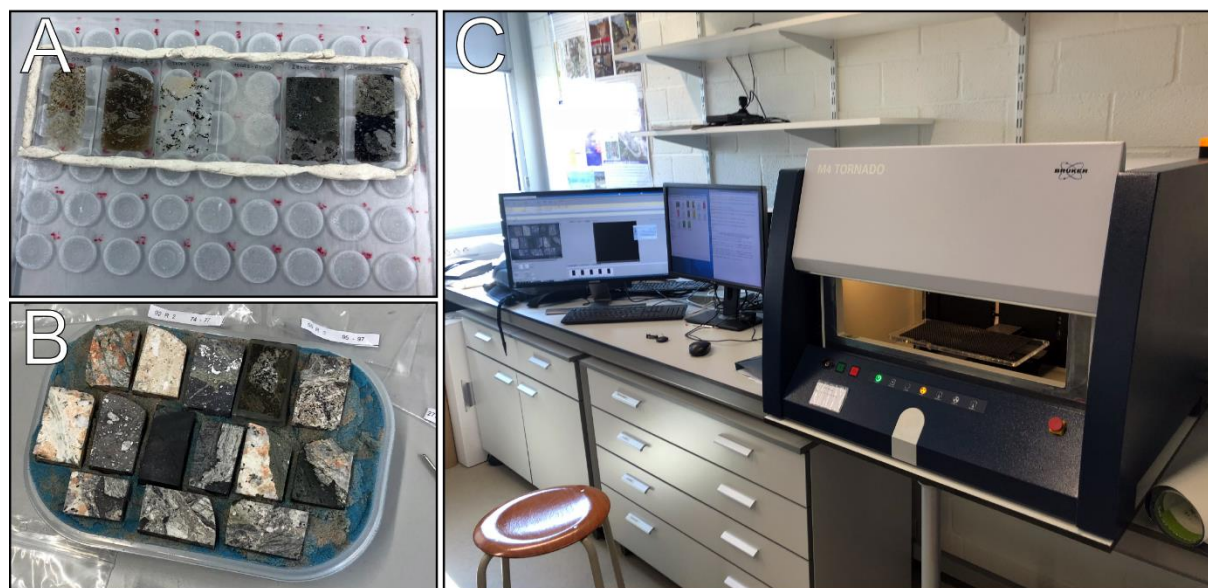
Figure 4.10. *A) Plastic sample holder for polished thin sections (Chicxulub peak ring samples) prior being inserted into the vacuum chamber for µXRF measurement. B) Chicxulub peak ring thick sections samples placed into a polypropylene holder filled with kinetic sand in order to have all samples on the same horizontal plane. C) The Bruker M4 Tornado µXRF instrument at Vrije Universiteit Brussels, Brussels, Belgium. The interior of the vacuum chamber with the xyz computer-guided stage is visible.*

The µXRF instrument at VUB was used to obtain chemical maps of some of the samples. It is equipped with a 30 W Rh anode as X-ray source, and two XFlash 430 silicon drift detectors, which were operated under maximum energy settings (600 µA, 50kV), without using a filter, and under near-vacuum conditions (20 mbar). The X-ray beam focused by the polycapillary lens yields a spot diameter of 25 µm. For all mappings, a standard integration time of 1 ms per pixel and a spacing (= spatial resolution) of 25 µm were used. The distribution of the moderately siderophile elements (Ni, Cr, and Co) within the Chicxulub peak ring impactites and target lithologies was investigated in order to check whether or not these elements are enriched in specific mineral phases, and, thus, if a meteoritic signature is present. To enhance the visualization of moderately siderophile elements on the maps, a second mapping was performed using an Aluminum 630 µm source filter, which reduces the X-ray signal for lighter major elements such as Al, Si, Ca, and K, and allows more sensitive detection of the trace elements (de Winter and Claeys, 2017; Feignon et al., 2022). The integration time was also longer, i.e., 5 ms per pixel.

The resulting spectra obtained by µXRF measurements were then converted in two types of chemical maps: (1) qualitative multi-element maps showing a color assigned to each element selected, where the color of every pixel is a tone produced by the combination of the selected colors (i.e., a ratio of the selected element abundances), and (2) semi-quantitative single-element so-called "heatmaps", showing the relative abundance variations of one selected

element according to a linear red-green-blue (RGB) color scale (from 0 to 255). The highest RGB value (255) corresponds to the highest X-ray intensity (i.e., the largest number of counts below the Kα peak) of the selected element. The RGB value of a pixel is calculated using its average RGB value and those of the eight surrounding pixels, corresponding to a square of 3 × 3 pixels, or 5,625 μm² (see details in Kaskes et al., 2021). To correctly visualize the distribution of Co, a peak deconvolution was applied in the M4 Bruker software to overcome the overlap between the Kα peak of Co, and the Kβ peak of Fe, at 6.93 and 7.06 keV, respectively (see publication in Chapter 7, Feignon et al., 2022).

Further quantification of major element compositions (bulk or in selected clasts) of the samples (thick sections) is possible using the Bruker M4 software by extraction of the spectra, and then by applying the Standardless Fundamental Parameter method (Sherman, 1955), which links the X-ray peak intensities with the respective elemental concentrations (de Winter et al., 2017; Vansteenberge et al., 2020). Also, the element maps can be used in order to quantify modal proportions of lithological components and textural characteristics (size, shape, orientation, and sorting) of these components, especially in heterogeneous samples such as suevite. As these quantification methods were not used for the present work, they are not discussed further. More information and discussion of these methods can be found in de Winter and Claeys (2017), Kaskes et al. (2021, 2022), and references therein.

4.2.5. Instrumental neutron activation analysis (INAA)

4.2.5.1. General principle

The instrumental neutron activation analysis (INAA) is a multi-element analytical technique, allowing precise (see Table 4.2) determination of bulk major and trace element abundances (up to 40 elements) of powdered or whole samples. The INAA investigations were performed at the Department of Lithospheric Research, University of Vienna, Vienna, Austria. This method is relatively non-destructive, as apart from crushing, no chemical treatment is needed. Prior to the INAA, the samples must be irradiated with neutrons (mostly thermal neutrons), which is typically done within a nuclear reactor. Consequently, a naturally occurring stable isotope is transformed into a short-lived radioactive isotope by neutron capture reaction. Then, the radioactive isotope undergoes radioactive decay, mostly β-decay associated with the emission of an X-ray or a γ-ray photon. The γ-ray energies are specific for each isotope. Thus, by measuring the intensities of the emitted γ-rays, the both type and amount of the various isotopes can be determined. Several analysis cycles (three cycles in the present work) are necessary to account for all the investigated elements, as the γ-ray spectrum changes with time due to the different half-lives of the various nuclides occurring in the samples. Quantification is finally done by comparing the γ-spectra produced with international reference materials. Detailed information on the INAA method can be found in, e.g., Ehmann and Vance (1991), Koeberl (1993, 1995), Gill (1997), and specific information on the current INAA procedures at the Department of Lithospheric Research (University of Vienna, Austria) can be found in Son and Koeberl (2005), Ferrière (2008), and Mader and Koeberl (2009). These references were used for the present summary.

Table 4.2. *Typical analytical precision (reproducibility) values for a variety of elements measured by the INAA method at the Department of Lithospheric Research, University of Vienna (Austria), derived from concentration measurements of international standard materials (AC-E granite, Allende carbonaceous meteorite (ALL), and SDO-1 shale) in 19 different sample batches. Standard deviation expressed in ppm, specified if otherwise. Data from Mader and Koeberl (2009).*

Element	AC-E		ALL		SDO-1	
	Standard deviation	rel.%	Standard deviation	rel.%	Standard deviation	rel.%
Na (wt.%)	0.19	4	0.01	2	0.01	3
K (wt.%)	0.43	11			0.25	10
Sc			0.75	6	0.69	6
Cr			236	7	4.95	7
Ni			1650	21	14	13
Fe (wt.%)	0.06	3	0.78	3	0.23	4
Co			34.4	5	1.87	5
Zn	15.7	7	8.96	8	5.71	9
Se					0.59	18
As			0.23	14	9.42	15
Br	0.3	32	0.49	75	0.69	82
Rb	9.43	6			7.14	6
Zr	9.92	5			29.6	5
Sb	0.30	80			0.66	17
Ba	5	9			264	50
Cs	0.18	6			0.37	6
La	3.08	5	0.09	15	1.76	5
Ce	6.66	4	0.28	16	3.41	4
Nd	10.1	13			114	165
Eu	0.40	23			0.06	4
Gd	2.30	13			3.85	50
Sm	1.70	8			0.90	8
Tb	0.42	8			0.08	8
Yb	1.26	7			0.18	5
Tm					0.14	22
Lu	0.49	21			0.17	30
Hf	1.39	5			0.21	5
Ta	0.64	7			0.06	8
W					1.17	61
Th	1.83	9			1.19	12
U	0.63	11			4.98	12

4.2.5.2. Sample preparation

About 100–150 mg of sample powder was weighed and deposited using a spatula (cleaned with acetone between each sample) in a previously cut polyethylene vial. After weighing, the vial was closed with a cap and labeled with the sample name. Samples are

grouped in batches of 17, plus three standard reference materials. It was checked that there was free space between sample material in the vial and the cap, and that no sample powder stuck between the vial and the cap, in order to avoid leaking. The same procedure was done with standard materials, excepted that the amount needed was 60–90 mg. The international reference materials used for INAA were the carbonaceous chondrite Allende (Smithsonian Institution, Washington DC, USA; Jarosewich et al., 1987), the Ailsa Craig granite AC-E (Centre de Recherche Pétrographiques et Géochimiques, Nancy, France; Govindaraju, 1989), and the Devonian Ohio shale SDO-1 (United States Geological Survey; Govindaraju, 1989). The closed vials were then placed upright in order to avoid that any sample or standard material remains stuck on the cap.

The vials need to be sealed in order to avoid material loss and/or radioactive contamination after irradiation. Sealing was done using a heated spatula passing on the seam between the vial and its cap. Testing of the vials sealing was made by holding them into hot water and it was looked for possible bubbles coming out of the vials interior. In this case, sealing was done again until the vials were fully leak-proofed.

Finally, before being transported for irradiation, the seventeen samples and three standard material batches were wrapped in a known position in plastic foil and finally packed in a polyethylene capsule for irradiation. The samples and standards were placed in four layers of five samples. The standard material vials were placed in the lowermost, middle, and uppermost layers in order to be able to apply a neutron flux correction by using the Na content in each of the standard materials (Mader and Koeberl, 2009).

4.2.5.3. Sample irradiation

In routine INAA, different sources can be used to irradiate samples, such as nuclear reactors (commonly used due to the high neutron flux from uranium fission), accelerators, or also radioisotopic emitters. For the present work, the capsules containing the sample batches were irradiated for 6 to 8 hours in the 250 kW TRIGA Mark II type research reactor at the Atomic Institute of the Austrian Universities, Vienna, Austria. The samples and standard materials were irradiated using a neutron flux of 2×10^{12} n cm^{-2} s^{-1} in the TRIGA reactor. The activity (A) of a given isotope, depending on the half-life of the intermediate nucleus, can be expressed by the following equation:

$$A = n.\phi.\sigma.(1 - e^{-ln2\frac{t_{irr}}{t_{1/2}}})$$

where n is the number of atoms of the target, ϕ is the neutron flux, σ is the neutron capture cross section (the probability of the interaction between a neutron and a target nuclide), t_{irr} is the irradiation time, and $t_{1/2}$ is the half-life of the nuclide. About 5 to 6 days after irradiation (this period corresponding to the cooling of irradiated samples), the capsules were transported back to the laboratory. Then, the samples vials were decontaminated in solutions of diluted HCl, diluted NaOH, and distilled water. After being dried, samples were ready for measurements.

4.2.5.4. Instrumentation used for INAA

In the INAA laboratory at the Department of Lithospheric Research, the measurement of the γ-rays emitted by the samples was done using four high-purity germanium (HpGe) semiconductor detectors (Canberra). The HpGe detectors are operating at liquid nitrogen temperature conditions, in order to minimize electronic noise and to prevent any damage to the lithium layer in the germanium crystals. The detectors are also protected by an aluminum cap, with a plastic foil on top. The relative efficiencies of the HpGe detectors used are ~12–45%, and their energy resolutions are of 1.76–1.85 keV (see Fig. 4.11). The signals recorded by the detectors were amplified in a built-in pre-amplifier, and then received and processed by Canberra DSP Model 2060 digital signal processors (DSP; Fig. 4.11). Then, the signals were transferred to the computer using acquisition interface modules (AIM) Canberra Model 556 (Fig. 4.11), producing spectra within the range of ~50–1800 keV, using 8,192 channels for the data memory. Every channel stores a signal having a given energy, and the amount of signals give a peak. The spectroscopy software GENIE^{TM} 2000 (Canberra) controls the data acquisition, storage, and evaluation.
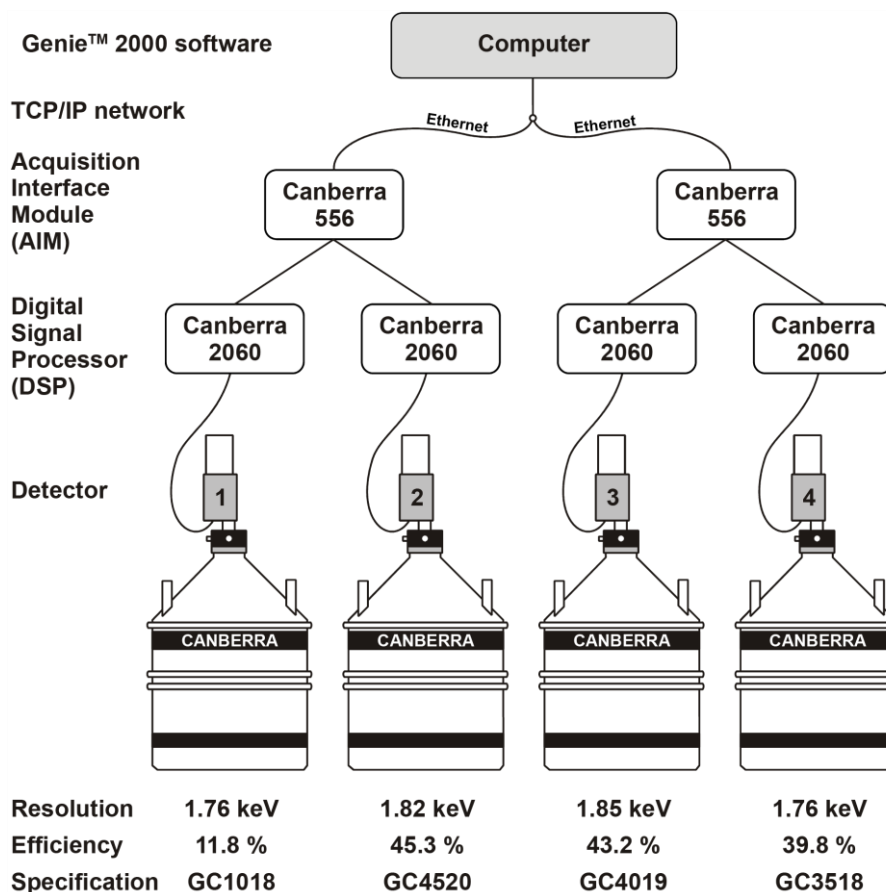
Figure 4.11. *Schematic configuration of the INAA instrumentation at the Department of Lithospheric Research, University of Vienna (modified from Mader and Koeberl, 2009).*

4.2.5.5. Measurement of the samples

During the period dedicated to measurements, when not analyzed, irradiated and decontaminated, samples were stored behind a lead shield to avoid exposition to radiation (even if the radiation levels are relatively low). Also, vials were checked for any damage that could have occurred after irradiation, and manipulations were reduced to the strict minimum. The samples were placed at the center of the HpGe detector, and samples information (name, weight, geometry) were provided in the software GENIE^{TM} 2000.

Measurements were made in three counting cycles (L1, L2, and L3), due to the different half-lives of the radioactive nuclides (see Table 4.3 for details). The duration (counting time) of each cycle is function of the sample quantity, nature, and irradiation parameters (e.g., activity). Importantly, the produced spectra need to be checked for a sufficient peak (signal) to background (noise) ratio. Thus, it is better to measure important samples and standards during long period of times (i.e., overnight, or over the weekend). The measurement cycle L1 was measured 5 days after irradiation, with each sample and standard being measured for at least 60 minutes. The cycle L1 is dedicated to the measurement of short-lived isotopes with half-lives of ~0.5–3 days (^{24}Na, ^{42}K, ^{76}As, ^{82}Br, ^{122}Sb, ^{140}La, ^{153}Sm, ^{169}Yb, ^{175}Yb, ^{177}Lu, ^{187}W, ^{198}Au, and ^{239}Np (for U)). The activity of the investigated samples was generally high, resulting in a dead-time more than 5–10%. The dead-time corresponds to the time loss due to an electronic overflow in the DSP (high count rates), mostly due to Na activity (half-life of 15 hours). In this case, either the sample was measured one day after, or at a distance of ~2 cm from the detector, with the sample placed on a 2-cm-sized plastic box put on the detector. Moreover, if a sample was measured in distance to the detector, all the other samples of the batch had to be measured the same way (i.e., with the same sample geometry) during the cycle. The cycle L1 was completed within 2–3 days (necessary), as after 10 half-lives, the signal would be too weak to obtain good results.

The measurement cycle L2 was started ~10 days after L1, and the measuring times for each sample and standard were ~3–4 hours (and could be up to 7 hours, depending on the sample). The isotopes measured during L2 were ^{46}Sc, ^{51}Cr, ^{59}Fe, ^{58}Co (for Ni), ^{86}Rb, ^{85}Sr, ^{95}Zr, ^{131}Ba, ^{140}La, ^{141}Ce, ^{147}Nd, ^{153}Sm, ^{152}Eu, ^{160}Tb, ^{170}Tm, ^{169}Yb, ^{175}Yb, ^{177}Lu, ^{181}Hf, ^{182}Ta, and ^{233}Pa (for Th).

Finally, cycle L3 was performed 3–4 weeks after L2, after most of the short-lived isotopes have decayed beyond the detection limit. The measurement time for each sample and standard was ~12–24 hours (24 hours in most cases). The isotopes measured during L3 were ^{46}Sc, ^{51}Cr, ^{59}Fe, ^{58}Co (for Ni), ^{60}Co, ^{65}Zn, ^{75}Se, ^{86}Rb, ^{85}Sr, ^{95}Zr, ^{134}Cs, ^{131}Ba, ^{141}Ce, ^{152}Eu, ^{153}Gd, ^{160}Tb, ^{170}Tm, ^{181}Hf, ^{182}Ta, ^{192}Ir, and ^{233}Pa (for Th). In any case, a longer measuring time was preferred to obtain better measurements.

Table 4.3. *Elements measured using INAA. The isotopes measured during analysis, as well as energy lines, half-lives, and measuring cycles, are reported. The energy line and half-live data are from Firestone and Shirley (1996), with h for hour, d for day, and y for year. Units are ppm, except as noted.*

Element	Isotope measured	Energy lines (keV)	Half-life ($t_{1/2}$)	Measurement cycle
Na (wt.%)	^{24}Na	1368.6	14.96 h	L1
K (wt.%)	^{42}K	1524.7	12.36 h	L1
Sc	^{46}Sc	889.3; 1120.5	83.79 d	L2, L3
Cr	^{51}Cr	320.1	27.70 d	L2, L3
Fe (wt.%)	^{59}Fe	192.3; 1099.2; 1291.6	44.50 d	L2, L3
Co	^{60}Co	1173.2; 1332.5	5.27 y	L3
Ni	^{58}Co	810.8	70.82 d	L2, L3
Zn	^{65}Zn	1115.5	244.26 d	L3
As	^{76}As	559.1	26.32 h	L1
Br	^{82}Br	554.3; 776.5	35.30 h	L1
Sr	^{85}Sr	514.0	64.84 d	L2, L3
Rb	^{86}Rb	1076.6	18.63 d	L2, L3
Zr	^{95}Zr	724.2; 756.7	64.02 d	L2, L3
Sb	^{124}Sb	1691.0	60.0 d	L3
	^{122}Sb	564.1	2.70 d	L1
Cs	^{134}Cs	795.8	2.06 y	L3
Ba	^{131}Ba	496.3	11.50 d	L2, L3
La	^{140}La	328.8; 487.0; 1596.2	1.68 d	L1, L2
Ce	^{141}Ce	145.4	32.50 d	L2, L3
Nd	^{147}Nd	91.1; 531.0	10.98 d	L2
Sm	^{153}Sm	103.2	46.27 h	L1, L2
Eu	^{152}Eu	121.8; 1408.0	13.54 y	L2, L3
Gd	^{153}Gd	97.4; 103.2	241.6 d	L3
Tb	^{160}Tb	298.6; 897.4; 966.2; 1178.0	72.3 d	L2, L3
Tm	^{170}Tm	84.3	128.6 d	L2, L3
Yb	^{175}Yb	282.5; 396.3	4.18 d	L1, L2
	^{169}Yb	177.2; 198.0	32.03 d	L1, L2
Lu	^{177}Lu	208.4	6.73 d	L1, L2
Hf	^{181}Hf	482.2	42.39 d	L2, L3
Ta	^{182}Ta	67.7; 222.1; 1221.4; 1231.0	114.43 d	L2, L3
W	^{187}W	685.8	23.72 h	L1
Ir (ppb)	^{192}Ir	299.0; 308.5; 316.5; 468.1	73.83 d	L3
Au (ppb)	^{198}Au	411.8	2.70 d	L1
Th	^{233}Pa	300.3; 312.2	26.97 d	L2, L3
U	^{239}Np	228.2; 277.6	2.36 d	L1

4.2.5.6. Data processing and corrections

In order to determinate element concentrations in the investigated samples, several corrections were applied (following background subtraction and peak area calculation). After the completion of all counting cycles, sample information was checked (name, weight, geometry, acquisition time), and the acquired spectra were calibrated using GENIE™ 2000 in order to check that the peaks of each spectrum were in a correct position with no shifting (they

should not deviate more than ~0.5–1 keV from their theoretical position). Several other corrections were applied, namely, decay time correction, dead time correction, normative time correction, geometry correction, and neutron flux correction. As samples and standard materials were not measured simultaneously, a recalculation to a normative time was necessary for comparison, i.e., the decay time correction (f_z), given by the following equation:

$$f_z = e^{ln2\frac{\Delta t}{t_{1/2}}}$$

where Δt is the decay time, and $t_{1/2}$ is the half-live of the nuclide.

The dead time correction (f_p) was done automatically during signal processing. Also, as the activity of the samples and standards decreased with time, correction of the measuring times and decay rates of the different nuclides was necessary. This operation was the normative time correction (f_n), which was done following the equation:

$$f_n = \frac{1 - e^{-ln2\frac{t_{std}}{t_{1/2}}}}{1 - e^{-ln2\frac{t_{sample}}{t_{1/2}}}}$$

where t_{std} is the measurement time of the standard, and t_{sample} is the measurement time of the sample.

Depending on the geometry of the sample (i.e., sample located on the detector surface, or at a specific distance to the detector), a geometry correction (f_g) was applied when needed. Also, if there were heterogeneities in the neutron flux that the samples were subjected to in the irradiation reactor, a flux correction (f_f) is applied, as the position of each sample and standard in a batch is known. After these corrections, the element concentrations were finally calculated using the following equation:

$$c_{sample} = c_{std}\frac{W_{std} \times A_{sample}}{W_{sample} \times A_{std}}$$

where c is the element concentration, W is the weight of the element, and A is the peak area. The calculation of element concentrations was performed automatically using the custom-made PC-based Neutron Activation Analysis (PNAA) software (Möslinger, 2006). In general, after integration of the acquired data and peak search for all spectra of a batch, the concentrations are obtained by using standard materials for the calibration, and then the concentrations are calculated for each sample compared to each of the standards. The PNAA calculations are made of several steps, including, determination of the peak position and area, efficiency correction, nuclide identification, and detection limits. The PNAA calculations produced an Excel-file providing the element concentrations (in ppm) from each measuring cycle of each sample.

The final steps of data checking were done manually on the produced Excel-files, with each sample and standard represented as a single worksheet. The calculation of element concentrations was made by averaging several values calibrated from one or more standard materials, from L1 to L3, according to the nuclide. First, a neutron flux correction factor is calculated, and, if varying more than ~5 rel.%, the neutron flux correction was done. Second, detection limits were indicated as red numbers in the worksheets, with the "<" sign before the number. In this case, these values were not used for the calculation. Third, a manual check was made in the "averaging" column, showing the element concentrations in a sample. It is

important to verify, for example, if one or more values are outliers. Also, some element contents were not calculated automatically due to being below the detection limit, and, in this case, the value was selected manually (the lowest available number was used). The concentrations of Na, K, and Fe were converted in wt.%, while the Ir and Au contents were converted in ppb (with a multiplication factor of 0.2 applied for Au). After this step, the final result is available. A final check was made by looking at the rare earth elements (REEs) normalized abundance pattern of the corresponding sample. As REEs (except Eu and Ce, depending on the oxidation state), do not normally fractionate relative to each other, the pattern should appear as a rather smooth line. If not the case, further corrections can be applied. In this study, the Tm contents calculated were too low despite applying all corrections. Consequently, these were not included in the presented results.

The following major trace element contents (in ppm, specified if other) were measured by bulk INAA analysis: Na (wt.%), K (wt.%), Sc, Cr, Fe (wt.%), Co, Ni, Zn, Ga, As, Se, Br, Rb, Sr, Zr, Sb, Cs, Ba, La, Ce, Nd, Sm, Eu, Gd, Tb, Tm, Yb, Lu, Hf, Ta, W, Os, Ir, Au, Th, and U (concentrations of underlined elements were preferentially used in the following chapters due to either that they are not measured by bulk XRF analysis, or that their precisions and accuracies are better than for XRF). The replicate analysis (n=8) of the international standard materials (AC-E, ALL, and SDO-1) yielded reproducibilities for trace element contents on the order of ~2 to 15 rel.% (see also, Table 4.2; Mader and Koeberl, 2009). More details on the accuracy and precision of the INAA method can be found in, e.g., Koeberl (1993), Son and Koeberl (2005), and Mader and Koeberl (2009).

4.2.6. Mass spectrometry

Mass spectrometry was used to measure isotopic ratios at very high precision, as well as concentrations of selected elements with very low detection limits (such as ppb, or even ppt). In the framework of this thesis, mass spectrometry was used in order to determine Rb–Sr, Sm–Nd, and Re–Os isotope ratios, as well as highly siderophile element (HSE; Ir, Os, Pt, and Re) contents of selected samples (see details in publication in Chapter 7, Feignon et al., 2022).

4.2.6.1. General principle

The basic idea behind mass spectrometry (MS) is to use a magnetic field to separate ionized atoms (and/or molecules) based on their mass. A mass spectrometer is composed of three major components: (1) an ion source (where the sample is ionized), (2) a magnetic analyzer (i.e., a magnet), and (3) an ion collector (Fig. 4.12). During analysis, all three parts of the mass spectrometer are put under vacuum conditions. There are different types of mass spectrometers. In this study, the main MS technique used was the thermal ionization mass spectrometer (TIMS) for Rb–Sr, Sm–Nd, and Re–Os isotopic investigations. Thus, the principle of TIMS is mainly described here, while the measurement of HSE contents (by inductively coupled plasma mass spectrometry, ICP-MS) is described in the related sub-section.

For TIMS analysis, the sample (in the form of a purified solid sample or as an aqueous solution) is loaded on a high purity, refractory metal filament (Kawai et al., 2001). The metals generally used are Re, Ta, W, and Pt. Generally, the ion source is made of an arrangement of

two, or even three filaments, for decoupling evaporation and ionization processes. The first filament is used for exhaustive evaporation of the sample by resistive heating, while the second heated filament causes ionization of the atoms (e.g., elements with ionization potentials below 7 eV can be efficiently vaporized and ionized at temperatures ~1000–2500 °K). For Rb–Sr and Sm–Nd isotopes analysis, samples were loaded on a Re filament, and two filaments were used for ionization. In the case of Re–Os isotopes analysis, a single Pt filament was used. Depending on the ionization potential of the selected elements, commonly, positive atomic or molecular ions are used for TIMS analysis (e.g., for Rb–Sr, Sm–Nd isotopes investigations). Thus, the TIMS is set in positive mode (P-TIMS). Meanwhile, elements such as Os or Re have a lower ionization potential when using negative ions (e.g., OsO_3^-). Thus, the first section of the mass spectrometer is depolarized to allow measurement of negative ions, setting the TIMS in negative mode (N-TIMS).
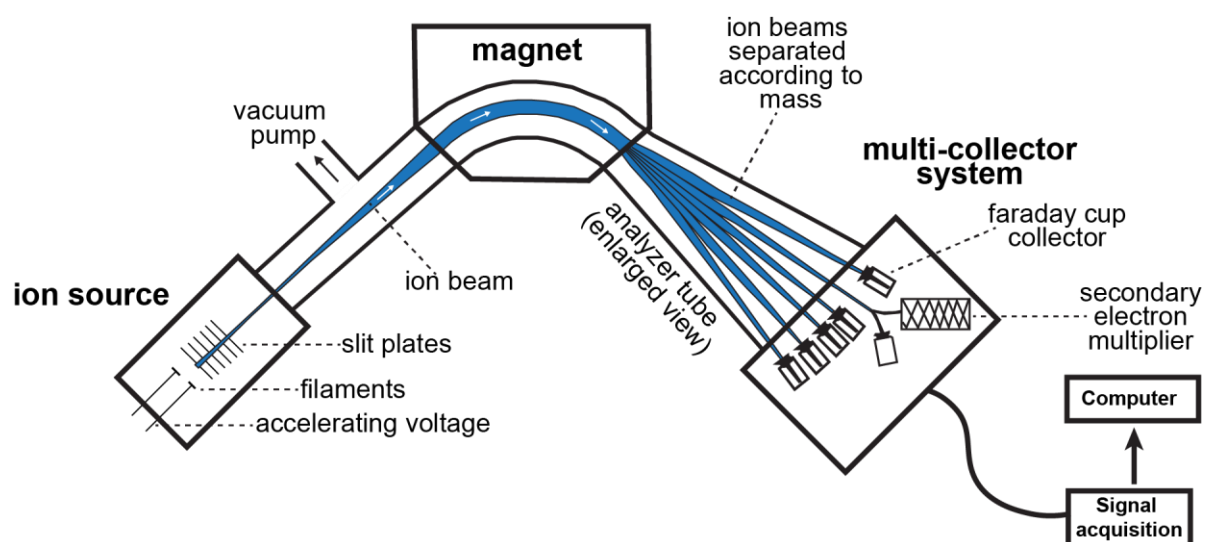
Figure 4.12. *Schematic diagram of a multi-collector TIMS, equipped with a secondary electron multiplier.*

The resulting ions are then accelerated by a high voltage electric field, and collimated into a beam by means of spaced slit plates. The accelerated ion beam enters a magnetic field generated by an electromagnet (Fig. 4.12). The positions and shapes of the pole pieces of the magnet are such that they produce magnetic field lines perpendicular to the direction of the ion beam. The ions are deflected by the magnetic field according to their mass-to-charge ratio (i.e., the heavier ions are less deflected than the lighter ones). Importantly, this technique only allows to measure the mass number, thus, isobaric (i.e., atoms with the same mass number but with different atomic numbers) or mass interferences can occur. Consequently, it is generally required to perform a chemical separation and purification of samples to isolate the element(s) of interest before starting measurement (e.g., by isotope dilution technique; see descriptions of the chemical separation procedures for Os isotopes, HSEs, Rb–Sr, and Sm–Nd isotopes in sections 4.2.6.2 and 4.2.6.3).

The deflected ions (according to their masses) continue to travel as separated beams through the analyzer tube and finally reach the collector slit, where they generate an electrical charge. The collector records either the current produced or the charge induced by the ions

impacting its surface. In recent TIMS instruments, the collector slit incorporates a multi-Faraday cup detector system, as well as a secondary electron multiplier (amplifying the incident charges) for measuring isotope amounts of minor isotopes. The accelerating voltage and the magnetic field are adjusted in order to focus the ion beams of the isotope of interest through the collector slit and then into the Faraday cup(s). The other ion beams collide with a grounded slit plate or with the metallic walls of the tube and are neutralized. By using multiple collectors (Faraday cups), several isotopic ion beams can be detected and measured simultaneously, improving the precision of measured isotope ratios. The received signal(s) is amplified and measured digitally, and sent to the computer for isotope ratios calculations. The spectrum obtained consists of a series of peaks identifying each isotope. The height of these peaks is proportional to the relative abundances of the isotopes. The final abundances or isotopic ratios of the elements of interests are calculated offline, after applying corrections (e.g., subtracting background noise and "blank" result, etc.).

Given the high sensitivity of MS, several parameters have to be taken into account as they could be a source of error in the isotopic ratios or concentrations obtained. These parameters include the environmental contamination occurring during sample chemical preparation for separating elements, and also instrument-related processes such as mass (isobaric) interference and mass fractionation. Generally, the amounts of the selected elements in the samples for isotopic analysis are very low ($\sim< 1$ µg [µg $= 10^{-6}$ g] to less than $\sim<1$ ng (ng $= 10^{-9}$ g])), while they also occur in the environment (e.g., Pb) and can contaminate the sample during the laboratory preparation for analysis. In order to account for the contamination induced by laboratory procedures, "blanks" are prepared in addition to the selected samples. These "blanks" are measured by taking an imaginary sample through all the chemical preparation steps. The final solution obtained is measured to determine the amount of environmental contamination. In the case of typical, whole-rock samples, acceptable maximum total chemistry blanks should normally be from less than 1 ng (e.g., for Sr and Nd) to less than 1 pg (pg $= 10^{-12}$ g; e.g., for Os). As stated above, mass interference could occur even if separation chemistry is properly done. For example, in the case of Os isotopic chemistry which was performed in this study, the ^{187}Os isotope has the same mass than ^{187}Re. After Os separation, Re can still be present (in a very small amount) in the Pt filament, or also in the solutions used for chemistry. To correct the amount of ^{187}Os from the mass interference caused by ^{187}Re, the signal of ^{185}Re isotope is measured, as there is no ^{185}Os isotope. Then, after measurement, using the known ^{185}Re/^{187}Re isotopic ratio in natural samples (0.59738; Gramlich et al., 1973), it is possible to calculate the amount of ^{187}Re and correct the ^{187}Os/^{188}Os ratio from the mass fractionation. Additionally, in the ion source of TIMS, mass-dependent fractionation occurs, leading to analytical artifacts. The evaporation and ionization processes are mass dependent, with the required energy to break chemical bonds lower for lighter isotopes than for heavier ones. The vaporization/ionization rate is not the same for isotopes of different masses, leading to a variation in the isotopic ratio with time. The lighter isotopes will evaporate and ionize first, while, after some time, the remaining sample material to measure will be enriched in heavier isotopes. The mass fractionation is internal to each TIMS instrument, thus, corrections to obtain the true isotope ratio value are made using linear or power law, in addition to the use of literature data. Replicate analyses of international standard materials are also performed in order to account for the TIMS measurement uncertainties and reproducibilities. More information on

mass spectrometry, TIMS, and the different isotopic systems can be found in e.g., Potts (1987), Gill (1997), de Groot (2004), Faure and Mensing (2004), Aggarwal (2016), Dickin (2018), Walther and Wendt (2020); these references were used for the elaboration of this review.

4.2.6.2. Re-Os isotopic analysis

As presented in Chapter 2, the use of $^{187}Os/^{188}Os$ ratios and Os abundances in impactites samples can be a powerful and sensitive tool in order to detect a contamination by the meteorite projectile (>0.01%), coupled with the analysis of the other HSE contents (see section 4.2.6.3). The Re–Os isotope systematics are also used for, e.g., dating meteorites, study the evolution of seawater composition through time, or as a complementary dating and source tracer tool for terrestrial rocks, in addition to Rb–Sr, Sm–Nd, and U–Pb isotopes (Faure and Mensing, 2004; Dickin, 2018). Osmium has seven naturally occurring isotopes (^{184}Os, ^{186}Os, ^{187}Os, ^{188}Os, ^{189}Os, ^{190}Os, and ^{192}Os), with the Re–Os method based on the β-decay of ^{187}Re to stable ^{187}Os (the half-life of ^{187}Re is ~42 Ga). Apart from ^{187}Re, the other naturally occurring Re isotope is ^{185}Re.

The sample chemistry (isotope dilution) procedure aims to separate Os from all other HSEs (which have also to be separated from the sample powder), following the methods described in, e.g., Cohen and Waters (1996), Birck et al. (1997), Pearson and Woodland (2000), Luguet et al. (2015), and Schulz et al. (2016), used for the following summary. Figure 4.13 presents a chart summarizing the chemical separation procedure. The separation of HSEs and Os was done in the clean room laboratory of the Department of Lithospheric Research, University of Vienna, equipped with six laminar flow hoods, clean air workstations, Milli-Q water (ultrapure water), acid distillation systems, air-conditioned, and with HEPA-filtered air.

Eighteen powdered samples from the IODP-ICDP Expedition 364 drill core were selected for Os isotopic analysis, and HSE abundance measurements, i.e., upper impact melt rock (n = 6), lower impact melt-bearing unit (n = 5), suevite (n = 2), granite (n = 2), dacite (n = 1), dolerite (n = 1), and amphibolite (n = 1). For more details on these lithologies, see Chapter 3.

Before the sample preparation itself, acids that will be used for the chemical separation of Os were purified to remove any traces of Os or Re that may be present. Hydrochloric acid (HCl), nitric acid (HNO₃), and hydrobromic acid (HBr) were purified by elbow distillation, and HNO₃ was also purified from Re by sparging. Sulfuric acid (H₂SO₄) and hydrofluoric acid (HF) were not purified as H₂SO₄ is only used in a small amount (10 µL), and HF is not used during Os preparation for analysis. Additionally, the Savillex PFA (Perfluoroalkoxy) beakers that will be used for the chemistry were cleaned using acetone, HBr, and HNO₃, and glass vials were cleaned using HF, and then for 3–4 hours with aqua regia (acid mixture composed of 3 mL HNO₃ and 2 mL HCl) at 270 °C and 70 bars in an Anton-Paar high pressure asher. This cleaning step lasts generally for several days.

About ~0.3 to 0.6 g of homogenized sample powder were weighed and spiked with a mixed tracer solution (10 µL of spike were added) composed of ^{185}Re, ^{190}Os, ^{191}Ir, and ^{194}Pt (Fig. 4.13). The element abundances within the spike are known, and one isotope of each element composing the spike is artificially enriched. Therefore, knowing the sample and spike weight, the isotopic composition of the mixture can be used to calculate the amount of the selected elements (here Ir, Os, Pt, and Re) in the sample (see details in Faure and Mensing,

2004; Dickin, 2018). The "picrite" spike was used, as it is dedicated to typical crustal rock samples, while the "basalt" spike, being ten times less concentrated than the "picrite" spike, is used for the blank, allowing to better identify background level during the analysis. The spiked samples were placed in glass vials and digested in 5 mL aqua regia at 270 °C and 100–130 bars in the Anton-Paar high pressure asher for 5 hours (Fig. 4.13).
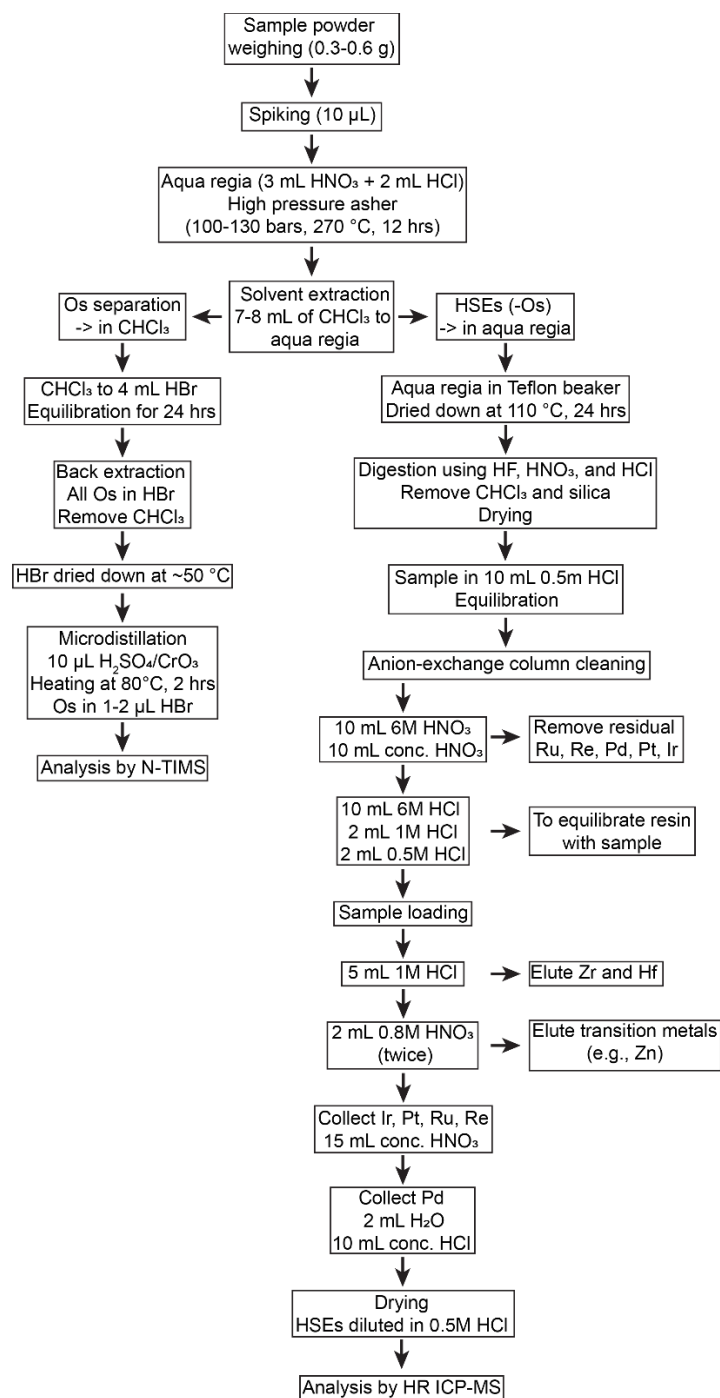
Figure 4.13. *Flow chart describing the Os and other HSEs separation procedure used for this work. Details on each of the steps are provided in the text. Adapted from Pearson and Woodland (2000).*

The total duration of the high pressure asher program was ~12–13 hours, as the temperature increased for ~2 hours from room temperature to ~200 °C, stayed at ~200 °C for ~3 hours, then increased for ~1 hour to ~270 °C and stayed at this level for 5 hours, before decreasing to room temperature for ~2–3 hours (pressure remained constant). During this time, the glass vials were sealed with Teflon paper and a glass cap. It was suggested that such high pressure digestion techniques allow the complete release of Os from the sample (more complete attack of HSE-bearing phases) and its complete equilibration with the ^{190}Os from the spike (Cohen and Waters, 1996; Meisel and Moser, 2004).

The next step of the chemistry is called "solvent extraction" (Fig. 4.13). After opening the glass vials, one pipette of chloroform ($CHCl_3$) was added to the aqua regia to proceed to Os separation. Chloroform has a high partition coefficient with Os, allowing its separation from the other HSEs. Carbon tetrachloride (CCl_4) was more efficient than chloroform to separate Os, but is not used anymore for solvent extraction due to its high toxicity. As the density of chloroform is higher than aqua regia, the two liquids mingle in two layers with the chloroform at the bottom part of the glass vials and the aqua regia above. The liquid mixture was extracted (but not the undissolved fragments remaining) and placed in a centrifuge tube. For few minutes, tubes were placed in a centrifuge. Then, chloroform was collected carefully from the centrifuge tube and put into a previously prepared Savillex PFA beaker (labelled "Os") containing 4 mL HBr. Then, ~2 and ~1 mL of chloroform were further added to the aqua regia in order to separate the maximum possible amount of Os from the other HSEs, and then collected into the "Os" beaker. The "Os" beakers containing the mingled mixture of chloroform (reddish liquid) and HBr (yellow liquid) were placed for 24 hours in the centrifuge. Finally, the aqua regia containing the HSEs minus Os was collected in a beaker labelled "HSEs" and dried down (beaker with open cap) on a hot plate at 110 °C for 24 hours (see section 4.2.6.3).

The following step of the Os preparation for the analysis is the "back extraction". The affinity and stability of Os is higher with HBr, forming hexabromo-Os complex $OsBr_6^{2-}$, than with chloroform. Thus, chloroform was removed from the "Os" beaker to leave only HBr inside. Then the "Os" beakers were wrapped in Al foils and dried on a hot plate at ~50 °C.

Further purification of Os was made using the so-called microdistillation technique. The remaining sample dry residue from the "back extraction" was dissolved in a small quantity (~20 μL) of concentrated HBr, and placed within the cap of a conical beaker. The HBr was evaporated with the cap heated at ~80 °C on a hot plate. Then, the dried residue of Os was dissolved in 10 μL of H_2SO_4 containing CrO_3, acting as an oxidizing agent (the Os complex $OsBr_6^{2-}$ was oxidized to OsO_4). A drop (20 μL) of HBr was placed in the tip of the conical beaker which was then closed and placed upside down and wrapped in an Al foil, excepted the beaker tip (Fig. 4.14). The conical beaker was heated during 2 hours at 80 °C. The conical beaker was then opened and put back to its normal position, with the HBr evaporated down to ~1–2 μL, completing the Os purification by microdistillation, and preparing it for TIMS analysis.
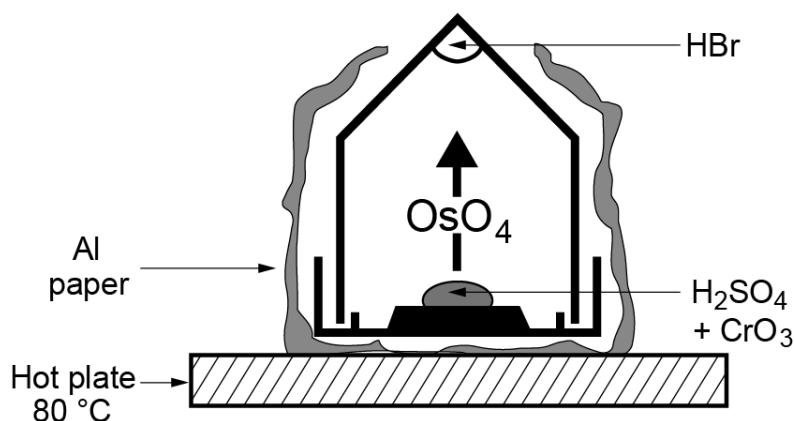
Figure 4.14. *Schematic representation of the final purification of Os by microdistillation, see details in text. Modified from Birck et al. (1997).*

Determination of the $^{187}Os/^{188}Os$ ratios and Os concentrations were performed at the Department of Lithospheric Research, University of Vienna, using a ThermoFinnigan Triton TIMS, operating in negative ion mode (N-TIMS). Osmium was loaded as a bromide on Pt ribbon filaments covered with $NaOH/Ba(OH)_2$ used as an activator enhancing the production of negative thermal ions (see details in Creaser et al., 1991; Völkening et al., 1991). The runs were performed with an oxygen bleed in order to raise ionization yields (Schulz et al., 2016). Osmium was emitted and measured as OsO_3^- ions in "peak jumping" mode using the secondary electron multiplier detector, which offers more sensitivity than Faraday cups. No isobaric interferences attributable to W- or Pt-oxides were observed, whereas isobaric interferences of ^{187}Re on ^{187}Os were monitored by measuring $^{185}ReO_3^-$ (mass 233), and corrected if observed. Mass fractionation was corrected offline using $^{192}Os/^{188}Os = 3.083$ (Brandon et al., 2005; Luguet et al., 2008). The Os total procedural blank was ~0.4 pg (n = 2) contributing less than 0.5% to the measured Os concentrations of the samples.

In order to check the state of the instrument (signal quality, contamination), repeated N-TIMS measurements (n = 3) of 10 pg loads of a Durham Romil Osmium external Standard (DROsS) were performed using the secondary electron multiplier at signal intensities similar to those typically achieved during sample measurement runs (~1,000 to ~100,000 counts on mass 240, i.e., $^{192}OsO_3^-$). The DROsS measurements yielded an average $^{187}Os/^{188}Os$ ratio of 0.16088 ± 00056, $^{189}Os/^{188}Os$ ratio of 1.2167 ± 0.0040, and $^{190}Os/^{188}Os$ ratio of 1.9782 ± 0.0080. These values are in agreement within the 2σ uncertainty of the average values reported by Luguet et al. (2008), obtained for much larger Os loads of DROsS. The long-term external reproducibilities are $\pm 0.4\%$ for $^{187}Os/^{188}Os$, $\pm 0.2\%$ for $^{189}Os/^{188}Os$, and $\pm 0.3\%$ for $^{190}Os/^{188}Os$ ratios. Alongside the samples, replicate measurements of internal reference standard materials were also performed to monitor the analytical quality. The standard materials measured were the lherzolite UB-N (Meisel et al., 2003) and the komatiite OKUM (Potts and Meisel, 2015). All analyses of international standard materials reproduced the certified values within 2σ error.

4.2.6.3. Highly siderophile elements content analysis

After the "solvent extraction" (see section 4.2.6.2), the "HSEs" beakers were dried down (beaker with open cap) on a hot plate at 110 °C for 24 hours. Afterwards, concentrated HF was added in the beaker, which was put on the hot plate table top (with closed cap), and then dried down. Then, 14 M HNO_3 was added and dried down again. These steps allow full digestion of any remaining undissolved silicate material, the removal of residual chloroform, the destruction of residual organics, and ensure a better recovery of Re (Ishikawa et al., 2014), though to also have a lithophile affinity (e.g., Luguet et al., 2007; Mallmann and O'Neill, 2007). Then, 6M HCl is put in the beaker and dried down at 130 °C, followed by 1M HCl (table top drying). Finally, sample was diluted in 10 mL of 0.5M HCl, constituting the loading solution, kept on the hot plate at 100 °C, before being transferred in a centrifuge tube. Centrifugation was done. The HSEs are separated from the matrix using 1 mL of resin BioRad AG1 X8, 200 to 400 mesh, in polypropylene columns with 2 mL resin capacity and 10 mL reservoir (according to procedure outlined in, e.g., Rehkämper and Halliday, 1997; Pearson and Woodland, 2000; Coggon et al., 2013; Luguet et al., 2015). Before loading sample, the resin was cleaned and equilibrated using the following reagents: 6M (10 mL) and concentrated HNO_3 (10 mL, elution of residual Ru, Re, Pd, Pt, and Ir), and then 6M HCl (10 mL, reconversion of the resin to its chloride form), 1M (2 mL), and 0.5M HCl (2 mL, equilibration of the resin before sample loading). This creates a non-reducing environment for the sample, in order to minimize any reduction of Ir^{4+} in solution. The sample (within 10 mL of 0.5M HCl) was loaded into the column. Afterwards, 5 mL of 1M HCl were added to the column in order to remove Zr and Hf, followed by two times 2 mL of 0.8M HNO_3 which elute transition metals such as Zn. Following these steps, Ir, Pt, Re, and Ru (not measured) were collected in a beaker using 15 mL of concentrated HNO_3. After adding 2 mL of H_2O which neutralize HNO_3, Pd was collected in a separate beaker, further dried down at ~60 °C. However, Pd was not measured in the framework of this study. The beakers containing the recovered HSEs of interest (Ir, Pt, and Re) for each sample were subsequently dried down and re-dissolved in 0.5M HCl.

The selected HSE (Ir, Pt, and Re) abundances were measured using a Thermo Fisher Element XR high resolution inductively coupled plasma mass spectrometer (HR ICP-MS) in single collector mode at the Steinmann Institute at the University of Bonn, Germany. In contrast to TIMS, the ICP-MS uses plasma as ionization source. The plasma torch composed of ionized Ar gas, reaching temperature of ~5,000 °C, causing a very efficient ionization of most elements (Houk, 1986). The very high temperature of the plasma ensures that nearly all of the ions formed are monoatomic. Therefore, the ICP-MS reach very high sensitivity in measuring element abundances, with detection limits as low as ppt (pg/g). For the HSE analysis, samples (in the form of a HSE-bearing solution for each) were sprayed in the plasma chamber, and the resulting ions measured. Detailed descriptions of the measurement procedure are provided in Coggon et al. (2015), Wainwright et al. (2015), and Van Acken et al. (2016). The HSE concentrations were measured in single collector mode. A 1 ppb in-house, multi-element HSE standard solution was measured at the beginning, middle, and end of the analytical session in order to monitor the instrumental drift. The mass bias was corrected relative to this standard solution using ratios of 0.5986 for $^{185}Re/^{187}Re$, 0.5957 for $^{191}Ir/^{193}Ir$, and 0.2117 for $^{198}Pt/^{195}Pt$, and corrections were insignificant for all samples. Additionally, isobaric interferences caused by Hf

on Ir and Pt were monitored and corrected for offline. In order to determine the oxide production, 1 ppb HSE solutions doped in Hf were measured at the beginning, middle, and end of each analytical session. Rhenium, Ir, and Pt were measured using a cyclonic borosilicate glass spray chamber. Total procedural blanks for this study (n = 2) 0.5–1 pg for Ir, 10–30 pg for Pt, and 3–4 pg for Re. Blank correction for procedural blank was achieved by subtracting the blank contribution from the amount of analyte detected. Due to the often very low HSE concentrations of the analyzed samples, blank corrections were applied in all cases. With respect to individual samples, these blanks resulted in variable uncertainties for the calculated concentrations in the range of 1–60% for Ir, 1–70% for Pt, and <1–30% for Re (highest uncertainties for low HSE dacite (238R1_101–103.5), granites (136R2_20–25 and 200R3_12.5–15), and amphibolite (80R2_61–63.5) samples; see details in publication in Chapter 7, Feignon et al., 2022). As for Os content and isotopic analysis, replicate measurements of international standard materials were done alongside the samples, i.e., UB_N lherzolite (Meisel et al., 2003) and OKUM komatiite (Potts and Meisel, 2015). All analyses of reference materials reproduce certified values within 2σ error.

4.2.6.4. Rb-Sr and Sm-Nd isotopic analysis

As the impact cratering process offers unique access to rocks located in deeper level of the crust (see Chapter 1), the use of Rb–Sr and Sm–Nd isotope systematics in pre-impact lithology samples recovered in the Expedition 364 drill core can bring new and important information on the Yucatán basement rocks (e.g., crystallization and alteration ages, sources, etc.). Sixteen granite, four dolerite, two dacite, and two felsite samples were selected for Rb–Sr and Sm–Nd isotope investigations. The sample preparation (separation of Sr and Nd from the whole rock sample powder) and analysis follow relatively similar steps than for Re–Os isotopes investigations. More details on Rb–Sr and Sm–Nd isotope systematics can be found in Faure and Mensing (2004) and Dickin (2018).
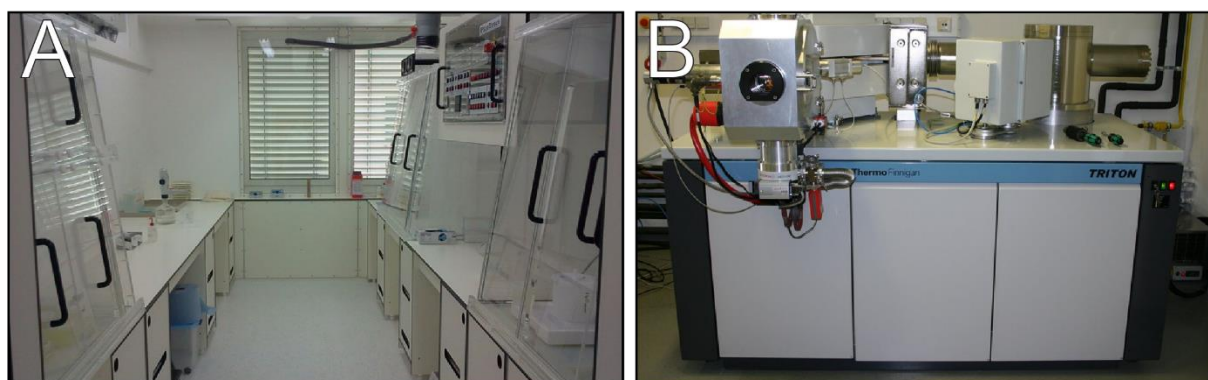
Figure 4.15. *A) The clean room laboratory at the Department of Lithospheric Research, University of Vienna. This facility is suitable for chemical separation of elements for isotopic analysis (e.g., Re–Os, Rb–Sr, and Sm–Nd). Photograph available at: https://lithosphere.univie.ac.at/forschung/labors/reinraumlabor/. B) The Thermo-Finnigan Triton TIMS instrument at the Department of Lithospheric Research, University of Vienna. Photograph available at: https://lithosphere.univie.ac.at/forschung/labors/tims/.*

The Sr and Nd isotopic analytical work was performed at the Department of Lithospheric Research, University of Vienna, with the sample preparation taking place in the clean laboratory (Fig. 4.15). Approximately 50–100 mg of whole rock powders were weighed, and then digested in Savillex PFA beakers using an ultra-pure mixture of HF and HNO_3 (4:1 ratio). In order to make sure that insoluble phases, such as zircon, were fully digested, the beakers (with cap tightly closed) were placed on a hot plate for 2–4 weeks at 100–120 °C. After acid evaporation, the residue was treated with repeated treatment by 6M HCl, resulting in clear solutions.

The separation of Sr and REEs was performed using a BioRad AG 50W-X8, 200 to 400 mesh resin, with 2.5M and 4.0M HCl used as eluants. Then Nd was separated from the REEs using Teflon-coated bis-(2-ethylhexyl) phosphoric acid (HDEHP) and 0.22M HCl as eluant. The isolated element fractions (1 µL) were loaded on a Re double filament assembly and run in static, and positive mode on a Thermo-Finnigan Triton (P-TIMS, Fig. 4.15), as Sr and Nd are ionized as positive ions. The maximum procedural blanks were <1 ng for Sr and 40 pg for Nd, which can be considered negligible for the purpose of this study. Mass fractionation was corrected for $^{88}Sr/^{86}Sr = 8.3752$ and $^{146}Nd/^{144}Nd = 0.7219$, respectively. Samples were measured in two successive batches. Mean $^{87}Sr/^{86}Sr$ of 0.710260 ± 0.000004 (batch 1, n = 5) and 0.710257 ± 0.000006 (batch 2, n = 5) were determined for the NBS987 (Sr) and mean $^{143}Nd/^{144}Nd$ ratios of 0.511846 ± 0.000003 (batch 1, n = 5) and 0.511841 ± 0.000002 (batch 2, n = 5) for the La Jolla (Nd) international standards during the period of investigation. Uncertainties quoted represent 2σ errors of the mean. The isotopic ratios $^{87}Rb/^{86}Sr$ and $^{147}Sm/^{144}Nd$ were derived from Rb/Sr and Sm/Nd ratios obtained following Rb–Sr and Sm–Nd concentration measurements performed by XRF and INAA, respectively. The assigned uncertainties to $^{87}Rb/^{86}Sr$ and $^{147}Sm/^{144}Nd$ are 1 and 7 rel%, respectively, with an uncertainty on Rb, Sr, Sm, and Nd measurements of 1, 0.4, 2, and 5 rel%, respectively (Son and Koeberl, 2005; Mader and Koeberl, 2009; Nagl and Mader, 2019).

The $^{143}Nd/^{144}Nd$ ratios are expressed in ε notation, where $(\varepsilon_{Nd})_t$ indicates the deviation in parts in 10^4 of the $^{143}Nd/^{144}Nd$ ratios from the chondritic uniform reservoir (CHUR). When t = 0, the $(^{143}Nd/^{144}Nd)_{CHUR}$ ratio used to calculate the $(\varepsilon_{Nd})_{t=0}$ is the present-day value of 0.512638 (DePaolo and Wasserburg, 1976):

$$(\varepsilon_{Nd})_{t=0} = \left(\frac{\left(^{143}Nd/^{144}Nd\right)_{sample}}{0.512638} - 1 \right) \times 10^4$$

When t ≠ 0, the $(^{143}Nd/^{144}Nd)_{CHUR}$ ratio needs to be recalculated for the age of interest. The results of the Rb–Sr and Sm–Nd isotope analyses are presented and discussed in the publication in Chapter 6 (Feignon et al., 2021) and in Chapter 8.

References

Aggarwal S. K. 2016. Thermal ionization mass spectrometry (TIMS) in nuclear science and technology – a review. *Analytical Methods* 8:942. https://doi.org/10.1039/c5ay02816g.

Beckhoff B., Kanngießer B., Langhoff N., Wedell R., and Wolff, H. 2006. *Handbook of Practical X-Ray Fluorescence Analysis*. Springer Science & Business Media, New York. 863 p. https://doi.org/10.1007/978-3-540-36722-2.

Birck J. L., Barman M. R., and Capmas F. 1997. Re-Os isotopic measurements at the femtomole level in natural samples. *Geostandards Newsletter* 21:19–27. https://doi.org/10.1111/j.1751-908X.1997.tb00528.x.

Brandon A. D., Humayun M., Puchtel I. S., Leya I., and Zolensky M. 2005. Osmium Isotope Evidence for an s-Process Carrier in Primitive Chondrites. *Science* 309:1233–1236. https://doi.org/10.1126/science.1115053.

Cavosie A. J., Timms N. E., Ferrière L., and Rochette P. 2018. FRIGN zircon–The only terrestrial mineral diagnostic of high-pressure and high-temperature shock deformation. *Geology* 46:891–894. https://doi.org/10.1130/G45079.1.

Coggon J. A., Luguet A., Nowell G. M., and Appel P. W. U. 2013. Hadean mantle melting recorded by southwest Greenland chromitite [186]Os signatures. *Nature Geoscience* 6:871–874. https://doi.org/10.1038/ngeo1911.

Coggon J., Luguet A., Fonseca R., Lorand J. P., Heuser A., and Appel P. 2015. Understanding Re-Os systematics and model ages in metamorphosed Archean ultramafic rocks: A single mineral to whole-rock investigation. *Geochimica et Cosmochimica Acta* 167:205–240. https://doi.org/10.1016/j.gca.2015.07.025.

Cohen A. S. and Waters F. G. 1996. Separation of osmium from geological materials by solvent extraction for analysis by thermal ionisation mass spectrometry. *Analytica Chimica Acta* 332:269–275. https://doi.org/10.1016/0003-2670(96)00226-7.

Creaser R. A., Papanastassiou D. A., and Wasserburg G. J. 1991. Negative thermal ion mass-spectrometry of osmium, rhenium and iridium. *Geochimica et Cosmochimica Acta* 55:397–401. https://doi.org/10.1016/0016-7037(91)90427-7.

de Groot P. A. 2004. *Handbook of stable isotope analytical techniques*. Elsevier, Amsterdam. 1234 p.

de Winter N. J. and Claeys P. 2016. Micro X-ray fluorescence (µXRF) line scanning on Cretaceous rudist bivalves: A new method for reproducible trace element profiles in bivalve calcite. *Sedimentology* 64:231–251. https://doi.org/10.1111/sed.12299.

DePaolo D. J. and Wasserburg G. J. 1976. Nd isotopic variations and petrogenetic models. *Geophysical Research Letters* 3:249–252. https://doi.org/10.1029/GL003i005p00249.

Dickin A. P. 2018. *Radiogenic Isotope Geology, Third Edition.* Cambridge University Press, Cambridge. 482 p.

Dressler B. O., Sharpton V. L., and Schuraytz B. C. 1998. Shock metamorphism and shock barometry at a complex impact structure: Slate Islands, Canada. *Contributions to Mineralogy and Petrology* 130:275–287. https://doi.org/10.1007/s004100050365.

Duboc O., Robbe A., Santner J., Folegnani G., Gallais P., Lecanuet C., Zehetner F., Nagl P., and Wenzel W. W. 2019. Silicon Availability from Chemically Diverse Fertilizers and Secondary Raw Materials. *Environmental Science & Technology* 53:5359–5368. https://doi.org/10.1021/acs.est.8b06597.

Ehmann W. D. and Vance D. E. 1991. *Radiochemistry and nuclear methods of analysis*. John Wiley and Sons, New York. 531 p.

Emmons R. C. 1943. The universal stage (with five axes of rotation). *Geological Society of America Memoir* 8, 205 p. https://doi.org/10.1130/MEM8.

Engelhardt W. v. and Bertsch W. 1969. Shock induced planar deformation structures in quartz from the Ries crater, Germany. *Contributions to Mineralogy and Petrology* 20:203–234. https://doi.org/10.1007/BF00377477.

Faure G. and Mensing T. M. 2004. *Isotopes: Principles and applications, Third Edition*. John Wiley & Sons, Hoboken, New Jersey. 897 p.

Feignon J.-G., Ferrière L., Leroux H., and Koeberl C. 2020. Characterization of shocked quartz grains from Chicxulub peak ring granites and shock pressure estimates. *Meteoritics & Planetary Science* 55:2206–2223. https://doi.org/10.1111/maps.13570.

Feignon J.-G., de Graaff S. J., Ferrière L., Kaskes P., Déhais T., Goderis S., Claeys P., and Koeberl C. 2021. Chicxulub impact structure, IODP-ICDP Expedition 364 drill core: Geochemistry of the granite basement. *Meteoritics & Planetary Science* 56:1243–1273. https://doi.org/10.1111/maps.13705.

Feignon J.-G., Schulz T., Ferrière L., Goderis S., de Graaff S. J., Kaskes K., Déhais T., Claeys P., and Koeberl C. 2022. Search for a meteoritic component within the impact melt rocks of the Chicxulub impact structure peak ring, Mexico. *Geochimica et Cosmochimica Acta* 323:74–101. https://doi.org/10.1016/j.gca.2022.02.006.

Feldman V. I. 1992. The conditions of shock metamorphism. In *Large meteorite impacts and planetary evolution*, edited by B. O. Dressler, R. A. F. Grieve, and V. L. Sharpton. Geological Society of America Special Paper #293. Geological Society of America, Boulder, Colorado. pp. 121–132.

Fel'dman V. I., Sazonova L. V., and Kotel'nikov S. I. 1996. Distribution of the shock pressure in the rocks of the Vorotilov hole, Puchezh-Katunki astrobleme. *Doklady Akademii Nauk SSSR* 349:658–660. In Russian.

Ferrière L. 2008. *Shock metamorphism and geochemistry of impactites from the Bosumtwi impact structure: A case study of shock-induced deformations and transformations in quartz and associated methodology*. PhD thesis, University of Vienna, Austria. 279 p.

Ferrière L., Koeberl C., Ivanov B. A., and Reimold W. U. 2008. Shock metamorphism of Bosumtwi impact crater rocks, shock attenuation, and uplift formation. *Science* 322:1678–1681. https://doi.org/10.1126/science.1166283.

Ferrière L., Morrow J. R., Amgaa T., and Koeberl C. 2009. Systematic study of universal-stage measurements of planar deformation features in shocked quartz: Implications for statistical significance and representation of results. *Meteoritics & Planetary Science* 44:925–940. https://doi.org/10.1111/j.1945-5100.2009.tb00778.x.

Firestone R. B. and Shirley V. S. 1996. *Table of Isotopes*, 8th ed. (volume I and II). John Wiley & Sons, New York. 224 p.

French B. M. 1998. *Traces of catastrophe: A handbook of shock-metamorphic effects in terrestrial meteorite impact structures*. LPI Contribution #954. Houston, Texas: Lunar and Planetary Institute. 120 p. https://www.lpi.usra.edu/publications/books/CB-954/CB-954.intro.html.

French B. M. 2005. The universal stage user's guide (updated). B. M. French: Shock metamorphism course, University of Vienna. 201 p.

Gauglitz G. and Moore D. S. 2014. *Handbook of Spectroscopy, Vol. 4.* John Wiley & Sons, Weinheim. 1993 p.

Gill R. 1997. *Modern Analytical Geochemistry: an Introduction to Quantitative Chemical Analysis Techniques for Earth, Environmental and Materials Scientists*. Routledge, London. 342 p. https://doi.org/10.4324/9781315844381.

Govindaraju K. 1989. 1989 compilation of working values and sample description for 272 geostandards. *Geostandards Newsletter* 13:1–113. https://doi.org/10.1111/j.1751-908X.1989.tb00476.x.

Gramlich J. W., Murphy T. J., Garner E. L., and Shields W. R. 1973. Absolute isotopic abundance ratio and atomic weight of a reference sample of rhenium. *Journal of Research of the National Bureau of Standards* 77A:691–698. https://doi.org/10.6028/jres.077A.040.

Grieve R. A. F. and Robertson P. B. 1976. Variations in shock deformation at the Slate Islands impact structure, Lake Superior, Canada. *Contributions to Mineralogy and Petrology* 58:37–49. https://doi.org/10.1007/BF00384743.

Holm-Alwmark S., Ferrière L., Alwmark C., and Poelchau M. H. 2018. Estimating average shock pressures recorded by impactite samples based on universal stage investigations of planar deformation features in quartz—Sources of error and recommendations. *Meteoritics & Planetary Science* 53:110–130. https://doi.org/10.1111/maps.13029.

Hörz F. 1968. Statistical measurements of deformation structures and refractive indices in experimentally shock loaded quartz. In *Shock metamorphism of natural materials*, edited by French B. M. and Short N. M. Baltimore, Maryland: Mono Book Corporation. pp. 243–253.

Houk R. S. 1986. Mass spectrometry of inductively coupled plasmas. *Analytical Chemistry* 58:97A–105A. https://doi.org/10.1021/ac00292a003.

Huffman A. R. and Reimold W. U. 1996. Experimental constraints on shock-induced microstructures in naturally deformed silicates. *Tectonophysics* 256:165–217. https://doi.org/10.1016/0040-1951(95)00162-X.

Ishikawa A., Senda R., Suzuki K., Dale C. W., and Meisel T. 2014. Re-evaluating digestion methods for highly siderophile element and ^{187}Os isotope analysis: Evidence from geological reference materials. *Chemical Geology* 384:27–46. https://doi.org/10.1016/j.chemgeo.2014.06.013.

Jarosewich E., Clarke R. S. Jr., and Barrows J. N. 1987. The Allende meteorite reference sample. *Smithsonian Contributions to the Earth Sciences* 27:1–49. https://doi.org/10.5479/si.00810274.27.1.

Kaskes P., Déhais T., de Graaff S. J., Goderis S., and Claeys P. 2021. Micro–X-ray fluorescence (µXRF) analysis of proximal impactites: High-resolution element mapping, digital image analysis, and quantifications. In *Large meteorite impacts and planetary evolution VI*, edited by W. U. Reimold and C. Koeberl. Geological Society of America Special Paper #550. Geological Society of America, Boulder, Colorado. pp. 171–206. https://doi.org/10.1130/2021.2550(07).

Kaskes P., de Graaff S. J., Feignon J.-G., Déhais T., Goderis S., Ferrière L., Koeberl C., Smit J., Wittmann A., Gulick S., Debaille V., Matielli N., and Claeys P. 2022. Formation of the crater suevite sequence from the Chicxulub peak ring: a petrographic, geochemical, and sedimentological characterization. *Geological Society of America Bulletin* 134:895–927. https://doi.org/10.1130/B36020.1.

Kawai Y., Nomura M., Murata H., Susuki T., and Fujii Y. 2001. Surface ionization of alkaline earth iodides in double filament system. *International Journal of Mass Spectrometry* 206:1–5. https://doi.org/10.1016/S1387-3806(00)00351-1.

Koeberl C. 1993. Instrumental neutron activation analysis of geochemical and cosmochemical samples: a fast and reliable method for small sample analysis. *Journal of Radioanalytical and Nuclear Chemistry* 168:47–60. https://doi.org/10.1007/BF02040877.

Koeberl C. 1995. Neutron activation analysis. In *Methods and instrumentations: results and recent developments*, edited by A. S. Marfunin. Springer-Verlag, Berlin, Heidelberg, New York. pp. 322–329.

Losiak A., Golebiowska I., Ferrière L., Wojciechowski J., Huber M. S., and Koeberl C. 2016. WIP: A web-based program for indexing planar features in quartz grains and its usage. *Meteoritics & Planetary Science* 51:647–662. https://doi.org/10.1111/maps.12614.

Luguet A., Shirey S. B., Lorand J.-P., Horan M. F., and Carlson R. W. 2007. Residual platinum-group minerals from highly depleted harzburgites of the Lherz massif (France) and their role in HSE fractionation of the mantle. *Geochimica et Cosmochimica Acta* 71:3082–3097. https://doi.org/10.1016/j.gca.2007.04.011.

Luguet A., Nowell G. M., and Pearson D. G. 2008. ^{184}Os/^{188}Os and ^{186}Os/^{188}Os measurements by negative thermal ionization mass spectrometry (N-TIMS): effects on interfering element and mass fractionation corrections on data accuracy and precision. *Chemical Geology* 248:342–362. https://doi.org/10.1016/j.chemgeo.2007.10.013.

Luguet A., Behrens M., Pearson D. G., Koenig S., and Herwartz D. 2015. Significance of the whole rock Re-Os ages in cryptically and modally metasomatized cratonic peridotites – Constraints from the HSE-Se-Te systematics. *Geochimica et Cosmochimica Acta* 164:441–463. https://doi.org/10.1016/j.gca.2015.06.016.

Mader D. and Koeberl C. 2009. Using instrumental neutron activation analysis for geochemical analyses of terrestrial impact structures: Current analytical procedures at the University of Vienna Geochemistry Activation Analysis Laboratory. *Applied Radiation and Isotopes* 67:2100–2103. https://doi.org/10.1016/j.apradiso.2009.04.014.

Mallmann G. and O'Neill H. St. C. 2007. The effect of oxygen fugacity on the partitioning of Re between crystals and silicate melt during mantle melting. *Geochimica et Cosmochimica Acta* 71:2837–2857. https://doi.org/10.1016/j.gca.2007.03.028.

Meisel T. and Moser J. 2004. Reference materials for geochemical PGE analysis: new analytical data for Ru, Rh, Pd, Os, Ir, Pt and Re by isotope dilution ICP-MS in 11 geological reference materials. *Chemical Geology* 208:319–338. https://doi.org/10.1016/j.chemgeo.2004.04.019.

Meisel T., Reisberg L., Moser J., Carignan J., Melcher F., and Brügmann G. 2003. Re–Os systematics of UB-N, a serpentinized peridotite reference material. *Chemical Geology* 201:161–179. https://doi.org/10.1016/S0009-2541(03)00234-1.

Morgan J. V., Gulick S., Mellet C. L., Green S. L., and Expedition 364 Scientists 2017. *Chicxulub: Drilling the K-Pg impact crater*. Proceedings of the International Ocean Discovery Program, 364. International Ocean Discovery Program, College Station, Texas. 164 p.

Möslinger M. 2006. PNAA version 1.0—User manual. Unpublished, 18p.

Müller W. F. and Défourneaux M. 1968. Deformationsstrukturen-im Quarz als Indikator für Stosswellen: Eine experimentelle Untersuchung an Quartz-Einkristallen. *Zeitschrift für Geophysik* 34:483–504.

Nagl P. and Mader D. 2019. X-ray fluorescence (XRF) and instrumental neutron activation analysis (INAA) for the geochemical analysis of rocks, presented on in-house control samples (abstract). *Mitteilungen der Österreichischen Mineralogischen Gesellschaft* 165:67.

Nisbet E. G., Dietrich V. J., and Esenwien A. 1979. Routine trace element determinations in silicate minerals and rocks by X-ray fluorescence. *Fortschritte der Mineralogie* 57:264–279.

Norrish K. and Chappell B. W. 1967. X-ray fluorescence spectrography. In *Physical Methods of Determinative Mineralogy*, edited by J. Zussman. Academic Press, London and New York. pp. 161–214.

Pearson D. G. and Woodland S. J. 2000. Solvent extraction/anion exchange separation and determination of PGEs (Os, Ir, Pt, Pd, Ru) and Re-Os isotopes in geological samples by isotope dilution ICP-MS. *Chemical Geology* 165:87–107. https://doi.org/10.1016/S0009-2541(99)00161-8.

Petrakakis K. and Nagl P. 1993. Program MAJORS (1986–1993), Version 11/93. Institute of Petrology, University of Vienna.

Potts P. J. 1987. *A handbook of silicate rock analysis*. Blackie, Glasgow. 622 p. https://doi.org/10.1007/978-94-015-3988-3.

Potts P. J. and Meisel T. 2015. Certificate of Analysis, IAG OKUM (Ultramafic rock). International Association of Geoanalysts. Available online at http://www.iageo.com.

Potts P. J., Bowles J. F. W., Reed S. J. B., and Cave M. R. 1995. *Microprobe techniques in the Earth sciences*. Chapman & Hall, London. 419 p. https://doi.org/10.1007/978-1-4615-2053-5.

Rae A. S. P., Collins G. S., Grieve R. A. F., Osinski G. R., and Morgan J. V. 2017. Complex crater formation: Insights from combining observations of shock pressure distribution with numerical models at the West Clearwater Lake impact structure. *Meteoritics & Planetary Science* 52:1330–1350. https://doi.org/10.1111/maps.12825.

Rehkämper M. and Halliday A. N. 1997. Development and application of new ion-exchange techniques for the separation of the platinum group and other siderophile elements from geological samples. *Talanta* 44:663–672. https://doi.org/10.1016/S0039-9140(96)02100-5.

Reinhard M. 1931. *Universaldrehtischmethoden*. Birkhäuser, Basel, Switzerland. 118 p.

Schulz T., Luguet A., Wegner W., van Acken D., and Koeberl C. 2016. Target rocks, impact glasses, and melt rocks from the Lonar crater, India: Highly siderophile element systematics and Sr-Nd-Os isotopic signatures. *Meteoritics & Planetary Science* 51:1323–1339. https://doi.org/10.1111/maps.12665.

Sherman J. 1955. The theoretical derivation of fluorescent X-ray intensities from mixtures. *Spectrochimica Acta* 7:283–306. https://doi.org/10.1016/0371-1951(55)80041-0.

Son T. H. and Koeberl C. 2005. Chemical variation within fragments of Australasian tektites. *Meteoritics & Planetary Science* 40:805–815. https://doi.org/10.1111/j.1945-5100.2005.tb00156.x.

Stöffler D. and Langenhorst F. 1994. Shock metamorphism of quartz in nature and experiment: I. Basic observation and theory. *Meteoritics & Planetary Science* 29:155–181. https://doi.org/10.1111/j.1945-5100.1994.tb00670.x.

Van Acken D., Hoffmann J. E., Schorscher J. H. D., Schulz T., Heuser A., and Luguet A. 2016. Mantle sources of High-Al komatiites from the Mesoarchaean Quebra Osso Group, Minas Gerais, Brazil: Trace elements, HSE systematics and Os isotopic signatures. *Chemical Geology* 422:108–121. https://doi.org/10.1016/j.chemgeo.2015.12.015.

Vansteenberge S., de Winter N. J., Sinnesael M., Xueqin Z., Verheyden S., and Claeys P. 2020. Benchtop μXRF as a tool for speleothem trace elemental analysis: Validation, limitations and application on an Eemian to early Weichselian (125–97 ka) stalagmite from Belgium. *Palaeogeography, Palaeoclimatology, Palaeoecology* 538:109460. https://doi.org/10.1016/j.palaeo.2019.109460.

Völkening J., Walczyk T., and Heumann K. G. 1991. Osmium isotope ratio determinations by negative thermal ionization mass-spectrometry. *International Journal of Mass Spectrometry and Ion Processes* 105:147–159. https://doi.org/10.1016/0168-1176(91)80077-Z.

Wainwright A. N., Luguet A., Fonseca R. O. C., and Pearson D. G. 2015. Investigating metasomatic effects on the [187]Os isotopic signature: A case study on micrometric base metal

sulfides in metasomatised peridotite from the Letlhakane kimberlite (Botswana). *Lithos* 232:35–48. https://doi.org/10.1016/j.lithos.2015.06.017.

Walther C. and Wendt K. 2020. Radioisotope mass spectrometry. In *Handbook of Radioactivity Analysis (Fourth Edition)*, edited by M. F. L'Annunziata. Elsevier, Amsterdam. pp. 861–898. https://doi.org/10.1016/B978-0-12-814397-1.00008-X.

Watt I. M. 1997. *The principles and practice of electron microscopy, 2nd ed.* Cambridge University Press, Cambridge. 484 p. https://doi.org/10.1017/CBO9781139170529.

Xie X., Yan M., Wang C., Li L., and Shen H. 1989. Geochemical Standard Reference Samples GSD 9–12, GSS 1–8 and GSR 1–6. *Geostandards Newsletter* 13:83–179. https://doi.org/10.1111/j.1751-908X.1989.tb00469.x.

CHAPTER 5: Characterization of shocked quartz grains from Chicxulub peak ring granites and shock pressure estimates

Authors

Jean-Guillaume Feignon, Ludovic Ferrière, Hugues Leroux, and Christian Koeberl.

Publication status

Personal contribution

Sample selection, petrographic descriptions, universal stage investigations, scanning electron microscope observations, shock pressure estimates, interpretation of the results, writing (original draft), writing (revision and editing).

Characterization of shocked quartz grains from Chicxulub peak ring granites and shock pressure estimates

Jean-Guillaume FEIGNON [iD]*[1], Ludovic FERRIÈRE [iD][2], Hugues LEROUX [iD][3], and Christian KOEBERL [iD][1]

[1]Department of Lithospheric Research, University of Vienna, Althanstrasse 14, A-1090, Vienna, Austria
[2]Natural History Museum, Burgring 7, A-1010 Vienna, Austria
[3]Univ-Lille, CNRS, INRAE, Centrale Lille, UMR 8207 – UMET – Unité Matériaux et transformations, 59655 Villeneuve d'Ascq, France
*Corresponding author. E-mail: jean-guillaume.feignon@univie.ac.at

Abstract–Planar deformation features (PDFs) in quartz are a commonly used and well-documented indicator of shock metamorphism in terrestrial rocks. The measurement of PDF orientations provides constraints on the shock pressure experienced by a rock sample. A total of 963 PDF sets were measured in 352 quartz grains in 11 granite samples from the basement of the Chicxulub impact structure's peak ring (IODP-ICDP Expedition 364 drill core), with the aim to quantify the shock pressure distribution and a possible decay of the recorded shock pressure with depth, in the attempt to better constrain shock wave propagation and attenuation within a peak ring. The investigated quartz grains are highly shocked (99.8% are shocked), with an average of 2.8 PDF sets per grain; this is significantly higher than in all previously investigated drill cores recovered from Chicxulub and also for most K-Pg boundary samples (for which shocked quartz data are available). PDF orientations are roughly homogenous from a sample to another sample and mainly parallel to $\{10\bar{1}3\}$ and $\{10\bar{1}4\}$ orientations (these two orientations representing on average 68.6% of the total), then to $\{10\bar{1}2\}$ orientation, known to form at higher shock pressure. Our shock pressure estimates are within a narrow range, between ~16 and 18 GPa, with a slight shock attenuation with increasing depth in the drill core. The relatively high shock pressure estimates, coupled with the rare occurrence of basal PDFs, i.e., parallel to the (0001) orientation, suggest that the granite basement in the peak ring could be one of the sources of the shocked quartz grains found in the most distal K-Pg boundary sites.

INTRODUCTION

Quartz grains with shock metamorphic features, commonly referred to as "shocked quartz," are a typical diagnostic criterion used for the identification of hypervelocity impact structures on Earth (e.g., Stöffler and Langenhorst 1994; Grieve et al. 1996; French 1998; French and Koeberl 2010; Deutsch et al. 2015; Stöffler et al. 2017; and references therein). In addition to the simple optical properties of quartz and its natural abundance in terrestrial crustal rocks, its shock metamorphic features, forming at a wide pressure range, are well characterized. Upon shock compression, quartz develops irregular fractures (which are not diagnostic shock effects) and several types of planar microstructures, including planar fractures (PFs), feather features (FFs), and planar deformation features (PDFs), all of them being crystallographically controlled (e.g., French and Short 1968; Engelhardt and Bertsch 1969; Stöffler and Langenhorst 1994; Grieve et al. 1996; French 1998; French and Koeberl 2010; Poelchau and Kenkmann 2011; Ferrière and Osinski 2013; and references therein).

Planar fractures start to form at pressures ~>5 GPa; they are parallel open fractures with a spacing of ~15–20 μm or more (see e.g., Stöffler and

[Correction added on 24 October 2020 after first online publication: author name Ludovic FerriÈre is amended with Ludovic Ferrière.]

Langenhorst 1994; Grieve et al. 1996; French and Koeberl 2010; Ferrière and Osinski 2013; and references therein). Feather features, which are assumed to start to form at pressures ~>7 GPa, are narrowly spaced, short, parallel to subparallel lamellae that branch off of PFs (see Poelchau and Kenkmann 2011). In this study, we focused our attention on PDFs, which start forming ~>8 to 10 GPa and that are composed of narrow, straight, individual planar lamellae (usually less than 200 nm thick) of amorphous material, forming parallel sets spaced 2–10 μm apart (e.g., Engelhardt and Bertsch 1969; Stöffler 1972; Stöffler and Langenhorst 1994). In metamorphosed and altered rocks, PDFs can be recrystallized, but they are still optically visible due to decoration of arrays of small fluid inclusions (Goltrant et al. 1992; Trepmann and Spray 2006).

At pressures higher than 30–35 GPa for non-porous crystalline rocks (such as the samples investigated here), but already at pressures as low as ~5.5 GPa for porous sandstones (Kieffer et al. 1976; Stöffler and Langenhorst [1994] and references therein; Kowitz et al. 2013a, 2013b, 2016), diaplectic quartz glass forms by solid-state transformation, without melting. In porous sandstones and pressures as low as ~7.5 GPa, high-pressure polymorphs of quartz such as coesite and stishovite may form (Mansfeld et al. 2017; Folco et al. [2018], and references therein), whereas for non-porous crystalline rocks, coesite and stishovite form at pressure ranges between 30 and 60 GPa and between 12 and 45 GPa, respectively (e.g., Stöffler and Langenhorst [1994], and references therein). At high temperature (>1500 °C), without necessarily requiring high shock pressures, quartz melts and forms lechatelierite, a monomineralic quartz melt (Stöffler and Langenhorst 1994; French and Koeberl [2010], and references therein).

Planar fractures and PDFs are generally oriented parallel to planes of low Miller–Bravais indices, such as (0001) and {10$\bar{1}$1} for PFs and (0001), {10$\bar{1}$3}, and {10$\bar{1}$2} for PDFs (see Ferrière et al. [2009a], and references therein). In crystals showing a (strong) undulose extinction (easily visible under the optical microscope in cross-polarized light), due to a plastic deformation of the crystal lattice (e.g., Trepmann and Spray 2005), the PDFs can look curved. In some rare cases, kinkbands can be seen.

The orientation of PDFs can be characterized and measured using the transmission electron microscope (TEM; e.g., Goltrant et al. 1991), or with a spindle stage (e.g., Bohor et al. 1987) when dealing with single quartz grains. However, to measure and index a large number of PDF sets in a large number of grains in a given sample, only the universal stage (U-stage) technique can be used efficiently; this method is inexpensive, but time consuming if one is to obtain statistically robust, significant, and precise results (see recommendations in Ferrière et al. 2009a; Holm-Alwmark et al. 2018).

The different shock metamorphic features described above and in particular PDFs are important for the investigation of shock pressures experienced by a given rock sample, as the formation of specific PDF orientations depends on the shock pressure, allowing pressure to be derived based on PDF orientation statistics. The shock pressure calibration is based on shock experiments (e.g., Hörz 1968; Müller and Défourneaux 1968). Shock barometry studies have improved the understanding of crater formation processes, in particular shock wave propagation and attenuation with increasing distance from the point of impact, and in some cases to tentatively estimate from which part of the target rock (i.e., sampling horizon) samples were derived before being ejected and incorporated into proximal impactites or even distal ejecta (e.g., Nakano et al. 2008). Moreover, shock barometry results can be integrated to develop and constrain numerical modeling of impact crater, from central uplift (e.g., Ferrière et al. 2008) to peak ring formation (e.g., Rae et al. 2019).

The ~200 km diameter (e.g., Gulick et al. 2013) Chicxulub impact structure, located mostly on the Yucatán peninsula (Mexico), was identified following large-scale negative Bouguer gravity anomaly and magnetic anomalies (Fig. 1). The characterization of shocked quartz grains in samples derived from inside the structure confirmed its impact origin (Penfield and Camargo 1981; Hildebrand et al. 1991). The impact structure is buried under Cenozoic limestones, and the only surface expression of the structure is a ring of cenotes (i.e., water-filled sinkholes). The Chicxulub impact structure, 66.05 Myr old (Sprain et al. 2018), is related to the Cretaceous–Paleogene (K-Pg) boundary, which is evidenced by a distinct ejecta distribution pattern related to distance from the Chicxulub (Alvarez et al. 1980; Smit 1999; Schulte et al. 2010). Impact ejecta material can be found in several K-Pg boundary layers across the world. Shocked quartz grains with PDFs in K-Pg boundary layers were first described by Bohor et al. (1984) and then found in more than 50 K-Pg sites worldwide (e.g., Bohor et al. 1987; Claeys et al. 2002). Chicxulub is the only known impact structure on Earth with a well-preserved, nearly intact, peak ring (80–90 km in diameter), indicated by seismic reflection and refraction surveys (Gulick et al. [2013], and references therein).

Investigating the rocks that make up this peak ring and its nature, chemistry, and origin, as well as its formation mechanism, were some of the primary aims
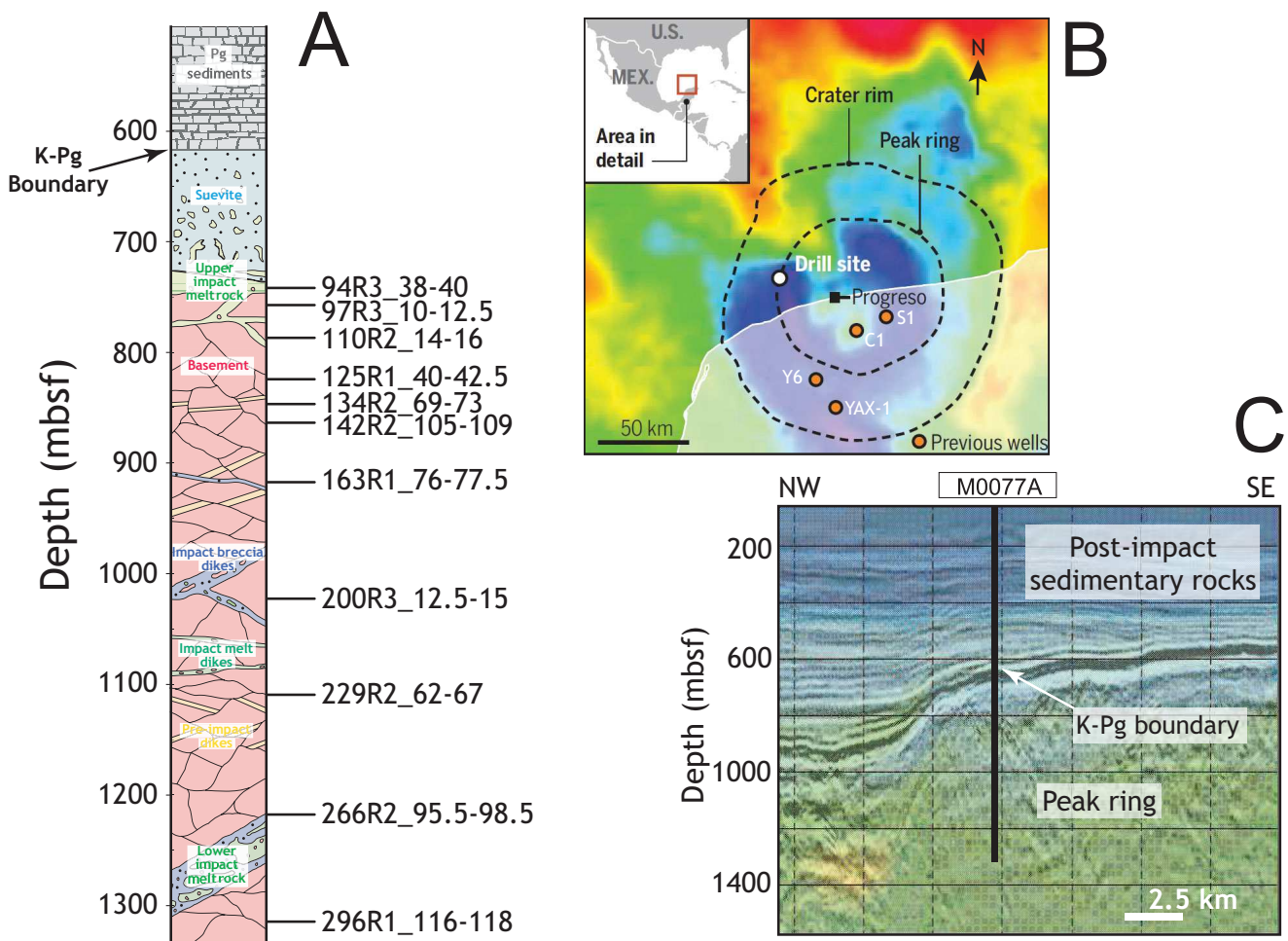
Fig. 1. A) Simplified representation of the stratigraphic log of hole M0077A with the location of the samples that were investigated in this study. Sample references are indicated on the right side of the log (modified from Morgan et al. 2016). B) Drilling site location on the Bouguer gravity anomaly map of the impact structure. Locations of previous drill cores Y6 and YAX-1 are also shown (modified from Hand 2016). C) Radial seismic profile of the peak ring at the drilling site and borehole location (from Morgan et al. 2016). (Color figure can be viewed at wileyonlinelibrary.com.)

of the IODP-ICDP Expedition 364 (Morgan et al. 2017). A continuous core (M0077A) was recovered between 505.7 and 1334.7 mbsf (meters below sea floor). It was divided in three main lithological units (1) a "postimpact" Cenozoic sedimentary rocks section (from 505.7 to 617.3 mbsf), (2) an "upper peak ring" section (from 617.3 to 747.0 mbsf) comprised of ~105 m melt-bearing polymict impact breccia (suevite) overlaying ~25 m of impact melt rocks, and (3) a "lower peak ring" section (from 747.0 to 1334.7 mbsf) consisting of granitoid (coarse-grained granite with aplite and pegmatite facies dikes) intruded by several pre-impact subvolcanic dikes and intercalations of millimeter to decameter suevite and impact melt rocks (Fig. 1). The occurrence of crystalline basement rocks at such depths suggests that they were uplifted at least 2.25 km (Morgan et al. 2016). The peak ring was then

intensively altered by a long living, more than 1 Ma, hydrothermal system (Kring et al. 2020).

In this study, we focus on investigations of shocked quartz grains in granite samples recovered from the "lower peak ring" section with the aim to quantify the shock pressure distribution and a possible decay of the recorded shock pressure with depth. The investigated samples represent a large and unique unit of mid-crustal basement rocks (derived from 8–10 km depth; Morgan et al. 2016) that were shocked and then moved outward and upward, then inward before collapsing outward (see e.g., figures in Riller et al. [2018] and Rae et al. [2019]), thus offering the unique opportunity to study and to constrain shock pressures recorded in rocks forming a peak ring as well as to better constrain shock wave propagation and attenuation in a peak ring. In addition, because the

investigated rock unit is possibly one of the sources of shocked quartz grains found in ejecta from numerous K-Pg boundary sites, our results are also here compared with previous PDF measurements published on proximal and distal sites (Nakano et al. [2008], and references therein).

MATERIALS AND METHODS

Forty-one polished thin sections were prepared from a selected number of granite samples taken at regular intervals between 747.0 and 1334.7 mbsf, in the "lower peak ring" section. They were investigated for their shock metamorphic features in quartz and in other minerals using an optical microscope equipped with a U-stage at the University of Vienna and a JEOL JSM-6610 variable pressure (VP) scanning electron microscope (SEM) at the Natural History Museum (Vienna, Austria). An FEI Tecnai G2 20 transmission electron microscope (TEM) on focused ion beam (FIB) foils was also used at the University of Lille (Villeneuve d'Ascq, France) to better characterize the nature of the PDFs. Ten thin sections were selected for additional investigation using the U-stage (Fig. 1; Table 1). In addition, one granite clast in an impact melt rock sample (94R3_38-40) located in the lower part of the "upper peak ring" section, at 743.6 mbsf, was also investigated for comparison, resulting in a total of 11 thin sections investigated. They were selected due to their relative abundance in quartz grains (at least 20 grains per thin section). Additionally, due to the limitations of the U-stage method, quartz grains should be preferentially located in the central part of the thin section to be investigated (i.e., in the case of rectangular thin sections like those that we have investigated here, only about 3/5 of the section can be investigated with the U-stage). In order to obtain reliable statistics on PDF orientations, at least 75 PDF sets were measured for each sample (Ferrière et al. 2009a).

Measurements of the crystallographic orientation of PDFs were obtained using a U-stage (Emmons 1943) mounted on an optical microscope and following the method described in Stöffler and Langenhorst (1994) and Ferrière et al. (2009a). This technique consists of four main steps, including (1) measuring the studied quartz grain c-axis; (2) determining the poles perpendicular to planes of all PDFs visible in the quartz grain investigated; (3) plotting on a stereographic Wulff net the c-axis and poles to all PDF sets; and (4) indexing, where possible, the PDFs measured using the new stereographic projection template (NSPT), allowing the indexing of 15 typical PDF crystallographic orientations in quartz, within a 5° envelop of measurement error (Ferrière et al. [2009a] and

references therein). In this study, c-axis and PDF sets were measured twice, that is, the c-axis and PDFs are measured, then the inner stage is rotated 180° and the measurements are repeated. This is done in order to avoid measurement errors. For some orientations (c-axis and/or PDF sets), a difference of 2–3° was common from the first measurement to the second, inducing in a few cases a slightly higher error than the previously stated 5°. When a set of PDF orientations does not plot inside the envelope of typical PDF orientations from the NSPT, the set is considered as unindexed.

The measurements were indexed using both the manual and the automated methods, using the web-based indexing program (WIP; Losiak et al. 2016). The manual indexing was done at first then using WIP in order to verify the results obtained with the manual indexing method. The manual indexing allows to correct the artificially higher proportion of $\{10\bar{1}4\}$ orientations as found using WIP due to the program failing at considering $\{10\bar{1}4\}$ as a minor orientation, subordinate to the $\{10\bar{1}3\}$ orientation. In case of a measurement in the overlapping area between $\{10\bar{1}4\}$ and $\{10\bar{1}3\}$, the orientation was recorded as $\{10\bar{1}3\}$ (Ferrière et al. 2009a; Holm-Alwmark et al. 2018). In the case of grains displaying a strong undulose extinction, the c-axis has to be measured in several areas of the grain, and only the manual indexing method allows us to index the PDFs relative to each other, whereas each measurement has to be considered as a separate grain in WIP.

All the calculated frequencies presented in this study are absolute frequencies, as described by Engelhardt and Bertsch (1969). They are calculated as the number of symmetrically equivalent planes measured in n quartz grains, divided by the total number of measured PDF sets in n quartz grains.

For assigning average shock pressures to each given sample, the method described in Holm-Alwmark et al. (2018) was used. This method is adapted to estimate shock pressures in non-porous crystalline rocks. To summarize, the average shock pressure for a given sample is derived from a classification of each quartz grain in the sample depending of the measured orientations of PDFs. A shock pressure is assigned to each quartz grain, then a mean value is calculated, giving an average shock pressure for the sample. Holm-Alwmark et al. (2018) defined six different classification types: quartz grains with no PDFs and from A to D types. Quartz grains with no PDFs were assigned a shock pressure of 5 GPa, which is the mean pressure between the onset of shatter cones (2 GPa; e.g., French 1998) and the formation of type A grains. Type A grains (7.5 GPa) contain exclusively basal PDFs (parallel to [0001]). Type B grains (15 GPa) contain PDFs that are parallel to one or more $\{10\bar{1}3\}$- or

Table 1. Petrographic description of the investigated granite samples, based on optical microscopy observations.

Sample	Depth (mbsf)	Lithologies	Main mineral phases	Accessory minerals	Shock/deformation features	Alteration features
94R3_38-40	743.6	Partly digested coarse-grained granite clast (2–3 cm, grain size: ~0.1 to 1.1 cm) included in dark gray, clast-poor (clast size <1 mm) impact melt rock (+some brown greenish veins) with flowing texture. Clasts are undigested rock clasts or individual minerals, both with reaction rims. Matrix glassy and very finely crystallized (microliths)	Granite: K-Feldspar, Quartz, Plagioclase, Micas (completely decomposed). Impact melt: Clasts: quartz, K-feldspar and plagioclase. Matrix: Microliths of plagioclase and pyroxene	Apatite, Titanite, Zircon, Magnetite (?)	Fractures. Microbrecciated areas at the granite rim. Quartz shocked with multiple decorated PDF sets, PFs and FFs, toasted and undulose extinction. Titanite heavily fractured. Ballen quartz (type V; in impact melt rock)	Postimpact calcite filling vesicles (in impact melt rock) and fractures (in granite)
97R3_10-12.5	752.5	Coarse-grained granite (Grain size: ~0.2 to 1.5 cm)	K-feldspar, Quartz, Plagioclase, Biotite (rare and mostly chloritized)	Chlorite, Muscovite, Apatite, Titanite, Zircon, Epidote, Magnetite	Fractures. Cataclasite (submillimetric) vein cutting the thin section, microbrecciated quartz, and feldspars (grains subrounded). Some minerals are sheared. Quartz shocked with multiple decorated PDF sets, PFs and FFs, undulose extinction, some kinkbanding. PFs in feldspars. Kinkbanding in biotite. Apatite and titanite with planar microstructures	Strong sericitization in feldspars cores, less at the rim. Postimpact calcite filling fractures
110R2_14-16	788.1	Coarse-grained granite (Grain size: ~0.1–0.5 cm)	K-feldspar, Quartz, Plagioclase, Chloritized biotite	Chlorite, Muscovite, Titanite, Magnetite, Apatite, Zircon	Fracturing. Small cataclasite vein with microbrecciated shocked quartz and feldspar. Shocked quartz with PFs, FFs and decorated PDFs (up to 3 visible, undulose extinction. Titanite strongly fractured. Kinkbanding common in muscovite and chlorite	Few calcite filling fractures. Variable sericitization of feldspar

Table 1. *Continued.* Petrographic description of the investigated granite samples, based on optical microscopy observations.

Sample	Depth (mbsf)	Lithologies	Main mineral phases	Accessory minerals	Shock/deformation features	Alteration features
125R1_40-42.5	826.7	Coarse-grained granite (Grain size: ~0.1–1.2 cm)	K-feldspar, Quartz, Plagioclase, Biotite (chloritized)	Chlorite, Muscovite, Apatite, Titanite, Magnetite, Zircon	Fracturing. Quartz shocked with PFs, FFs, and multiple decorated PDF sets. Shearing, PFs, and planar microstructures in feldspar. Planar microstructures in apatite. Kinkbanding common in biotite-chlorite	Post-impact calcite filling some fractures
134R2_69-73	845.9	Coarse-grained granite (Grain size: 0.5–1.5 cm)	K-feldspar, Quartz, Plagioclase, Biotite (chloritized)	Muscovite, Apatite, Titanite, Epidote, Zircon, Magnetite	Strong fracturing. Shocked quartz with PFs, FFs, and decorated PDFs. PFs in feldspar. Shearing and strong fracturing in epidote. Shearing in apatite. Kinkbanding in chlorite/micas	Sericitization of feldspar. Postimpact calcite filling fractures
142R2_105-109	861.9	Coarse-grained granite (Grain size: ~0.5–1.0 cm)	K-feldspar, Quartz, Plagioclase, Biotite (rare and chloritized)	Chlorite, Titanite, Apatite, Magnetite	Fracturing. Shocked quartz with PFs, FFs, and decorated PDFs (2–3 sets commonly visible), undulose extinction. PFs (up to 2 sets) and planar microstructures in feldspar. Clear planar microstructures in titanite	Variable sericitization of feldspar. Some postimpact calcite filling in calcite
163R1_76-77.5	915.5	Coarse-grained granite (Grain size ~0.5–1.5 cm)	K-feldspar, Quartz, Plagioclase, Biotite (strong chloritization)	Chlorite, Titanite, Magnetite, Zircon, Monazite [?]	Shocked quartz with PFs, FFs, and slightly decorated PDFs (up to 3 sets observed), undulose extinction. Fracturing and planar microstructures in feldspar, titanite	Sericitization common in feldspar. Some fractures filled with opaque minerals
200R3-12.5-15	1021.0	Coarse-grained granite (Grain size: ~0.2–0.8 cm)	K-feldspar, Quartz, Plagioclase, Biotite (rare and often chloritized)	Chlorite, Muscovite, Apatite, Titanite, Zircon, Epidote, Magnetite	Fracturing. Thin cataclastic areas with microbrecciated quartz and feldspar (subrounded). Quartz with PFs, FFs, and decorated PDFs, low undulose extinction. Kinkbanding (common) in micas/chlorite. Planar microstructures in apatite (2 sets) and titanite	Strong sericitization in some feldspars. Postimpact calcite filling fractures

Table 1. *Continued.* Petrographic description of the investigated granite samples, based on optical microscopy observations.

Sample	Depth (mbsf)	Lithologies	Main mineral phases	Accessory minerals	Shock/deformation features	Alteration features
229R2_62-67	1107.2	Coarse-grained granite (Grain size: <0.1–1.3 cm)	K-feldspar Quartz Plagioclase	Muscovite Chlorite Apatite Titanite Epidote (Fe) Magnetite Zircon Monazite (?)	Open fracture Quartz with PFs, FFs, and decorated PDFs, K-feldspar with PFs, and planar microstructures Planar microstructures in apatite and titanite Kinkbanding in micas/chlorite (common) Shearing in feldspar, apatite	Sericitization in feldspar Some postimpact calcite
266R2_95.5-98.5	1220.5	Coarse-grained granite (Grain size: < 0.8 cm)	K-feldspar Quartz Plagioclase Biotite	Muscovite Chlorite Opaque minerals (Magnetite [?]) Apatite Epidote Titanite	Strong fracturing, few shearing Cataclasite area with quartz, feldspar, and opaque minerals no mineral deformation Shocked quartz with PFs, FFs, and decorated PDFs (1–2 sets visible) Planar microstructures in feldspar Kinkbanding and fracturing (common) in biotite	Some sericitization in plagioclase Fracture filling with opaque minerals Low chloritization of biotite
296R1_116-118	1311.1	Coarse-grained granite (Grain size: ~0.5–1.5 cm)	K-feldspar Quartz Plagioclase	Few/tiny accessory phases Chlorite (former biotite) Muscovite Apatite Magnetite Zircon	Thin cataclasite veins with shocked minerals (quartz and felsdpar) Strong fracturing Shearing in minerals Shocked quartz with PFs, FFs, and decorated PDF sets (at least 2 visible), common undulose extinction Kinkbanding in plagioclase and rare in quartz	Postimpact calcite filling fractures and partially filling PFs in quartz Some sericite in plagioclase

{10$\bar{1}$4}-equivalent plane(s). Type B2 grains (16.5 GPa) contain three or more PDFs with {10$\bar{1}$3}- or {10$\bar{1}$4}-equivalent planes. Type C grains (17 GPa) contain PDFs with high index orientation(s), such as {11$\bar{2}$2} and/or {22$\bar{4}$1}, and type D grains (20 GPa) contain PDFs parallel to one or more {10$\bar{1}$2}-equivalent orientation(s). An additional type, type E, was added by Fel'dman (1994) corresponding to quartz grains transformed to diaplectic glass. However, no type E grains were identified in any of the investigated samples.

RESULTS AND DISCUSSION

Sample Descriptions

The investigated samples mainly consist of pervasively deformed, locally micro-brecciated (presence of cataclastic veins) and sheared, coarse-grained leucogranite (Fig. 2). The grain size ranges from ~0.2 to 4 cm, but also submillimeter-sized grains occur in cataclasite veins crosscutting some of the granite samples. Some of the cataclasites exhibit a greenish color, due to a hydrothermal overprint (Kring et al. 2020). The mineral assemblage consists mainly of K-feldspar (orthoclase, ~25–40%); plagioclase (~25–35%), which is often highly sericitized; quartz (~25–35%); and, to a lesser extent, biotite (~1–5%), often chloritized. The main accessory minerals are muscovite, (fluor)apatite, titanite, epidote (piemontite), zircon, (titano)magnetite, and allanite. Other accessory minerals, including monazite, ilmenite, rutile, chalcopyrite, cobaltoan pyrite, stolzite/raspite, galena, uranothorite, and uranothorianite, were also detected during our SEM survey. Shock features were observed in alkali-feldspar and plagioclase (i.e., PFs filled with opaque minerals and also some possible PDFs; see Pittarello et al. 2020), titanite, and apatite (with different types of planar microstructures; Timms et al. 2019; Cox et al. 2020). Kinkbanding is common in biotite, muscovite, and chlorite, and is also observed, to a lesser extent, in plagioclase and quartz. Postimpact calcite veinlets commonly cut the granite (see details in Table 1).

The investigated granite clast (3.5 cm in size) in sample 94R3_38-40 occurs in a dark-greenish, clast-poor, impact melt rock sample. Other clasts in this impact melt rock sample (<1 mm size) include granite and mineral clasts, such as K-feldspar, plagioclase, shocked quartz (with PDFs, some toasted), and ballen silica of type V (i.e., characterized by a chert-like texture that formed following a complete recrystallization of the ballen; see Ferrière et al. 2009b), and, to a lesser extent, calcite (see Table 1).

In the selected thin sections, a total of 352 quartz grains were investigated. Nearly all (99.8%) of the observed grains are shocked (only one apparently unshocked quartz grain was seen during our survey), including PFs with (or without) FFs and PDFs (up to 7 sets of PDFs as seen under the U-stage). In addition, almost all quartz grains show undulose extinction which can be occasionally extreme, and in a few cases kinkbands (Fig. 3). As seen under the optical microscope and further documented under the SEM, the PFs enhance fluid circulation inside the grains as shown by the corroded margins of the PFs and the presence of postimpact, secondary calcite filling the PFs. Similar observations were made by Kring et al. (2020) on granite samples from the peak ring. The PDFs are decorated with trails of vugs or tiny fluid inclusions. The TEM observations allow us to resolve the PDFs at high magnification, showing that they are composed of aligned fluid inclusions or vugs and dislocations (Fig. 3), microstructures typical of annealed PDFs. Free dislocations and subgrain boundaries were also observed. Dislocations preferentially occur along the fluid inclusions trails. No glass-bearing lamellae were detected in the investigated samples. The observation that PDFs are annealed and decorated indicates that the originally amorphous PDFs were recrystallized during a postshock thermal episode. Kinkbanding of some shocked quartz grains shows that, after the propagation of the shock wave and formation of the PDFs, the granitoids from the "lower peak ring" section were subject to intense stress and were sheared, as also indicated by mineral-specific fracturing and localized cataclasites (Rae et al. 2019).

Crystallographic Orientations of the PDFs

The U-stage was used to characterize the crystallographic orientation of both PFs and PDFs in quartz grains. In total, 963 sets of PDF (and 97 sets of PF) were measured in 352 quartz grains, resulting in an average of ~2.8 PDF sets per grain (see Table 2).

PFs are mainly oriented parallel to {10$\bar{1}$1} (~60%), (0001) (~20%), and, to a lesser extent, to {10$\bar{1}$3} (~8%) orientations.

Figure 4 and Table 3 show the PDFs orientation frequencies and the proportion of unindexed sets. Our measurements for all the granite samples, including also the granite clast in impact melt rock, show that PDFs with {10$\bar{1}$3} and {10$\bar{1}$4} orientations are most abundant, together representing 68.6% of the total measured orientations. Then, by decreasing abundances, PDFs parallel to {10$\bar{1}$2} (7.4%), {10$\bar{1}$1} (3.7%), {11$\bar{2}$2} (3.1%), and {22$\bar{4}$1} (3.0%) occur, with variations from sample to sample (see Fig. 4 and Table 3). Other orientations have frequencies below 2% with only a few basal PDFs (i.e., parallel to [0001]; 1.7%). No PDFs with {51$\bar{6}$0} orientation were observed in our survey.
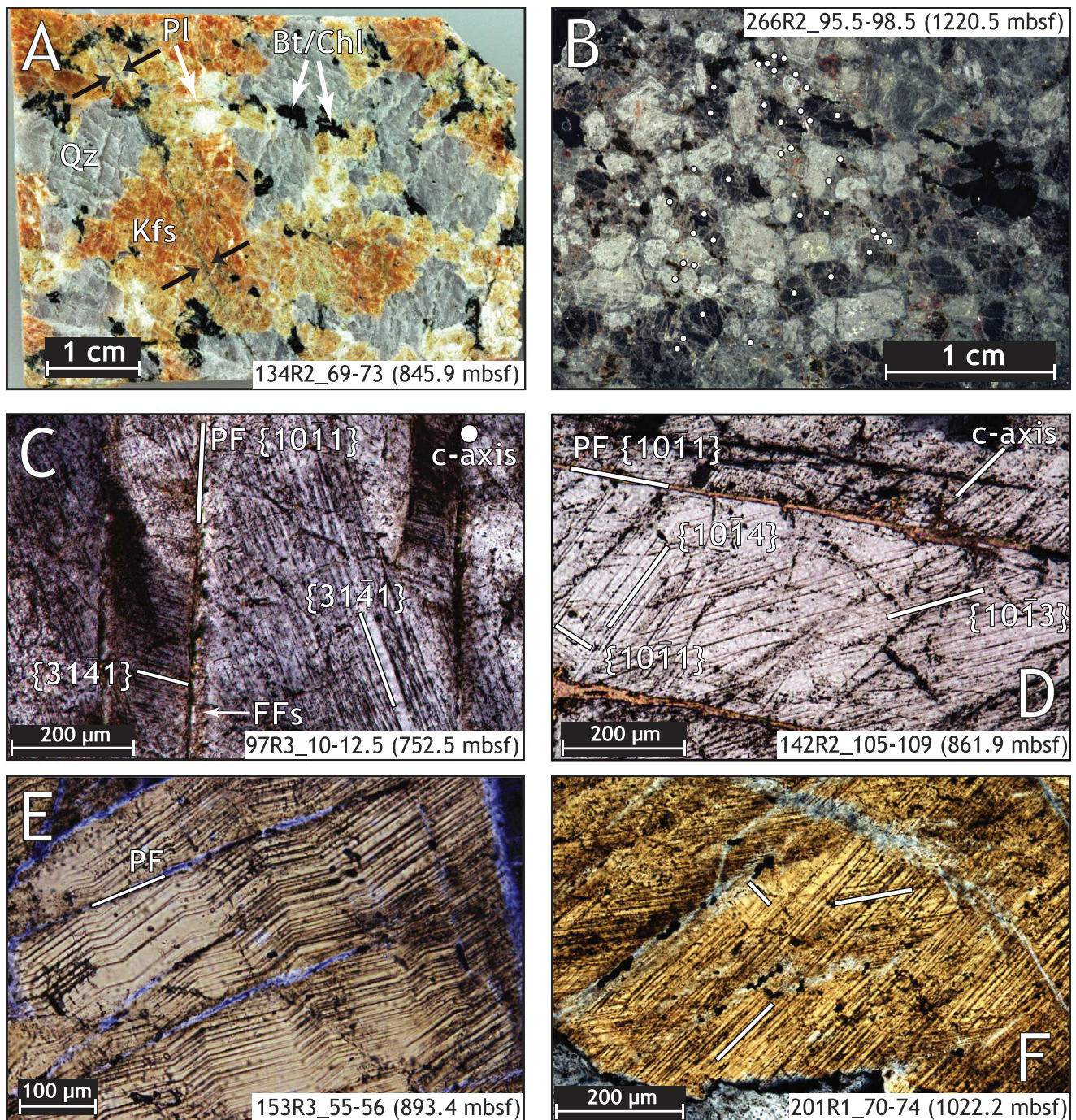
Fig. 2. Macrophotograph (A) and thin section scan (B) of typical coarse-grained granite samples from the "lower peak ring" section that were investigated in this study. See Table 1 for the petrographic descriptions. A) All minerals are highly fractured. A thin greenish (hydrothermally altered) cataclasite vein cross-cut the sample on the left side (black arrows). Bt: biotite, Chl: chlorite, Kfs: K-feldspar, Pl: plagioclase, and Qz: quartz. B) Thin section scan of one of the granite samples investigated under the U-stage. The white dots indicate the positions of the investigated quartz grains. Thin section photomicrographs of shocked quartz grains (all in cross polarized light). C) Shocked quartz with one set of PF with branched FFs and two sets of decorated PDFs; as indicated, the *c*-axis of the grain is perpendicular to the field of view. The deformation of the crystal is evidenced with the undulose extinction. D) Quartz grain with one set of PF filled with postimpact calcite and three sets of decorated PDFs. E) Shocked quartz with kinkbanding. As the kinkbanding affected both PF and PDF, it must have occurred after the onset of PF and PDF formation (this specific sample was not measured with U-stage). F) Shocked quartz grain with two prominent decorated PDF sets and a third set of PDFs that are barely visible in this photograph, but are indicated with a white mark (sample not measured with the U-stage). (Color figure can be viewed at wileyonlinelibrary.com.)
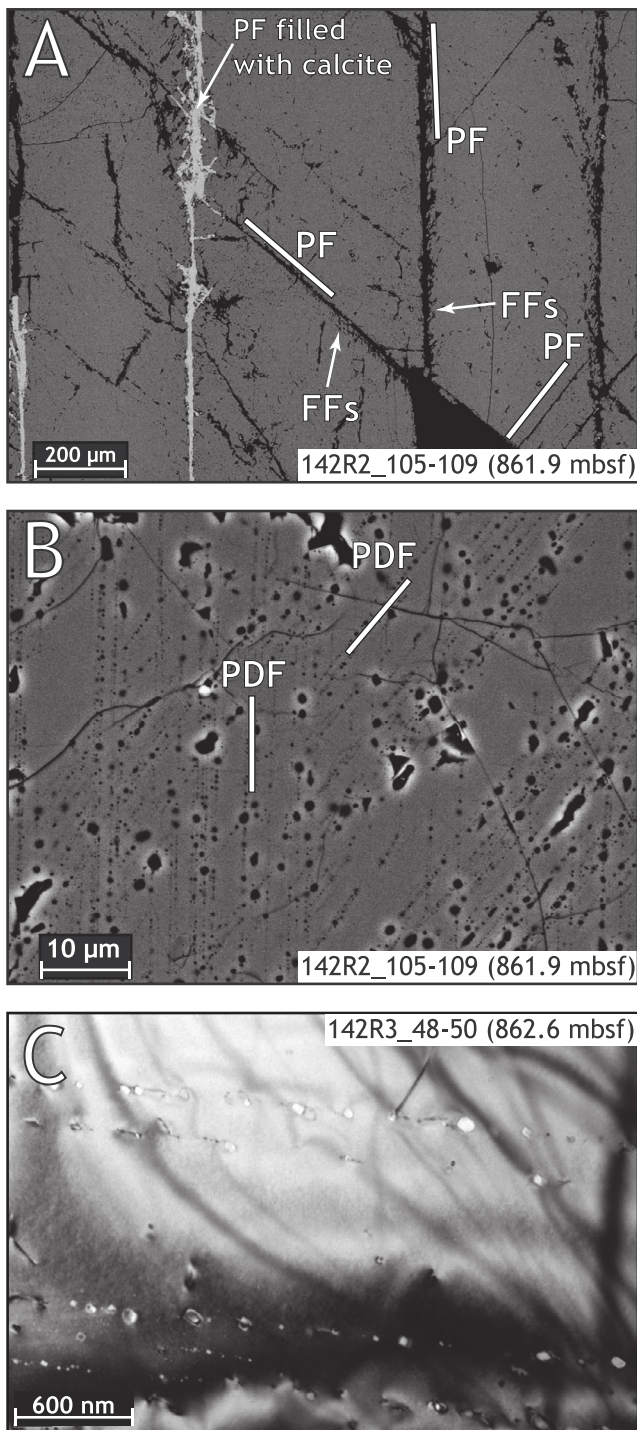
Fig. 3. A and B) SEM backscattered electron (BSE) images of shocked quartz grains from sample 142R2_105-109. A) Shocked quartz grain with three sets of PFs, including one set filled with postimpact calcite. The FFs are also evidenced, branching off the PFs. Note in both PFs and FFs cases the dissolution of quartz at the margins. B) Two sets of highly decorated PDFs. C) Bright field transmission electron microscope (TEM) micrograph of a quartz grain with one set of decorated PDFs. Aligned fluid inclusions or vugs are visible as well as dislocations, preferentially occurring along the vugs/fluid inclusions.

The frequency of unindexed sets is below 15%, on average of 6.1%, which is reasonable considering that quartz grains often exhibit strong undulose extinction. Only one sample (296R1_116-118) has nearly 15% of unindexed sets as it was the first sample investigated using the U-stage by J.-G. F. In order to confirm the reliability of the data, the sample 200R3_12.5-15 was measured twice, by two different users with varying experience. The results gave a similar pattern, except for the $\{22\bar{4}1\}$ orientation, which was slightly more abundant in the second measurement, but this minor difference does not affect the shock pressure estimate.

The PDF orientation frequencies for all the samples are broadly similar, with some outliers. The granite clast sample (sample 94R3_38-40) shows a pattern very similar to the one of the upper samples, except for the $\{11\bar{2}1\}$ orientation, which is significantly more abundant, representing 6.4% of the total, to be compared to less than 2% for the other samples of the upper part of the investigated granite unit. Interestingly, an increase in the $\{10\bar{1}2\}$ orientation frequency is seen with decreasing depth. A similar trend is also observed, to a lesser extent, for the $\{11\bar{2}2\}$ and $\{22\bar{4}1\}$ orientations.

The majority of the investigated quartz grains have three sets of PDFs, representing on average 34.7% of the total (see Fig. 5), whereas the quartz grains with two sets of PDFs represent on average 29.0% of the total. The average number of PDF sets per grain seems to slightly decrease with increasing depth (see Table 3 and Fig. 6). The three deepest samples investigated have mainly shocked quartz grains with two sets of PDFs, representing from 36.8% to 48.6% of the total, whereas the shallowest samples in the unit have a majority of quartz grains with three sets of PDFs, representing from 30.4% to 48.1% of the total. The sample 97R3_10-12.5 shows a higher proportion of quartz grains with four sets of PDF (representing 26.5% of the total) than all the other investigated samples whereas the granite clast sample has a significantly higher abundance of quartz grains with five sets of PDFs (representing 30.4% of the total). All these observations are indicative of a slight decrease of the shock intensity with increasing depth in the core.

Shock Pressure Estimates

Based on our U-stage results, and following the shock pressure estimation model of Holm-Alwmark et al. (2018), the granites from the "lower peak ring" section record shock pressures between ~16 and 18 GPa (see Table 3 and Fig. 6). Our shock pressure estimates are consistent with observations published on zircon grains from the same granite unit, indicating that the shock pressure was <20 GPa (Timms et al. 2019). In

Table 2. Summary of PDF set abundances in quartz grains and results of our universal-stage investigations of 11 thin sections of granites from the Chicxulub impact structure peak ring.

Sample	Depth (mbsf)	Number of grains	% grains with PDFs	Number of sets	Average number of sets/grain
94R3_38-40[a]	743.6	23	100	78	3.4
97R3_10-12.5	752.5	34	100	97	2.9
110R2_14-16	788.1	34	100	102	3.0
125R1_40-42.5	826.7	23	100	72	3.1
134R2_69-73	845.9	29	100	91	3.1
142R2_105-109	861.9	27	100	79	2.9
163R1_76-77.5	915.5	27	100	78	2.9
200R3-12.5-15	1021.0	38	100	90	2.4
229R2_62-67	1107.2	39	97.4	111	2.8
266R2_95.5-98.5	1220.5	43	100	84	2.0
296R1_116-118	1311.1	35	100	81	2.3
Total		352	99.8	963	2.8

[a]Granite clast in impact melt rock.
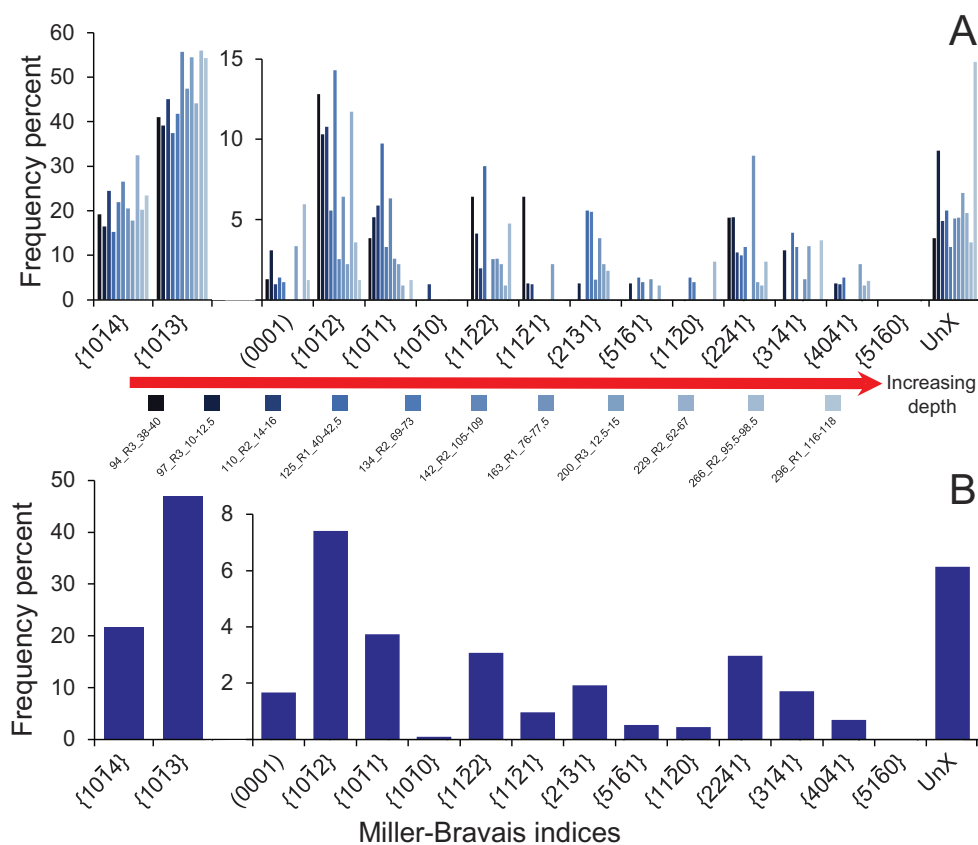
Fig. 4. A and B) Histograms showing the absolute frequencies of PDF orientations (Miller–Bravais indices). With the exception of the (0001) orientation, all the orientations are ranked with increasing angle between the *c*-axis and the pole to PDFs. UnX = unindexed. A) Detailed histogram for each investigated sample, with increasing depth from the darkest to the lightest bar (i.e., from left to right). B) Histogram showing a compilation of all our measurements. (Color figure can be viewed at wileyonline library.com.)

addition, a shock pressure range of ~16–18 GPa is also in good agreement with the presence of TiO_2-II as described by Schmieder et al. (2019). Although the range of pressure estimates is very narrow, taking into account the errors associated with the measurements, a slight shock attenuation with increasing depth is

Table 3. Crystallographic orientation abundances of PDFs (%) derived from universal-stage measurements of shocked quartz grains in granites from the Chicxulub impact structure peak ring and shock pressure estimates.

Sample	Depth (mbsf)	c (0001)	{$10\bar{1}4$}	ω, ω' {$10\bar{1}3$}	π, π' {$10\bar{1}2$}	r, z {$10\bar{1}1$}	m {$10\bar{1}0$}	ξ {$11\bar{2}2$}	s {$11\bar{2}1$}	ρ {$21\bar{3}1$}	x {$51\bar{6}1$}	a {$11\bar{2}0$}	{$22\bar{4}1$}	{$31\bar{4}1$}	t {$40\bar{4}1$}	k {$51\bar{6}0$}	Unindexed	Average shock pressure (GPa)[b]
94R3_38-40[a]	743.6	1.3	19.2	41.0	12.8	3.9	n.d.	6.4	6.4	n.d.	n.d.	n.d.	5.1	n.d.	n.d.	n.d.	3.9	17.7
97R3_10-12.5	752.5	3.1	16.5	39.2	10.3	5.2	n.d.	4.1	1.0	1.0	1.0	n.d.	5.2	3.1	1.0	n.d.	9.3	17.2
110R2_14-16	788.1	1.0	24.5	45.1	10.8	5.9	1.0	1.9	1.0	n.d.	n.d.	n.d.	2.9	n.d.	1.0	n.d.	4.9	17.4
125R1_40-42.5	826.7	1.4	15.3	37.5	5.6	9.7	n.d.	8.3	n.d.	5.6	1.4	1.4	2.8	4.2	1.4	n.d.	5.6	17.0
134R2_69-73	845.9	1.1	22.0	41.8	14.3	3.3	n.d.	n.d.	n.d.	5.5	1.1	1.1	3.3	3.3	n.d.	n.d.	3.3	17.6
142R2_105-109	861.9	n.d.	26.6	55.7	2.5	6.3	n.d.	2.5	n.d.	1.3	n.d.	n.d.	n.d.	n.d.	n.d.	n.d.	5.1	16.6
163R1_76-77.5	915.5	n.d.	20.5	47.4	6.4	2.6	n.d.	2.6	2.2	3.8	1.3	n.d.	9.0	1.3	n.d.	n.d.	5.1	17.0
200R3_12.5-15	1021.0	3.3	17.8	54.4	2.2	2.2	n.d.	2.2	2.2	2.2	n.d.	n.d.	1.1	3.3	2.2	n.d.	6.7	16.2
229R2_62-67	1107.2	n.d.	32.4	44.1	11.7	0.9	n.d.	0.9	n.d.	1.8	0.9	n.d.	0.9	n.d.	0.9	n.d.	5.4	17.0
266R2_95.5-98.5	1220.5	6.0	20.2	56.0	3.6	n.d.	n.d.	4.8	n.d.	n.d.	n.d.	2.4	2.4	n.d.	1.2	n.d.	3.6	15.8
296R1_116-118	1311.1	1.2	23.5	54.3	1.2	1.2	n.d.	n.d.	n.d.	n.d.	n.d.	n.d.	3.0	3.7	n.d.	n.d.	14.8	15.8
Average all samples		1.7	21.7	47.0	7.4	3.7	0.1	3.1	1.0	1.9	0.5	0.4	3.0	1.7	0.7	n.d.	6.1	16.8

[a]Granite clast in impact melt rock.
[b]Using Holm-Alwmark et al. (2018) calibration.
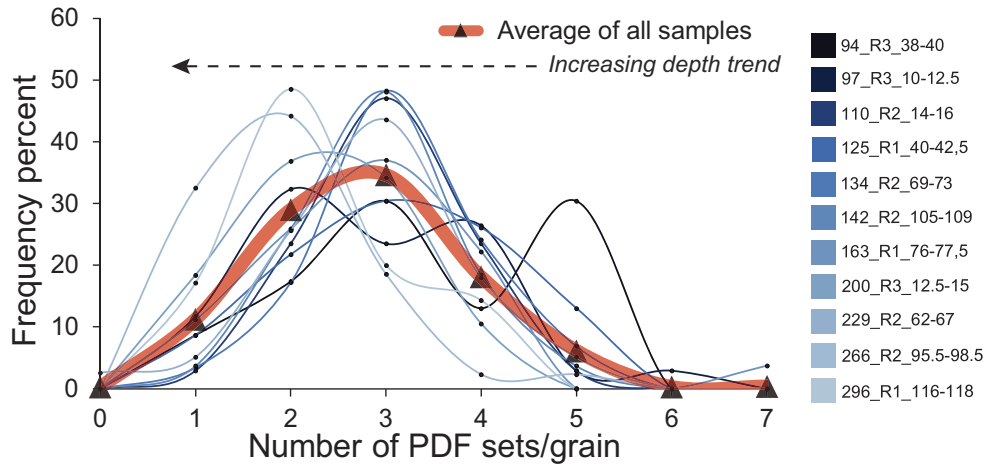
Fig. 5. Frequency of the number of PDF sets per grain for each investigated sample (same color code as for Figure 4). The average abundance for all sample is shown as bold curve and black triangles. There is a clear decrease in the abundance of shocked quartz grains with three sets of PDFs with increasing depth whereas the proportion of shocked quartz grains with two sets of PDFs increases inversely. The granite clast in impact melt rock sample 94R3_38-40 is clearly distinguishable here, with a significantly higher abundance of shocked quartz grains with five sets of PDFs (i.e., representing 30.4%). (Color figure can be viewed at wileyonlinelibrary.com.)
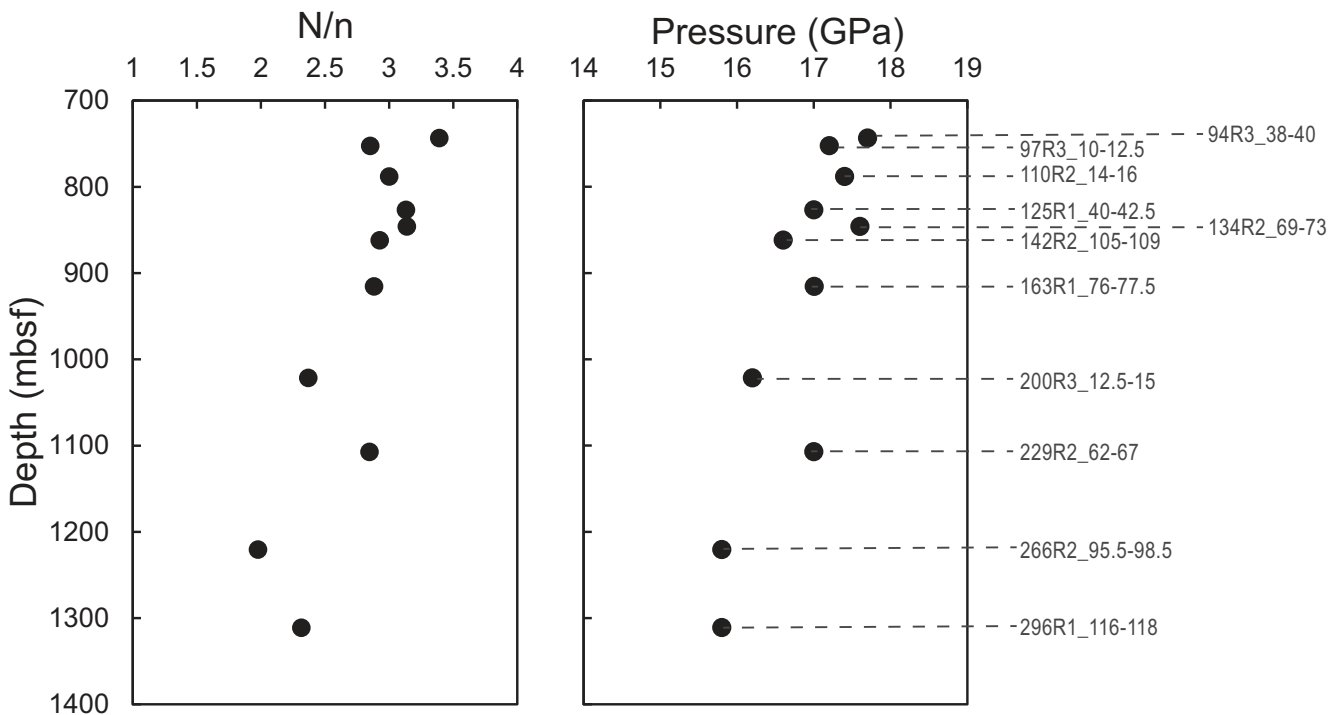
Fig. 6. Average number of PDF sets per grain (i.e., N/n, with N the number of PDF sets/grain and n the number of measured quartz grains; left) and estimated shock pressure (right) for each sample versus depth. In both cases, a slightly, but significant, decreasing of the values with increasing depth is visible, indicating a slight shock attenuation with increasing depth within the "lower peak ring" granite basement. Sample 229R2_62-67 is somewhat out of the general trend (i.e., it shows a slightly higher shock pressure than the neighbor samples), likely due to the fact that the thin section was prepared from a granite that is in direct contact with an aplite (i.e., the thin section was prepared at less than 1 cm from the contact), and such a textural change can induce a slight pressure excursion.

noticeable. The observed slight shock attenuation is highlighted by the abundance of PDFs parallel to the $\{10\bar{1}2\}$ orientation, that is, known to form at pressures of at least 20 GPa (Hörz 1968), significantly more abundant in the upper section of the granite basement (representing between 6% and 14% of the total) than in

the lower section (representing less than 3% of the total). The slight shock attenuation with increasing depth is also supported by the decreasing abundance of quartz grains with three sets of PDFs with increasing depth (see Fig. 6). This further supports the suggestion that the upper section of the granite basement experienced slightly higher shock pressures than the lower section.

The granite clast in impact melt rock located just on top of the granite unit rock investigated here recorded the highest shock pressure (17.7 GPa) of all the investigated samples. This is not surprising because this clast is derived from a section shocked at higher pressures that was either assimilated in the impact melt or that was ejected.

In general, our shock pressure estimates are slightly lower than the shock pressures derived from the dynamic collapse model for peak ring formation as modeled for the Chicxulub impact structure by Rae et al. (2019). In this model, the peak shock pressure calculated during the shock and decompression stage for the peak ring material is 22.2 GPa. This suggests either that the modeled peak shock pressures for the peak ring material are slightly overestimated or that the investigated "lower peak ring" granite was derived from a somewhat different area from the peak ring that experienced slightly lower shock pressure than the area selected in the model by Rae et al. (2019). In any case, our results can be used in order to further constrain the peak ring formation model.

Comparison with Previous Studies

The average abundance of shocked quartz grains in the investigated samples is 99.8% of the total number of quartz grains. This is significantly higher than the abundance of shocked quartz grains reported in previous studies of several K-Pg boundary sites worldwide. In terrestrial (non-marine) K-Pg sites, a very low number, from less than 2% (see Morgan et al. 2006; Nakano et al. 2008) to as much as ~25%, of the quartz grains are shocked (see Bohor et al. 1984, 1987; Izett 1990). Samples from oceanic drill cores recovered in the Atlantic and in the Pacific show on average a much higher abundance of shocked quartz grains, with about 36% and 23%, respectively (Morgan et al. 2006), and up to 63% in some Pacific sites according to Bostwick and Kyte (1996). The large difference in the abundance of shocked quartz grains from a study to another for the same geographical area can be explained by differences in the used protocols (e.g., sample selection, separation technique used, and preparation). Thus, comparison of different studies and derived numbers/proportions can be challenging. For example,

the estimated dilution of the proportion of shocked quartz grains by detrital quartz can vary significantly (Morgan et al. 2006). Interestingly, the fraction of shocked quartz grains reported for suevites from drill cores YAX-1 (Nakano et al. 2008) and Y6 (Sharpton et al. 1992), both recovered within the impact structure, is 31% and 33%, respectively. Only at K-Pg sites in the United States and Canada, the abundance of shocked quartz grains is much higher, but still lower compared to the samples investigated in this work, with ~80% of the quartz grains being shocked (Morgan et al. 2006).

The average number of PDF sets per grain recorded in the peak ring granite samples is also higher than in any other previously studied K-Pg boundary sites and drill cores in which an average from 1.4 to 2 PDF sets/grain were observed (Grieve and Alexopoulos 1988; Morgan et al. 2006; Nakano et al. 2008). Only the shocked quartz grains in Y6 drill core, with an average of 2.4 PDF sets/grain (Sharpton et al. 1992), and in some Western U.S. K-Pg sites, with an average of 2.8 PDF sets/grain (Izett 1990), show values approaching or similar to those that we have obtained from the investigated granite unit. Bohor et al. (1984, 1987) reported a higher average number of "planar features," 4.1 and 3.5, respectively, but it is not clear if all these features were indeed PDFs.

The PDF orientations and their abundances in our study show patterns generally similar to those obtained for distal K-Pg sites in Europe, the Pacific Ocean, North America, and in the YAX-1 drill core (Badjukov et al. 1986; Bohor et al. 1987; Grieve and Alexopoulos 1988; Izett 1990; Bostwick and Kyte 1996; Nakano et al. 2008) with the $\{10\bar{1}3\}$ orientation being the most abundant one, followed by the $\{10\bar{1}2\}$ orientation. It should be noted that in most studies published before 2009, the $\{10\bar{1}4\}$ orientation was not considered (i.e., some of these orientations were indexed as $\{10\bar{1}3\}$ orientations, other were unindexed), as it was only introduced later by Ferrière et al. (2009a). Another striking similarity between our results and those obtained for distal ejecta and YAX-1 samples is the absence or very low abundance of basal PDFs, parallel to (0001).

Interestingly, in two proximal K-Pg boundary sites investigated by Nakano et al. (2008; i.e., Moncada and Peñalver Formations, in Mexico), both located less than 800 km away from the center of the Chicxulub impact structure, the abundance of basal PDFs is up to 7.0% of the total measured orientations, and a similar abundance was found in the suevite unit from the Y6 drill core (Y6-N14) as reported by Sharpton et al. (1992). It was suggested by Nakano et al. (2008) that because PDFs with the (0001) orientation develop at the

lowest shock pressure (i.e., ~7.5 GPa), these shocked quartz grains were derived from lower shock pressure zones than the other grains derived from more central parts of the crater. Moreover, the formation of basal PDFs parallel to the (0001) plane, which represents mechanical Brazil micro-twin lamellae, requires a shear component, whereas other PDF orientations do not (e.g., Goltrant et al. 1991, 1992; Trepmann and Spray 2005). The difference in terms of recorded shock pressures between YAX-1 and Y6 drill cores is likely the result of a different sampling horizon. In addition, an increase of the recorded shock pressure in distal ejecta with increasing distance from the crater was evidenced either by the increasing average number of PDF sets/grain (Morgan et al. 2006) or by the increasing abundance of orientations that are known to form at higher shock pressures (Alvarez et al. 1995; Nakano et al. 2008). Shock pressures recorded for the quartz grains in this study are very similar to those recorded for quartz grains from distal K-Pg sites. Consequently, we can assume that the lower peak ring granite is probably the source material for the shocked quartz grains found in distal K-Pg boundary sites. The occurrence of spinel group minerals (picotite) at some of the distal K-Pg sites also suggests that some grains originate from the crystalline portion of the Chicxulub peak ring, that is, were derived from pre-impact dikes of dolerite as suggested by Schmieder et al. (2017). However, a comparison of our results with existing published data is somewhat challenging. Shocked quartz grains investigated in K-Pg sites and in previous drill cores occur as single, submillimetric grains in sedimentary (calcareous clastic, clays) deposits or suevite, whereas the shock quartz grains investigated in this study are generally larger, up to 15 mm in size, and from a crystalline (granitic) basement that was not reworked by any sedimentary process that may induce a significant dilution with local detrital unshocked quartz grains (i.e., what would affect the relative abundance of shocked quartz grains in a given unit, but not the PDF orientations nor the average number of PDF sets per grain; Claeys et al. 2002; Morgan et al. 2006). Moreover, comparing PDF orientations is not straightforward due to somewhat different methodologies used and the way the data are presented.

CONCLUSIONS

Our observations and results on shocked quartz grains confirm that the rocks of the granite basement unit in the Chicxulub impact structure peak ring are moderately shocked, as is indicated by the high abundance of shock features, such as PFs, FFs, and PDFs in quartz. The PDF orientation distribution

patterns in the peak ring granite are very similar to the distribution for distal K-Pg sites and the YAX-1 drill core, with the $\{10\bar{1}3\}$ orientations being the most abundant orientation and a very low abundance of basal PDFs compared to more proximal samples, that is, less than 800 km away from crater center (Nakano et al. 2008) and in the Y6 drill core (Sharpton et al. 1992), suggesting that the "lower peak ring" granite is possibly the source material of the shocked quartz grains found in distal K-Pg boundary sites.

Almost all quartz grains investigated are shocked at pressures between ~16 and 18 GPa, with a slight shock attenuation with increasing depth, highlighted by the increasing abundance of PDFs parallel to $\{10\bar{1}2\}$ orientation, known to develop at higher shock pressures (Hörz 1968) and the increasing average number of PDF sets per grain with decreasing depth. The abundance of shocked quartz and the average number of PDF sets per grain in this study is somewhat higher than in samples recovered in previous Chicxulub drill cores and from most K-Pg boundaries.

Editorial Handling—Dr. Jeffrey Plescia

REFERENCES

Alvarez L. W., Alvarez W., Asaro F., and Michel H. V. 1980. Extraterrestrial cause for the Cretaceous-Tertiary extinction. *Science* 208:1095–1108.

Alvarez W., Claeys P., and Kieffer S. W. 1995. Emplacement of K/T boundary shocked quartz from Chicxulub crater. *Science* 269:930–935.

Badjukov D. D., Nazarov M. A., and Suponeva I. V. 1986. Shocked quartz grains from K/T boundary sediments

(abstract). 17th Lunar and Planetary Science Conference. pp. 18–19.

Bohor B. F., Foord E. E., Modreski P. J., and Triplehorn D. M. 1984. Mineralogic evidence for an impact event at the Cretaceous-Tertiary boundary. *Science* 224:867–869.

Bohor B. F., Modreski P. J., and Foord E. E. 1987. Shocked quartz in the Cretaceous-Tertiary boundary clays: Evidence for a global distribution. *Science* 236:705–708.

Bostwick J. A. and Kyte F. T. 1996. The size abundance of shocked quartz in Cretaceous-Tertiary boundary sediments from the Pacific Basin. In *The Cretaceous-Tertiary event and other catastrophes in Earth history*, edited by Ryder G., Fastovsky D., and Gartner S. Geological Society of America Special Paper 307. Boulder, Colorado: Geological Society of America. pp. 403–415.

Claeys P., Kiessling W., and Alvarez W. 2002. Distribution of Chicxulub ejecta at the Cretaceous-Tertiary boundary. In *Catastrophic events and mass extinctions: Impact and beyond*, edited by Koeberl C. and MacLeod G. Geological Society of America Special Paper 356. Boulder, Colorado: Geological Society of America. pp. 55–68.

Cox M. A., Erickson T. M., Schmieder M., Christoffersen R., Ross D. K., Cavosie A. J., Bland P. A., Kring D. A., and IODP–ICDP Expedition 364 Scientists. 2020. High-resolution microstructural and compositional analyses of shock deformed apatite from the peak ring of the Chicxulub impact crater. *Meteoritics & Planetary Science* 19 p. https://doi.org/10.1111/maps.13541.

Deutsch A., Poelchau M., and Kenkmann T. 2015. Impact metamorphism in terrestrial and experimental cratering events. In *EMU notes in mineralogy—Volume 15 Planetary mineralogy*, edited by Lee M. R. and Leroux H. London: European Mineralogical Union and the Mineralogical Society of Great Britain & Ireland. pp. 89–127.

Emmons R. C. 1943. The universal stage (with five axes of rotation). *Geological Society of America Memoir* 8:205p.

Engelhardt W. von and Bertsch W. 1969. Shock induced planar deformation structures in quartz from the Ries crater, Germany. *Contributions to Mineralogy and Petrology* 20:203–234.

Fel'dman V. I. 1994. The conditions of shock metamorphism. In *Large meteorite impacts and planetary evolution*, edited by Dressler B. O. Grieve R. A. F. and Sharpton V. L. Geological Society of America Special Paper 293. Boulder, Colorado: Geological Society of America. pp. 121–132.

Ferrière L., Koeberl C., Ivanov B. A., and Reimold W. U. 2008. Shock metamorphism of Bosumtwi impact crater rocks, shock attenuation, and uplift formation. *Science* 322:1678–1681.

Ferrière L., Morrow J. R., Amgaa T., and Koeberl C. 2009a. Systematic study of universal-stage measurements of planar deformation features in shocked quartz: Implications for statistical significance and representation of results. *Meteoritics & Planetary Science* 44:925–940.

Ferrière L., Koeberl C., and Reimold U. W. 2009b. Characterisation of ballen quartz and cristobalite in impact breccias: New observations and constraints on ballen formation. *European Journal of Mineralogy* 21:203–217.

Ferrière L. and Osinski G. R. 2013. Shock metamorphism. In *Impact cratering: Processes and products*, edited by Osinski G. R. and Pierazzo E. Chichester, UK: Blackwell Publishing Ltd. pp. 106–124.

Folco L., Mugnaioli E., Gemelli M., Masotta M., and Campanale F. 2018. Direct quartz-coesite transformation in shocked porous sandstone from Kamil crater (Egypt). *Geology* 46:739–742.

French B. M. 1998. Traces of catastrophe: A handbook of shock-metamorphic effects in terrestrial meteorite impact structures. LPI Contribution 954. Houston, Texas: Lunar and Planetary Institute. 120 p.

French B. M. and Koeberl C. 2010. The convincing identification of terrestrial meteorite impact structures: What works, what doesn't, and why. *Earth-Science Reviews* 98:123–170.

French B. M. and Short N. M. 1968. *Shock metamorphism of natural materials*. Baltimore, Maryland: Mono Book Corporation. 644 p.

Goltrant O., Cordier P., and Doukhan J.-C. 1991. Planar deformation features in shocked quartz: A transmission electron microscopy investigation. *Earth and Planetary Science Letters* 106:103–115.

Goltrant O., Leroux H., Doukhan J.-C., and Cordier P. 1992. Formation mechanisms of planar deformation features in naturally shocked quartz. *Physics of the Earth and Planetary Interiors* 74:219–240.

Grieve R. A. F. and Alexopoulos J. 1988. Microscopic planar features in quartz from Scollard Canyon, Alberta, and the Cretaceous-Tertiary boundary event. *Canadian Journal of Earth Science* 25:1530–1534.

Grieve R. A. F., Langenhorst F., and Stöffler D. 1996. Shock metamorphism of quartz in nature and experiment: II. Significance in geoscience. *Meteoritics & Planetary Science* 31:6–35.

Gulick S., Christeson G., Barton P., Grieve R., Morgan J., and Urrutia-Fucugauchi J. 2013. Geophysical characterization of the Chicxulub impact crater. *Reviews of Geophysics* 51:31–52.

Hand E. 2016. Updated: Drilling of dinosaur-killing impact crater explains buried circular hills. *Science Magazine*. https://doi.org/10.1126/science.aaf5684

Hildebrand A. R., Penfield G. T., Kring D. A., Pilkington M., Camargo Z. A., Jacobsen S. B., and Boynton W. V. 1991. Chicxulub crater: A possible Cretaceous/Tertiary boundary impact crater on the Yucatán Peninsula, Mexico. *Geology* 19:867–871.

Holm-Alwmark S., Ferrière L., Alwmark C., and Poelchau M. H. 2018. Estimating average shock pressures recorded by impactite samples based on universal stage investigations of planar deformation features in quartz—Sources of error and recommendations. *Meteoritics & Planetary Science* 53:110–130.

Hörz F. 1968. Statistical measurements of deformation structures and refractive indices in experimentally shock loaded quartz. In *Shock metamorphism of natural materials*, edited by French B. M. and Short N. M. Baltimore, Maryland: Mono Book Corporation. pp. 243–253.

Izett G. A. 1990. *The Cretaceous/Tertiary boundary interval, Raton Basin, Colorado and New Mexico*. Geological Society of America Special Paper 249. Boulder, Colorado: Geological Society of America. 100 p.

Kieffer S. W., Phakey P. P., and Christie J. M. 1976. Shock processes in porous quartzite: Transmission electron microscope observations and theory. *Contributions to Mineralogy and Petrology* 59:41–93.

Kowitz A., Schmitt R. T., Reimold W. U., and Hornemann U. 2013a. The first MEMIN shock recovery experiments at low shock pressure (5–12.5 GPa) with dry, porous sandstone. *Meteoritics & Planetary Science* 48:99–114.

Kowitz A., Güldemeister N., Reimold W. U., Schmitt R. T., and Wünnemann K. 2013b. Diaplectic quartz glass and SiO$_2$ melt experimentally generated at only 5 GPa shock pressure in porous sandstone: Laboratory observations and meso-scale numerical modeling. *Earth and Planetary Science Letters* 384:17–26.

Kowitz A., Güldemeister N., Schmitt R. T., Reimold W. U., Wünnemann K., and Holzwarth A. 2016. Revision and recalibration of existing shock classifications for quartzose rocks using low-shock pressure (2.5–20 GPa) recovery experiments and mesoscale numerical modeling. *Meteoritics & Planetary Science* 51:1741–1761.

Kring D. A., Tikoo S. M., Schmieder M., Riller U., Rebolledo-Vieyra M., Simpson S. L., Osinski G. R., Gattacceca J., Wittmann A., Verhagen C. M., Cockell C. S., Coolen M. J. L., Longstaffe F. J., Gulick S. P. S., Morgan J. V., Bralower T. J., Chenot E., Christeson G. L., Claeys P., Ferrière L., Gebhardt C., Goto K., Green S. L., Jones H., Lofi J., Lowery C. M., Ocampo-Torres R., Perez-Cruz L., Pickersgill A. E., Poelchau M. H., Rae A. S. P., Rasmussen C., Sato H., Smit J., Tomioka N., Urrutia-Fucugauchi J., Whalen M. T., Xiao L., and Yamaguchi K. E. 2020. Probing the hydrothermal system of the Chicxulub impact crater. *Science Advances*. 6: eaaz3053. https://doi.org/10.1126/sciadv.aaz3053.

Losiak A., Golebiowska I., Ferrière L., Wojciechowski J., Huber M. S., and Koeberl C. 2016. WIP: A web-based program for indexing planar features in quartz grains and its usage. *Meteoritics & Planetary Science* 51:647–662.

Mansfeld U., Langenhorst F., Ebert M., Kowitz A., and Schmitt R. T. 2017. Microscopic evidence of stishovite generated in low-pressure shock experiments on porous sandstone: Constraints on its genesis. *Meteoritics & Planetary Science* 52:1449–1464.

Morgan J., Lana C., Kearsley A., Coles B., Belcher C., Montanari S., Diaz-Martinez E., Barbosa A., and Neumann V. 2006. Analyses of shocked quartz at the global K-P boundary indicate an origin from a single, high-angle, oblique impact at Chicxulub. *Earth and Planetary Science Letters* 251:264–279.

Morgan J. V., Gulick S. P. S., Bralower T., Chenot E., Christeson G., Claeys P., Cockell C., Collins G. S., Coolen M. J. L., Ferrière L., Gebhardt C., Goto K., Jones H., Kring D. A., Le Ber E., Lofi J., Long X., Lowery C., Mellett C., Ocampo-Torres R., Osinski G. R., Perez-Cruz L., Pickersgill A., Pölchau M., Rae A., Rasmussen C., Rebolledo-Vieyra M., Riller U., Sato H., Schmitt D. R., Smit J., Tikoo S., Tomioka N., Urrutia-Fucugauchi J., Whalen M., Wittmann A., Yamaguchi K. E., and Zylberman W. 2016. The formation of peak rings in large impact craters. *Science* 354:878–882.

Morgan J., Gulick S., Mellet C. L., and Green S. L. and the Expedition 364 Scientists. 2017. *Chicxulub: Drilling the K-Pg impact crater*. Proceedings of the International Ocean Discovery Program, 364. College Station, Texas: International Ocean Discovery Program. 164 p.

Müller W. F. and Défourneaux M. 1968. Deformationsstrukturen-im Quarz als Indikator für Stosswellen: Eine experimentelle Untersuchung an Quartz-Einkristallen. *Zeitschrift für Geophysik* 34:483–504.

Nakano Y., Goto K., Matsui T., Tada R., and Tajika E. 2008. PDF orientations in shocked quartz grains around the Chicxulub crater. *Meteoritics & Planetary Science* 43:745–760.

Penfield G. T. and Camargo Z. A. 1981. Definition of a major igneous zone in the central Yucatán platform with aeromagnetics and gravity. *Society of Exploration Geophysicists Technical Program, Abstracts, and Biographies* 51:37.

Pittarello L., Ferrière L., Feignon J.-G., Osinski G. R., and Koeberl C. 2020. Preferred orientation distribution of shock-induced planar microstructures in quartz and feldspar. *Meteoritics & Planetary Science* 55:1082–1092.

Poelchau M. H. and Kenkmann T. 2011. Feather features: A low-shock-pressure indicator in quartz. *Journal of Geophysical Research* 116:B02201.

Rae A. S. P., Collins G. S., Poelchau M., Riller U., Davison T. M., Grieve R. A. F., Osinski G. R., Morgan J. V., and IODP-ICDP Expedition 364 Scientists. 2019. Stress-strain evolution during peak-ring formation: A case study of the Chicxulub impact structure. *Journal of Geophysical Research: Planets* 124:396–417.

Riller U., Poelchau M. H., Rae A. S. P., Schulte F. M., Collins G. S., Melosh H. J., Grieve R. A. F., Morgan J. V., Gulick S. P. S., Lofi J., Diaw A., McCall N., Kring D. A., and IODP-ICDP Expedition 364 Science Party. 2018. Rock fluidization during peak-ring formation of large impact structures. *Nature* 562:511–518.

Schmieder M., Kring D. A., and the IODP-ICDP Expedition 364 Science Party. 2017. Petrology of target dolerite in the Chicxulub peak ring and a possible source of K/Pg boundary picotite spinel (abstract #1964). 48th Lunar and Planetary Science Conference. CD-ROM.

Schmieder M., Erickson T. M., and Kring D. A. and the IODP-ICDP Expedition 364 Science Party. 2019. Microstructural characterization of TiO$_2$-II in the chicxulub peak ring (abstract #1568). 50th Lunar and Planetary Science Conference. CD–ROM.

Schulte P., Alegret L., Arenillas I., Arz J. A., Barton P. J., Bown P. R., Bralower T. J., Christeson G. L., Claeys P., Cockell C. S., Collins G. S., Deutsch A., Goldin T. J., Goto K., Grajales-Nishimura J. M., Grieve R. A. F., Gulick S. P. S., Johnson K. R., Kiessling W., Koeberl C., Kring D. A., MacLeod K. G., Matsui T., Melosh J., Montanari A., Morgan J. V., Neal C. R., Nichols D. J., Norris R. D., Pierazzo E., Ravizza G., Rebolledo-Vieyra M., Reimold W. U., Robin E., Salge T., Speijer R. P., Sweet A. R., Urrutia-Fucugauchi J., Vajda V., Whalen M. T., and Willumsen P. S. 2010. The Chicxulub asteroid impact and mass extinction at the Cretaceous-Paleogene boundary. *Science* 327:1214–1218.

Sharpton V. L., Dalrymple G. B., Marin L. E., Ryder G., Schuraytz B. C., and Urrutia-Fucugauchi J. 1992. New links between the Chicxulub impact structure and the Cretaceous/Tertiary boundary. *Nature* 359:819–821.

Smit J. 1999. The global stratigraphy of the Cretaceous-Tertiary boundary impact ejecta. *Annual Review of Earth and Planetary Sciences* 27:75–113.

Sprain C. J., Renne P. R., Clemens W. A., and Wilson G. P. 2018. Calibration of chron C29r: New high-precision geochronologic and paleomagnetic constraints from the Hell Creek region, Montana. *Geological Society of America Bulletin* 130:1615–1644.

Stöffler D. 1972. Deformation and transformation of rock-forming minerals by natural and experimental shock processes. I. Behavior of minerals under shock compression. *Fortschritte der Mineralogie* 49:50–113.

Stöffler D. and Langenhorst F. 1994. Shock metamorphism of quartz in nature and experiment: I. Basic observation and theory. *Meteoritics* 29:155–181.

Stöffler D., Hamann C., and Metzler K. 2017. Shock metamorphism of planetary silicate rocks and sediments: Proposal for an updated classification system. *Meteoritics & Planetary Science* 53:5–49.

Timms N. E., Pearce M. A., Erickson T. M., Cavosie A. J., Rae A. S. P., Wheeler J., Wittman A., Ferrière L., Poelchau M. H., Tomioka N., Collins G. S., Gulick S. P. S., Rasmussen C., Morgan J. V., IODP-ICDP Expedition 364 Scientists. 2019. New shock microstructures in titanite ($CaTiSiO_5$) from the peak ring of the Chicxulub impact structure, Mexico. *Contributions to Mineralogy and Petrology* 174:38. https://doi.org/10.1007/s00410-019-1565-7.

Trepmann C. A. and Spray J. G. 2005. Planar microstructures and Dauphiné twins in shocked quartz from the Charlevoix impact structure, Canada. In *Large meteorite impacts III*, edited by Kenkmann T., Hörz F., and Deutsch A. Geological Society of America Special Paper 384. Boulder, Colorado: Geological Society of America. pp. 315–328.

Trepmann C. A. and Spray J. G. 2006. Shock-induced crystal-plastic deformation and post-shock annealing of quartz: Microstructural evidence from crystalline target rocks of the Charlevoix impact structure, Canada. *European Journal of Mineralogy* 18:161–173.

CHAPTER 6: Chicxulub impact structure, IODP-ICDP Expedition 364 drill core: Geochemistry of the granite basement

Authors

Jean-Guillaume Feignon, Sietze J. de Graaff, Ludovic Ferrière, Pim Kaskes, Thomas Déhais, Steven Goderis, Philippe Claeys, and Christian Koeberl.

Publication status

Personal contribution

Sample selection, petrographic descriptions, optical microscope observations, scanning electron microscope observations, micro-X-ray fluorescence chemical mapping of some of the presented samples, sample preparation for geochemical analysis, instrumental neutron activation analysis (trace element abundances), assistance during thermal ionization mass spectrometry (TIMS) measurement of Sr–Nd isotopic ratios, processing and interpretation of the results, writing (original draft), writing (revision and editing).

Chicxulub impact structure, IODP-ICDP Expedition 364 drill core: Geochemistry of the granite basement

Jean-Guillaume FEIGNON [1]*, Sietze J. DE GRAAFF [2,3], Ludovic FERRIÈRE [4],
Pim KASKES [2,3], Thomas DÉHAIS [2,3], Steven GODERIS [2], Philippe CLAEYS [2], and
Christian KOEBERL [1]

[1]Department of Lithospheric Research, University of Vienna, Althanstrasse 14, Vienna A-1090, Austria
[2]Research Unit: Analytical, Environmental & Geo-Chemistry, Department of Chemistry, Vrije Universiteit Brussel,
AMGC-WE-VUB, Pleinlaan 2, Brussels 1050, Belgium
[3]Laboratoire G-Time, Université Libre de Bruxelles, Av. F.D. Roosevelt 50, Brussels 1050, Belgium
[4]Natural History Museum, Burgring 7, Vienna A-1010, Austria
*Corresponding author. E-mail: jean-guillaume.feignon@univie.ac.at

Abstract–The IODP-ICDP Expedition 364 drilling recovered a 829 m core from Hole M0077A, sampling ~600 m of near continuous crystalline basement within the peak ring of the Chicxulub impact structure. The bulk of the basement consists of pervasively deformed, fractured, and shocked granite. Detailed geochemical investigations of 41 granitoid samples, that is, major and trace element contents, and Sr–Nd isotopic ratios are presented here, providing a broad overview of the composition of the granitic crystalline basement. Mainly granite but also granite clasts (in impact melt rock), granite breccias, and aplite were analyzed, yielding relatively homogeneous compositions between all samples. The granite is part of the high-K, calc-alkaline metaluminous series. Additionally, they are characterized by high Sr/Y and $(La/Yb)_N$ ratios, and low Y and Yb contents, which are typical for adakitic rocks. However, other criteria (such as Al_2O_3 and MgO contents, Mg#, K_2O/Na_2O ratio, Ni concentrations, etc.) do not match the adakite definition. Rubidium–Sr errorchron and initial $^{87}Sr/^{86}Sr_{t=326Ma}$ suggest that a hydrothermal fluid metasomatic event occurred shortly after the granite formation, in addition to the postimpact alteration, which mainly affected samples crosscut by shear fractures or in contact with aplite, where the fluid circulation was enhanced, and would have preferentially affected fluid-mobile element concentrations. The initial $(\varepsilon_{Nd})_{t=326Ma}$ values range from −4.0 to 3.2 and indicate that a minor Grenville basement component may have been involved in the granite genesis. Our results are consistent with previous studies, further supporting that the cored granite unit intruded the Maya block during the Carboniferous, in an arc setting with crustal melting related to the closure of the Rheic Ocean associated with the assembly of Pangea. The granite was likely affected by two distinct hydrothermal alteration events, both influencing the granite chemistry: (1) a hydrothermal metasomatic event, possibly related to the first stages of Pangea breakup, which occurred approximately 50 Myr after the granite crystallization, and (2) the postimpact hydrothermal alteration linked to a long-lived hydrothermal system within the Chicxulub structure. Importantly, the granites sampled in Hole M0077A are unique in composition when compared to granite or gneiss clasts from other drill cores recovered from the Chicxulub impact structure. This marks them as valuable lithologies that provide new insights into the Yucatán basement.

INTRODUCTION

The ~200 km diameter (e.g., Gulick et al. 2013) and 66.05 Myr old (Sprain et al. 2018) Chicxulub impact structure is located in the northwestern part of the Yucatán peninsula (Mexico, Fig. 1). The characterization of shocked quartz grains in samples derived from within the structure confirmed its impact origin (Penfield and Camargo 1981; Hildebrand et al. 1991). Chicxulub is the only known terrestrial impact structure with a nearly intact, well-preserved peak ring (e.g., Morgan et al. 1997, 2016) and it is related to the Cretaceous–Paleogene boundary and the non-avian dinosaur extinction (Swisher et al. 1992; Smit 1999; Schulte et al. 2010; Chiarenza et al. 2020; Goderis et al. 2021). The structure was formed by the impact of an ~12 km diameter carbonaceous chondrite-like body (Shukolyukov and Lugmair 1998; Quitté et al. 2007; Goderis et al. 2013; Collins et al. 2020) on an ~3 km thick Mesozoic carbonate and evaporite platform overlying crystalline basement rock (e.g., Morgan et al. [2016] and references therein).

Today, the impact structure is buried under ~1 km of Cenozoic limestones, with its only surface expression being a ring of cenotes (i.e., water-filled sinkholes). Consequently, the direct study of the different lithologies occurring in the impact structure (i.e., a variety of impact breccias, impact melt rocks, and (shocked) pre-impact basement rocks) is only possible either by investigating ejecta material (Belza et al. 2015) or by using samples recovered by scientific drilling programs (e.g., Koeberl and Sigurdsson 1992; Koeberl 1993a; Belza et al. 2012) or petroleum exploration campaigns (e.g., Lopez Ramos 1975; Hildebrand et al. 1991; Swisher et al. 1992; Urrutia-Fucugauchi et al. 1996; Claeys et al. 2003; Tuchscherer et al. [2004a] and references therein). Drilling campaigns were conducted within the impact structure by Petróleos Méxicanos (PEMEX), recovering the Chicxulub–1 (C–1) and Yucatan–6 (Y6) cores, which sampled melt-bearing impact breccia (suevite) and impact melt rock (e.g., Hildebrand et al. 1991; Kring and Boynton 1992; Swisher et al. 1992; Schuraytz et al. 1994; Ward et al. 1995; Claeys et al. 2003; Kettrup and Deutsch 2003); and by the International Continental Scientific Drilling Program (ICDP), recovering the Yaxcopoil–1 (Yax–1) core (e.g., Tuchscherer et al. 2004a, 2004b, 2005, 2006).

Pre-impact basement material was generally found as clasts in the suevite units recovered in previous drill core campaigns, with a wide variety of target lithologies being reported, including Cretaceous sedimentary platform rocks (a 616 m thick megablock of limestones, dolomites, and anhydrites was identified in the Yax–1 drill core, e.g., Dressler et al. 2003; Wittmann et al. 2004; Belza et al. 2012), granites, orthogneisses, amphibolites, quartzites,

quartz-mica schists, and dolerites (e.g., Sharpton et al. 1992; Kettrup et al. 2000; Claeys et al. 2003; Kettrup and Deutsch 2003; Schmitt et al. 2004; Tuchscherer et al. 2005). Importantly, no large unit of the underlying crystalline basement material was ever recovered in any of the previous drill core campaigns.

A large crystalline basement unit composed mainly of granite was recovered for the first time in the Chicxulub peak ring drilled during the joint International Ocean Discovery Program (IODP) and ICDP Expedition 364 (see the IODP-ICDP Expedition 364 Drill Core section and Morgan et al. 2017). This unit represents the main focus of this study. In order to better characterize the granite basement, we present the results of the major and trace element analyses of 41 granitoid samples, including Sr–Nd isotopic analyses for 16 samples, from the "lower peak ring" section. A comparison with chemical data for granites and granitic gneisses from previous studies is also presented. Our investigations of a large set of granite samples offer a unique opportunity to constrain the chemistry and sources of the granite, a major component to the impactites recovered in the drill core; how it was affected by the impact event; and, more generally, refine the Yucatán basement geology.

THE CHICXULUB IMPACT STRUCTURE

Geological Setting

The crystalline basement rocks forming the Yucatán platform belong to the Maya block (Fig. 1), which is generally described as encompassing the Yucatán peninsula, the northeast of Mexico, the coastal plains of the western and northern Gulf of Mexico, and the Chiapas massif complex (Keppie et al. 2011; Weber et al. 2012, 2018), with its north and northeastern boundaries bordered by continental shelves and oceanic lithosphere (Alaniz-Álvarez et al. 1996; Keppie et al. 2011). The Maya block was thought to be bordered in the northwest by the Oaxaquia block (Grenvillian-aged); in the southwest by the Cuicateco complex; and in the south by the Polochic, Motagua, and Jocotlán-Chamaleón fault systems (Fig. 1), making the separation with the Caribbean plate (Dengo 1969; Donnelly et al. 1990; Weber et al. 2012, 2018). However, the exact geographical area covered by the Maya block remains a topic of discussion. Indeed, the work by Ortega-Gutiérrez et al. (2018) suggests that the Chiapas massif (or Southern Maya) forms a distinct lithotectonic domain (Fig. 1), characterized by the presence of medium- to high-grade metamorphic rock outcrops that were not observed in the Maya block (Weber et al. 2008; Ortega-Gutiérrez et al. 2018). The
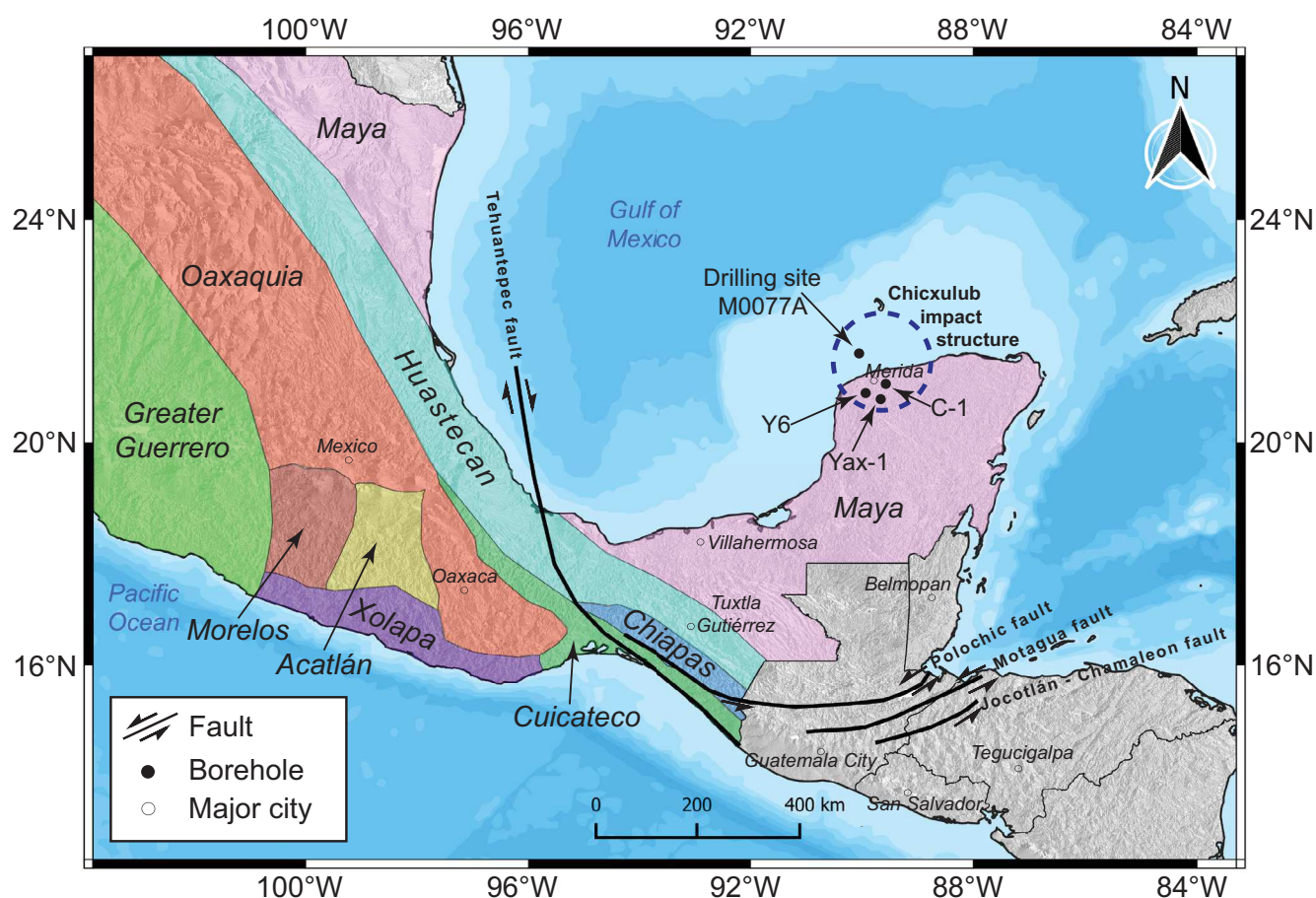
Fig. 1. Map of southeast Mexico with the main tectonostratigraphic domains proposed by Ortega-Gutiérrez et al. (2018), major faults, and the Chicxulub impact structure (dashed circle; 200 km in diameter) with the IODP-ICDP Expedition 364 (M0077A) and previous drilling (Y6, Yax–1, and C–1) locations reported (modified from Weber et al. 2012, 2018; Ortega-Gutiérrez et al. 2018). SRTM data can be found online at: https://www2.jpl.nasa.gov/srtm/cbanddataproducts.html. (Color figure can be viewed at wileyonlinelibrary.com.)

Chiapas massif would be separated from the Maya block by the Paleozoic-aged Huastecan orogenic belt. This orogenic system is mostly buried and extends from the Ouachita suture belt in Northwest Mexico to the Polochic, Motagua, and Jocotlán-Chamaleón fault systems in Guatemala. Consequently, the Huastecan orogenic belt separates the Maya block from the Oaxaquia and Cuicateco terranes in the west and southwest, respectively (Fig. 1).

The material composing the Maya block is mainly Pan-African–aged, such as tholeiitic dolerite intruded in Grenvillian Novillo gneiss in the Cd. Victoria area, yielding an Ar/Ar age of 546 ± 5 Ma (Keppie et al. 2011). In addition, the age of zircon grains found in ejected material at various K–Pg boundary locations and from boreholes inside the Chicxulub impact structure range mainly between 550 and 545 Ma, just after the Cambrian–Precambrian boundary (Krogh

et al. 1993; Kettrup and Deutsch [2003] and references therein; Kamo et al. 2011; Keppie et al. 2011), suggesting that a predominantly late Ediacaran crystalline basement constitutes the northern part of the Yucatán peninsula (Ortega-Gutiérrez et al. 2018). The Sm–Nd T_{DM} model ages reported from orthogneisses, impact melt rock, impact glass, and amphibolites display a wide range between 1.4 and 0.7 Ga, suggesting the involvement of a Grenvillian component during the formation of Yucatán crystalline basement (Kettrup and Deutsch 2003; Keppie et al. 2011). Granites and zircon grains with younger ages (late Paleozoic, ~320–345 Ma) are also reported, but are comparatively rare (Kamo and Krogh 1995; Kamo et al. 2011; Keppie et al. 2011).

While the exact extent of the lithotectonic domains remains up for debate, paleomagnetic reconstructions indicate that the Maya block, and more precisely the Yucatán-Chiapas block, separated from Texas (southern

margin of Laurentia) during the breakup of Pangea during the Late Triassic (~230 Ma). The Yucatán-Chiapas block then rotated ~40° (up to 60° for the Yucatán basement, independently from the Chiapas block) anticlockwise as the Gulf of Mexico opened. The rotation was accommodated by the presence of a transform fault marking the boundary between continental and oceanic crust offshore the east coast of Mexico (Dickinson and Lawton 2001; Steiner 2005). The seafloor spreading began during the Callovian (~164 Ma). The rotation ceased by the Berriasian (~139 Ma), and, since then, the Yucatán block has remained geologically stable (see detailed geotectonic reconstructions in Dickinson and Lawton 2001; Steiner [2005] and references therein). At the time of the Chicxulub impact event, at ~66.05 Ma (Sprain et al. 2018), the Yucatán basement was covered by an approximately 3 km thick carbonate platform composed of limestone, dolomite, marl, and anhydrite (Lopez Ramos 1975; Kring 2005). Additionally, the platform was covered by seawater, deepening to the north and northeast with an average water depth of ~600 m (Gulick et al. 2008).

During the impact event, the target rocks (sedimentary rocks and the underlying basement rocks) were either vaporized, melted, shocked, ejected from the crater, uplifted, injected as melt into the structure, and/or incorporated into gravity flows during crater modification (Morgan et al. 2016; Gulick et al. 2019; de Graaff et al. 2021). Rock fluidization rapidly led to the formation of a central peak ring inside the structure (Riller et al. 2018; Rae et al. 2019). Afterward, the peak ring was intensively altered by a long-lived, by more than one million years, hydrothermal system (Kring et al. 2020).

The impact structure site was finally covered by carbonates and evaporites from the Cretaceous to the Quaternary, forming the current subsurface geology of the Yucatán peninsula (Lopez Ramos 1975; Hildebrand et al. 1991), and preserving the impact structure and its peak ring from erosion.

IODP-ICDP Expedition 364 Drill Core

Investigating the rocks that make up the peak ring in order to understand its nature, chemistry, and origin, as well as its formation mechanism, was one of the primary goals of the IODP-ICDP Expedition 364 (e.g., Morgan et al. 2017). A continuous core from Hole M0077A (see Fig. 2) was recovered between 505.7 and 1334.7 mbsf (meters below sea floor). Four main lithological units were identified, including (1) a "postimpact" Cenozoic sedimentary rock section (from 505.7 to 617.3 mbsf); (2) a melt-bearing, polymict, impact breccia (suevite) section (from 617.3 to

721.6 mbsf); overlaying (3) an impact melt rock and green schlieren unit (from 721.6 to 747.0 mbsf), or "upper impact melt rock" unit (Morgan et al. 2017; de Graaff et al. 2021). The lower and thicker recovered unit (4), the so-called "lower peak ring" section (from 747.0 to 1334.7 mbsf), consists of granitoid (coarse-grained granite with centimeter to decimeter aplite and pegmatite facies areas) intruded by several pre-impact subvolcanic dikes and intercalations of millimeter to decameter suevite-like breccia and impact melt rocks (Morgan et al. 2017). The latter has been discussed in detail, and referred to as the "lower impact melt-bearing unit" (LIMB), by de Graaff et al. (2021).

The "lower peak ring" section represents a large, nearly uninterrupted crystalline basement rock unit, and is the main focus of this study. The occurrence of crystalline basement rocks at such relatively shallow depths suggests that they were uplifted from a pre-impact depth of 8–10 km (Morgan et al. 2016; Riller et al. 2018). The basement rocks are shocked, with most of the minerals showing signs of shock metamorphism. Shock pressures experienced by the granite were estimated between ~16 and 18 GPa (Feignon et al. 2020).

Zhao et al. (2020) reported on the investigation of nine granite samples and suggested that these late Paleozoic granites are K-rich adakitic rocks that formed following the melting of a thickened crust with a residue of garnet-bearing amphibolite or garnet-bearing granulite. However, the term "adakitic" should be used with care in this context, as a full set of criteria should be used in addition to the used Sr/Y and La/Yb ratios to define an adakitic rock (see Moyen 2009). The long-lasting hydrothermal system, which occurred within Chicxulub (e.g., Kring et al. 2020), may also have had a significant effect on the bulk granite geochemistry as also suggested by de Graaff et al. (2021).

Granite Ages

Dating on the Hole M0077A granites was performed on zircon and yield late Paleozoic (Carboniferous) U–Pb ages of 326 ± 5 Ma (Rasmussen et al. 2019; Zhao et al. 2020) and 334 ± 2.3 Ma (Ross et al. 2021). More recent ages (215 ± 28 to 260 ± 9 Ma) were obtained for allanite and probably recorded allanite growth during alteration events, while zircon ages represent the igneous crystallization (Wittmann et al. 2018). A similar late Paleozoic age, albeit with large uncertainty, of 478 ± 110 Ma, was obtained in zircons from Yax–1 impact breccia (Schmieder et al. 2017). These ages contrast the mostly dominant Pan-African–aged zircon population recovered from K–Pg boundary sites and previous drill cores (e.g., Krogh et al. 1993; Kamo et al. 2011; Keppie et al. 2011).
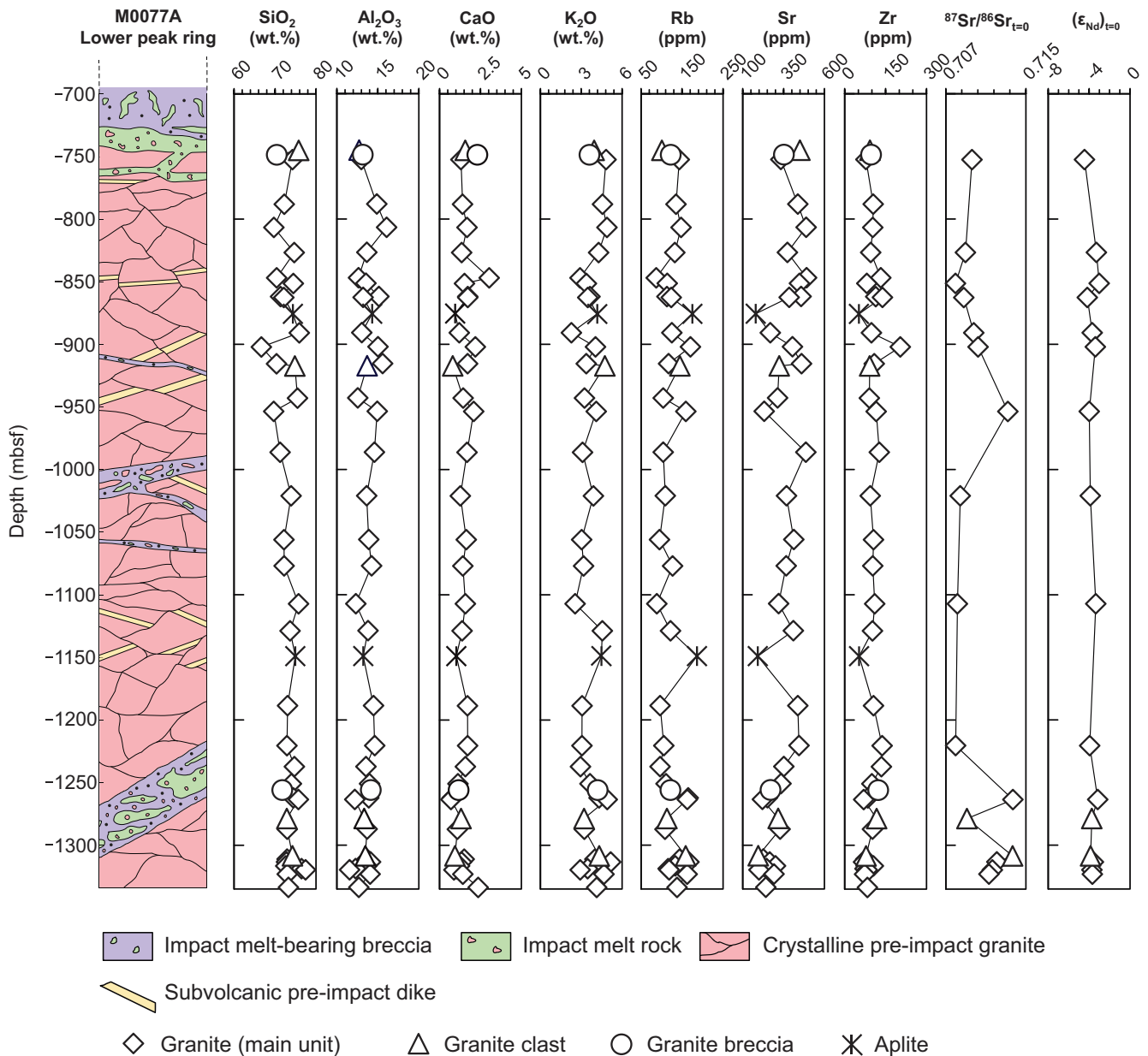
Fig. 2. Lithostratigraphy of the "lower peak ring" section (747.0–1334.7 mbsf) of the Hole M0077A core (from de Graaff et al. 2021), comparing the concentration variations of selected major (SiO_2, Al_2O_3, CaO, K_2O), trace elements (Rb, Sr, Zr), and Sr–Nd isotopic compositions with depth in the investigated samples. (Color figure can be viewed at wileyonlinelibrary.com.)

Using the ages presented in both Zhao et al. (2020) and Ross et al. (2021), we can assume that these granites were probably emplaced during the Carboniferous. During this period, the Yucatán block was located at the edge of the Gondwana craton and recorded arc magmatism originating from the subduction of oceanic crust of the Rheic ocean beneath the northern edge of Gondwana before its collision with Laurentia (Pangean assembly) according to the geotectonic reconstructions of Dickinson and Lawton (2001).

MATERIALS AND METHODS

Sample Selection

Forty-one samples ranging from 20 to 50 g in mass were prepared from a selected number of granitoid samples taken at regular intervals between 745.1 and 1334.7 mbsf. Sample nomenclature used in this study corresponds to Core#Section#_Top(cm)–Bottom(cm) and indicates the exact sampling interval as defined in Morgan et al. (2017), while the centimeters indicate the

distance in a core section from the top. The uppermost sample consists of a granite clast located in the upper impact melt rock (Unit 3), whereas the other samples were taken from the "lower peak ring" section. Due to the size of core samples (8 cm diameter), special care was taken to select representative equigranular granite samples to assess any compositional variation with core depth; texture change; and the effects of shock, fracturing, and other types of chemical alteration as well as the fluid circulation following the onset of the hydrothermal system. As such, three samples exhibiting a porphyritic texture (with large K-feldspar crystals up to 7 cm in size) were excluded from the scope of this study, as their chemistry would be biased by K-feldspar accumulation rather than representing whole rock composition.

The majority of the selected samples ($n = 33$) were taken from the main granite unit (i.e., granites sampled from the continuous granite interval of at least 1 m in thickness). In addition, samples of granite clasts in impact melt rock ($n = 4$), one from the "upper impact melt rock" and the remaining three from the LIMB, were selected. A granite clast was considered in this study as having a size smaller than one meter throughout the drill core. Additionally, two granite breccias as well as two aplites were selected to assess any chemical variation related to petrographic textures. Sample locations and their relative depths within the core are shown in Fig. 2 and Table 1.

Petrographic Investigations

Polished thin sections of the samples were prepared and investigated for their mineralogy, textures, and shock metamorphic features in minerals using optical microscopy at the University of Vienna and a JEOL JSM-6610 variable pressure (VP) scanning electron microscope (SEM) at the Natural History Museum (Vienna, Austria). Additionally, detailed investigations on shocked quartz grains were made on 11 thin sections using a universal stage (see Feignon et al. 2020).

Major Element Mapping

Energy-dispersive micro X-ray fluorescence (μXRF) was performed on 20 granite samples at the Vrije Universiteit Brussels (VUB) using a Bruker M4 Tornado benchtop μXRF surface scanner equipped with an Rh tube as X-ray source and two XFlash 430 Silicon Drift detectors. This technique produced high-resolution elemental distribution maps by scanning flat sample surfaces (i.e., polished thin and thick sections), in a rapid, nondestructive, and cost-efficient way (e.g., de Winter and Claeys 2016; Kaskes et al. 2021). The μXRF

mapping was performed with two detectors and maximized X-ray source energy settings (50 kV and 600 μA, without any filter). The measurements were carried out under near vacuum conditions (20 mbar) with a spatial resolution of 25 μm and an integration time of 1 ms per 25 μm. This approach resulted in qualitative multi-element maps and semiquantitative single-element heat maps, in which the highest spectral peak for one element (i.e., the largest number of counts below the—in general—Kα peak) corresponds to the pixel in the sample with the highest possible RGB value (i.e., 255).

Geochemical Analysis

The samples were crushed in polyethylene wrappers and then powdered in an agate bowl using a Retsch RS200 vibratory disk mill. The obtained sample powders were then stored in clean, hermetically sealed, polyethylene vials.

Major Element Analysis

Samples were measured by means of glass bead-based X-ray fluorescence (XRF). The analyses were performed using an X-ray spectrometer PHILIPS PW2404 at the Department of Lithospheric Research (University of Vienna, Austria) with a super sharp end window tube and an Rh-anode. The element concentrations were determined using calibration curves established using international reference materials. Accuracy and precision values (in wt%) are about 0.6 for SiO_2 and Fe_2O_3, 0.3 for Al_2O_3, 0.2 for Na_2O, 0.07 for MgO and CaO, 0.03 for TiO_2 and K_2O, 0.02 for P_2O_5, and 0.01 for MnO.

Approximately 3 g of homogenized rock powder was weighed in a porcelain crucible that was previously heated at 1050 °C for at least 3 h and cooled down to room temperature in a desiccator. For LOI determination, the crucible with rock powder was placed into an oven at 110 °C overnight, and weighed again. Next, the crucible with rock powder was placed into a muffle furnace at 850 °C for 3 h, and weighed one final time. The LOI was then calculated.

Fused beads were prepared by adding 0.8 g of the calcined sample powder to 8.0 g of a di-lithium tetraborate and di-lithium metaborate (Fluxana FX-X65-2) mixture (2:1 ratio). This mixture was then poured into a crucible of platinum and gold and fused using a PANalytical EAGON 2 furnace.

Trace Element Analysis

Trace element concentrations were both measured using bulk XRF and instrumental neutron activation analysis (INAA). The bulk XRF measurement for trace element concentrations was done on pressed powder

Table 1. Major element concentrations (in wt%) of all the investigated samples from the Expedition 364 Chicxulub drill core, namely granites (from the main unit), granite clasts, granite breccias, and aplites, as determined using bulk XRF.

Sample	Depth (mbsf)	SiO_2	TiO_2	Al_2O_3	Fe_2O_3*	MnO	MgO	CaO	Na_2O	K_2O	P_2O_5	LOI	Total	K_2O/Na_2O	A/CNK	Mg#
Granites (from the main unit)																
97R3_10–12.5	752.5	74.3	0.16	13.0	1.07	0.02	0.46	1.31	3.71	4.82	0.05	1.06	99.90	1.30	0.94	40
110R2_14–16	788.1	72.3	0.21	14.9	1.09	0.02	0.47	1.41	4.82	4.56	0.05	b.d.l.	99.76	0.95	0.96	40
116R2_58–62	806.7	69.7	0.21	16.1	1.28	0.02	0.61	1.68	4.75	4.88	0.07	1.34	100.63	1.03	0.99	42
125R1_40–42.5	826.7	74.7	0.14	13.7	0.90	0.01	0.36	1.36	4.36	4.27	0.04	0.52	100.31	0.98	0.96	38
134R3_75–79	846.9	70.4	0.26	12.6	1.60	0.04	1.32	3.04	4.52	2.91	0.08	2.28	99.10	0.64	0.78	56
136R2_20–25	851.4	74.5	0.12	13.5	0.67	0.01	0.33	1.53	4.67	3.38	0.03	1.08	99.85	0.72	0.96	43
142R2_105–109	861.9	71.4	0.20	15.1	1.50	0.02	0.62	1.73	5.05	3.64	0.07	0.01	99.32	0.72	0.98	39
142R3_48–50	862.6	72.2	0.38	13.2	2.55	0.04	0.94	1.73	4.23	3.48	0.20	0.70	99.60	0.82	0.95	36
153R1_47–50.5	890.8	75.9	0.24	13.0	1.04	0.01	0.56	1.21	5.38	2.27	0.10	1.04	100.81	0.42	0.96	45
156R3_11–15	902.1	66.7	0.48	15.0	3.76	0.06	1.35	2.19	4.93	4.04	0.34	0.49	99.32	0.82	0.91	36
163R1_76–77.5	915.5	70.4	0.22	15.6	1.47	0.02	0.61	1.72	5.41	3.37	0.09	0.62	99.47	0.62	0.99	39
172R1_118–121	942.9	75.5	0.15	12.6	0.83	0.02	0.36	1.45	4.41	3.24	0.04	1.10	99.64	0.73	0.94	40
176R2_112–116	953.6	69.7	0.26	14.9	1.50	0.02	0.55	2.09	4.04	4.10	0.09	2.64	99.89	1.01	1.00	36
188R2_11–13.5	986.2	71.3	0.27	14.6	1.82	0.03	0.74	1.68	5.22	3.09	0.13	0.67	99.48	0.59	0.97	38
200R3_12.5–15	1021.0	73.9	0.24	13.6	1.23	0.02	0.49	1.27	4.28	3.89	0.05	1.05	100.10	0.91	1.01	38
212R1_129–131.5	1056.0	72.2	0.19	13.9	1.28	0.02	0.57	1.64	4.90	3.03	0.04	1.21	98.95	0.62	0.97	41
219R1_105.5–108	1077.0	72.2	0.21	14.2	1.48	0.04	0.62	1.43	5.24	3.17	0.06	0.64	99.34	0.60	0.97	39
229R2_62–67	1107.2	75.8	0.21	12.3	1.32	0.03	0.59	1.58	4.30	2.55	0.07	1.15	99.87	0.59	0.97	41
236R1_90–92.5	1128.8	73.7	0.20	13.8	1.29	0.02	0.56	1.38	3.89	4.55	0.06	0.60	100.05	1.17	1.00	40
256R1_70–72.5	1188.6	73.1	0.20	14.5	1.57	0.02	0.66	1.71	5.08	3.06	0.07	0.60	100.51	0.60	0.98	39
266R2_95.5–98.5	1220.5	72.9	0.29	14.6	1.74	0.02	0.61	1.72	5.01	3.05	0.11	0.47	100.55	0.61	1.00	35
272R1_28–30.5	1237.2	74.8	0.26	13.5	1.58	0.02	0.56	1.58	5.01	2.94	0.09	0.77	101.10	0.59	0.95	35
276R2_62–64.5	1250.9	74.0	0.18	14.0	1.26	0.01	0.55	1.13	5.03	3.64	0.06	0.69	100.55	0.72	0.98	40
280R1_47–49	1262.2	74.5	0.13	13.9	0.96	0.03	0.36	0.78	4.52	4.30	0.04	0.57	100.04	0.95	1.03	37
280R2_51.5–53.5	1263.5	75.7	0.13	12.2	0.87	0.01	0.33	0.70	3.80	4.91	0.06	0.46	99.15	1.29	0.95	37
288R1_61–64	1287.2	73.0	0.19	13.7	1.14	0.02	0.51	1.09	5.42	3.22	0.07	0.44	98.80	0.59	0.95	41
296R1_116–118	1311.1	73.0	0.16	13.7	1.28	0.03	0.30	1.51	4.50	4.00	0.07	1.29	99.78	0.89	0.94	26
297R1_36–38	1313.4	72.8	0.14	14.1	1.23	0.01	0.29	1.35	4.22	5.16	0.05	1.25	100.62	1.22	0.94	27
298R1_41–43	1316.5	72.6	0.23	13.7	1.25	0.02	0.48	1.23	4.66	4.29	0.09	1.04	99.56	0.92	0.94	37
298R3_1.5–3.5	1318.7	76.5	0.13	12.3	0.71	0.01	0.28	1.05	4.38	3.46	0.04	0.83	99.63	0.79	0.95	38
299R1_52.5–55	1319.7	77.5	0.16	11.6	1.22	0.02	0.56	0.88	4.01	2.92	0.08	1.04	99.89	0.73	1.02	41
300R1_78–79.5	1323.1	73.0	0.17	14.1	0.91	0.02	0.25	1.43	4.46	4.67	0.06	1.33	100.35	1.05	0.94	30
303R2_82–84.5	1333.7	73.3	0.16	12.7	0.59	0.01	0.14	2.37	4.11	4.13	0.08	1.93	99.49	1.00	0.82	27
Granite clasts																
95R2_19–22	745.1	75.8	0.19	12.7	0.94	b.d.l.	0.63	1.57	3.82	3.95	0.09	0.53	100.23	1.03	0.95	51
163R3_52–57	917.3	74.8	0.19	13.7	0.94	0.01	0.61	0.81	4.11	4.73	0.06	0.71	100.70	1.15	1.03	50

Table 1. *Continued.* Major element concentrations (in wt%) of all the investigated samples from the Expedition 364 Chicxulub drill core, namely granites (from the main unit), granite clasts, granite breccias, and aplites, as determined using bulk XRF.

Sample	Depth (mbsf)	SiO_2	TiO_2	Al_2O_3	Fe_2O_3*	MnO	MgO	CaO	Na_2O	K_2O	P_2O_5	LOI	Total	K_2O/Na_2O	A/CNK	Mg#
285R2_26–28.5	1278.7	72.9	0.24	13.3	1.69	0.02	0.64	1.32	5.13	3.20	0.11	0.45	99.00	0.62	0.93	37
295R2_51–53	1308.5	74.3	0.13	13.5	1.01	0.01	0.26	0.95	4.36	4.32	0.05	0.80	99.61	0.99	0.99	28
Granite breccias																
96R2_50–52	748.7	70.5	0.23	13.2	1.62	0.04	1.10	2.32	4.39	3.61	0.08	2.14	99.15	0.82	0.86	51
1278R1_43–45	1256.0	71.8	0.22	14.1	1.69	0.02	0.67	1.17	4.90	4.21	0.10	0.53	99.43	0.86	0.96	38
Aplites																
147R2_0–3	875.7	74.4	0.05	14.3	0.55	0.01	0.07	0.96	5.12	4.17	0.02	0.54	100.17	0.81	0.97	16
242R3_23–26	1149.0	75.0	0.09	13.2	0.59	0.02	0.15	1.03	4.37	4.48	0.03	0.66	99.60	1.03	0.95	28

b.d.l. = below detection limit; LOI = loss on ignition.
*Iron oxide reported as total ferrous Fe.

pellets. The latter were prepared by mixing 0.5 mL of an aqueous polyvinyl alcohol solution (MERCK Mowiol) and approximately 10 g of non-ignited rock powder. The mixture was then placed in a hydraulic press, applying a pressure of approximately 16 tons per square centimeter. The pressed powder pellets were then dried in an oven at 70 °C overnight. Tool cleaning was done using acetone. The trace element concentrations were then obtained by using the intensities at peak and background positions, which were measured on blank specimens for interpolating background intensity at the peak position (Nisbet et al. 1979).

For bulk INAA analysis, between 100 and 150 mg of dried rock powder was placed in small polyethylene vials that were sealed to avoid any leaking of material and/or radioactive contamination after irradiation. The same was done for international reference materials (standards ACE granite, ALL Allende carbonaceous chondrite meteorite, and SDO-1 shale) but using less material (60–90 mg). Samples were then packed in groups of 17, to which three standard samples were added.

Samples and standards were irradiated together for 8 h in the 250 kW Triga reactor of the Atomic Institute of the Austrian Universities at a neutron flux of 2×10^{12} n cm^{-2} s^{-1}. Samples and standards were then measured with coaxial Canberra HpGe detectors in three cycles (L1, L2, and L3). The cycle L1 was measured ~5 days after irradiation. Each sample is measured for at least 60 min. Cycle L2 was done ~10 days after irradiation, with ~3–4 h measuring time for each sample. Finally, the Cycle L3 was performed 3–4 weeks after irradiation and the samples were measured for at least 12 h (generally 24 h in this study). Data obtained were then processed automatically by computer, and neutron flux correction was applied. Finally, the data were checked manually. Replicate analysis of international reference materials ACE, ALL, and SDO-1 ($n = 8$) yielded reproducibilities for trace element contents on the order of ~2 to 15 rel%. More details on instrumentation, accuracy, and precision of this method can be found in, for example, Koeberl (1993b), Son and Koeberl (2005), and Mader and Koeberl (2009).

Sr–Nd Isotopic Analysis

The Sr and Nd isotopic analytical work was performed at the Department of Lithospheric Research (University of Vienna, Austria). Sixteen of the 41 aforementioned samples were selected, including granite ($n = 14$) and granite clasts ($n = 2$).

Rock powders (approximately 50–100 mg) were digested in tightly screwed Savillex beakers using an ultra-pure mixture of HF:HNO$_3$ (4:1 ratio) for 2–

4 weeks at 100–120 °C on a hot plate, in order to make sure the insoluble phases, such as zircon, were fully digested. After acid evaporation, repeated treatment of the residue using 6 M HCl resulted in clear solutions. Element isolation for Sr and rare earth elements (REE) was performed using AG 50W-X8 (200–400 mesh, Bio-Rad) resin and 2.5 and 4.0 M HCl as eluants. Neodymium was separated from the REE group using Teflon-coated HDEHP and 0.22 M HCl as eluant. Maximum total procedural blanks were <1 ng for Sr and 40 pg for Nd, which can be considered negligible for the purpose of this work. The isolated element fractions were loaded on an Re double filament assembly and run in static mode on a Thermo-Finnigan Triton thermal ionization mass spectrometer (TIMS) instrument. Mass fractionation was corrected for $^{88}Sr/^{86}Sr = 8.3752$ and $^{146}Nd/^{144}Nd = 0.7219$, respectively. Samples were measured in two successive batches. Mean $^{87}Sr/^{86}Sr$ of 0.710260 ± 0.000004 (batch 1, $n = 5$) and 0.710257 ± 0.000006 (batch 2, $n = 5$) were determined for the NBS987 (Sr) and mean $^{143}Nd/^{144}Nd$ ratios of 0.511846 ± 0.000003 (batch 1, $n = 5$) and 0.511841 ± 0.000002 (batch 2, $n = 5$) for the La Jolla (Nd) international standards during the period of investigation. Uncertainties quoted represent 2σ errors of the mean. The isotopic ratios $^{87}Rb/^{86}Sr$ and $^{147}Sm/^{144}Nd$ were derived from Rb/Sr and Sm/Nd ratios obtained following Rb–Sr and Sm–Nd concentration measurements performed by XRF and INAA, respectively. The assigned uncertainties to $^{87}Rb/^{86}Sr$ and $^{147}Sm/^{144}Nd$ are 1 and 7%, respectively, with an uncertainty on Rb, Sr, Sm, and Nd measurements of 1, 0.4, 2, and 5%, respectively (Son and Koeberl 2005; Mader and Koeberl 2009; Nagl and Mader 2019).

RESULTS

Petrography

Granites and Granite Clasts

The investigated samples mainly consist of equigranular coarse-grained, holocrystalline and phaneritic leucogranite. The bulk mineral assemblage is mainly composed of orange to brownish K-feldspar (orthoclase, ~25–50 vol%); plagioclase (~15–35 vol%); quartz (~15–35 vol%); and, to a lesser extent, biotite (generally 1–5 vol%). Two samples (156R3_11–15 and 272R1_28–30.5) display a higher biotite content of ~10 vol%. The grain size varies from ~0.5 to 4 cm for K-feldspar, plagioclase, and quartz, and from ~0.1 to 1 cm for biotite (Figs. 3 and 4). Textural and compositional variations are common throughout the granite unit. The main accessory minerals are muscovite, (fluor)apatite, titanite, secondary epidote (piemontite) located in cataclasite areas or associated with calcite veins, zircon, (titano)magnetite, and allanite. Other accessory minerals, including monazite, ilmenite, rutile, chalcopyrite, cobaltoan pyrite, stolzite/raspite, galena, uranothorite, and uranothorianite, were also detected during an SEM survey (Fig. 5). These accessory phases represent <1 vol% of the mineral assemblage and grain size is never more than 0.5 mm. Alteration is pervasive, as evidenced by epidote mineralization; sericitization of plagioclases; common chloritization of biotite; and the presence, to some extent, of secondary albite/K-feldspar veins crosscutting the granite unit (Fig. 4) (see also Kring et al. 2020). Granite alteration appears to be more pronounced in close proximity to impact melt rock dikes and along fractures.

The granite unit is pervasively deformed to different degrees from one sample to another, ranging from not or slightly deformed to displaying strong mineral deformation associated with foliation, this ductile deformation is thought to be pre-impact, providing evidence for local shear zones cutting the granite (see Fig. 3B). In addition, fracturing and shearing that occurred during the impact are abundant, as well as the presence of cataclasite veins made of microbrecciated material (mainly submillimeter-sized feldspars and quartz grains, as well as calcite) cross-cutting the granite (from millimeter to several centimeters in thickness, see Figs. 3C, 3D, and 4). In some cases, the cataclasites exhibit a greenish color associated with the presence of secondary epidote (piemontite), likely due to hydrothermal alteration (Kring et al. 2020). Postimpact calcite veinlets commonly cut through the granite samples. These veinlets are clearly indicated by µXRF mapping (Fig. 6). In addition, calcite fillings are observed in some planar fractures (PFs) within quartz grains (see also Ferrière et al. 2017; Feignon et al. 2020).

Impact-induced shock metamorphic features are apparent in most rock-forming minerals, that is, multiple sets of PFs, feather features (FFs), in average 2.8 sets of planar deformation features (PDFs), undulose extinction, and occasional kinkbanding in quartz grains (for details, see Feignon et al. 2020); in alkali-feldspar and plagioclase (i.e., PFs filled with opaque minerals and also some possible PDFs; see Pittarello et al. 2020), titanite, and apatite (with different types of planar microstructures; Timms et al. 2019; Cox et al. 2020). Kinkbanding is common in biotite, muscovite, and chlorite and also observed, to a lesser extent, in plagioclase and in quartz (Figs. 4D–F).
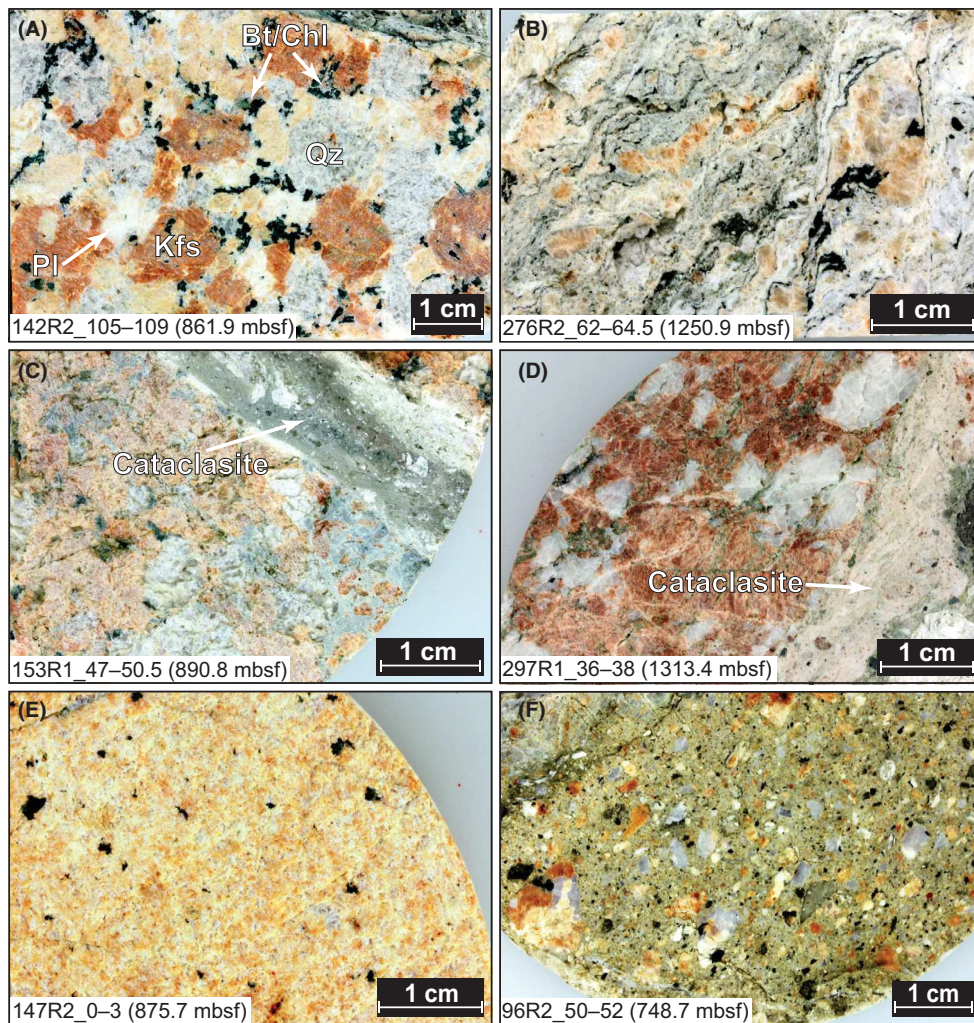
Fig. 3. Macrophotographs of the different sample types from the "lower peak ring" section of the Hole M0077A core investigated in this study. A) Coarse-grained granite, relatively undeformed with limited fracturing, exhibiting the typical paragenesis: K-feldspar (Kfs), quartz (Qz), plagioclase (Pl), biotite (Bt), and chlorite (Chl). B) Highly deformed granite sample with foliated minerals. C and D) Granite samples cross-cut by centimeter-sized cataclasite veins made up of microbrecciated material. The alteration is occurring mainly at the contact between the granite and cataclasite in (D), with greenish mineralization. E) Typical aplite sample with a fine-grained mineralogy and a low-biotite content. F) One of the two investigated granite breccia samples comprises a greenish-gray matrix with mainly K-feldspar and quartz as mineral clasts. (Color figure can be viewed at wileyonlinelibrary.com.)

Granite Breccias

Two of the investigated samples consist of monomict granite breccia. The upper sample (96R2_50–52, 748.7 mbsf) is made of subrounded, ~0.5 mm mineral clasts (mainly quartz and K-feldspar) with rare occurrence (<2 vol%) of biotite (Figs. 3F and 6E). The matrix (~45 vol%) is made of brecciated quartz; K-feldspar; and, to a lesser extent, calcite. The clastic breccia shows no signs of melting.

The second sample (278R1_43–45, 1256.0 mbsf) is similarly brecciated (with ~50 vol% of matrix), but more strongly deformed than 96R2_50–52, with a clear mylonitic-like texture. In addition, the breccia is in contact with a large, 7 cm sized, coarse-grained granite.

Aplites

Samples 147R2_0–3 and 242R3_23–26 (875.7 and 1149.0 mbsf, respectively) are aplites with a fine-grained (average mineral size is <1 mm), homogeneous, equigranular texture (Fig. 3E). The main mineral phases are K-feldspar, quartz, and plagioclase whereas biotite is nearly absent (<1 vol%). Plagioclase exhibits sericitization and some calcite veins crosscut the samples. Shock features in the form of PFs and up to
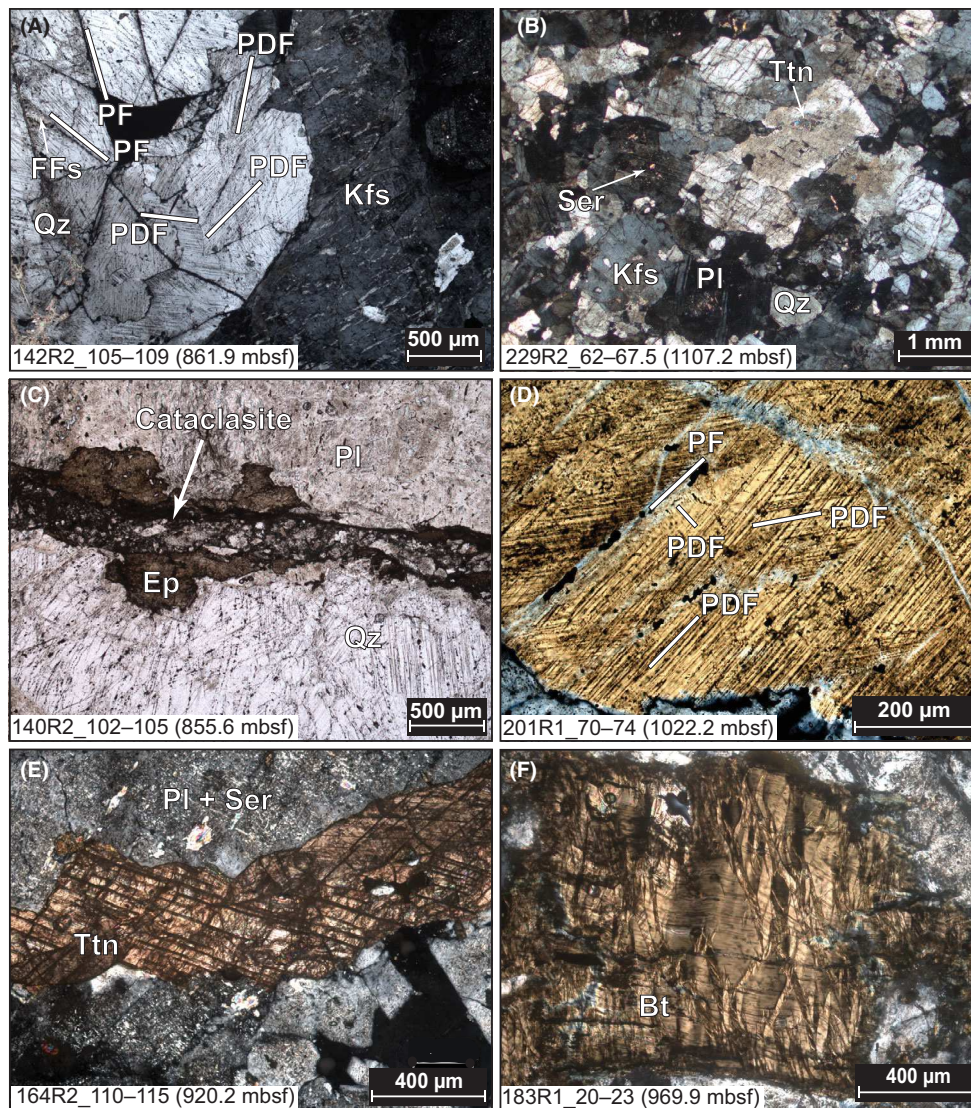
Fig. 4. Thin section photomicrographs (all in cross-polarized light except C in natural transmitted light). A) Typical granite sample with K-feldspar (Kfs) and quartz (Qz) crystals. Quartz is shocked with at least two sets of PF (with FFs) and several sets of PDF, not all shown for image clarity. No obvious shock features are visible on the K-feldspar in this case. B) Granite sample with a finer mean grain size, near aplitic texture. Plagioclase (Pl) is sericitized. Ttn = titanite. C) Cataclasite vein, characterized by brecciated quartz and feldspars, crossing the field of view. Epidote crystals (Ep, piemontite) are localized at the contact between cataclasite and the host rock (i.e., in this case mainly quartz and feldspars). D) Shocked quartz grain with two prominent decorated PDF sets. A third set of PDFs and a set of PFs, barely visible on this photograph, are also indicated with white marks. E) A titanite crystal with well-developed shock-induced planar microstructures (at least two sets visible) next to a sericitized (Ser) plagioclase. F) Large well-developed kinkbands in biotite (Bt). (Color figure can be viewed at wileyonlinelibrary.com.)

three sets of PDFs are observed in quartz grains, while shock microstructures are in some cases also observed in plagioclase.

Geochemistry

Major element contents of all investigated granitoid samples are presented in Table 1 and averaged trace element compositions for each type of sample (i.e.,

granite from the main unit, granite clast, granite breccia, and aplite) are presented in Table 2. Trace element compositions for all 41 investigated samples are reported in Data S1 in supporting information. Strontium and Nd isotopic data are reported in Table 3. In order to allow a discussion of the geochemical patterns of the investigated samples, the contents of selected major (SiO_2, Al_2O_3, CaO, and K_2O) and trace (Ba, Sr, Zr) elements, $^{87}Sr/^{86}Sr$ and $(\varepsilon_{Nd})_{t=0}$
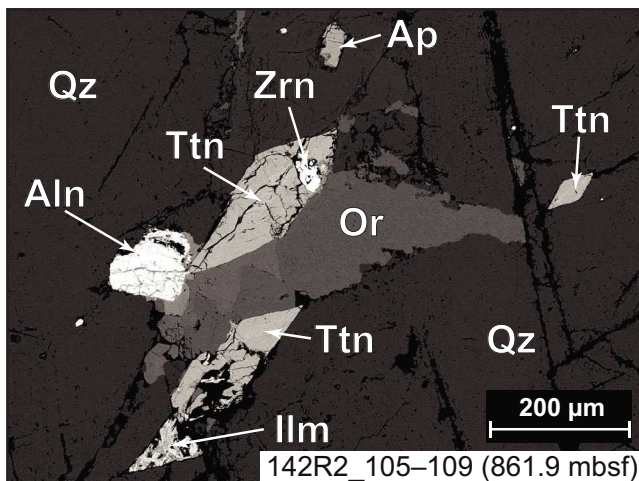
Fig. 5. SEM backscattered electron (BSE) image of an assemblage of the most commonly encountered accessory minerals in the investigated granite samples. Qz = quartz; Or = orthoclase; Ttn = titanite; Ap = apatite; Zrn = zircon; Aln = allanite; Ilm = ilmenite. (Color figure can be viewed at wileyonlinelibrary.com.)

have been plotted against depth from 745.1 to 1333.7 mbsf (Fig. 2). The LOI recorded for all the samples is relatively low (<2.6%, average of $0.91 \pm 0.55\%$, $n = 41$); thus, the data were not recalculated on an LOI-free basis, as this would not change the major element contents significantly. Interestingly, the highest LOI values (>1.5%) are observed for samples located in proximity (<0.5 m) of fractures, shearing areas, and/or dikes (both pre- and postimpact in origin), supporting more pronounced granite alteration near these features, as observed in the petrographic investigations.

Major Elements

Major elements show broadly similar patterns with few exceptions (see Fig. 7), independently of the sample type (granite, granite clast, granite breccia, or aplite) or

the depth in the drill core (Fig. 2), and represent the most evolved lithology compared to pre-impact dikes, suevites, and impact melt rocks (Morgan et al. 2017). Nearly all the samples show a granitic composition, with the SiO_2 and total alkali ($Na_2O + K_2O$) contents ranging from 69.68 to 77.45 wt% and from 6.85 and 9.38 wt%, respectively. Two samples plot outside the granite field and display a monzo-granitic composition with 156R3_11–15 having the lowest SiO_2 content (66.66 wt%) and 8.97 wt% total alkalis, whereas 116R2_58–62 shows the highest total alkali content (9.63 wt%) and 69.73 wt% SiO_2. The investigated granitoid sample suite spreads between the calc-alkaline and the high-K calc-alkaline series (Ewart 1982), with K_2O contents ranging from 2.27 to 5.16 wt%. The Al_2O_3 contents show a continuous, decreasing trend from 16.06 to 11.55 wt% and are accompanied by increasing SiO_2 concentrations. A less pronounced decreasing trend can be noticed for CaO concentration (0.70–3.04 wt%), while other major elements in the investigated samples do not show a clear trend with increasing SiO_2 concentrations but exhibit rather relatively low and homogeneous compositions with limited variations in the $Fe_2O_3^*$ (0.55–2.55 wt%), TiO_2 (0.05–0.38 wt%), and MgO (0.07–1.32 wt%) contents, highlighting the evolved nature of these samples relative to the other lithologies present in the drill core (i.e., suevites, impact melt rocks, and pre-impact dikes, such as dolerite and dacite; see e.g., Morgan et al. 2017; de Graaff et al. 2021). Additionally, the very high SiO_2 contents of all granite samples characterized here indicate a higher degree of fractionation.

The main outlier is sample 156R3_11–15, the least evolved sample with a quartz-monzonite composition, having the highest contents in Fe_2O_3 (3.76 wt%), MgO (1.35 wt%), TiO_2 (0.48 wt%), and P_2O_5 (0.34 wt%) of the investigated sample suite. These relatively high contents can be explained petrographically, as this sample contains ~10% of biotite; additionally, apatite

Fig. 6. Micro-XRF overview of representative investigated granitoid samples thick sections. A) Multi-element (Fe–Si–Ca–K) maps of eight samples. The upper row displays four granites from the main unit, highlighting some of the textural differences. The granite sample 134R3_75–79 is in contact with a dolerite dike and crosscut by several calcite veins. A large cataclasite vein occurs in sample 153R1_47–50.5. Iron is more abundant at the contact between cataclasite and granite while the matrix is relatively enriched in K, thus dominated by brecciated K-feldspar; then quartz; and, to a lesser extent, calcite (Ca-rich area within the cataclasite). The lower row shows two granite clasts, one aplite, and one granite breccia samples. The bulk geochemistry of all these samples is fairly similar; however, the main differences are textural (i.e., deformation; alteration features; or, to a lesser extent, interaction with impact melt rock or dike). B) Strontium distribution map (heatmap) of the same samples shown in (A). The plus and minus on the color scale indicate a high or a low abundance of Sr, respectively. These eight granitoid samples were mapped simultaneously, resulting in a semiquantitative distribution of Sr. Strontium contents display variations from one sample to another. While it is mostly concentrated in plagioclase, a relatively higher Sr content is observed in the Ca-rich area of the cataclasite. The lower Sr content in granite clast 295R2_51–53 is also confirmed by INAA and isotopic analysis (Table 3). Scanned images of thick sections are available in Fig. S1 in supporting information. IMR = impact melt rock. (Color figure can be viewed at wileyonlinelibrary.com.)
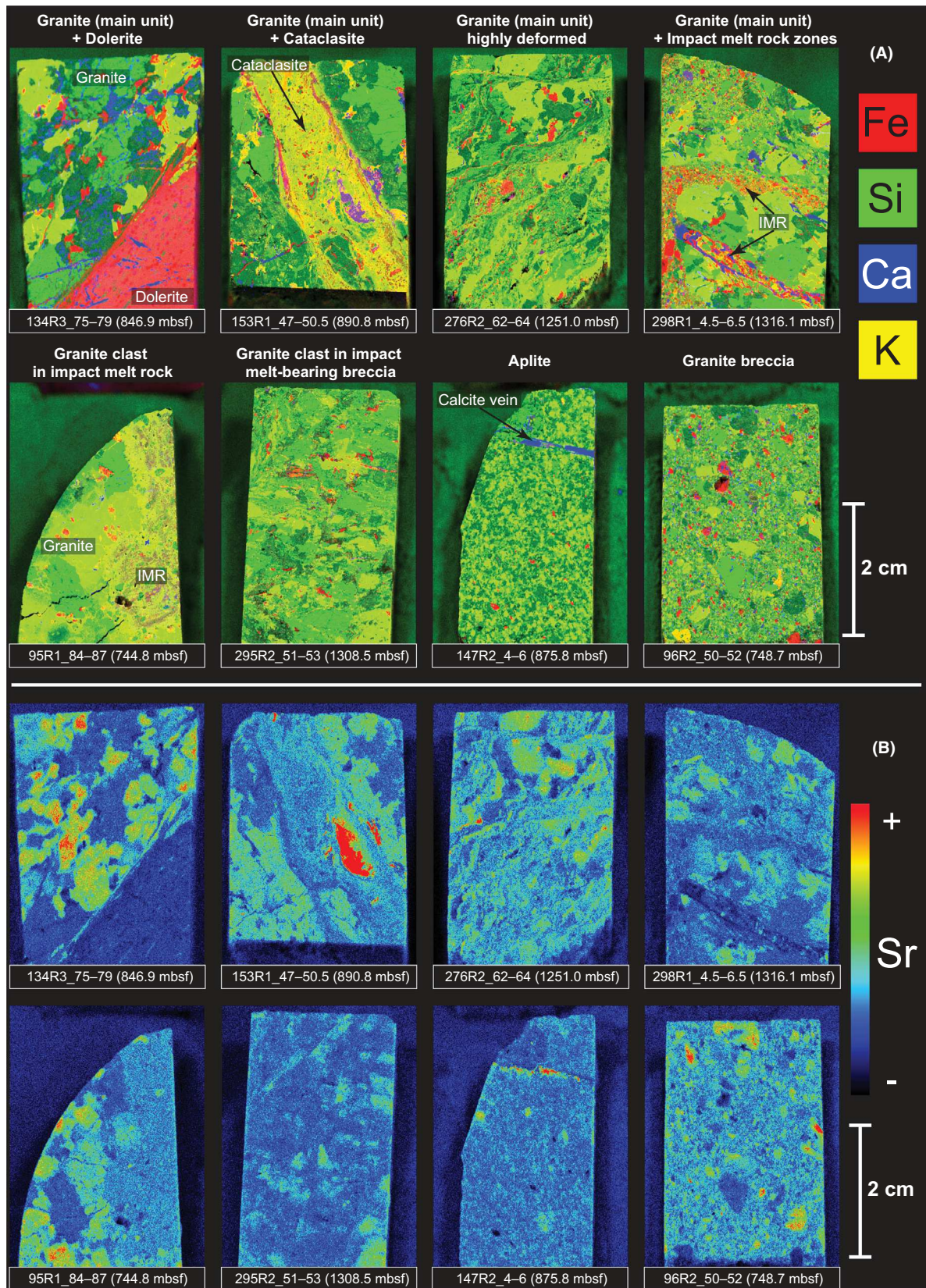
Table 2. Averages and range of trace element contents (all in ppm) for each of the investigated sample types from the Expedition 364 Chicxulub drill core (i.e., granites from the main unit, granite clasts, granite breccias, and aplites) as obtained using INAA and bulk XRF. Detailed results for each sample are available in Data S1.

	Granites (n = 33)		Granite clasts (n = 4)		Granite breccias (n = 2)		Aplites (n = 2)	
	Average	Range	Average	Range	Average	Range	Average	Range
Sc	3.07	1.57–7.82	3.20	2.72–4.06	4.16	3.84–4.49	2.72	1.98–3.46
V*	28.8	12.5–76.0	26.6	18.4–30.1	42.6	36.4–48.7	10.8	6.70–14.8
Cr	11.4	7.27–21.2	10.8	9.67–11.8	20.9	10.9–30.9	6.26	5.41–7.10
Co	3.33	1.22–10.1	3.45	1.91–6.45	4.52	3.42–5.62	0.72	0.52–0.92
Ni*	3.91	1.80–10.2	4.45	2.70–7.10	9.40	4.60–14.2	0.70	0.50–0.90
Cu*	18.4	8.40–123	13.1	9.90–19.0	17.1	12.2–21.9	13.8	11.0–16.5
Zn*	26.2	4.00–89.8	17.4	6.30–25.6	20.5	11.9–29.0	10.6	7.30–13.8
As*	1.50	b.d.l.–3.10	2.27	b.d.l.–4.60	2.20	1.40–3.00	1.75	1.70–1.80
Rb*	126	87.1–171	129	101–159	122	122–122	181	175–187
Ba*	468	229–847	391	211–532	343	266–420	176	170–182
Th*	11.4	5.20–20.0	15.3	8.90–26.3	11.4	9.70–13.1	15.1	13.6–16.5
U*	7.50	3.80–30.2	6.20	2.90–9.20	6.10	5.20–7.00	8.10	5.30–10.9
Nb*	6.49	3.20–12.2	6.13	5.50–7.00	7.05	5.60–8.50	12.5	11.8–13.2
Ta	0.60	0.30–0.95	0.59	0.46–0.76	0.65	0.52–0.79	1.55	1.14–1.97
La	15.0	2.10–30.5	11.3	4.60–14.4	16.7	12.7–20.7	7.50	10.4–4.50
Ce	29.6	9.70–56.2	26.3	10.1–34.0	27.3	26.3–28.3	13.6	10.6–16.5
Pb*	25.3	13.4–98.5	22.6	17.5–33.3	152	24.1–280	32.7	26.2–39.2
Sr*	351	200–491	321	195–450	311	270–352	185	179–192
Nd	11.2	4.00–23.0	11.3	8.40–13.0	15.1	15.0–15.3	7.10	5.80–8.30
Zr*	103	69.2–204	94.9	78.4–117	110	97.3–123	52.7	52.6–52.8
Cs	1.51	0.75–4.87	1.18	0.57–1.50	1.19	1.10–1.30	1.52	1.38–1.67
Hf	3.08	2.03–5.91	2.74	2.42–3.38	3.51	3.06–3.97	2.74	2.63–2.86
Sm	2.38	1.09–5.96	2.39	1.74–3.10	2.80	2.54–3.10	2.48	2.66–2.29
Eu	0.45	0.27–0.85	0.46	0.34–0.60	0.53	0.46–0.60	0.40	0.40–0.40
Gd	2.03	1.03–4.56	1.87	1.24–2.52	1.96	1.32–2.60	2.00	1.54–2.46
Tb	0.16	0.10–0.36	0.16	0.13–0.20	0.21	0.19–0.20	0.23	0.20–0.26
Yb	0.60	0.23–1.04	0.55	0.35–0.70	0.62	0.48–0.76	0.75	0.61–0.90
Y*	5.97	3.70–10.9	6.45	5.60–7.50	8.05	6.80–9.30	7.20	6.20–8.20
Lu	0.08	0.05–0.14	0.09	0.06–0.10	0.11	0.08–0.14	0.10	0.10–0.10
K/Rb	256	158–319	282	250–332	249	234–264	193	192–194
Sr/Y	62.2	36.6–123	49.8	29.6–59.9	40.4	29.0–51.8	26.4	21.8–30.9
(La/Yb)$_N$	19.0	2.85–40.9	15.8	4.64–25.9	20.3	11.3–29.4	7.50	3.40–11.6

b.d.l. = below detection limit.
*Measured with XRF.

and titanite grains are also relatively more abundant than in the other investigated samples.

The relatively high CaO content (2.09–3.04 wt%) observed in four granite and in one granite breccia samples can be explained by (1) the presence of calcite-filled fractures, evidenced by the µXRF mapping of sample 134R3_75–79 (Fig. 6A), the sample with the highest measured CaO contents (3.04 wt%), and the significant presence of calcite in the matrix of the granite breccia sample (see Fig. 6A), respectively, and/ or (2) a higher proportion of plagioclase as is the case for sample 156R3_11–15, which displays ~35 vol% plagioclase and a lower abundance of calcite veins relative to the other CaO-rich granites.

Based on the $Al_2O_3/(Na_2O + K_2O)$ versus $Al_2O_3/(CaO + Na_2O + K_2O)$ diagram (see Fig. 10), the

investigated samples are metaluminous to weakly peraluminous. The K_2O/Na_2O ratios of the granitoids range from 0.42 to 1.30, with an average of 0.84 ± 0.21.

Trace Elements

Concerning trace element contents presented in CI-chondrite-normalized diagrams (Fig. 8), with normalization values from McDonough and Sun (1995), the granites from the main unit (Fig. 8A) show similar patterns to one another and to literature data (Zhao et al. 2020; de Graaff et al. 2021), with enriched compositions relative to CI-chondritic values. Fluid-mobile elements, such as Ba and U, are highly enriched, with samples 298R1_41–43 and 300R1_78–79.5, located in the lower part of the basement (1316.5 and 1323.1 mbsf, respectively), and highly fractured,

Table 3. Rb–Sr and Sm–Nd isotopic compositions of 14 granites and two granite clasts from the Expedition 364 Chicxulub drill core.

Sample	Depth (mbsf)	Rb (ppm)	Sr (ppm)	^{87}Rb/^{86}Sr[a]	^{87}Sr/^{86}Sr[b]	(^{87}Sr/^{86}Sr)$_{I=326Ma}$	Sm (ppm)	Nd (ppm)	^{147}Sm/^{144}Nd[a]	^{143}Nd/^{144}Nd[c]	ε_{Nd}[d]	(ε_{Nd})$_{I=326Ma}$	T^{Nd}_{DM} (326Ma) (Ga)[e]
Granites													
97R3_10–12.5	752.5	143	333	1.2431	0.709614	0.70385	1.73	10.0	0.1025	0.512410	−4.4	−0.5	1.1
125R1_40–42.5	826.7	132	374	1.0217	0.708963	0.70422	1.70	8.03	0.1285	0.512470	−3.3	−0.4	1.1
136R2_20–25	851.4	114	447	0.7382	0.707975	0.70455	1.09	4.10	0.1607	0.512484	−3.0	−1.5	1.2
142R3_48–50	862.6	124	384	0.9347	0.708807	0.70447	4.09	23.0	0.1075	0.512424	−4.2	−0.5	1.1
153R1_47–50.5	890.8	125	269	1.3452	0.709801	0.70356	2.00	10.0	0.1209	0.512449	−3.7	−0.5	1.2
156R3_11–15	902.1	171	404	1.2254	0.710231	0.70454	1.20	19.0	0.0382	0.512464	−3.4	3.2	0.8
176R2_112–116	953.6	159	231	1.9933	0.713210	0.70396	1.94	14.0	0.0838	0.512433	−4.0	0.7	1.0
200R3_12.5–15	1021.0	109	368	0.8573	0.708447	0.70447	2.47	13.9	0.1074	0.512439	−3.9	−0.2	1.1
229R2_62–67	1107.2	89	319	0.8075	0.708159	0.70441	2.02	14.0	0.0872	0.512467	−3.3	1.2	0.9
266R2_95.5–98.5	1220.5	106	444	0.6910	0.707981	0.70477	2.16	16.0	0.0816	0.512436	−3.9	0.8	1.0
280R2_51.5–53.5	1263.5	163	220	2.1457	0.713705	0.70375	2.80	10.4	0.1628	0.512477	−3.1	−1.7	1.2
297R1_36–38	1313.4	167	265	1.8248	0.712105	0.70364	1.36	4.00	0.2055	0.512454	−3.6	−4.0	1.4
299R1_52.5–55.5	1319.7	118	200	1.7083	0.711652	0.70373	1.39	9.00	0.0934	0.512447	−3.7	0.6	1.0
300R1_78–79.5	1323.1	162	291	1.6118	0.711322	0.70384	3.25	11.8	0.1659	0.512449	−3.7	−2.4	1.2
Granite clasts													
285R2_26–28.5	1278.7	113	317	1.0319	0.709111	0.70432	3.10	12.6	0.1487	0.512447	−3.7	−1.7	1.2
295R2_51–53	1308.5	159	195	2.3614	0.713686	0.70273	1.82	13.0	0.0846	0.512440	−3.9	0.8	1.0

[a]Uncertainties on ^{87}Rb/^{86}Sr and ^{147}Sm/^{144}Nd are ±1.0% and ±5.0%, respectively.
[b]The uncertainty on ^{87}Sr/^{86}Sr ratio is ±2σ = 0.000004.
[c]The uncertainty on ^{143}Nd/^{144}Nd ratio is ±2σ = 0.000004.
[d]Calculated using ^{143}Nd/^{144}Nd$_{CHUR}$ = 0.512638 (DePaolo and Wasserburg 1976). CHUR = chondritic uniform reservoir.
[e]Two-stage Nd model age calculated following the method of Liew and Hofmann (1988) with ^{143}Nd/^{144}Nd$_{DM}$ = 0.513151, ^{147}Sm/^{144}Nd$_{DM}$ = 0.219, and ^{147}Sm/^{144}Nd$_{CC}$ = 0.12. DM = depleted mantle; CC = continental crust.
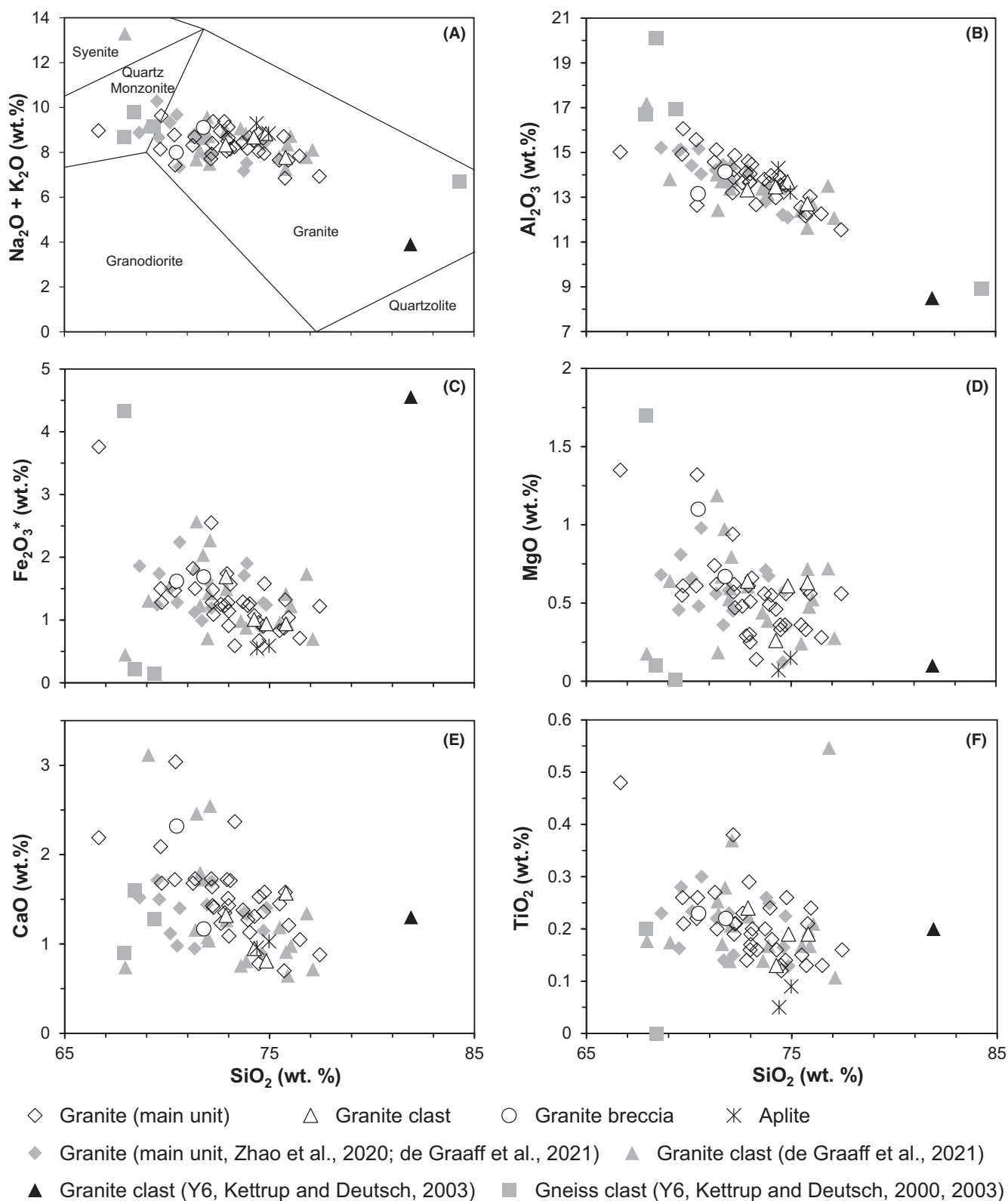
Fig. 7. A) Total alkalis versus SiO$_2$ (TAS) diagram (upper left) modified from Middlemost (1994). B–F) Harker diagrams of Al$_2$O$_3$, Fe$_2$O$_3$* (total ferrous Fe), MgO, CaO, and TiO$_2$ versus SiO$_2$ for the investigated granite, granite clast, granite breccia, and aplite samples.

showing values more than 1000 times the CI-chondritic value for U, whereas a depletion of Pb is observed for nearly all the samples. In contrast, Nb and Ta show a relative depletion, while Zr and Hf show a moderate enrichment, relative to neighboring trace elements, a pattern typical of arc-type magmatism (Pearce et al. 1984). Otherwise, the granites are mainly characterized by light rare earth elements (LREE) with concentrations higher than 10 times CI-chondritic values and lower contents of heavy rare earth elements (HREE), below 10 times the CI-chondritic values, and displaying a relatively flat pattern. No pronounced positive or negative Eu anomalies were recorded. Additionally, Yb shows a slight negative anomaly relative to Er and Y (Yb^* is 0.81 ± 0.30, $Yb^* = Yb_N/[Er_N \times Y_N]^{0.5}$, $n = 33$) in some of the samples. While similar Yb negative anomalies may previously have been observed, Yb is more slightly depleted relative to Lu in the samples investigated by Zhao et al. (2020) and de Graaff et al. (2021), and thus, an analytical artifact cannot be fully excluded here. Negative Yb anomalies require highly reducing conditions to occur and are typically coupled with clear Eu anomalies (Hsu 2003), which are not observed in our samples. Finally, some samples show either a depletion or an enrichment in some elements relative to the large majority of the granites. Sample 136R2_20–25 is depleted in La and Nd (an Nd depletion is also observed for 297R1_36–38), whereas sample 153R1_47–50.5 exhibits no depletion in Pb compared to the other investigated samples.

The trace element compositions of the granite clasts are plotted in Fig. 8B. The concentrations for the plotted elements are within the range of the investigated granite samples from the main unit, with only sample 95R2_19–22 showing a small depletion in La and Ce and an enriched Sr composition compared to the other clasts investigated.

The trace element contents of the two investigated granite breccia samples are shown in Fig. 8C. Sample 278R1_43–45 does not exhibit any significant differences compared to the main granite suite, whereas sample 96R2_50–52 shows a clear enrichment in Pb (280 ppm relative to the <99 ppm in the main granite group), which may be explained by the presence of a Pb-bearing phase (e.g., sulfide minerals). These secondary phases are commonly observed in the impact melt-bearing breccias (see Kring et al. 2020), making this Pb-enrichment secondary. The Pb composition of this specific sample (as for granite 153R1_47–50.5) is similar to that of the "upper impact melt rock" sample 100_2_89.5_91.5 investigated by de Graaff et al. (2021) and may have a similar secondary Pb-enriched component.

The two investigated aplites (Fig. 8D) have trace element composition patterns somewhat similar to those of the granites, with only a slight enrichment in Ta and a depletion in Ba and Zr concentrations. Sample 147R2_0–3 is also slightly depleted in La concentrations compared to the granites. However, in bivariate immobile trace element diagrams (Fig. 9), the aplites plot slightly outside of the main trend as defined by the granites; the difference is even more striking in the Ta versus Nb diagram (Fig. 9B).

Sr–Nd Isotopic Ratios

In the 16 investigated granite samples (including two granite clasts from the lower part of the core; samples 285R2_26–28.5 and 295R2_51–53), the element concentrations range from 89 to 171 ppm Rb, 195 to 447 ppm Sr, 1.1 to 4.1 ppm Sm, and 4.1 to 23 ppm Nd. The granite clasts do not have distinct Rb–Sr/Nd–Sm concentrations relative to the main granite group (Table 3). The Rb/Sr and Sm/Nd ratios vary from 0.24 to 0.82 and from 0.14 to 0.27, respectively. Only granite 156R3_11–15 shows a lower Sm/Nd ratio of 0.06.

The present-day $^{87}Sr/^{86}Sr$ ratios show a clear variability, ranging from 0.70798 and 0.71371 (Table 3). Interestingly, the samples located close to the bulk of the LIMB, in the lower part of the granite unit (at 1263.5 mbsf, $n = 6$), where several impact melt rock and suevite dikes occur, and where the granite exhibits higher degrees of deformation relative to the upper samples, generally display more radiogenic compositions than in the upper part ($n = 10$), with average $^{87}Sr/^{86}Sr$ of 0.711930 and 0.709319, respectively. Only sample 176R2_112–116 (953.6 mbsf) has a distinct, more radiogenic composition in the upper part of the granite unit, with an $^{87}Sr/^{86}Sr$ of 0.713210. This particular sample is characterized by the presence of 2–3 mm cataclasites and is near a contact with a 10 cm thick, pervasive, shear zone. The $^{87}Rb/^{86}Sr$ ratios range from 0.6910 to 2.3614. Samples in close proximity to the LIMB display a generally higher $^{87}Rb/^{86}Sr$ ratio (average of 1.7807) compared to the samples located in the upper part of the granite unit (average of 1.0857). The investigated samples form an isochron between $^{87}Sr/^{86}Sr$ and $^{87}Rb/^{86}Sr$ (see Fig. 11C). Given the estimated errors on the $^{87}Sr/^{86}Sr$ and $^{87}Rb/^{86}Sr$ ratios, the isochron has a very high scattering with a mean square of weighed deviates (MSWD) of 25. The MSWD of the isochron is well above the value for a statistically acceptable isochron, defined at <~2.5 by Brooks et al. (1972), and, thus, should be considered to represent an errorchron, indicating that the Rb–Sr system has not been completely reset. The apparent regression age is calculated to be 273 ± 21 Ma, with an initial $^{87}Sr/^{86}Sr$
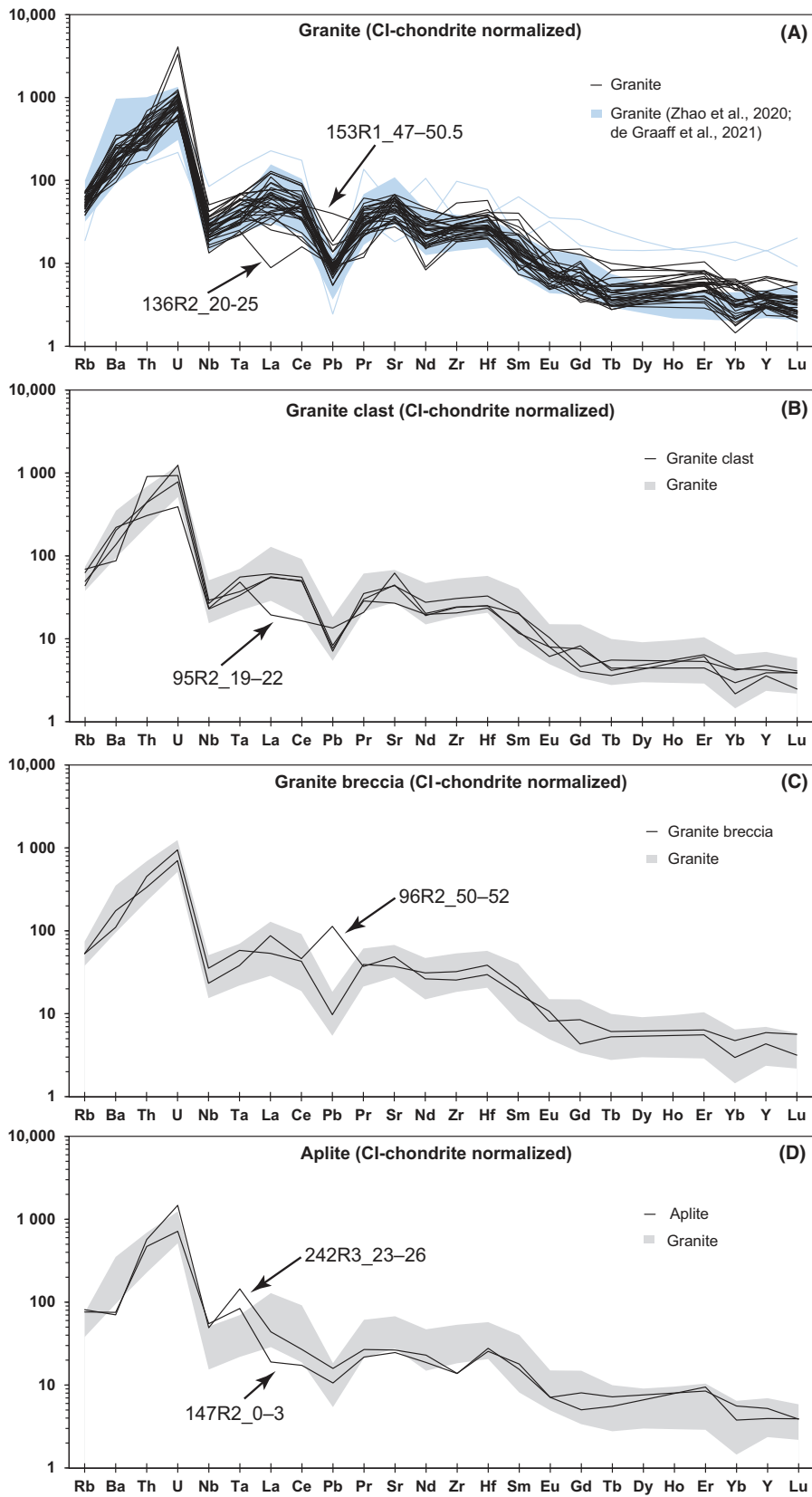
Fig. 8. A–D) CI-chondrite-normalized trace element compositions, with normalization values from McDonough and Sun (1995). A) The blue area in the upper diagram represents the compositions from previous work made on granite from the M0077A core (Zhao et al. 2020; de Graaff et al. 2021). B–D) The gray outline represents the main composition of all the granite samples investigated in this study, to allow a comparison with the granite clast, breccia, and aplite samples. Investigated samples have highly similar patterns, except one granite breccia with a significant Pb positive anomaly that may due to the presence of a Pb-bearing phase. (Color figure can be viewed at wileyonlinelibrary.com.)

of 0.705164 ± 0.0003. However, given the high uncertainty on age determination and its deviation from the well-constrained U–Pb Carboniferous ages obtained in zircons by Zhao et al. (2020) and Ross et al. (2021), this apparent age obtained from the errorchron corresponds to a disturbance of the Rb–Sr system (see the Discussion section).

In contrast, current $^{143}Nd/^{144}Nd$ ratios display limited variations (0.512410–0.512484) and $(\varepsilon_{Nd})_{t=0}$ values plot in a narrow range between -4.4 and -3.0 for all the investigated samples. The corresponding $^{147}Sm/^{144}Nd$ ratios vary from 0.0816 to 0.2055, while granite sample 156R3_11–15 shows a lower $^{147}Sm/^{144}Nd$ ratio of 0.0382 (Table 3). There is no significant difference observed between samples in the upper part of the granite unit and the samples in the lower part, next to the LIMB, indicating that Nd remained mostly unaffected by alteration processes.

Based on the work of Zhao et al. (2020), the initial $^{87}Sr/^{86}Sr$ and ε_{Nd} are calculated using $t = 326$ Ma. Initial $(^{87}Sr/^{86}Sr)_{t=326Ma}$ are 0.70273–0.70477, while $(\varepsilon_{Nd})_{t=326Ma}$ vary from -4.0 to 3.2 (see Fig. 11A). The Nd two-stage model age (DePaolo 1981; Liew and Hofmann 1988) $T_{DM2(326Ma)}$ ranges between 0.8 and 1.4 Ga. The model ages are relatively similar for all samples (Table 3).

DISCUSSION

Granite Characterization

In general, the granitoids investigated in this study (i.e., granites, granite clasts, brecciated granites, and aplites) are relatively homogeneous in terms of their major element content (i.e., limited variations in composition or well-defined compositional trends). Only a single outlier compared to the other granitoids, the quartz-monzonite sample (156R3_11–15), with higher major element contents other than SiO_2, as well as enrichments in Zr and Hf, is noted. The relatively high proportion of plagioclase (~35 vol%), biotite (~10 vol%), and zircon may explain the distinct chemical composition of this sample. No samples with clearly distinct compositions were identified, suggesting that the investigated granite clasts all belong to the main granite unit, and that the granite breccias did not experience

significant interaction with lithologies other than granite during their emplacement. Additionally, the textural variations (i.e., degree of deformation, presence of cataclasite veins) observed during petrographic investigations (see the Petrography section 4.1) within the main granite unit do not significantly affect the major element contents. As a result, for simplicity, all the investigated samples are from here onward termed "granite" (whether they are granite clasts or granite breccia samples; also including the aplite samples [except where indicated], which are a fine-grained equivalent of granite).

The granite samples are characterized by a decreasing Al_2O_3 and, to a lesser extent, CaO content, with increasing degrees of differentiation, as is commonly associated with fractionation of plagioclase (Langmuir et al. 1992; Sisson and Grove 1993), although the variation of modal mineral components (mainly the K-feldspar content relative to plagioclase) may contribute, to some extent, to these trends. However, the Al_2O_3 contents are relatively high, indicating a retention of plagioclase in the granite, albeit to a limited extent as no positive Eu anomaly is observed in any of the investigated samples. This observation further supports that the granites represent intrusions rather than cumulates (see also de Graaff et al. 2021). None of the samples investigated in this study display a distinct trace element composition that would either suggest interaction with other lithologies within the core (i.e., impact melt rock or pre-impact volcanic dikes) or a distinct granite type other than arc derived, implying that the granites sampled in the Hole M0077A core are related to a single magmatic intrusion event.

Our petrographic investigations and previous studies have highlighted the pervasive alteration of the recovered rocks from IODP-ICDP Expedition 364 drill core (Morgan et al. 2017; Simpson et al. 2020; de Graaff et al. 2021), following the onset of a long-living hydrothermal system (Kring et al. 2020) that could have affected the whole rock compositions, especially the mobile elements like Ba, Rb, and U. Immobile incompatible elements, especially high field strength elements (HFSE) like Zr, Hf, Nb, and Ta, are less affected by alteration processes, and can thus be used to trace the magmatic signatures of the granite samples
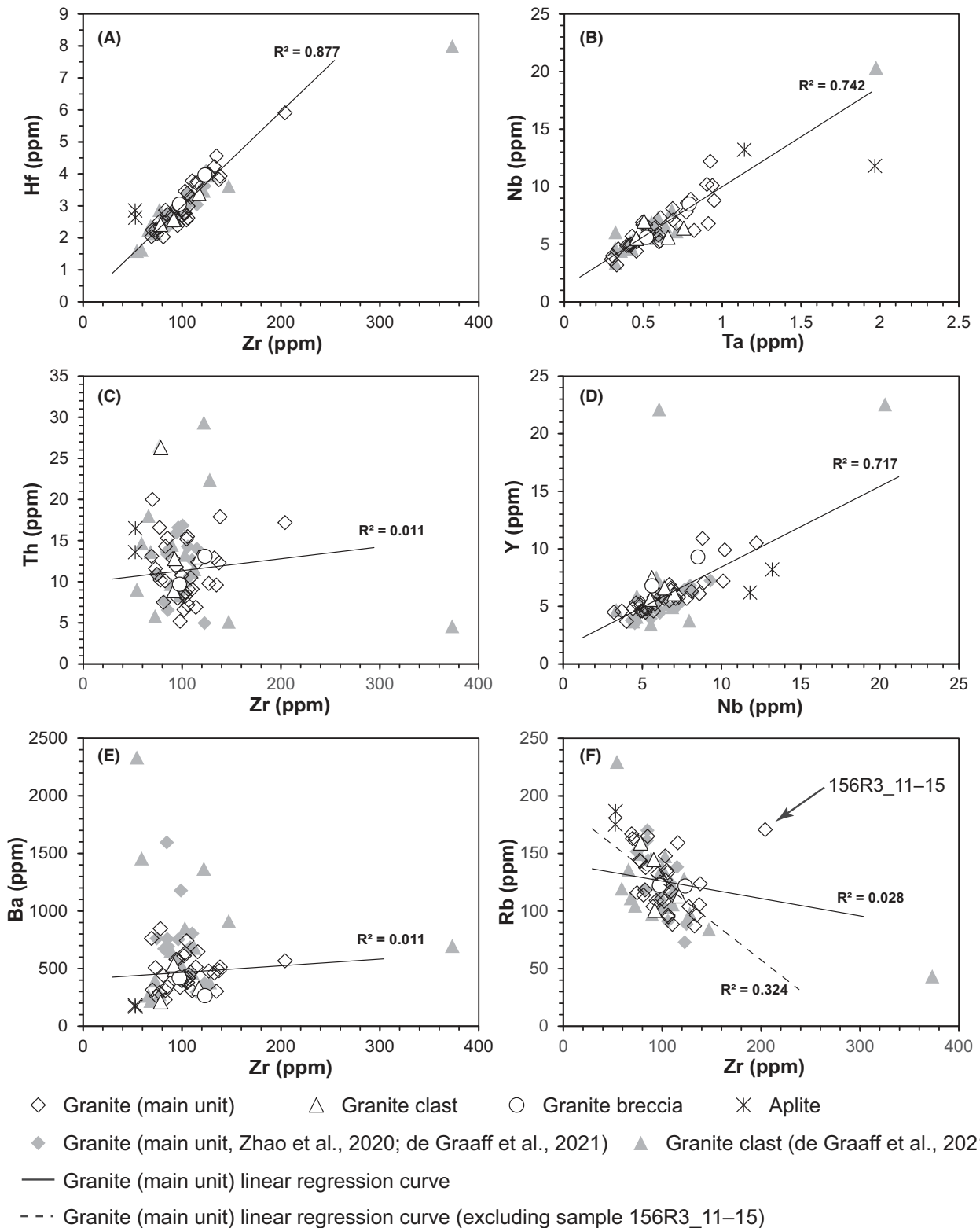
Fig. 9. A–F) Bivariate diagrams on trace element variations in granite samples. The trend line is calculated based on the main granite unit samples only. Zr versus Hf, Ta versus Nb, and Nb versus Y show strong covariations with R^2 above 0.7. The aplites plot slightly outside the main trend. Th, Ba, and Rb abundances are more scattered. In the Rb versus Zr diagram, the dashed trend line is calculated excluding the outlier samples enriched in Zr (i.e., sample 156R3_11–15) providing a better, although still low, covariation (R^2 of 0.324).

(e.g., Pearce et al. 1984; Pearce 2014). Strong linear covariations for all sample groups, with the notable exception of the aplite samples, which plot outside the main trend, are observed between Zr and Hf, Ta and Nb, and Nb and Y (Fig. 9). A similar linear correlation is observed when plotting Zr and V versus TiO_2 content (see Fig. S2 in supporting information). In contrast, Th, Ba, and U contents are more scattered when plotted versus Zr concentrations. A similar scattering is observed for Rb, but with a slightly lower importance than for Th, Ba, and U (Fig. 9 and Fig. S2). The decoupling between immobile and these mobile elements therefore indicates that they were probably affected by alteration. Additionally, as already shown in de Graaff et al. (2021), no covariation is observed between La and Zr (Fig. S2) in the granites investigated, with the $(La/Yb)_N$ ratio displaying strong variation (from ~3 to ~41) while Yb_N has relatively similar contents. This observation confirms that La must have been remobilized by alteration processes within the Chicxulub impact structure (de Graaff et al. 2021).

In order to assess the degree of hydrothermal alteration of the investigated samples, the K/Rb ratio was used to discriminate between altered and less altered granites. According to Helvaci and Griffin (1983), less altered and unaltered crustal rocks show K/Rb ratio <300, while in the case of hydrothermally altered rocks, the K/Rb ratio is typically between 400 and 500. The average K/Rb ratio of the investigated samples is of 256 for the main granite group, 282 for the granite clasts, 249 for the granite breccias, and 193 for the aplites (Table 2). Four of the investigated samples exhibit K/Rb ratios slightly above 300, that is, granite clast 95R2_19–22 with a K/Rb of 332, and granite samples 110R2_14–16, 116R2_58–62, and 236R1_90–92.5 with K/Rb of 314, 306, and 319, respectively (Table 2). However, great care should be taken with the use of this ratio, as, on the one hand, Rb contents are decoupled relative to immobile elements like Zr, and on the other hand, postimpact K-metasomatism was clearly indicated throughout the Chicxulub impact structure and in the entire drill core (Hecht et al. 2004; Kring et al. 2020), and, thus, K/Rb and Na_2O/K_2O ratios may not totally reflect the original, primary magmatic signature of the Chicxulub granites.

As described in the Trace Elements section, the trace element contents of the granite indicate a typical arc-like signature characterized by Ta and Nb depletions (see also de Graaff et al. 2021) coupled with slight Lu (HREE) enrichment relative to HREE Yb, which is compatible with a source melted with garnet in the residue as also reported by Zhao et al. (2020) and de Graaff et al. (2021). Using the chemical classification

of Pearce et al. (1984) to decipher the tectonic context of the granite formation, the Rb content is plotted versus Y + Nb concentrations (Fig. 10B), as Rb and Nb are affected in a similar way by mantle heterogeneities, while Y remains unaffected. Even though some scattering of the data is noticed, all the samples plot within the volcanic arc granite field, close to or on the limit with the syn-collision granite array, which may suggest a transition between arc magmatism and a collisional context (Fig. 10B).

Interestingly, the two investigated aplite samples plot within the enriched-MORB array (Fig. 10C); together with their immobile element compositions (Fig. 9), this may suggest that the aplites were emplaced as dikes during a distinct event, with a more "enriched-MORB"-like source, or may result from a remelting of granite material (e.g., through local changes in the solidus temperature caused by fluid circulation or during a thermal event), or may be the result of a different crystallization stage of the granite. Further investigations are needed in order to confirm their origin.

The present-day more radiogenic $^{87}Sr/^{86}Sr$ and higher $^{87}Rb/^{86}Sr$ ratios are observed for samples in proximity to the LIMB (below 1263.5 mbsf), where the granites are generally highly deformed and crosscut by numerous, more or less thick, impact melt rock dikes, and for sample 176R2_112–116, recovered from a much shallower depth, at 953.6 mbsf, which is in contact with a 3–4 mm thick cataclasite. While these more radiogenic granites display slightly higher Rb contents (average 147 ppm) compared to the less radiogenic granites (average 127 ppm), they display a more pronounced depletion in Sr, with average concentrations of 357 and 258 ppm for the less radiogenic and the more radiogenic granites, respectively. These observations clearly indicate that the granite experienced hydrothermal alteration, affecting both Rb and Sr contents (as well as other mobile elements such as Ba, Th, and U), and that the impact-related features (i.e., impact melt rock dikes, cataclasites, shock-induced fractures at the mineral scale) may have enhanced the hydrothermal fluid circulation. The mobilization and slight enrichment in Rb (and also in other mobile trace elements) could be attributed to hydrothermal fluid alteration and/or to the supply of crustal material, while the Sr depletion could be related to the hydrothermal alteration of plagioclase, evidenced by the high level of sericitization occurring in plagioclases (Plimer and Elliott 1979; Cruciani et al. 2017).

However, fluid alteration by seawater alone cannot fully explain the present-day more radiogenic $^{87}Sr/^{86}Sr$ ratios measured, as the present-day $^{87}Sr/^{86}Sr$ of seawater is estimated at ~0.709 (Veizer 1989). Thus,
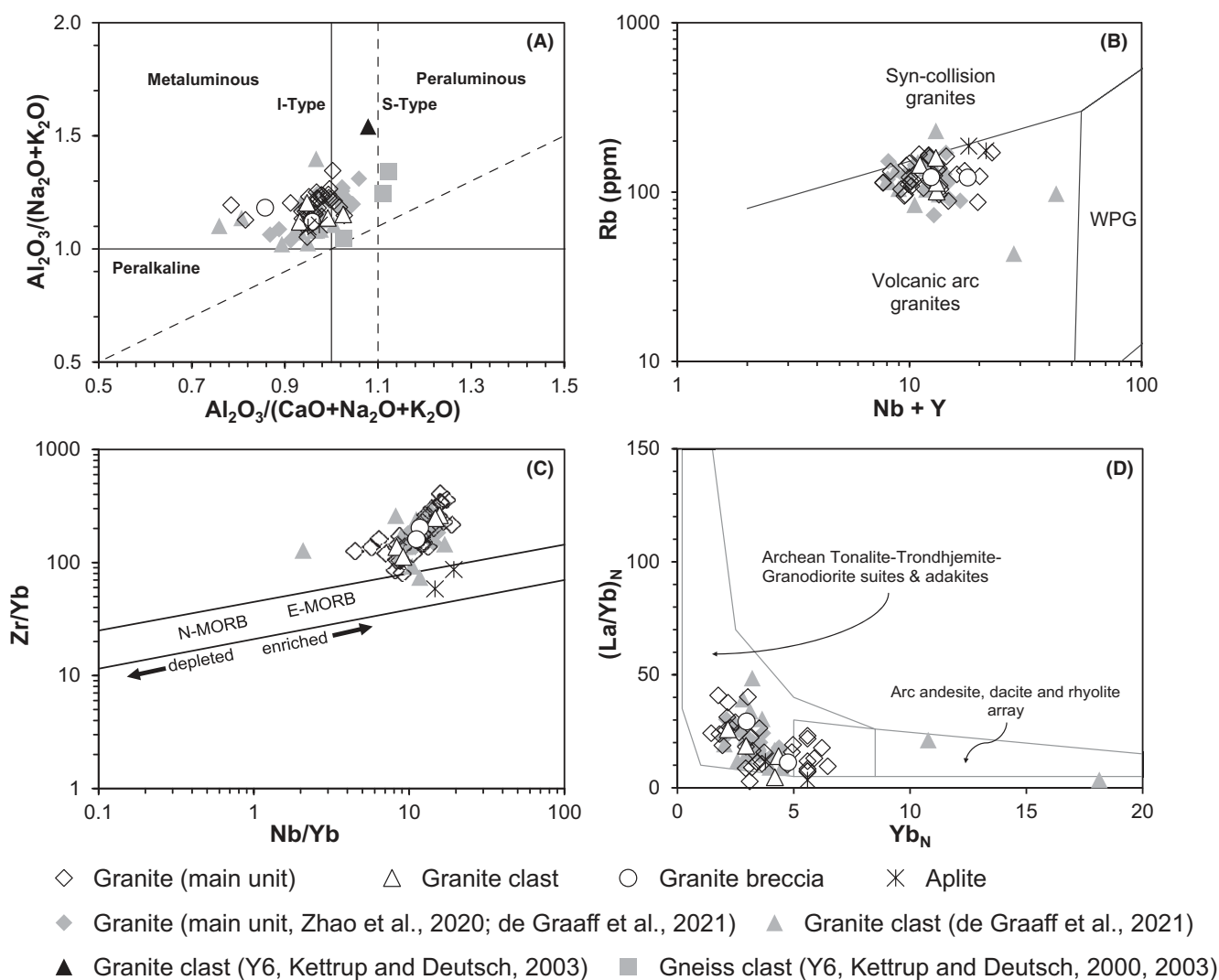
Fig. 10. A) A/NK versus A/CNK discriminating diagram, with A = Al_2O_3, C = CaO, N = Na_2O, and K = K_2O, all in molar proportions (modified from Maniar and Picolli 1989). The majority of the investigated granites in M0077A core are metaluminous with a weakly peraluminous character, associated with I-Type granites. Y6 clasts have a more peraluminous affinity. None of the investigated samples show a peralkaline character. B) Rb versus Nb + Y diagram, discriminating the granite tectonic context, as defined by Pearce et al. (1984). WPG = within-plate granite. The M0077A core granites are characterized as volcanic arc granite, with only one sample plotting in the syn-collision granite array. C) Zr/Yb versus Nb/Yb diagram (modified from Macdonald et al. 2000). N-MORB = normal mid-oceanic ridge basalt; E-MORB = enriched mid-oceanic ridge basalt. The granite, granite clast, and breccia samples plot outside the MORB array, indicating that they are derived from a different source, probably enriched. However, the two aplite samples are located in the E-MORB area, suggesting that they could have formed from a source with a different chemical composition. D) $(La/Yb)_N$ versus $(Yb)_N$ with the typical fields for adakites and normal-arc volcanic rocks (Martin et al. 2005). A significative number of the granite samples plots in the overlapping area between adakites and "normal" arc-rocks. Interestingly, two granite clasts recovered by de Graaff et al. (2021) have a distinct composition with high $(Yb)_N$ and low $(La/Yb)_N$ typical for "normal" arc volcanic rocks.

hydrothermal alteration following the impact cannot solely account for the more radiogenic $^{87}Sr/^{86}Sr$ ratios measured in 10 of the investigated samples (Table 3).

The apparent age of 273 ± 21 Ma determined by the whole-rock errorchron (Fig. 11C), younger than the Carboniferous ages reported in Zhao et al. (2020) and Ross et al. (2021), indicates that the Rb–Sr system was

likely disrupted (i.e., open system behavior), within ~50 Myr after granite crystallization and, thus, could account for another, older, metasomatic event that affected the Chicxulub granite unit. Following this event, the already altered granite was affected by postimpact hydrothermal overprint. Moreover, this apparent age overlaps within uncertainty with the age
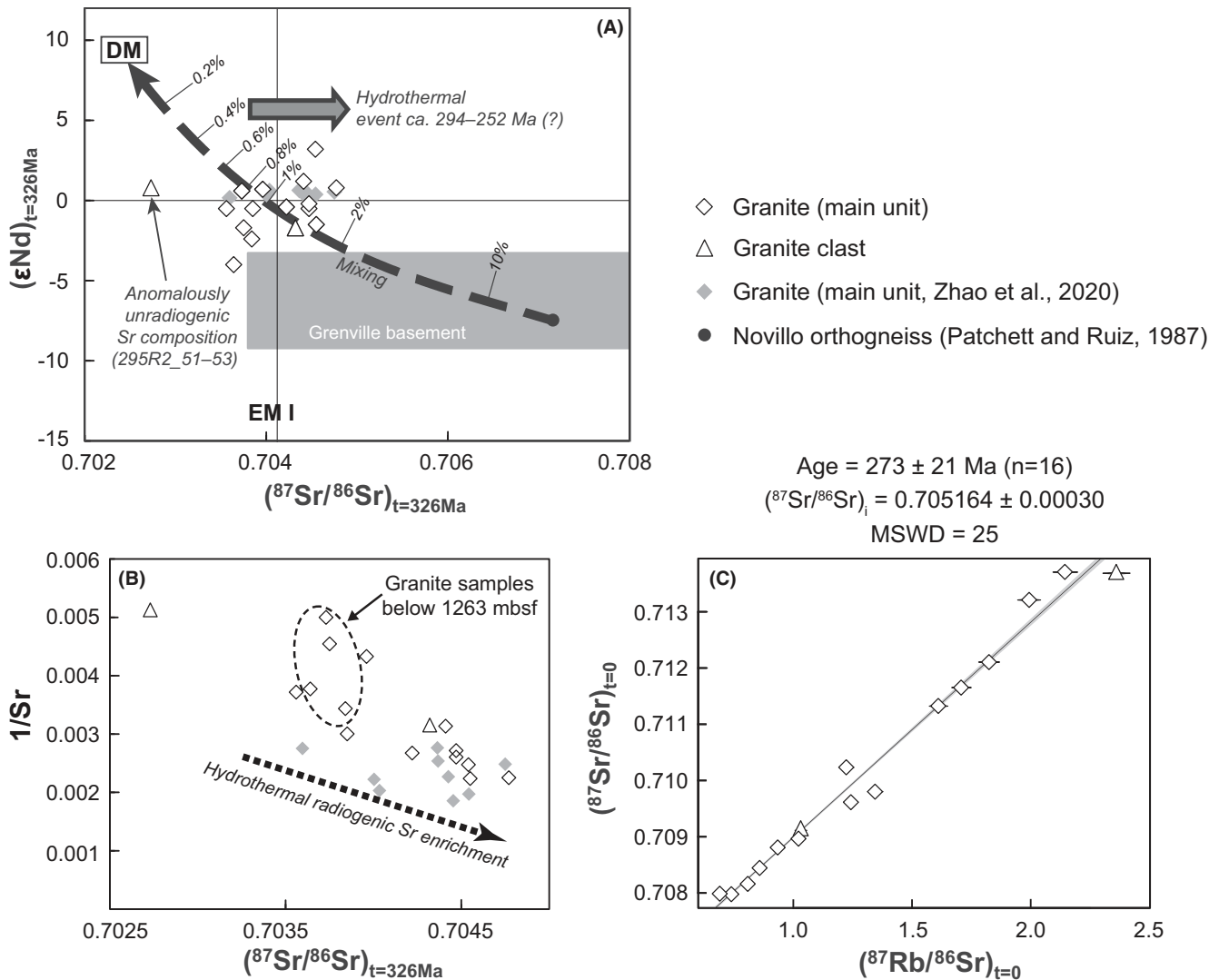
Fig. 11. Strontium–Nd isotopic compositions of 14 granite samples from the main unit and two granite clasts. M0077A granite Sr–Nd isotopic data from Zhao et al. (2020) are also reported for comparison. A) Initial $(\varepsilon_{Nd})_{t=326Ma}$ and $(^{87}Sr/^{86}Sr)_{t=326Ma}$ ratios. The Grenvillian basement area is drawn from data of Patchett and Ruiz (1987) and Weber and Köhler (1999). The Novillo Gneiss composition is from Patchett and Ruiz (1987). The mixing model calculation, DM, and EM I compositions at $t = 326$ Ma are calculated from Faure and Mensing (2004), with DM = depleted mantle, and EM I = enriched mantle I. B) Strontium concentration (expressed as 1/Sr) versus initial $(^{87}Sr/^{86}Sr)_{t=326Ma}$. With increasing Sr concentration, Sr is becoming more radiogenic and thus may be consistent with addition, a short time after granite crystallization, of radiogenic Sr (and of Rb, to enhance this difference over time) by hydrothermal enrichment. However, the samples in proximity to the LIMB, in the lower part of the granite unit (dashed circle) are among the least Sr-rich (and least radiogenic) and perhaps have experienced more "recent" limited addition of Rb (related with the postimpact hydrothermal system). C) $^{87}Sr/^{86}Sr$ versus $^{87}Rb/^{86}Sr$. Isochron of all the investigated samples ($n = 16$). A strong scattering is noticed with an MSWD of 25. The uncertainty of age and $(^{87}Sr/^{86}Sr)_i$ is expressed with a 2σ interval.

recorded in allanite, that is, 215 ± 28 to 260 ± 9 Ma (Wittmann et al. 2018), and, thus, probably corresponds to the same hydrothermal event. Taking into account these parameters, and given the high uncertainty on the apparent age, a metamorphic/hydrothermal fluid metasomatism during the late Triassic, possibly related to the intracontinental extension, which occurred during

the initial breakup of Pangea (Dickinson and Lawton 2001; Steiner 2005), might be the best candidate to explain the apparent Rb–Sr errorchron age and allanite ages.

The age-corrected, initial $(^{87}Sr/^{86}Sr)_{t=326Ma}$ and $(\varepsilon_{Nd})_{t=326Ma}$ compositions suggest that the granites may have formed following a mixing between a mantle-

derived component, which could be relatively similar in composition to the Pan-African Stony Mountain gabbro (Pollock and Hibbard 2010), as suggested by Zhao et al. (2020), and a minor contribution of a moderately enriched, Grenvillian, crustal component, which could be similar to the Novillo Gneiss (Fig. 11A), located in the Oaxaquian crust, in northeastern Mexico (Patchett and Ruiz 1987), even though the data display some scattering. The presence of a Grenvillian component is suggested by the $T_{DM2(t=326Ma)}$ of 0.8–1.4 Ga recorded by the samples. Additionally, the assimilation of the Oaxaquian crust in the Pan-African granitoids of the northern Maya block was previously suggested by Lopez et al. (2001). Three granite samples (156R3_11–15, 229R2_62–67, and 266R2_95.5–98.5) plot in the +ve area (i.e., displaying positive $[\varepsilon_{Nd}]_{t=326Ma}$ and radiogenic $[^{87}Sr/^{86}Sr]_{t=326Ma}$, see Fig. 11A). These samples, albeit not showing strong evidence for mineral deformation, are cross-cut by shear fractures (however, it cannot be excluded that these features were formed following the impact) or, in the case of sample 229R2_62–67, are in contact with aplite, which enhanced fluid circulation. They infer addition of radiogenic Sr but not evolved Nd, thus indicating consistent hydrothermal fluid metasomatism. Given the apparent Rb-Sr errorchron and allanite ages, the Late Triassic metasomatic event could explain these three specific compositions, by possibly adding metasomatic Rb in a relatively short timescale after granite crystallization. The possibility of metasomatic ^{87}Rb enrichment is also indicated by the $(^{87}Sr/^{86}Sr)_{t=326Ma}$ becoming more radiogenic with increasing Sr concentration (Faure and Mensing 2004) (Fig. 11B).

The granite clast sample 295R2_51–53 displays a distinctly lower initial $(^{87}Sr/^{86}Sr)_{t=326Ma}$ of 0.70273 and not evolved $(\varepsilon_{Nd})_{t=326Ma}$ of 0.8, while having the highest $^{87}Rb/^{86}Sr$ (2.3614) of all investigated samples. Petrologically, this sample is highly deformed, with mineral ductile deformation and pervasive shear fracture networks throughout, which could be either a record of the late Triassic metamorphic event, or of postimpact deformation. Addition of Rb during the onset of the postimpact hydrothermal system, at temperatures of ~300–400 °C as estimated by Kring et al. (2020) and Simpson et al. (2020), may explain the particular composition of this sample, as this "recent" Rb would not have had the time to decay. Interestingly, granite samples from the lower part of the granite unit (below 1263 mbsf, $n = 4$) may also have been affected, to a lesser extent, by this "recent" Rb enrichment related to the postimpact hydrothermal system (Fig. 11B), as they display more radiogenic $^{87}Sr/^{86}Sr$ (average 0.712196) and higher $^{87}Rb/^{86}Sr$ (average 1.82265) compared to the granite samples in the upper part of the granite unit (average $^{87}Sr/^{86}Sr$ and $^{87}Rb/^{86}Sr$ of 0.709319 and 1.08574, respectively), and thus back-calculate to unradiogenic $(^{87}Sr/^{86}Sr)_{t=326Ma}$ with an average of 0.703740. However, the Sr depletion observed in these granites and possibly related to hydrothermal alteration of plagioclase (sericitization), could also explain these compositions and may have occurred either (or both) during the Late Triassic metasomatic event or during the postimpact alteration, although the latter is more probable as the Sr depletion only occurs in the lower granite samples, in proximity to the LIMB and cataclastites.

The available data seem to indicate that the Chicxulub peak ring granites were affected by at least two hydrothermal alteration/metasomatic events, that is, a first event taking place approximately 50 Myr after granite formation (273 ± 21 Ma), and a second event related to the postimpact hydrothermal alteration (as the result of a hydrothermal system active for more than 1 Myr after the impact event at 66.05 Ma). However, some care should be taken in these interpretations, as it is not possible to fully disentangle the specific effects of the Late Triassic metasomatic event from the postimpact hydrothermal alteration event. In addition, the granite samples may not have kept their original magmatic Rb-Sr isotopic signature due to these alteration events.

Comparison with Granitoid Lithologies from the Chicxulub Impact Structure

Geochemical data available for granitoid rocks (clasts) from other drill cores recovered inside the Chicxulub impact structure were compared to the obtained results (Figs. 7–11). The geochemistry of nine granite samples from the "lower peak-ring" section of the Hole M0077A drill core was investigated by Zhao et al. (2020), while six granites from the main unit and 18 granite clasts were investigated by de Graaff et al. (2021). Major and trace element compositions of the granite samples from the main unit and the majority of the clasts in Zhao et al. (2020) and de Graaff et al. (2021) show no significant differences from the samples in this study, albeit a minor Eu negative anomaly with an Eu* of 0.77 ± 0.02 (Eu* = $Eu_N/[Sm_N \times Gd_N]^{0.5}$) was recorded in four granite clasts and one granite from the main unit in de Graaff et al. (2021). Moreover, de Graaff et al. (2021) describe a granitic clast with a syenite composition (13.3 wt% $Na_2O + K_2O$), and two granitic samples at 730.3 and 1287.8 mbsf with distinct enrichments in the HREE and LREE contents (Fig. 8). Additionally, these two granite clasts show a distinct Sr/Y, $(La/Yb)_N$, Y, and $(Yb)_N$ (Fig. 10D), which is most comparable to "normal" arc-related rocks. The former

was interpreted to be a textural characteristic related to it being an alkali-feldspar dominated sample while the latter two clasts were interpreted to either reflect granite clasts that were significantly affected by an interaction with the host impact melt rock or they were derived from a granitic body distinct from the main granite unit sampled in the Hole M0077A core (de Graaff et al. 2021).

Based on the investigation of a limited number of granite samples, Zhao et al. (2020) characterized the granites as "adakitic rocks" due to their anomalously high Sr/Y and $(La/Yb)_N$ ratios and low Y content and low $(Yb)_N$. However, the term "adakite" (or "adakitic") is often used to cover a large range of rocks with different characteristics and/or formation processes (Moyen 2009). More conservatively applied, the term adakite is restricted to the type of rock called "high silica adakite" (HSA), which is formed by the melting of metabasalts from oceanic crust slab (e.g., Martin et al. 2005). High Sr/Y and $(La/Yb)_N$ ratios are not the only criteria used to define an adakite; thus, in order to decipher the "adakitic" nature of the Chicxulub granites, the parameters defined by Defant and Drummond (1990), Martin et al. (2005), and Moyen (2009) were used in this work. A comparative table summarizes the difference between HSA rocks and the investigated granites (Table 4).

In this study, the investigated granites yield Sr/Y and $(La/Yb)_N$ ratios with wide variations, from 22 to 123 and 3 to 41, respectively. Based on $(La/Yb)_N$ versus $(Yb)_N$, the granites effectively plot in the adakite field as defined in Martin et al. (2005) (Fig. 10D). However, an overlap between adakitic compositions and "normal" arc compositions is noticeable in this diagram, and in addition, de Graaff et al. (2021) demonstrated that La was mobilized by alteration processes. It is important to highlight here that the investigated aplite samples yield values of Sr/Y and $(La/Yb)_N$ of 26 and 7.5, below the adakitic thresholds of 40 and 10, respectively (Table 4). In addition, with Al_2O_3 content below 15 wt%, FeO + MgO + MnO + TiO_2 contents <7 wt%, Mg# <50, K_2O/Na_2O above 0.4 (revealing a more potassic composition), and low Cr and Ni contents (suggesting a more evolved source), the investigated granites are distinctly different from a typical "adakitic rock." In addition, in the Zr/Yb versus Nb/Yb diagram (Fig. 10C), the granites, granite clasts, and granite breccias plot outside the MORB array, further supporting a contribution of an enriched (or possibly crustal) endmember in the granite genesis. Combined with the Nd isotopic data, this indicates a formation process distinct from adakites (Moyen 2009). Thus, the investigated granites should be termed high-K (high-Sr/Y or high $(La/Yb)_N$), calc-alkaline granites.

Granite-like lithologies were also sampled and investigated in the Y6 core (Kettrup et al. 2000; Kettrup and Deutsch 2003), that is, one granite and four granitic gneiss clasts in the suevite. Only major element and Sr–Nd isotopic data are available for these clast samples. The Y6 granite clast shows a composition distinct from the Expedition 364 granite samples and is highly silicic (81.9 wt% SiO_2) and subalkaline. The gneiss clast samples exhibit more variations with 67.9–84.3 wt% SiO_2 and have peraluminous compositions. These distinct compositions highlight the variety of evolved lithologies represented in the Yucatán peninsula crystalline basement and found as clasts in impact breccia and impact melt rock samples.

Table 4. Comparison between the average composition of the high silica adakite (HSA) and the investigated granites samples from the Expedition 364 Chicxulub drill core, using all the criteria defined for adakitic rocks in addition to Sr/Y and $(La/Yb)_N$ ratios (Defant and Drummond 1990; Martin et al. 2005; Moyen 2009).

	HSA Adakites average values*	Average granites	Average granite clasts	Average granite breccias	Average aplites
SiO_2 (wt%)	>56	73.1	74.4	71.1	74.7
Al_2O_3 (wt%)	>15	14	13	14	14
MgO (wt%)	<3	0.6	0.5	0.9	0.1
FeO + MgO + MnO + TiO_2 (wt%)	≈7	2.0	1.8	2.6	0.7
Mg#	≈50	38	41	44	22
K_2O/Na_2O	≈0.4	0.8	0.9	0.8	0.9
Y (ppm)	<18	6.0	6.5	8.1	7.2
Yb (ppm)	<1.9	0.6	0.6	0.6	0.8
Cr (ppm)	≈36	19	11	26	13
Ni (ppm)	≈24	3.9	4.5	9.4	0.7
Sr/Y	>40	62	50	40	26
$(La/Yb)_N$	>10	19	16	20	7.5

*As defined by Defant and Drummond (1990), Martin et al. (2005), and Moyen (2009).

While the Sr–Nd isotopic composition recorded by Zhao et al. (2020) is similar to our "group 1" (i.e., the least altered granites), the Sr–Nd isotopic ratios of the Y6 granite and three of the gneiss clasts exhibit distinct, more enriched crustal signatures (Fig. 11). The fourth gneiss clast (Y6 N14 p4a) has a high $(^{87}Sr/^{86}Sr)_{t=0}$ of 0.732676 and chondritic $(\varepsilon_{Nd})_{t=0}$ of 0.0, and represents another, distinct component of the Yucatán target (Kettrup and Deutsch 2003).

The Nd model ages (one- or two-stage model ages termed as T_{DM1} and T_{DM2}, respectively) calculated for the most primitive samples ($T_{DM2(326Ma)}$ of 0.8–1.2 Ga) encompass the calculated model age range of Zhao et al. (2020), with $T_{DM2(326Ma)}$ for the granites between 1.0 and 1.1 Ga. Crystalline basement clasts recovered within impact breccia and impact melt rocks yield T_{DM1} between 0.7 and 1.4 Ga, while impact melt rocks have T_{DM1} of 1.1–1.2 Ga (Kettrup et al. 2000; Kettrup and Deutsch 2003; Keppie et al. 2011). This implies that the northern Maya block and the granite investigated here involved Grenville-aged material during their formation (Keppie et al. 2012).

In general, our results are consistent with previous studies on a more limited set of samples (see Zhao et al. 2020; de Graaff et al. 2021), and further support that the investigated granite unit could be related with arc magmatism during the closure of the Rheic ocean and Pangea assembly in the Carboniferous (Zhao et al. 2020; Ross et al. 2021). Conversely, a similar granite type was not sampled in any previous drill cores, including Y6 (Kettrup et al. 2000; Kettrup and Deutsch 2003). However, the Expedition 364 drill core offers only a limited view of the extension of this granite unit; thus, care should be taken when discussing geodynamic implications of the data.

CONCLUSIONS

The granite from the "lower peak-ring" section in the IODP-ICDP Expedition 364 Hole M0077A drill core can be defined as coarse-grained, phaneritic with K-feldspar (orthoclase), plagioclase, quartz, and biotite as the main mineral phases. In addition to the main granite unit, granite clasts, granite breccias, and aplites and pegmatites are observed. Impact-induced deformations are pervasive with fracturing, shearing, and the presence of cataclasite veins and shock metamorphic features in minerals (such as PFs, FFs, and PDFs in quartz, but also a large set of shock metamorphic features in all other minerals composing the granites).

Despite numerous textural changes, the chemical composition of the granite inside the peak ring is broadly homogeneous and defines the studied samples

as high-K (high-Sr/Y or high $[La/Yb]_N$), calc-alkaline granites.

The major and trace element patterns suggest a formation by fractional crystallization with moderate plagioclase fractionation. However, initial Sr–Nd isotopic data reveal a more complex origin, with admixture of a Grenvillian crust component during the granite genesis, as suggested by the two-stage Nd model ages $T_{DM2(326Ma)}$ of 0.8–1.2 Ga. Additionally, the granite experienced a hydrothermal fluid metasomatic/metamorphic event, indicated by the radiogenic Sr enrichment and allanite crystallization. An apparent errorchron age of 273 ± 21 Ma indicates that this may be related to the intracontinental extension that occurred at the Yucatán peninsula during the late Triassic initial breakup of Pangea. However, the high uncertainty on the apparent age may also reflect the effect of postimpact alteration, which is also recorded in the granites, and thus disturbed the Rb-Sr system even more, adding complexity to the data interpretation. Additionally, the granites in the vicinity of impact melt rock or cataclasite dikes, mainly in the lower part of the granite unit, seem to have experienced, to some extent, alteration from the long-lasting, postimpact hydrothermal system, through addition of more recent Rb. Strontium depletion, related to the hydrothermal alteration of plagioclase, is also observed in these samples, without allowing any conclusion on which hydrothermal event was the cause of this Sr depletion. Other fluid mobile elements, such as Ba, Th, and U, have also been affected, probably by both hydrothermal events.

Our results are consistent with previous work conducted on granite samples recovered at site M0077, supporting that the calc-alkaline to high-K calc-alkaline granites located in the Chicxulub impact structure peak ring were formed in an arc tectonic context, intruding the Maya block during the closure of the Rheic ocean and assembly of Pangea.

Data Availability Statement—The data that support the findings of this study are available in the supplementary material of this article.

Editorial Handling—Dr. Jeffrey Plescia

REFERENCES

Alaniz-Álvarez S. A., van der Heyden P., Nieto-Samaniego A. F., and Ortega-Gutiérrez F. 1996. Radiometric and kinematic evidence for Middle Jurassic strike-slip faulting in southern Mexico related to the opening of the Gulf of Mexico. *Geology* 24:443–446.

Belza J., Goderis S., Keppens E., Vanhaecke F., and Claeys P. 2012. An emplacement mechanism for the mega-block zone within the Chicxulub crater (Yucatán, Mexico) based on chemostratigraphy. *Meteoritics & Planetary Science* 47:400–413.

Belza J., Goderis S., Smit J., Vanhaecke F., Baert K., Terryn H., and Claeys P. 2015. High spatial resolution geochemistry and textural characteristics of 'microtektite' glass spherules in proximal Cretaceous-Paleogene sections: Insights into glass alteration patterns and precursor melt lithologies. *Geochimica et Cosmochima Acta* 152:1–38.

Brooks C., Hart S. R., and Wendt I. 1972. Realistic use of two-error regression treatment as applied to rubidium-strontium data. *Reviews of Geophysics and Space Physics* 10:551–557.

Chiarenza A. A., Farnsworth A., Mannion P. D., Lunt D. J., Valdes P. J., Morgan J. V., and Allison P. A. 2020. Asteroid impact, not volcanism, caused the end-Cretaceous dinosaur extinction. *Proceedings of the National Academy of Sciences* 117:17,084–17,093.

Claeys P., Heuschkel S., Lounejeva-Baturina E., Sanchez-Rubio G., and Stöffler D. 2003. The suevite of drill hole Yucatàn 6 in the Chicxulub impact crater. *Meteoritics & Planetary Science* 38:1299–1317.

Collins G. S., Patel N., Davison T. M., Rae A. S. P., Morgan J. V., Gulick S. P. S., IODP-ICDP Expedition 364 Science Party, and Third-Party Scientists. 2020. A steeply-inclined trajectory for the Chicxulub impact. *Nature Communications* 11:1480. https://doi.org/10.1038/s41467-020-15269-x

Cox M. A., Erickson T. M., Schmieder M., Christoffersen R., Ross D. K., Cavosie A. J., Bland P. A., Kring D. A., and IODP–ICDP Expedition 364 Scientists. 2020. High-resolution microstructural and compositional analyses of shock deformed apatite from the peak ring of the Chicxulub impact crater. *Meteoritics & Planetary Science* 55:1715–1733.

Cruciani G., Franceschelli M., and Puxeddu M. 2017. U-, Pb-enrichment, Sr-depletion produced by water-rock interaction processes within the eclogitic oceanic crust of Ordovician age in NE Sardinia. *Procedia Earth and Planetary Science* 17:508–511.

Defant M. J. and Drummond M. S. 1990. Derivation of some modern arc magmas by melting of young subducted lithosphere. *Nature* 347:662–665.

de Graaff S. J., Kaskes P., Déhais T., Goderis S., Debaille V., Matielli N., Ross C. H., Gulick S. P. S., Feignon J.-G., Ferrière L., Koeberl C., Smit J., and Claeys P. 2021. New insights into the formation and emplacement of impact melt rocks of the Chicxulub impact structure, Mexico, following the 2016 IODP-ICDP Expedition 364. *Geological Society of America Bulletin.* https://doi.org/10.1130/B35795.1.

Dengo G. 1969. Problems of tectonic relations between Central America and the Caribbean. *Gulf Coast Association of Geological Societies Transactions* 19:311–320.

DePaolo D. J. 1981. Trace element and isotopic effects of combined wallrock assimilation and fractional crystallization. *Earth and Planetary Science Letters* 53:189–202.

DePaolo D. J. and Wasserburg G. J. 1976. Nd isotopic variations and petrogenetic models. *Geochemistry* 3:249–252.

de Winter N. J. and Claeys P. 2016. Micro X-ray fluorescence (µXRF) line scanning on Cretaceous rudist bivalves: A new method for reproducible trace element profiles in bivalve calcite. *Sedimentology* 64:231–251.

Dickinson W. R. and Lawton T. F. 2001. Carboniferous to Cretaceous assembly and fragmentation of Mexico. *Geological Society of America Bulletin* 113:1142–1160.

Donnelly T. W., Horne G. S., Finch R. C., and López-Ramos E. 1990. Northern Central America; the Maya and Chortis blocks. In *The Caribbean region; The Geology of North America*, edited by Dengo G. and Case J. E. Boulder, Colorado: Geological Society of America. pp. 371–396.

Dressler B. O., Sharpton V. L., Morgan J., Moran D., Smit J., Stöffler D., and Urrutia J. 2003. Investigating a 65-Ma-old smoking gun: Deep drilling of the Chicxulub impact structure. *Eos, Transactions, American Geophysical Union* 84:125–130.

Ewart A. 1982. The mineralogy and petrology of Tertiary-recent orogenic volcanic rocks: With a special reference to the andesitic-basaltic compositional range. In *Andesites: Orogenic andesites and related rocks*, edited by Thorpe R. S. Chichester, UK: Wiley. pp. 25–95.

Faure G. and Mensing T. M. 2004. *Isotopes: Principles and applications*. Hoboken, New Jersey: John Wiley & Sons Inc.

Feignon J.-G., Ferrière L., Leroux H., and Koeberl C. 2020. Characterization of shocked quartz grains from Chicxulub peak ring granites and shock pressure estimates. *Meteoritics & Planetary Science* 55:2206–2223.

Ferrière L., Rae A. S. P., Poelchau M., Koeberl C., and the IODP-ICDP Expedition 364 Science Party. 2017. Macro- and microscopic evidence of impact metamorphism in rocks from the Chicxulub peak ring IODP-ICDP expedition 364 drill core (abstract #1600). 48th Lunar and Planetary Science Conference. CD-ROM.

Goderis S., Sato H., Ferrière L., Schmitz B., Burney D., Kaskes P., Vellekoop J., Wittmann A., Schulz T., Chernonozhkin S. M., Claeys P., de Graaff S. J., Déhais T., de Winter N. J., Elfman M., Feignon J.-G., Ishikawa A., Koeberl C., Kristiansson P., Neal C. R., Owens J. D., Schmieder M., Sinnesael M., Vanhaecke F., Van Malderen S. J. M., Bralower T. J., Gulick S. P. S., Kring D. A., Lowery C. M., Morgan J. V., Smit J., Whalen M. T., and IODP-ICDP Expedition 364 Scientists. 2021. Globally distributed iridium layer preserved within the Chicxulub impact structure. *Science Advances* 7:abe3647.

Goderis S., Tagle R., Belza J., Smit J., Montanari A., Vanhaecke F., Erzinger J., and Claeys P. 2013. Reevaluation of siderophile element abundances and ratios across the Cretaceous-Paleogene (K–Pg) boundary: Implications for the nature of the projectile. *Geochimica et Cosmochimica Acta* 120:417–446.

Gulick S. P. S., Barton P. J., Christeson G. L., Morgan J. V., McDonald M., Mendoza-Cervantes K., Pearson Z. F., Surendra A., Urrutia-Fucugauchi J., Vermeesch P. M., and Warner M. R. 2008. Importance of pre-impact crustal structure for the asymmetry of the Chicxulub impact crater. *Nature Geoscience* 1:131–135.

Gulick S. P. S., Christeson G. L., Barton P. J., Grieve R. A. F., Morgan J. V., and Urrutia-Fucugauchi J. 2013. Geophysical characterization of the Chicxulub impact crater. *Reviews of Geophysics* 51:31–52.

Gulick S. P. S., Bralower T. J., Ormö J., Hall B., Grice K., Schaefer B., Lyons S., Freeman K. H., Morgan J. V., Artemieva N., Kaskes P., de Graaff S. J., Whalen M. T., Collins G. S., Tikoo S. M., Verhagen C., Christeson G. L., Claeys P., Coolen M. J. L., Goderis S., Goto K., Grieve R. A. F., McCall N., Osinski G. R., Rae A. S. P., Riller U., Smit J., Vajda V., Wittmann A., and Expedition 364 Scientists. 2019. The first day of the Cenozoic. *Proceedings of the National Academy of Sciences* 116:19,342–19,351.

Hecht L., Wittmann A., Schmitt R.-T., and Stöffler D. 2004. Composition of impact melt particles and the effects of post-impact alteration in suevitic rocks at the Yaxcopoil-1 drill core, Chicxulub crater, Mexico. *Meteoritics & Planetary Science* 39:1169–1186.

Helvaci C. and Griffin W. L. 1983. Metamorphic feldspathization of metavolcanics and granitoids, Avnik area, Turkey. *Contributions to Mineralogy and Petrology* 83:309–319.

Hildebrand A. R., Penfield G. T., Kring D. A., Pilkington M., Camargo Z. A., Jacobsen S. B., and Boynton W. V. 1991. Chicxulub crater: A possible Cretaceous/Tertiary boundary impact crater on the Yucatán Peninsula, Mexico. *Geology* 19:867–871.

Hsu W. 2003. Rare earth element geochemistry and petrogenesis of Miles (IIE) silicate inclusions. *Geochimica et Cosmochimica Acta* 67:4807–4821.

Kamo S. L. and Krogh T. E. 1995. Chicxulub crater source for shocked zircon crystals from the Cretaceous-Tertiary boundary layer, Saskatchewan: Evidence from new U-Pb data. *Geology* 23:281–284.

Kamo S. L., Lana C., and Morgan J. V. 2011. U-Pb ages of shocked zircon grains link distal K–Pg boundary sites in Spain and Italy with the Chicxulub impact. *Earth and Planetary Science Letters* 310:401–408.

Kaskes P., Déhais T., de Graaff S. J., Goderis S., and Claeys P. 2021. Micro–X-ray fluorescence (μXRF) analysis of proximal impactites: High-resolution element mapping, digital image analysis, and quantifications. In *Large meteorite impacts and planetary evolution VI: Geological Society of America special paper 550*, edited by Reimold W. U. and Koeberl C. Boulder, Colorado: Geological Society of America. pp. 171–206. https://doi.org/10.1130/2021.2550(07)

Keppie J. D., Dostal J., Norman M., Urrutia-Fucugauchi J., and Grajales-Nishimura M. 2011. Study of melt and a clast of 546 Ma magmatic arc rocks in the 65 Ma Chicxulub bolide breccia, northern Maya block, Mexico: Western limit of Ediacaran arc peripheral to northern Gondwana. *International Geology Review* 53:1180–1193.

Keppie J. D., Murphy J. B., Nance R. D., and Dostal J. 2012. Mesoproterozoic Oaxaquia-type basement in peri-Gondwanan terranes of Mexico, the Appalachians and Europe: T_{DM} age constraints on extent and significance. *International Geology Review* 54:313–324.

Kettrup B. and Deutsch A. 2003. Geochemical variability of the Yucatàn basement: Constraints from crystalline clasts in Chicxulub impactites. *Meteoritics & Planetary Science* 38:1079–1092.

Kettrup B., Deutsch A., Ostermann M., and Agrinier P. 2000. Chicxulub impactites: Geochemical clues to the precursor rocks. *Meteoritics & Planetary Science* 35:1229–1238.

Koeberl C. 1993a. Chicxulub crater, Yucatàn: Tektites, impact glasses, and the geochemistry of target rocks and breccias. *Geology* 21:211–214.

Koeberl C. 1993b. Instrumental neutron activation analysis of geochemical and cosmochemical samples: A fast and reliable method for small sample analysis. *Journal of Radioanalytical and Nuclear Chemistry* 168:47–60.

Koeberl C. and Sigurdsson H. 1992. Geochemistry of impact glasses from the K/T boundary in Haiti: Relation to smectites and a new type of glass. *Geochimica et Cosmochimica Acta* 56:2113–2129.

Kring D. A. 2005. Hypervelocity collisions into continental crust composed of sediments and an underlying crystalline basement: Comparing the Ries (~ 24 km) and Chicxulub (~ 180 km) impact craters. *Geochemistry* 65:1–46.

Kring D. A. and Boynton W. V. 1992. Petrogenesis of an augite-bearing melt rock in the Chicxulub structure and its relationship to K/T impact spherules in Haiti. *Nature* 358:141–144.

Kring D. A., Tikoo S. M., Schmieder M., Riller U., Rebolledo-Vieyra M., Simpson S. L., Osinski G. R., Gattacceca J., Wittmann A., Verhagen C. M., Cockell C. S., Coolen M. J. L., Longstaffe F. J., Gulick S. P. S., Morgan J. V., Bralower T. J., Chenot E., Christeson G. L., Claeys P., Ferrière L., Gebhardt C., Goto K., Green S. L., Jones H., Lofi J., Lowery C. M., Ocampo-Torres R., Perez-Cruz L., Pickersgill A. E., Poelchau M. H., Rae A. S. P., Rasmussen C., Sato H., Smit J., Tomioka N., Urrutia-Fucugauchi J., Whalen M. T., Xiao L., and Yamaguchi K. E. 2020. Probing the hydrothermal system of the Chicxulub impact crater. *Science Advances* 6:eaaz3053.

Krogh T. E., Kamo S. L., Sharpton V. L., Marin L. E., and Hildebrand A. R. 1993. U-Pb ages of single shocked

zircons linking distal K/T ejecta to the Chicxulub crater. *Nature* 366:731–734.

Langmuir C. H., Klein E. M., and Plank T. 1992. Petrological systematics of mid-ocean ridge basalts: Constraints on melt generation beneath ocean ridges. In *Mantle flow and melt generation at mid-ocean ridges*, edited by Morgan J. P., Blackman D. K., and Sinton J. M. Geophysical Monograph Series, Volume 71. Washington, D.C.: American Geophysical Union. pp. 183–280.

Liew T. C. and Hofmann A. W. 1988. Precambrian crustal components, plutonic associations, plate environment of the Hercynian fold belt of central Europe: Indications from a Nd and Sr isotopic study. *Contributions to Mineralogy and Petrology* 98:129–138.

Lopez R., Cameron K. L., and Jones N. W. 2001. Evidence for Paleoproterozoic, Grenvillian and Pan-African age Gondwana crust beneath northeastern Mexico. *Precambrian Research* 107:195–214.

Lopez Ramos E. 1975. Geological summary of the Yucatan peninsula. In *The Gulf of Mexico and the Caribbean*, edited by Nairn A. E. M. and Stehli F. G. Boston, Massachusetts: Springer. pp. 257–282.

Macdonald R., Hawkesworth C. J., and Heath E. 2000. The Lesser Antilles volcanic chain: A study in arc magmatism. *Earth-Science Reviews* 49:1–76.

Mader D. and Koeberl C. 2009. Using instrumental neutron activation analysis for geochemical analyses of terrestrial impact structures: Current analytical procedures at the University of Vienna Geochemistry Activation Analysis Laboratory. *Applied Radiation and Isotopes* 67:2100–2103.

Maniar P. D. and Piccoli P. M. 1989. Tectonic discrimination of granitoids. *Geological Society of America Bulletin* 101:635–643.

Martin H., Smithies R. H., Rapp R. P., Moyen J.-F., and Champion D. C. 2005. An overview of adakite, tonalite-trondjhemite-granodiorite (TTG) and sanukitoid: Relationships and some implications for crustal evolution. *Lithos* 79:1–24.

McDonough W. F. and Sun S. 1995. The composition of the Earth. *Chemical Geology* 120:223–253.

Middlemost E. A. K. 1994. Naming materials in the magma/igneous rock system. *Earth-Science Reviews* 37:215–224.

Morgan J., Warner M., the Chicxulub Working Group, Brittan J., Buffler R., Camargo A., Christeson G., Denton P., Hildebrand A., Hobbs R., Macintyre H., Mackenzie G., Maguire P., Marin L., Nakamura Y., Pilkington M., Sharpton V., Snyder D., Suarez G., and Trejo A. 1997. Size and morphology of the Chicxulub impact crater. *Nature* 390:472–476.

Morgan J. V., Gulick S. P. S., Bralower T., Chenot E., Christeson G., Claeys P., Cockell C., Collins G. S., Coolen M. J. L., Ferrière L., Gebhardt C., Goto K., Jones H., Kring D. A., Le Ber E., Lofi J., Long X., Lowery C., Mellett C., Ocampo-Torres R., Osinski G. R., Perez-Cruz L., Pickersgill A., Pölchau M., Rae A., Rasmussen C., Rebolledo-Vieyra M., Riller U., Sato H., Schmitt D. R., Smit J., Tikoo S., Tomioka N., Urrutia-Fucugauchi J., Whalen M., Wittmann A., Yamaguchi K. E., and Zylberman W. 2016. The formation of peak rings in large impact craters. *Science* 354:878–882.

Morgan J., Gulick S., Mellet C. L., Green S. L., and Expedition 364 Scientists. 2017. *Chicxulub: Drilling the K-Pg impact crater*. Proceedings of the International Ocean Discovery Program, 364. College Station, Texas: International Ocean Discovery Program. 164 p.

Moyen J.-F. 2009. High Sr/Y and La/Yb ratios: The meaning of the "adakitic signature." *Lithos* 112:556–574.

Nagl P. and Mader D. 2019. X-ray fluorescence (XRF) and instrumental neutron activation analysis (INAA) for the geochemical analysis of rocks, presented on in-house control samples (abstract). *Mitteilungen der Österreichischen Mineralogischen Gesellschaft* 165:67.

Nisbet E. G., Dietrich V. J., and Esenwien A. 1979. Routine trace element determinations in silicate minerals and rocks by X-ray fluorescence. *Fortschritte der Mineralogie* 57:264–279.

Ortega-Gutiérrez F., Elías-Herrera M., Morán-Zenteno D. J., Solari L., Weber B., and Luna-González L. 2018. The pre-Mesozoic metamorphic basement of Mexico, 1.5 billion years of crustal evolution. *Earth-Science Reviews* 183:2–37.

Patchett P. J. and Ruiz J. 1987. Nd isotopic ages of crust formation and metamorphism in the Precambrian of eastern and southern Mexico. *Contributions to Mineralogy and Petrology* 96:523–528.

Pearce J. A. 2014. Immobile element fingerprinting of ophiolites. *Elements* 10:101–108.

Pearce J. A., Harris N. B. W., and Tindle A. G. 1984. Trace element discrimination diagrams for the tectonic interpretation of granitic rocks. *Journal of Petrology* 25:956–983.

Penfield G. T. and Camargo Z. A. 1981. Definition of a major igneous zone in the central Yucatán platform with aeromagnetics and gravity. *Society of Exploration Geophysicists Technical Program, Abstracts, and Biographies* 51:37.

Pittarello L., Ferrière L., Feignon J.-G., Osinski G. R., and Koeberl C. 2020. Preferred orientation distribution of shock-induced planar microstructures in quartz and feldspar. *Meteoritics & Planetary Science* 55:1082–1092.

Plimer I. R. and Elliott S. M. 1979. The use of Rb/Sr ratios as guide to mineralization. *Journal of Geochemical Exploration* 12:21–34.

Pollock J. C. and Hibbard J. P. 2010. Geochemistry and tectonic significance of the Stony Mountain gabbro, North Carolina: Implications for the Early Paleozoic evolution of Carolinia. *Gondwana Research* 17:500–515.

Quitté G., Robin E., Levasseur S., Capmas F., Rocchia R., Birck J.-L., and Allègre C. J. 2007. Osmium, tungsten, and chromium isotopes in sediments and in Ni-rich spinel at the K-T boundary: Signature of a chondritic impactor. *Meteoritics & Planetary Science* 42:1567–1580.

Rae A. S. P., Collins G. S., Poelchau M., Riller U., Davison T. M., Grieve R. A. F., Osinski G. R., Morgan J. V., and IODP-ICDP Expedition 364 Scientists. 2019. Stress-strain evolution during peak-ring formation: A case study of the Chicxulub impact structure. *Journal of Geophysical Research: Planets* 124:396–417.

Rasmussen C., Stockli D. F., Ross C. H., Pickersgill A., Gulick S. P., Schmieder M., Christeson G. L., Wittmann A., Kring D. A., Morgan J. V., and Expedition 364 Science Party. 2019. U-Pb memory behavior in Chicxulub's peak ring—Applying U-Pb depth profiling to shocked zircon. *Chemical Geology* 525:356–367.

Riller U., Poelchau M. H., Rae A. S. P., Schulte F. M., Collins G. S., Melosh H. J., Grieve R. A. F., Morgan J. V., Gulick S. P. S., Lofi J., Diaw A., McCall N., Kring D.

A., and IODP-ICDP Expedition 364 Science Party. 2018. Rock fluidization during peak-ring formation of large impact structures. *Nature* 562:511–518.

Ross C. H., Stockli D. F., Rasmussen C., Gulick S. P. S., de Graaff S. J., Claeys P., Zhao J., Xiao L., Pickersgill A. E., Schmieder M., Kring D. A., Wittmann A., and Morgan J. 2021. Evidence of Carboniferous arc magmatism preserved in the Chicxulub impact structure. *Geological Society of America Bulletin.* https://doi.org/10.1130/B35831.1.

Schmieder M., Shaulis B. J., Lapen T. J., and Kring D. A. 2017. U-Th–Pb systematics in zircon and apatite from the Chicxulub impact crater, Yucatán, Mexico. *Geological Magazine* 155:1330–1350.

Schmitt R. T., Wittmann A., and Stöffler D. 2004. Geochemistry of drill core samples from Yaxcopoil-1, Chicxulub impact crater, Mexico. *Meteoritics & Planetary Science* 39:979–1001.

Schulte P., Alegret L., Arenillas I., Arz J. A., Barton P. J., Bown P. R., Bralower T. J., Christeson G. L., Claeys P., Cockell C. S., Collins G. S., Deutsch A., Goldin T. J., Goto K., Grajales-Nishimura J. M., Grieve R. A. F., Gulick S. P. S., Johnson K. R., Kiessling W., Koeberl C., Kring D. A., MacLeod K. G., Matsui T., Melosh J., Montanari A., Morgan J. V., Neal C. R., Nichols D. J., Norris R. D., Pierazzo E., Ravizza G., Rebolledo-Vieyra M., Reimold W. U., Robin E., Salge T., Speijer R. P., Sweet A. R., Urrutia-Fucugauchi J., Vajda V., Whalen M. T., and Willumsen P. S. 2010. The Chicxulub asteroid impact and mass extinction at the Cretaceous-Paleogene boundary. *Science* 327:1214–1218.

Schuraytz B. C., Sharpton V. L., and Marín L. E. 1994. Petrology of impact-melt rocks at the Chicxulub multiring basin, Yucatán, Mexico. *Geology* 22:868–872.

Sharpton V. L., Dalrymple G. B., Marin L. E., Ryder G., Schuraytz B. C., and Urrutia-Fucugauchi J. 1992. New links between the Chicxulub impact structure and the Cretaceous/Tertiary boundary. *Nature* 359:819–821.

Shukolyukov A. and Lugmair G. W. 1998. Isotopic evidence for the Cretaceous-Tertiary impactor and its type. *Science* 282:927–930.

Simpson S. L., Osinski G. R., Longstaffe F. J., Schmieder M., and Kring D. A. 2020. Hydrothermal alteration associated with the Chicxulub impact crater upper peak-ring breccias. *Earth and Planetary Science Letters* 547:116425.

Sisson T. W. and Grove T. L. 1993. Temperatures and H$_2$O contents of low-MgO high-alumina basalts. *Contributions to Mineralogy and Petrology* 113:167–184.

Smit J. 1999. The global stratigraphy of the Cretaceous-Tertiary boundary impact ejecta. *Annual Review of Earth and Planetary Sciences* 27:75–113.

Son T. H. and Koeberl C. 2005. Chemical variation within fragments of Australasian tektites. *Meteoritics & Planetary Science* 40:805–815.

Sprain C. J., Renne P. R., Clemens W. A., and Wilson G. P. 2018. Calibration of chron C29r: New high-precision geochronologic and paleomagnetic constraints from the Hell Creek region, Montana. *Geological Society of America Bulletin* 130:1615–1644.

Steiner M. B. 2005. Pangean reconstruction of the Yucatan Block: Its Permian, Triassic, and Jurassic geologic and tectonic history. In *The Mojave-Sonora Megashear hypothesis: Development, assessment, and alternatives*, edited by Anderson T. H., Nourse J. A., McKee J. W.,

and Steiner M. B. Geological Society of America Special Paper 393. Boulder, Colorado: Geological Society of America. pp. 457–480.

Swisher C. C., Grajales-Nishimura J. M., Montanari A., Margolis S. V., Claeys P., Alvarez W., Renne P., Cedillo-Pardoa E., Maurrasse F.-J.-M.-R., Curtis G. H., Smit J., and McWilliams M. O. 1992. Coeval ^{40}Ar/^{39}Ar ages of 65.0 million years ago from Chicxulub crater melt rock and Cretaceous-Tertiary boundary tektites. *Science* 257:954–958.

Timms N. E., Pearce M. A., Erickson T. M., Cavosie A. J., Rae A. S. P., Wheeler J., Wittman A., Ferrière L., Poelchau M. H., Tomioka N., Collins G. S., Gulick S. P. S., Rasmussen C., Morgan J. V., and IODP-ICDP Expedition 364 Scientists. 2019. New shock microstructures in titanite (CaTiSiO$_5$) from the peak ring of the Chicxulub impact structure, Mexico. *Contributions to Mineralogy and Petrology* 174:38.

Tuchscherer M. G., Reimold W. U., Koeberl C., and Gibson R. L. 2004a. Major and trace element characteristics of impactites from the Yaxcopoil-1 borehole, Chicxulub structure, Mexico. *Meteoritics & Planetary Science* 39:955–978.

Tuchscherer M. G., Reimold W. U., Koeberl C., Gibson R. L., and de Bruin D. 2004b. First petrographic results on impactites from the Yaxcopoil-1 borehole, Chicxulub structure, Mexico. *Meteoritics & Planetary Science* 39:899–930.

Tuchscherer M. G., Reimold W. U., Koeberl C., and Gibson R. L. 2005. Geochemical and petrographic characteristics of impactites and Cretaceous target rocks from the Yaxcopoil-1 borehole, Chicxulub impact structure, Mexico: Implications for target composition. *Meteoritics & Planetary Science* 40:1513–1536.

Tuchscherer M. G., Reimold W. U., Gibson R. L., de Bruin D., and Späth A. 2006. Major and trace element compositions of melt particles and associated phases from the Yaxcopoil-1 drill core, Chicxulub impact structure, Mexico. *Meteoritics & Planetary Science* 41:1361–1379.

Urrutia-Fucugauchi J., Marin L., and Trejo-Garcia A. 1996. UNAM scientific drilling program of Chicxulub impact structure—Evidence for a 300 kilometer crater diameter. *Geophysical Research Letters* 23:1565–1568.

Veizer J. 1989. Strontium isotopes in seawater through time. *Annual Review of Earth and Planetary Sciences* 17:141–167.

Ward W. C., Keller G., Stinnesbeck W., and Adatte T. 1995. Yucatán subsurface stratigraphy: Implications and constraints for the Chicxulub impact. *Geology* 23:873–876.

Weber B. and Köhler H. 1999. Sm–Nd, Rb–Sr and U–Pb geochronology of a Grenville Terrane in Southern Mexico: Origin and geologic history of the Guichicovi Complex. *Precambrian Research* 96:145–262.

Weber B., Valencia V. A., Schaaf P., Pompa-Mera V., and Ruiz J. 2008. Significance of provenance ages from the Chiapas Massif Complex (Southeastern Mexico): Redefining the Paleozoic basement of the Maya Block and its evolution in a Peri-Gondwanan realm. *The Journal of Geology* 116:619–639.

Weber B., Scherer E. E., Martens U. K., and Mezger K. 2012. Where did the lower Paleozoic rocks of Yucatan come from? A U-Pb, Lu–Hf, and Sm–Nd isotope study. *Chemical Geology* 312–313:1–17.

Weber B., González-Guzmán R., Manjarrez-Juárez R., de León A. C., Martens U., Solari L., Hecht L., and Valencia

V. 2018. Late Mesoproterozoic to Early Paleozoic history of metamorphic basement from the southeastern Chiapas Massif Complex, Mexico, and implications for the evolution of NW Gondwana. *Lithos* 300–301:177–199.

Wittmann A., Kenkmann T., Schmitt R. T., Hecht L., and Stöffler D. 2004. Impact-related dike breccia lithologies in the ICDP drill core Yaxcopoil-1, Chicxulub impact structure, Mexico. *Meteoritics & Planetary Science* 39:931–954.

Wittmann A., van Soest M., Hodges K. V., Darling J. R., Morgan J. V., Gulick S. P. S., Stockli D., Rasmussen C., Kring D. A., and Schmieder M. 2018. Petrology and radioisotopic ages of allanite in the peak ring of the Chicxulub impact crater (abstract #6286). 81st Annual Meeting of The Meteoritical Society, Moscow, Russia. LPI Contribution 2067.

Zhao J., Xiao L., Gulick S. P. S., Morgan J. V., Kring D. A., Urrutia-Fucugauchi J., Schmieder M., de Graaff S. J., Wittmann A., Ross C. H., Claeys P., Pickersgill A., Kaskes P., Goderis S., Rasmussen C., Vajda V., Ferrière L., Feignon J.-G., Chenot E., Perez-Cruz L., Sato H., Yamaguchi K., and IODP-ICDP Expedition 364 Scientists. 2020. Geochemistry, geochronology and petrogenesis of Maya Block granitoids and dykes from the Chicxulub impact crater, Gulf of Mexico: Implications for the assembly of Pangea. *Gondwana Research* 82:128–150.

SUPPORTING INFORMATION

Additional supporting information may be found in the online version of this article.

Data S1. Raw geochemical data for major elements, trace elements, and Sr–Nd isotopic analyses.

Fig. S1. Thick sections mosaic scan of selected granite, granite clast granite breccia, and aplite samples investigated using μXRF Three samples were taken from a different interval than the samples used for geochemical investigations; however, they are located very close within few centimeters from each other and thus, the chemical variation should be negligible.

Fig. S2. Bivariate diagrams of V and Zr versus TiO_2, and La and U versus Zr.

Supplementary material Figure S2. Thick sections mosaic scan of selected granite, granite clast, granite breccia and aplite samples investigated using µXRF. Three samples were taken from a different interval than the samples used for geochemical investigations, however they are located very close (within few centimeters) from each other, and thus, the chemical variation should be negligible.

| 134R3_75-79 846.9 mbsf (coarse granite with dolerite) XRF, INAA | 153R1_47-50,5 890.8 mbsf (coarse granite with cataclasite) XRF, INAA + Sr | 276R2_62-64 1251.0 mbsf (coarse granite heavily deformed) XRF, INAA | 298_1_4,5_6,5 1316.1 mbsf (coarse granite with IMR zones) *XRF, INAA done on 298R1_41-43* |

| 95_1_84_87 744.8 mbsf (granite clast inside IMR) *XRF, INAA done on 95_2_19_22* | 295_2_51_53 1308.5 mbsf (granite clast inside suevite) XRF, INAA + Sr | 147_2_4_6 875.8 mbsf (aplite) XRF, INAA done on 147_2_0_3 | 96_2_50_52 748.7 mbsf (granite breccia) XRF, INAA |

3 cm
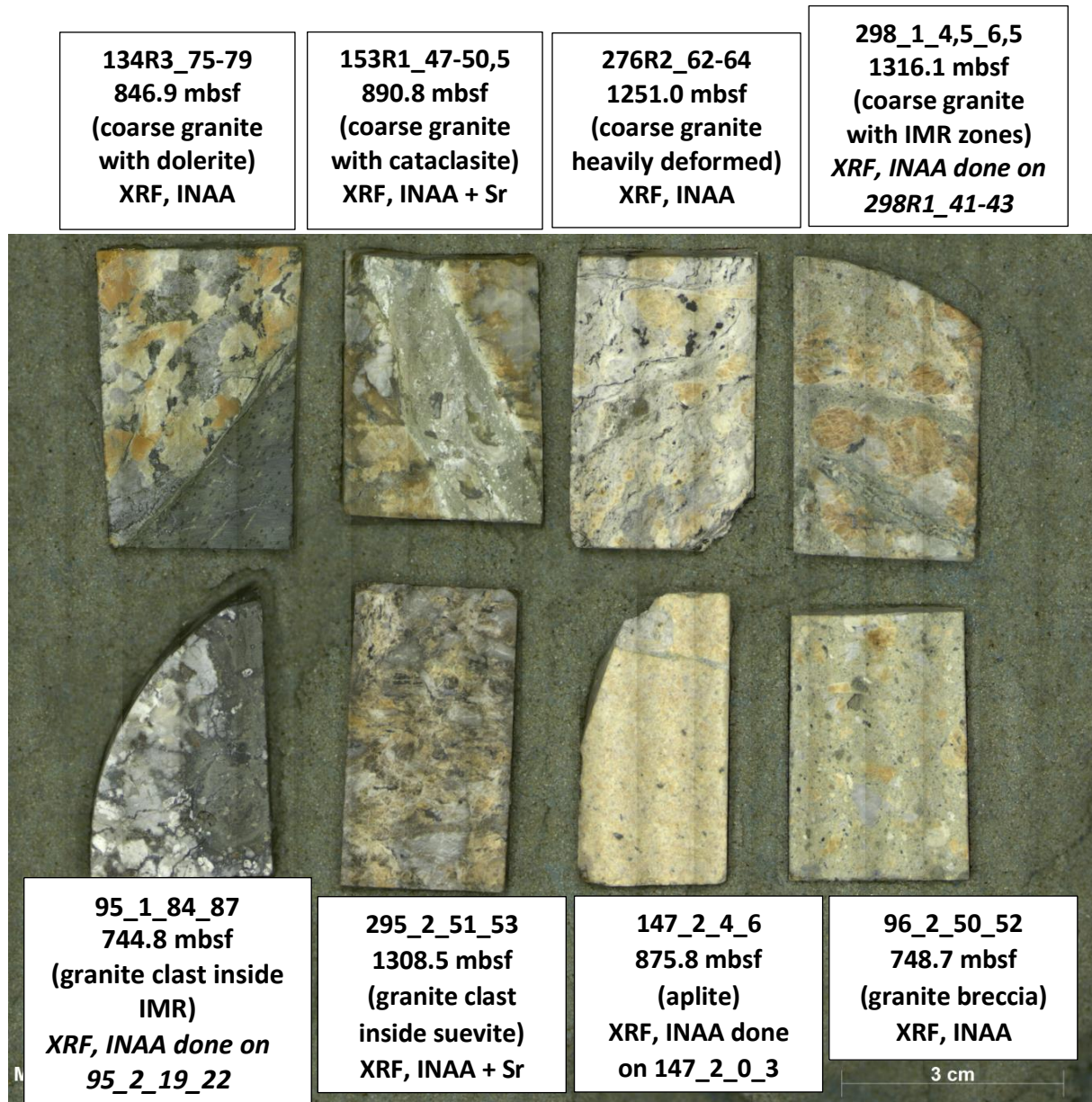
Supplementary Material Figure S3. Bivariate diagrams of V and Zr versus TiO_2. A strong co-variation is observed with R^2 values of 0.834 and 0.860 for V and Zr, respectively. The legend is the same as in Fig. 2, with open diamonds for the granite from the main unit, triangles for the granite clasts, circles for the granite breccias, and stars for the aplite dikes.

For the diagram of V versus TiO_2, gray diamonds are data from Zhao et al. (2020), all granite samples from the main unit.

For the diagram of Zr versus TiO_2, gray diamonds are data from granite samples from the main unit, from both Zhao et al. (2020) and de Graaff et al. (2021), while gray triangles are granite clast compositions from de Graaff et al. (2021).
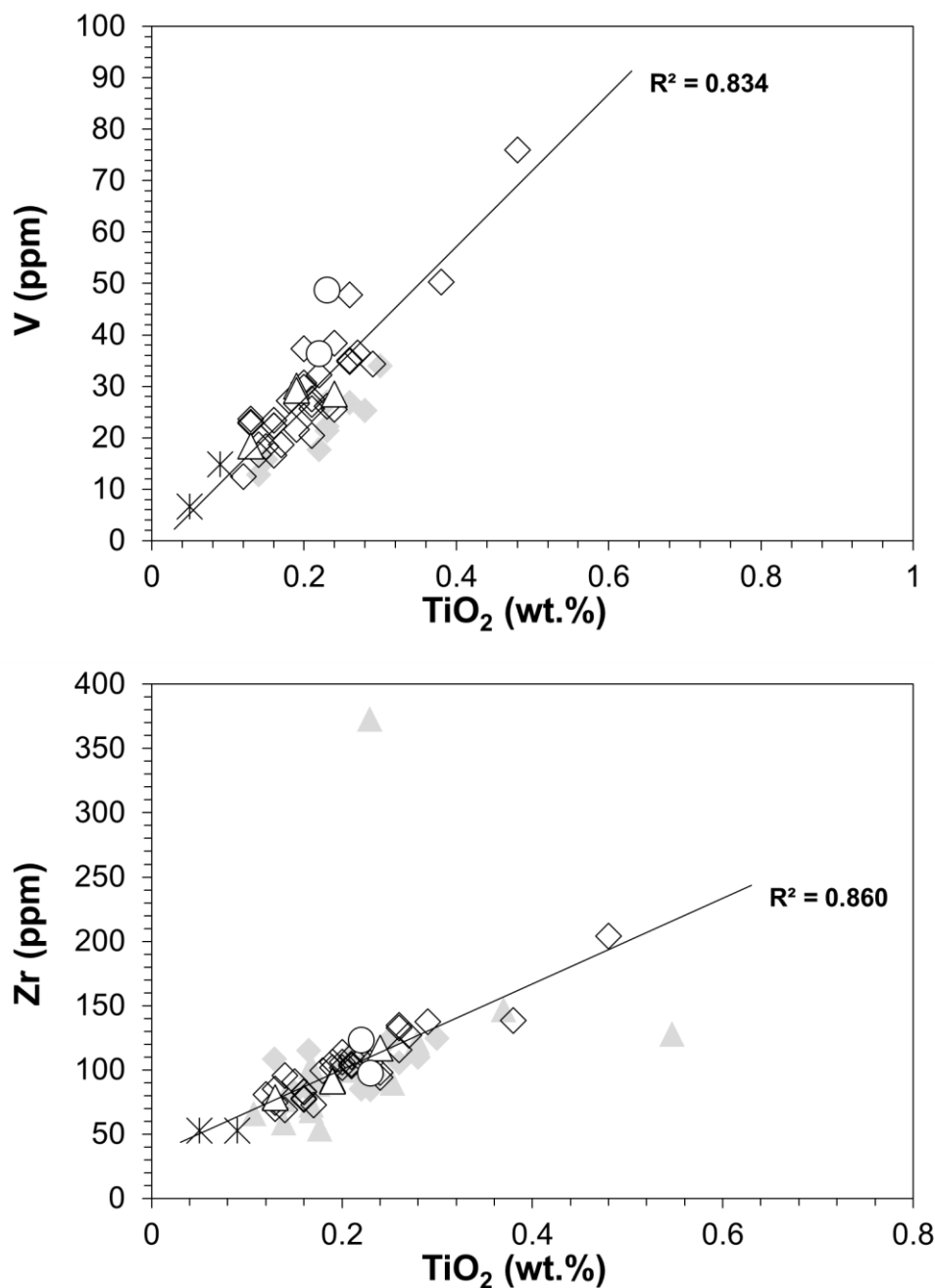
CHAPTER 7: Search for a meteoritic component within the impact melt rocks of the Chicxulub impact structure peak ring, Mexico

Authors

Jean-Guillaume Feignon, Toni Schulz, Ludovic Ferrière, Steven Goderis, Sietze J. de Graaff, Pim Kaskes, Thomas Déhais, Philippe Claeys, and Christian Koeberl.

Publication status

Personal contribution

Sample selection, petrographic descriptions, optical microscope observations, micro-X-ray fluorescence chemical mapping of some of the presented samples, sample preparation for geochemical analysis, instrumental neutron activation analysis (trace element abundances), assistance during thermal ionization mass spectrometry (TIMS) measurement of Re–Os isotopic ratios, processing and interpretation of the results, writing (original draft), writing (revision and editing).

Search for a meteoritic component within the impact melt rocks of the Chicxulub impact structure peak ring, Mexico

Jean-Guillaume Feignon [a,*], Toni Schulz [a,b], Ludovic Ferrière [c], Steven Goderis [d], Sietze J. de Graaff [d,e], Pim Kaskes [d,e], Thomas Déhais [d,e], Philippe Claeys [d], Christian Koeberl [a]

[a] *Department of Lithospheric Research, University of Vienna, Althanstrasse 14, A-1090 Vienna, Austria*
[b] *Institute for Geology and Mineralogy, University of Cologne, Zülpicher Strasse 49b, 50674 Cologne, Germany*
[c] *Natural History Museum, Burgring 7, 1010 Vienna, Austria*
[d] *Research Unit: Analytical, Environmental & Geo-Chemistry, Department of Chemistry, Vrije Universiteit Brussel, AMGC-WE-VUB, Pleinlaan 2, 1050 Brussels, Belgium*
[e] *Laboratoire G-Time, Université Libre de Bruxelles, Av. F.D. Roosevelt 50, 1050 Brussels, Belgium*

Abstract

Constraining the degree of preservation of a meteoritic signature within an impact structure provides vital insights in the complex pathways and processes that occur during and after an impact cratering event, providing information on the fate of the projectile. The IODP-ICDP Expedition 364 drilling recovered a ~829 m continuous core (M0077A) of impactites and basement rocks within the ~200-km diameter Chicxulub impact structure peak ring. No highly siderophile element (HSE) data have been reported for any of the impact melt rocks of this drill core to date. Previous work has shown that most Chicxulub impactites contain less than 0.1% of a chondritic component. Only few impact melt rock samples in previous drill cores recovered from the Chicxulub might contain such a signal. Therefore, we analyzed impact melt rock and suevite samples, as well as pre-impact lithologies of the Chicxulub peak ring, with a focus on the HSE concentrations and Re–Os isotopic compositions.

Similar to the concentrations of the other major and trace elements, those of the moderately siderophile elements (Cr, Co, Ni) of impact melt rock samples primarily reflect mixing between a mafic (dolerite) and felsic (granite) components, with the incorporation of carbonate material in the upper impact melt rock unit (from 715.60 to 747.02 meters below seafloor). The HSE concentrations of the impact melt rocks and suevites are generally low (<39 ppt Ir, <96 ppt Os, <149 ppt Pt), comparable to the values of the average upper continental crust, yet three impact melt rock samples exhibit an enrichment in Os (125–410 ppt) and two of them also in Ir (250–324 ppt) by one order of magnitude relative to the other investigated samples. The $^{187}Os/^{188}Os$ ratios of the impact melt rocks are highly variable, ranging from 0.18 to 2.09, probably reflecting heterogenous target rock contributions to the impact melt rocks. The significant amount of mafic dolerite (mainly ~20–60% and up to 80–90%), which is less radiogenic ($^{187}Os/^{188}Os$ ratio of 0.17), within the impact melt rocks makes an unambiguous identification of an extraterrestrial admixture challenging. Granite samples have unusually low $^{187}Os/^{188}Os$ ratios (0.16 on average), while impact melt rocks and suevites broadly follow a mixing trend between upper continental crust and chondritic/mantle material. Only one of the investigated samples of the upper impact melt rock unit could also be interpreted in terms of a highly diluted (~0.01–0.05%) meteoritic component. Importantly, the impact melt rocks and pre-impact lithologies were affected by post-impact hydrothermal alteration processes, probably remobilizing Re and Os. The mafic contribution, explaining the least

* Corresponding author.
  E-mail address: jean-guillaume.feignon@univie.ac.at (J.-G. Feignon).

75

radiogenic $^{187}Os/^{188}Os$ values, is rather likely. The low amount of meteoritic material preserved within impactites of the Chicxulub impact structure may result from a combination of the assumed steeply-inclined trajectory of the Chicxulub impactor (enhanced vaporization, and incorporation of projectile material within the expansion plume), the impact velocity, and the volatile-rich target lithologies.

1. INTRODUCTION

The Chicxulub impact structure, ∼200-km-in-diameter (Gulick et al., 2013) and 66.05 Myr old (Sprain et al., 2018), is located in the northwestern part of the Yucatán peninsula, Mexico (Fig. 1). The circular structure was identified based on the observation of large-scale negative Bouguer gravity and magnetic anomalies (Hildebrand et al., 1991, and references therein). The identification and characterization of shocked quartz grains in drill core samples from within the structure was used to confirm its impact origin (Hildebrand et al., 1991). Chicxulub is the only known impact structure on Earth with a well-preserved peak ring (e.g., Morgan et al., 2016, and references therein). The structure formed following the oblique impact of a ∼12-km-diameter body (Collins et al., 2020) on a target rock made of ∼3-km thick, Mesozoic carbonate and evaporite, platform overlying crystalline basement rocks (Lopez

Ramos, 1975; Urrutia-Fucugauchi et al., 2011; Morgan et al., 2016). The Chicxulub impact event coincides with the end of the Mesozoic Era, which is marked by the Cretaceous-Paleogene (K–Pg) boundary, and the extinction of, for instance, the non-avian dinosaurs (e.g., Swisher et al., 1992; Smit, 1999; Schulte et al., 2010; DePalma et al., 2019; Chiarenza et al., 2020). The K–Pg impact event is marked in the geologic record by a thin layer of clay, which has, so far, been found in more than 350 terrestrial and marine sites around the world (e.g., Smit, 1999; Claeys et al., 2002; Schulte et al., 2010).

An iridium enrichment several thousand times higher than the average upper continental crust (UCC) value (average composition of Earth's continental crust ∼0.02 ppb Ir; Peucker-Ehrenbrink and Jahn, 2001) was first characterized in the K–Pg layer sites of Gubbio (Italy) and Caracava (Spain), leading to the hypothesis of a large impact event as the cause of the mass extinction at the K–Pg boundary
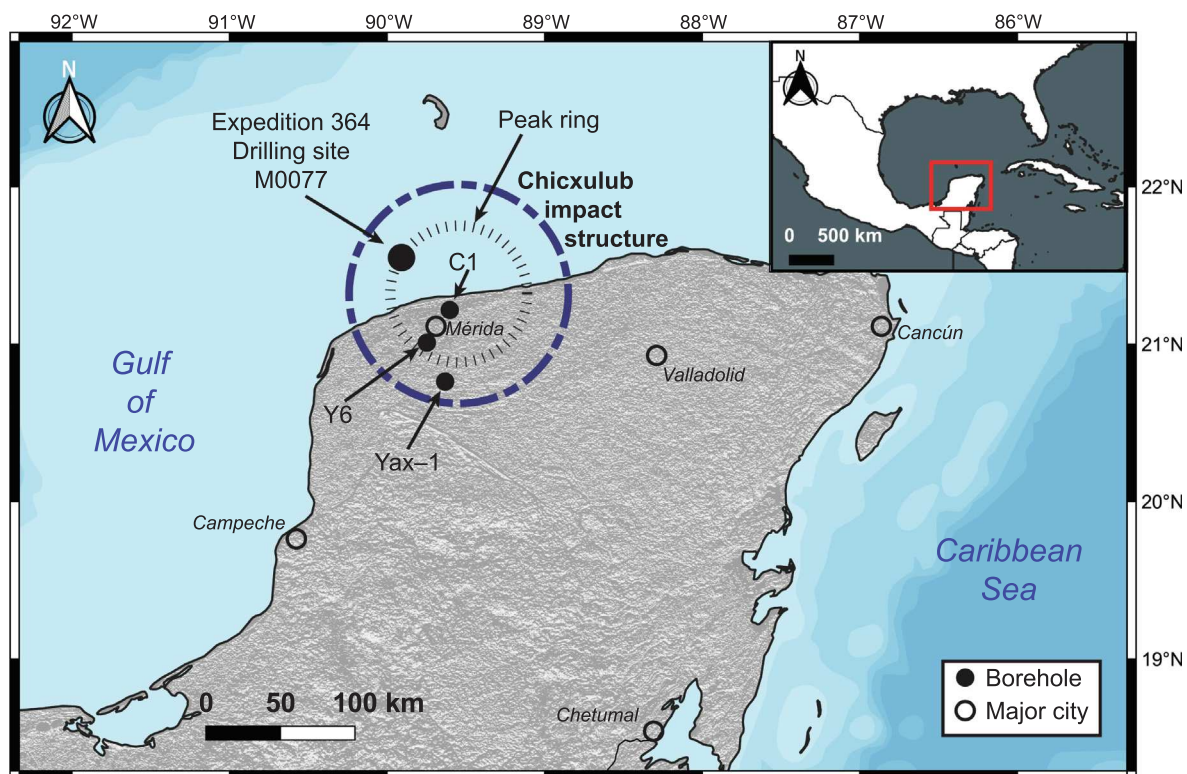

Fig. 1. Map and digital elevation model of the Yucatán peninsula, SE Mexico, showing the 200-km-diameter Chicxulub impact structure (dashed line) and the peak ring (thin circle within). The locations of the M0077A drill core, as well as other drill cores within the impact structure that are discussed in the text, are shown for reference.

(Alvarez et al., 1980; Smit and Hertogen, 1980). Subsequent investigations at other K–Pg boundary sites measured Ir enrichments of up to 87 ppb (Claeys et al., 2002). Enrichments in moderately (e.g., Cr, Co, and Ni), and other highly siderophile elements (Ru, Rh, Pd, Re, Os, Pt, and Au; HSE) were also found at a number of K–Pg boundary sites (see Schulte et al., 2010; Goderis et al., 2013, and references therein). The projectile component in the boundary layer was determined to be of carbonaceous chondritic composition (Kyte, 1998; Trinquier et al., 2006; Quitté et al., 2007; Goderis et al., 2013). Since then, iridium, and, more broadly, the HSE (e.g., Os, Pt) contents, as well as Re–Os isotopic compositions, have been identified as geochemical tracers to reveal a projectile component in ejecta (e.g., Koeberl et al., 2012; Koeberl, 2014). Other impactites, and, more specifically, impact melt rocks can also contain traces of the original projectile (e.g., Palme et al., 1978; Morgan et al., 1979, Tagle and Hecht, 2006; Koeberl et al., 2012; Koeberl, 2014). Such meteoritic material was identified, using the aforementioned geochemical tools, within the large Vredefort impact structure (South Africa) Granophyre, displaying HSE abundances and Re–Os isotopic compositions that can only be explained by the addition of ~0.2% of chondritic material (French et al., 1989; Koeberl et al., 1996). Similarly, an unambiguous meteoritic contribution was identified within the chemically homogeneous impact melt rock body of the Morokweng impact structure (~70–80-km-diameter, South Africa), with an estimated chondritic contribution between ~2 and ~5% (e.g., Koeberl et al., 1997; Koeberl and Reimold, 2003). Additionally, a preserved, 25-cm sized meteorite clast was discovered within the impact melt rocks recovered from a drill core (Maier et al., 2006). In the case of Morokweng, the meteoritic component is relatively abundant and is homogeneously distributed within the impact melt rocks (Koeberl et al., 1997), in contrast to the impact melt rocks from other impact structures (Koeberl, 1998). The average $^{187}Os/^{188}Os$ ratio of the UCC is ~1.4 (Peucker-Ehrenbrink and Jahn, 2001), while undifferentiated meteoritic material (i.e., chondrites) shows significantly less radiogenic $^{187}Os/^{188}Os$ ratios of ~0.12–0.13 (Fischer-Gödde et al., 2010). In addition, chondrites are characterized by elevated HSE abundances, e.g., an average of ~600 ppb Os, ~500–600 ppb Ir, and ~1100 ppb Pt (Horan et al., 2003; Tagle and Berlin, 2008; Fischer-Gödde et al., 2010). Although terrestrial mantle rocks have similarly low $^{187}Os/^{188}Os$ ratios, on the order of ~0.13 (Meisel et al., 2001), their HSE concentrations are at least two orders of magnitude lower compared to chondrites with, e.g., values of ~3.9 ppb Os, ~3.5 ppb Ir, and ~7.6 ppb Pt (Becker et al., 2006). On the other hand, UCC values are ~0.03 ppb Os, ~0.02 ppb Ir, and ~0.51 ppb Pt (Peucker-Ehrenbrink and Jahn, 2001). Consequently, the addition of even a small amount of chondritic material to crustal target rocks associated with a meteorite impact can lead to a significant change of the $^{187}Os/^{188}Os$ signature and the HSE concentrations of the impactites (Walker et al., 2002; Koeberl et al., 2012; Koeberl, 2014, and references therein). However, having a mix of lithologies, including a significant mafic component (or HSE-rich target rock) within the impactites,

may simulate a meteoritic component (but requires independent petrographic and/or geochemical confirmation of the presence of such a large mafic component) (see also, Lambert, 1982; McDonald et al., 2007).

Up to now, the presence of a distinct meteoritic component in impactites, comparable to that observed in, for example, Vredefort, Morokweng, or in the East Clearwater Lake (Grieve et al., 1980) impact structures, is rather rare. For the Chicxulub impact structure, several studies came up with mostly a low or heterogeneously distributed meteoritic component within the impactites (Koeberl et al., 1994; Gelinas et al., 2004; Tagle et al., 2004; Tuchscherer et al., 2004a; Goderis et al., 2021). In 2016, the joint International Ocean Discovery Program (IODP) and International Continental Scientific Drilling Program (ICDP) Expedition 364 drilling recovered a ~829 m continuous core (in Hole M0077A) of impactites and basement rocks within the ~200-km diameter (Gulick et al., 2013) Chicxulub impact structure peak ring (Morgan et al., 2016). While an unambiguous meteoritic component was identified in the upper part of the "transitional unit" of the Expedition 364 core (Goderis et al., 2021), the potential presence of a projectile contribution is still to be determined in the impact melt rock units of the core. In order to detect and to constrain the distribution of an extraterrestrial component in rocks forming the Chicxulub peak ring, we have conducted geochemical and isotopic investigations on a selection (n = 33) of impact melt rock, suevite, and pre-impact crystalline lithologies from this drill core, with a specific focus on selected moderately siderophile trace elements (Cr, Co, and Ni), selected HSEs (Re, Os, Ir, and Pt), and Re–Os isotope compositions. The characterization of a wide range of target rock lithologies drilled in this core allows us to identify their respective contributions to the HSE budget and to the Re–Os isotope composition to ascertain whether a meteoritic component is preserved within the impact melt rocks of the peak ring structure. Constraining the degree of preservation of a meteoritic signature within an impact structure provides vital insights in the complex pathways and processes that occur during and after a large impact cratering event.

2. SUMMARY OF PREVIOUS GEOCHEMICAL AND ISOTOPIC WORK ON CHICXULUB AND ITS GLOBALLY DISTRIBUTED EJECTA

The Chicxulub impact structure is buried under ~1 km of Cenozoic limestones, with a ring of cenotes (i.e., water-filled sinkholes) as its only surface expression. Consequently, the direct study of the different lithologies occurring within the impact structure (i.e., a variety of impact breccias, impact melt rocks, and (shocked) pre-impact target rocks), and, thus, the relative abundance of a meteoritic component in these lithologies, relies largely on investigating samples recovered by scientific drilling programs and petroleum exploration campaigns (e.g., Lopez Ramos, 1975; Hildebrand et al., 1991; Koeberl and Sigurdsson, 1992; Kring and Boynton, 1992; Swisher et al., 1992; Koeberl, 1993a; Koeberl et al., 1994; Sharpton et al., 1996; Urrutia-Fucugauchi et al., 1996; Claeys et al., 2003;

Tuchscherer et al., 2004a, and references therein; Belza et al., 2012). Several drilling campaigns were conducted within the impact structure by Petróleos Méxicanos (PEMEX), including Chicxulub–1 (C1) and Yucatán–6 (Y6) cores (Fig. 1), which sampled several impactite units, mainly melt-bearing impact breccias (suevites) and impact melt rocks (e.g., Hildebrand et al., 1991; Kring and Boynton, 1992; Swisher et al., 1992; Schuraytz et al., 1994; Ward et al., 1995; Claeys et al., 2003; Kettrup and Deutsch, 2003); and by the ICDP, recovering the Yax-copoil–1 (Yax–1) core (e.g., Tuchscherer et al., 2004a, 2004b, 2005, 2006).

Several studies have tried to identify and/or quantify the presence of a meteoritic component within the impactites recovered in C1, Y6, and Yax–1 drill cores. Most of the investigated impact melt rock and suevite samples in the Yax–1 drill core display low Ir contents, generally below 100 ppt, and HSE abundance patterns similar to those of the UCC (Tagle et al., 2004; Tuchscherer et al., 2004a). Clast-rich (with quartz, feldspar, anhydrite, and carbonate clasts) impact melt rock sample Y6-N19 from the Y6 drill core shows similar upper crustal HSE composition (Tagle et al., 2004). In these impactites, the meteoritic component, if present, corresponds to the equivalent of less than 0.05% chondrite (Tagle et al., 2004). Minor enrichments were measured in three samples from Yax–1, i.e., (1) a clast-supported, reworked suevite, with limestone, fossils, and melt fragments at 800.4 m depth in the core, (2) a fine-grained, carbonate groundmass supported suevite containing melt particles at 844.8 m depth, and (3), a polymict impact melt breccia with a fine-grained carbonate groundmass at 890.5 m depth (Tuchscherer et al., 2004a). The Ir contents of these samples are up to ~400 ppt, which is higher by a factor of 50 compared to other impactites from Yax–1 and upper crustal values (Tuchscherer et al., 2004a). These Ir enrichments were thought to be indicative of a minor, heterogeneously distributed, meteoritic signature within the impactites (Tuchscherer et al., 2004a). Other impact melt rock samples from Yax–1 were investigated by Gelinas et al. (2004), revealing variable Os contents, ranging from 11 to 368 ppt, and corresponding $^{187}Os/^{188}Os$ ratios, which range from ~0.19 to ~2.31. These data were interpreted to indicate the presence of a minor and heterogeneously distributed chondritic component, equivalent to less than 0.1% of a chondritic admixture in four samples but less than 0.01% of such a component in nine samples. Only two studies reported elevated Ir contents, potentially indicative of a meteoritic component in C1 and Y6 impact melt rocks. Iridium concentrations of ~6 and ~13.8 ppb, respectively were measured in powder splits (i.e., aliquot from the same prepared powder) from C1 and Y6 impact melt rocks (Koeberl et al., 1994; Schuraytz et al., 1996). The powder split from C1, showing a high Ir content (~6 ppb), also has a high Os concentration of ~25 ppb, associated with a subchondritic $^{187}Os/^{188}Os$ ratio of ~0.11. This was explained as representing an admixture of ~3% of meteoritic material (Koeberl et al., 1994). However, other studies failed to reproduce these anomalies in Y6 and C1 (see also, Tagle et al., 2004, and references therein).

The most compelling evidence of a chemical contamination from the projectile is found in distal K–Pg impact ejecta, including Ir and other HSEs enrichments in the K–Pg clay layer at different sites worldwide (Schulte et al., 2010; Goderis et al., 2013). In a few cases, this analysis was also coupled with Re–Os and Cr isotope compositions that were interpreted to reflect the signature of a carbonaceous chondrite component (Shukolyukov and Lugmair, 1998; Trinquier et al., 2006; Quitté et al., 2007). Notably, a 2.5-mm lithic clast (included in a ~4-mm-sized light-brown clay inclusion), interpreted as an altered carbonaceous chondrite, was found in drill core from Deep Sea Drilling Project (DSDP) Hole 576, which sampled marine K–Pg sediments from the North Pacific Ocean, and is considered to represent material from the Chicxulub projectile (Kyte, 1998). In contrast, the proximal K–Pg ejecta deposits found around the Gulf of México, which are thicker than distal ejecta (i.e., from a few centimeters to tens of meters of clastic beds) and were formed following high-energy sediment transport (tsunami or gravity flows), show a more moderate Ir anomaly due to dilution processes, with an Ir content generally below 1.5 ppb (e.g., Smit, 1999; Claeys et al., 2002; Schulte et al., 2010; Goderis et al., 2013; Sanford et al., 2016). This is similar to the Ir anomaly found at the top of the transitional unit in the Expedition 364 M0077A drill core (Goderis et al., 2021).

3. THE IODP-ICDP EXPEDITION 364 DRILL CORE

The IODP-ICDP Expedition 364 successfully recovered a continuous core between 505.7 and 1334.7 meters below seafloor (mbsf) into the Chicxulub impact structure peak ring (Figs. 1–2a). The drilling took place offshore of the Yucatán peninsula at site M0077A (21.45°N, 89.95°W; Morgan et al., 2017).

The drill core was subdivided in four main lithological units (see Morgan et al., 2017), consisting of: (1) a ~112 m "post-impact" Cenozoic sedimentary rock section (from 505.70 to 617.33 mbsf), further divided in seven lithostratigraphic subunits, with the deepest sub-unit (unit 1G) defined as a ~75-cm thick, fine-grained, and carbonate-rich transitional unit (from 616.58 to 617.33 mbsf) in which the Ir anomaly (~1.0 ppb) was found (Goderis et al., 2021); (2) a ~98 m impact melt-bearing polymict impact breccia (defined as suevite) unit (from 617.33 to 715.60 mbsf), further subdivided in three sub-units, i.e., with increasing depth, the bedded suevite (617.33–620.88 mbsf), the graded suevite (620.88–710.01 mbsf), and the non-graded suevite (710.01–715.60 mbsf), according to the classification of the suevite sequence proposed by Kaskes et al. (2022); (3) an ~31 m thick impact melt rock sequence (from 715.60 to 747.02 mbsf), composed of two intermingled, and distinct chemically, impact melt rock phases, i.e., a SiO_2-rich and trachyandesitic black melt, and a CaO-rich green phase, made of mainly secondary clay minerals and sparitic calcite (Morgan et al., 2017; de Graaff et al., 2022; Schulte et al., 2021; Kaskes et al., 2022). The impact melt rock sequence can be subdivided in three subunits, i.e., the upper part, a brecciated
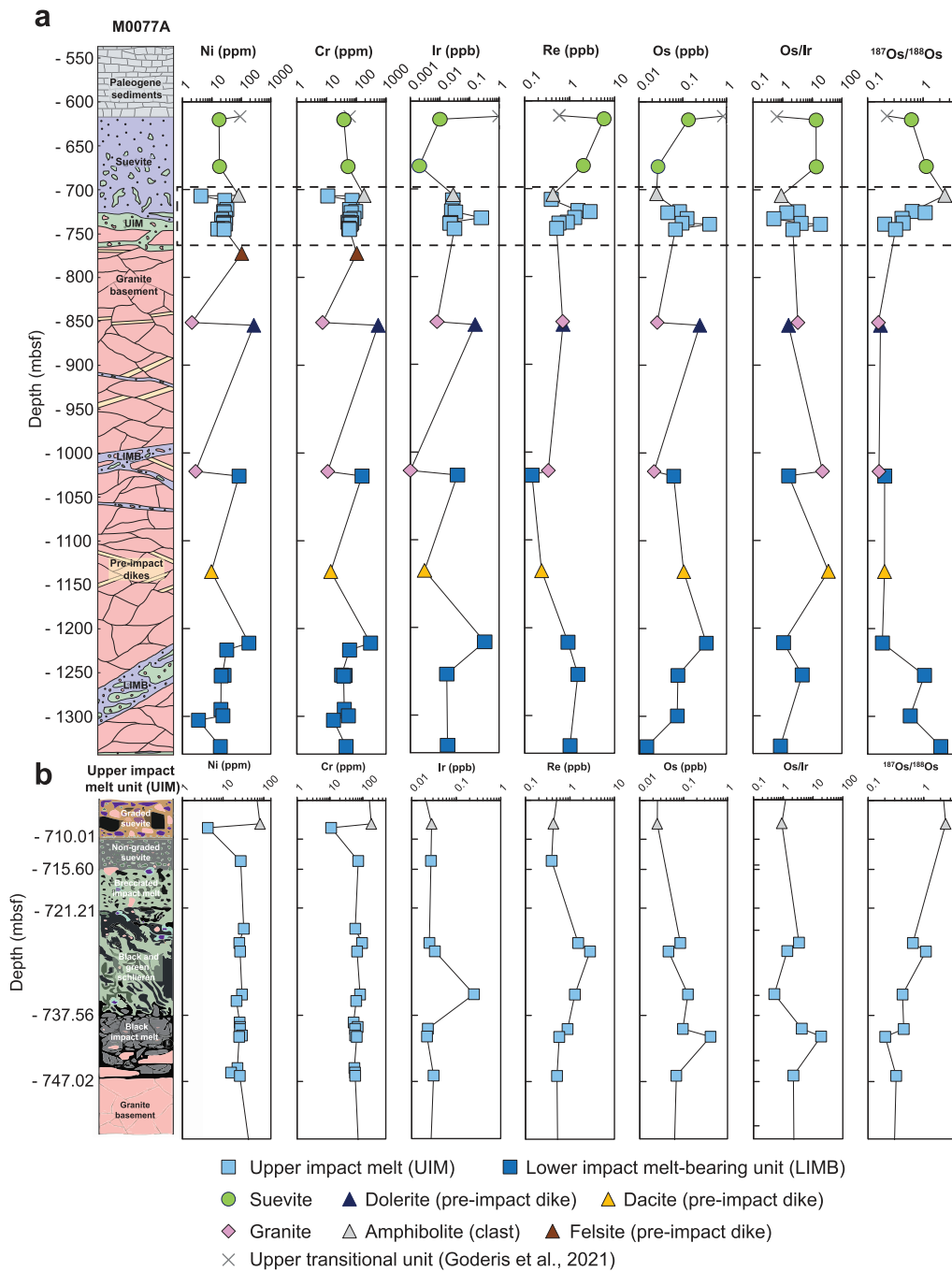
Fig. 2. a) Lithostratigraphy of the M0077A drill core (∼550.0–1334.7 mbsf, modified from de Graaff et al., 2022), comparing the concentration variations of selected moderately siderophile elements (Cr and Ni), HSEs (Os, Ir, Re), Os/Ir, and $^{187}Os/^{188}Os$ isotopic compositions with depth in the investigated samples. Cobalt concentrations are varying similarly to Cr, and Ni. Values from the upper transitional unit (Goderis et al., 2021) are shown to highlight the differences in HSE and Os isotopic compositions. The dashed frame represents the UIM interval shown in (b). b) Schematic representation of the main lithological and textural characteristics of the UIM sequence, located above the shocked granite unit (modified from Schulte et al., 2021, with the interval names defined in Kaskes et al., 2022), and showing the same selected elements, elemental ratios, and isotopic composition as in (a).

impact melt rock with angular black impact melt fragments in a green phase matrix (from 715.60 to 721.21 mbsf), then a schlieren texture between both black impact melt rock and the green phase (from 721.21 to 737.56 mbsf), and the lower part of the unit (from 737.56 to 747.02 mbsf) is

composed of black impact melt rock only, with the occurrence of crystalline basement clasts (Schulte et al., 2021; de Graaff et al., 2022; Kaskes et al., 2022); and (4), a crystalline basement rock unit (from 747.02 to 1334.69 mbsf) mainly made of shocked, fractured, and deformed,

coarse-grained granite, with locally aplitic and pegmatitic textures. The granite is defined as a high-K calc-alkaline granite; it was shocked at pressures estimated between ~16 and 18 GPa, and undergone both pre- and post-impact pervasive hydrothermal alteration (Feignon et al., 2020, 2021; Kring et al., 2020; Zhao et al., 2020; de Graaff et al., 2022). The granite unit is pervasively intruded by pre-impact subvolcanic dikes, including dolerite, felsite, and dacite, as well as by impact-related dikes (i.e., impact melt rock and impact melt rock-bearing breccia; Morgan et al., 2017; de Graaff et al., 2022). These impact-related dikes are more abundant in the lower part of the granite unit, between 1206.98 to 1334.69 mbsf, and display varying degrees of brecciation and deformation.

In this study we use the four units mentioned above, as defined in Morgan et al. (2017), with units (2) and (3) representing the "upper peak ring" section, while the unit (4) represents the "lower peak ring" section. The subunits used for the "upper peak ring" section are those described in Kaskes et al. (2022). The impact melt rock samples comprise impact melt rock clasts located in the suevite unit (2) described in Kaskes et al. (2022), samples from the upper impact melt rock (UIM) unit (3) as presented in de Graaff et al. (2022), and samples from the lower impact melt rock-bearing unit (LIMB), with all the impact melt rock and impact melt rock-bearing units found in the granite unit (4) considered to be part of the LIMB, as in de Graaff et al. (2022).

Previous work on impact melt rocks from the Hole M0077A drill core showed that they have mainly an andesitic composition (54.4–71.7 wt.%), resulting from the mixing and melting of mafic and felsic target rock compositions, with the dolerite and granitoid possibly representing the major components, in addition to varying degrees of carbonate admixture (de Graaff et al., 2022). While the LIMB shows no indication of carbonate dilution, the UIM is characterized by the presence of a carbonate component, as well as undigested carbonate clasts (de Graaff et al., 2022). The origin of the LIMB is debated with de Graaff et al. (2022) interpreting it as impact melt rock that has been injected into the crystalline target rock during the first phases of crater formation (compression and excavation stages) and that then brecciated after the central uplift collapse. In contrast, Riller et al. (2018) proposed that the LIMB was emplaced at the end of the peak ring formation, following entrainment and trapping of melt bodies within target rock thrust zones.

So far, meteoritic matter was only found in the upper part of the so-called "transitional unit", where a thin gray-green marlstone layer (616.55–616.58 mbsf) was identified, below the Danian pelagic limestone (Lowery et al., 2018; Gulick et al., 2019; Whalen et al., 2020). The interval between 616.55 and 616.58 mbsf is characterized by significant enrichments in Ni (50–100 ppm), Ir (~1.0 ppb), and HSEs (Os, Ru, Pt, and Pd), in addition to lower initial $^{187}Os/^{188}Os_i$ ratio (0.224–0.250) when compared to the lower part of the "transitional unit" (0.281–0.367) and the UCC values (Table 1; Goderis et al., 2021). The meteoritic contribution in the gray-green marlstone layer is estimated at ~0.1% chondritic (Goderis et al., 2021).

4. ANALYTICAL METHODS

Samples with masses ranging from ~20 to 50 g were crushed in polyethylene wrappers and then powdered in an agate bowl using a Retsch RS200 vibratory disc mill at the University of Vienna. Macrophotographs of the main sample types investigated are presented in Fig. 3. Details on sample material, i.e., petrographic descriptions, and major element compositions, can be found in the Supplementary Material.

4.1. Trace element analysis

Trace element concentrations (including Cr, Co, and Ni) were measured using bulk XRF as well as Instrumental Neutron Activation Analysis (INAA). The bulk XRF measurements for trace element concentrations were done on pressed powder pellets. Sample preparation and measurement was done following the methodology described in Feignon et al. (2021). The international reference material used for bulk XRF trace element concentration calibration was GSR 1–6 (Xie et al., 1989).

For bulk INAA analysis, international reference materials used were Ailsa Craig granite AC-E (Centre de Recherches Pétrographiques et Géochimiques, Nancy, France), the carbonaceous chondrite Allende (ALL; Smithsonian Institution, Washington DC, USA), and the Devonian Ohio shale SDO-1 (USGS). The reproducibility for trace elements is on the order of ~2–15% relative standard deviation. The details on instrumentation, accuracy, and precision of this method are given in, e.g., Koeberl (1993b), Son and Koeberl (2005), Mader and Koeberl (2009), Feignon et al. (2021), and references therein.

4.2. Micro-X-ray fluorescence

In addition to the bulk powder geochemical techniques, we applied energy-dispersive micro-X-ray fluorescence (μXRF) mapping of 17 polished thick sections in order to get a better understanding of the distribution of major and trace elements (specifically Ni, Cr, and Co) within the different Chicxulub impactite and target lithologies and to investigate whether specific mineral phases are enriched in moderately siderophile elements and thus a potential meteoritic signature. For this, an M4 Tornado benchtop μXRF surface scanner (Bruker Nano GmbH, Berlin, Germany) equipped with a Rh tube as X-ray source and two XFlash 430 Silicon Drift detectors was used at the Vrije Universiteit Brussel, Belgium (VUB). The μXRF mapping was performed under near-vacuum conditions (20 mbar), using both detectors at maximized X-ray source energy settings (50 kV and 600 μA) and with a spot size and spatial resolution of 25 μm in combination with an integration time of 5 ms per pixel. For the first major element measurement run no specific X-ray source filter was applied, but to enhance the visualization of moderately siderophile elements such as Cr, Co, and Ni, an Aluminum 630 μm filter was applied during a second mapping. This filter allows for a more sensitive detection of trace elements by reducing the X-ray signal for lighter major elements such as Al, Si,

Table 1
Summary table with average moderately and highly siderophile elements, and Os isotope data of investigated samples from this study and from the available literature on the IODP-ICDP Expedition 364 (M0077A Hole) drill core, as well as from previous cores (i.e., Yax−1, Y6, and C1) from the Chicxulub impact structure. Outlier impact melt samples are also presented. n/a: not available, n.d.: non detectable, (?) ambiguous.

Sample group (site or core; lithology)	Cr (ppm)	Co (ppm)	Ni (ppm)	Re (ppb)	Os (ppb)	Ir (ppb)	Pt (ppb)	(^{187}Os/^{188}Os)	Range of meteoritic contribution (%)
M0077A core									
Average green marlstone (Goderis et al., 2021; n = 3)	24.7	8.01	68.0	0.32	0.82	1.27	3.87	0.23	<0.05–0.1%
Average transitional unit (Goderis et al., 2021; n = 27)	17.0	11.3	38.9	0.69	0.44	0.27	2.23	0.28	~0.05%
Average suevite (n = 2)	45.3	10.6	17.8	3.90	0.08	0.006	0.08	0.88	<0.01%
Average UIM (n = 15)	61.5	13.4	24.1	1.14	0.14	0.06	0.10	0.52	n.d.–0.05%
91R1_102–104.5*	82.3	15.6	29.2	1.29	0.13	0.25	0.10	0.42	~0.01–0.05%
93R2_11–12.5*	65.4	14.3	24.8	0.57	0.41	0.02	0.08	0.20	~0.1%(?)
Average LIMB (n = 10)	77.9	20.7	43.1	0.90	0.11	0.10	0.15	0.82	n.d.–0.1%(?)
265R2_9–11*	299	58.2	180	0.82	0.34	0.32	0.35	0.18	~0.1%(?)
Average dolerites (n = 1)	542	68.3	266	0.71	0.25	0.16	0.35	0.17	n.d.
Average amphibolites (n = 1)	181	32.4	81.0	0.42	0.03	0.03	0.21	2.47	n.d.
Average felsites (n = 1)	105	26.2	103	n/a	n/a	n/a	n/a	n/a	n.d.
Average dacites (n = 1)	13.7	8.22	9.60	0.24	0.11	0.003	0.04	0.20	n.d.
Average granites (n = 2)	9.10	2.30	2.45	0.52	0.02	0.005	0.09	0.16	n.d.
Yax-1 core									
Suevites (Tagle et al., 2004; n = 5)	55.2	15.0	17.8	n/a	n/a	0.06	0.52	n/a	<0.05%
Impactites (Tuchscherer et al., 2004a; n = 43)	42.0	7.09	21.2	n/a	n/a	<0.4	n/a	n/a	<0.1%
Impactites (Gelinas et al., 2004; n = 16)	n/a	n/a	n/a	0.06	0.10	n/a	n/a	0.63	<0.01–0.1%
Y6 core									
Y6-N19 Impact melt sample (Schuraytz et al., 1996; Tagle et al., 2004)	15	42	15	n/a	n/a	0.06–13.8	0.45	n/a	<0.01–3%
C1 core									
Data from Koeberl et al. (1994), n = 2	114	14.8	40.0	1.28	12.6	6.00	n/a	0.31	0.01–5%
K-Pg boundary clays									
Data from Goderis et al. (2013)	111	46.2	199	n/a	n/a	5.96	10.2	n/a	~0.1–>5%
Data from Quitté et al. (2007), n = 11	n/a	n/a	n/a	7.38	9.31	n/a	n/a	0.22	<0.05–>5%
Fossil meteorite (Kyte, 1998)	6540	76.0	1370	n/a	n/a	690	n/a	n/a	n/a
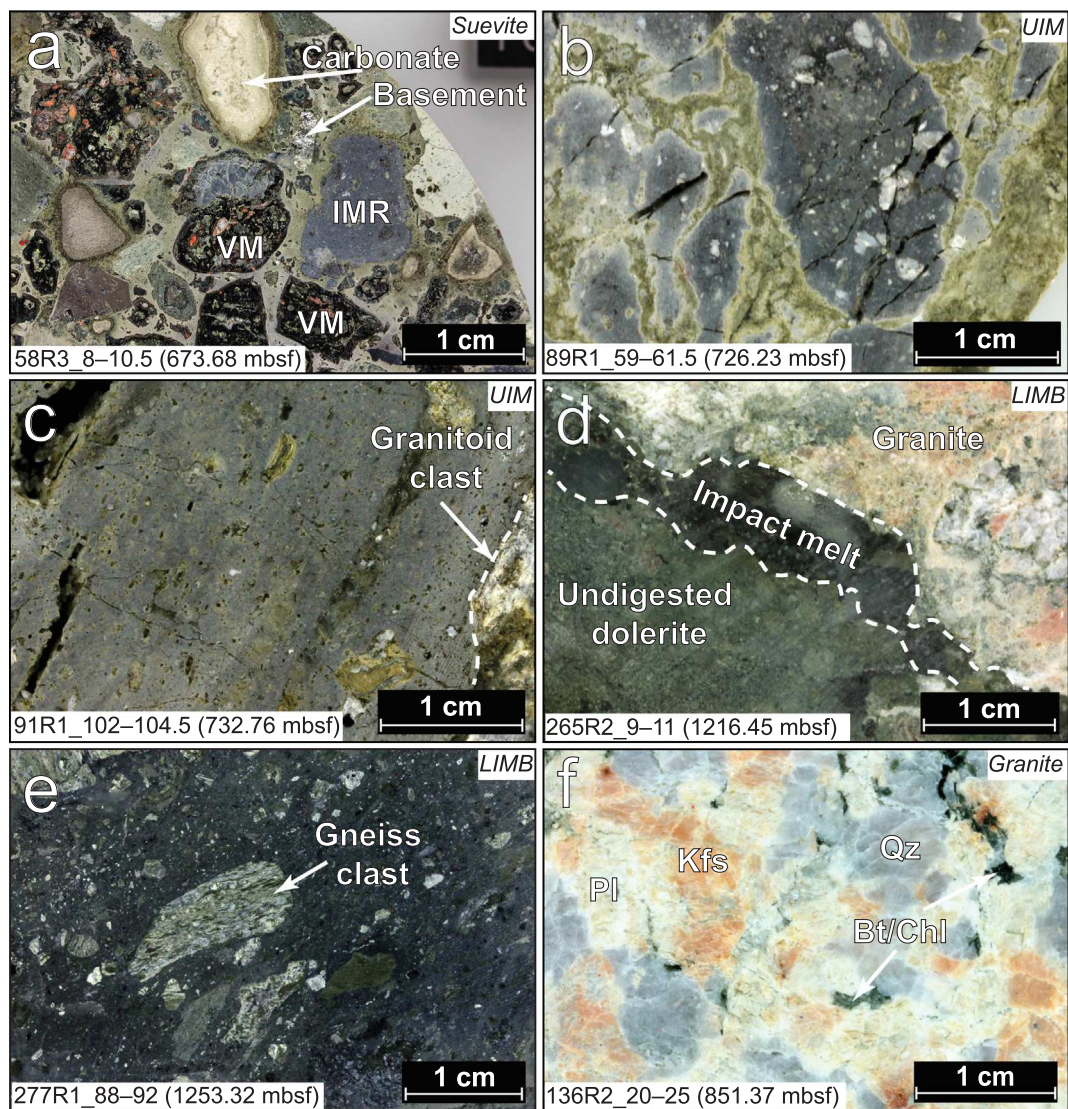
Fig. 3. Macrophotographs of the main sample types encountered. a) Suevite sample from the graded suevite unit (Kaskes et al., 2022) showing several types of centimeter-sized clasts, i.e., carbonates, impact melt rock (IMR), altered vitric melt (VM), and crystalline basement, embedded in a clastic matrix. b–c) Upper impact melt rock samples, with (b) showing the schlieren texture between mingled black impact melt rock and the carbonate-rich, altered, green phase, as well as abundant open fractures crosscutting the sample, and (c) a black melt rock-dominated sample with greenish altered area, clast-poor and vesiculated. A large centimetric granitoid clast is visible on the right side. d–e) Lower impact melt-bearing unit samples, with (d) a relatively thin impact melt intruding at the contact between the granite unit and a dolerite dike, leading to the partial melting of the dolerite, and (e) relatively clast-rich impact melt rock with a large sub-angular gneiss clast. f) Typical coarse-grained granite (pre-impact lithology), relatively undeformed and with limited fracturing, exhibiting the typical paragenesis (i.e., Kfs: K-feldspar, Qz: quartz, Pl: plagioclase, Bt: biotite, and Chl: chlorite). Additional macrophotographs of other pre-impact lithologies are shown in Fig. S1.

Ca, and K (de Winter and Claeys, 2017). This combined approach resulted in qualitative multi-element maps and semi-quantitative single-element heatmaps for a range of elements, in which the highest X-ray intensity for the elements' $K\alpha$-line corresponds to the pixel in the sample with the highest possible red-green-blue value (i.e., 255; Kaskes et al., 2021). To correctly visualize the distribution of Co, a peak deconvolution was applied in the M4 Bruker software to overcome the overlap between the $K\alpha$ peak of Co and the $K\beta$ peak of Fe (at 6.93 and 7.06 keV, respectively).

4.3. HSE concentrations and ^{187}Os/^{188}Os analysis

About ~0.4 to ~0.6 g of homogenized sample powder was spiked with a mixed tracer solution composed of ^{185}Re, ^{190}Os, ^{191}Ir, and ^{194}Pt isotopes and digested in 5 ml acid mixture (HNO$_3$-HCl: 3 + 2 ml) at 270 °C and 100–130 bars in an Anton-Paar high pressure asher for 5 h. After digestion, Os was separated from the other HSEs using a CCl$_4$/HBr liquid extraction procedure (Cohen and Waters, 1996). Osmium was further purified using a H$_2$SO$_4$/H$_2$CrO$_4$ microdistillation technique (Birck et al.,

1997). After Os extraction, all other HSEs were separated by ion-exchange chromatography using the procedure outlined in Pearson and Woodland (2000).

Measurements of Os concentrations and $^{187}Os/^{188}Os$ ratios were carried out at the Department of Lithospheric Research at the University of Vienna, Austria. Osmium was loaded as a bromide on Pt filaments covered with a $NaOH/Ba(OH)_2$ activator (Völkening et al., 1991; Creaser et al., 1991). Analyses were performed using a ThermoFinnigan Triton Thermal Ionization Mass Spectrometer (TIMS), operating in negative ion mode. Isobaric interferences attributable to W- or Pt-oxides were not observed. Isobaric interferences of ^{187}Re on ^{187}Os were monitored by measuring $^{185}ReO_3^-$ (mass 233) and corrected if observed. Mass fractionation was corrected offline using $^{192}Os/^{188}Os = 3.083$ (Brandon et al., 2005; Luguet et al., 2008). The Os total procedural blank was ~0.4 pg (n = 2) contributing less than 0.5% to the measured Os concentrations of the samples.

Repeated Negative-TIMS measurements (n = 3) of 10 pg loads of a DROsS (Durham Romil Osmium Standard) solution were performed using the electron multiplier at signal intensities that were typically achieved during the sample runs (~1,000 to ~100,000 counts on mass 240 = $^{192}OsO^{-3}$). The DROsS measurements yielded an average of 0.16088 ± 56 for $^{187}Os/^{188}Os$, 1.2167 ± 40 for $^{189}Os/^{188}Os$, and 1.9782 ± 80 for $^{190}Os/^{188}Os$ ratios (errors refer to the last two digits). These values agree within the 2σ uncertainty of the average values reported by Luguet et al. (2008), obtained for much larger Os loads of DROsS. The long-term external reproducibilities are ± 0.4% for $^{187}Os/^{188}Os$, ± 0.2% for $^{189}Os/^{188}Os$, and ± 0.3% for $^{190}Os/^{188}Os$ ratios.

Rhenium and HSE concentrations were measured using a Thermo Fisher Element XR ICP-MS in single collector mode at the Steinmann Institute at the University Bonn, Germany, using methods described in Luguet et al. (2015). Instrumental drift was monitored using a 1 ppb in-house multi-element HSE standard solution measured at the beginning, middle, and end of the analytical session. Mass bias was corrected relative to this standard solution using ratios of 0.5986 for $^{185}Re/^{187}Re$, 0.5957 for $^{191}Ir/^{193}Ir$ and 0.2117 for $^{198}Pt/^{195}Pt$ and corrections were insignificant for all samples. Additionally, isobaric interferences caused by Hf on Ir and Pt were monitored and corrected for offline. To determine the oxide production, Hf-doped 1 ppb HSE solutions were run at the beginning, middle, and end of each analytical session. Rhenium, Ir, and Pt were measured using a cyclonic borosilicate glass spray chamber. Total procedural blanks for this study (n = 2) were 3–4 pg for Re, 0.5–1 pg for Ir, and 10–30 pg for Pt. Blank correction for procedural blank is achieved by direct subtraction of the blank contribution from the gross amount of analyte detected. Due to the often very low HSE contents of the analyzed samples, blank corrections were applied in all cases. With respect to individual samples, these blanks resulted in variable uncertainties for the calculated concentrations in the range of <1–30% for Re, 1–60% for Ir, and 1–70% for Pt (highest uncertainties for low HSE dacite (238R1_101–103.5), granites (136R2_20–25 and 200R3_12.5–15), and amphibolite (80R2_61–63.5) samples.

Analytical quality was monitored with repeated measurements of reference materials UB-N (lherzolite; Meisel et al., 2003) and OKUM (komatiite; Potts and Meisel, 2015) processed alongside the samples. All analyses of reference materials reproduce certified values within 2σ error.

5. RESULTS

5.1. Moderately siderophile element variations

Concentrations for the moderately siderophile elements, i.e., Cr, Co, and Ni contents are presented in Fig. 4, together with values for the "transitional unit" (Goderis et al., 2021), K–Pg clays (Goderis et al., 2013), and previously investigated granites (Feignon et al., 2021), for comparison. Chromium, Co, and Ni contents all plot between two endmembers, i.e., the granite with the lowest measured Cr, Co, and Ni concentrations (i.e., with 7.3–10.9, 1.90–2.69, and 2.10–2.80 ppm, respectively), and the dolerite which by far shows the highest Cr, Co, and Ni contents, with 542, 68.3, and 266 ppm, respectively. The Cr, Co, and Ni contents of others lithologies, i.e., impact melt rocks, suevites, amphibolite, dacite, and felsite, broadly spread between these two endmembers, with a strong linear correlation observed between all samples (correlation factor $R^2 = 0.95$ for Ni versus Cr, and $R^2 = 0.93$ for Ni versus Co). In most of the impact melt rock and suevite samples, the Cr, Co, and Ni contents show a relatively narrow range, of 22.5–25, 9.68–20.0, and 15.7–32.2 ppm, respectively. Two impact melt rock samples, i.e., 80R2_126–128 impact melt clast, and 294R1_67.5–70 from the LIMB, have moderately siderophile element contents similar to the granites, with 10.9 ppm Cr, 7.48 ppm Co, and 4.20 ppm Ni, and 17.0 ppm Cr, 7.76 ppm Co, 3.50 ppm Ni, respectively. Two other impact melt rocks from the LIMB, i.e., 202R2_48.5–53 and 265R2_9–11, are relatively enriched in Cr, Co, and Ni, in comparison to the other impact melt rocks, with 155 ppm Cr, 25.2 ppm Co, and 83.7 ppm Ni, and 299 ppm Cr, 58.2 ppm Co, and 180 ppm Ni, respectively. The amphibolite has a composition similar to the LIMB sample 202R2_48.5–53 with 181 ppm Cr, 32.4 ppm Co, and 81.0 ppm Ni, while the felsite is slightly enriched in Ni, relative to Cr and Co (see Fig. 4c) with 105 ppm Cr, 26.2 ppm Co, and 103 ppm Ni. On the other hand, the dacite displays lower contents of Cr, Co, and Ni, albeit higher than for the granites, with 13.7, 8.22, and 9.60 ppm, respectively. Generally, the transitional unit samples (Goderis et al., 2021) are depleted in Cr (average of 17.3 ppm) but show similar Co contents (average 10.6 ppm), relative to the investigated samples (Fig. 4 and Table 1). In contrast, the transitional unit samples investigated in Goderis et al. (2021) show a distinct enrichment in Ni (average of 68 ppm) relative to most of the samples investigated here (Fig. 4 and Table 1). The Cr/Ni of impact melt rocks ranges between 1.41 and 4.85 (with an average of 2.43), which is significantly higher than the Cr/Ni for CI-chondrite material, i.e., ~0.26 (Tagle and Berlin, 2008), and close to average UCC values (~2.0; Rudnick and Gao, 2014, and references therein). Importantly, the Cr/Ni and Cr/Co ratios of the investigated impact melt rocks
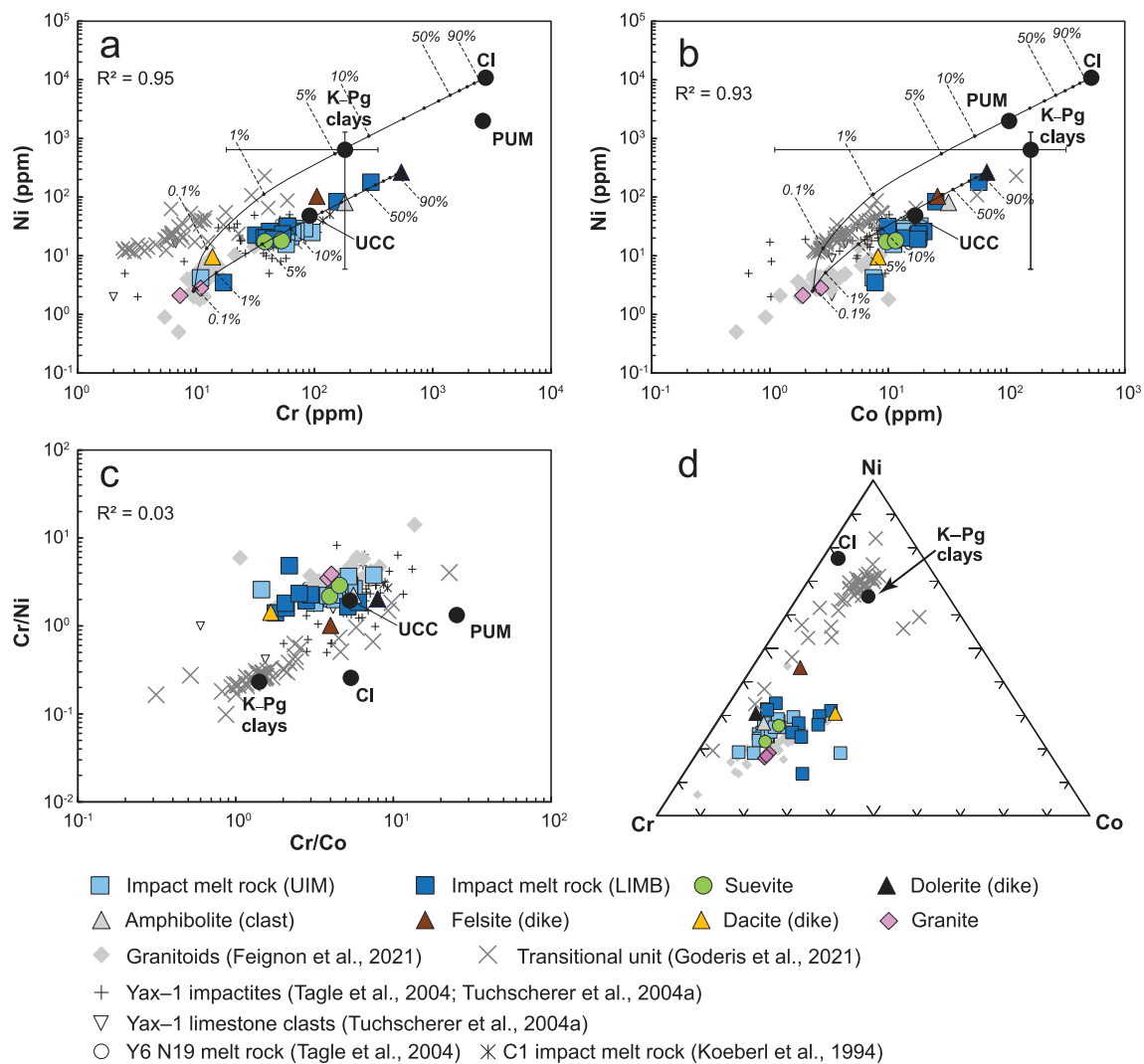
Fig. 4. a–d) Content of the investigated samples for moderately siderophile elements (Cr, Co, and Ni). For comparison, the Ni, Cr, and Co compositions of samples from granitoids as well as the transitional unit (M0077A drill core), and other drill cores were included. The average compositions of K–Pg clays (taking into account the slight variation between proximal and distal sites), CI-chondrites (CI), and primitive upper mantle (PUM), are from Goderis et al. (2013), Tagle and Berlin (2008), and Lubetskaya and Korenaga (2007), respectively. a–b) Bivariate diagrams of Ni versus Cr, and Ni versus Co. All the samples display strong covariations with R^2 above 0.9. Mixing lines are drawn between (1) average granite and CI-chondrite compositions and (2) average granite and dolerite compositions. All the investigated samples broadly follow the mixing line (2). c) Interelement ratio diagram of Cr/Ni versus Cr/Co. d) Ternary diagram of Cr, Ni, and Co, highlighting the Ni-enrichment occurring in the transitional unit samples.

and suevites plot between the pre-impact lithologies compositions, without any sample displaying a composition close to the CI-chondrite component. Six LIMB samples plot between the granite and the dacite compositions, the latter having a higher Co content, and thus, a lower Cr/Co (1.67) than the granite (3.85–4.05). The granites show relatively low Cr, Co, and Ni contents, of 5.40–30.9, 0.50–10.1, and 0.5–14.2 ppm, respectively (this study and Feignon et al., 2021), compared to the average UCC composition (Fig. 4; Rudnick and Gao, 2014, and references therein).

5.2. Micro-X-ray fluorescence

The distribution of the most important major and trace elements (±ppm level) is visualized in the μXRF maps of

Fig. 5. Polished thick sections were scanned of which bulk powder data was available, resulting in a representative sample set of two suevites, one amphibolite, seven UIM samples, one dolerite, one dacite, and five LIMB samples (Fig. 5a). The major element trends are shown in an Fe-Si-Ca-K multi-element map and a single-element Ca heat-map (Fig. S5). Suevite and UIM samples are clearly enriched in Ca, present as carbonate clasts, sparry calcite (green schlieren), and calcite veins. The amphibolite, dolerite, dacite, and LIMB samples are depleted in Ca and yield, in general, more Fe-rich phases. The single-element heat-maps of the moderately siderophile elements Cr, Co, and Ni (measured with an Al 630 μm X-ray source filter) are shown in Fig. 5b–d and display clear enrichments in these three elements in amphibolite (80R2_61–63.5), dolerite
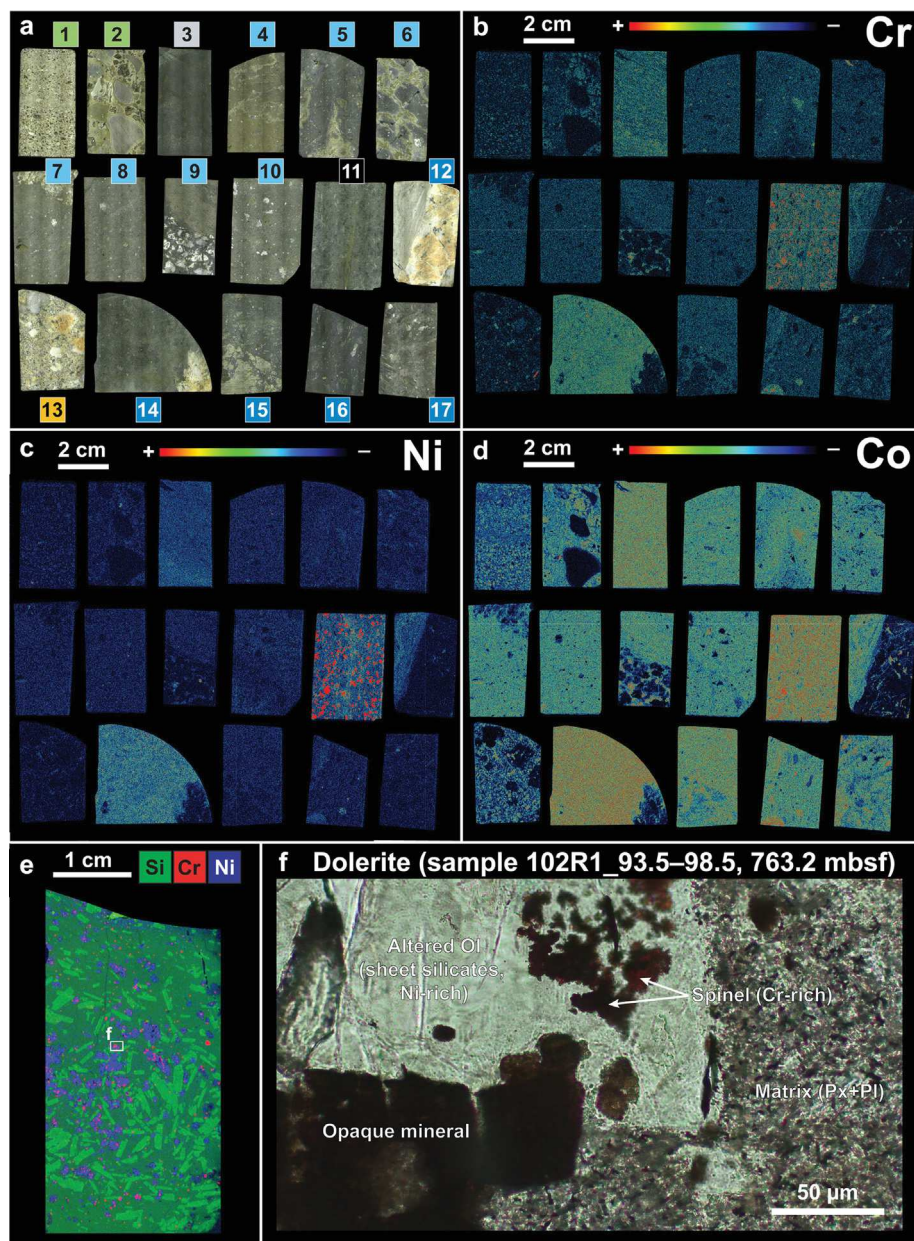
Fig. 5. High-resolution micro-X-ray fluorescence (μXRF) mapping results. a) Scanned image overview of the 17 M0077A impactite and target lithology samples, from upper left to lower right: two suevites, one amphibolite, seven UIM samples, one dolerite, one LIMB, one dacite, and four LIMB samples. Sample details are indicated below. b-d) Single-element distribution maps (or 'heatmaps') of Cr, Co, and Ni, measured using an Al-630 μm X-ray source filter and peak deconvolution applied on the Co map. e) Multi-element map showing the distribution of Si, Cr, and Ni within dolerite sample 102R1_93.5–98.5 (763.2 mbsf). The colors allow to distinguish the different mineral phases forming the dolerite, i.e., plagioclase (light green), altered olivine (blue), spinel-group and opaque minerals (red). The dark green represents the dolerite matrix. Nickel (and Co) are mainly concentrated in altered olivine, while Cr is concentrated in spinel-group minerals. f) Thin section microphotograph (plane polarized light) of dolerite sample shown in Fig. 5e, showing the Ni, Cr, and Co carrier mineral phases. Ol: olivine, Px: pyroxene, and Pl: plagioclase. Sample details with sample ID, lithology/unit, and core depth: 1) 41R1_106–108 (bedded suevite unit, 620.4 mbsf); 2) 53R3_6–8 (graded suevite unit, 673.7 mbsf); 3) 80R2_61–63.5 (amphibolite, 706.6 mbsf); 4) 83R1_22–24.5 (UIM, 712.3 mbsf); 5) 88R3_45–47.5 (UIM, 724.9 mbsf); 6) 89R1_59–61.5 (UIM, 726.2 mbsf); 7) 91R1_102–104.5 (UIM, 732.8 mbsf); 8) 93R1_21–23.5 UIM, 738.1 mbsf); 9) 93R2_11–12.5 (UIM, 739.1 mbsf); 10) 95R2_45–47.5 (UIM, 745.3 mbsf); 11) 140R2_5–8 (dolerite, 854.6 mbsf); 12) 202R48.5–53 (LIMB, 1026.3 mbsf); 13) 238R1_101–103.5 (dacite, 1135.1 mbsf); 14) 265R2_16–19 (LIMB, 1216.6 mbsf, from the same LIMB dike as sample 265R2_9–11); 15) 277R1_88–92 (LIMB, 1253.3 mbsf); 16) 292R2_66–68.5 (LIMB, 1299.4 mbsf); 17) 303R3_22.5–25 (LIMB, 1334.4 mbsf).

(140R2_5–8), and LIMB (265R2_16–19) samples, compared to the other samples. Ni and Cr hotspots in the dolerite sample overlap with enrichments in Mg (not shown here) and – in combination with petrographic analysis – these Ni rich phases are linked to altered olivine minerals, while the Cr-rich phases are linked to spinel group and opa-

que minerals (see Fig. 5e-f). For the other samples, the enrichments in Ni, Cr, and Co show a uniform pattern and, therefore, cannot be associated with any specific mineral phase.

5.3. Highly siderophile element concentrations

Chondrite-normalized highly siderophile element (HSE) abundance patterns (Os, Ir, Pt, and Re) are presented in Fig. 6. Concentrations of the HSE are shown in Fig. 7 and provided in Table 2. The Ir and Os contents of the impact melt rocks (i.e., both UIM and LIMB) are generally relatively low, ranging from 17 to 39 ppt, and 15 to 96 ppt, respectively, similar to the average UCC composition (i.e., ~31 ppt Os, and ~22 ppt Ir; Peucker-Ehrenbrink and Jahn, 2001). Only two samples, 91R1_102–104.5 from the UIM, and 265R2_9–11 from the LIMB, show enrichments in Ir and Os concentrations by one order of magnitude, with 250 ppt Ir and 125 ppt Os, and 324 ppt Ir and 344 ppt Os, respectively. Additionally, the UIM sample 93R2_11–12.5 displays only an enrichment in Os, with 410 ppt, but a UCC-like Ir content of 22 ppt. Suevite samples are characterized by Os (27–134 ppt), and Ir (2–10 ppt) contents which are relatively similar to (for Os) and lower than (for Ir) those of impact melt rocks. The granite and amphibolite display Os contents of 22–26 ppt, comparable to the UCC composition. The Ir contents of granite range, between 1–8 ppt which is lower than the average UCC value of ~22 ppt (Peucker-Ehrenbrink and Jahn, 2001). The dacite has an Os concentration of 105 ppt, associated with an Ir content of 3 ppt. Given the higher uncertainty (see Section 5.4), some care should be taken with the samples
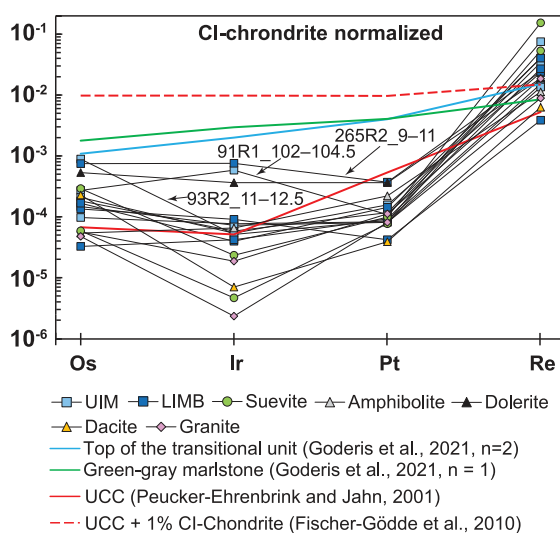
Fig. 6. CI-chondrite-normalized HSE abundance patterns, with normalization values from McDonough and Sun (1995). The impact melt samples generally display crustal HSE compositions with only three samples enriched in Os and/or Ir, which are still lower than those of the upper transitional unit and green-gray marlstone samples from the core section 40R1 (Goderis et al., 2021). Rhenium is generally enriched relative to both the upper continental crust and the transitional unit and was probably added following post-impact alteration from a long-lived hydrothermal system (Kring et al., 2020).

exhibiting very low Ir contents (<10 ppt). In contrast, the dolerite sample constitutes a more enriched lithology, with Os and Ir concentrations reaching 245 and 156 ppt, respectively. The dolerite Os and Ir composition reveals mantle-like affinity, plotting toward the primitive upper mantle (and chondritic) composition (Fig. 7), with a Os/Ir of 1.57, close to the primitive upper mantle value of 1.12 (Becker et al., 2006), and the chondritic Os/Ir of ~1.07 (Fischer-Gödde et al., 2010). Platinum concentrations for the UIM and LIMB samples range between 40 and 352 ppt, values which are below the average UCC Pt content of ~510 ppt (Peucker-Ehrenbrink and Jahn, 2001). Similarly to Ir and Os, only LIMB sample 265R2_9–11 is clearly enriched in Pt, at 352 ppt, while the second highest Pt content is two times lower, i.e., 149 ppt in UIM sample 93R1_21–23.5. In the case of the suevite samples, Pt contents are relatively similar to those of impact melt rocks with 73–94 ppt. Pre-impact lithologies display Pt concentrations of 77–106 ppt for granite and dacite, whereas amphibolite and dolerite show higher contents (i.e., 210 and 346 ppt, respectively). Finally, Re contents in impact melt rocks are more scattered relative to the other investigated HSEs, ranging from 145 to 2828 ppt. The Ir/Pt of the impact melt rocks varies from 0.13 to 2.43, higher than the UCC Ir/Pt of ~0.04 (Peucker-Ehrenbrink and Jahn, 2001), and encompassing the primitive upper mantle and CI-chondrite Ir/Pt ratio of ~0.45 and ~0.48, respectively (Becker et al., 2006; Fischer-Gödde et al., 2010). The Re contents are high (>1200 ppt) in UIM samples displaying the green phase (i.e., 88R3_45–47.5, 89R1_59–61.5, and 91R1_102–104.5), which are characterized by elevated CaO contents. Similar high Re contents are observed in the lower transitional unit, characterized also by very high CaO, i.e., generally more than 40 wt.% (Goderis et al., 2021). Suevites are characterized by elevated Re contents (2003–5800 ppt), while pre-impact lithologies display Re contents ranging from 237 to 710 ppt. Interelement plots between Os and Ir ($R^2 = 0.20$), and Ir and Pt ($R^2 = 0.53$) are shown on Fig. 7, demonstrating a relative decoupling between these elements, albeit less important in the case of Ir and Pt.

5.4. Re–Os isotope systematics

Measured $^{187}Os/^{188}Os$ ratios for 18 samples are given in Table 2 and range between 0.20 and 1.09, while Re–Os isotopic compositions are reported in Fig. 8. Measured $^{187}Os/^{188}Os$ ratios in the impact melt rocks display significant variations, ranging from an unradiogenic value of 0.1840 for the LIMB sample 265R2_9–11 to a more radiogenic value of 2.086 for the LIMB sample 303R3_22.5–25. A relatively good correlation ($R^2 = 0.80$) is noted between measured $^{187}Os/^{188}Os$ ratios and the Os concentrations in the impact melt rocks (Fig. 9b), with the more unradiogenic $^{187}Os/^{188}Os$ ratios in samples with the highest Os contents. The suevite samples have $^{187}Os/^{188}Os$ ratios of 0.6163 (for sample 41R1_106–108), and 1.1390 (for sample 58R3_8–10.5), broadly within the range of the impact melt rocks. Compared to impactite samples, the dolerite and the dacite samples show less radiogenic compositions, with $^{187}Os/^{188}Os$ ratios of 0.1700 and 0.2015, accompanied by
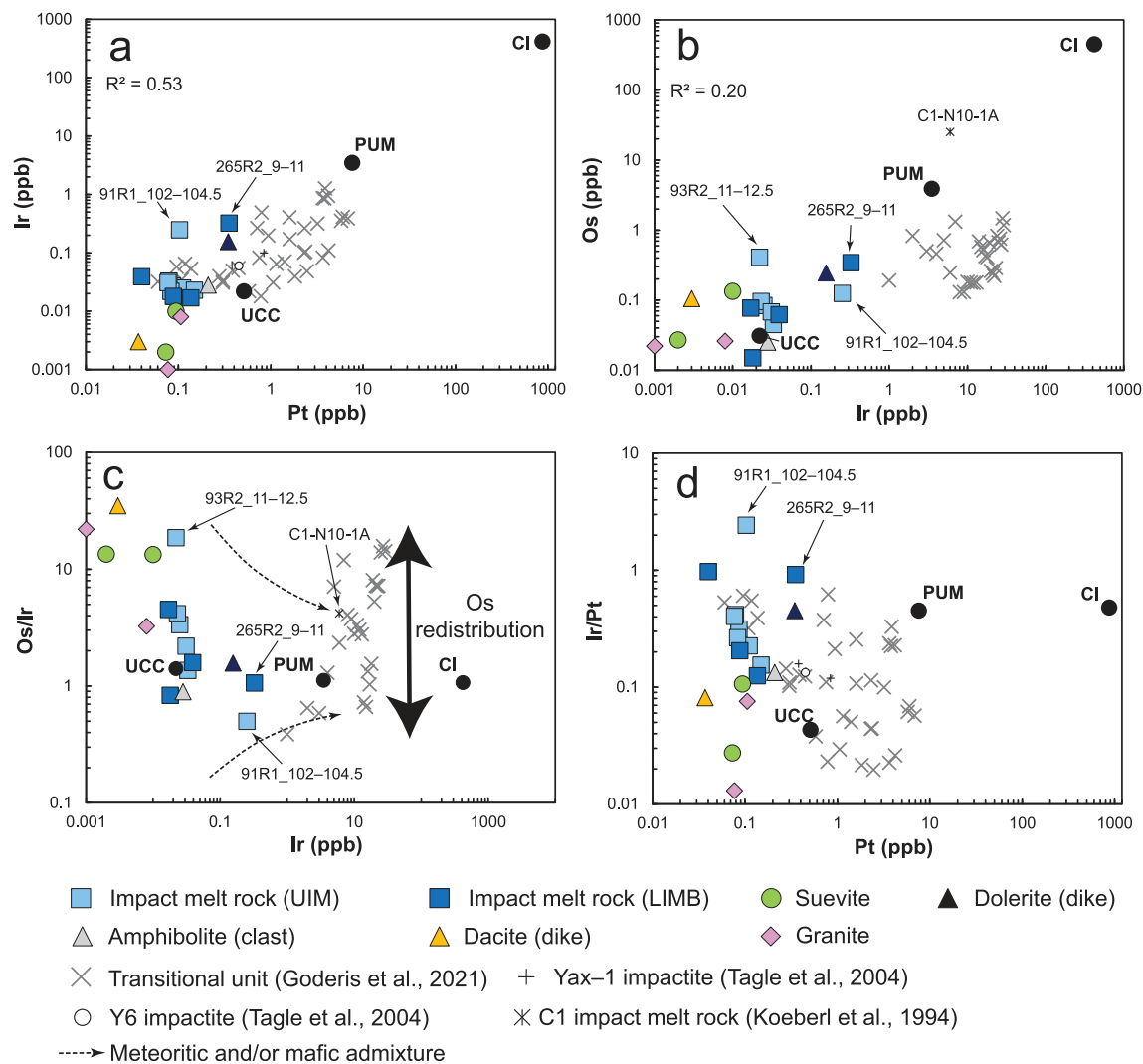
Fig. 7. Highly siderophile element compositions of the investigated samples, with average compositions of upper continental crust (UCC), primitive upper mantle (PUM), and CI-chondrites (CI) from Peucker-Ehrenbrink and Jahn (2001), Becker et al. (2006), and Fischer-Gödde et al. (2010), respectively. a–b) Bivariate diagrams of Ir versus Pt, and Os versus Ir. The impact melt samples generally display limited covariation. c) Os/Ir versus Ir diagram showing a slight trend towards PUM and CI composition for two impact melt samples, while transitional unit samples (Goderis et al., 2013) are clearly more enriched in Ir than the PUM composition, supporting the presence of meteoritic material within the transitional unit. d) Ir/Pt ratio versus Pt diagram, with impact melt samples plotting generally towards UCC compositions as no clear enrichment in Pt was observed.

relatively high Os contents of 245 and 105 ppt, respectively. While having relatively low Os contents, i.e., 22–26 ppt, the two granite samples are characterized by $^{187}Os/^{188}Os$ ratios, ranging from $\sim$0.157 to $\sim$0.161, well below the average UCC value of $\sim$1.4 (Peucker-Ehrenbrink and Jahn, 2001). Finally, the amphibolite displays a more radiogenic composition than all the other samples, with a $^{187}Os/^{188}Os$ ratio of $\sim$2.47, associated with a very low Os content of 25 ppt.

Measured $^{187}Os/^{188}Os$ ratios were back-calculated to 66.05 Ma (Table 2; Sprain et al., 2018). Recalculation to the time of impact is preferred here to know the Os isotopic composition at the time of formation of the impact melt rocks. Both measured and age-corrected $^{187}Os/^{188}Os$ ratios are similar, excepted for the amphibolite sample which has a measured $^{187}Os/^{188}Os$ ratio of $\sim$2.47 and an age-corrected

$^{187}Os/^{188}Os$ ratio of $\sim$2.39. Therefore, the $^{187}Os/^{188}Os$ ratios provided in the text refer to measured values, the age-corrected values being stated in other cases.

The $^{187}Re/^{188}Os$ ratios of the impact melt rocks vary from as low as $\sim$6.7 to as high as $\sim$341, with the highest $^{187}Re/^{188}Os$ ratio (i.e., one UIM and two LIMB samples with $^{187}Re/^{188}Os$ higher than 100) observed in samples that have high $^{187}Os/^{188}Os$ ratios, i.e., above 1 (Fig. 8a). Elevated $^{187}Re/^{188}Os$ are reported for suevite samples with values of 201 for 41R1_106–108, and 350 for 58R3_8–10.5. Dolerite and dacite display lower $^{187}Re/^{188}Os$ ratios compared to the ones discussed above, with 13.5 and 10.6, respectively. The amphibolite and granite samples have $^{187}Re/^{188}Os$ ratios of 79.8 and 72.7–125, respectively. When plotting $^{187}Os/^{188}Os$ versus $^{187}Re/^{188}Os$ ratios for impact

melt rock samples, we obtain a so-called "errorchron" (see Fig. 8a), with a high scattering indicated by a mean square weighted deviation (MSWD) of 67, associated with an apparent age of 339 ± 113 Ma. This apparent age is similar, but with a higher uncertainty, as the U–Pb ages obtained on zircons from the granite, clustering around 334 ± 2.3 Ma (Ross et al., 2022).

6. DISCUSSION

6.1. Geochemistry of the impact melt rocks: mixing of felsic and mafic target lithologies

The major and trace element results (Tables S2 and S3), as well as petrographic observations for the investigated samples are in excellent agreement with previous work on impact melt rocks from the Chicxulub Expedition 364 drill core by de Graaff et al. (2022) and Schulte et al. (2021), which suggested that they formed by mixing and melting of granite and dolerite pre-impact basement rocks mainly, with (or without) incorporation of carbonate target rock material. While trace element compositions are relatively similar for both LIMB and UIM samples, with some variations only observed for specific trace elements (see Fig. S4), the major element contents of the two impact melt rocks units display more significant compositional variations. These are probably related to the heterogeneity of the impact melt, also in combination with a heterogeneous distribution of pre-impact lithology clasts at the hand sample scale (Morgan et al., 2017). Two mixing lines were calculated on a LOI-free basis for the CaO, MgO, Fe_2O_3, Al_2O_3, and TiO_2 contents (Fig. S3) between (1) dolerite and granite, representing the less evolved and the most evolved lithologies, as well as the most abundant pre-impact magmatic lithologies in the sample suite compared to the mafic amphibolite, which is far less abundant (found only as scarce, small centimeter-sized, clasts; see also, de Graaff et al., 2022), (2) average limestone composition (estimated by de Graaff et al., 2022) and granite to highlight the addition of carbonate material (or not) within the impact melt rocks. The LIMB samples plot relatively well along the mixing line between dolerite and granite for MgO, Fe_2O_3, and TiO_2, with a limited offset. In the case of CaO, LIMB samples show a clear offset, being depleted relative to the mixing line. They seem to follow a trend between the granite composition and the composition of LIMB sample 265R2_9–11, which is characterized by having a major and trace element composition similar to dolerite (i.e., a basaltic composition with low SiO_2 and high Fe_2O_3 and MgO contents). This genetic link is confirmed by µXRF mapping (Fig. S5) and petrographic investigations, which show that this sample is mainly a partially melted dolerite dike, with no contribution from a granitic component in the impact melt rock. Additionally, variations in the CaO content were observed between two dolerite dikes by de Graaff et al. (2022), with CaO contents ranging from as low as 2.40 wt.% to up to 10.7 wt.%. These variations in the CaO content in dolerite may be due to a variable abundance of post-impact calcite veins crosscut-

ting the dolerite. Consequently, the LIMB probably results from the mixing between a granitic (felsic) and a dolerite (mafic) component characterized by low CaO contents (below 5 wt.%). In the case of the UIM (and suevite) samples, µXRF maps (Fig. S5) and petrographic observations have shown that carbonate material is mainly present as carbonate clasts and as sparry calcite within the green schlieren-textured matrix. These trends are also reflected in terms of whole-rock major element contents, with the UIM and suevite samples generally plotting in the area between the granite–dolerite and the granite–limestone mixing lines, and displaying enrichment in CaO and depletions in MgO, Fe_2O_3, and, to a lesser extent, TiO_2 contents (Fig. S3). The abundance of carbonate material within the UIM is even more significant in samples displaying the schlieren texture, or dominated by the green phase, i.e., located between 712.30 and 737.10 mbsf. These samples have an average CaO content of 11.2 wt.%, more than the double compared to the other UIM samples, with an average CaO content of 4.72 wt.%. The 80R2_126–128 sample, which is an impact melt rock clast within the suevite unit, shows a CaO content and an overall major element composition closer to the LIMB than to the UIM (i.e., having an evolved composition with 66.3 wt.% SiO_2, and plotting on or in proximity to the granite–dolerite mixing line), thus, this impact melt sample incorporated a relative limited amount of carbonate material. The carbonate component is even more abundant in the suevite samples, which have up to 28.6 wt.% CaO in the investigated samples (i.e., values up to 40.5 wt.% CaO were reported in the upper part of the suevite sequence by Kaskes et al., 2022). The Al_2O_3 contents for both LIMB and UIM are more scattered, probably an effect, as already noted in our petrographic observations and in previous works, of the presence of clay minerals (phyllosilicates) resulting from low-temperature alteration of (vitric) melt (see also, Kring et al., 2020; Simpson et al., 2020; Schulte et al., 2021; de Graaff et al., 2022). According to mixing calculation of de Graaff et al. (2022), most of the impact melt rock major element compositions may be explained by the mixing of ~30–60% of dolerite with the granite (see also Supplementary Material).

Regarding the trace element data, the CI-chondrite-normalized trace element abundance pattern of the LIMB sample 267R3_52.5–55.5 is highly similar to those of the granites, suggesting that this lithology dominates the composition of the whole sample (Fig. S4). This is further supported by petrographic observations, indicating a higher abundance of clasts and brecciated granitoid-derived material relative to the other LIMB samples investigated, and is also in agreement with the major element analysis, as this sample shows the most felsic composition of all LIMB samples. On the other hand, the dolerite affinity of LIMB sample 265R2_9–11 is also reflected in the trace element compositions with, similarly to dolerite, depletions in Rb, Ba, and Th (Fig. S4 and Table S3). These observations further highlight the heterogeneous nature of the impact melt rocks (i.e., both UIM and LIMB) and their incomplete mixing, as indicated by the flow textures and the presence of undigested clasts, in major element, and, to a lesser extent, trace element compositions.

Table 2

Moderately and highly siderophile element abundances and Re–Os isotopic compositions of impact melt rocks, suevites, and pre-impact lithologies. Cr and Co contents were obtained by INAA, while Ni contents were obtained using bulk XRF measurements. *Sample investigated for HSE-Os analysis.

Sample	Depth (mbsf)	Cr (ppm)	Co (ppm)	Ni (ppm)	Re (ppb)	Os (ppb)	Ir (ppb)	Pt (ppb)	$^{187}Os/^{188}Os$	2σ	$^{187}Re/^{188}Os$	2σ	$(^{187}Os/^{188}Os)_i$
Impact melt rocks (UIM)													
80R2_126–128	707.2	10.9	7.48	4.20	—	—	—	—	—	—	—	—	—
83R1_22–24.5*	712.3	72.2	12.8	27.2	0.387	—	0.027	0.086	—	—	—	—	—
88R1_12–14.5	722.7	58.8	18.5	32.2	—	—	—	—	—	—	—	—	—
88R3_45–47.5*	724.9	94.9	12.7	25.0	1.528	0.084	0.025	0.111	0.6374	0.0090	92.545	2.776	0.6374
89R1_59–61.5*	726.2	67.1	12.8	26.2	2.828	0.045	0.033	0.079	1.0900	0.0300	341.210	10.240	1.0900
91R1_102–104.5*	732.8	82.3	15.6	29.2	1.290	0.125	0.250	0.103	0.4154	0.0240	51.029	1.531	0.4154
91R2_89–91.5	733.8	62.7	11.9	21.4	—	—	—	—	—	—	—	—	—
92R2_89–91.5	737.1	52.3	12.8	25.5	—	—	—	—	—	—	—	—	—
92R3_39–41	737.8	69.6	15.6	26.2	—	—	—	—	—	—	—	—	—
93R1_21–23.5*	738.1	57.8	15.1	26.0	0.883	0.096	0.023	0.149	0.4363	0.0095	45.555	1.367	0.4363
93R1_121–123.5	739.1	58.1	13.7	29.0	—	—	—	—	—	—	—	—	—
93R2_11–12.5*	739.3	65.4	14.3	24.8	0.573	0.410	0.022	0.083	0.2025	0.0028	6.722	0.202	0.2025
95R1_18–20	744.1	55.3	12.5	22.5	—	—	—	—	—	—	—	—	—
95R1_84–87	744.8	57.6	11.1	15.7	—	—	—	—	—	—	—	—	—
95R2_45–47.5*	745.3	58.3	13.8	25.8	0.511	0.068	0.031	0.077	0.3189	0.0035	36.835	1.105	0.3189
Impact melt rocks (LIMB)													
202R2_48.5–53*	1026.3	155	25.2	83.7	0.145	0.062	0.039	0.040	0.2029	0.001	11.277	0.338	0.2029
265R2_9–11*	1216.5	299	58.2	180	0.915	0.344	0.324	0.352	0.1844	0.002	12.760	0.383	0.1844
267R3_52.5–55.5	1224.4	59.1	9.88	31.7	—	—	—	—	—	—	—	—	—
277R1_59.5–62	1253.0	31.8	17.8	22.5	—	—	—	—	—	—	—	—	—
277R1_88–92*	1253.3	41.7	20.0	26.0	1.524	0.077	0.017	0.136	1.0610	0.024	105.910	3.180	1.0610
277R2_25–27	1253.9	37.5	18.1	20.6	—	—	—	—	—	—	—	—	—
290R1_66–68	1292.0	39.2	14.0	20.2	—	—	—	—	—	—	—	—	—
292R2_66–68.5*	1299.4	53.9	18.1	23.7	—	0.075	—	—	0.5851	0.030	—	—	—
294R1_67.5–70	1304.4	17.0	7.76	3.50	—	—	—	—	—	—	—	—	—
303R3_22.5–25*	1334.4	45.0	17.8	19.2	1.014	0.015	0.018	0.088	2.0860	0.016	309.600	9.290	2.0860
Suevites													
41R1_106–108*	620.4	38.1	9.68	17.5	5.800	0.134	0.010	0.094	0.6163	0.0017	201.67	—	0.6163
58R3_8–10.5*	673.7	52.5	11.5	18.1	2.003	0.027	0.002	0.073	1.1390	0.0170	350.31	—	1.1390
Pre-impact lithologies													
80R2_61–63.5 (amphibolite)*	706.6	181	32.4	81.0	0.424	0.025	0.028	0.210	2.4740	—	79.790	—	2.3862
105R2_83–89 (felsite)	772.8	105	26.2	103	—	—	—	—	—	—	—	—	—
140R2_5–8 (dolerite)*	854.6	542	68.3	266	0.710	0.245	0.156	0.346	0.1700	0.0040	13.547	—	0.1700
238R1_101–103.5 (dacite)*	1135.1	13.7	8.22	9.60	0.237	0.105	0.003	0.037	0.2015	0.0069	10.600	—	0.2015
136R2_20–25 (granite)*	851.4	7.3	1.90	2.10	0.698	0.026	0.008	0.106	0.1569	0.0098	124.56	—	0.1569
200R3_12.5–15 (granite)*	1021.0	10.9	2.69	2.80	0.335	0.022	0.001	0.077	0.1609	0.0081	72.710	—	0.1609
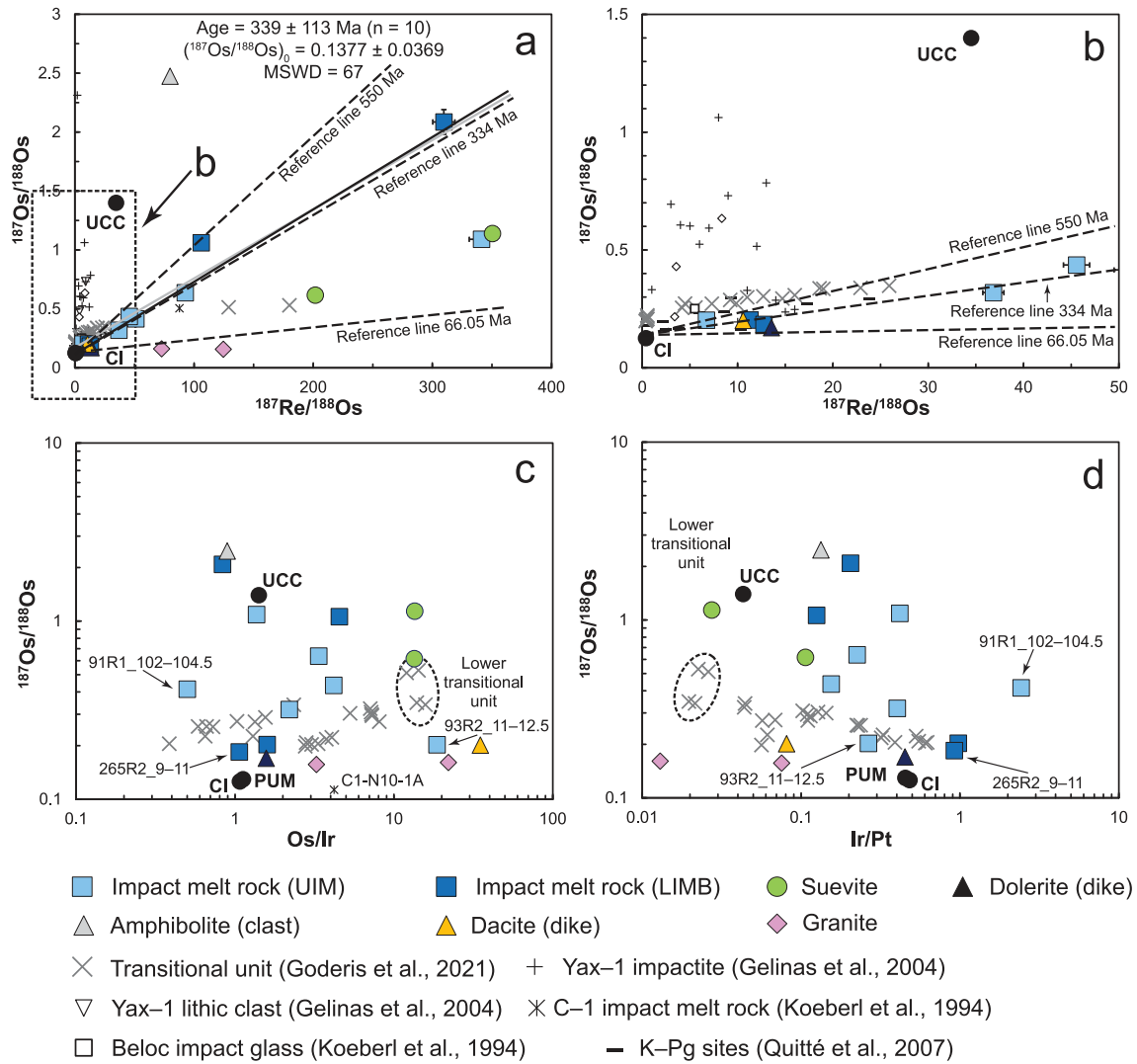
Fig. 8. a) Re–Os isotopic compositions of the investigated samples. An isochron was calculated, using IsoplotR (Vermeesch, 2018), for impact melt rocks (black line), giving an errorchron (high MSWD). The calculated apparent age and characteristics of the errorchron are given within the plot. The calculated uncertainty on the apparent age is two sigma with overdispersion. For comparison, a second isochron (gray line) is calculated for the transitional unit samples (Goderis et al., 2021). The transitional unit errorchron gives an apparent age of 333 ± 100 Ma, a $^{187}Os/^{188}Os_i$ of 0.20763, and a MSWD of 1200. Strong variations in the $^{187}Re/^{188}Os$ ratios are also observed. The dashed frame represents the Fig. 8b. b) Enlarged view of (a) with two isotopic trends that can be identified, i.e., the trend formed by the investigated samples, and similar to the Re–Os compositions in the transitional unit, K–Pg boundary sites, Beloc impact glass, and some Yax–1 samples, and a second trend formed by Yax–1 samples between chondritic and crustal compositions. In (a) and (b) two calculated reference lines for ~66.05 (age of the impact) and ~334 Ma (age of the granite) were added. A ~550 Ma (Pan-African) reference line was also added in (a). The Os isotopic signature of the granites plots towards the ~66.05 Ma reference line, which may indicate that the system was disrupted by the impact. c) Osmium isotopic composition versus Os/Ir ratio. UIM sample 93R2_11–12.5 has a composition similar to those of the lower transitional unit, characterized by a high abundance of sulfide minerals. d) Osmium isotopic composition versus Ir/Pt ratio. In contrast to Fig. 8c, sample 93R2_11–12.5 shows a composition closer to the mantle/chondritic compositions. The average values of upper continental crust (UCC), primitive upper mantle (PUM), and CI-chondrite (CI) are derived from Peucker-Ehrenbrink and Jahn (2001), Meisel et al. (2001), and Fischer-Gödde et al. (2010).

6.2. Search for the presence of an impactor component

There is no obvious correlation of Cr, Co, Ni, HSE abundances, and the Re–Os isotopic compositions with depth in the core (see Fig. 2), nor any specific enrichment in the abundances of these elements in a given unit or lithology. Only a decrease of the Re concentrations and the $^{187}Os/^{188}Os$ ratio is present in the UIM samples with increasing depth (from nearly crustal values to unradiogenic values; Fig. 2b), however, this is probably due to textural variations (i.e., with the green phase being absent in the lower part of the UIM) and further supports that the chemical and isotope variations observed are mainly related to the lithological nature of the samples, and/or to some
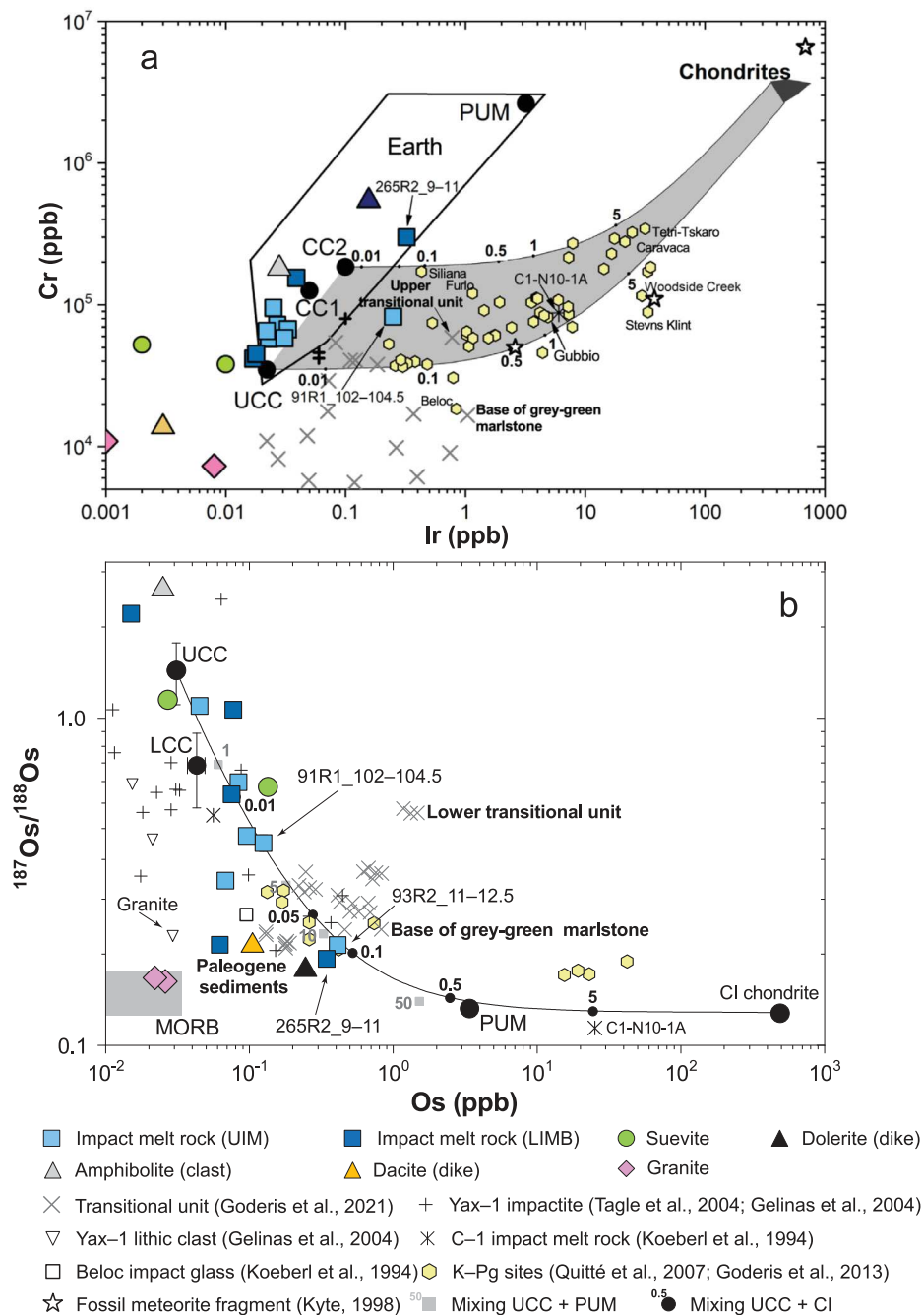
Fig. 9. a) Diagram of Cr versus Ir concentrations (modified from Tagle and Hecht, 2006; Goderis et al., 2021) presenting data from the investigated samples in this study, compared to the transitional unit samples, K–Pg boundary sites, Yax–1 impactites (Tagle et al., 2004), and a fossil meteorite fragment. The data are also compared with Cr and Ir compositions of various terrestrial lithologies and chondrites. The gray area displays the mixing trajectories between chondritic meteoritic material and crustal terrestrial target rocks. Earth field, upper continental crust (UCC), continental crust (CC), primitive upper mantle (PUM) compositions are from Tagle and Hecht (2006), and references therein. Suevites, granites and dacite are plotting well outside the typical terrestrial values with low Cr and Ir content. b) Osmium isotopic ratio versus Os concentration (based on Tagle and Hecht (2006), and references therein), with measured $^{187}Os/^{188}Os$ ratio versus Os concentration in the investigated samples, and compared with samples from the transitional unit (core section 40R1), impactites from Yax–1 (Gelinas et al., 2004), C1, Beloc impact glass, and other K–Pg boundary sites. Os isotopic composition of lithic clasts found in Yax–1 is also presented, especially the unradiogenic granite highlighted by an arrow. The curve represents a mixing line between upper continental crust (UCC) and CI-chondrite composition. The impact melt and suevite samples from drill core M0077A display relatively important variations in $^{187}Os/^{188}Os$ ratio, with several samples broadly following both the mixing curves between UCC and CI-chondrites, and UCC and primitive upper mantle (PUM), making the disentanglement between the mantle and meteoritic component impossible. The largest measured meteoritic contribution in the impact melt samples from the peak ring is between ∼0.01 and 0.05%. With the two unradiogenic impact melt rocks more probably representing a mafic component or the effects of post-impact hydrothermal alteration. The measured granite samples display unusually unradiogenic $^{187}Os/^{188}Os$ ratios, plotting within the MORB field (Schiano et al., 1997).

heterogeneities within the impact melt rocks. Similarly, a decrease with increasing depth in the core is also observed for the CaO content of the UIM samples, probably indicating that the carbonate component is less abundant within the deepest part of the UIM unit. Thus, Re is expected to be enriched in Ca-rich lithologies, such as the green phase of the UIM, as well as suevite samples, according to their Re and CaO compositions.

In general, the moderately siderophile elements (Cr, Co, and Ni) compositions of the investigated impact melt rocks are relatively homogeneous, broadly comprised between the pre-impact lithology compositions, with no sample plotting close to the CI-chondrite component (Fig. 4). These trends in Cr, Co, and Ni are also visualized by µXRF mapping (Fig. 5b–d), showing low abundance values in the suevites, UIM, and dacite samples, in contrast to enriched values for the amphibolite, dolerite, and LIMB sample 265R2_16–19 (which is from the same LIMB dike as 265R2_9–11) and to a lesser degree sample 202R2_48.5–53. The main information given is the enrichment in Ni and Cr observed within the decomposed olivines, and the spinel-group minerals, respectively (see Fig. 5e–f), in dolerite samples. Indeed, previous observations on dolerite have shown the presence of numerous submicroscopic crystallites of Ni- and Co-bearing Fe-sulfides (containing up to ∼10 wt.% Ni and ∼1 wt.% Co) within the sheet silicate aggregates replacing olivine (see also de Graaff et al., 2022 and Supplementary Material). Applying µXRF mapping on all of the 17 samples at the same time has the benefit that it displays a high-resolution (sub-mm), semi-quantitative overview of the enrichments and depletions of selected elements in the different lithological and mineralogical phases (Kaskes et al., 2021).

When calculating mixing lines between the granite and the dolerite end-members in the case of Ni versus Cr, and Ni versus Co (Fig. 4a–b), both UIM and LIMB samples plot along this mixing line with no or only minor offsets along the granite–CI-chondrite mixing line. The moderately siderophile element compositions of the UIM and LIMB may be reproduced by the admixture of ∼5–20%, and up to ∼80% of dolerite component to the granite. In contrast, the "transitional unit" samples and K–Pg boundary clays (Goderis et al., 2013, and references therein; Goderis et al., 2021) show a clear enrichment in Ni (Fig. 4), which is characteristic of the incorporation of chondritic material (Tagle and Berlin, 2008). Therefore, the Cr, Co, and Ni contents in impact melt rocks from the Chicxulub peak ring are mostly derived from the mixing between the dolerite (specifically the incorporation of Ni, Cr, and Co carrier phases) and granite components. Importantly, these moderately siderophile elements grant further insight into target rock contributions to the impact melt rock but yield no distinct proof of meteoritic admixture.

The HSE abundance patterns of most of the impact melt rocks (Fig. 6) are typical for crustal composition, as shown by their low Os, Ir, and Pt contents, suggesting no or no significant admixture of a meteoritic component to these samples. The Os/Ir, Ir and Pt contents of impact melt rocks and suevites mostly spread between the pre-impact lithologies compositions. This suggests that the variation of Os/Ir, as

well as the Ir and Pt contents in impact melt rocks and suevites seems mainly due to a mixing between these pre-impact components, and more specifically between granite and dolerite, without being affected by another external process. Additionally, nearly all the impact melt rock samples exhibit typical terrestrial Cr and Ir compositions (Fig. 9a), the exception being the Ir and, to a lesser extent, Cr concentrations of the suevite, dacite, and granite samples (i.e., lower than typical terrestrial values; Fig. 9a), confirming the low siderophile element content of some of the target lithologies, although an additional effect by hydrothermal alteration cannot be excluded.

Only three samples, two from the UIM (samples 91R1_102–104.5 and 93R2_11–12.5) and one from the LIMB (sample 265R2_9–11) show a clear enrichment in Os and/or in Ir relative to the average UCC composition (Fig. 6) and were thus considered as good candidates for potentially having incorporated a meteoritic component. However, the enrichment observed in these samples is below those recorded in the upper transitional unit and the green-gray marlstone in core 40R, in which an unambiguous meteoritic component was found (Goderis et al., 2021). Based on our petrographic investigations, as well as major and trace elements analysis, the impact melt rock sample 265R2_9–11 mainly consists of melted dolerite. Moreover, the Cr and Ir composition of this sample plots within terrestrial array (Fig. 9a), towards the primitive upper mantle, confirming the mantle-like (mafic) affinity of this specific impact melt rock sample. The HSE and Os isotopic compositions of sample 265R2_9–11 are also very similar to those measured in the dolerite sample (Table 2). Following these observations, the observed enrichment in HSE in this sample relative to the other impact melt samples (Fig. 6) is interpreted to be probably associated with the incorporation of dolerite, rather than a meteoritic admixture.

For the 93R2_11–12.5 UIM sample, only high Os was measured (410 ppt), whereas Ir content is low (22 ppt), resulting in a high Os/Ir ratio of 18.6. Similarly, high Os/Ir ratio (12.0–15.8), associated with high Ni, Os, Re, and Pt content, but low Ir contents, were measured in the lower part of the "transitional unit", more specifically in the section between 617.32 and 617.34 mbsf (Goderis et al., 2021). They were thought to be the result of hydrothermal remobilization of HSEs of crustal and possibly meteoritic origin, while Ir, being less mobile (Racki et al., 2011; Schmitz et al., 2011; Krull-Davatzes et al., 2012) compared to, e.g., Os, Re, and Pt, was not affected (Goderis et al., 2021). Unlike the samples from the "transitional unit", no distinct enrichment in Ni, Re, and Pt content is observed in our sample, suggesting that perhaps Os was remobilized. This sample also exhibits the second highest Cu content (49.3 ppm), compared to the average Cu content of ∼27 ppm for the UIM samples (see Table S3). This suggests this sample experienced, to some extent, hydrothermal alteration with the formation of chalcopyrite, also observed commonly in impact melt rock by Kring et al. (2020). Therefore, the less radiogenic $^{187}Os/^{188}Os$ signature measured (0.2025) compared to other impact melt samples could either be due to a ∼0.1% contribution of chondritic

material or a ~10% of a mantle component, with the latter being more probable as the Cr and Ir contents of this sample plot within the terrestrial field (Fig. 9a). Additionally, a Re-loss following post-impact hydrothermal alteration may also explain the low $^{187}Os/^{188}Os$ ratio measured in sample 93R2_11–12.5.

Finally, the UIM sample 91R1_102–104.5 displays enrichments in both Os and Ir relative to the UCC composition, i.e., 125 and 250 ppt, respectively, and plots toward the primitive upper mantle and CI-chondrite compositions in the Os/Ir ratio versus Ir content diagram (Fig. 7c). Importantly, no dolerite clasts were noticed during our petrographic investigations, and the major element composition is not mafic (i.e., 58.7 wt.% SiO_2). Based on the Cr versus Ir diagram, and the Os isotopic composition (Fig. 9), we estimate that the UIM sample 91R1_102–104.5 may contain a distinct but highly diluted meteoritic component, at most about 0.01 to 0.05%. However, the $^{187}Os/^{188}Os$ ratio of 0.4154, close to crustal values (Fig. 9b), does not unambiguously confirm that the HSE and Os isotopic compositions are of meteoritic origin. Sample 91R1_102–104.5 also has the highest As content of all UIM samples, of 10.8 ppm, three times more than the average of 3.7 ppm for the UIM samples (see Table S3). Arsenic is generally known to be an important constituent of geothermal fluids (Ballantyne and Moore, 1988). The Cu content of this sample is lower (15.6 ppm) than the UIM average, suggesting that post-impact hydrothermal fluid alteration implying sulfide minerals precipitation (Kring et al., 2020) probably did not affect significantly the HSE abundances and the Os isotopic composition. However, the mafic component present within the impact melt rocks could also explain the specific HSE content and Re–Os isotopic composition of this sample. In this case, it is difficult to unambiguously verify the presence of a small meteoritic component.

The majority of impact melt rocks and the suevites $^{187}Os/^{188}Os$ ratios broadly follow the mixing lines between (1) UCC and CI-chondrite and (2) UCC and primitive upper mantle, which also corresponds to a line between amphibolite and dolerite (and even dacite) compositions (Fig. 9b). Based on the major element data, mixing between dolerite and amphibolite cannot explain the andesitic composition of impact melt rocks. The dacite is also relatively rare, with only three dikes identified throughout the entire core (Morgan et al., 2017; de Graaff et al., 2022), and a significant contribution from this lithology to the Os isotopic composition seems unlikely.

The terrestrial Cr and Ir signature of the majority of the impact melt rocks suggests that the $^{187}Os/^{188}Os$ isotopic ratio variation likely represents mixing between a mantle-like component and a crustal component, although the granite (and dacite) samples display unusual, MORB-like $^{187}Os/^{188}Os$ ratios, coupled with very low Cr and Ir contents (see next section). Finally, both the amphibolite and LIMB sample 303R3_22.5–25 are characterized by supracrustal $^{187}Os/^{188}Os$ isotopic ratios of 2.47 and 2.09, and low Os contents of 15 and 25 ppt, respectively. However, the $^{187}Re/^{188}Os$ ratio of the amphibolite is lower (~79.8) than that of sample 303R3_22.5–25 (~309), and these two

samples do not seem to follow an isochron. As such, the high $^{187}Re/^{188}Os$ ratio measured in LIMB sample 303R3_22.5–25 suggests, more probably, a late addition of Re, perhaps from hydrothermal fluid origin. Therefore, the HSE contents and the Re–Os isotopic composition of the impact melt rocks and suevites indicate a highly heterogeneous distribution of both pre-impact material and the occurrence of a highly diluted possible meteoritic component in a single UIM sample.

This heterogeneity, associated with previous petrographic investigations, suggests that during its formation, the impact melt rock did not have sufficient time to fully homogenize and experienced a fast quenching, especially in the case of the UIM (see Schulte et al., 2021). The combined major element, moderately siderophile elements, and Ir–Pt data are consistent with mixing line between granite and dolerite. However, Re–Os isotopic data are inconsistent with such a mixture. This may suggest that the Os isotopic composition and HSE patterns within the impact melt rocks and suevites underwent modifications induced by the post-impact hydrothermal alteration (Simpson et al., 2020), remobilizing both Re and Os, that the granite samples represent outlier compositions, or that another currently unsampled component contributed to the impact melt. The siderophile elements, as well as Re–Os isotopic signatures of the granite may have been affected by pre-impact hydrothermal metasomatic event(s) that occurred approximately 50 Myr after granite formation (Feignon et al., 2021). The obtained data illustrate the challenges to characterize and unambiguously identify a distinct projectile contamination in the presence of a mafic component and/or with a hydrothermal overprint.

6.3. Alteration and hydrothermal overprint

Previous work and observations (Morgan et al., 2017; Kring et al., 2020) have indicated evidence for alteration and hydrothermal overprint throughout the entire drill core. The post-impact hydrothermal system was long lived, occurring for at least 1 Myr (Kring et al., 2020). This hydrothermal overprint is evidenced by the occurrence of secondary minerals, such as clay, chlorite, pyrite, etc., that were observed within the impactites (i.e., both impact melt rocks and suevites), as well as in the pre-impact material (Kring et al., 2020; Goderis et al., 2021). Following this evidence, in the presence of a high amount of sulfide minerals, chalcophile elements (Cu, Zn) may be redistributed and lead to local enrichments. Such enrichments in Cu and Zn, as well as Ni, are seen in the lower transitional unit (617.32 to 617.34 mbsf; Goderis et al., 2021). Indeed, not only chalcophile, but also siderophile elements may be redistributed and this could explain some of the features observed in some samples, like the low amount of Cr, Co, and Ni of the granites compared to the average UCC composition, and the fractionated Os/Ir and Ir/Pt ratios (Table 1, Figs. 4a–b, 6).

Rhenium, and, to a lesser extent, Os are also known to be highly mobile during alteration and weathering processes (Wallace et al., 1990; Jaffe et al., 2002; Wimpenny et al., 2007; Aiglsperger et al., 2021). The Re concentrations

of impact melt rocks and suevites are scattered, but in general higher than the average UCC Re content (Fig. 6), and even higher than the Re contents of the transitional unit (Goderis et al., 2021), suggesting a significant hydrothermal remobilization of Re within the suevites and impact melt rocks. This is further supported by the large number of samples displaying a very high $^{187}Re/^{188}Os$ ratio, plotting far to the right of the "errorchron" (Fig. 8). The "errorchron" given by the measured $^{187}Os/^{188}Os$ versus the $^{187}Re/^{188}Os$ ratios has significant scatter (Fig. 8a–b), with Re–Os isotopic compositions varying from unradiogenic, i.e., chondritic (and mantle-like) compositions to Re-rich compositions. However, none of the pre-impact lithologies have $^{187}Re/^{188}Os$ ratios higher than ~125, further supporting a probable late addition of Re, driven by the hydrothermal cell. Even if the apparent age shows a large uncertainty (339 ± 113 Ma), it is within the range of the granite age of ~334 ± 2.3 Ma obtained for zircons (Ross et al., 2022). Transitional unit samples (Goderis et al., 2021) also yield a relatively similar apparent age of ~333 ± 100 Ma (Fig. 9a), which may confirm that the granite represents the main felsic component for most impact melt rocks, and more generally, impactites of the Chicxulub peak ring. However, both measured $^{187}Os/^{188}Os$ ratios of granite samples plot along the 66.05 Ma (impact age) reference line, in contradiction with its estimated age. This possibly indicates that the Re–Os isotopic system was disturbed following the impact event.

The granite Re–Os isotopic signature is highly unusual, plotting in the MORB array (Fig. 9b), i.e., with low Os content (22–26 ppt), which are values relatively typical, albeit slightly lower than, upper crustal rocks (~31 ppt; Peucker-Ehrenbrink and Jahn, 2001), whereas the measured $^{187}Os/^{188}Os$ ratio is highly unradiogenic (0.16), and thus similar to mantle values (~0.13; Meisel et al., 2001). Additionally, the Ir contents (1–8 ppt) are below UCC composition (~22 ppt; Peucker-Ehrenbrink and Jahn, 2001). A similar unusually low $^{187}Os/^{188}Os$ ratio is observed for the dacite (0.20) associated with a low Ir content (3 ppt). The $^{187}Re/^{188}Os$ ratio of the granites are also relatively high, i.e., ~73 and ~124 (Fig. 8a), suggesting they may have been affected by the addition of Re following the hydrothermal overprint. In the case of the dacite, the $^{187}Re/^{188}Os$ ratio is relatively low (~11). Possibly, the Os was also remobilized by the long-lived post-impact hydrothermal system in the granite and dacite samples, as the granite plots close to the 66.05 Ma reference line on the Re–Os isotopic diagram (Fig. 8a). The remobilization may have been eased by the high porosity of the granites (10% on average; Christeson et al., 2018) which could have further enhanced fluid circulation. One granite clast investigated in Yax–1 drill core has a similar low Os concentration of ~29 ppt and is coupled with a relatively unradiogenic $^{187}Os/^{188}Os$ ratio of 0.2169 (see Fig. 9b; Gelinas et al., 2004). This may suggest that the unusual Re–Os isotopic signature of the investigated granites is not restricted to our samples from the Hole M0077A drill core, but could represent a common feature within the Chicxulub impact structure, highlighting the effects of post-impact hydrothermal alteration. However, no further investigations were made to

assess the degree of alteration experienced by this granite in Yax–1. Thus, the unusual Os isotopic signature of the granites and dacite may be related to the hydrothermal overprint that affected this granite, rather than representing a primary magmatic, or source inherited signal. Further investigations on additional samples would be needed to confirm this trend.

6.4. Comparison with other Chicxulub drill cores

Our geochemical investigations of the HSE contents and Re–Os isotope systematics in impact melt rocks are compared with results obtained for the "transitional unit" of the Chicxulub peak ring (core 40R) presented by Goderis et al. (2021). Unlike the impact melt rocks from our study, the transitional unit displays unambiguous evidence for a meteoritic component admixture, with generally high Ni, Os, Ir, and Pt contents (see Figs. 4–6 and Table 1). Samples from the transitional unit show compositions more comparable to chondritic addition to the local background signature (Figs. 6–8), whereas the Ir/Pt and Os/Ir ratios show variations similar to those of the impact melt rocks from this study. The $^{187}Os/^{188}Os$ isotopic composition of the transitional unit is more homogeneous and covers a relatively narrow range (~0.21–0.35, excluding the lower transitional unit samples) compared to impact melt rocks and suevites from this study. Within the transitional unit, contamination by up to ~0.1% of meteoritic material was found (Goderis et al., 2021). This is nearly one order of magnitude higher compared to the hypothetic meteoritic contamination of up to ~0.01–0.05% recorded in UIM sample 91R1_102–104.5 (Fig. 9). This suggests a higher dilution and heterogeneous distribution of the meteoritic matter in the impact melt rock units, or that only the mafic component was present. On the other hand, the dolerite, representing the mafic component, appears to have contributed significantly to the HSE budget and to the Re–Os isotopic signature observed in some impact melt rock samples (e.g., sample 265R2_9–11).

The Cr, Co, Ni, and HSE concentrations of impact melt rocks and suevites are also similar to those previously measured in impactites recovered in other drill cores, i.e., C1, Y6, and Yax–1 (Koeberl et al., 1994; Tuchscherer et al., 2004a; Tagle et al., 2004; Gelinas et al., 2004). Comparable variations in the $^{187}Os/^{188}Os$ ratio, from radiogenic crustal to unradiogenic (i.e., chondritic) values, were measured in previous drill cores (Table 1; see also Koeberl et al., 1994; Gelinas et al., 2004). The meteoritic component is difficult to discern, and compositions are broadly within the range of those of the UCC, and, when identified, the admixture of meteoritic material to the impactites is not higher than ~0.1%. The Cr versus Ir compositions of impactites from the Yax–1 and Y6 drill cores (Fig. 9a) measured by Tagle et al. (2004) are close to the overlapping area between the continental crust–chondrites mixing area and the Earth field shown in Fig. 9a, and thus might indicate a barely resolvable meteoritic component. Additionally, the Yax–1 impactites have relatively mafic to intermediate compositions (44.2–55.8 wt.% SiO_2), and thus, may also reflect a possible contribution of a mafic component, excluding

impactites displaying a significant (>10 wt.% CaO) carbonate component (Tagle et al., 2004; Tuchscherer et al., 2004a). This poses further implications regarding the origin of the HSE and Re–Os compositions of the impactite samples from Yax–1, as even if a minor heterogeneous meteoritic component may be present, the contribution from a mafic lithology cannot be excluded or disentangled. Additionally, Tuchscherer et al. (2004a) explained the composition of Yax–1 impactites, especially in the green impact melt breccia (unit 4, 861–884 meters depth), by the presence of a significant mafic component. Mafic clasts were identified in impact-melt bearing polymict impact breccias from Yax–1, e.g., gabbro and amphibolite, but no dolerite (samples YAX-1_836.34 and Yax-1_832.83; Kring, 2005, and references therein; Schmieder et al., 2017). Amphibolite was also identified as a clast in the Y6 core (sample Y6 N14 p4c; Kettrup and Deutsch, 2003). The only exception where a significant impactor component was identified in Chicxulub drill core material was in the case of powdered splits of impact melt rock from the C1 (C1-N10-1A, 1393–1394 meters below sea level) and Y6 (Y6-N19, 1377–1379.5 meters below sea level) drill cores (Sharpton et al., 1992; Koeberl et al., 1994; Schuraytz et al., 1996). These samples display high Ir and Os concentrations, up to ~15 ppb and ~25 ppb, respectively, associated with a chondritic $^{187}Os/^{188}Os$ ratio, corresponding to a contribution of chondritic material of up to ~5% (Fig. 9b). However, their interpretation remains difficult due to their stratigraphic position and may represent atypical sample heterogeneity, as the HSEs in these samples do not show chondritic elemental abundance ratios and may represent a mafic component that was not sampled (Sharpton et al., 1992; Koeberl et al., 1994; Schuraytz et al., 1996). Additionally, subsequent investigations of sample Y6-N19 revealed significant hydrothermal alteration (e.g., anhydrite veining, zeolites, and secondary calcite) and did not find such high Ir contents (<0.01 ppb; Kring and Boynton, 1992; Tagle et al., 2004, and references therein).

When adding available $^{187}Os/^{188}Os$ and $^{187}Re/^{188}Os$ isotope data from previous work (see Table 1), the Re–Os isotopic signatures recorded in the transitional unit, Yax–1 and C1 drill cores, and in K–Pg sites around the globe (Koeberl et al., 1994; Gelinas et al., 2004; Quitté et al., 2007; Goderis et al., 2021) follow broadly the same trend as the studied impact melt rocks, but show generally lower $^{187}Re/^{188}Os$ ratio (<30) towards chondritic/mantle-like compositions, with only two transitional unit samples having a $^{187}Re/^{188}Os$ ratio higher than 100. These two latter samples are from the bottom of the transitional unit (617.34 mbsf) where a strong hydrothermal signature in HSE pattern and pyrite chemistry is identified (Goderis et al., 2021), and thus, support a late addition of Re, explaining these high $^{187}Re/^{188}Os$ ratios. Therefore, the impact melt, suevite, and even granite samples displaying $^{187}Re/^{188}Os$ higher than 100 represent compositions in accordance with a post impact hydrothermal overprint which caused an addition of Re after remobilization of this element. Regarding the Yax–1 impactites (Gelinas et al., 2004), while some of these follow the same trend as the previously described samples, a second trend, albeit somewhat

scattered towards the average UCC, as well as the amphibolite sample, for the Re–Os isotopic composition can be identified and may represent a different crustal component, or a larger proportion of amphibolite, that could have been incorporated within Yax–1 impactites but not in C-1 or in the M0077A drill core, or even in the K–Pg boundary sites. A contribution of the amphibolite, albeit small, may also explain the difference observed between the calculated initial transitional unit (0.2076) and the impact melt rock (0.1377) $^{187}Os/^{188}Os$ ratios (Fig. 8a). This second trend does not follow the calculated ~66.05, ~334 Ma, and ~550 Ma (Pan-African) reference lines in Fig. 8a–b. Thus, even a more pronounced addition of Pan-African material, thought to be an important component of the Yucatán peninsula basement rocks (Zhao et al., 2020; Feignon et al., 2021, and references therein), does not explain the Re–Os isotopic composition of these Yax–1 impactites.

Therefore, the common features of the impact melt rocks, and more broadly, impactites recovered in drill cores within the Chicxulub impact structure (including the Hole M0077A core) are, on the one hand their relatively similar Ni, Cr, Co, and HSE compositions, and, on the other hand the strong heterogeneity of HSE distribution from a sample to another, at a relatively small scale (Koeberl et al., 1994; Tagle et al., 2004; Tuchscherer et al., 2004a; Goderis et al., 2021). Generally, the incorporation of meteoritic material is low (up to ~0.1% in rare samples; Gelinas et al., 2004; Goderis et al., 2021), compared to the more distal K–Pg boundary layers displaying contributions of meteoritic material of up to ~5%, and to the upper transitional unit topping the peak ring, recording unambiguously the admixture of chondritic material (see Fig. 9; Quitté et al., 2007; Goderis et al., 2013; Goderis et al., 2021). Moreover, the heterogeneous distribution of meteoritic material within the impact melt rocks seems to be a common feature of the Chicxulub impact structure, and not only restricted to the peak ring. The absence of a high amount of projectile component within the impact melt rocks (and more generally all impactites) of the Chicxulub structure may be due to the role played by the nature of the interface between the target rock and the impactor in the admixture process, as suggested by Tagle et al. (2004). In the case of Chicxulub, the crystalline basement was covered with volatile-rich layers, i.e., ~3-km-thick carbonate platform, anhydrite, and seawater (Lopez Ramos, 1975; Kring, 2005), which may have prevented the mixing process between the meteoritic material and the target rock (Tagle et al., 2004).

6.5. Lack of ubiquitous impactor signal explained

No distinct HSE composition from dolerite and other pre-impact lithologies was measured in the investigated Chicxulub peak ring impact melt rock samples, which does not allow to unambiguously distinguish between a mafic and a meteoritic contribution to the impact melt rocks. Previous work on Chicxulub impactites from within the impact structure (Koeberl et al., 1994; Gelinas et al., 2004; Tagle et al., 2004; Tuchscherer et al., 2004a) indicates that probably only a minor meteoritic material was incorporated (and heterogeneously) in the impactites. Interestingly, a
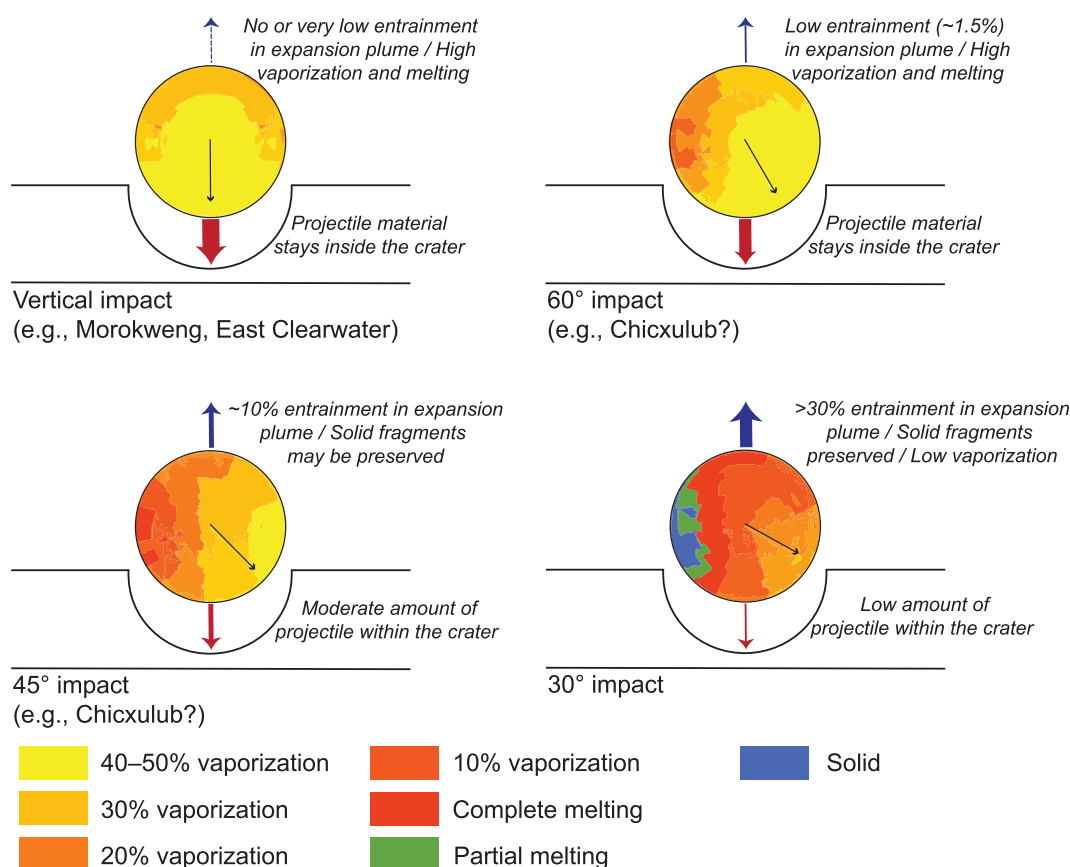
Fig. 10. Diagram modified from Pierazzo and Melosh (2000), showing the distribution of vaporization and melting inside a 10-km diameter projectile according to the impact angle relative to the target surface. In the case of vertical and steeply-inclined (60°) impact, significant vaporization and melting occur, with the meteoritic material being mainly concentrated at the bottom of the crater. The proportion of projectile material ejected and entrained within the expansion plume increases with decreasing angle (percentages provided are given at t = 3 s after the impact; Pierazzo and Melosh, 1999).

possible explanation for this low incorporation of the projectile could be the impact angle, as numerical modeling suggests that the Chicxulub impact structure formed, most probably, following an oblique impact, with an angle between 45 and 60° to the horizontal (Collins et al., 2020). This is an important aspect to consider because the impact angle has an effect on the amount of projectile vaporization, which decreases with the impact angle (Pierazzo and Melosh, 2000). For vertical and steeply-inclined (60°) impacts, at least ~30% of the impactor mass is vaporized, the remaining part being generally completely melted (see Fig. 11 of Pierazzo and Melosh, 2000). Below 60°, parts of the projectile may survive as solid fragments (from the trailing half of the projectile, subject to lesser shock pressures), with the vaporization becoming nearly non-existent for very shallow impact angles (~15°). For the assumed 45–60° impact angle of the Chicxulub impact event, a substantial proportion of the impactor material was likely vaporized (~10–30%, see Fig. 10) and melted (Pierazzo and Melosh, 1999, 2000), and deposited outside the impact crater, as indicated by the marine Os isotopic composition record and Ir concentrations (Paquay et al., 2008).

The preservation within the K–Pg boundary ejecta of a significant meteoritic component (e.g., Quitté et al., 2007;

Goderis et al., 2013), and of a small, 2.5 mm, (fossil) meteorite fragment (Kyte, 1998), is consistent with the scenario of an oblique impact event, probably below 60°, where parts of the impactor survived as solid phase and/or melted material, according to hydrocode modeling (Pierazzo and Melosh, 1999, 2000). For 45 and 60° impact angles, ~10% and ~1.5% of the projectile is entrained within the expansion plume, respectively (Fig. 10; Pierazzo and Melosh, 1999). However, as the numerical simulation ends only 3 seconds after the impact, it is possible that these percentages represent minimal estimates, as the expansion plume should develop over a longer duration (Pierazzo and Melosh, 1999). Hydrocode modeling has shown, especially for steeply-inclined impact (60°), that the projectile material stays mainly inside the crater, and moves downward (Pierazzo and Melosh, 2000). Therefore, in this case, the preserved meteoritic material may be located in the deepest impact melt rock units (up to ~3 km depth, Morgan et al., 2016) of the Chicxulub impact structure, rather than in the shallowest impact melt rocks investigated here. Unfortunately, these deep impact melt rocks were not yet recovered by any of the available drill cores.

An impact angle closer to 45° would be more consistent in order to explain the observed distribution of meteoritic matter, which is concentrated mainly in the K–Pg impact

ejecta, and also the preservation of a solid meteorite fragment in sediments retrieved from a K–Pg boundary in the North Pacific Ocean (Kyte, 1998), which seems unlikely at higher impact angles (Fig. 10). The vaporization and ejection of the meteoritic matter may have prevented its incorporation at high amounts within the impact structure, and may explain the generally low (<0.1%) meteoritic contamination measured in the Chicxulub impactites. The sheer volume of impact melt rocks produced at Chicxulub, may have enhanced the dilution of impactor component (see also Grieve and Cintala, 1992), and could also explain this low, or not detectable, meteoritic contribution.

6.6. Implications for projectile material identification and distribution in large impact structures

Similarly low levels of meteoritic material in the impactites was found in several impact structures around the world (e.g., Bosumtwi, Manicouagan, Lake Saint Martin, Ries), suggesting possibly similar mechanisms of formation of the impactites (Tagle et al., 2004, and references therein). On a broader perspective, similar impact processes, e.g., an oblique impact event, may be involved to explain the lack of a detectable meteoritic component within the aforementioned impact structures (Pierazzo and Melosh, 2000). Difficulties with unambiguously identifying a meteoritic signature in impact melt rocks using the HSEs budget and Re–Os isotopic system were also encountered in impact structures characterized by target lithologies that contain a large mafic component and/or that were affected by hydrothermal alteration. The Lonar crater, located in India, formed in mafic (i.e., basalt) target rock (Schulz et al., 2016). Lonar crater basalts have relatively unradiogenic $^{187}Os/^{188}Os$ ratios, but still higher than the Chicxulub peak ring dolerite (∼0.35, and two radiogenic basalts with $^{187}Os/^{188}Os$ ratios above 1.5; Schulz et al., 2016). Some impactites at Lonar crater have significantly higher HSE abundances relative to basalt, as well as distinct Re–Os isotopic ratios, which allows for the identification of a meteoritic contribution of ∼0.02% (Schulz et al., 2016). However, results of Cr isotopic studies suggest significant incorporation of chondritic material, i.e., between ∼1–3% (Mougel et al., 2019). Impact spherules have been found to contain even larger contributions, i.e., up to 8% (Das Gupta et al., 2017). Another example is the Bosumtwi impact structure in Ghana, where the target rock has unusually high HSE contents, and thus, it was not possible to identify, and to quantify an unequivocal impactor contribution distinct from the crustal contribution in impactite samples recovered within the crater or in the proximal ejecta deposits (see also Goderis et al., 2007; McDonald et al., 2007). However, Koeberl and Shirey (1993) have shown (using Re and Os concentrations and Os isotopic compositions) that about 0.6% of a meteoritic component is incorporated in Ivory Coast tektites (i.e., distal ejecta from the Bosumtwi crater).

While at several large impact structures, such as Chicxulub, no or only minimal projectile contamination was detected in impactites from within the crater and/or in proximal ejecta deposits, there are other cases where a significant amount of meteoritic component was identified within the impact structure. An homogeneous chondritic contribution of ∼2–5%, as well as a preserved meteorite fragment were identified within the impact melt rocks from the Morokweng impact structure (Koeberl et al., 1997; Koeberl and Reimold, 2003; Maier et al., 2006). Similarly, the investigated impact melt rocks from the ∼22-km diameter East Clearwater Lake impact structure revealed the presence of ∼8% of CI chondrite material (Grieve et al., 1980). In these two cases, the scenario of a vertical, or nearly vertical impact event relative to the target surface, where most of the projectile material stays within the crater (Fig. 10; Pierazzo and Melosh, 2000) are favored. The preservation of a meteorite fragment within the Morokweng impact melt rocks may also be explained by a relatively low impact velocity, with possibly a lower degree of vaporization and melting of the projectile (Maier et al., 2006). In the case of the East Clearwater Lake impact structure, it is suggested that peak shock pressures in the order of ∼300 GPa were sufficient to vaporize the silicate component, but only melt the metal fraction of the projectile (Grieve et al., 1980). Therefore, the investigation of HSE abundances and Re–Os isotopic signatures of the impact melt rocks and ejecta deposits of large impact structures may provide useful information on the processes involved in the distribution of the impactor material.

7. CONCLUSIONS

As shown using major and trace element whole-rock concentrations, μXRF mapping, petrographic investigations, and consistent with previous works, the impact melt rocks in the Chicxulub peak ring mainly reflect mixing between a felsic and a mafic target lithology component (i.e., granite and dolerite). In the upper impact melt unit (UIM), carbonate material was also incorporated both within the green schlieren phase, and as clasts within the silicate black impact melt. Other pre-impact lithologies, such as dacite, amphibolite, and felsite, appear not to have contributed to the impact melt rock significantly.

While previous work at K–Pg boundary sites around the world, and also to some extent within the Chicxulub impact structure, has identified the presence of meteoritic matter, the impact melt rocks within the peak ring structure have a more complex geochemical signature. Most notably, the post-impact hydrothermal overprint as well as the mafic target rock contribution have affected the HSE compositions and the Re–Os isotopic signature significantly. The main mafic lithology in the Hole M0077A core is dolerite (with an accumulation of Ni and Co in pseudomorphosed olivine, and of Cr in spinel-group minerals), which shows a mantle-like signature with enrichments in the HSEs, and low $^{187}Os/^{188}Os$ ratio comparable to chondritic values, preventing an unambiguous identification of a contamination by the projectile). The effects of post-impact hydrothermal alteration also play an important role in remobilizing elements such as Ni, Re (especially with a late addition of Re, increasing the measured $^{187}Re/^{188}Os$ ratios of suevites, some impact melt rocks, and, to a lesser extent, granites), and Os either by fluid circulation or accumulation of HSEs

in sulfide phases (Goderis et al., 2021). Consequently, contributions of mafic material and hydrothermal overprint seem to be the most likely explanations for the observed HSE and Re–Os isotopic compositions within the Chicxulub peak ring impact melt rock. Nonetheless a potential meteoritic component in the impact melt cannot be fully excluded either, as a single UIM sample (91R1_102–104.5) indicates a possible projectile contribution of ~0.01–0.05%, nearly an order of magnitude lower than that recorded in the transitional unit, and in the Yax–1 drill core.

To summarize, at least five processes led to the currently observed impact melt rock moderately siderophile element, HSE, and Re–Os isotopic compositions: (1) enhanced excavation, vaporization of the impactor following a steeply inclined (possibly ~45°) impact, preventing and/or limiting the incorporation of meteoritic material (ejection within the expansion plume) within the impact melt rocks, (2) melting and mixing of a mafic (potentially dolerite) and a felsic (likely granite) component, with the incorporation of variable contributions of carbonate, and (3) the addition of a minor meteoritic component, (4) fast quenching (Schulte et al., 2021) leading to a heterogeneous chemical composition and distribution of the HSE–Os isotopic composition, and (5) remobilization of some moderately and HSEs such as Ni, Re, and Os following the onset of a long-living, post-impact hydrothermal system, further modifying the HSE budget. The variations in moderately siderophile element, HSE, and Re–Os isotopic compositions, reflect large heterogeneity within the impact melt, similar to what has been observed in previous works on impact melt rocks from different drill cores within the Chicxulub impact structure. This suggests that during its formation, the impact melt did not have sufficient time to fully homogenize, both physically and chemically, and that this process seems to be common to the entire Chicxulub impact structure and not restricted to the peak ring. The Chicxulub peak ring impact melt rocks represent an important example of the challenges associated with the unambiguous identification of a meteoritic component within terrestrial impact structures.

Declaration of Competing Interest

The authors declare that they have no known competing financial interests or personal relationships that could have appeared to influence the work reported in this paper.

APPENDIX A. SUPPLEMENTARY MATERIAL

Supplementary data to this article can be found online at https://doi.org/10.1016/j.gca.2022.02.006.

REFERENCES

Aiglsperger T., González-Jiménez J. M., Proenza J. A., Galí S., Longo F., Griffin W. L. and O'Reilly S. Y. (2021) Open System Re-Os Isotope Behavior in Platinum-Group Minerals during Lateritization? *Minerals* **11**, 1083.

Alvarez L. W., Alvarez W., Asaro F. and Michel H. V. (1980) Extraterrestrial cause for the Cretaceous-Tertiary extinction. *Science* **208**, 1095–1108.

Ballantyne J. M. and Moore J. N. (1988) Arsenic geochemistry in geothermal systems. *Geochim. Cosmochim. Acta* **52**, 475–483.

Becker H., Horan M. F., Walker R. J., Gao S., Lorand J.-P. and Rudnick R. L. (2006) Highly siderophile element composition of the Earth's primitive upper mantle: Constraints from new data on peridotite massifs and xenoliths. *Geochim. Cosmochim. Acta* **70**, 4528–4550.

Belza J., Goderis S., Keppens E., Vanhaecke F. and Claeys P. (2012) An emplacement mechanism for the mega-block zone within the Chicxulub crater, (Yucatán, Mexico) based on chemostratigraphy. *Meteorit. Planet. Sci.* **47**, 400–413.

Birck J. L., Barman M. R. and Capmas F. (1997) Re-Os isotopic measurements at the femtomole level in natural samples. *Geost. Newslett.* **21**, 19–27.

Brandon A. D., Humayun M., Puchtel I. S., Leya I. and Zolensky M. (2005) Geochemistry: Osmium isotope evidence for an s-process carrier in primitive chondrites. *Science* **309**, 1233–1236.

Chiarenza A. A., Farnsworth A., Mannion P. D., Lunt D. J., Valdes P. J., Morgan J. V. and Allison P. A. (2020) Asteroid impact, not volcanism, caused the end-Cretaceous dinosaur extinction. *Proc. Natl. Acad. Sci.* **117**, 17084–17093.

Christeson G. L., Gulick S. P. S., Morgan J. V., Gebhardt C., Kring D. A., Le Ber E., Lofi J., Nixon C., Poelchau M., Rae A. S. P., Rebolledo-Vieyra M., Riller U., Schmitt D. R., Wittmann A., Bralower T. J., Chenot E., Claeys P., Cockell C. S., Coolen M. J. L., Ferrière L., Green S., Goto K., Jones H., Lowery C. M., Mellett C., Ocampo-Torres R., Perez-Cruz L., Pickersgill A. E., Rasmussen C., Sato H., Smit J., Tikoo S. M., Tomioka N., Urrutia-Fucugauchi J., Whalen M. T., Xiao L. and Yamaguchi K. E. (2018) Extraordinary rocks from the peak ring of the Chicxulub impact crater: P-wave velocity, density, and porosity measurements from IODP/ICDP Expedition 364. *Earth Planet. Sci. Lett.* **495**, 1–11.

Claeys P., Kiessling W. and Alvarez W. (2002) Distribution of Chicxulub ejecta at the Cretaceous–Tertiary boundary. In *Catastrophic events and mass extinctions: impacts and beyond* (eds. C. Koeberl and K. G. MacLeod). Geological Society of America Special Paper 356, Boulder, Colorado, pp. 55–68.

Claeys P., Heuschkel S., Lounejeva-Baturina E., Sanchez-Rubio G. and Stöffler D. (2003) The suevite of drill hole Yucatàn 6 in the Chicxulub impact crater. *Meteorit. Planet. Sci.* **38**, 1299–1317.

Cohen A. S. and Waters F. G. (1996) Separation of osmium from geological materials by solvent extraction for analysis by thermal ionization mass spectrometry. *Anal. Chim. Acta* **332**, 269–275.

Collins G. S., Patel N., Davison T. M., Rae A. S. P., Morgan J. V., Gulick S. P. S. and IODP-ICDP Expedition 364 Science Party and Third-Party Scientists (2020) A steeply-inclined trajectory for the Chicxulub impact. *Nat. Commun.* **11**, 1480.

Creaser R. A., Papanastassiou D. A. and Wasserburg G. J. (1991) Negative thermal ion mass-spectrometry of osmium, rhenium and iridium. *Geochim. Cosmochim. Acta* **55**, 397–401.

Das Gupta R., Banerjee A., Goderis S., Claeys P., Vanhaecke F. and Chakrabarti R. (2017) Evidence for a chondritic impactor, evaporation-condensation effects and melting of the Precambrian basement beneath the 'target' Deccan basalts at Lonar crater, India. *Geochim. Cosmochim. Acta* **215**, 51–75.

de Graaff S. J., Kaskes P., Déhais T., Goderis S., Debaille V., Ross C. H., Gulick S. P. S., Feignon J.-G., Ferrière L., Koeberl C., Smit J., Matielli N. and Claeys P. (2022) New insights into the formation and emplacement of impact melt rocks within the Chicxulub impact structure, following the 2016 IODP-ICDP Expedition 364. *Geol. Soc. Am. Bull.* **134**, 293–315.

de Winter N. J. and Claeys P. (2017) Micro X-ray fluorescence (µXRF) line scanning on Cretaceous rudist bivalves: A new method for reproducible trace element profiles in bivalve Calcite. *Sedimentology* **64**, 231–251.

DePalma R. A., Smit J., Burnham D. A., Kuiper K., Manning P. L., Oleinik A., Larson P., Maurrasse F. J., Vellekoop J., Richards M. A. and Gurche L. (2019) A seismically induced onshore surge deposit at the KPg boundary, North Dakota. *Proc. Natl. Acad. Sci.* **116**, 8190–8199.

Feignon J.-G., Ferrière L., Leroux H. and Koeberl C. (2020) Characterization of shocked quartz grains from Chicxulub peak ring granites and shock pressure estimates. *Meteorit. Planet. Sci.* **55**, 2206–2223.

Feignon J.-G., de Graaff S. J., Ferrière L., Kaskes P., Déhais T., Goderis S., Claeys P. and Koeberl C. (2021) Chicxulub impact structure, IODP-ICDP Expedition 364 drill core: Geochemistry of the granite basement. *Meteorit. Planet. Sci.* **56**, 1243–1273.

Fischer-Gödde M., Becker H. and Wombacher F. (2010) Rhodium, gold and other highly siderophile element abundances in chondritic meteorites. *Geochim. Cosmochim. Acta* **74**, 356–379.

French B. M., Orth C. J. and Quintana C. R. (1989) Iridium in the Vredefort bronzite granophyre: Impact melting and limits on a possible extraterrestrial component. In *Proceedings, 19th Lunar and Planetary Science Conference*. Cambridge University Press, Cambridge/Houston, TX, Lunar and Planetary Institute, pp. 733–744.

Gelinas A., Kring D. A., Zurcher L., Urrutia-Fucugauchi J., Morton O. and Walker R. J. (2004) Osmium isotope constraints on the proportion of bolide component in Chicxulub impact melt rocks. *Meteorit. Planet. Sci.* **39**, 1003–1008.

Goderis S., Tagle R., Schmitt R. T., Erzinger J. and Claeys P. h. (2007) Platinum group elements provide no indication of a meteoritic component in ICDP cores from the Bosumtwi crater, Ghana. *Meteorit. Planet. Sci.* **42**, 731–741.

Goderis S., Tagle R., Belza J., Smit J., Montanari A., Vanhaecke F., Erzinger J. and Claeys P. (2013) Reevaluation of siderophile element abundances and across the Cretaceous-Paleogene (K–Pg) boundary: Implications for the nature of the projectile. *Geochim. Cosmochim. Acta* **120**, 417–446.

Goderis S., Sato H., Ferrière L., Schmitz B., Burney D., Kaskes P., Vellekoop J., Wittmann A., Schulz T., Chernonozhkin S. M., Claeys P., de Graaff S. J., Déhais T., de Winter N. J., Elfman M., Feignon J.-G., Ishikawa A., Koeberl C., Kristiansson P., Neal C. R., Owens J. D., Schmieder M., Sinnesael M., Vanhaecke F., Van Malderen S. J. M., Bralower T. J., Gulick S. P. S., Kring D. A., Lowery C. M., Morgan J. V., Smit J., Whalen M. T. and IODP-ICDP Expedition 364 Scientists (2021) Globally distributed iridium layer preserved within the Chicxulub impact structure. *Sci. Adv.* **7**, eabe3647.

Grieve R. A. F. and Cintala M. J. (1992) An analysis of differential impact melt-crater scaling and implications for the terrestrial impact record. *Meteoritics* **27**, 526–538.

Grieve R. A. F., Palme H. and Plant A. G. (1980) Siderophile-rich particles in the melt rocks at the E. Clearwater impact structure, Quebec: their characteristics and relationship to the impacting body. *Contrib. Mineral. Petrol.* **75**, 187–198.

Gulick S. P. S., Christeson G. L., Barton P. J., Grieve R. A. F., Morgan J. V. and Urrutia-Fucugauchi J. (2013) Geophysical characterization of the Chicxulub impact crater. *Rev. Geophys.* **51**, 31–52.

Gulick S. P. S., Bralower T. J., Ormö J., Hall B., Grice K., Schaefer B., Lyons S., Freeman K. H., Morgan J. V., Artemieva N., Kaskes P., de Graaff S. J., Whalen M. T., Collins G. S., Tikoo S. M., Verhagen C., Christeson G. L., Claeys P., Coolen M. J. L., Goderis S., Goto K., Grieve R. A. F., McCall N., Osinski G. R., Rae A. S. P., Riller U., Smit J., Vajda V., Wittmann A. and the Expedition 364 Scientists, (2019) The first day of the Cenozoic. *Proc. Natl. Acad. Sci. USA* **116**, 19342–19351.

Hildebrand A. R., Penfield G. T., Kring D. A., Pilkington M., Camargo Z. A., Jacobsen S. B. and Boynton W. V. (1991) Chicxulub crater: A possible Cretaceous/Tertiary boundary impact crater on the Yucatán Peninsula, Mexico. *Geology* **19**, 867–871.

Horan M. F., Walker R. J., Morgan J. W., Grossman J. N. and Rubin A. E. (2003) Highly siderophile elements in chondrites. *Chem. Geol.* **196**, 27–42.

Jaffe L. A., Peucker-Ehrenbrink B. and Petsch S. T. (2002) Mobility of rhenium, platinum group elements and organic carbon during black shale weathering. *Earth Planet. Sci. Lett.* **198**, 339–353.

Kaskes P., Déhais T., de Graaff S. J., Goderis S. and Claeys P. (2021) Micro–X-ray fluorescence (µXRF) analysis of proximal impactites: High-resolution element mapping, digital image analysis, and quantifications. In *Large Meteorite Impacts and Planetary Evolution VI: Geological Society of America Special Paper 550* (eds. W. U. Reimold and C. Koeberl). Geological Society of America Special Paper 550, Boulder, Colorado, pp. 171–206.

Kaskes P., de Graaff S. J., Feignon J.-G., Déhais T., Goderis S., Ferrière L., Koeberl C., Smit J., Wittmann A., Gulick S., Debaille V., Matielli N. and Claeys P. (2022) Formation of the Crater Suevite Sequence from the Chicxulub Peak Ring: a Petrographic, Geochemical, and Sedimentological Characterization. *Geol. Soc. Am. Bull.* **134**, 895–927.

Kettrup B. and Deutsch A. (2003) Geochemical variability of the Yucatàn basement: Constraints from crystalline clasts in Chicxulub impactites. *Meteorit. Planet. Sci.* **38**, 1079–1092.

Koeberl C. (1993a) Chicxulub Crater, Yucatan: Tektites, impact glasses, and the geochemistry of target rocks and breccias. *Geology* **21**, 211–214.

Koeberl C. (1993b) Instrumental neutron activation analysis of geochemical and cosmochemical samples: a fast and reliable method for small sample analysis. *J. Radioanal. Nucl. Chem.* **168**, 47–60.

Koeberl C. (1998) Identification of meteoritical components in impactites. In *Meteorites: Flux with Time and Impact Effects* (eds. M. M. Grady, R. Hutchison, G. J. H. McCall and D. A. Rothery). Geological Society Special Publication 140, London, United Kingdom, pp. 133–152.

Koeberl C. (2014) The Geochemistry and Cosmochemistry of Impacts. In *Treatise on Geochemistry (Second Edition)*, Volume 2 (eds. H. D. Holland and K. K. Turekian). Elsevier, Amsterdam, Netherlands, pp. 73–118.

Koeberl C. and Reimold W. U. (2003) Geochemistry and petrography of impact breccias and target rocks from the 145 Ma Morokweng impact structure, South Africa. *Geochim. Cosmochim. Acta* **67**, 1837–1862.

Koeberl C. and Shirey S. B. (1993) Detection of a Meteoritic Component in Ivory Coast Tektites with Rhenium-Osmium Isotopes. *Science* **261**, 595–598.

Koeberl C. and Sigurdsson H. (1992) Geochemistry of impact glasses from the K/T boundary in Haiti: Relation to smectites and a new type of glass. *Geochim. Cosmochim. Acta* **56**, 2113–2129.

Koeberl C., Sharpton V. L., Schuraytz B. C., Shirey S. B., Blum J. D. and Marin L. E. (1994) Evidence for a meteoritic component in impact melt rock from the Chicxulub structure. *Geochim. Cosmochim. Acta* **58**, 1679–1684.

Koeberl C., Reimold W. U. and Shirey S. B. (1996) Re–Os isotope and geochemical study of the Vredefort Granophyre: Clues to the origin of the Vredefort structure, South Africa. *Geology* **24**, 913–916.

Koeberl C., Armstrong R. A. and Reimold W. U. (1997) Morokweng, South Africa: A large impact structure of Jurassic-Cretaceous boundary age. *Geology* **25**, 731–734.

Koeberl C., Claeys P., Hecht L. and McDonald I. (2012) Geochemistry of impactites. *Elements* **8**, 37–42.

Kring D. A. (2005) Hypervelocity collisions into continental crust composed of sediments and an underlying crystalline basement: Comparing the Ries (~24 km) and Chicxulub (~180 km) impact craters. *Geochemistry* **65**, 1–46.

Kring D. A. and Boynton W. V. (1992) Petrogenesis of an augite-bearing melt rock in the Chicxulub structure and its relationship to K/T impact spherules in Haiti. *Nature* **358**, 141–144.

Kring D. A., Tikoo S. M., Schmieder M., Riller U., Rebolledo-Vieyra M., Simpson S. L., Osinski G. R., Gattacceca J., Wittmann A., Verhagen C. M., Cockell C. S., Coolen M. J. L., Longstaffe F. J., Gulick S. P. S., Morgan J. V., Bralower T. J., Chenot E., Christeson G. L., Claeys P., Ferrière L., Gebhardt C., Goto K., Green S. L., Jones H., Lofi J., Lowery C. M., Ocampo-Torres R., Perez-Cruz L., Pickersgill A. E., Poelchau M. H., Rae A. S. P., Rasmussen C., Sato H., Smit J., Tomioka N., Urrutia-Fucugauchi J., Whalen M. T., Xiao L. and Yamaguchi K. E. (2020) Probing the hydrothermal system of the Chicxulub impact crater. *Sci. Adv.* **6**, eaaz3053.

Krull-Davatzes A. E., Lowe D. R. and Byerly G. R. (2012) Mineralogy and diagenesis of 3.24 Ga meteorite impact spherules. *Precambrian Res.* **196–197**, 128–148.

Kyte F. T. (1998) A meteorite from the Cretaceous/Tertiary boundary. *Nature* **396**, 237–239.

Lambert P. (1982) Anomalies within the system: Rochechouart target rock meteorite. In *Geological Implications of Impacts of Large Asteroids and Comets on Earth*. Geological Society of America Special Paper 190, Boulder, Colorado, pp. 57–68.

Lopez Ramos E. (1975) Geological Summary of the Yucatan Peninsula. In *The Gulf of Mexico and the Caribbean* (eds. A. E. M. Nairn and F. G. Stehli). Springer, Boston, MA, pp. 257–282.

Lowery C. M., Bralower T. J., Owens J. D., Rodríguez-Tovar F. J., Jones H., Smit J., Whalen M. T., Claeys P., Farley K., Gulick S. P. S., Morgan J. V., Green S., Chenot E., Christeson G. L., Cockell C. S., Coolen M. J. L., Ferrière L., Gebhardt C., Goto K., Kring D. A., Lofi J., Ocampo-Torres R., Perez-Cruz L., Pickersgill A. E., Poelchau M. H., Rae A. S. P., Rasmussen C., Rebolledo-Vieyra M., Riller U., Sato H., Tikoo S. M., Tomioka N., Urrutia-Fucugauchi J., Vellekoop J., Wittmann A., Xiao L., Yamaguchi K. E. and Zylberman W. (2018) Rapid recovery of life at ground zero of the end-Cretaceous mass extinction. *Nature* **558**, 288–291.

Lubetskaya T. and Korenaga J. (2007) Chemical composition of Earth's primitive mantle and its variance: 1. Method and results. *J. Geophys. Res.* **112**, B03211.

Luguet A., Nowell G. M. and Pearson D. G. (2008) $^{184}Os/^{188}Os$ and $^{186}Os/^{188}Os$ measurements by negative thermal ionization mass spectrometry (N-TIMS): effects on interfering element and mass fractionation corrections on data accuracy and precision. *Chem. Geol.* **248**, 342–362.

Luguet A., Behrens M., Pearson D. G., Koenig S. and Herwartz D. (2015) Significance of the whole rock Re-Os ages in cryptically and modally metasomatized cratonic peridotites – Constraints from the HSE-Se-Te systematics. *Geochim. Cosmochim. Acta* **164**, 441–463.

Mader D. and Koeberl C. (2009) Using Instrumental Neutron Activation Analysis for geochemical analyses of terrestrial impact structures: Current analytical procedures at the University of Vienna Geochemistry Activation Analysis Laboratory. *Appl. Radiat. Isot.* **67**, 2100–2103.

Maier W. D., Andreoli M. A., McDonald I., Higgins M. D., Boyce A. J., Shukolyukov A., Lugmair G. W., Ashwal L. D., Gräser P., Ripley E. M. and Hart R. J. (2006) Discovery of a 25-cm asteroid clast in the giant Morokweng impact crater, South Africa. *Nature* **441**, 203–206.

McDonald I., Peucker-Ehrenbrink B., Coney L., Ferrière L., Reimold W. U. and Koeberl C. (2007) Search for a meteoritic component in drill cores from the Bosumtwi impact structure, Ghana: Platinum group element contents and osmium isotopic characteristics. *Meteorit. Planet. Sci.* **42**, 743–753.

McDonough W. F. and Sun S. (1995) The composition of the Earth. *Chem. Geol.* **120**, 223–253.

Meisel T., Walker R. J., Irving A. J. and Lorand J.-P. (2001) Osmium isotopic compositions of mantle xenoliths: a global perspective. *Geochim. Cosmochim. Acta* **65**, 1311–1323.

Meisel T., Reisberg L., Moser J., Carignan J., Melcher F. and Brügmann G. (2003) Re–Os systematics of UB-N, a serpentinized peridotite reference material. *Chem. Geol.* **201**, 161–179.

Morgan J. V., Gulick S. P. S., Bralower T., Chenot E., Christeson G., Claeys P., Cockell C., Collins G. S., Coolen M. J. L., Ferrière L., Gebhardt C., Goto K., Jones H., Kring D. A., Le Ber E., Lofi J., Long X., Lowery C., Mellett C., Ocampo-Torres R., Osinski G. R., Perez-Cruz L., Pickersgill A., Pölchau M., Rae A., Rasmussen C., Rebolledo-Vieyra M., Riller U., Sato H., Schmitt D. R., Smit J., Tikoo S., Tomioka N., Urrutia-Fucugauchi J., Whalen M., Wittmann A., Yamaguchi K. E. and Zylberman W. (2016) The formation of peak rings in large impact craters. *Science* **354**, 878–882.

Morgan J., Gulick S., Mellet C. L. and Green S. L. (2017) Chicxulub: Drilling the K-Pg impact crater. In *and the Expedition 364 Scientists*. International Ocean Discovery Program, College Station, Texas, p. 164 p..

Morgan J. W., Janssens M.-J., Hertogen J., Gros J. and Takahashi H. (1979) Ries impact crater, southern Germany: search for meteoritic material. *Geochim. Cosmochim. Acta* **43**, 803–815.

Mougel B., Moynier F., Koeberl C., Wielandt D. and Bizzarro M. (2019) Identification of a meteoritic component using chromium isotopic composition of impact rocks from the Lonar impact structure, India. *Meteorit. Planet. Sci.* **54**, 2592–2599.

Palme H., Janssens M. J., Takahashi H., Anders E. and Hertogen J. (1978) Meteoritic material at five large impact craters. *Geochim. Cosmochim. Acta* **42**, 313–323.

Paquay F. S., Ravizza G. E., Dalai T. K. and Peucker-Ehrenbrink B. (2008) Determining chondritic impactor size from the marine osmium isotope record. *Science* **320**, 214–218.

Pearson D. G. and Woodland S. J. (2000) Solvent extraction/anion exchange separation and determination of PGEs (Os, Ir, Pt, Pd, Ru) and Re-Os isotopes in geological samples by isotope dilution ICP-MS. *Chem. Geol.* **165**, 87–107.

Peucker-Ehrenbrink B. and Jahn B.-M. (2001) Rhenium-osmium isotope systematics and platinum group element concentrations: Loess and the upper continental crust. *Geochem. Geophys. Geosyst.* **2**, 1061.

Pierazzo E. and Melosh H. J. (1999) Hydrocode modeling of Chicxulub as an oblique impact event. *Earth Planet. Sci. Lett.* **165**, 163–176.

Pierazzo E. and Melosh H. J. (2000) Hydrocode modeling of oblique impacts: The fate of the projectile. *Meteorit. Planet. Sci.* **35**, 117–130.

Potts P. J. and Meisel T. (2015) Certificate of Analysis, IAG OKUM (Ultramafic rock). International Association of Geoanalysts. Available online at http://www.iageo.com.

Quitté G., Levasseur S., Capmas F., Rocchia R., Birck J. L. and Allègre C. J. (2007) Osmium, tungsten, and chromium isotopes in sediments and in Ni-rich spinel at the K-T boundary: signature of a chondritic impactor. *Meteorit. Planet. Sci.* **42**, 1567–1580.

Racki G., Machalski M., Koeberl C. and Harasimiuk M. (2011) The weathering-modified iridium record of a new Cretaceous-Palaeogene site at Lechówka near Chelm, SE Poland, and its palaeobiologic implications. *Acta Palaeontol. Pol.* **56**, 205–215.

Riller U., Poelchau M. H., Rae A. S. P., Schulte F. M., Collins G. S., Melosh H. J., Grieve R. A. F., Morgan J. V., Gulick S. P. S., Lofi J., Diaw A., McCall N., Kring D. A. and IODP-ICDP Expedition 364 Science Party (2018) Rock fluidization during peak-ring formation of large impact structures. *Nature* **562**, 511–518.

Ross C. H., Stockli D. F., Rasmussen C., Gulick S. P. S., de Graaff S. J., Claeys P., Zhao J., Xiao L., Pickersgill A. E., Schmieder M., Kring D. A., Wittmann A. and Morgan J. V. (2022) Evidence of Carboniferous arc magmatism preserved in the Chicxulub impact structure. *Geol. Soc. Am. Bull.* **134**, 241–260.

Rudnick R. L. and Gao S. (2014) Composition of the Continental Crust. In *Treatise on Geochemistry (Second Edition)*, Volume 4 (eds. H. D. Holland and K. K. Turekian). Elsevier, Amsterdam, Netherlands, pp. 1–51.

Sanford J. C., Snedden J. W. and Gulick S. P. S. (2016) The Cretaceous-Paleogene boundary deposit in the Gulf of Mexico: Large-scale oceanic basin response to the Chicxulub impact. *J. Geophys. Res. Solid Earth* **121**, 1240–1261.

Schiano P., Birck J.-L. and Allègre C. J. (1997) Osmium-strontium-neodymium-lead isotopic covariations in mid-ocean ridge basalt glasses and the heterogeneity of the upper mantle. *Earth Planet. Sci. Lett.* **150**, 363–379.

Schmieder M., Shaulis B. J., Lapen T. J. and Kring D. A. (2017) U-Th-Pb systematics in zircon and apatite from the Chicxulub impact crater, Yucatán, Mexico. *Geol. Mag.* **155**, 1330–1350.

Schmitz B., Heck P. R., Alwmark C., Kita N. T., Meier M. M. M., Peucker-Ehrenbrink B., Ushikubo T. and Valley J. W. (2011) Determining the impactor of the Ordovician Lockne crater: oxygen and neon isotopes in chromite versus sedimentary PGE signatures. *Earth Planet. Sci. Lett.* **306**, 149–155.

Schulte F. M., Wittmann A., Jung S., Morgan J. V., Gulick S. P. S., Kring D. A., Grieve R. A. F., Osinski G. R., Riller U. and IODP-ICDP Expedition 364 Science Party (2021) Ocean resurge-induced impact melt dynamics on the peak-ring of the Chicxulub impact structure, Mexico. *Int. J. Earth Sci.* **110**, 2619–2636.

Schulte P., Alegret L., Arenillas I., Arz J. A., Barton P. J., Bown P. R., Bralower T. J., Christeson G. L., Claeys P., Cockell C. S., Collins G. S., Deutsch A., Goldin T. J., Goto K., Grajales-Nishimura J. M., Grieve R. A. F., Gulick S. P. S., Johnson K. R., Kiessling W., Koeberl C., Kring D. A., MacLeod K. G., Matsui T., Melosh J., Montanari A., Morgan J. V., Neal C. R., Nichols D. J., Norris R. D., Pierazzo E., Ravizza G., Rebolledo-Vieyra M., Reimold W. U., Robin E., Salge T., Speijer R. P., Sweet A. R., Urrutia-Fucugauchi J., Vajda V., Whalen M. T. and Willumsen P. S. (2010) The Chicxulub asteroid impact and mass extinction at the Cretaceous-Paleogene boundary. *Science* **327**, 1214–1218.

Schulz T., Luguet A., Wegner W., van Acken D. and Koeberl C. (2016) Target rocks, impact glasses, and melt rocks from the Lonar crater, India: Highly siderophile element systematics and Sr-Nd-Os isotopic signatures. *Meteorit. Planet. Sci.* **51**(7), 1323–1339.

Schuraytz B. C., Sharpton V. L. and Marín L. E. (1994) Petrology of impact-melt rocks at the Chicxulub multiring basin, Yucatán, Mexico. *Geology* **22**, 868–872.

Schuraytz B. C., Lindstrom D. J., Marín L. E., Martinez R. R., Mittlefehldt D. W., Sharpton V. L. and Wentworth S. J. (1996) Iridium metal in Chicxulub impact melt: forensic chemistry on the K-T smoking gun. *Science* **271**, 1573–1576.

Sharpton V. L., Dalrymple G. B., Marin L. E., Ryder G., Schuraytz B. C. and Urrutia-Fucugauchi J. (1992) New links between the Chicxulub impact structure and the Cretaceous/Tertiary boundary. *Nature* **359**, 819–821.

Sharpton V. L., Lee S., Ryder G. and Schuraytz B. C. (1996) A model of the Chicxulub impact basin based on evaluation of geophysical data, well logs, and drill core samples. In *The Cretaceous-Tertiary Event and Other Catastrophes in Earth History* (eds. G. Ryder, D. E. Fastovsky and S. Gartner). Geological Society of America Special Paper 307, Boulder, Colorado, pp. 55–74.

Shukolyukov A. and Lugmair G. W. (1998) Isotopic evidence for the Cretaceous-Tertiary impactor and its type. *Science* **282**, 927–930.

Simpson S. L., Osinski G. R., Longstaffe F. J., Schmieder M. and Kring D. A. (2020) Hydrothermal alteration associated with the Chicxulub impact crater upper peak-ring breccias. *Earth Planet. Sci. Lett.* **547**(116425), 12p.

Smit J. (1999) The global stratigraphy of the Cretaceous-Tertiary boundary impact ejecta. *Annu. Rev. Earth. Planet. Sci.* **27**, 75–113.

Smit J. and Hertogen J. (1980) An extraterrestrial event at the Cretaceous-Tertiary boundary. *Nature* **285**, 198–200.

Son T. H. and Koeberl C. (2005) Chemical variation within fragments of Australasian tektites. *Meteorit. Planet. Sci.* **40**, 805–815.

Sprain C. J., Renne P. R., Clemens W. A. and Wilson G. P. (2018) Calibration of chron C29r: New high-precision geochronologic and paleomagnetic constraints from the Hell Creek region, Montana. *Geol. Soc. Am. Bull.* **130**, 1615–1644.

Swisher C. C., Grajales-Nishimura J. M., Montanari A., Margolis S. V., Claeys P., Alvarez W., Renne P., Cedillo-Pardoa E., Maurrasse F. J.-M. R., Curtis G. H., Smit J. and McWilliams

M. O. () Coeval ^{40}Ar/^{39}Ar ages of 65.0 million years ago from Chicxulub crater melt rock and Cretaceous-Tertiary boundary tektites. *Science* **257**, 954–958.

Tagle R. and Berlin J. (2008) A database of chondrite analyses including platinum group elements, Ni Co, Au, and Cr: Implications for the identification of chondritic projectiles. *Meteorit. Planet. Sci.* **43**, 541–559.

Tagle R. and Hecht L. (2006) Geochemical identification of projectiles in impact rocks. *Meteorit. Planet. Sci.* **41**, 1721–1735.

Tagle R., Erzinger J., Hecht L., Schmitt R. T., Stöffler D. and Claeys P. (2004) Platinum group elements in impactites of the ICDP Chicxulub drill core Yaxcopoil-1: Are there traces of the projectiles? *Meteorit. Planet. Sci.* **39**, 1009–1016.

Trinquier A., Birck J. L. and Allègre C. J. (2006) The nature of the KT impactor. A ^{54}Cr reappraisal. *Earth Planet. Sci. Lett.* **241**, 780–788.

Tuchscherer M. G., Reimold W. U., Koeberl C. and Gibson R. L. (2004a) Major and trace element characteristics of impactites from the Yaxcopoil-1 borehole, Chicxulub structure, Mexico. *Meteorit. Planet Sci.* **39**, 955–978.

Tuchscherer M. G., Reimold W. U., Koeberl C., Gibson R. L. and de Bruin D. (2004b) First petrographic results on impactites from the Yaxcopoil-1 borehole, Chicxulub structure, Mexico. *Meteorit. Planet. Sci.* **39**, 899–930.

Tuchscherer M. G., Reimold W. U., Koeberl C. and Gibson R. L. (2005) Geochemical and petrographic characteristics of impactites and Cretaceous target rocks from the Yaxcopoil-1 borehole, Chicxulub impact structure, Mexico: Implications for target composition. *Meteorit. Planet. Sci.* **40**, 1513–1536.

Tuchscherer M. G., Reimold W. U., Gibson R. L., de Bruin D. and Späth A. (2006) Major and trace element compositions of melt particles and associated phases from the Yaxcopoil-1 drill core, Chicxulub impact structure, Mexico. *Meteorit. Planet. Sci.* **41**, 1361–1379.

Urrutia-Fucugauchi J., Marin L. and Trejo-Garcia A. (1996) UNAM scientific drilling program of Chicxulub impact structure-Evidence for a 300 kilometer crater diameter. *Geophys. Res. Lett.* **23**, 1565–1568.

Urrutia-Fucugauchi J., Camargo-Zanoguera A., Perez-Cruz L. and Perez-Cruz G. (2011) The Chicxulub multi-ring impact crater, Yucatan carbonate platform, Gulf of Mexico. *Geofis. Int.* **50**, 99–127.

Vermeesch P. (2018) IsoplotR: a free and open toolbox for geochronology. *Geosci. Front.* **9**, 1479–1493.

Völkening J., Walczyk T. and Heumann K. G. (1991) Osmium isotope ratio determinations by negative thermal ionization mass-spectrometry. *Int. J. Spectrom. Ion Process.* **105**, 147–159.

Wallace M. W., Gostin V. A. and Keays R. R. (1990) Acraman impact ejecta and host shales: Evidence for low-temperature mobilization of iridium and other platinoids. *Geology* **18**, 132–135.

Walker J. W., Prichard H. M., Ishiwatari A. and Pimentel M. (2002) The osmium isotopic composition of convecting upper mantle deduced from ophiolite chromites. *Geochim. Cosmochim. Acta* **66**, 329–345.

Ward W. C., Keller G., Stinnesbeck W. and Adatte T. (1995) Yucatán subsurface stratigraphy: Implications and constraints for the Chicxulub impact. *Geology* **23**, 873–876.

Whalen M. T., Gulick S. P. S., Lowery C. M., Bralower T. J., Morgan J. V., Grice K., Schaefer B., Smit J., Ormö J., Wittmann A., Kring D. A., Lyons S., Goderis S. and IODP-ICDP Expedition 364 Scientists (2020) Winding down the Chicxulub impact: The transition between impact and normal marine sedimentation near ground zero. *Mar. Geol.* **430** 106368.

Wimpenny J., Gannoun A., Burton K. W., Widdowson M., James R. H. and Gislason S. R. (2007) Rhenium and osmium isotope and elemental behaviour accompanying laterite formation in the Deccan region of India. *Earth Planet. Sci. Lett.* **261**, 239–258.

Xie X., Yan M., Wang C., Li L. and Shen H. (1989) Geochemical Standard Reference Samples GSD 9–12, GSS 1–8 and GSR 1–6. *Geostandards Newslett.* **13**, 83–179.

Zhao J., Xiao L., Gulick S. P. S., Morgan J. V., Kring D. A., Urrutia-Fucugauchi J., Schmieder M., de Graaff S. J., Wittmann A., Ross C. H., Claeys P., Pickersgill A., Kaskes P., Goderis S., Rasmussen C., Vajda V., Ferrière L., Feignon J.-G., Chenot E., Perez-Cruz L., Sato H., Yamaguchi K. and IODP-ICDP Expedition 364 Scientists (2020) Geochemistry, geochronology and petrogenesis of Maya Block granitoids and dykes from the Chicxulub Impact Crater, Gulf of México: Implications for the assembly of Pangea. *Gondwana Res.* **82**, 128–150.

Associate editor: Marc Norman

SUPPLEMENTARY MATERIAL

Search for a meteoritic component within the impact melt rocks of the Chicxulub impact structure peak ring, Mexico

Jean-Guillaume Feignon[1], Toni Schulz[1,2], Ludovic Ferrière[3], Steven Goderis[4], Sietze J. de Graaff[4,5], Pim Kaskes[4,5], Thomas Déhais[4,5], Philippe Claeys[4] and Christian Koeberl[1]

[1]Department of Lithospheric Research, University of Vienna, Althanstrasse 14, A-1090 Vienna, Austria.

[2]Institute for Geology und Mineralogy, University of Cologne, Zülpicher Strasse 49b, 50674 Cologne, Germany.

[3]Natural History Museum, Burgring 7, 1010 Vienna, Austria.

[4]Research Unit: Analytical, Environmental & Geo-Chemistry, Department of Chemistry, Vrije Universiteit Brussel, AMGC-WE-VUB, Pleinlaan 2, 1050 Brussels, Belgium.

[5]Laboratoire G-Time, Université Libre de Bruxelles, Av. F.D. Roosevelt 50, 1050 Brussels, Belgium.

*Corresponding author: jean-guillaume.feignon@univie.ac.at

i

SUPPLEMENTARY TEXT

I) PETROGRAPHIC DESCRIPTION OF SAMPLE MATERIAL

The sample nomenclature used in this study corresponds to Core#Section#_Top(cm)–Bottom(cm) and indicates the exact sampling interval (see also, Morgan et al., 2017), while the centimeters indicate the distance in a core section, from the top of the section. In total, thirty-three samples were investigated for their major and trace elements, i.e., twenty-five impact melt rock samples, both from the upper impact melt rock (UIM, n = 15), and from the LIMB (n = 10), suevites (n = 2), and samples of pre-impact lithologies (n = 6, i.e., two granite samples, one amphibolite (clast), one dolerite, one dacite, and one felsite). Among these thirty-three samples, seventeen were further investigated for their HSE concentrations and Re–Os isotope compositions, i.e., impact melt rocks (i.e., both UIM (n = 7) and LIMB (n = 5) samples), suevite samples (n = 2), and samples of pre-impact lithologies (n = 5, i.e., two granite samples, one amphibolite (clast), one dacite, and one dolerite). This selection allows to estimate the contribution of pre-impact lithologies to the HSE abundances and Re–Os isotope characteristics of impact melt rocks, and to a lesser extent, suevites, and possibly identify any additional contribution of a meteoritic component. Detailed petrographic descriptions of the different samples are also provided in the supplementary Table S1.

I.1) Suevite

Two suevite samples were selected in the framework of this study. They are located in the bedded suevite (sample 41R1_106–108, 620.35 mbsf) and in the graded suevite (sample 58R3_8–10.5, 673.68 mbsf) sections, according to the classification of the suevite unit by Kaskes et al. (2022). Suevite sample 41R1_106–108 is macroscopically gray-green in color, fine-grained (clast size < 0.3 cm, and generally < 0.1 cm), well-sorted, with a bedding clearly visible (see Fig. 3). The clastic matrix consists of micritic carbonate, while angular, green-brownish vitric melt clasts (i.e., quenched melt) are commonly observed, together with carbonate clasts, rare ballen silica of type V (i.e., chert-like recrystallized ballen quartz; Ferrière et al., 2009), and shocked (PDFs are visible) and toasted quartz grains. The suevite sample 58R3_8–10.5 (Figs. 3a and S1a) is characterized by a larger clast size (generally between ~0.5 and ~1.0 cm in size), while the matrix is clastic, made of fragments of carbonate, quartz, and aluminosilicates. Clasts comprise brownish and altered vitric melt exhibiting reaction rims with the matrix, carbonate, and impact melt rock (clast-poor, with abundant microcrystalline plagioclase and rarer pyroxene within the groundmass),

ii

carbonate and mineral clasts consisting of shocked quartz grains or plagioclase. A detailed petrographic description of the M0077A suevite sequence is given in Kaskes et al. (2022).

I.2) Impact melt rock clasts in suevite and upper impact melt rock unit (UIM)

      The impact melt samples were selected between 707.22 mbsf and 745.33 mbsf. The two upper samples (i.e., 80R2_126–128 and 83R1_22–24.5, at 707.22 mbsf and 712.30 mbsf, respectively) consist of impact melt rock clasts included in the suevite unit. The six UIM samples located between 722.71 and 737.10 mbsf consist of black impact melt rock intermingled with a green phase, forming schlieren texture (Figs. 3b–S1a). Finally, the last seven UIM samples, located between 737.78 and 745.33 mbsf, consist only of black impact melt rock. Some of the investigated samples were in contact with large granitoid clasts, up to several centimeters in size, embedded in the impact melt, especially at the base of the UIM (Fig. 3c), but care was taken to only investigate the impact melt rocks, excluding those large clasts.

      Macroscopically, impact melt clast samples 80R2_126–128 and 83R1_22–24.5 are relatively clast poor (<10 vol%), with clasts less than 0.5 cm in size, and exhibit a greenish color due to alteration. Microscopically, they are characterized by a high abundance of brownish clay minerals in the matrix. The clasts are mainly undigested carbonate and quartz, with ballen silica of type V. For simplicity, as these two samples do not exhibit distinct petrographic features relative to the other UIM samples, the impact melt rock clasts are included in the UIM, except where specified.

      In the UIM samples, the black impact melt rock appears macroscopically relatively homogeneous and clast-poor (~1.5–7 vol%, Figs. 3c and S1c), with the clast size generally being less than 1 cm. The matrix of the black impact melt rock appears to be either glassy (vitric) or is composed of microcrystalline, and acicular plagioclase (<50 µm), with microlites of pyroxene, to a lesser extent, as well as some clay and opaque minerals. For some samples, the microlites and undigested clasts are oriented along the flow direction, indicating a hyalopilitic texture. Mainly shocked, undigested to partially digested and altered granitoid clasts (i.e., displaying rounded to angular shapes) were observed in the investigated samples. A few undigested and partially digested gneiss and dolerite clasts were also seen, but in a lower proportion (<0.5 vol%). Mica-schist clasts were also documented in the UIM (Morgan et al., 2017), but were not observed in our samples. Vesicles are generally filled with sparitic calcite. Mineral clasts, probably derived from the

crystalline basement rocks, mainly consist of quartz, feldspars (i.e., plagioclase and K-feldspar), with more rarely also carbonates (see also de Graaff et al., 2022). Reaction rims are commonly observed around both crystalline and mineral clasts, indicating a reaction with the groundmass material. Shock metamorphic features, i.e., several sets of planar deformation features (PDFs), and toasting is common in quartz grains (either included in pre-impact basement rock clasts or as undigested quartz grains within the impact melt rock). Additionally, ballen silica of type V were also detected (Fig. S1c).

The green phase, forming the main component of the upper part of the UIM as well as the schlieren texture, highlighting the immiscibility with the black impact melt rock, is fine-grained with phyllosilicates (exhibiting a radial disposition in some areas), which may be saponite-like sheet silicate according to Slivicki et al. (2019), and sparitic calcite (from microcrystalline to more than 1 mm in size) representing the main mineral phases. The calcite grain sizes increase from microcrystalline at the contact with the black impact melt rock to millimeter-sized towards the center of the green phase. Opaque minerals are also observed within the green phase. Other phases, such as garnet and sporadic fluorite, were also documented in the green phase (Slivicki et al., 2019; Schulte et al., 2021), but not detected in our samples. In addition, brownish, angular to sub-angular clasts of altered impact melt rock were seen. Rare calcite veins crosscutting both the black impact melt rock and the green phase also occur.

I.3) Lower impact melt-bearing unit (LIMB)

The two upper samples from the LIMB (i.e., 202R2_48.5–53, at 1026.31 mbsf, and 265R2_9–11, at 1216.45 mbsf) were taken from thin impact melt dikes, less than 30 cm thick, crosscutting the granite unit. The remaining samples belong to the main body forming the LIMB between 1224.44 and 1334.38 mbsf, characterized by an alternation of impact melt rocks, polymict impact breccias, and centimeter-to-meter-sized basement (granite) clasts.

At the macroscopic scale, the impact melt rock of this unit is black, whereas brecciated material appears more or less gray. The LIMB displays large textural variations, from microcrystalline, clast-poor impact melt, to brecciated basement and impact melt rock material. Flow banding is observed in some samples (e.g., 265R2_9–11, 267R3_52.5–55.5, 277R2_25–27, and 294R1_67.5–70) and absent in other ones. The texture of the matrix varies from microcrystalline (plagioclase and pyroxene microlites) to microbrecciated crystalline basement

material. Several types of clasts are observed in the investigated samples, i.e., mineral clasts (quartz, feldspars, and pyroxenes) derived from the crystalline basement, shocked granitoid (common), gneiss, and dolerite (Figs. 3d–e, and S1d), similar to what have been previously described in Morgan et al. (2017) and in de Graaff et al. (2022). Quartz grains embedded in the LIMB, and the granitoid clasts, are shocked, with PDFs in quartz grains. Generally, toasted quartz is also observed, but is rarer than in the UIM. No ballen silica was observed in the investigated LIMB samples. Additionally, no carbonate clasts were reported, with only some occurrence of secondary calcite veins, which is in agreement with Kring et al. (2020), and de Graaff et al. (2022). Clast size in the investigated samples ranges from less than 1 millimeter to up to several centimeters.

Sample 265R2_9–11 (1216.45 mbsf) is quite distinct from the other LIMB samples investigated. It is derived from a ~10 cm thick dike cross cutting the granite unit and represents a partially melted dolerite dike (see Fig. 3d). At proximity to the contact with the granite, the impact melt is clast-poor and displays infiltrations within the dolerite (made of equigranular laths of plagioclase and pyroxene, and sheet silicates forming pseudomorphs after olivine) towards the center of the dike. With increasing distance from the impact melt, the dolerite appears "pristine" (i.e., non-melted), while small acicular plagioclases and pyroxenes within the melt matrix are also observed.

I.4) Pre-impact lithologies

Several different pre-impact lithologies have been sampled, namely granite, dolerite, amphibolite, dacite, and felsite. While the granite is the main lithology forming the "lower peak ring" section, the other pre-impact lithologies occur either as centimeter-to-meter-sized undigested clasts in suevites and impact melt rocks, or as dikes, having thicknesses from few centimeters to several meters, cross-cutting the granite unit (see also, Morgan et al., 2016, 2017). Detailed petrographic descriptions of the pre-impact lithologies are given in Feignon et al. (2020, 2021), and in de Graaff et al. (2022).

Two granite samples (136R2_20–25, and 200R3_12.5–15, at 851.37 and 1020.96 mbsf, respectively) were selected from the main granite unit. The dolerite (140R2_5–8 at 854.59 mbsf), felsite (105R2_83–89 at 772.83 mbsf), and dacite (238R1_101–103.5 at 1135.05 mbsf) samples are from dikes crosscutting the granite unit. Finally, the amphibolite sample (80R2_61–63.5 at

v

706.57 mbsf) is a clast embedded in a large, ~40-cm-sized impact melt rock clast (from which the 80R2_126–128 sample originates), itself included in the graded suevite.

The two selected granite samples (136R2_20–25 and 200R3_12.5–15) are coarse-grained, equigranular, and phaneritic. The bulk mineral assemblage is mainly composed of K-feldspar, plagioclase (often sericitized), quartz, and, to a lesser extent, biotite which is often chloritized (Figs. 3f–S1f). Mineral grains are in general undeformed. The grain size varies from ~0.2 cm to up to ~1 cm. Shock metamorphic features are visible in most rock-forming minerals. Detailed petrographic descriptions of granite and associated shock metamorphic features can be found in Timms et al. (2019), Cox et al. (2020), Feignon et al. (2020, 2021), Pittarello et al. (2020), and de Graaff et al. (2022).

The dolerite sample (140R2_5–8) is derived from a ~1.8 m pre-impact dike crosscutting the granite unit. It is holocrystalline, porphyritic, and fine-grained, with a mineral size of ~0.2–0.3 mm and up to 0.5 mm in the matrix and between 2 and 3 mm for the phenocrysts. The main phenocrysts are subhedral to euhedral plagioclase and pyroxene, with plagioclase exhibiting the largest and most abundant phenocrysts. Pyroxene crystals are heavily fractured and altered. The dolerite also contains serpentinized olivine, i.e., olivine which was replaced by mafic sheet silicates. Opaque and spinel-group (possibly picotite) minerals were also observed (see Fig. 5e–f), in agreement with previous observations of Schmieder et al. (2017a, 2017b) and de Graaf et al. (2022). The matrix is composed of finely crystallized pyroxene, greenish amphibole poikilitically enclosing plagioclase laths, and less abundant opaques minerals (Fig. S1e).

The felsite sample (105R2_83–89) is from a ~60 cm thick dike crosscutting the upper part of the granite unit, sampled close to the contact with the granite. This dike was at first identified as a clast-poor impact melt rock (Morgan et al., 2017) and later reclassified as felsite (de Graaff et al., 2022). It is fine-grained, porphyritic, with the phenocrysts (generally 0.1–0.5 mm in size) consisting of feldspars (i.e., K-feldspar and plagioclase), rare pyroxene, quartz (shocked with up to two PDF sets), and also zoisite. The matrix is microcrystalline and mainly made of acicular plagioclase.

The dacite (238R1_101–103.5) was sampled from a ~1-m-thick dike crosscutting the granite unit. Its texture is porphyritic, holocrystalline, with subhedral to euhedral plagioclases up to 1 cm in size. Plagioclase crystals, which are the most abundant mineral phase, are found either as single tabular crystals or forming aggregates, exhibiting common zoning, and often sericitized.

Quartz grains up to 0.5 cm in size are also observed and shocked (PDFs are visible). The matrix is mainly composed (in decreasing abundance) of fine-grained (~100–600 μm) plagioclase, quartz, and chloritized biotite.

The amphibolite clast sample (80R2_61–63.5) is holocrystalline, equigranular, and fine-grained (~100–400 μm), mainly composed of amphibole, plagioclase, and more rarely of quartz and pyroxene (see Fig. S2). Quartz grains are shocked, with at least one set of PDFs, while amphiboles are highly fractured. A few reddish veinlets crosscut the amphibolite.

II) MAJOR ELEMENT ANALYSIS

Major element concentrations were measured by means of glass bead-based X-ray fluorescence (XRF) following the methodology outlined in Feignon et al. (2021). The analyses were performed using a PHILIPS PW2404 X-ray spectrometer at the Department of Lithospheric Research (University of Vienna, Austria) with a super-sharp end-window tube and a Rh-anode.

The element concentrations were determined using calibration curves established using international reference materials SG1-A (granite), TDB-1 (diabase), BHVO-2 (ocean island basalt), and JH-1 (hornblendite). Accuracy and precision values (in wt.%) are about 0.6 for SiO_2, 0.5 for Fe_2O_3, 0.3 for Al_2O_3, 0.2 for Na_2O, 0.05 for CaO, 0.04 for MgO, 0.02 for TiO_2, K_2O, and P_2O_5, and 0.01 for MnO. More details on instrumentation of bulk XRF measurements can be found in, e.g., Nagl and Mader (2019) and Duboc et al. (2019).

III) MAJOR ELEMENT VARIATIONS

Due to the large variation in loss on ignition (LOI) observed between the different lithologies (i.e., from <1 wt.% for the amphibolite clast to nearly ~18 wt.% in suevite) the major element data presented here and in Fig. S3 were recalculated on a LOI-free basis, allowing a better disentanglement of the impact melt rock and suevite components. Non-recalculated major element data for all the investigated samples are provided in Table S2.

Suevite samples display a clear enrichment in CaO (up to 28.6 wt.% CaO in sample 41R1_106–108) relative to impact melt rocks (with the exception of two UIM samples) and the investigated pre-impact lithologies, indicating a significant carbonate component contribution. Consequently, other major element contents are relatively low, with 45.7–53.7 wt.% SiO_2, 10.6–

vii

12.5 wt.% Al_2O_3, or similar to UIM samples with 4.10–4.60 wt.% Fe_2O_3, 4.45–5.14 wt.% MgO, and 0.44–0.52 wt.% TiO_2.

The impact melt rocks (both UIM and LIMB samples) mainly have a trachyandesitic composition as is indicated by the total alkali versus SiO_2 (TAS) diagram (Fig. S3a), however, several outliers are present. All the investigated samples broadly follow the alkaline series (Fig. S3a).

The UIM samples display clear variations in SiO_2, total alkalis (Na_2O+K_2O), CaO, and, to a lesser extent, MgO contents, with 50.5–66.3 wt.%, 5.86–9.25 wt.%, 3.20–19.2 wt.%, and 1.21–6.78 wt.%, respectively. It is worth noting that three UIM samples (88R1_12–14.5, 89R1_59–61.5, and 92R2_89–91.5), characterized by a pronounced schlieren component, are clearly enriched in CaO (13.3–19.2 wt.%) relative to the other UIM samples (3.20–7.58 wt.%). Other major elements, such as Al_2O_3, Fe_2O_3, and TiO_2, show more limited variations, with contents of 12.1–18.3 wt.%, 3.61–6.18 wt.%, and 0.56–0.86 wt.%, respectively.

The LIMB samples (excluding sample 265R2_9–11) display less variation in SiO_2 and total alkali contents than the UIM samples (54.5–68.5 and 6.44–8.61 wt.%, respectively), whereas significant variability in Fe_2O_3 and MgO content (Figs. S3c–d) is seen from one sample to another, ranging from 3.83–9.33 wt.%, and 2.81–8.35 wt.%, respectively. The Fe_2O_3, MgO, and, to a lesser extent, TiO_2 concentrations (0.32–1.04 wt.%) in the LIMB form a relative continuum between dolerite and granite composition, i.e., a continuous decrease with increasing SiO_2 content. The CaO content in all the LIMB samples is lower than in the UIM, with limited variation (1.49–3.32 wt.%). Contents of Al_2O_3 have a narrow range, i.e., 14.3–16.8 wt.%. Sample 265R2_9–11 represents a clear outlier, with a mafic composition similar to dolerite, i.e., having the lowest SiO_2 and total alkali contents (48.7 and 4.11 wt.%, respectively), combined with the highest Fe_2O_3 and MgO contents (13.3 and 14.2 wt.%, respectively) of all the investigated LIMB samples. This is in agreement with petrographic observations made on this specific sample (i.e., a partially melted dolerite dike).

Concerning the pre-impact lithologies, two clear end-members are apparent: (1) the mafic dolerite (plotting in the basalt field in the TAS diagram; Fig. S3a), the least evolved lithology with 47.1 wt.% SiO_2 and 3.01 wt.% total alkali, a high Fe_2O_3 and MgO contents, with 12.6 and 12.1 wt.%, respectively, and the highest TiO_2 concentration of all the investigated samples, with 1.19 wt.%; and (2) the evolved granites, displaying 74.6–75.4 wt.% SiO_2 and 8.15–8.25 wt.% total

viii

alkali, and the lowest amounts of Fe_2O_3 (0.68–1.24 wt.%), MgO (0.33–0.49 wt.%), CaO (1.28–1.55wt.%), and TiO_2 (0.12–0.24 wt.%) compared to the other samples. The amphibolite is also relatively mafic, between the basaltic and the trachybasaltic compositions, with 51.7 wt.% SiO_2, 5.10 wt.% total alkali, 10.12 wt.% Fe_2O_3, and 7.46 wt.% MgO. The felsite represents an intermediate composition (trachyandesite) and is characterized by the highest amount of total alkali of all pre-impact lithologies (i.e., 8.72 wt.%), and a SiO_2 content of 54.9 wt.%. Finally, the dacite sample is the second most evolved pre-impact lithology after the granites, displaying a trachytic composition in the TAS diagram, with 68.9 wt.% SiO_2 and 8.50 wt.% total alkali, and low Fe_2O_3 (2.89 wt.%) and MgO (1.43 wt.%). It is worth noting that all the investigated magmatic pre-impact lithologies have CaO contents below 10 wt.% (i.e., 1.28–8.26 wt.%).

IV) TRACE ELEMENT VARIATIONS

Trace element compositions of the impact melt rocks (i.e., both UIM and LIMB samples), suevites, and pre-impact lithologies are provided in Table S3. The different lithologies (excluding the dolerite, the dacite, and the felsite, which are discussed below) display relatively similar CI-chondrite-normalized patterns, with limited variations between samples (Fig. S4). In general, CI-chondrite normalized patterns relatively similar to that of the granites are observed (Feignon et al., 2021). However, the heavy rare earth elements (HREE), from Tb to Lu, are enriched and display a relatively flat chondrite-normalized pattern in impact melt rocks, suevites, and amphibolite, compared to the granites, which display a decreasing abundance for the HREE. In impact melt rock, suevite, and amphibolite samples, fluid-mobile elements, such as Ba, Sr, Th, and U, are enriched from 100 to up to 1,000 times the CI-chondritic values, as well as La and Ce which display an enrichment relative to CI-chondritic values between ~40 and ~200 times, while Nb and Ta are relatively depleted compared to the neighboring elements. A significant negative Pb anomaly is also observed for all the investigated samples, except in the case of granite 136R2_20–25 where the negative Pb anomaly is less pronounced. Only two LIMB samples display a distinct pattern, i.e., sample 267R3_52.5–55.5, which is depleted in HREE relative to the other impact melt rock and suevite samples (i.e., showing a pattern similar to the granites), and sample 265R2_9–11, with depletions in Rb, Ba, and Th, relative to the other impact melt rock and suevite samples, which is comparable to the pattern observed for dolerite. Suevite sample 41R1_106–108 displays a clear enrichment in Sr. The dolerite sample is relatively depleted in Rb, Ba, and Th compared to the

granite compositions, and the REE pattern is similar to those of impact melt rocks, suevites, and amphibolite, with the HREE being enriched compared to the granites. The dacite shows a pattern relatively similar to those of the granites, being slightly enriched in La, Ce, and Sr, while the HREE are similar to those of the most enriched granites. Of the two granites investigated here, only sample 136R2_20–25 displays depletions in La and Nd relative to the granite composition from Feignon et al. (2021). Finally, the felsite shows a clear enrichment in nearly all the trace elements, having a clear distinct pattern from the other lithologies. Only Nb, Ta, and Pb are similar to the other investigated samples. The felsite is also slightly depleted in Zr and Hf relative to the neighboring trace elements.

x

SUPPLEMENTARY FIGURES

xi
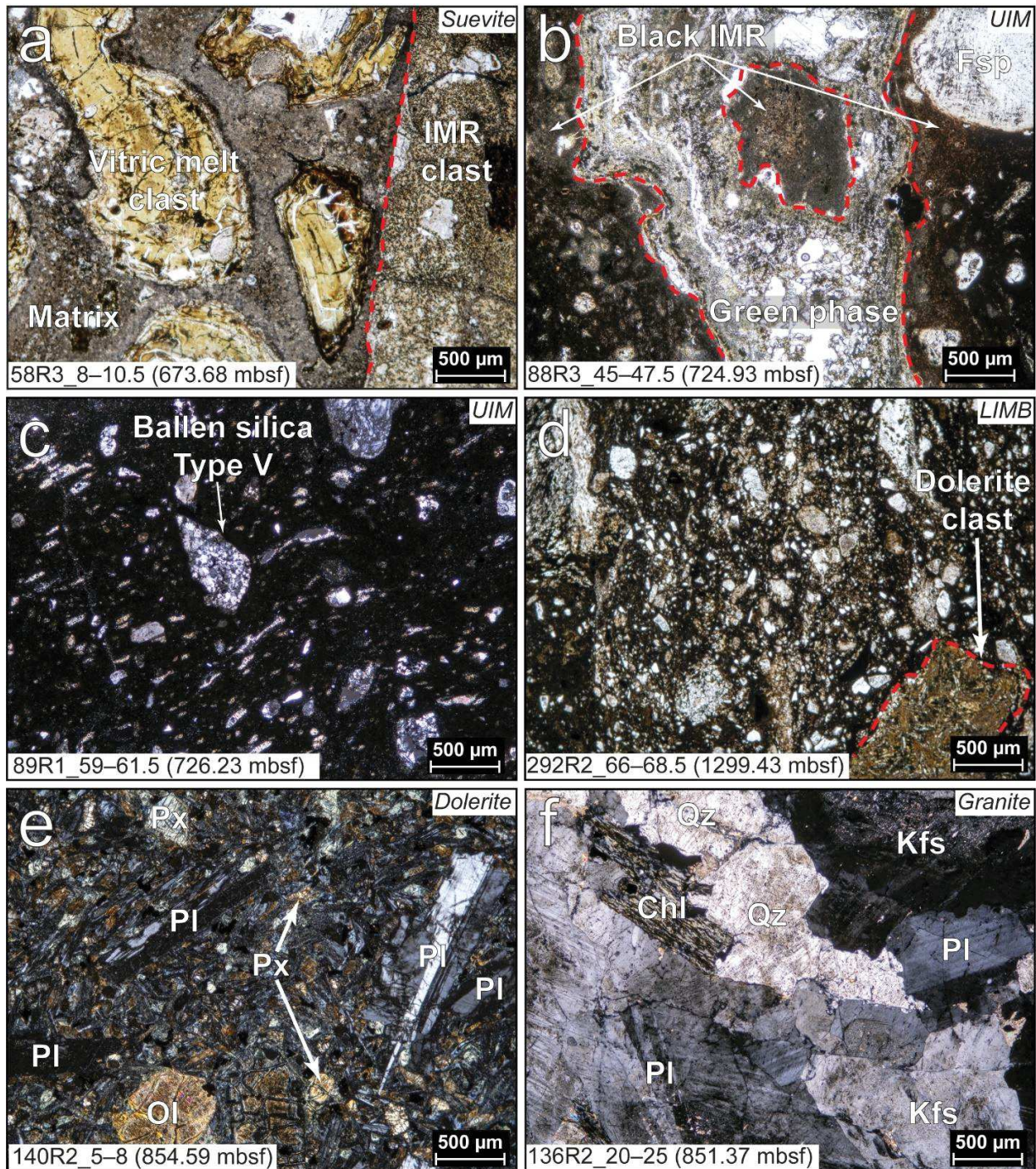
Figure S1. Thin section photomicrographs (a, b, and d in plane polarized light, and c, e, and f in cross polarized light). a) Microphotograph of suevite sample shown in Fig. 3a, mainly composed of altered vitric melt clasts embedded in a clastic matrix. Mineral clasts are also present within the matrix, such as quartz and calcite. A large impact melt rock (IMR) clast is located on the right side. b–c) Upper impact melt rock samples with (b) displaying a green phase (carbonate-rich with reaction rims) area crosscutting the black impact melt rock (IMR). A black impact melt clast is included within the green phase. A rounded, undigested feldspar crystal (Fsp) is visible on the upper right. c) Typical black impact melt rock, clast-poor, with the clasts consisting mainly of undigested minerals, including a ballen silica type V. Additionally, the clasts seem oriented following the flowing direction of the impact melt. d) Lower impact melt-bearing unit sample, clearly enriched in clasts compared to the two previous samples. A large dolerite clast is also included within the impact melt. e) Porphyritic dolerite with large plagioclase (Pl) crystals, the smaller crystals consist mainly of plagioclase and pyroxene (Px). A possible altered olivine (Ol) is also observed due to its typical euhedral shape. f) Typical granite sample with K-feldspar (Kfs), plagioclase (Pl), quartz (Qz) and chlorite (Chl) crystals, with the chlorite probably representing former biotite. The quartz is shocked with at least two sets of planar deformation feature (PDF) sets (difficult to discern at this scale).
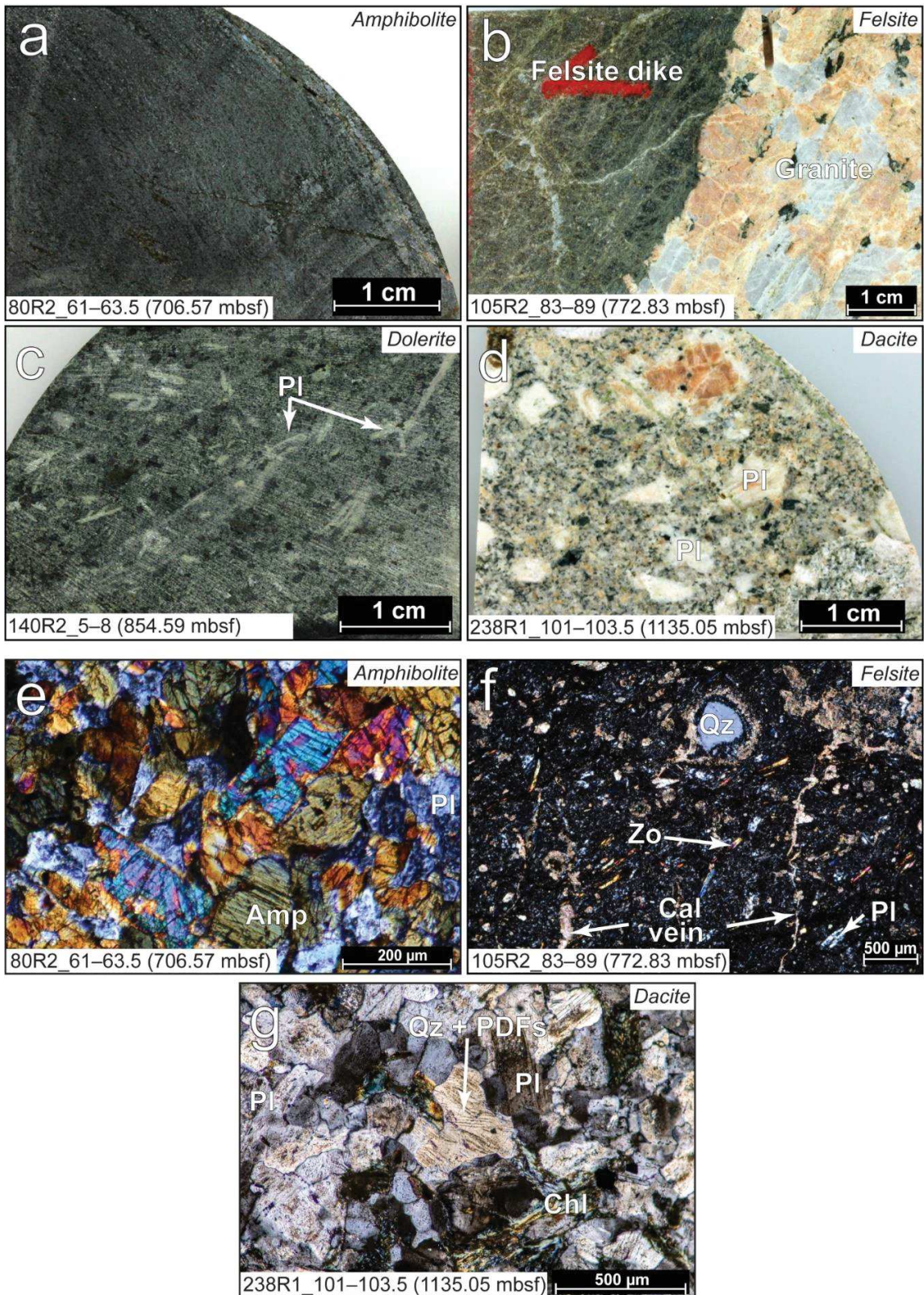
Figure S2. Macro- and microphotographs of pre-impact lithogies. (a) Macrophotograph of investigated amphibolite clast. The texture is homogeneous and microcrystalline. (b) Macrophotograph of a felsite dike, in contact with granite. The felsite is heavily fractured. The fractures are commonly filled by calcite. In contrast to the neighboring granite, the minerals are not easily visible at the macroscopic scale. (c) Macrophotograph of a dolerite sample displaying porphyritic texture. The main mineral phases are pyroxene and plagioclase (Pl). (d) Macrophotograph of a dacite sample. Plagioclase (Pl) is the main mineral phase and the texture is porphyritic. Quartz and biotite (commonly chloritized) are the other main mineral phases. Mineral fracturing is common. (e) Microphotograph (crossed polars) of amphibolite. The texture is equigranular, with amphibole (Amp) and plagioclase (Pl) as the main components. (f) Microphotograph (crossed polars) of felsite sample, finely crystallized with thin plagioclase (Pl) and zoisite (Zo). Quartz (Qz) is also observed (uncommon) and is here surrounded by a calcite reaction rim. The quartz grain is shocked with at least two sets of planar deformation features (barely visible here). Calcite (Cal) is also abundant in the form of veins crosscutting the sample. (g) Microphotograph (crossed-polars) of the dacite matrix, revealing abundant quartz (Qz) and plagioclase (Pl) minerals, associated with chlorite (Chl, former biotite). Sericitization of plagioclase is visible, while the quartz grain in the center display at least two visible sets of planar deformation features (PDFs), typical of shock metamorphism.

xiv
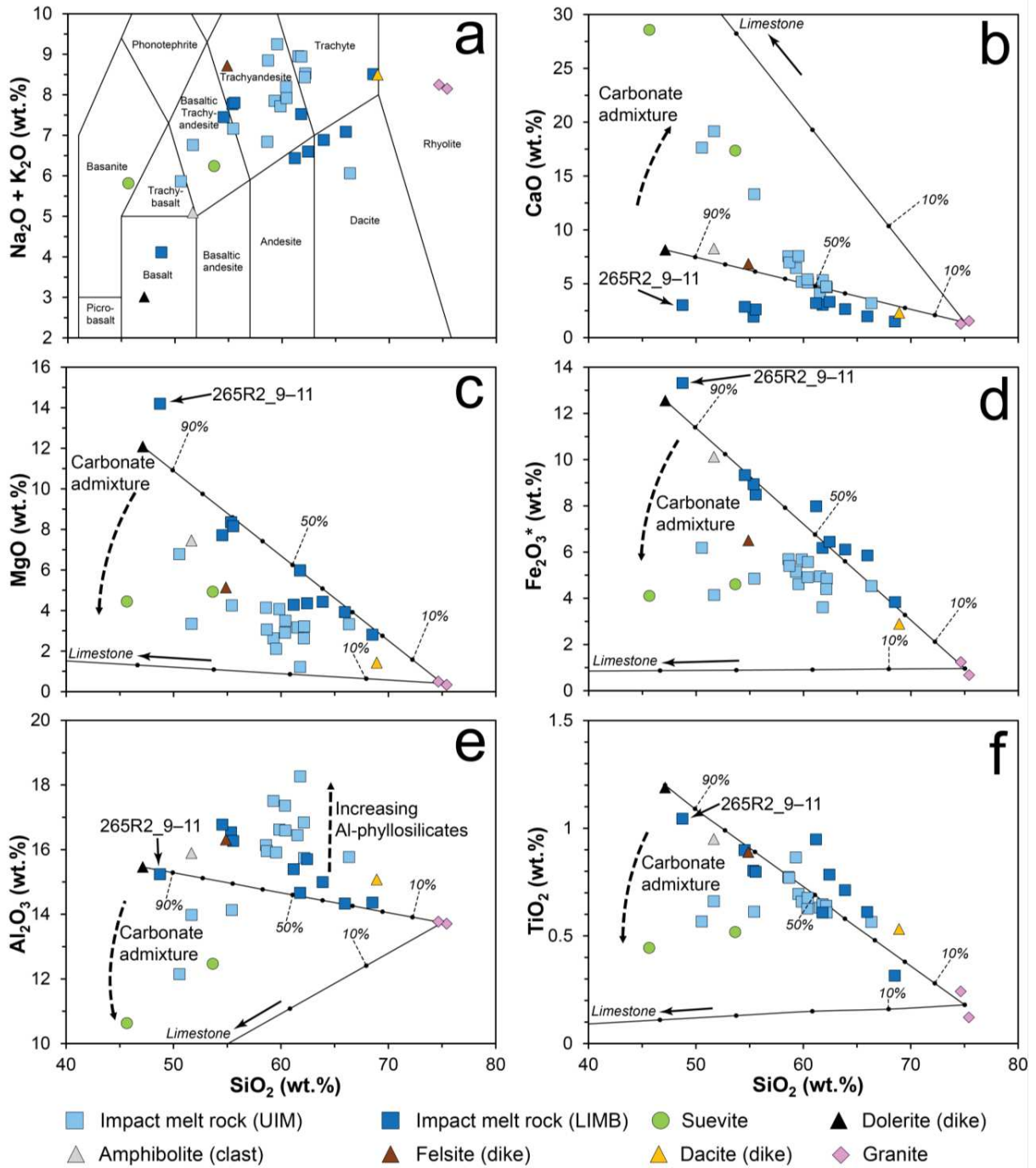
Figure S3. a) Total alkalis versus SiO$_2$ (TAS) diagram (upper left) modified from Le Bas et al. (1986). b–f) Harker diagrams of CaO, MgO, Fe$_2$O$_3$* (total ferrous Fe), Al$_2$O$_3$, and TiO$_2$ versus SiO$_2$ for the investigated UIM, LIMB, suevite, granite, dolerite, amphibolite, felsite, and dacite samples. All the data is recalculated on a LOI-free basis. Two mixing lines are drawn: (1) between the average of the two granites and the dolerite compositions, and (2) between the average granite composition and the average limestone clast composition (i.e., recalculated on a LOI-free basis: SiO$_2$: 4.06 wt.%, TiO$_2$: b.d.l. (absence of TiO$_2$ was assumed), Al$_2$O$_3$: 0.44 wt.%, Fe$_2$O$_3$* = 0.74 wt.%, MgO: 2.65 wt.%, and CaO: 90.8 wt.%) recorded by de Graaff et al., (2022).
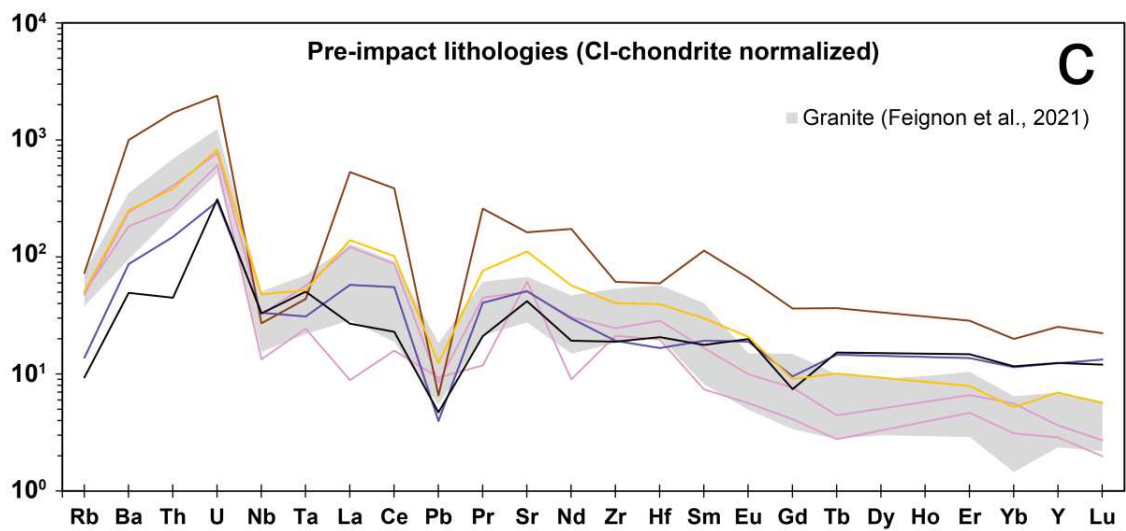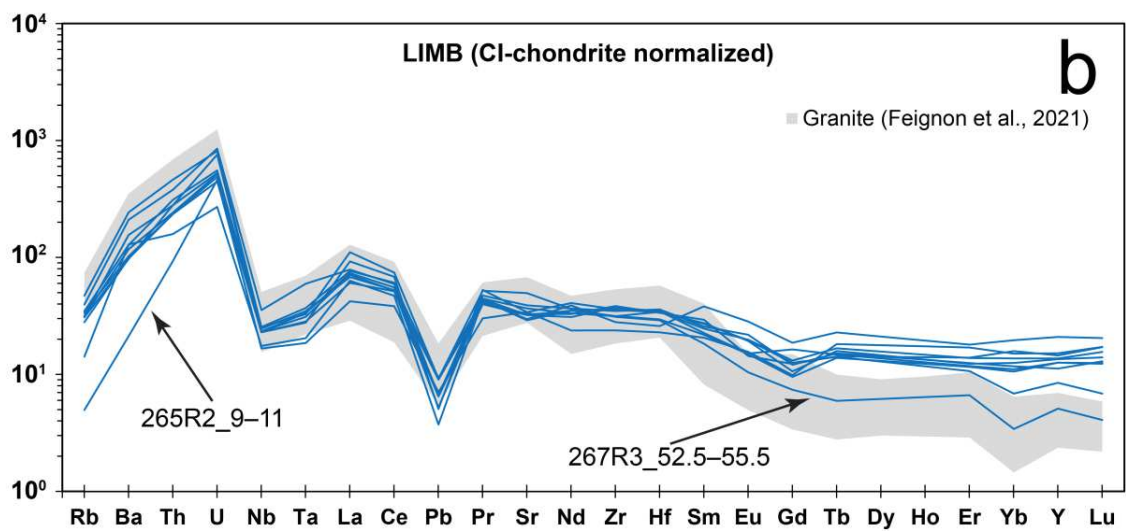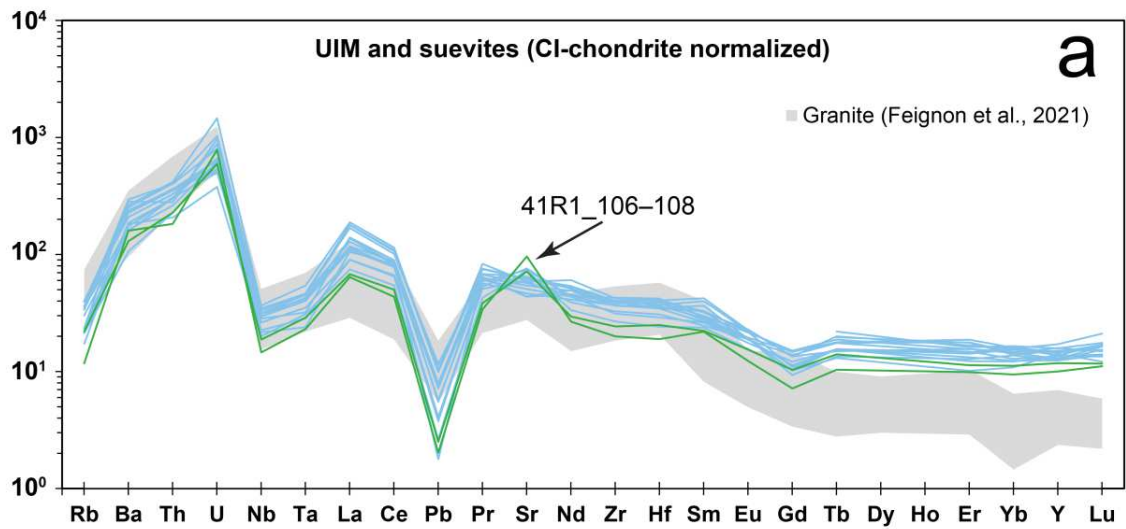
xvi

Figure S4. CI-chondrite-normalized trace element compositions of (a) impact melt rocks from UIM and suevites, (b) impact melt rocks from LIMB, and (c) pre-impact lithologies, with normalization values from McDonough and Sun (1995). The gray area represents the main composition of the granite unit based on Feignon et al. (2021). Investigated impact melt rocks display relatively similar patterns excepted for 265R2_9–11, which is depleted in Rb, Ba, and Th, and for 267R3_52.5–55 which has a HREE pattern similar to those of granite (i.e., depleted relative to the other impact melt rock samples). The upper suevite sample (41R1_106–108) displays a positive anomaly in Sr.
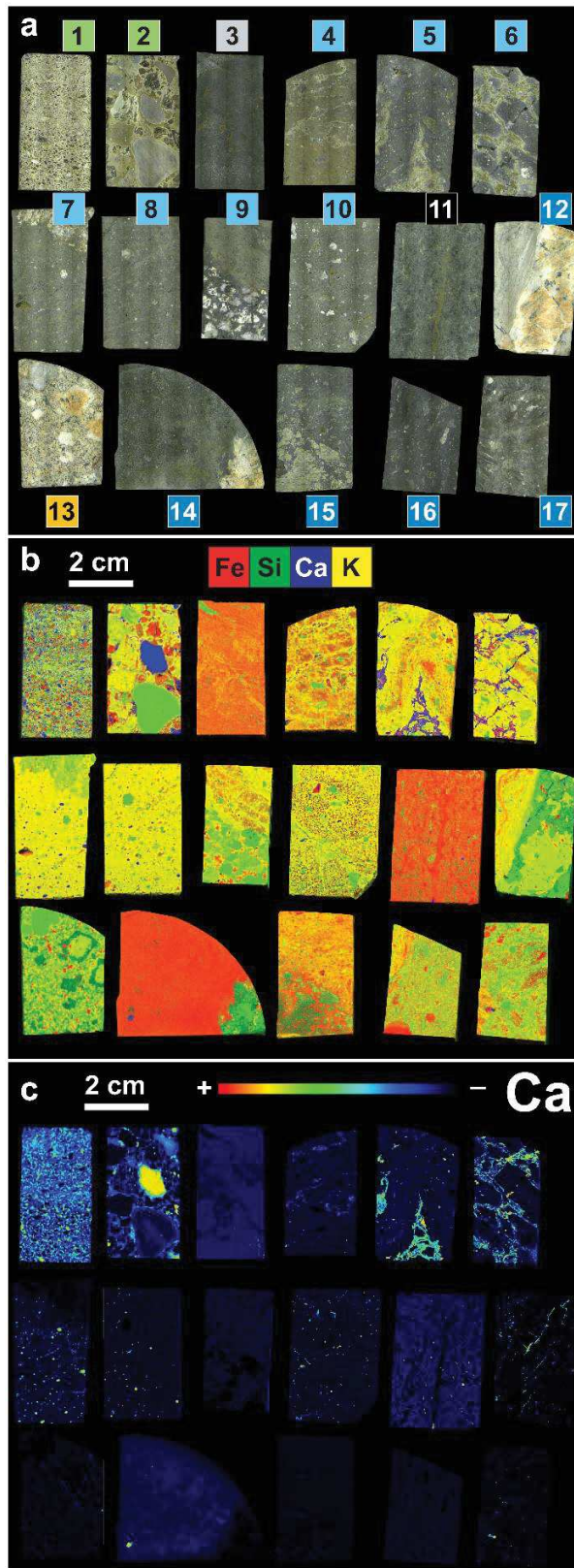
Figure S5. High-resolution micro-X-ray fluorescence (µXRF) mapping results. a) Scanned image overview of the 17 M0077A impactite and target lithology samples, from upper left to lower right: two suevites, one amphibolite, seven UIM samples, one dolerite, one LIMB, one dacite, and four LIMB samples. Sample details are indicated below. b) Multi element map showing the distribution of Fe, Si, Ca, and K. c) Single element heatmap of Ca. Sample details with sample ID, lithology/unit, and core depth: 1) 41R1_106–108 (bedded suevite unit, 620.4 mbsf); 2) 53R3_6–8 (graded suevite unit, 673.7 mbsf); 3) 80R2_61–63.5 (amphibolite, 706.6 mbsf); 4) 83R1_22–24.5 (UIM, 712.3 mbsf); 5) 88R3_45–47.5 (UIM, 724.9 mbsf); 6) 89R1_59–61.5 (UIM, 726.2 mbsf); 7) 91R1_102–104.5 (UIM, 732.8 mbsf); 8) 93R1_21–23.5 UIM, 738.1 mbsf); 9) 93R2_11–12.5 (UIM, 739.1 mbsf) ; 10) 95R2_45–47.5 (UIM, 745.3 mbsf); 11) 140R2_5–8 (dolerite, 854.6 mbsf); 12) 202R48.5–53 (LIMB, 1026.3 mbsf); 13) 238R1_101–103.5 (dacite, 1135.1 mbsf); 14) 265R2_16–19 (LIMB, 1216.6 mbsf, from the same LIMB dike as sample 265R2_9–11); 15) 277R1_88–92 (LIMB, 1253.3 mbsf); 16) 292R2_66–68.5 (LIMB, 1299.4 mbsf); 17) 303R3_22.5–25 (LIMB, 1334.4 mbsf).

SUPPLEMENTARY TABLES

Table S1. Thin section petrographic descriptions of the investigated samples. Samples highlighted in grey were selected for HSE and Re–Os isotopic analysis.

Sample	Depth (mbsf)	Description
Amphibolite clast		
80R2 61–63.5 (amphibolite clast)	706.57	Homogeneous sample, finely crystallized (mineral size 100–400 µm), rare quartz grains, shocked with one PDF set observed, undulose extinction. Minerals seem to be slightly foliated, main minerals are plagioclase, amphibole and px(?), highly fractured (shock microstructures). Amphibolite clast
Impact melt rocks (UIM)		
80R2_126–128	707.2	No thin section available. Macrosample greenish, possible flowing structure is visible. Clast poor, alteration is significant.
83R1_22–24.5*	712.3	Strongly altered impact melt rock with 1-2 mm thick greenish veins filled with secondary clay minerals. Clast-poor, carbonate clasts and quartz (ballen noticed), clast size is less than 0.5 cm, one clast of granitoid is noted with K-feldspar and quartz, matrix seems to be finely crystallized but overprinted with alteration.
88R1_12–14.5	722.71	Schlieren texture with black and green melts. Black melt: matrix is finely crystallized (microliths of plagioclase) but brownish suggesting some alteration, clast poor (mainly mineral clasts, quartz dominant, less occurrence of K-feldspar) Quartz grains are generally toasted, some ballen silica is observed. Carbonate clasts are rare. Green melt: Calcite/carbonate is the main phase, very fine + strong alteration with clay minerals.
88R3_45–47.5*	724.9	Black melt dominant compared to green melt. Green melt is carbonate rich, strongly altered. Contact between the two melt phases is sharp. Black melt is clast poor, with some mineral orientated in the flowing direction. Clasts are mainly quartz grain (both shocked and ballen silica), rare carbonate grains with reaction rim. Matrix is glassy and very finely cristallized (plagioclase microliths?). Post-impact calcite vein crosscut both melts.
89R1_59–61.5*	726.2	Sample with schlieren of green melt. Black melt is clast poor, one large gneiss clast (2-3 mm) is observed. Mineral clasts mainly quartz, carbonate, one plagioclase observed among the clast. Green melt is similar to previous sample. Quartz grains are shocked and toasted, ballen silica also noticed. Open fractures commonly observed crosscutting the sample at the macroscopic scale.
91R1_102–104.5*	732.8	Black impact melt rock sample. Was in contact with a centimetric granite clast (removed for geochemical investigations). In contrast to previous samples, no flowing texture visible. Clast poor with microlithic matrix. Clast population include quartz grains, carbonates, and felspars. Quartz grains are toasted, ballen silica type V. Calcite veins are crosscuting the sample. The partially digested granitoid clast (1-cm size) is also observed in the thin section. Some greenish areas seem to indicate alteration.
91R2_89–91.5	733.8	No thin section available. Macrosample is black melt rock. Slight greenish area. Large (0.5 cm) gneiss clast). Flowing texture not really visible.
92R2_89–91.5	737.1	Impact melt rock with schlieren of green melt rock. Flowing texture visible in the black melt. Otherwise, similar to samples with schlieren. Carbonate-rich green melt with clay mineral alteration.
92R3_39–41	737.8	Black impact melt rock sample. Zeolite alteration visible at the naked eye. Fiscrete flowing texture in the matrix. However, clasts are undeformed. Similar to previous black melt rock samples.
93R1_21–23.5*	738.1	No thin section available. Homogeneous black melt sample. Clast poor, however seem to exhibit some diffuse greenish alteration of the mesostasis (matrix). Vesicles of 1-3 mm (unfilled). No flowing texture visible.
93R1_121–123.5	739.1	Similar to previous sample in the same section. However, at the macroscopic scale, the sample exhibits a "patchy" texture, with brownish-greenish patches and darker, black areas in between. Seem, as the previous one, to have more vesiculation. Small brownish altered globules are observed. Carbonates are nearly absent. Very clast poor sample (only some undigested quartz grains that are toasted and shocked).
93R2_11–12.5*	739.3	Sample in contact with a granitoid clast (1-2 cm) which was removed for geochemical investigations. The granitoid clast (mainly quartz and K-feldspar, maybe plagioclase) is not fully digested and is crosscut by cataclasite material and the impact melt with recrystallization of plagioclase (acicular). Strong mineral deformation. The impact melt rock is the black melt, clast poor, no carbonate clast observed, otherwise similar to previous black melt samples.

xx

95R1_18–20	744.1	Black impact melt rock in contact with a 3cm granitoid clast partially digested. Still clast poor, but clasts seem more abundant than for samples from the core section 93R1. Clasts are generally millimetric, with quartz grains the main population and, to a lesser extent, feldspar. Diffuse, greenish alteration is also visible.
95R1_84–87	744.8	Similar to previous sample. Patchy texture is observed at the macroscopic scale.
95R2_45–47.5*	745.3	No thin section available. Black impact melt rock with mainly undigested quartz and basement clasts. Similar to previous core section 95R samples.

Impact melt rocks (LIMB)

202R2_48.5–53*	1026.3	Impact melt rock in contact with granite. Clast poor in proximity to the granite, the matrix becomes more brecciated with increasing distance to the granite, with a lesser melt abundance. Undigested quartz mineral clasts (shocked with PDF, some are toasted) are abundant, K-feldspar and calcite are also noticed. In proximity with the granite, the matrix is glassy, with no microliths visible.
265R2_9–11*	1216.5	Impact melt rock in contact with granite. Quite heterogeneous structure. In proximity with the granite, black to brownish impact melt rock, exhibiting flowing structure at the macroscopic scale. Matrix is made of microliths. Undigested shocked quartz (PDFs observed) and, to a lesser extent, pyroxene constitute the clast population. Intercalation of more crystallized material is also noticed. When going further away from the granite, the impact melt is more heavily crystallized with plagioclase and pyroxene laths. The matrix is brown and microliths are more abundant. The repartition is not homogeneous as recrystallized Plagioclase and pyroxene are more abundant in some area, while others have more microlithic melt. This may be a partially digested dolerite (or mafic basement clast). Some altered olivines are also observed.
267R3_52.5–55.5	1224.4	No thin section available. Black to grayish impact melt rock, flowing structure are visible. Seem clast-enriched compared to the upper impact melt rock. Clast are submillimetric, with quartz dominating the clast population.
277R1_59.5–62	1253.0	Impact melt rock clast rich, with large, subcentimetric to centimetric basement clasts (gneiss, granite). Quartz are the main mineral clasts.
277R1_88–92*	1253.3	Similar as previous sample, basement clasts are embedded in a black, homogeneous melt, where microliths are absent in some place or, when present, seem to be altered. Areas exhibiting brownish color (alteration). Large 1.5 cm gneiss clast. Carbonate clast are absent.
277R2_25–27	1253.9	Black impact melt rock with greenish areas, indicating that some alteration affected this sample. Part of the impact melt exhibit clear flowing structures with elongated minerals. Some aletered brownish to orange glassy clasts are present. 1 cm gneiss clast. In the gneiss clast, intercalations of finely crystallized plagioclase (like shards) veins. Recrystallizations of pl and maybe px (as shards) are also observed in the impact melt itself.
290R1_66–68	1292.0	Impact melt rock, clast rich. One part of the sample is made of black impact melt rock with partially digested and undigested basement clasts (gneiss, granite). The matrix is made of black melt, microliths seem barely visible. Some greenish alteration veins. Quartz is also the main mineral clast (shocked with PDF, rarely toasted). The other half of the sample is made of large plagioclase and pyroxene laths (generally 0.5 cm long). Minerals are heavily fractured. Intercalation of finely crystallized plagioclase and px veins.
292R2_66–68.5*	1299.4	Black impact melt rock, homogeneous. Large clasts are less abundant than previous samples (from section 277R), and smaller (no more than 1 cm size). However, the impact melt is clast rich, as submillimetric clasts are abundant, generally shocked quartz, plagioclase and K-feldspar. Rare undigested pyroxene are also noted. No flowing structure clearly visible.
294R1_67.5–70	1304.4	Grayish impact melt rock with strong flow banding texture (mineral well elongated in the direction of the flow). In contact with a large 2-3 cm gneiss clast. Feldspar vein is crosscutting the impact melt.
303R3_22.5–25*	1334.4	Impact melt rock (black). Melt is black to brownish. Quartz is shocked and sometimes toasted. The impact melt is "mingled" with more brecciated material (mainly granitic material (Quartz+felsdpars). Melt seems to have a low abundance of microliths (or even none).

Suevites

| 41R1_106–108 | 620.4 | Typical suevite, matrix with micritic carbonate, bedding clearly visible in the texture. Clasts of relatively small size, i.e., millimetric to submillimetric (clasts consist mainly of carbonate (fossils) + rare quartz grains (ballen silica type V) + abundant angulous altered glass brownish-greenish (alteration with clay minerals?) + quartz is toasted + one shocked quartz with two PDF sets |

xxi

58R3_8–10.5	673.7	Suevite, larger clast size than for 41R1 106–108 sample (0.5 to centimetric). Brownish glass clast, altered and fractured, reaction rim around these clast. Matrix clastic with quartz, carbonate, seems more hydrothermally altered (presence of opaque phases inside, more brownish), large centimetric carbonate clasts, rare quartz grain, ballen type v noticed, toasted quartz, imr clast (clast poor) in the imr -> mainly quartz grains (shocked and toasted) with pdfs, one plagioclase, a larger carbonate clast with reaction rim, matrix of the imr finely crystallized (microlithic plagio abundant and probably px)

Pre-impact dikes

105R2 83–89 (felsite)	772.83	Felsite dike cross cutting granite sample. Contact with granite is sharp, slightly porphyritic (feldspar and px the main porphyritic crysts). Finely crystallized (acicular plagioclase microliths). Calcite, and, to a lesser extent, quartz (shocked with PDFs (2 set)) also occur. The felsite seem heavily altered with several calcite veins crosscutting the sample and high abundance of brownish veins. The calcite seems to have replaced a former anhedral mineral.
140R2 5–8 (dolerite)	854.59	Fine-grained dolerite, porphyritic. Plagioclase and pyroxene are the main mineral phases. Relatively high abundance of opaque minerals. Occurrence of calcite in veins as well as veins filled with finely crystallized plagioclase. Pyroxenes are highly fractured and plagioclases seem to underwent some alteration. Olivine also occurs and is highly altered, generally replaced by sheet silicates (probable serpentinization).
238R1 101–103.5 (dacite)	1135.05	Porphyritic dacite, with millimetric plagioclase crystals in a microcrystalline matrix (plagioclase and quartz). Quartz is shocked with occurrence of PDFs. Rarer K-feldspars are observed. Minor opaque minerals, biotite (often chloritized), apatite, titanite. Microstructures are observed in apatite (1 set). Plagioclase is sericitized (common).

Granites

136R2_20–25	851.37	Coarse-grained granite (Grain size up to 1 cm). K-feldspar, Quartz, Plagioclase (often sericitized), Chloritized biotite Apatite, Titanite, Magnetite. Fracturing is quite abundant. Some fractures are filled with calcite and crosscut the granite. Quartz with PFs, FFs, and decorated PDFs. Kinkbanding (common) in micas/chlorite.
200R3_12.5–15	1021.0	Coarse-grained granite (Grain size: ~0.2–0.8 cm). With K-feldspar, Quartz, Plagioclase, Biotite (rare and often chloritized), Muscovite, Apatite, Titanite, Zircon, Epidote, Magnetite. Fracturing is observed. Thin cataclastic areas with microbrecciated quartz and feldspar (subrounded). Quartz with PFs, FFs, and decorated PDFs, low undulose extinction Kinkbanding (common) in micas/chlorite. Planar microstructures in apatite (2 sets) and titanite.

xxii

Table S2. Major element concentrations (in wt.%) of the investigated samples from the Chicxulub peak ring drill core, according to sample type and determined using bulk XRF. Iron oxide is reported as total ferrous Fe (Fe_2O_3*). LOI: loss on ignition. *Sample selected for HSE–Os analysis.

Sample	Depth (mbsf)	SiO_2	TiO_2	Al_2O_3	Fe_2O_3*	MnO	MgO	CaO	Na_2O	K_2O	P_2O_5	LOI	Total	Na_2O+K_2O
Impact melt rocks (UIM)														
80R2_126–128	707.2	63.5	0.54	15.1	4.33	0.10	3.18	3.06	3.80	2.00	0.11	3.06	98.74	5.80
83R1_22–24.5*	712.3	56.1	0.74	15.5	5.45	0.07	3.96	7.24	4.01	2.54	0.16	3.14	98.87	6.55
88R1_12–14.5	722.7	45.4	0.58	12.3	3.64	0.11	2.94	16.8	3.35	2.59	0.13	11.5	99.35	5.94
88R3_45–47.5*	724.9	57.7	0.84	17.0	5.00	0.08	2.55	6.28	4.41	3.22	0.16	1.89	99.10	7.63
89R1_59–61.5*	726.2	51.6	0.57	13.2	4.52	0.10	3.96	12.4	3.39	3.28	0.13	6.70	99.83	6.67
91R1_102–104.5*	732.8	56.4	0.74	15.3	5.19	0.13	2.94	6.71	3.97	4.53	0.16	2.83	98.93	8.50
91R2_89–91.5	733.8	57.4	0.67	15.4	4.45	0.14	2.03	7.31	3.89	5.03	0.15	3.27	99.73	8.92
92R2_89–91.5	737.1	44.6	0.50	10.7	5.45	0.13	5.98	15.6	2.97	2.20	0.12	10.1	98.29	5.17
92R3_39–41	737.8	60.5	0.62	16.2	4.86	0.09	3.11	4.03	4.12	4.68	0.14	2.04	100.36	8.80
93R1_21–23.5*	738.1	60.3	0.59	15.3	4.70	0.09	3.12	4.52	4.26	4.01	0.14	2.03	99.03	8.27
93R1_121–123.5	739.1	58.1	0.64	16.1	5.52	0.07	3.95	5.04	3.90	3.59	0.14	1.51	98.62	7.49
93R2_11–12.5*	739.3	58.9	0.66	16.2	5.43	0.07	3.41	4.98	4.33	3.39	0.15	1.47	98.95	7.72
95R1_18–20	744.1	58.8	0.61	16.9	4.78	0.06	2.83	5.27	4.26	3.72	0.14	2.37	99.73	7.98
95R1_84–87	744.8	60.3	0.63	17.8	3.52	0.05	1.18	5.2	4.14	4.58	0.14	1.87	99.37	8.72
95R2_45–47.5*	745.3	60.2	0.62	16.3	4.26	0.05	2.54	4.60	4.42	3.75	0.14	1.97	98.88	8.17
Impact melt rocks (LIMB)														
202R2_48.5–53*	1026.3	57.9	0.57	13.7	5.79	0.10	5.60	2.85	3.61	3.44	0.11	4.51	98.22	7.05
265R2_9–11*	1216.5	45.3	0.97	14.2	12.4	0.20	13.2	2.80	3.52	0.30	0.12	5.29	98.21	3.82
267R3_52.5–55.5	1224.4	67.4	0.31	14.1	3.77	0.07	2.76	1.47	4.29	4.08	0.09	1.86	100.24	8.37
277R1_59.5–62	1253.0	53.1	0.77	15.9	8.57	0.13	8.01	1.86	5.02	2.43	0.17	3.51	99.43	7.45
277R1_88–92*	1253.3	53.0	0.76	15.5	8.09	0.14	7.78	2.49	4.36	3.08	0.17	2.81	98.16	7.44
277R2_25–27	1253.9	52.2	0.86	16.1	8.93	0.21	7.38	2.74	4.71	2.42	0.21	2.97	98.71	7.13
290R1_66–68	1292.0	61.9	0.69	14.5	5.92	0.17	4.29	2.57	4.37	2.30	0.16	1.95	98.86	6.67
292R2_66–68.5*	1299.4	62.1	0.78	15.6	6.41	0.20	4.33	3.30	4.25	2.31	0.17	1.68	101.14	6.56
294R1_67.5–70	1304.4	59.4	0.92	15.0	7.75	0.17	4.16	3.11	4.79	1.46	0.38	2.31	99.42	6.25
303R3_22.5–25*	1334.4	64.8	0.60	14.1	5.75	0.11	3.85	1.94	4.31	2.65	0.16	1.93	100.17	6.96
Suevites														
41R1_106–108*	620.4	36.0	0.35	8.37	3.23	0.17	3.50	22.5	3.01	1.57	0.09	18.2	96.89	4.58
58R3_8–10.5*	673.7	46.6	0.45	10.8	4.00	0.10	4.28	15.1	2.81	2.61	0.10	12.8	99.63	5.42
Pre-impact lithologies														
80R2_61–63.5 (amphibolite)*	706.6	50.6	0.93	15.6	9.91	0.25	7.30	8.09	3.69	1.30	0.29	0.79	98.69	4.99
105R2_83–89 (felsite)	772.8	50.6	0.82	15.0	6.00	0.16	4.74	6.32	3.24	4.80	0.49	5.67	97.88	8.04
140R2_5–8 (dolerite)*	854.6	44.4	1.12	14.6	11.8	0.27	11.4	7.68	2.32	0.52	0.11	3.89	98.11	2.84
238R1_101–103.5 (dacite)*	1135.1	67.4	0.52	14.7	2.83	0.05	1.40	2.26	4.61	3.70	0.28	1.04	98.80	8.31
136R2_20–25 (granite)*	851.4	74.5	0.12	13.5	0.67	0.01	0.33	1.53	4.67	3.38	0.03	1.08	99.85	8.05
200R3_12.5–15 (granite)*	1021.0	73.9	0.24	13.6	1.23	0.02	0.49	1.27	4.28	3.89	0.05	1.05	100.10	8.17

Table S3. Trace element contents (in ppm, or as specified otherwise) for each sample type (i.e., impact melt rock, suevite, and pre-impact lithologies) as obtained using INAA and bulk XRF. b.d.l.: below detection limit. *Sample selected for HSE–Os analysis.

Sample	Depth (mbsf)	Na (wt.%)	K (wt.%)	Fe (wt.%)	Sc	V	Cr	Co	Ni	Cu	Zn	As	Rb	Ba	Th	U
Method used		INAA	INAA	INAA	INAA	XRF	INAA	INAA	XRF	XRF	XRF	XRF	XRF	XRF	XRF	XRF
Impact melt rocks (UIM)																
80R2_126–128	707.2	2.60	1.47	2.88	15.4	92.5	10.9	7.48	4.20	10.4	68.2	2.10	39.7	441	6.00	2.80
83R1_22–24.5*	712.3	2.75	1.72	3.57	18.9	134	72.2	12.8	27.2	11.5	74.2	3.30	53.4	450	8.70	6.50
88R1_12–14.5	722.7	2.48	2.50	2.49	16.2	90.4	58.8	18.5	32.2	12.1	197	7.50	50.0	393	7.60	4.60
88R3_45–47.5*	724.9	3.35	2.89	3.73	23.2	131	94.9	12.7	25.0	9.00	300	5.80	54.0	684	8.10	7.20
89R1_59–61.5*	726.2	2.56	2.69	3.26	16.4	92.5	67.1	12.8	26.2	28.3	91.1	4.50	69.3	385	8.80	4.90
91R1_102–104.5*	732.8	2.98	3.70	3.93	21.0	126	82.3	15.6	29.2	15.6	111	10.8	79.6	420	8.90	3.70
91R2_89–91.5	733.8	2.82	3.21	3.11	18.5	114	62.7	11.9	21.4	14.0	99.8	3.20	92.4	504	9.50	4.90
92R2_89–91.5	737.1	2.08	1.47	3.78	13.3	82.6	52.3	12.8	25.5	22.6	119	2.90	48.7	257	6.60	4.50
92R3_39–41	737.8	3.35	4.47	3.70	19.3	109	69.6	15.6	26.2	42.6	85.0	3.20	91.1	546	10.2	4.00
93R1_21–23.5*	738.1	3.27	3.29	3.45	16.5	101	57.8	15.1	26.0	42.1	86.5	2.20	83.3	548	10.6	3.80
93R1_121–123.5	739.1	2.67	2.59	3.66	17.1	114	58.1	13.7	29.0	40.6	82.0	1.00	68.1	569	10.7	4.40
93R2_11–12.5*	739.3	3.17	2.54	4.06	19.6	116	65.4	14.3	24.8	49.3	79.1	1.50	77.4	573	10.5	4.70
95R1_18–20	744.1	3.19	3.06	3.37	16.2	106	55.3	12.5	22.5	36.8	118	3.60	79.6	712	11.6	5.90
95R1_84–87	744.8	3.21	4.14	2.56	16.6	98.2	57.6	11.1	15.7	56.1	164	5.00	90.6	638	12.1	10.8
95R2_45–47.5*	745.3	3.24	2.80	3.03	18.3	92.0	58.3	13.8	25.8	36.7	201	6.10	80.9	608	11.7	7.60
Impact melt rocks (LIMB)																
202R2_48.5–53*	1026.3	2.78	2.63	4.42	11.1	86.5	155	25.2	83.7	28.7	101	0.80	91.0	506	11.0	6.30
265R2_9–11*	1216.5	2.56	b.d.l.	9.30	48.2	260	299	58.2	180	62.9	176	1.20	11.4	51.1	2.70	3.40
267R3_52.5–55.5	1224.4	2.95	2.85	2.55	6.87	49.0	59.1	9.88	31.7	60.6	48.0	0.60	108	585	13.4	6.00
277R1_59.5–62	1253.0	3.42	1.81	5.45	18.4	115	31.8	17.8	22.5	43.3	124	2.30	70.6	234	8.10	5.60
277R1_88–92*	1253.3	2.96	1.84	5.59	20.3	123	41.7	20.0	26.0	44.4	103	2.90	77.0	247	6.80	3.30
277R2_25–27	1253.9	3.44	1.78	6.26	23.2	144	37.5	18.1	20.6	43.8	106	1.60	64.3	236	6.80	3.60
290R1_66–68	1292.0	3.03	1.16	4.30	18.0	109	39.2	14.0	20.2	47.4	100	2.40	72.6	283	7.00	3.80
292R2_66–68.5*	1299.4	3.33	1.42	4.96	23.2	137	53.9	18.1	23.7	51.2	173	3.10	72.5	375	8.10	3.90
294R1_67.5–70	1304.4	3.55	1.00	5.33	23.5	87.6	17.0	7.76	3.50	17.3	94.2	2.20	32.6	311	4.60	2.00
303R3_22.5–25*	1334.4	2.97	1.66	4.01	16.7	108	45.0	17.8	19.2	13.0	45.9	0.80	80.1	308	9.00	4.10
Suevites																
41R1_106–108*	620.4	2.33	1.37	2.33	10.6	85.8	38.1	9.68	17.5	22.0	26.9	6.20	27.0	385	5.30	5.80
58R3_8–10.5*	673.7	2.28	2.39	3.03	13.6	90.3	52.5	11.5	18.1	22.6	57.4	3.00	50.6	313	6.60	4.40
Pre-impact lithologies																
80R2_61–63.5 (amphibolite)*	706.6	1.30	0.91	7.14	33.7	274	181	32.4	81.0	21.2	108	1.40	31.6	210	4.30	2.20
105R2_83–89 (felsite)	772.8	2.54	3.45	4.65	22.0	193	105	26.2	103	28.9	107	22.1	168	2406	49.4	17.7
140R2_5–8 (dolerite)*	854.6	1.82	<0.8	9.39	40.7	233	542	68.3	266	110	99.9	4.30	21.5	119	1.30	2.30
238R1_101–103.5 (dacite)*	1135.1	3.59	2.34	2.27	5.44	56.2	13.7	8.22	9.60	105	54.1	2.00	118	604	11.1	6.10
136R2_20–25 (granite)*	851.4	3.23	2.65	0.45	1.57	12.5	7.3	1.90	2.10	13.6	12.2	1.90	114	440.8	7.5	4.5
200R3_12.5–15 (granite)*	1021.0	3.44	3.18	0.97	2.66	25.6	10.9	2.69	2.80	10.2	24.8	1.60	109	579.8	11.8	5.7

*Sample investigated for HSE-Os analysis

Table S3. *(Continued).*

Sample	Depth (mbsf)	Nb	Ta	La	Ce	Pb	Sr	Nd	Zr	Cs	Hf	Sm	Eu	Gd	Tb	Yb	Y	Lu
Method used		XRF	INAA	INAA	INAA	XRF	XRF	INAA	XRF	INAA	INAA	INAA	INAA	INAA	INAA	INAA	XRF	INAA
Impact melt rocks (UIM)																		
80R2_126–128	707.2	5.20	0.33	25.0	50.6	4.40	393	22.4	139	1.83	3.63	5.38	1.07	b.d.l.	0.71	2.23	23.7	0.38
83R1_22–24.5*	712.3	6.80	0.43	33.1	54.9	19.4	467	23.8	151	0.18	3.57	4.86	1.23	4.53	0.63	2.34	24.9	0.37
88R1_12–14.5	722.7	5.40	0.39	21.3	39.8	9.30	552	20.0	119	0.21	2.99	3.87	1.08	3.11	0.47	1.75	22.3	0.30
88R3_45–47.5*	724.9	7.50	0.57	27.1	48.7	18.0	532	20.1	164	0.25	4.33	4.31	1.22	3.33	0.56	2.47	22.7	0.42
89R1_59–61.5*	726.2	6.30	0.48	21.4	40.8	10.1	431	17.8	125	0.31	3.17	3.64	1.06	3.46	0.56	1.96	21.1	0.33
91R1_102–104.5*	732.8	7.10	0.58	27.8	53.5	13.6	316	20.9	149	0.40	3.98	4.42	1.21	4.61	0.68	2.37	22.8	0.40
91R2_89–91.5	733.8	7.10	0.54	25.9	47.8	14.1	337	18.8	141	0.38	3.56	3.89	0.99	3.71	0.56	2.07	21.2	0.34
92R2_89–91.5	737.1	4.80	0.42	17.6	33.4	6.50	526	15.3	102	0.41	2.49	3.51	0.88	3.17	0.56	1.99	19.5	0.34
92R3_39–41	737.8	7.50	0.62	30.5	51.0	17.8	318	22.7	146	0.43	4.09	4.86	1.05	4.24	0.63	2.52	21.6	0.41
93R1_21–23.5*	738.1	7.50	0.57	32.4	51.6	19.7	367	20.0	140	0.21	3.75	4.22	1.10	4.51	0.64	2.57	23.1	0.41
93R1_121–123.5	739.1	7.70	0.59	36.8	56.9	21.6	451	22.0	152	0.21	3.68	4.61	1.14	4.27	0.69	2.51	26.0	0.44
93R2_11–12.5*	739.3	7.90	0.63	42.4	67.0	24.4	448	23.4	154	0.26	4.22	4.73	1.29	4.10	0.72	2.53	26.9	0.52
95R1_18–20	744.1	8.30	0.63	42.2	65.5	25.9	450	24.5	153	0.17	3.81	5.92	1.24	b.d.l.	0.79	2.65	24.8	0.43
95R1_84–87	744.8	8.80	0.74	44.6	70.4	24.6	425	27.6	161	0.21	4.17	6.26	1.27	4.13	0.54	2.32	20.2	0.40
95R2_45–47.5*	745.3	8.30	0.62	39.9	62.0	28.6	414	20.3	151	0.25	4.00	4.04	1.08	2.85	0.49	2.21	19.7	0.38
Impact melt rocks (LIMB)																		
202R2_48.5–53*	1026.3	8.50	0.81	18.7	36.3	23.0	266	15.2	120	0.96	3.53	4.01	1.10	3.84	0.51	1.10	13.3	0.17
265R2_9–11*	1216.5	4.00	0.25	10.0	23.5	17.4	247	10.8	90.9	0.71	2.35	3.05	0.88	3.02	0.66	2.42	23.8	0.42
267R3_52.5–55.5	1224.4	6.10	0.45	26.3	45.5	22.7	359	16.6	119	0.64	2.98	2.71	0.59	2.26	0.21	0.55	8.00	0.10
277R1_59.5–62	1253.0	5.60	0.42	16.8	31.9	22.3	238	15.0	147	0.63	3.46	4.33	0.81	3.76	0.52	2.55	22.8	0.42
277R1_88–92*	1253.3	5.50	0.38	14.4	31.5	16.0	233	14.1	143	0.71	3.57	3.34	0.85	5.00	0.53	1.78	19.8	0.31
277R2_25–27	1253.9	5.50	0.38	21.9	41.9	12.5	247	18.6	138	0.66	3.49	4.06	1.09	3.25	0.57	2.02	21.2	0.34
290R1_66–68	1292.0	5.60	0.45	17.4	34.0	16.4	233	16.0	136	1.11	3.52	3.65	1.12	4.02	0.60	2.21	21.5	0.38
292R2_66–68.5*	1299.4	6.10	0.50	18.1	37.3	16.4	283	16.7	133	1.29	3.70	3.80	1.23	3.70	0.55	1.89	17.6	0.32
294R1_67.5–70	1304.4	4.20	0.28	15.0	28.8	9.20	215	17.8	107	1.80	2.67	5.65	1.59	5.70	0.82	3.15	32.8	0.50
303R3_22.5–25*	1334.4	5.90	0.47	16.1	32.2	12.8	211	16.1	121	0.87	3.04	3.23	0.84	2.91	0.50	1.70	19.8	0.30
Suevites																		
41R1_106–108*	620.4	3.50	0.31	15.2	26.7	5.00	698	12.2	76.2	3.77	1.95	3.24	0.69	2.19	0.37	1.52	15.7	0.27
58R3_8–10.5*	673.7	4.50	0.39	16.1	30.7	6.20	518	13.5	92.8	2.52	2.57	3.29	0.87	3.16	0.51	1.80	18.5	0.29
Pre-impact lithologies																		
80R2_61–63.5 (amphibolite)*	706.6	8.00	0.42	13.7	33.8	9.80	370	13.6	73.3	0.64	1.72	2.85	1.06	2.92	0.53	1.84	19.4	0.33
105R2_83–89 (felsite)	772.8	6.50	0.60	126	236	16.2	1177	79.2	234	2.42	6.13	16.8	3.73	11.1	1.32	3.21	39.7	0.55
140R2_5–8 (dolerite)*	854.6	7.90	0.69	6.38	14.1	11.6	303	8.79	72.1	1.47	2.12	2.62	1.12	2.27	0.55	1.87	19.5	0.30
238R1_101–103.5 (dacite)*	1135.1	11.5	0.71	32.9	62.3	30.7	806	26.1	154	0.92	4.07	4.42	1.17	2.77	0.36	0.84	10.9	0.14
136R2_20–25 (granite)*	851.4	3.20	0.33	4.71	9.54	23.0	447	4.10	81.1	0.77	2.03	1.09	0.32	1.26	0.07	0.50	4.50	0.05
200R3_12.5–15 (granite)*	1021.0	7.80	0.77	23.7	40.4	20.9	368	13.9	94.1	1.08	2.93	2.47	0.56	2.34	0.13	0.90	5.70	0.07

REFERENCES

Cox M. A., Erickson T. M., Schmieder M., Christoffersen R., Ross D. K., Cavosie A. J., Bland P. A., Kring D. A. and IODP–ICDP Expedition 364 Scientists (2020) High-resolution microstructural and compositional analyses of shock deformed apatite from the peak ring of the Chicxulub impact crater. *Meteorit. Planet. Sci.* **55**, 1–19. https://doi.org/10.1111/maps.13541.

de Graaff S. J., Kaskes P., Déhais T., Goderis S., Debaille V., Ross C. H., Gulick S. P. S., Feignon J.-G., Ferrière L., Koeberl C., Smit J., Matielli N. and Claeys P. (2022). New insights into the formation and emplacement of impact melt rocks within the Chicxulub impact structure, following the 2016 IODP-ICDP Expedition 364. *Geol. Soc. Am. Bull.* **134**, 293–315. https://doi.org/10.1130/B35795.1.

Duboc O., Robbe A., Santner J., Folegnani G., Gallais P., Lecanuet C., Zehetner F., Nagl P. and Wenzel W. W. (2019) Silicon availability from chemically diverse fertilizers and secondary raw materials. *Environ. Sci. Technol.* **53**, 5359–5368. https://doi.org/10.1021/acs.est.8b06597.

Feignon J.-G., Ferrière L., Leroux H. and Koeberl C. (2020) Characterization of shocked quartz grains from Chicxulub peak ring granites and shock pressure estimates. *Meteorit. Planet. Sci.* **55**, 2206–2223. https://doi.org/10.1111/maps.13570.

Feignon J.-G., de Graaff S. J., Ferrière L., Kaskes P., Déhais T., Goderis S., Claeys P. and Koeberl C. (2021) Chicxulub impact structure, IODP-ICDP Expedition 364 drill core: Geochemistry of the granite basement. *Meteorit. Planet. Sci.* **56**, 1243–1273. https://doi.org/10.1111/maps.13705.

Ferrière L., Koeberl C. and Reimold U. W. (2009) Characterisation of ballen quartz and cristobalite in impact breccias: New observations and constraints on ballen formation. *Eur. J. Mineral.* **21**, 203– 217. https://doi.org/10.1127/0935-1221/2009/0021-1898.

Kaskes P., de Graaff S. J., Feignon J.-G., Déhais T., Goderis S., Ferrière L., Koeberl C., Smit J., Wittmann A., Gulick S., Debaille V., Matielli N. and Claeys P. (2022) Formation of the Crater Suevite Sequence from the Chicxulub Peak Ring: a Petrographic, Geochemical, and Sedimentological Characterization. *Geol. Soc. Am. Bull.* **134**, 895–927. https://doi.org/10.1130/B36020.1.

Kring D. A., Tikoo S. M., Schmieder M., Riller U., Rebolledo-Vieyra M., Simpson S. L., Osinski G. R., Gattacceca J., Wittmann A., Verhagen C. M., Cockell C. S., Coolen M. J. L., Longstaffe F. J., Gulick S. P. S., Morgan J. V., Bralower T. J., Chenot E., Christeson G. L., Claeys P., Ferrière L., Gebhardt C., Goto K., Green S. L., Jones H., Lofi J., Lowery C. M., Ocampo-Torres R., Perez-Cruz L., Pickersgill A. E., Poelchau M. H., Rae A. S. P., Rasmussen C., Sato H., Smit J., Tomioka N., Urrutia-Fucugauchi J., Whalen M. T., Xiao L. and Yamaguchi K. E. (2020) Probing the hydrothermal system of the Chicxulub impact crater. *Sci. Adv.* **6**, eaaz3053. https://doi.org/10.1126/sciadv.aaz3053.

Le Bas M. J., Le Maitre R. W., Streckeisen A. and Zanettin, B. (1986) A chemical classification of volcanic rocks based on the total alkali–silica diagram. *J. Petrol.* **27**, 745–750. https://doi.org/10.1093/petrology/27.3.745.

McDonough, W.F. and Sun, S. 1995. The composition of the Earth. *Chem. Geol.* **120**, 223-253. https://doi.org/10.1016/0009-2541(94)00140-4.

Morgan J. V., Gulick S. P. S., Bralower T., Chenot E., Christeson G., Claeys P., Cockell C., Collins G. S., Coolen M. J. L., Ferrière L., Gebhardt C., Goto K., Jones H., Kring D. A., Le Ber E., Lofi J., Long X., Lowery C., Mellett C., Ocampo-Torres R., Osinski G. R., Perez-Cruz L., Pickersgill A., Pölchau M., Rae A., Rasmussen C., Rebolledo-Vieyra M., Riller U., Sato H., Schmitt D. R., Smit J., Tikoo S., Tomioka N., Urrutia-Fucugauchi J., Whalen M., Wittmann A., Yamaguchi K. E. and Zylberman W. (2016) The formation of peak rings in large impact craters. *Science* **354**, 878–882. https://doi.org/10.1126/science.aah6561.

xxvii

Morgan J., Gulick S., Mellet C. L., Green S. L. and the Expedition 364 Scientists (2017) Chicxulub: Drilling the K-Pg impact crater. *Proceedings of the International Ocean Discovery Program, 364*. College Station, Texas: International Ocean Discovery Program. 164 p.

Nagl P. and Mader D. (2019) X-Ray Fluorescence (XRF) and Instrumental Neutron Activation Analysis (INAA) for the Geochemical Analysis of Rocks, Presented on In-House Control Samples. *Mitteilungen der Österreichischen Mineralogischen Gesellschaft* **165**, 67.

Pittarello L., Ferrière L., Feignon J.-G., Osinski G. R. and Koeberl C. (2020) Preferred orientation distribution of shock-induced planar microstructures in quartz and feldspar. *Meteorit. Planet. Sci.* **55**, 1082–1092. https://doi.org/10.1111/maps.13490.

Schmieder M., Kring D. A., and the IODP-ICDP Expedition 364 Science Party. (2017a) Petrology of target dolerite in the Chicxulub peak ring and a possible source of K/Pg boundary picotite spinel. *48th Lunar Planet. Sci. Conf.* Lunar Planetary Institute, Houston. Abstract #1235.

Schmieder M., Kring D.A., Goderis S., Claeys Ph., Coolen M. J. L., Wittmann A., Expedition 364 Science Party. (2017b) Secondary Sulfides in Hydrothermally Altered Impactites and Basement Rocks of the Chicxulub Peak Ring – A Preliminary Survey. *80th Annu. meet. Meteorit. Soc.* Lunar Planetary Institute, Santa Fe, New Mexico. Abstract #6139.

Schulte F. M., Wittmann A., Jung S., Morgan J. V., Gulick S. P. S., Kring D. A., Grieve R. A. F., Osinski G. R., Riller U. and IODP-ICDP Expedition 364 Science Party (2021). Ocean resurge-induced impact melt dynamics on the peak-ring of the Chicxulub impact structure, Mexico. *Int. J. Earth Sci.* **110**, 2619–2636. https://doi.org/10.1007/s00531-021-02008-w.

Slivicki S. J., Schmieder M., Kring D.A. and the IODP-ICDP Expedition 364 Science Party (2019) Petrologic analysis of green-black impact melt rock with a history of hydrothermal alteration at Chicxulub. *50th Lunar Planet. Sci. Conf.* Lunar Planetary Institute, Houston. Abstract #2132.

xxviii

Timms N. E., Pearce M. A., Erickson T. M., Cavosie A. J., Rae A. S. P., Wheeler J., Wittmann A., Ferrière L., Poelchau M. H., Tomioka N., Collins G. S., Gulick S. P. S., Rasmussen C., Morgan J. V. and IODP-ICDP Expedition 364 Scientists (2019) New shock microstructures in titanite (CaTiSiO$_5$) from the peak ring of the Chicxulub impact structure, Mexico. *Contrib. Mineral. Petrol.* **174**, 38. https://doi.org/10.1007/s00410-019-1565-7.

CHAPTER 8: Potpourri

This last chapter presents further detailed investigations conducted on impactite samples from the IODP-ICDP Expedition 364 drill core which are not presented in the publications in Chapters 5, 6, and 7. These include descriptions of shock features in minerals other than quartz within samples from the granite unit, petrographic and geochemical characterization of the suevite unit, as well as a short complementary discussion of the Rb–Sr and Sm–Nd isotopic compositions of the pre-impact dikes, and also a general conclusion summarizing processes occurring in pre-impact lithologies, suevites, and impact melt rocks to form the currently observed lithological sequence of the Chicxulub impact structure peak ring. Some of the results presented and discussed here (below) were integrated with several co-authored publications, here listed in chronological order of publication:

- Pittarello et al. 2020. Preferred orientation distribution of shock-induced planar microstructures in quartz and feldspar. *Meteoritics & Planetary Science* 55:1082–1092. https://doi.org/10.1111/maps.13490.

- Goderis et al. 2021. Globally distributed iridium layer preserved within the Chicxulub impact structure. *Science Advances* 7:eabe3647. https://doi.org/10.1126/sciadv.abe3647.

- de Graaff et al. 2022. New insights into the formation and emplacement of impact melt rocks within the Chicxulub impact structure, following the 2016 IODP-ICDP Expedition 364. *Geological Society of America Bulletin* 134:293–315. https://doi.org/10.1130/B35795.1.

- Kaskes et al. 2022. Formation of the crater suevite sequence from the Chicxulub peak ring: A petrographic, geochemical, and sedimentological characterization. *Geological Society of America Bulletin* 134:895–927. https://doi.org/10.1130/B36020.1.

- de Graaff et al. The Chicxulub impact structure reveals the first in-situ Jurassic-aged magmatic intrusions of the Yucatán Peninsula, Mexico. *Lithos* (submitted 2022-06-12).

8.1. Shock features in minerals other than quartz

As shown in Chapter 5 (Feignon et al., 2020), quartz grains in the granitic basement of the M0077A drill core are heavily fractured and shocked, with common occurrence of several sets of planar fractures (PFs), in some cases with associated feather features (FFs), and planar deformation features (PDFs) having crystallographic orientations indicating shock pressures of 17 ± 1 GPa. Apart from quartz, some shock-induced effects and microstructures were also observed in other minerals, including plagioclase, biotite, titanite, apatite, and zircon grains.

In contrast to shock metamorphic features in quartz, those in feldspar/plagioclase grains have to date not been investigated/described in such details (e.g., Stöffler, 1967; Ostertag, 1983; Pittarello et al., 2013; Pickersgill et al., 2021). In addition to shock pressures, parameters such as the chemical composition (Ca-rich or Na-rich varieties), the complex crystallography (biaxial, with monoclinic and triclinic symmetries), and also the fact that feldspars are more subject to alteration than quartz, will affect the development of shock metamorphic features (Stöffler et al., 2018, and references therein; Pittarello et al., 2020). The main shock microstructures previously observed in feldspars consist of PFs, PDFs, and alternating

amorphous microtwins, with the presence of PDFs seemingly limited to intermediate to albitic (Na-rich) terms (Stöffler, 1967; Dworak, 1969; Gibbons and Ahrens, 1977; Ostertag, 1983; Langenhorst et al., 1995; Pittarello et al., 2013; Jaret et al., 2014; Pickersgill et al., 2015).
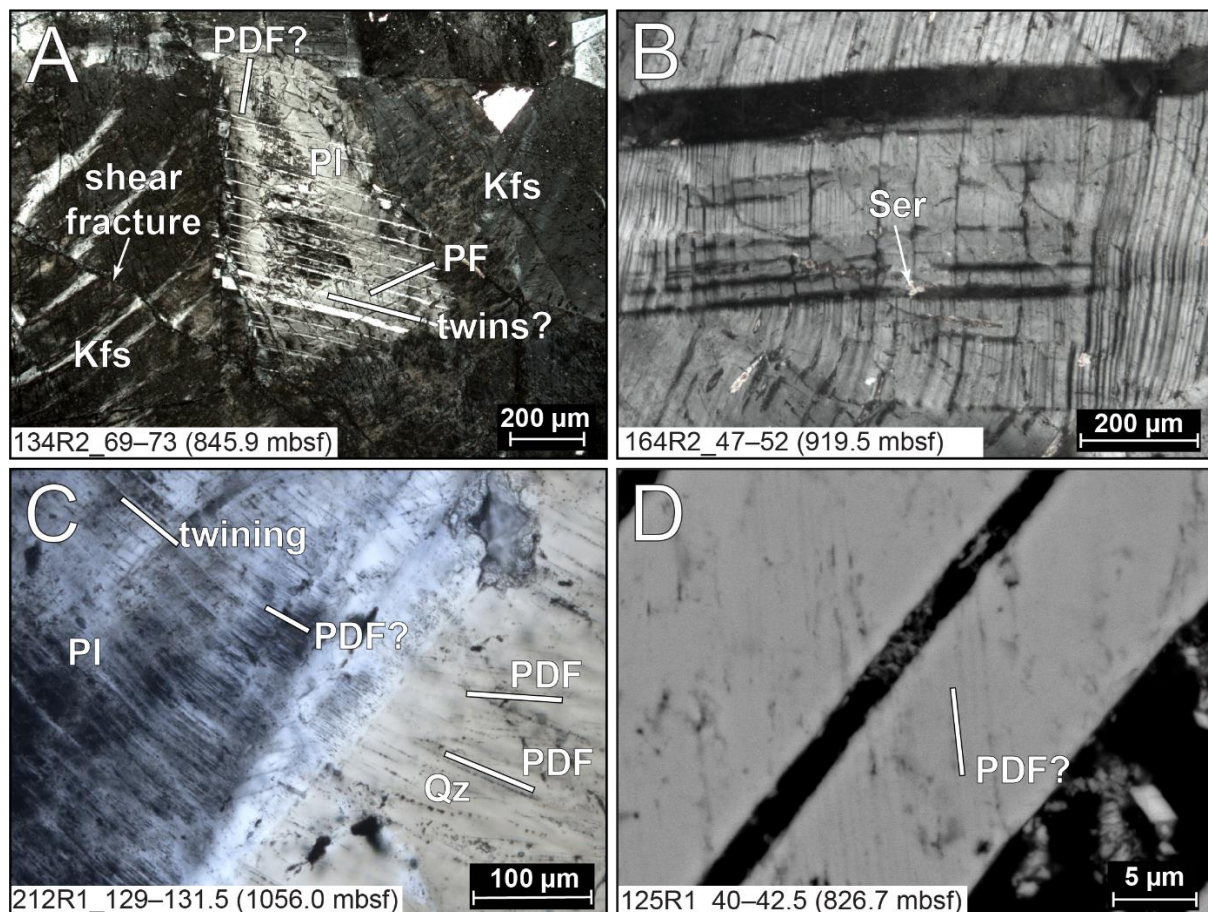

Figure 8.1. *A–C) Thin section photomicrographs (all in cross-polarized light) of shocked plagioclase (Pl) grains within granite samples. A) Plagioclase grain showing twinning and one set of planar fractures (PF). A possible set of planar deformation features (PDF) is also visible in the upper part of the grain. The grain shows signs of alteration mainly in its center part. Kfs: K-feldspar. B) Plagioclase grain showing kinkbanding and some sericitization (Ser). C) Contact between a plagioclase and a shocked quartz (Qz) grain with two visible PDF sets. The rim of the plagioclase shows intense twining and a possible set of PDF. D) Back-scattered electron (BSE) image of a plagioclase grain, with barely visible thin planar microstructures, which are possible PDFs.*

The associated shock pressures necessary to form PDFs in plagioclase were estimated at between 18–22 and 24–34 GPa, with increasing albite composition (Stöffler et al., 2018, and references therein). In the case of plagioclase crystals in granite samples from the Chicxulub peak ring, they are commonly altered (sericitization), especially within grain cores, possibly hiding shock-induced planar microstructures. In general, planar microstructures, such as microtwins, PFs, and likely PDFs, were observed in plagioclase minerals (locally at the albite-rich rim of the grains, where alteration is generally more limited than in the core), with a lower abundance than in quartz (Fig. 8.1; see details in Pittarello et al., 2020). Given that the estimated

shock pressure range to form PDFs in plagioclase is slightly higher than in quartz, these observations seem in accordance with the shock pressure estimates (16–18 GPa) obtained from PDFs measurements in quartz grains (Feignon et al., 2020).
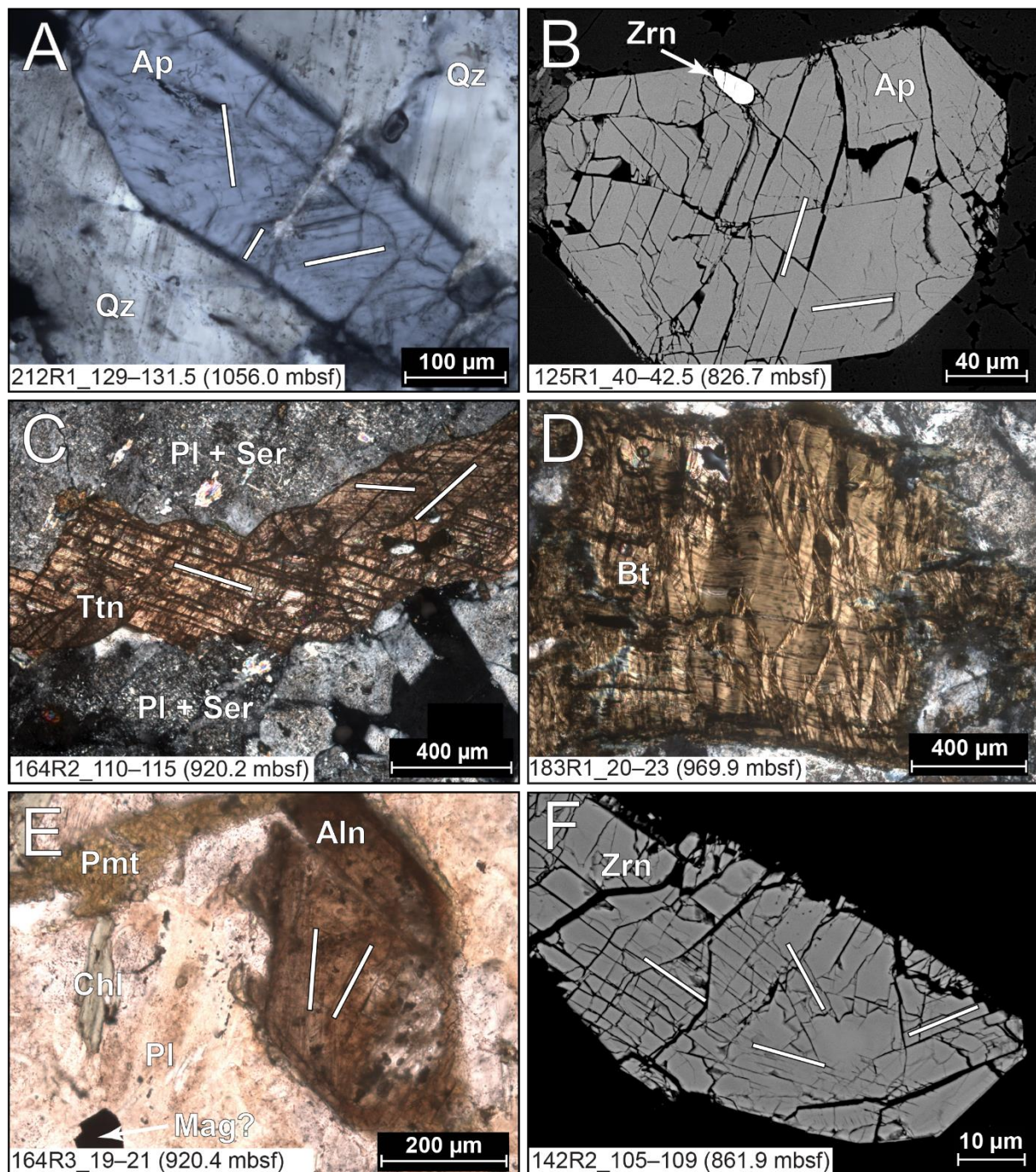

Figure 8.2. *A) Cross-polarized light photomicrograph of an apatite (Ap) grain showing three visible sets of planar microstructures. The apatite grain is located within a shocked quartz (Qz) displaying two visible PDF sets. The host rock is a granite. B) Scanning electron microscope BSE image of an apatite grain (with also a zircon grain, noted Zrn) highly fractured, with at least two sets of planar fractures visible. The host rock is a granite. C) Cross-polarized photomicrograph of a titanite (Ttn) grain with well-developed sets of planar microstructures. Two sets are clearly visible, while the third one is hardly visible on this photomicrograph. The*

titanite grain is surrounded by strongly sericitized (Ser) plagioclase (Pl). The host rock is a dacite. D) Cross-polarized photomicrograph of well-developed kinkbands in biotite (Bt) within a granite. E) Natural transmitted light image of a well-preserved allanite (Aln) crystal displaying two sets of planar microstructures. The host rock is a dacite. Chl: chlorite; Pmt: piemontite (epidote); Mag: magnetite. F) Scanning electron microscope BSE image of a strongly fractured zircon grain within a granite sample; At least four orientations of (planar) fractures are visible.

In apatite grains, shock-induced microstructures described in previous works include PFs, recrystallization, microvesicles, crystal-plastic deformation, and cataclastically deformed zones (e.g., Wittmann et al., 2013; Cavosie and Centeno, 2014; Alwmark et al., 2017; Słaby et al., 2017; McGregor et al., 2018, 2020; Birski et al., 2019; Černok et al., 2019; Kenny et al., 2020). The PFs in apatite consist of multiple sets of parallel, planar microstructures crossing the grain, with a typical spacing of 5–10 µm between each PF (Cavosie and Centeno, 2014; McGregor et al., 2018; Montalvo et al., 2019). Previous observations in natural samples from e.g., the Santa Fe impact structure (USA) and the Nicholson Lake impact structure (Canada) have identified PFs in apatite grains composing rocks that have experienced shock pressures between ~10 and 20 GPa (Cavosie and Centeno, 2014; McGregor et al., 2018; Montalvo et al., 2019). In the investigated granite samples from the Chicxulub peak ring, optical microscope and SEM observations have shown that apatite grains (euhedral to subhedral basal and prismatic sections) display generally PFs, with up to three visible sets per grain, in addition to irregular fracturing (see Fig. 8.2A–B). Also, SEM investigations have shown that apatite is enriched in fluor, and, thus, can be defined as a fluorapatite, with zoning observed in some grains. Further investigations of apatite grains from the Chicxulub peak ring Expedition 364 drill core samples by Cox et al. (2020) have shown that some apatite grains show also cataclastically deformed zones and granular textures, and that PFs are oriented along either $\{\bar{2}110\}$, $\{2\bar{1}\bar{1}0\}$, $\{\bar{1}\bar{1}20\}$, or $\{11\bar{2}0\}$ plans. Cox et al. (2020) also shown that the formation of shock microstructures in apatite grains is highly influenced by the petrographic context.

Planar microstructures previously observed in titanite include deformation twins lamellae, organized in two sets (Mügge, 1889), shown to form at pressures of ~0.5–0.8 GPa, and a twin mode defined as {221}<110>, with {221} being the twinning plane, and <110> the shear direction (Borg, 1970; Borg and Heard, 1972). However, such a twinning can be the result of endogenic tectonic/metamorphic processes, and, thus, cannot be used as a shock metamorphism indicator (Borg and Heard, 1972; Bonamici et al., 2015). Globally, the microstructures observed in titanite grains from naturally shocked rocks were not characterized in much detail, but only described as 'planar fractures', 'mechanical twins', and/or 'planar features' (e.g., Koeberl et al., 1996; Papapavlou et al., 2018), and their crystallographic orientations were not determined. In the recovered coarse-grained granite, and also dacite samples from the Chicxulub peak ring, a number of titanite grains were observed, up to ~2 mm-long for the largest grains, and often associated with other accessory phases, such as apatite, zircon, and epidote. Typically, titanite grains show up to three visible sets of planar microstructures (twin lamellae) a few micrometers wide, and generally straight (Fig. 8.2C). A few titanite grains show a nearly granular texture. A detailed study of shock microstructures in titanite grains in impactites from the Chicxulub peak ring by Timms et al. (2019) have shown

that the deformation twins are oriented along $\{\bar{1}11\}$ and $\{130\}$ orientations, different from the $\{221\}$ twins recorded in tectonically deformed titanite. These authors have proposed that such twins can be used as an indicator of shock metamorphism knowing that they occur in granite samples shocked at pressure of ~17 GPa (i.e., shock pressure based on investigations in quartz grains; Feignon et al., 2020). Additionally, the high-pressure titanite polymorph TiO_2-II (riesite), forming at shock pressures below 20 GPa and stable up to 400 °C was identified within granite rocks (Kring et al., 2020, and references therein).

Zircon grains in impactites from the Chicxulub peak ring observed by SEM display generally one or more sets of planar fractures, together with irregular fractures (Fig. 8.2F). No shock twins, or reidite were identified in our suite of samples, but no systematic search was conducted. Similar observations were made, except the identification of rare mechanical twins (but no reidite) in zircons from the granite basement (Timms et al., 2019; Cox et al., 2020; Zhao et al., 2021). In contrast, zircon grains within felsic clasts from the suevite unit exhibit reidite, twinning, and granular zircon including the so-called "former reidite in granular neoblastic" (FRIGN) zircon, indicating shock pressures of >30 GPa (see details in Zhao et al., 2021). Also, a detailed study of 429 zircon grains in granitic rocks from the peak ring identified a unique zircon-reidite intergrowth and three grains with shock twins, suggesting an amplified shock pressure of up to 25 GPa, due to shock impedance differences between the host minerals associated with the zircon grain (see details in Wittmann et al., 2021).

In granite samples, a number of micas grains, mainly biotite, chloritized biotite, and muscovite display more or less well-developed kinkbands, a sign of compression (Fig. 8.2D). Because kinkbanding starts to form at relatively low shock pressures (~0.1–0.5 GPa, can also be formed during tectonic processes; e.g., Stöffler et al., 2018, and references therein), the abundance of mica grains with kinkands is not surprising. Additionally, planar microstructures were observed in a few allanite grains, when those were not too strongly altered (Fig. 8.2E).

All these observations of shock-induced microstructures in plagioclase and accessory minerals within the granite unit of the Chicxulub peak ring further support that the shock pressure experienced by the granite was generally below about 20 GPa. This is in accordance with the shock pressure estimates obtained from PDF orientations measurements in quartz grains (see publication in Chapter 5, Feignon et al., 2020).

8.2. The suevite unit of the M0077A drill core

In the following section, the main petrographic observations and bulk geochemical (major and trace elements) investigations made on suevite samples are described. These results were largely integrated into the detailed study by Kaskes et al. (2022). The suevite (or polymict impact melt-bearing breccia) unit was identified as a ~104 m thick sequence, occurring between 617.3 and 721.6 meters below seafloor (mbsf), and it was divided into three subunits (Morgan et al., 2017). Previous studies on the suevite unit have characterized its geophysical properties (Christenson et al., 2018) and its macroscopic and hydrothermal features were also investigated in great detail (Kring et al., 2020). Digital image analysis (Osinski et al., 2020), geological line logging and machine learning clast analysis of core sample photographs (Gulick et al., 2019; Örmo et al., 2021) were also performed. The main characteristics of the suevite unit highlighted

by these studies were the high degree of hydrothermal alteration it experienced, its relatively high porosity, and a moderate sorting. In order to explain the sorting of the suevite, it was proposed that it was due to melt-water interaction, relatively similar to phreatomagmatic explosions that are observed for volcanoes (Gulick et al., 2019; Osinski et al., 2020), and by a powerful resurge going back into the crater (Gulick et al., 2019; Örmo et al., 2021). However, the detailed petrography (clast types, groundmass) of the suevite, as well as its geochemistry, are not well constrained. Thus, this was the main focus of the study by Kaskes et al. (2022), in order to address this issue and to better disentangle the formation processes of the suevite unit.

8.2.1. Petrographic observations

8.1.2.1. Suevite clast types and matrix

Based on optical microcopy observations, several clast types were identified within the suevite unit of the M0077A core, i.e., impact melt rock clasts (glassy and microcrystalline), crystalline basement clasts (mafic and felsic), mineral clasts, and carbonate clasts. These different clasts can be observed in the macrophotographs presented in Appendix A. Also, macrophotographs and thin section photomicrographs of typical suevite samples and some clasts are presented in Figures 8.3 and 8.4.

The impact melt rock clasts constitute the main component of the clast population of the suevite unit. They can be subdivided into two types: (1) glassy (or vitric) melt clasts, and (2) microcrystalline melt clasts. The vitric melt clasts have a glassy appearance, varying in color from yellow-green to orange-brown, without any visible microliths (holohyaline texture), generally an angular shape, and also show vesiculation, with sparry calcite filling of the vesicles. These clasts are generally highly altered, with the presence of clay minerals (phyllosilicates), hiding the original impact melt clast. Vitric melt clasts represent ~40–70 vol% of the clast population throughout the suevite unit (Kaskes et al., 2022). The microcrystalline impact melt rock clasts are composed of acicular plagioclase and pyroxene microliths, with varying degrees of alteration to phyllosilicates. In the most altered areas, the microliths are generally poorly preserved. The microcrystalline impact melt rock clasts appear brownish to black in color in thin section, with both clast-poor and clast-rich varieties observed throughout the suevite unit, and with sizes varying from few millimeters to tens of centimeters (e.g., a black microcrystalline impact melt rock clast of ~60 cm occurs in core section 80R2, 706.3–106.9 mbsf). The clasts within the microcrystalline impact melt rock clasts consists mainly of undigested mineral clasts (generally quartz and K-feldspar), as well as basement clasts such as granite or gneiss, and rarely amphibolite or dolerite, having sizes from <0.5 mm to several centimeters. According to Kaskes et al. (2022), these microcrystalline impact melt rock clasts constitute ~10–45 vol% of the entire clast population.

The crystalline basement clasts can be subdivided into felsic basement and mafic basement clasts. In general, the lithologies and their petrography are similar to those described in Feignon et al. (2021, 2022) and de Graaff et al. (2022). The felsic basement clasts have a relatively low abundance throughout the suevite unit (<10 vol%; Kaskes et al., 2022). The most common felsic clasts consist of granite composed of quartz, K-feldspar, plagioclase (all with abundances of ~25–40 vol%), and minor biotite (<5 vol%) often chloritized as a consequence

of alteration. Most of the granite clasts are deformed, fractured (with partial filling of the fractures with matrix material), with quartz grains showing strong undulose extinction, and appearing commonly toasted, which is interpreted to be a consequence of high post-shock temperatures (Whitehead et al., 2002; Ferrière et al., 2009a). Other shock metamorphic features observed in quartz grains within granite clasts include PFs, PDFs (with up to three sets visible, but in general only one or two sets can be observed per grain under the optical microscope), and also rather rare kinkbanding in biotite. The relative abundance of PDFs in quartz grains of the granite clasts is lower than the average 2.8 PDF sets per grain observed in the granitic basement of the M0077A drill core (see details in Feignon et al., 2020). The other felsic basement clasts observed are rare gneisses, mostly in the middle and lower parts of the suevite unit, with the first occurrence of a gneiss clast within microcrystalline impact melt rock clast in suevite sample 50R3_24–26.5 (at 648.8 mbsf). The gneiss clasts are composed of preferentially oriented quartz grains (~0.1–0.5 mm in size), alternating with bands rich in mica minerals (mainly biotite, <100 µm in size), and rarer K-feldspars (~0.2–1.0 mm in size), and iron oxide mineral grains. Mafic basement clasts (dolerite and amphibolite clasts) are rare (<5 vol%; Kaskes et al., 2022), and only observed in the middle and lower parts of the suevite unit (first occurrence of a mafic clast, a dolerite, in sample 56R2_95–97.5, at 667.2 mbsf). The dolerite clasts are either equigranular or porphyritic in texture. The porphyritic dolerite clasts are composed of relatively euhedral plagioclase laths (~0.3–1.5 mm in size), pyroxene (~0.1–0.5 mm in size), and opaque minerals within a microlithic matrix composed mainly of finely crystallized plagioclase and pyroxene. The equigranular dolerite clasts display the same mineral assemblage, with mineral sizes smaller than for the porphyritic dolerite (i.e., <0.5 mm). The amphibolite clasts show evidence of metamorphism with a slight foliation observed in the rock texture. Amphibolite clasts are fine-grained (mineral sizes of ~100–400 µm), holocrystalline, and composed of oriented greenish amphibole, plagioclase, and more rarely quartz and pyroxene. Quartz grains are shocked with at least one set of PDFs, while amphiboles are highly fractured. A large, ~40 cm amphibole clast occurs in core section 80R2 (sample 80R2_61–63.5, at 706.6 mbsf).

Mineral clasts within the suevite include isolated minerals (mainly quartz and feldspar) derived from the felsic basement, with similar textures as those observed in granitic clasts. Isolated quartz grains show similar shock features as previously described in granite clasts. Additionally, ballen quartz is relatively common, from type II to type V, with a chert-like texture (see Ferrière et al., 2009b). Angular silica mineral clasts were also observed within the suevite, and consist of microcrystalline quartz showing a speckled texture, different from quartz observed within other crystalline basement clasts.
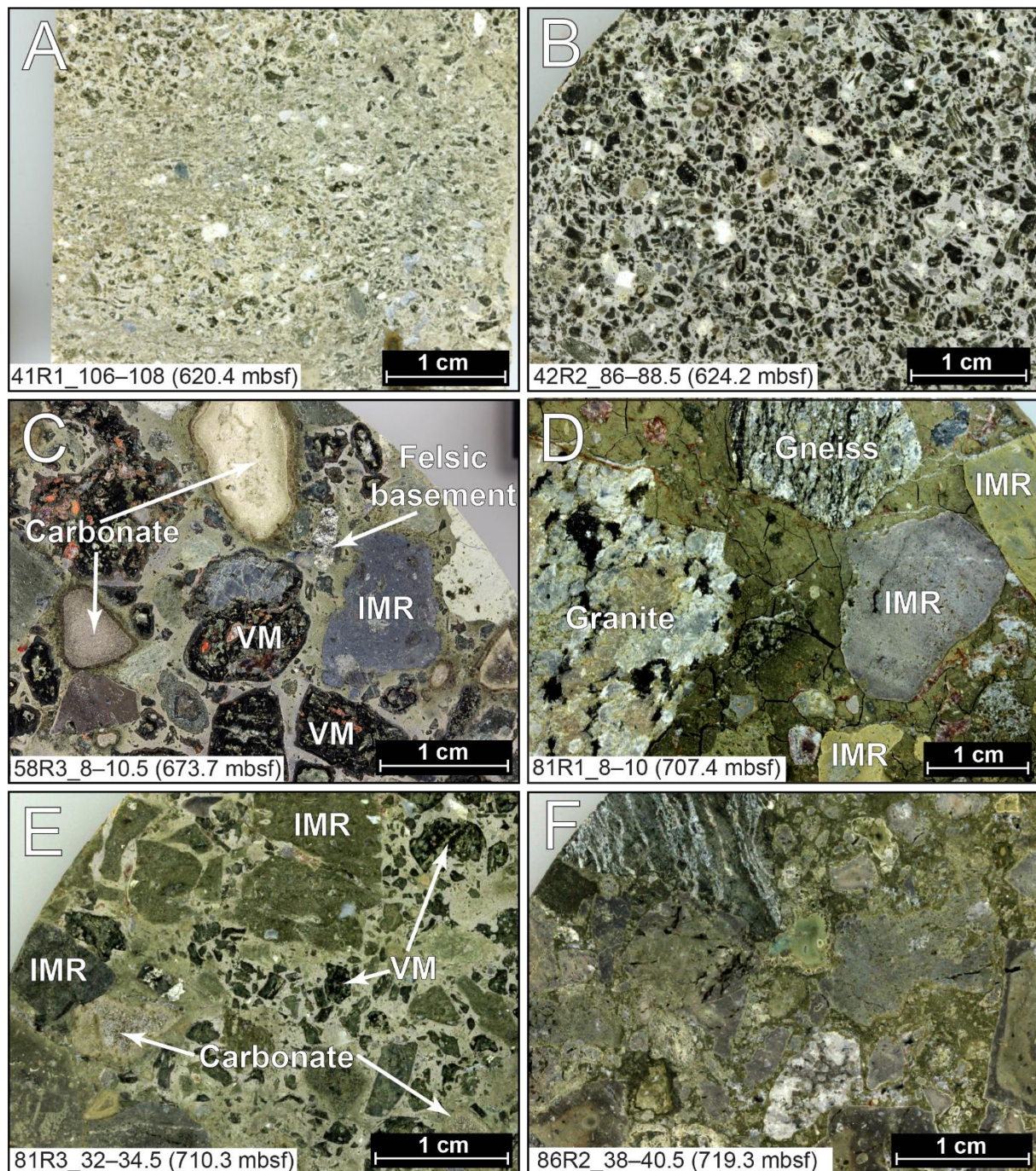
Figure 8.3. *Macrophotographs of typical suevite samples taken throughout the suevite unit, as well as a brecciated impact melt rock sample (F). A) Bedded suevite subunit sample characterized by a fine-grained texture, and mainly composed of greenish vitric impact melt and carbonate clasts. The bedding is mainly visible in the center part of the sample. B) Fine-grained sample from the upper part of the graded suevite subunit. No obvious orientation of the clasts is visible in this case. Vitric and microcrystalline impact melt clasts constitute the main population, with rarer carbonate and felsic basement clasts, embedded in a micritic carbonate matrix. C) Graded suevite sample recovered deeper in the suevite unit than sample in (B). The larger size of the clasts is obvious, with several centimeter-sized clasts, i.e., carbonates, microcrystalline impact melt rock (IMR), altered vitric impact melt (VM), and felsic basement clasts. D) Suevite sample from the lower part of the graded suevite subunit. The poor-*

sorting is visible, and clasts of more than one centimeter in size are common, with a wide variety of different lithologies, i.e., impact melt rock clasts (IMR), granite, and gneiss in this case. Small clasts consist generally of crystalline basement derived mineral clasts, and rarer carbonates. The matrix is also strongly altered and display desiccation cracks. E) Sample from the non-graded suevite subunit, characterized by a poor-sorting, and with the clast population being dominated by vitric and microcrystalline impact melt rock clasts, with rarer carbonate clasts, while crystalline basement clasts are nearly absent. F) Brecciated impact melt rock sample, composed mainly of black microcrystalline impact melt rock fragments embedded within a greenish-dark matrix showing flow texture, similar to the green schlieren observed in the upper impact melt rock unit (Unit 3 in Morgan et al., 2017). A granitic clast is visible in the lower part of the sample.

Carbonate clasts are commonly observed throughout the entire suevite sequence, with an abundance of ~10–25 vol% (Kaskes et al., 2022). They show a large variety of carbonate rocks, including boundstones, rudstones, micritic wackestones, and packstones. Fossils are generally preserved within these carbonate clasts, including, foraminifera, bivalves, gastropods, and echinoids. Other carbonate clasts are more or less rounded, and composed of calcite, from microcrystalline in size to sparry calcite of up to several millimeters in size, with reaction rims around these clasts. Kaskes et al. (2022) identified these latter carbonate clasts as reacted carbonate clasts, as they do not preserve fossils or depositional features, such as bedding, in contrast to the former primary carbonate clasts. Importantly, no evaporite clasts were observed (e.g., anhydrite, gypsum), in contrast to those observed in Y6, UNAM, and Yax-1 drill cores (see details in Chapter 3; Rebolledo-Vieyra et al., 2000; Claeys et al., 2003; Dressler et al., 2003, 2004; Stöffler et al., 2004; Urrutia-Fucugauchi et al., 2004, 2008). This confirms the previous observations of Gulick et al. (2019), suggesting that evaporite sulfate minerals are preferentially vaporized during the excavation stage, and/or also that evaporite rocks were fractured in larger fragments than carbonate clasts, and were ejected and deposited outside the Chicxulub peak ring area.

The matrix (or groundmass) of the suevite is mainly composed of micritic, rounded carbonate grains, and can also be termed as particulate or clastic matrix (Stöffler and Grieve, 2007). The matrix volume in the suevite varies from ~35 to 50 vol% from a sample to another (Kaskes et al., 2022). In addition to micritic carbonate, some quartz grains can also occur. In addition, depending on the degree of hydrothermal alteration, matrix can be altered, with the presence of phyllosilicates, and even desiccation cracks that are visible at the macroscopic scale, especially in the lower part of the suevite unit (e.g., samples 72R1_94.5–99, 73R1_20–23, and 76R1_117–119.5, at 698.0, 699.3, and 703.6 mbsf, respectively), making difficult the characterization of the nature of the matrix. The matrix in the lowermost part of the suevite unit is less sorted than elsewhere in the sequence, with the occurrence of large carbonate particles up to ~200 µm surrounded by smaller calcite grains. The matrix also contains foraminifera that can be observed throughout the entire suevite unit. More details on the clast types and matrix petrography and geochemistry can be found in Kaskes et al. (2022).
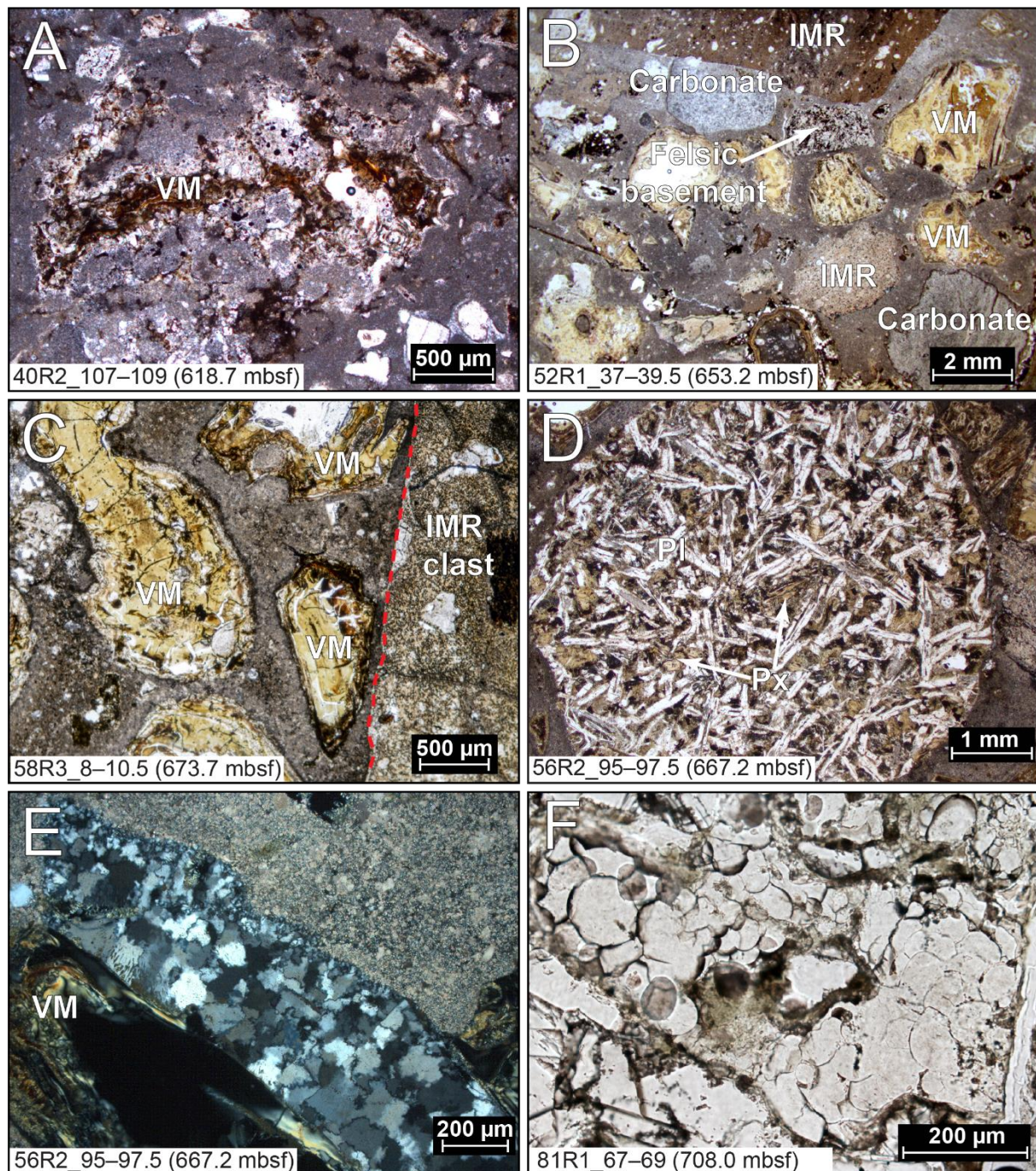
Figure 8.4. *Thin section photomicrographs of typical features observed in samples from the suevite unit. Apart from (E) which is in cross-polarized light, all the other photographs were taken in natural transmitted light. A) Bedded suevite sample, characterized by a fine-grained texture, an abundant micritic carbonate matrix, and mainly composed of vitric impact melt clasts (VM). The vitric melt clast here is partly altered with the presence of clay minerals and secondary calcite. B) Typical graded suevite sample, rich in vitric impact melt clasts (VM), with a clast-poor microcrystalline impact melt rock clast (IMR), felsic basement (granodiorite?) clast, and carbonate clasts (one with brown reaction rim and fossils preserved inside in the lower part of the photograph). C) Graded suevite sample, similar to (B), with larger clast size, and vitric impact melt clasts. D) Rounded porphyritic dolerite clast (in a graded suevite sample), composed of plagioclase laths and small pyroxene and opaque (iron oxide) mineral*

grains. E) Ballen silica (type V) grain, with a typical "chert-like" texture, indicating the full recrystallization of the ballen (see Ferrière et al., 2009b). The grain is in contact with a vitric melt clast, and the micritic carbonate matrix of the suevite. F) Ballen silica (type II; Ferrière et al., 2009b) as part of a silica mineral clast within the basal part of the graded suevite.

8.1.2.2. Stratigraphic evolution of the suevite unit

Macroscopic and petrographic observations of the suevite unit in core M0077A highlight some variations throughout the suevite sequence (Figs. 8.3–8.4). The uppermost part of the suevite unit is marked by a relatively sharp contact at 617.33 mbsf, with a laminated carbonate siltstone belonging to the so-called "transitional unit" (Unit 1G, 617.58–617.33 mbsf) which has been extensively described (Morgan et al., 2017; Bralower et al., 2020; Whalen et al., 2020; Goderis et al., 2021; see also Chapter 3), on top of a fine-grained suevite, gray-brown in color at the macroscopic scale.

From core level 617.33 mbsf downward, the suevite appears fine-grained, green-brownish in color, with clasts generally not larger than ~1 mm, and is mainly matrix-supported. Also, clear horizontal bedding is visible until sample 41R2_50–54 (621.25 mbsf). The matrix contains abundant sparry calcite and foraminifera, while vitric melt clasts represent the main clast population, and rare carbonate clasts, microcrystalline impact melt rock clasts, and isolated quartz grains probably derived from the felsic basement. Kaskes et al. (2022) also identified, in sample 41R1_105–109, a preserved silicate "glass" (mostly altered to clay minerals) impact spherule of 1.2 mm in diameter.

Below core level 621.25 mbsf, and first observed in sample 41R2_131–133.5 (622.06 mbsf), the suevite color changes from green-brown to blue-green-gray. Until sample 49R1_64–66.5 (644.33 mbsf), the suevite is relatively fine-grained, well-sorted, and characterized by a coarsening trend with increasing depth (clast size from ~1–3 mm in section 41R2 to ~2–8 mm in section 49R1). The clast population is dominated by vitric and microcrystalline impact melt rock clasts, and minor carbonate, mineral, felsic, and mafic basement clasts. At depths between 644.33 (sample 49R1_64–66.5) and 663.04 mbsf (sample 55R1_105–107), the clast size is relatively constant, with even a slight fining in samples within section 54R, with a similar clast population. Then, from 663.04 to 677.11 mbsf (sample 59R3_95–97), the clast size increases with depth, and the suevite becomes medium-grained, less well sorted, with clasts larger than 1 cm occurring together with clasts of ~2–5 mm in size. Globally, the suevite in core interval 621.25–677.11 mbsf is matrix-supported, with limited alteration (i.e., relatively low occurrence of phyllosilicates hiding the matrix texture), an no specific orientation of the clasts is noted. Going downward within the core, from 677.11 mbsf on, the suevite shows a coarsening with increasing depth (dominated by clasts of ~1–5 cm in size), and a texture becoming more clast-supported with increasing depth. The matrix also becomes green to dark brown in color, indicating a high degree of hydrothermal alteration, later confirmed in thin sections (i.e., presence of phyllosilicates and reddish mineralization). Also, especially in samples located in core sections 67R1, 72R1, 73R1, 76R1, and 77R1 (691–704 mbsf), fracturing is important, with the notable occurrence of desiccation cracks in the matrix and in some vitric impact melt clasts. While the clast population is dominated by vitric impact melt (often heavily altered and with vesicles filled with sparry calcite) and microcrystalline impact melt rock clasts, carbonate clasts

are slightly less abundant than in the upper part of the suevite, and are observed together with mineral clasts, felsic and mafic basement clasts. The suevite sequence shows two large black, clast-poor impact melt rock clasts (~60 and ~90 cm in size) in core sections 80R2 (706.4–707.3 mbsf) and 81R2 (709.1–710.0 mbsf), with also a ~40 cm amphibolite clast observed in the impact melt rock clast within core section 80R2 (sample 80R2_61–63.5, 706.57 mbsf).

Below the impact melt rock clast from ~710 mbsf, the suevite appears poorly sorted, with no trend in clast size with increasing depth, as fine-grained suevite (e.g., 81R3_32–34.5, 710.31 mbsf, with clasts of ~1–5 mm in size) alternates with coarser areas (e.g., 82R1_35–38.5, 710.74 mbsf, with the occurrence of a ~40 cm limestone clast). The clasts are mainly vitric and microcrystalline impact melt clasts, as well as carbonate clasts, with a low abundance of felsic (granitic?) basement clasts, generally less than 5 mm in size. The clastic matrix is composed of subrounded carbonate fragments (up to ~200 µm in size), and shows a relatively poor sorting. Preserved foraminifera are also observed within the matrix. Suevite with similar petrography is observed until sample 84R3_27–29.5 (715.09 mbsf) and can be observed in half-core scans until ~715.60 mbsf, also confirmed by Kaskes et al. (2022).

From core level 715.60 mbsf and downward to 721.62 mbsf (lower limit of unit 2C; Morgan et al., 2017), the matrix color transition from dark gray-brown to greenish. Macroscopically, the lithology shows mainly carbonate and felsic basement clasts, and an increasing proportion of black impact melt clasts with increasing depth within the greenish matrix. Microscopically, the matrix is dominated by sparry calcite and phyllosilicates, similarly to the green schlieren observed in the upper part of the upper impact melt rock unit (unit 3A 721.62–737.56 mbsf), which is described in details in de Graaff et al. (2022), and in publication Chapter 7 (Feignon et al., 2022). Thus, the core section between 715.60 and 721.62 mbsf could be interpreted as a larger green schlieren area, with larger calcite crystals and a lower proportion of black impact melt rock than in core section below 721.62 mbsf.

8.2.2. Geochemistry of the suevite unit

Whole rock major and trace element concentration analyses were performed on 24 suevite samples using XRF and INAA analysis, and presented in Figures 8.5 (composition according to stratigraphic position within the core), 8.6 (major element compositions according to SiO_2), and 8.7 (CI-chondrite normalized trace element abundances), respectively. Samples containing large clasts were excluded from the analysis, in order to obtain relatively representative compositions. Suevite samples are characterized by a high loss on ignition (LOI), between 10.6 and 24.3 wt.% (see Feignon et al., 2022). Consequently, the major element data presented here and in Figures 8.5 and 8.6 were recalculated on a LOI-free basis, allowing a better comparison between the different suevite samples and with the other lithologies. Non-recalculated major element data for all the investigated samples are provided in Appendix B.

Bulk CaO and SiO_2 represent the main components of the suevite unit, with a combined contribution higher than 67 wt.%, and up to nearly 80 wt.%. When plotted against depth (Fig. 8.5), CaO and SiO_2 show a symmetric pattern. The CaO contents in the uppermost part of the suevite unit (~617–621 mbsf) are high, exceeding 25 wt.%, and up to 34.4 wt.% measured in the uppermost investigated suevite sample (40R2_107–109, 618.7 mbsf). Then, between ~621 to ~684 mbsf, CaO contents in suevite samples are relatively stable, between 12.9–19.0 wt.%,

while between ~702 and 716 mbsf, the values show more scattering (two suevite samples with CaO contents of 18.7 and 17.7 wt.%, and the two lowermost measured suevite samples having the highest CaO contents, i.e., 38.3 and 39.4 wt.%, see Fig. 8.5). As only four samples were investigated for major element data in the lower part of the suevite unit, it makes difficult to confirm the presence of a pattern in major element contents in this part of the suevite unit. Also, the two impact melt clasts (80R2_126–128, and 83R1_22–24.5, located at 707.2 and 712.3 mbsf, respectively), and the amphibolite clast have low CaO contents (3.20–8.26 wt.%). Below ~716 mbsf, the CaO content in the upper impact melt rock (UIM) decreases with increasing depth in the core, from 24.9 wt.% in UIM sample 86R1_19–21.5 (717.8 mbsf) to less than 5.0 wt.% in UIM samples below 737 mbsf.
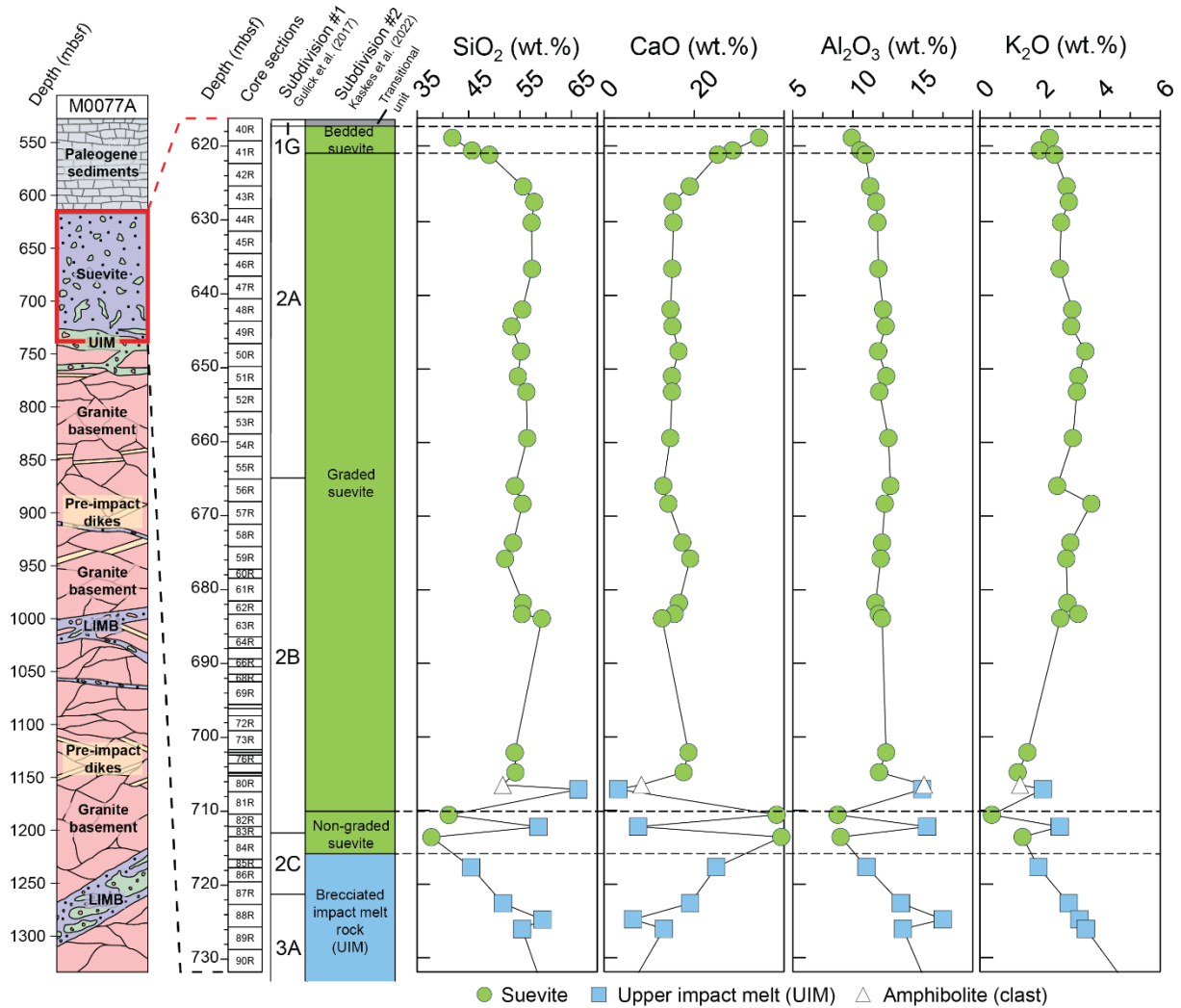
Figure 8.5. *Lithostratigraphy of the M0077A drill core with a focus on the stratigraphy of the suevite unit and adjacent units (interval ~616–732 meters below seafloor [mbsf]), modified from Kaskes et al. (2022). The core sections numbers are indicated adjacent to the depths, then is indicated the subdivision of the suevite unit made by Morgan et al. (2017), followed by the classification of the suevite sequence as proposed by Kaskes et al. (2022). The four columns on the right side allow to compare the variation of selected major elements (SiO2, CaO, Al2O3, and K2O) with depth in the investigated samples. UIM: upper impact melt rock unit, LIMB: lower impact melt bearing unit.*

As indicated earlier, the SiO_2, and, to a lesser extent, Al_2O_3 contents display patterns symmetric to CaO content (Fig. 8.5). For example, SiO_2 contents are low in the uppermost part of the suevite (<49 wt.%), and then increase with increasing depth (52–59 wt.% between 625 and 705 mbsf), before being relatively low again in the two lowermost suevite samples investigated (37.8–41.2 wt.%). Bulk Fe_2O_3, K_2O, Na_2O, and MgO contents show relatively consistent values throughout the suevite unit (Fig. 8.5).
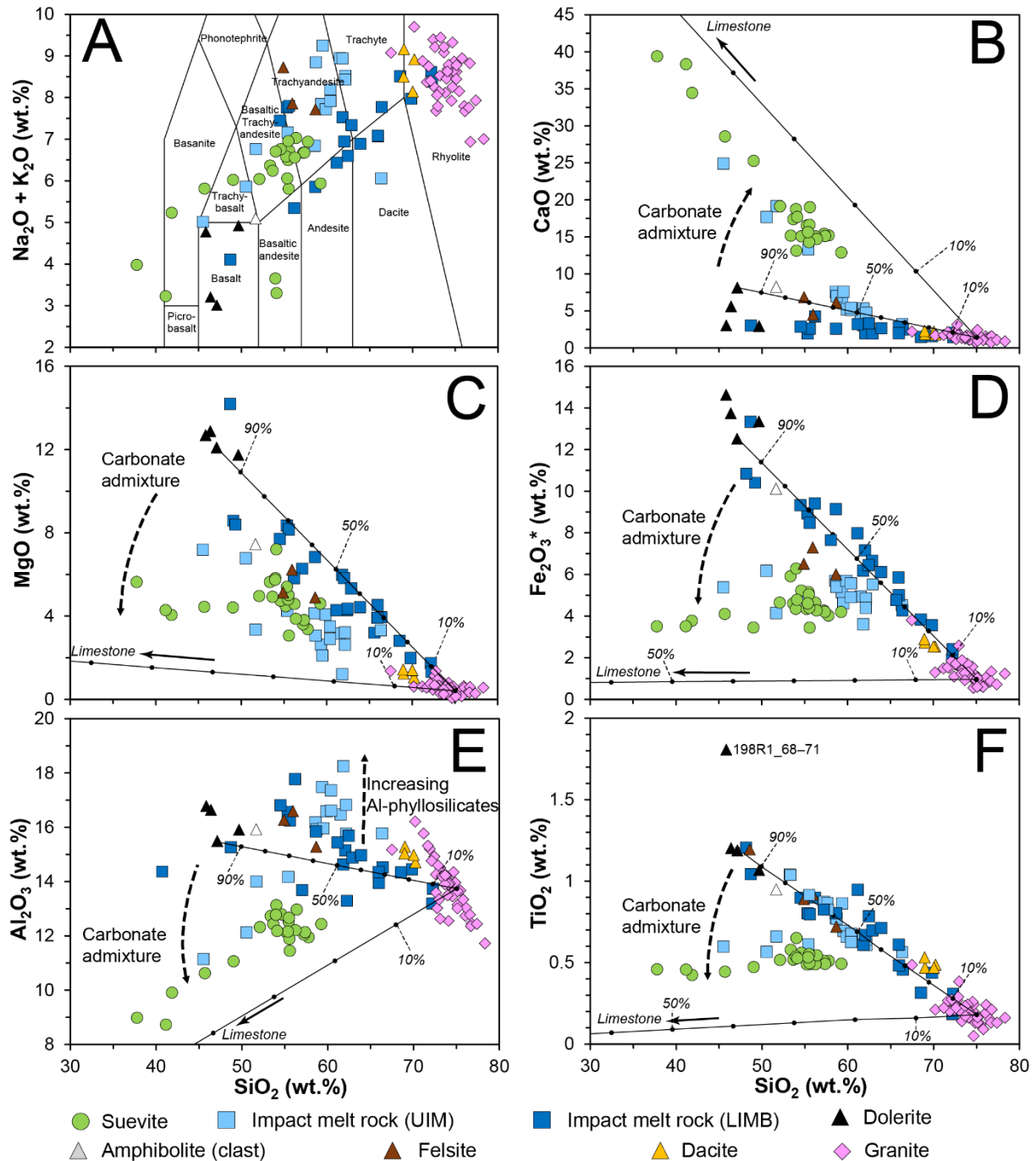
Figure 8.6. *A) Total alkalis versus SiO_2 (TAS) diagram modified from Le Bas et al. (1986). B– F) Harker variation diagrams of CaO, MgO, Fe_2O_3* (total ferrous Fe), Al_2O_3, and TiO_2 versus SiO_2 for the investigated suevite, UIM, LIMB, granite, dolerite, amphibolite, felsite, and dacite samples. All the data are recalculated on a LOI-free basis. Two mixing lines are drawn: (1)*

between dolerite and granitic compositions, and (2) between granitic and limestone composition (i.e., recalculated on a LOI-free basis: SiO_2: 4.06 wt.%, TiO_2: below detection limit (absence of TiO_2 was assumed), Al_2O_3: 0.44 wt.%, Fe_2O_3: 0.74 wt.%, MgO: 2.65 wt.%, and CaO: 90.8 wt.%) measured by de Graaff et al. (2022). Suevite major element compositions are relatively homogeneous, excepted for five, CaO-rich and SiO_2-poor samples, which plot towards the limestone endmember and are part of either the bedded suevite (uppermost three samples) or the non-graded suevite (lowermost two samples) subunits.*

The Harker variation diagrams presented in Fig. 8.6 allow to compare the bulk major element compositions of suevite samples with the other lithologies observed in the M0077A drill core, i.e., impact melt rocks and pre-impact lithologies. Importantly, carbonates, dolerite, and granitic endmembers compositions are represented, as the main contributor to the Chicxulub peak ring impactites compositions (de Graaff et al., 2022; Feignon et al., 2022). In general, the suevite unit shows major element compositions that are partly overlapping with the UIM (excepted for Al_2O_3), and forming a trend towards the carbonate endmember (Fig. 8.6). This suggests that the carbonate component is present in the suevite, as in the UIM (de Graaff et al., 2022), and even to a higher amount than in the UIM, while it is absent in the LIMB (de Graaff et al., 2022; Feignon et al., 2022). Also, suevite major element compositions plots generally in the area delimited by the dolerite-granite mixing line, highlighting the main contribution of these lithologies (mafic and felsic) to the suevite composition. The highest measured CaO amount can also be explained by the presence of large carbonate clasts, the cementation features of the matrix, and/or the presence of post-impact sparry calcite fillings (Kaskes et al., 2022).
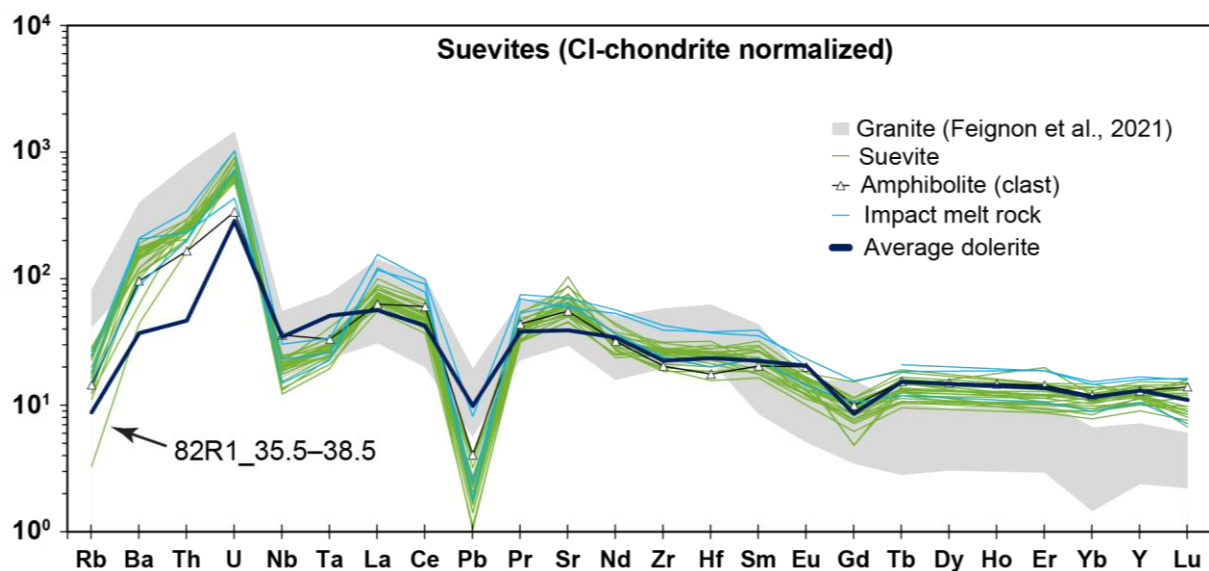
Figure 8.7. *CI-chondrite normalized trace element abundances of suevite samples. Generally, the abundance patterns are relatively similar for all suevite samples. Additionally, three impact melt rock samples are shown, which occur either as clasts within the suevite (80R2_126–128, and 83R1_22–24.5, at 707.2 and 712.3 mbsf, respectively), or belong to the brecciated impact melt rock located on the upper part of the upper impact melt rock (UIM) unit (86R1_19–21.5, 717.8 mbsf), formerly identified as suevite in Morgan et al. (2017). For comparison, granite*

composition range, average dolerite, and amphibolite clast (80R2_61–63.5, 706.6 mbsf) compositions are also shown. Normalization values from McDonough and Sun (1995).

The suevite samples display relatively similar CI-chondrite normalized trace element abundance patterns, with limited variation from a sample to another (Fig. 8.7). In general, suevite CI-chondrite normalized abundance patterns are relatively similar to those of granites (Feignon et al., 2021), excepted for Rb (with suevite samples being depleted in Rb relative to granites, but enriched relative to dolerite and amphibolite samples), and heavy rare earth elements (HREEs), from Tb to Lu, that are enriched relative to the granite but very similar to dolerite and amphibolite, with a flat pattern, whereas granite display decreasing abundances for HREEs. Fluid-mobile elements, such as, Ba, Th, U, and Sr, and also light rare earth elements such as La and Ce, are enriched in the suevite from 40 to more than 800 times the CI-chondrite values. In contrast, Nb and Ta are depleted relative to neighboring elements. A significant Pb anomaly is observed in all suevite samples, and is more important than for granites. No suevite sample display a distinct CI-chondrite normalized abundance pattern relative to other suevites, only suevite sample 82R1_35.5–38.5 (710.7 mbsf) is slightly depleted in Rb, Ba, and Th relative to the other suevites. Additionally, the impact melt clasts in sections 80R2 and 81R2 are enriched in trace elements relative to suevite, and a relatively similar pattern is observed for sample 86R1_19–21.5 (717.8 mbsf), which was petrographically described as similar to the green schlieren of the UIM, further suggesting that it does not belong to the suevite unit.

8.2.3. Re-classification of the suevite sequence

After completion of the IODP-ICDP Expedition 364 drilling, mainly based on macroscopic observations and geophysical data, a first classification of the suevite unit (Unit 2A–2C, 617.33–721.62 mbsf) was proposed, as part of the "upper peak ring" section, which also includes the upper impact melt rock unit (Unit 3A–3B, 721.62–747.02 mbsf) (Morgan et al., 2017; see also Chapter 3). Using detailed petrographic observations and geochemical investigations (including this work), and their detailed, multi-proxy approach, Kaskes et al. (2022) proposed a new classification of the suevite unit of the M0077A drill core. Consequently, the proposed total thickness of the suevite unit is ~98.3 m (from 617.33 to 715.60 mbsf), and this unit can be subdivided into three subunits, namely, from top to bottom: (1) the bedded suevite, (2) the graded suevite, and (3) the non-graded suevite. The suevite unit is located below the transitional unit (unit 1G) and above a section of brecciated impact melt rock (unit 3A) belonging to the UIM. A summary describing these three units is provided here, from the top to the bottom of the suevite unit, with the only difference being the proposition of a slightly (37 centimeters in total) thicker bedded suevite (from 617.33 to 621.25 mbsf) compared to Kaskes et al. (2022). Detailed descriptions and discussion of the new classification of the suevite sequence are provided in Kaskes et al. (2022).

The bedded suevite (617.33–621.25 mbsf) is ~3.9-m-thick and forms the uppermost part of the suevite unit. The upper limit of the bedded suevite with the transitional unit is marked by a sharp, stylolitized contact, and an increase in grain size between the transitional unit and the bedded suevite. Also, compared to the bedded suevite, the transitional unit is enriched in CaO and MnO, and generally depleted in trace elements (Goderis et al., 2021; Appendix C). This

subunit can be defined as fine-grained, well-sorted suevite with the presence of bedding. The clast population is dominated by vitric melt clasts, with rare carbonate clasts, mineral clasts derived from the basement, and microcrystalline impact melt rock clasts. In term of geochemistry, the bedded suevite shows increasing CaO contents with decreasing depth (25.3–34.4 wt.%) and low SiO_2 (41.9–49.0 wt.%), and Al_2O_3 (9.91–11.1 wt.%) relative to the other suevite subunits. The lower limit of the bedded suevite was placed at 621.25 mbsf (corresponding to sample 41R2_50–54), as it corresponds to the deepest level where bedding is macroscopically and microscopically visible, explaining the slight difference with the lower limit at 620.88 mbsf proposed by Kaskes et al. (2022). Also, this difference is within the spatial resolution of geophysical parameters such as seismic velocities which decreases from ~4200 to ~2600 m/s (Christeson et al., 2018; Kaskes et al., 2022).

The graded suevite (621.25–710.01 mbsf), ~89 m in thickness, represents the main part of the suevite sequence. The main characteristics of the graded suevite are a coarsening trend with increasing depth, with a relatively good sorting in the upper part of the subunit, and a relatively poor sorting in the lower part, and a relatively homogeneous geochemical composition for the entire suevite sequence (Figs. 8.5 and 8.6). However, the general coarsening trend with increasing depth is not fully continuous, with some grain size changes in the middle part of the graded suevite (clast size relatively constant, with even slight fining between ~644 and ~663 mbsf). While vitric and microcrystalline impact melt clasts dominate the clast population in the upper part of the bedded suevite, the felsic and mafic basement clasts, as well as the carbonate clasts, are more abundant than in the bedded suevite, especially in the coarse part of the graded suevite, while the matrix is composed of fine, micritic carbonate. Also, the lower part of the graded suevite (~680–710 mbsf) shows a high degree of hydrothermal alteration, with a change in matrix color from blue-green-gray above ~680 mbsf to greenish-dark brown, and a common alteration of the matrix and of the vitric melt clasts, indicated by the presence of phyllosilicates and also some desiccation cracks. The lower part of the graded suevite is marked by the presence of two large (~60 and ~90 cm in size) black aphanitic impact melt rock clasts, with the lower limit of the subunit defined at the bottom of the deepest large impact melt clast, at 710.01 mbsf. The boundary between units 2A and 2B defined in Morgan et al. (2017) was placed at 664.52 mbsf, corresponding to an oblique, erosional surface. However, the petrography of the suevite samples below and above this limit are similar in terms of matrix texture, clast population, and geophysical parameters, such as seismic velocity, density, and porosity values (Christeson et al., 2018; Gulick et al., 2019).

The basal part of the suevite unit, between 710.01 and 715.60 mbsf (~5.6 m thick), consists of a non-graded suevite. The non-graded suevite is distinct from the graded suevite in term of petrography and geochemistry. It is characterized by a relatively poor sorting, the absence of grading, and a fine-grained to coarse-grained texture from a sample to another. The suevite matrix is mainly dark-brown and contains carbonate fragments and foraminifera. The clast population is dominated by grayish impact melt rock and carbonate clasts, while felsic and mafic basement clasts are nearly absent, in contrast to the bottom part of the graded suevite. In terms of geochemistry, the non-graded suevite displays high CaO contents (38.3–39.4 wt.%) and low SiO_2 contents (37.8–41.2 wt.%) in the two samples measured in this subunit. However, the geochemical data from Kaskes et al. (2022) in the non-graded suevite indicate relatively scattered CaO and SiO_2 compositions. According to Kaskes et al. (2022) the core level 715.60

mbsf is marked by a variation in the nature of the matrix, from a clastic matrix dominated by carbonate fragments and foraminifera above this level, to a microcrystalline and macrocrystalline (sparry calcite) matrix below this level. This is confirmed by our observations with a similar transition between samples 84R3_27–29.5 (715.09 mbsf) and 85R1_30–31 (716.79 mbsf). The lithology below 715.60 mbsf is similar to the brecciated impact melt rock with black impact melt and green schlieren defined by Morgan et al. (2017) between 721.62 and 737.56 mbsf (unit 3A), with a higher proportion of green schlieren. Thus, the interval 715.60–721.62 mbsf was classified as a continuation of the upper impact melt rock unit, composed of brecciated impact melt rock, and further confirmed by geophysical observations (Christeson et al., 2018; Kaskes et al., 2022).

8.2.4. Suevite unit emplacement

The new classification of the suevite unit proposed by Kaskes et al. (2022) allows to refine the emplacement model of the proximal impactites of the Chicxulub impact structure, by linking observations with emplacement processes and (relative) timing of the emplacement. Here is proposed a summary of these emplacement processes for each subunit of the suevite (see also, Fig. 8.8). Detailed presentation and discussion of the emplacement mechanism of the suevite unit are provided in Kaskes et al. (2022).

After the excavation stage, a central uplift formed in the center of the transient cavity, before experiencing gravitational collapse to form the peak ring, and entraining crustal and impactite material (Fig. 8.8; Morgan et al., 2016; Riller et al., 2018; Rae et al., 2019). During the modification stage, the Chicxulub peak ring was composed of shocked granitic basement rocks (Feignon et al., 2020) covered by a ~30-m thick impact melt sheet (Fig. 8.8), corresponding to the upper impact melt rock unit (de Graaff et al., 2022), with an overlying ~6-m-thick, clast-rich impact melt rock unit composed of felsic basement and recrystallized carbonate clasts (de Graaff et al., 2022). It was proposed that the clasts were entrained by outward-flowing melt and density currents (Gulick et al., 2019; de Graaff et al., 2022). As the impact occurred in a shallow seawater environment, after the initial vaporization of the seawater and target rocks at the impact site, the water from the Gulf of Mexico flowed back into the crater, entering from a gap in the northeastern part of the inner rim of the crater, less than 30 minutes after the impact, based on the "dam-break" model (e.g., Smit et al., 1996; Gulick et al., 2019). The contact between seawater and the hot impact melt rock caused phreatomagmatic (melt-water) explosive interactions, with quench fragmentation of the impact melt as well as important emission of steam (Gulick et al., 2019; Osinski et al., 2020; Schulte et al., 2021). This phreatomagmatic fragmentation probably resulted in the formation of the green schlieren textures observed in the brecciated impact melt rock (Fig. 8.8), and were later replaced by sparry calcite due to hydrothermal and seawater alteration (Kring et al., 2020; Schulte et al., 2021). The brecciation of the impact melt rock did not penetrate deeper than 737.56 mbsf, as the green schlieren are not observed deeper within the impact melt rock unit (Kaskes et al., 2022). Also, given the high amount of foraminifera preserved in the non-graded suevite, and the low amount of crystalline basement clasts, it is likely that the seawater that entered the crater <30 minutes after the impact was relatively poor in rock debris (Fig. 8.8), only bringing material from the seabed, while impact melt and carbonate clasts were probably derived from the top of the impact

melt sheet (Kaskes et al., 2022). While the microcrystalline impact melt rock clasts are similar in texture to the black impact melt rock observed in the UIM and could represent brecciated fragment derived from the UIM, the abundant vitric melt clasts are probably the result of a fast quenching of the top of the impact melt sheet, and were subsequently fragmented due to phreatomagmatic interactions. Thus, the non-graded suevite unit was probably emplaced by phreatomagmatic processes leading to the formation of a hyaloclastite breccia-like deposit (Watton et al., 2013), which are generally observed at submarine or subglacial volcanoes when magma interacts with water or ice, and are characterized by a poorly-sorted, matrix-supported lithology enriched in quenched glassy fragments (Greenfield et al., 2020). An alternative, but relatively similar, model was proposed by Osinski et al. (2020), suggesting that the section between 712.83–721.62 mbsf (Unit 2C) was a product of high-energy molten fuel-coolant interaction, very similar to phreatomagmatic deposits. However, the phreatomagmatic deposits from the emplacement model of Osinski et al. (2020) should be well-sorted, which is not the case for the non-graded suevite.

Then, from ~710 mbsf, the graded suevite was emplaced over a thickness of ~89 m, with a fining trend and increased sorting with decreasing depth. The petrographic compositions (clast population and matrix), as well as the bulk major and trace element compositions are relatively similar throughout the unit. A wide variety of clasts are observed in this unit, but they remain relatively similar in term of proportions and chemical composition throughout the graded suevite. The lower seismic velocity, density, and higher porosity values of this unit relative to the non-graded suevite imply a rapid deposition and limited cementation (Christeson et al., 2018; Kaskes et al., 2022). Thus, the graded suevite can be interpreted as the product of a depositional event that occurred relatively rapidly after the impact, with a decreasing energy with time. The most likely scenario proposed is that a powerful ocean resurge occurred into the Chicxulub crater and acted as a sorting agent (Gulick et al., 2019). Similar suevitic and impact breccia sequences were observed in the impactites from the Chesapeake Bay impact structure (USA; see Dypvik et al., 2018; Kaskes et al., 2022, and references therein for detailed discussion). Given the wide variety of clast types observed, and the clast-supported nature of the basal part of the graded suevite, it is most probable that the ocean water from this ocean resurge was debris-rich, with these debris probably coming from the fallout, settling, and mixing of the proximal ejecta (Fig. 8.8). The abundant vitric melt clasts, and microcrystalline impact melt rock clasts present in the graded suevite were probably brought from other areas of the crater by the ocean resurge (Kaskes et al., 2022). With the increasing volume of water flooding into the crater cavity, the water-melt ratio became so high that it was no longer possible to sustain phreatomagmatic activity (Németh and Kósik, 2020). This suggests that the phreatomagmatic impact melt-water interactions were short lived, in accordance with the emplacement model proposed by Gulick et al. (2019), whereas Osinski et al. (2020) suggested that phreatomagmatic processes were also responsible of the deposition of unit 2B (664.52–712.83 mbsf) and the majority of unit 2A (617.33–664.52 mbsf). According to the "dam-break" model of Gulick et al. (2019), the flooding of the crater up to the depth of the peak ring was estimated to take ~30–60 minutes, and would correspond to the deposition of the non-graded suevite subunit and the basal part of the graded suevite. Most likely, the remaining part of the graded suevite was deposited in the following few hours, with clasts settling from the water

column, and a decreasing energy of the system which finally form the well-sorted, fine-grained upper part of the graded suevite (Fig. 8.8; Kaskes et al., 2022).

The bedded suevite, starting from 621.25 mbsf and up to 620.88 mbsf in the suevite sequence, is characterized by the occurrence of well-developed bedding, an increase in bulk CaO content, and also an increase in seismic velocity, density and a decrease in porosity values (Christeson et al., 2018), which are typical of a well-cemented unit, and longer depositional processes than for the non-graded and the graded suevite subunits, with also reworking occurring (Kaskes et al., 2022). The upper part of the suevite unit is commonly interpreted as the product of seiche waves occurring within the crater (Fig. 8.8; Smit et al., 1996; Gulick et al., 2019; Whalen et al., 2020). Here, the transition from graded suevite to bedded suevite at 621.25 mbsf (620.88 mbsf in Kaskes et al., 2022) marks the onset of the seiche waves after the ocean resurge deposit corresponding to the graded suevite. Kaskes et al. (2022) also characterized the uppermost 20 cm of the bedded suevite as being cross-bedded and coarser than the remaining part of this unit, implying a rapid sedimentation, and associated with vertical sedimentary structures interpreted as dewatering pipes or fluid and vapor channels associated with the hydrothermal system (Gulick et al., 2019; Kring et al., 2020). These features were interpreted as turbidites or density current deposits, typical of high energy conditions of depositions (Gulick et al., 2019). Gulick et al. (2019) suggested that this specific layer was deposited following the return of a reflected tsunami coming from the continental landmass, possibly the Mexican highlands, 800 km away to the W-SW of the crater, and that the reflected tsunami waves entered the Chicxulub impact structure within 24 hours after the impact. Thus, this indicates that, most probably, the entire suevite unit was deposited within only a day after the impact (Gulick et al., 2019).

Following the end of the bedded suevite deposition at 620.88 mbsf, the sedimentation continued at a much lower rate (low energy of the system), with a slow settling of thin particles forming the ~75-cm-thick transitional unit (Lowery et al., 2018; Bralower et al., 2020; Whalen et al., 2020). The transitional unit is then capped by a ~3-cm-thick gray-green marlstone layer which display a positive Ir anomaly, with Ir content of ~1.0 ppb, indicating the presence of an impactor component, and interpreted as representing atmospheric settling of fine meteoritic matter, which occurred <20 years after the impact (Goderis et al., 2021). This layer marks the end of deposition of the proximal impactite sequence within the M0077A drill core (Fig. 8.8).
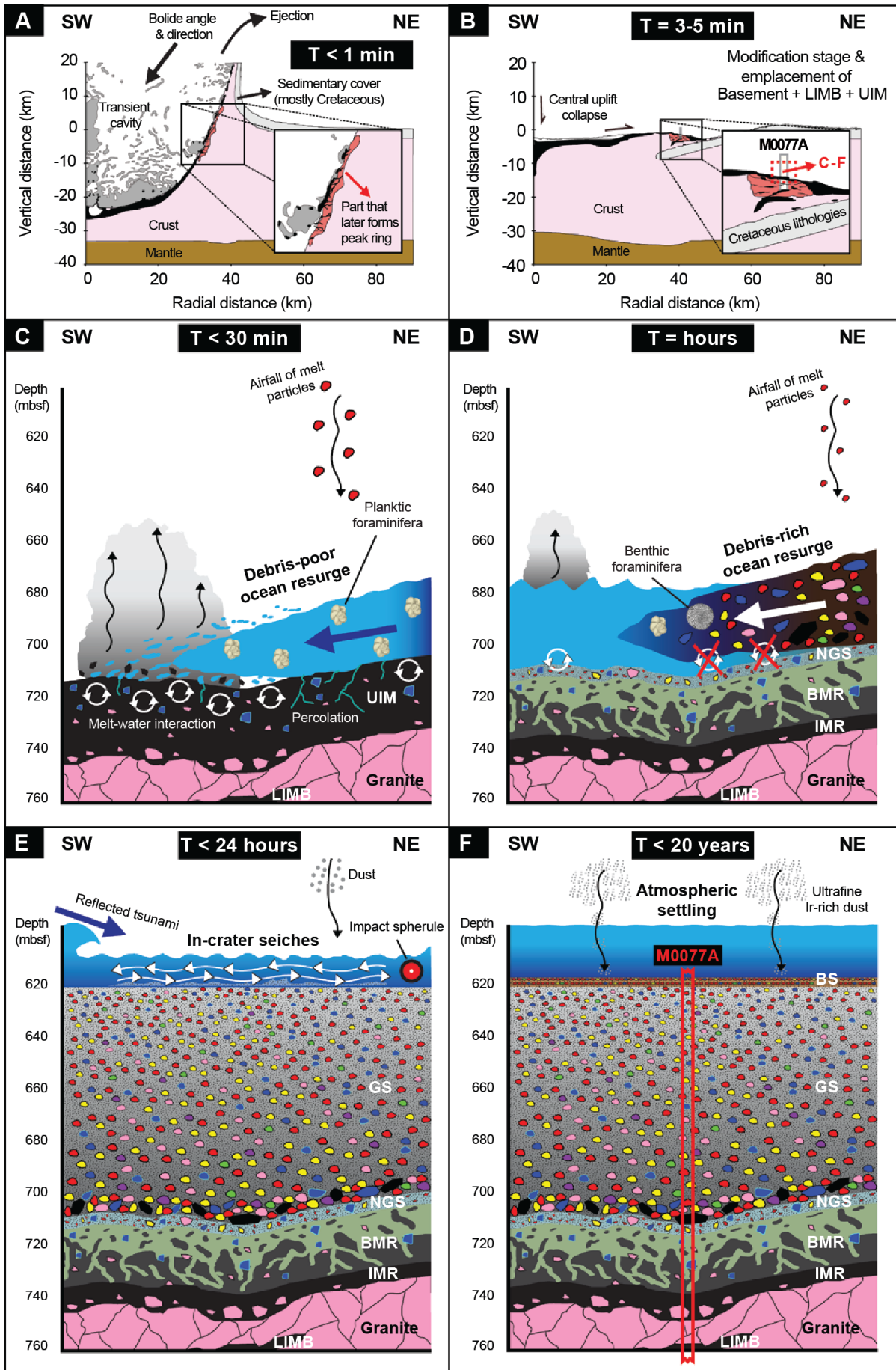
A — SW / NE — T < 1 min
Bolide angle & direction; Ejection; Transient cavity; Sedimentary cover (mostly Cretaceous); Crust; Mantle; Part that later forms peak ring

B — SW / NE — T = 3-5 min
Modification stage & emplacement of Basement + LIMB + UIM; Central uplift collapse; Crust; Mantle; Cretaceous lithologies; M0077A; C-F

C — SW / NE — T < 30 min
Airfall of melt particles; Planktic foraminifera; Debris-poor ocean resurge; Melt-water interaction; Percolation; UIM; Granite; LIMB

D — SW / NE — T = hours
Airfall of melt particles; Benthic foraminifera; Debris-rich ocean resurge; NGS; BMR; IMR; Granite; LIMB

E — SW / NE — T < 24 hours
Reflected tsunami; Dust; In-crater seiches; Impact spherule; GS; NGS; BMR; IMR; Granite; LIMB

F — SW / NE — T < 20 years
Atmospheric settling; Ultrafine Ir-rich dust; M0077A; BS; GS; NGS; BMR; IMR; Granite; LIMB

303

Figure 8.8. *Schematic representations of the several events that led to the emplacement of the suevite unit observed within the M0077A drill core (from Kaskes et al., 2022). A) Less than one minute after the impact, during the excavation stage, where target rocks experienced shock metamorphism, melting, and vaporization inside the transient cavity, and were also ejected outside of the crater (Morgan et al., 2016; Collins et al., 2020). B) About five minutes after the impact, the central uplift formed within the Chicxulub transient cavity, and subsequently collapsed due to gravity, leading to peak ring formation (e.g., Morgan et al., 2016; Riller et al., 2018). At this time, the peak ring was composed of granitic basement with injection of impact melt rocks (LIMB), and covered by the upper impact melt rock (UIM) unit (de Graaff et al., 2022). C) Focus on the peak ring area, less than thirty minutes after the impact, where first debris-poor seawater flooded the peak ring from a gap in the N-NE area of the crater inner rim. The ocean water interacted with the hot impact melt sheet, and percolated within the impact melt, resulting in intense quenching and fragmentation (phreatomagmatic activity). This subsequently brecciated the upper impact melt (BMR) sheet, forming the green schlieren textures observed in the upper part of the UIM (the non-brecciated, lower part of the UIM is then expressed as MR), as well as the ~5.6-m-thick, non-graded suevite unit (NS). D) During the following hours, the flooding of the crater continued with a high energy, debris-rich ocean resurge, which stopped the phreatomagmatic activity, and formed the ~89 m-thick graded suevite (GS). With the ocean resurge energy decreasing, the clast size is fining upward. E) After slow dissipation of the ocean resurge energy, seiche waves occurred within the crater, forming the reworked, fine-grained, ~3.9 m-thick bedded suevite (BS). Within this subunit, a preserved impact spherule, which was initially ejected from the crater and flowed back within, was identified by Kaskes et al. (2022). The top ~20 cm of the bedded suevite are marked by cross bedding, linked to the return of a reflected tsunami coming from the nearest landmass, within 24 hours after the impact (Gulick et al., 2019). F) The final stage of deposition of the impactite sequence within core M0077A occurred with the slow deposition of the ~75 cm-thick transitional unit, days to months after the impact (Lowery et al., 2018; Bralower et al., 2020; Whalen et al., 2020), further capped by a 3-cm-thick gray-green marlstone, characterized by a positive iridium anomaly. This was interpreted as corresponding to the settling of atmospheric dust ejected during the Chicxulub impact event, and enriched in meteoritic material. The deposition of the gray-green marlstone is thought to have occurred within 20 years after the impact (Goderis et al., 2021). The color of clasts within the suevite is: red: vitric impact melt clasts, yellow: microcrystalline impact melt rock clasts, pink: felsic basement clasts, purple: mafic basement clasts, green: silica mineral clasts, and blue: carbonate clasts.*

8.3. Isotopic compositions (Rb-Sr and Sm-Nd) of pre-impact dikes

In addition to the Rb–Sr and Sm–Nd isotopic compositions of granite samples, which are presented in the publication in Chapter 6 (Feignon et al., 2021), additional measurements were performed for seven pre-impact dike lithologies (i.e., three dolerite, two felsite, and two dacite samples), and for one lower impact melt-bearing unit sample (265R2_9–11, 1216.5 mbsf). This latter sample corresponds to a partially melted dolerite dike according to its petrographic and geochemical characteristics (Feignon et al., 2022). The isotopic data were integrated into a forthcoming publication by de Graaff et al. (submitted) and are presented here in Fig. 8.9, and in Appendix E.

The $^{87}Sr/^{86}Sr$ ratios and ε_{Nd} values were calculated using the impact age $t = 66.05$ Ma (Sprain et al., 2018). The $(^{87}Sr/^{86}Sr)_{t=66.05Ma}$ ratios of felsites, dacites, and lower impact melt rock range from 0.7053 to 0.7074, while granite samples have more radiogenic values towards and above seawater values (0.7073–0.7117), although these lithologies display relatively similar $(\varepsilon_{Nd})_{t=66.05Ma}$ values, between -3.7 and -2.1 (Fig. 8.9). The dolerites show similar offset towards seawater values, with more radiogenic $(^{87}Sr/^{86}Sr)_{t=66.05Ma}$ ratios of 0.7067–7073, similar to the other lithologies, but show less radiogenic $(\varepsilon_{Nd})_{t=66.05Ma}$ values ranging from -0.7 to 3.1, which possibly indicate an enriched mantle source signature (see also, de Graaff et al., submitted). The offset observed in $(^{87}Sr/^{86}Sr)_{t=66.05Ma}$ ratios of the pre-impact dike, and impact melt rock samples is probably indicative of the seawater alteration that occurred at the Chicxulub impact structure following the onset of a long-lived hydrothermal system, which may have overprinted to some extent the pristine isotopic compositions (Kring et al., 2020; Simpson et al., 2020; Feignon et al., 2021; de Graaff et al., 2022). Thus, some care should be taken in the interpretation of the data.

Dating of the dolerite, felsite, and dacite dikes was performed by de Graaff et al. (submitted) using U–Pb laser ablation inductively coupled plasma mass spectrometry in apatite and titanite crystals, yielding Carboniferous ages for the dacites (~322–317 Ma), overlapping with previously known ages of the granite basement unit, i.e., 326 ± 5 Ma (Zhao et al., 2020), and 334 ± 2.3 Ma (Ross et al., 2022). The dolerite yield Jurassic ages (~168–158 Ma), whereas the felsites show different ages, from Carboniferous (342.5 ± 4.3 Ma) to Jurassic (152.2 ± 11.4 Ma). These dating were performed on different samples than those presented in this study, but belong to the same dikes. Interestingly, the dolerites represent the first Jurassic lithology sampled within the Yucatán peninsula, and more broadly, in the southern Gulf of Mexico area (de Graaff et al., submitted).

Previous studies have shown that the granite basement in the M0077A drill core was emplaced during the Carboniferous in a volcanic arc tectonic context (Zhao et al., 2020; Feignon et al., 2021; de Graaff et al., 2022; Ross et al., 2022). The similar isotopic compositions of dacites and felsites with granites suggest that they formed in a similar geodynamic environment, except the felsite samples displaying a Jurassic age. The dolerites, however, represent a second, distinct magmatic phase that occurred during the Jurassic, accompanied by felsite that possibly formed as a consequence of dolerite emplacement (de Graaff et al., submitted).
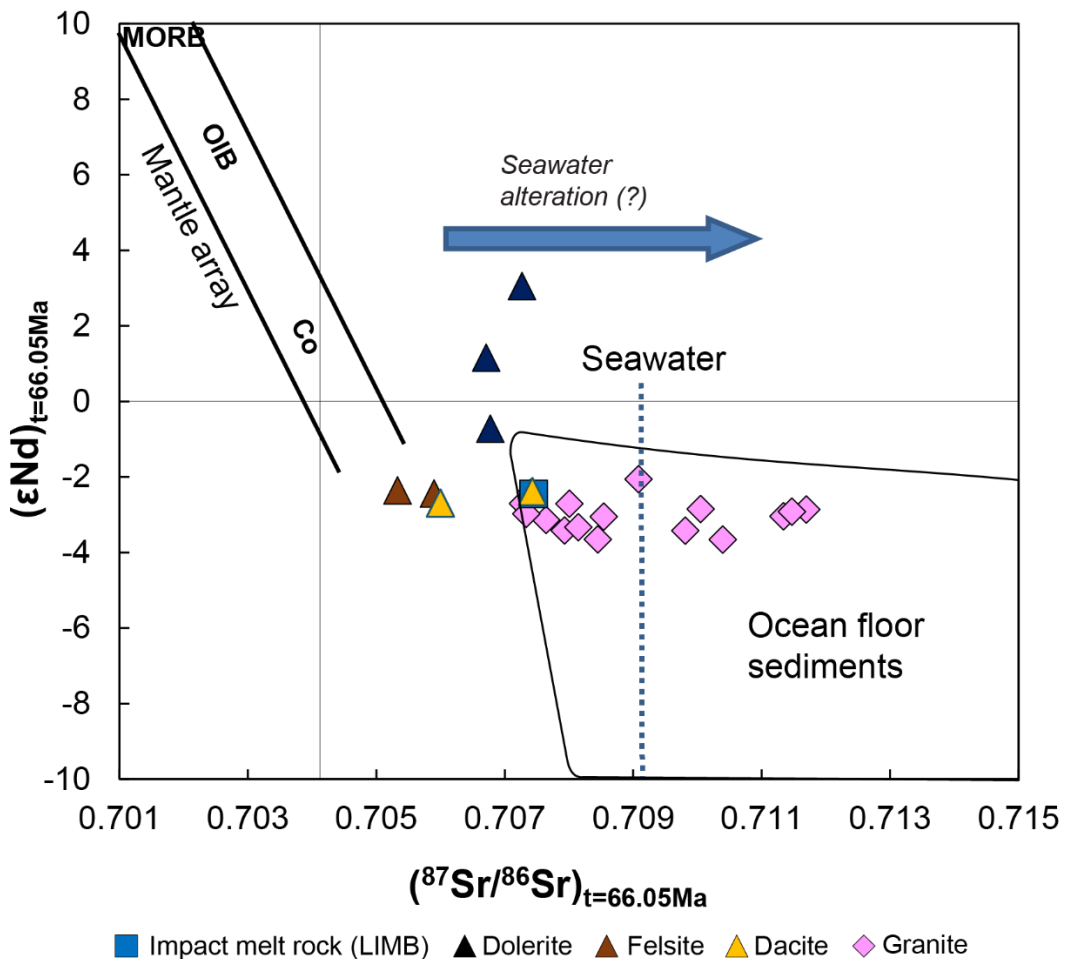
Figure 8.9. *Initial ($^{87}Sr/^{86}Sr)_{t=66.05Ma}$ ratios and ($\varepsilon Nd)_{t=66.05Ma}$ values for pre-impact dikes (dolerite, felsite, and dacite), lower impact melt bearing unit (LIMB), and granite samples (Feignon et al., 2021), The seawater and ocean floor sediments data are from White et al. (1985), Woodhead and Fraser (1985), and Ben Othman et al. (1989). The magmatic sources in the mantle array (from Philpotts and Ague, 2009) shown are: MORB: mid-ocean ridge basalt, OIB: oceanic islands basalt, and Co: continental flood basalts. Globally, the ($^{87}Sr/^{86}Sr)_{t=66.05Ma}$ ratios show an offset towards and beyond seawater values, possibly suggesting a seawater hydrothermal overprint event (the post-impact, long-lived hydrothermal system that occurred after the Chicxulub impact event; Kring et al., 2020). The ($\varepsilon Nd)_{t=66.05Ma}$ values are generally crustal for all samples, except dolerites, which display less radiogenic values, and possibly indicating an enriched mantle source (see details in de Graaff et al., submitted).*

Apart from hydrothermal alteration processes, the isotopic compositions of the dolerite dikes may be explained by the incorporation of a crustal component in the source region, while it would not correspond to typical mid-oceanic ridge basalt (MORB) or oceanic island basalt (OIB) dolerites. de Graaff et al. (submitted) further compared the M0077A drill core dolerites with other Jurassic-aged lithologies from the Gulf of Mexico, i.e., the Southern Louisiana salt dome xenoliths, consisting of alkalic igneous rocks (Stern et al., 2011), and dolerites recovered in Northwest Cuba (Allibon et al., 2008). de Graaff et al. (submitted) suggested that the dolerites from the Chicxulub peak ring and the Southern Louisiana salt dome xenoliths could be related to the opening of the Gulf of Mexico due to their similar Hf isotopes and REEs compositions,

while the Northwest Cuba Jurassic-aged dolerites show a distinct trace element and Nd isotope composition, suggesting a different source between the north and the south regions of the Gulf of Mexico.

8.4. Reconstruction of the Yucatan peninsula geological history and the Chicxulub impact event at the peak ring area

Following all of the investigations presented in this study, it is possible to compile a summary of the events that occurred before, during, and shortly after the Chicxulub impact event. The M0077A drill core recovered during the IODP-ICDP Expedition 364 in 2016 provides important insight for both the pre-impact geological setting of the Yucatán peninsula and the emplacement of the impactites within the impact structure, allowing to reconstruct a precise, possible scenario of the events. Thus, several steps can be identified using the detailed investigations made in this study, which further refine the impact scenario and its aftermath as presented in Chapter 3:

1) During the Carboniferous, a volcanic arc was active, with intrusion(s) of high-K calc-alkaline granite body/ies (334 ± 2.3 Ma) composed of K-feldspar, plagioclase, quartz, and minor biotite, further crosscut by dacite (~322–317 Ma) and possibly felsite (342.5 ± 4.3 Ma) dikes. The granite was intruded within the Pan-African Maya block, with the admixture of Grenvillian (0.8–1.2 Ga) crust during granite genesis. The arc tectonic context was probably linked with the closure of the Rheic ocean associated with the assembly of the Pangea (see Zhao et al., 2020; Feignon et al., 2021; de Graaff et al., 2022, submitted; Ross et al., 2022).

2) During the late Triassic, the initial breakup of the Pangea began, and was associated with intracontinental extension occurring at the Yucatán peninsula area. During this event, the granite experienced hydrothermal fluid/metasomatic alteration, and possible deformation (?) (273 ± 21 Ma), indicated by an enrichment in radiogenic Sr and the crystallization of allanite (Feignon et al., 2021).

3) During the Jurassic, a pervasive magmatic phase occurred, associated with the southern extension of the opening of the Gulf of Mexico, and possibly the anticlockwise rotation of the Yucatán basement (~164–139 Ma; Dickinson and Lawton, 2001; Steiner, 2005). During this magmatic event, the felsic basement of the Yucatán peninsula was intruded by dolerite (168–158 Ma) and minor felsite (152.2 ± 11.4 Ma) dikes (de Graaff et al., submitted).

4) From the Berriasian (~139 Ma) until the Chicxulub impact event (~66.05 Ma), the Yucatán block remained geologically stable, and was covered by an approximately ~3-km-thick carbonate platform composed of limestone, dolomite, marl, and anhydrite (López Ramos 1975; Kring, 2005). The sedimentary platform was also covered by seawater, deepening to the north and northeast with an average water depth of ~600 m (Gulick et al., 2008). It is assumed that the crystalline basement rocks mentioned above were located at depths of ~8–10 km (Morgan et al., 2016; Riller et al., 2018).

5) The Chicxulub impact crater was formed ~66.05 Ma, by the impact of a ~12-km diameter impactor with a carbonaceous chondrite-like composition (Kyte, 1998; Shukolyukov and Lugmair, 1998; Quitté et al., 2007; Goderis et al., 2013) in the Yucatán peninsula, coming from

the northeast, and with a steeply-inclined (~45–60°) trajectory (Collins et al., 2020; see also discussion and references in Feignon et al., 2022).

6) In the first minute after the impact, the contact and compression phase occurred, generating intense shock waves, causing compression, brecciation, melting, and vaporization of the target rock material, and nearly complete vaporization of the projectile (e.g., Collins et al., 2020). The granitic basement (recovered within the M0077A core) was shocked at pressures of 17 ± 1 GPa, forming shock metamorphic features in quartz grains (PFs, FFs, and PDFs), feldspars, biotite, apatite, titanite, and zircon grains (Feignon et al., 2020, and references therein; section 8.1, and references therein). Still in the first minute after the impact, the excavation stage started following the passage of rarefaction waves, forming a ~100 km-diameter, and ~20-km depth transient cavity. The excavation flow formed an impact plume composed of the vaporized, melted, and brecciated target material, also including impact spherules (Smit, 1999; Morgan et al., 2016; Riller et al., 2018; Gulick et al., 2019; Kaskes et al., 2022). At the same time, multiple melt injections occurred within the shocked crystalline basement, with a composition devoid of a carbonate component, and eventually forming the lower impact melt-bearing unit observed in core M0077A, which was suggested to occur in the early phases of the modification stage (de Graaff et al., 2022). At the same time, a minimum of ~1.5% to ~10% of the impactor material was entrained within the expansion plume, while the remaining volume of the projectile may have been preserved in deep impact melt rock bodies, as it moved downward (Pierazzo and Melosh, 2000; Feignon et al., 2022). An outward-moving tsunami formed across the Gulf of Mexico (e.g., Smit et al., 1996; Gulick et al., 2019).

7) Three minutes after the impact, the modification stage started, the transient cavity collapsed and an overheightened central uplift mainly composed of crustal rocks formed, before rapidly undergoing gravitational collapse (with rock fluidization occurring), resulting in lateral movements of crustal (further fracturing and deformation may have occurred within the granite) and impactite material, and finally forming the peak ring (Morgan et al., 2016; Riller et al., 2018; Rae et al., 2019). An ~30-m-thick impact melt rock sheet (probably formed mainly by a mixing between granitic and dolerite components, with no or very low impactor component; de Graaff et al., 2022; Feignon et al., 2022) was covering the peak ring, with the uppermost 6 m composed of felsic basement and carbonate clasts, granitic clasts were partially digested, and quartz grains toasted. Outward flowing melt and density currents may have carried carbonate clasts at the top of the peak ring, with the entrained carbonate partially melting at the contact of the hot impact melt sheet, and possibly forming mingling textures (Gulick et al., 2019; de Graaff et al., 2022). At the same time, large quantities of gases and dust were released into the atmosphere, with estimated volumes of 325 ± 130 Gt S, 425 ± 160 Gt CO_2, and 0.75–2.50 Gt of soot (Artemieva et al., 2017; Lyons et al., 2020).

8) Less than thirty minutes after the impact, a large gap at the north-northeast of the Chicxulub inner rim allowed debris-poor and carbonate-foraminifera-rich seawater to flow back into the crater, and came in contact with the hot impact melt sheet, causing phreatomagmatic interactions associated with steam formation and quench fragmentation of the impact melt (Gulick et al., 2019; Osinski et al., 2020). Brecciation of the upper part of the impact melt occurred, as well as the formation of green schlieren textures. Then, hyaloclastite breccia-like

deposits formed, resulting in the non-graded suevite unit, up to one hour after the impact (Kaskes et al., 2022).

9) In the following hours, the crater was continuously flooded by high-energy, debris-rich (probably coming from ejected material that was entrained within seawater) ocean resurge, which stopped the phreatomagmatic processes. The energy of the ocean resurge continuously decreased, and clasts (vitric impact melt, microcrystalline impact melt rock, felsic and mafic basement, and carbonates) settled through the water column, forming the fining-upward graded suevite.

10) Within a day after the impact, the bedded suevite emplaced, with lower-energy depositional processes than for the graded suevite. Reworking occurred, and is suggested to have been caused by seiche waves within the crater (Gulick et al., 2019; Whalen et al., 2020; Kaskes et al., 2022). Then, the reflected tsunami waves that reached continental landmass of central Mexico returned back into the crater, forming a ~20-cm cross bedded interval in the uppermost part of the bedded suevite (Gulick et al., 2019; Kaskes et al., 2022). At about the same time, ejected material within the impact plume fell back to the Earth's surface, at locations hundreds to thousand kilometers from the impact site, triggering global wildfires (e.g., Morgan et al., 2022, and references therein).

11) From days to months after the impact, the transitional unit was slowly deposited over ~75 cm above the suevite, forming dark-brown, fining-upward silt- and clay-sized limestone (Lowery et al., 2018; Bralower et al., 2020; Whalen et al., 2020).

12) Less than 20 years after the impact, the ultrafine meteoritic matter settled above the transitional unit, forming the gray-green marlstone layer, enriched in Ir (Goderis et al., 2021). The Chicxulub ejecta were also deposited all around the world, forming the well-known K–Pg boundary layer, enriched in meteoritic and shocked material (e.g., Alvarez et al., 1980; Kyte, 1998; Claeys et al., 2002; Goderis et al., 2013). Also, the fine dust and large volume of gases injected into the atmosphere caused a global darkening, an impact winter, with maximal temperature decreases of more than 20–30 °C between 2–4 years after the impact, which lasted for a decade before surface temperatures recovered to pre-impact levels, and also ocean acidification triggering K–Pg mass extinction (Morgan et al., 2022, and references therein). An alternative hypothesis suggests that the mass extinction may have occurred due to global firestorms, triggered by the reentry of ejected material within the atmosphere after the impact, which may have largely incinerated terrestrial ecosystems, and causing mass mortality of animals (Robertson et al., 2013). Another scenario proposed by Kaiho et al. (2016) suggests that the soot injection within the stratosphere did not induce a global darkening, but rather latitude-dependent climate changes (i.e., colder climates at mid–high latitudes and drought with milder cooling at low latitudes on land), inducing at first terrestrial extinctions for few years, followed by marine extinctions for a longer period of time (limited cessation of photosynthesis in oceans occurring a few months to 2 years after the impact, followed by surface water cooling of oceans within ~2 to 6 years after the impact). Years after the impact, life, in the form of nannoplankton and foraminifera, reappeared in the impact basin (Lowery et al., 2018). Following the impact winter, the long-term effect of CO_2 injected into the atmosphere from

target rock vaporization and global wildfires may have led to a global warming that lasted for ~100,000 years (Morgan et al., 2022, and references therein).

13) Approximately 30,000 years after the impact, abundant and diverse benthic organisms were established within the impact structure, indicating that seafloor conditions had returned to normal with a high-productivity ecosystem, with important organic matter flux (Lowery et al., 2018).

14) For more than one million years, a long-lived hydrothermal system took place within the Chicxulub impact structure, with initial temperatures of 300–400 °C, and led to alteration of the peak ring rocks, mainly by alkaline-saline water (Kring et al., 2020; Simpson et al., 2020). At the same time, and until today, normal sedimentation processes resumed within the Chicxulub impact structure, covering it with Paleogene sedimentary rocks.

15) About ten million years after the impact, the hydrothermal system became colder (~20–50 °C), allowing the formation of clay minerals throughout the suevite and upper impact melt rock units, by interaction with fluids mainly composed of meteoric water (Simpson et al., 2022).

References

Allibon J., Lapierre H., Bussy F., Tardy M., Cruz Gàmez E. M., and Senebier F. 2008. Late Jurassic continental flood basalt doleritic dykes in northwestern Cuba: remnants of the Gulf of Mexico opening. *Bulletin de la Société Géologique de France* 179:445–452. https://doi.org/10.2113/gssgfbull.179.5.445.

Alvarez L. W., Alvarez W., Asaro F., and Michel H. V. 1980. Extraterrestrial cause for the Cretaceous-Tertiary extinction. *Science* 208:1095–1108. https://doi.org/10.1126/science.208.4448.1095.

Alwmark C., Bleeker W., LeCheminant A., Page L., and Scherstén A. 2017. An Early Ordovician ^{40}Ar-^{39}Ar age for the ~50 km Carswell impact structure, Canada. *Geological Society of America Bulletin* 129:1442–1449. https://doi.org/10.1130/B31666.1.

Artemieva N., Morgan J., and Expedition 364 Science Party 2017. Quantifying the Release of Climate-Active Gases by Large Meteorite Impacts With a Case Study of Chicxulub. *Geophysical Research Letters* 44:10,180–10,188. https://doi.org/10.1002/2017GL074879.

Ben Othman D., White D., and Patchett J. 1989. The geochemistry of marine sediments, island arc magma genesis and crust-mantle recycling. *Earth and Planetary Science Letters* 94:1–21. https://doi.org/10.1016/0012-821X(89)90079-4.

Birski Ł., Słaby E., Wirth R., Koch-Müller M., Simon K., Wudarska A., Götze J., Lepland A., Hofmann A., and Kuras A. 2019. Archaean phosphates: a case study of transformation processes in apatite from the Barberton greenstone belt. *Contributions to Mineralogy and Petrology* 174:25. https://doi.org/10.1007/s00410-019-1560-z.

Bonamici C. E., Fanning C. M., Kozdon R., Fournelle J. H., and Valley J. W. 2015. Combined oxygen-isotope and U-Pb zoning studies of titanite: new criteria for age preservation. *Chemical Geology* 398:70–84. https://doi.org/10.1016/j.chemg eo.2015.02.002.

Borg I. Y. 1970. Mechanical <110> twinning in shocked sphene. *American Mineralogist* 55:1876–1888. https://pubs.geoscienceworld.org/msa/ammin/article-abstract/55/11-12/1876/540764/Mechanical-110-twinning-in-shocked-sphene1.

Borg I. Y. and Heard H. C. 1972. Mechanical twinning in sphene at 8 Kbar, 25° to 500° C. In *Studies in Earth and Space Sciences*, edited by R. Shagam, R. B. Hargraves, W. J. Morgan, F. B. Van Houten, C. A. Burk, H. D. Holland, and L. C. Hollister. Geological Society of America Memoirs #132, Geological Society of America, Boulder, Colorado, pp. 585–592. https://doi.org/10.1130/MEM132-p585.

Bralower T. J., Cosmidis J., Fantle M. S., Lowery C. M., Passey B. H., Gulick S. P. S., Morgan J. V., Vajda V., Whalen M. T., Wittmann A., Artemieva N., Farley K., Goderis S., Hajek E., Heaney P. J., Kring D. A., Lyons S. L., Rasmussen C., Sibert E., Rodríguez Tovar F. J., Turner-Walker G., Zachos J. C., Carte J., Chen S. A., Cockell C., Coolen M., Freeman K. H., Garber J., Gonzalez M., Gray J. L., Grice K., Jones H. L., Schaefer B., Smit J., and Tikoo S. M. 2020. The habitat of the nascent Chicxulub crater. *AGU Advances* 1:1–27. https://doi.org/10.1029/2020av000208.

Cavosie A. J. and Centeno C. L. 2014. Shocked apatite from the Santa Fe impact structure, (USA): A new mineral for studies of shock metamorphism. *45th Lunar and Planetary Science Conference*, abstract #1691.

Černok A., White L. F., Darling J., Dunlop J., and Anand M. 2019. Shock-induced microtextures in lunar apatite and merrillite. *Meteoritics & Planetary Science* 54:1262–1282. https://doi.org/10.1111/maps.13278.

Christeson G. L., Gulick S. P. S., Morgan J. V., Gebhardt C., Kring D. A., Le Ber E., Lofi J., Nixon C., Poelchau M., Rae A. S. P., Rebolledo-Vieyra M., Riller U., Schmitt D. R., Wittmann A., Bralower T. J., Chenot E., Claeys P., Cockell C. S., Coolen M. J. L., Ferrière L., Green S., Goto K., Jones H., Lowery C. M., Mellett C., Ocampo-Torres R., Perez-Cruz L., Pickersgill A. E., Rasmussen C., Sato H., Smit J., Tikoo S. M., Tomioka N., Urrutia-Fucugauchi J., Whalen M. T., Xiao L., and Yamaguchi K. E. 2018. Extraordinary rocks from the peak ring of the Chicxulub impact crater: P-wave velocity, density, and porosity measurements from IODP/ICDP Expedition 364. *Earth and Planetary Science Letters* 495:1–11. https://doi.org/10.1016/j.epsl.2018.05.013.

Claeys P., Kiessling W., and Alvarez W. 2002. Distribution of Chicxulub ejecta at the Cretaceous-Tertiary boundary. In *Catastrophic events and mass extinctions: impacts and beyond*, edited by C. Koeberl and K. G. MacLeod. Geological Society of America Special Paper #356. Geological Society of America, Boulder, Colorado. pp. 55–68. https://doi.org/10.1130/0-8137-2356-6.55.

Claeys P., Heuschkel S., Lounejeva-Baturina E., Sanchez-Rubio G., and Stöffler D. 2003. The suevite of drill hole Yucatàn 6 in the Chicxulub impact crater. *Meteoritics & Planetary Science* 38:1299–1317. https://doi.org/10.1111/j.1945-5100.2003.tb00315.x.

Collins G. S., Patel N., Davison T. M., Rae A. S. P., Morgan J. V., Gulick S. P. S., IODP-ICDP Expedition 364 Science Party, and Third-Party Scientists 2020. A steeply-inclined trajectory for the Chicxulub impact. *Nature Communications* 11:1480. https://doi.org/10.1038/s41467-020-15269-x.

Cox M. A., Cavosie A. J., Bland P. A., Miljkovic K., and Wingate M. T. D. 2018. Microstructural dynamics of central uplifts: reidite offset by zircon twins at the Woodleigh impact structure, Australia. *Geology* 46:983–986. https://doi.org/10.1130/G45127.1.

Cox M. A., Erickson T. M., Schmieder M., Christoffersen R., Ross D. K., Cavosie A. J., Bland P. A., Kring D. A., and IODP–ICDP Expedition 364 Scientists 2020. High resolution microstructural and compositional analyses of shock deformed apatite from the peak ring of the Chicxulub impact crater. *Meteoritics & Planetary Science* 55:1715–1733. https://doi.org/10.1111/maps.13541.

de Graaff S. J., Kaskes P., Déhais T., Goderis S., Debaille V., Ross C. H., Gulick S. P. S., Feignon J.-G., Ferrière L., Koeberl C., Smit J., Mattielli N., and Claeys P. 2022. New insights into the formation and emplacement of impact melt rocks within the Chicxulub impact structure, following the 2016 IODP-ICDP Expedition 364. *Geological Society of America Bulletin* 134:293–315. https://doi.org/10.1130/B35795.1.

de Graaff S. J., Ross C. H., Feignon J.-G., Kaskes P., Gulick S. P. S., Goderis, S., Déhais T., Debaille V., Ferrière L., Koeberl C., Mattielli N., Stockli D., and Claeys P. The Chicxulub impact structure reveals the first in-situ Jurassic-aged magmatic intrusions of the Yucatán Peninsula, Mexico. *Lithos* (submitted 2022-06-12).

Dickinson W. R. and Lawton T. F. 2001. Carboniferous to Cretaceous assembly and fragmentation of Mexico. *Geological Society of America Bulletin* 113:1142–1160. https://doi.org/10.1130/0016-7606(2001)113<1142:CTCAAF>2.0.CO;2.

Dressler B. O., Sharpton V. L., Morgan J., Buffler R., Moran D., Smit J., Stöffler D., and Urrutia J. 2003. Investigating a 65-Ma-old smoking gun: Deep drilling of the Chicxulub Impact Structure. *EOS, Transactions, American Geophysical Union* 84:125–130. https://doi.org/10.1029/2003EO140001.

Dressler B. O., Sharpton V. L., Schwandt C. S., and Ames D. 2004. Impactites of the Yaxcopoil-1 drilling site, Chicxulub impact structure: Petrography, geochemistry, and depositional environment. *Meteoritics & Planetary Science* 39:857–878. https://doi.org/10.1111/j.1945-5100.2004.tb00935.x.

Dworak U. 1969. Stoßwellenmetamorphose des Anorthosits vom Manicouagan Krater, Québec, Canada. *Contributions to Mineralogy and Petrology* 24:306–347. https://doi.org/10.1007/BF00371273.

Dypvik H., Gohn G. S., Edwards L. E., Horton J. W., Jr. Powars D. S., and Litwin R. J. 2018. Chesapeake Bay Impact Structure—Development of "Brim" Sedimentation in a Multilayered Marine Target. Geological Society of America Special Paper #537. Geological Society of America, Boulder, Colorado. pp. 1–68. https://doi.org/10.1130/2018.2537.

Feignon J.-G., Ferrière L., Leroux H., and Koeberl C. 2020. Characterization of shocked quartz grains from Chicxulub peak ring granites and shock pressure estimates. *Meteoritics & Planetary Science* 55:2206–2223. https://doi.org/10.1111/maps.13570.

Feignon J.-G., de Graaff S. J., Ferrière L., Kaskes P., Déhais T., Goderis S., Claeys P., and Koeberl C. 2021. Chicxulub impact structure, IODP-ICDP Expedition 364 drill core: Geochemistry of the granite basement. *Meteoritics & Planetary Science* 56:1243–1273. https://doi.org/10.1111/maps.13705.

Feignon J.-G., Schulz T., Ferrière L., Goderis S., de Graaff S. J., Kaskes K., Déhais T., Claeys P., and Koeberl C. 2022. Search for a meteoritic component within the impact melt rocks of the Chicxulub impact structure peak ring, Mexico. *Geochimica et Cosmochimica Acta* 323:74–101. https://doi.org/10.1016/j.gca.2022.02.006.

Ferrière L., Koeberl C., Reimold W. U., Hecht L., and Bartosova K. 2009a. The origin of "toasted" quartz in impactites revisited. *40th Lunar and Planetary Science Conference*, abstract #1751.

Ferrière L., Koeberl C., and Reimold W. U. 2009b. Characterization of ballen quartz and cristobalite in impact breccias: new observations and constraints on ballen formation. *European Journal of Mineralogy* 21:203–217. https://doi.org/10.1127/0935-1221/2009/0021-1898.

Gibbons R. V. and Ahrens T. J. 1977. Effects of shock pressures on calcic plagioclase. *Physics and Chemistry of Minerals* 1:95–107. https://doi.org/10.1007/BF00307982.

Goderis S., Tagle R., Belza J., Smit J., Montanari A., Vanhaecke F., Erzinger J., and Claeys P. 2013. Reevaluation of siderophile element abundances and across the Cretaceous–Paleogene (K–Pg) boundary: Implications for the nature of the projectile. *Geochimica et Cosmochimica Acta* 120:417–446. https://doi.org/10.1016/j.gca.2013.06.010.

Goderis S., Sato H., Ferrière L., Schmitz B., Burney D., Kaskes P., Vellekoop J., Wittmann A., Schulz T., Chernonozhkin S. M., Claeys P., de Graaff S. J., Déhais T., de Winter N. J., Elfman M., Feignon J.-G., Ishikawa A., Koeberl C., Kristiansson P., Neal C. R., Owens J. D., Schmieder M., Sinnesael M., Vanhaecke F., Van Malderen S. J. M., Bralower T. J., Gulick S. P. S., Kring D. A., Lowery C. M., Morgan J. V., Smit J., Whalen M. T., and IODP-ICDP Expedition 364 Scientists. 2021. Globally distributed iridium layer preserved within the Chicxulub impact structure. *Science Advances* 7:eabe3647. https://doi.org/10.1126/sciadv.abe3647.

Greenfield L., Millett J. M., Howell J., Jerram D. A., Watton T., Healy D., Hole M. J., and Planke S. 2020. The 3D facies architecture and petrophysical properties of hyaloclastite delta deposits: An integrated photogrammetry and petrophysical study from southern Iceland. *Basin Research* 32:1081–1104. https://doi.org/10.1111/bre.12415.

Gulick S. P. S., Barton P. J., Christeson G. L., Morgan J. V., McDonald M., Mendoza-Cervantes K., Pearson Z. F., Surendra A., Urrutia-Fucugauchi J., Vermeesch P. M., and Warner M. R. 2008. Importance of pre-impact crustal structure for the asymmetry of the Chicxulub impact crater. *Nature Geoscience* 1:131–135. https://doi.org/10.1038/ngeo103.

Gulick S. P. S., Bralower T. J., Ormö J., Hall B., Grice K., Schaefer B., Lyons S., Freeman K. H., Morgan J. V., Artemieva N., Kaskes P., de Graaff S. J., Whalen M. T., Collins G. S., Tikoo S. M., Verhagen C., Christeson G. L., Claeys P., Coolen M. J. L., Goderis S., Goto K., Grieve R. A. F., McCall N., Osinski G. R., Rae A. S. P., Riller U., Smit J., Vajda V., Wittmann A., and the Expedition 364 Scientists 2019. The first day of the Cenozoic. *Proceedings of the National Academy of Sciences of the United States of America* 116:19342–19351. https://doi.org/10.1073/pnas.1909479116.

Jaret S. J., Kah L. C., and Harris R. S. 2014. Progressive deformation of feldspar recording low-barometry impact processes, Tenoumer impact structure, Mauritania. *Meteoritics & Planetary Science* 49:1007–1022. https://doi.org/10.1111/maps.12310.

Kaiho K., Oshima N., Adachi K., Adachi Y., Mizukami T., Fujibayashi M., and Saito R. 2016. Global climate change driven by soot at the K-Pg boundary as the cause of the mass extinction. *Scientific Reports* 6:28427. https://doi.org/10.1038/srep28427.

Kaskes P., de Graaff S. J., Feignon J.-G., Déhais T., Goderis S., Ferrière L., Koeberl C., Smit J., Wittmann A., Gulick S. P. S., Debaille V., Matielli N., and Claeys P. 2022. Formation of the crater suevite sequence from the Chicxulub peak ring: A petrographic, geochemical, and sedimentological characterization. *Geological Society of America Bulletin* 134:895–927. https://doi.org/10.1130/B36020.1.

Kenny G. G., Karlsson A., Schmieder M., Whitehouse M. J., Nemchin A. A., and Bellucci J. J. 2020. Recrystallization and chemical changes in apatite in response to hypervelocity impact. *Geology* 48:19–23. https://doi.org/10.1130/G46575.1.

Koeberl C., Reimold W. U., Kracher A., Träxler B., Vormaier A., and Körner W. 1996. Mineralogical, petrological, and geochemical studies of drill core samples from the Manson impact structure, Iowa. In *The Manson impact structure, Iowa; anatomy of an impact crater*, edited by C. Koeberl and R. R. Anderson. Geological Society of America Special Paper #302, Geological Society of America, Boulder, Colorado, pp. 145–219. https://doi.org/10.1130/0-8137-2302-7.145.

Kring D. A. 2005. Hypervelocity collisions into continental crust composed of sediments and an underlying crystalline basement: Comparing the Ries (~24 km) and Chicxulub (~180 km) impact craters. *Geochemistry* 65:1–46. https://doi.org/10.1016/j.chemer.2004.10.003.

Kring D. A., Tikoo S. M., Schmieder M., Riller U., Rebolledo-Vieyra M., Simpson S. L., Osinski G. R., Gattacceca J., Wittmann A., Verhagen C. M., Cockell C. S., Coolen M. J. L., Longstaffe F. J., Gulick S. P. S., Morgan J. V., Bralower T. J., Chenot E., Christeson G. L., Claeys P., Ferrière L., Gebhardt C., Goto K., Green S. L., Jones H., Lofi J., Lowery C. M., Ocampo-Torres R., Perez-Cruz L., Pickersgill A. E., Poelchau M. H., Rae A. S. P., Rasmussen C., Sato H., Smit J., Tomioka N., Urrutia-Fucugauchi J., Whalen M. T., Xiao L., and Yamaguchi K. E. 2020. Probing the hydrothermal system of the Chicxulub impact crater. *Science Advances* 6:eaaz3053. https://doi.org/10.1126/sciadv.aaz3053.

Kyte F. T. 1998. A meteorite from the Cretaceous/Tertiary boundary. *Nature* 396:237–239. https://doi.org/10.1038/24322.

Langenhorst F., Joreau P., and Doukhan J. C. 1995. Thermal and shock metamorphism of the Tenham chondrite: A TEM examination. *Geochimica et Cosmochimica Acta* 59:1835–1845. https://doi.org/10.1016/0016-7037(95)00086-F.

López-Ramos E. 1975. Geological summary of the Yucatan peninsula. In *The Gulf of Mexico and the Caribbean*, edited by A. E. M. Nairn and F. G. Stehli. Springer, Boston, Massachusetts, pp. 257–282. https://doi.org/10.1007/978-1-4684-8535-6_7.

Lowery C. M., Bralower T. J., Owens J. D., Rodríguez-Tovar F., Jones H., Smit J., Whalen M. T., Claeys P., Farley K., Gulick S. P. S., Morgan J. V., Green S., Chenot E., Christeson G. L., Cockell C. S., Coolen M. J. L., Ferrière L., Gebhardt C., Goto K., Kring D. A., Lofi J., Ocampo-Torres R., Perez-Cruz L., Pickersgill A. E., Poelchau M. H., Rae A. S. P., Rasmussen C., Rebolledo-Vieyra M., Riller U., Sato H., Tikoo S. M., Tomioka N., Urrutia-Fucugauchi J., Vellekoop J., Wittmann A., Xiao L., Yamaguchi K. E., and Zylberman W. 2018. Rapid recovery of life at ground zero of the end-Cretaceous mass extinction. *Nature* 558:288–291. https://doi.org/10.1038/s41586-018-0163-6.

Lyons S. L., Karp A. T., Bralower T. J., Grice K., Schaefer B., Gulick S. P. S., Morgan J. V., and Freeman K. H. 2020. Organic matter from the Chicxulub crater exacerbated the K–Pg impact winter. *Proceedings of the National Academy of Sciences of the United States of America* 117:25327–25334. https://doi.org/10.1073/pnas.2004596117.

McDonough W. F. and Sun S. 1995. The composition of the Earth. *Chemical Geology* 120:223–253. https://doi.org/10.1016/0009-2541(94)00140-4.

McGregor M., McFarlane C. R. M., and Spray J. G. 2018. In situ LA-ICP-MS apatite and zircon U-Pb geochronology of the Nicholson Lake impact structure, Canada: shock and related thermal effects. *Earth and Planetary Science Letters* 504:185–197. https://doi.org/10.1016/j.epsl.2018.10.006.

McGregor M., Walton E. L., McFarlane C. R. M., and Spray J. G. 2020. Multiphase U-Pb geochronology of sintered breccias from the Steen River impact structure, Canada: Mixed target considerations for a Jurassic-Cretaceous boundary event. *Geochimica et Cosmochimica Acta* 274:136–156. https://doi.org/10.1016/j.gca.2020.01.052.

Montalvo P., Cavosie A., Kirkland C., Evans N., McDonald B., Talavera C., and Erickson T. 2019. Detrital shocked zircon provides first radiometric age constraint (<1472 Ma) for the Santa Fe impact structure, New Mexico, USA. *Geological Society of America Bulletin* 131:845–863. https://doi.org/10.1130/B31761.1.

Morgan J. V., Gulick S. P. S., Bralower T., Chenot E., Christeson G., Claeys P., Cockell C., Collins G. S., Coolen M. J. L., Ferrière L., Gebhardt C., Goto K., Jones H., Kring D. A., Le Ber E., Lofi J., Long X., Lowery C., Mellett C., Ocampo-Torres R., Osinski G. R., Perez-Cruz L., Pickersgill A., Poelchau M., Rae A., Rasmussen C., Rebolledo-Vieyra M., Riller U., Sato H., Schmitt D. R., Smit J., Tikoo S., Tomioka N., Urrutia-Fucugauchi J., Whalen M., Wittmann A., Yamaguchi K. E., and Zylberman W. 2016. The formation of peak rings in large impact craters. *Science* 354:878–882. https://doi.org/10.1126/science.aah6561.

Morgan J. V., Gulick S., Mellet C. L., Green S. L., and Expedition 364 Scientists 2017. *Chicxulub: Drilling the K-Pg impact crater*. Proceedings of the International Ocean Discovery Program, 364. International Ocean Discovery Program, College Station, Texas. 164 p.

Morgan J. V., Bralower T. J., Brugger J., and Wünnemann K. 2022. The Chicxulub impact and its environmental consequences. *Nature Reviews Earth & Environment* 3:338–354. https://doi.org/10.1038/s43017-022-00283-y.

Moser D. E., Cupelli C. L., Barker I. R., Flowers R. M., Bowman J. R., Wooden J., and Hart J. R. 2011. New zircon shock phenomena and their use for dating and reconstruction of large impact structures revealed by electron nanobeam (EBSD, CL, EDS) and isotopic U–Pb and (U–Th)/He analysis of the Vredefort dome. *Canadian Journal of Earth Sciences* 48:117–139. https://doi.org/10.1139/E11-011.

Mügge O. 1889. Über durch Druck entstandene Zwillinge von Titanit nach den Kanten [110] und [110]. *Neues Jahrbuch für Mineralogie, Geologie und Paläontologie* 11:98–115.

Németh K. and Kósik S. 2020. Review of explosive hydrovolcanism. *Geosciences* 10:1–27. https://doi.org/10.3390/geosciences10020044.

Ormö J., Gulick S. P. S., Whalen M. T., King Jr D. T., Sturkell E., and Morgan J. 2021. Assessing event magnitude and target water depth for marine-target impacts: Ocean resurge deposits in the Chicxulub M0077A drill core compared. *Earth and Planetary Science Letters* 564:116915. https://doi.org/10.1016/j.epsl.2021.116915.

Osinski G. R., Grieve R. A. F., Hill P. J. A., Simpson S. L., Cockell C., Christeson G. L., Ebert M., Gulick S., Melosh H. J., Riller U., Tikoo S. M., and Wittmann A. 2020. Explosive interaction of impact melt and seawater following the Chicxulub impact event. *Geology* 48:108–112. https://doi.org/10.1130/G46783.1.

Ostertag R. 1983. Shock experiments on feldspar crystals. *Journal of Geophysical Research: Solid Earth* 88:B364–B376. https://doi.org/10.1029/JB088iS01p0B364.

Papapavlou K., Darling J. R., Moser D. E., Barker I. R., White L. F., Lightfoot P. C., Storey C. D., and Dunlop J. 2018. U-Pb isotopic dating of titanite microstructures: potential implications for the chronology and identification of large impact structures. *Contributions to Mineralogy and Petrology* 173:82. https://doi.org/10.1007/s00410-018-1511-0.

Philpotts A. R. and Ague J. J. 2009. *Principles of igneous and metamorphic petrology, 2nd edition*. Cambridge University Press, Cambridge, UK. 667 p. https://doi.org/10.1017/CBO9780511813429.

Pickersgill A. E., Osinski G., and Flemming R. L. 2015. Shock effects in plagioclase feldspar from the Mistastin Lake impact structure, Canada. *Meteoritics & Planetary Science* 50:1546–1561. https://doi.org/10.1111/maps.12495.

Pickersgill, A. E., Jaret, S., Pittarello, L., Fritz, J., and Harris, R. 2021. Shock effects in feldspars: An overview. In *Large Meteorite Impacts and Planetary Evolution VI*, edited by W. U. Reimold and C. Koeberl. Geological Society of America Special Paper #550. Geological Society of America, Boulder, Colorado. pp. 537–549. https://doi.org/10.1130/2021.2550(23).

Pierazzo E. and Melosh H. J. 2000. Hydrocode modeling of oblique impacts: The fate of the projectile. *Meteoritics & Planetary Science* 35:117–130. https://doi.org/10.1111/j.1945-5100.2000.tb01979.x.

Pittarello L., Schulz T., Koeberl C., Hoffmann J. E., and Münker C. 2013. Petrography, geochemistry, and Hf-Nd isotope evolution of drill core samples and target rocks from the El'gygytgyn impact crater, NE Chukotka, Arctic Russia. *Meteoritics & Planetary Science* 48:1160–1198. https://doi.org/10.1111/maps.12088.

Pittarello L., Ferrière L., Feignon J.-G., Osinski G. R., and Koeberl C. 2020. Preferred orientation distribution of shock-induced planar microstructures in quartz and feldspar. *Meteoritics & Planetary Science* 55:1082–1092. https://doi.org/10.1111/maps.13490.

Quitté G., Levasseur S., Capmas F., Rocchia R., Birck J. L., and Allègre C. J. 2007. Osmium, tungsten, and chromium isotopes in sediments and in Ni-rich spinel at the K-T boundary: signature of a chondritic impactor. *Meteoritics & Planetary Science* 42:1567–1580. https://doi.org/10.1111/j.1945-5100.2007.tb00591.x.

Rae A. S. P., Collins G. S., Poelchau M., Riller U., Davison T. M., Grieve R. A. F., Osinski G. R., Morgan J. V., and IODP-ICDP Expedition 364 Scientists 2019. Stress-Strain Evolution During Peak-Ring Formation: A Case Study of the Chicxulub Impact Structure. *Journal of Geophysical Research: Planets* 124:396–417. https://doi.org/10.1029/2018JE005821.

Rebolledo-Vieyra M., Urrutia-Fucugauchi J., Marin L. E., Trejo-Garcia A., Sharpton V. L., and Soler-Arechalde A. M. 2000. UNAM scientific shallow-drilling program of the Chicxulub impact crater. *International Geology Review* 42:928–940. https://doi.org/10.1080/00206810009465118.

Riller U., Poelchau M. H., Rae A. S. P., Schulte F. M., Collins G. S., Melosh H. J., Grieve R. A. F., Morgan J. V., Gulick S. P. S., Lofi J., Diaw A., McCall N., Kring D. A., and IODP-ICDP Expedition 364 Science Party 2018. Rock fluidization during peak-ring formation of large impact structures. *Nature* 562:511–518. https://doi.org/10.1038/s41586-018-0607-z.

Robertson D. S., Lewis W. M., Sheehan P. M., and Toon O. B. 2013. K-Pg extinction: Reevaluation of the heat-fire hypothesis. *Journal of Geophysical Research: Biogeosciences* 118:329–336. https://doi.org/10.1002/jgrg.20018.

Ross C. H., Stockli D. F., Rasmussen C., Gulick S. P. S., de Graaff S. J., Claeys P., Zhao J., Xiao L., Pickersgill A. E., Schmieder M., Kring D. A., Wittmann A., and Morgan J. 2022. Evidence of Carboniferous arc magmatism preserved in the Chicxulub impact structure. *Geological Society of America Bulletin* 134:241–260. https://doi.org/10.1130/B35831.1.

Schulte F. M., Wittmann A., Jung S., Morgan J. V., Gulick S. P. S., Kring D. A., Grieve R. A. F., Osinski G. R., Riller U., and IODP-ICDP Expedition 364 Science Party 2021. Ocean resurge-induced impact melt dynamics on the peak-ring of the Chicxulub impact structure, Mexico. *International Journal of Earth Sciences* 110:2619–2636. https://doi.org/10.1007/s00531-021-02008-w.

Shukolyukov A. and Lugmair G. W. 1998. Isotopic evidence for the Cretaceous-Tertiary impactor and its type. *Science* 282:927–930. https://:doi.org/10.1126/science.282.5390.927.

Simpson S. L., Osinski G. R., Longstaffe F. J., Schmieder M., and Kring D. A. 2020. Hydrothermal alteration associated with the Chicxulub impact crater upper peak-ring breccias. *Earth and Planetary Science Letters* 547:116425. https://doi.org/10.1016/j.epsl.2020.116425.

Simpson S. L., Longstaffe F. J., Osinski G. R., Caudill C. M., and Kring D. A. 2022. A low-temperature, meteoric water-dominated origin for smectitic clay minerals in the Chicxulub impact crater upper peak ring, as inferred from their oxygen and hydrogen isotope compositions. *Chemical Geology* 588:120639. https://doi.org/10.1016/j.chemgeo.2021.120639.

Słaby E., Förster H. J., Wirth R., Wudarska A., Birski Ł., and Moszumańska I. 2017. Validity of the apatite/merrillite relationship in evaluating the water content in the Martian mantle: Implications from shergottite Northwest Africa (NWA) 2975. *Geosciences* 7:99. https://doi.org/10.3390/geosciences7040099.

Smit J. 1999. The global stratigraphy of the Cretaceous-Tertiary boundary impact ejecta. *Annual Review of Earth and Planetary Sciences* 27:75–113. https://doi.org/10.1146/annurev.earth.27.1.75.

Smit J., Roep T. B., Alvarez W., Montanari A., Claeys P., Grajales-Nishimura J. M., and Bermudez J. 1996. Coarse-grained, clastic sandstone complex at the K/T boundary around the Gulf of Mexico : Deposition by tsunami waves induced by the Chicxulub impact? In *The Cretaceous-Tertiary Event and Other Catastrophes in Earth History*, edited by G. Ryder, D. E. Fastovsky, and S. Gartner. Geological Society of America Special Paper #307, Geological Society of America, Boulder, Colorado, pp. 151–182. https://doi.org/10.1130/0-8137-2307-8.151.

Steiner M. B. 2005. Pangean reconstruction of the Yucatan Block: Its Permian, Triassic, and Jurassic geologic and tectonic history. In *The Mojave-Sonora Megashear hypothesis: Development, assessment, and alternatives*, edited by T. H. Anderson, J. A. Nourse, J. W. McKee, and M. B. Steiner. Geological Society of America Special Paper #393, Geological Society of America Boulder, Colorado, pp. 457–480. https://doi.org/10.1130/0-8137-2393-0.457.

Stern R. J., Anthony E. Y., Ren M., Lock B. E., Norton I., Kimura J. I., Miyazaki T., Hanyu T., Chang Q., and Hirahara Y. 2011. Southern Louisiana salt dome xenoliths: First glimpse of Jurassic (ca. 160 Ma) Gulf of Mexico crust. *Geology* 39:315–318. https://doi.org/10.1130/G31635.1.

Stöffler D. 1967. Deformation und Umwandlung von Plagioklas durch Stoßwellen in den Gesteinen des Nördlinger Ries. *Contributions to Mineralogy and Petrology* 16:50–113. https://doi.org/10.1007/BF00371608.

Stöffler D. and Grieve R. A. F. 2007. Impactites, Chapter 2.11. In *Metamorphic Rocks: A Classification and Glossary of Terms, Recommendations of the International Union of Geological Sciences*, edited by D. Fettes and J. Desmons. Cambridge University Press, Cambridge, United Kingdom. pp.82–92, 111–125, and 126–242.

Stöffler D., Artemieva N. A., Ivanov B. A., Hecht L., Kenkmann T., Schmitt R. T., Tagle R. A., and Wittmann A. 2004. Origin and emplacement of the impact formations at Chicxulub, Mexico, as revealed by the ICDP deep drilling Yaxcopoil-1 and by numerical modeling. *Meteoritics & Planetary Science* 39:1035–1067. https://doi.org/10.1111/j.1945-5100.2004.tb01128.x.

Stöffler D., Hamann C., and Metzler K. 2018. Shock metamorphism of planetary silicate rocks and sediments: Proposal for an updated classification system. *Meteoritics & Planetary Science* 53:5–49. https://doi.org/10.1111/maps.12912.

Timms N. E., Erickson T. M., Pearce M. A., Cavosie A. J., Schmieder M., Tohver E., Reddy M. A., Zanetti M. R., Nemchin A. A., and Wittmann A. 2017. A pressure-temperature phase diagram for zircon at extreme conditions. *Earth-Science Reviews* 165:185–202. https://doi.org/10.1016/j.earscirev.2016.12.008.

Timms N. E., Pearce M. A., Erickson T. M., Cavosie A. J., Rae A. S. P., Wheeler J., Wittman A., Ferrière L., Poelchau M. H., Tomioka N., Collins G. S., Gulick S. P. S., Rasmussen C., Morgan J. V., and IODP-ICDP Expedition 364 Scientists. 2019. New shock microstructures in titanite ($CaTiSiO_5$) from the peak ring of the Chicxulub impact structure, Mexico. *Contributions to Mineralogy and Petrology* 174:38. https://doi.org/10.1007/s00410-019-1565-7.

Urrutia-Fucugauchi J., Morgan J., Stöffler D., and Claeys P. 2004. The Chicxulub Scientific Drilling Project (CSDP). *Meteoritics & Planetary Science* 39:787–790. https://doi.org/10.1111/j.1945-5100.2004.tb00928.x.

Urrutia-Fucugauchi J., Chavez-Aguirre J. M., Pérez-Cruz L., and De la Rosa J. L. 2008. Impact ejecta and carbonate sequence in the eastern sector of the Chicxulub crater. *Comptes Rendus Geoscience* 340:801–810. https://doi.org/10.1016/j.crte.2008.09.001.

Watton T. J., Jerram D. A., Thordarson T., and Davies R. J. 2013. Three-dimensional lithofacies variations in hyaloclastite deposits. *Journal of Volcanology and Geothermal Research* 250:19–33. https://doi.org/10.1016/j.jvolgeores.2012.10.011.

Whalen M. T., Gulick S. P. S., Lowery C. M., Bralower T. J., Morgan J. V., Grice K., Schaefer B., Smit J., Ormö J., Wittmann A., Kring D. A., Lyons S., Goderis S., and IODP-ICDP Expedition 364 Scientists 2020. Winding down the Chicxulub impact: The transition between impact and normal marine sedimentation near ground zero. *Marine Geology* 430:106368. https://doi.org/10.1016/j.margeo.2020.106368.

White W. M., Dupre B., and Vidal P. 1985. Isotope and trace element geochemistry of sediments from the Barbados ridge and Demerara Plain region, Atlantic Ocean. *Geochimica et Cosmochimica Acta* 49:1875–1886. https://doi.org/10.1016/0016-7037(85)90082-1.

Whitehead J., Spray J. G., and Grieve R. A. F. 2002. Origin of "toasted" quartz in terrestrial impact structures. *Geology* 30:431–434. https://doi.org/10.1130/0091-7613(2002)030<0431:OOTQIT>2.0.CO;2.

Wittmann A., Goderis S., Claeys P., Vanhaecke F., Deutsch A., and Adolph L. 2013. Petrology of impactites from El'gygytgyn crater: Breccias in ICDP-drill core 1C, glassy impact melt rocks and spherules. *Meteoritics & Planetary Science* 48:1199–1235. https://doi.org/10.1111/maps.12019.

Wittmann A., Cavosie A. J., Timms N. E., Ferrière L., Rae A., Rasmussen C., Ross C., Stockli D., Schmieder M., Kring D. A., Zhao J., Xiao L., Morgan J. V., Gulick S. P. S., and the IODP-ICDP Expedition 364 Scientists. 2021. Shock impedance amplified impact deformation of zircon in granitic rocks from the Chicxulub impact crater. *Earth and Planetary Science Letters* 575:117201. https://doi.org/10.1016/j.epsl.2021.117201.
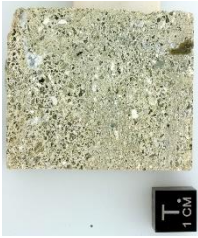
Woodhead J. D. and Fraser D. G. 1985. Pb, Sr and [10]Be isotopic studies of volcanic rocks from the Northern Mariana Islands. Implications for magma genesis and crustal recycling in the Western Pacific. *Geochimica et Cosmochimica Acta* 49:1925–1930. https://doi.org/10.1016/0016-7037(85)90087-0.

Zhao J., Xiao L., Gulick S. P. S., Morgan J. V., Kring D. A., Urrutia-Fucugauchi J., Schmieder M., de Graaff S. J., Wittmann A., Ross C. H., Claeys P., Pickersgill A., Kaskes P., Goderis S., Rasmussen C., Vajda V., Ferrière L., Feignon J.-G., Chenot E., Perez-Cruz L., Sato H., Yamaguchi K., and IODP-ICDP Expedition 364 Scientists. 2020. Geochemistry, geochronology and petrogenesis of Maya Block granitoids and dykes from the Chicxulub impact crater, Gulf of Mexico: Implications for the assembly of Pangea. *Gondwana Research* 82:128–150. https://doi.org/10.1016/j.gr.2019.12.003.

Zhao J., Xiao L., Xiao Z., Morgan J. V., Osinski G. R., Neal C. R., Gulick S. P. S., Riller U., Claeys P., Zhao S., Prieur N. C., Nemchin A., Yu S., and IODP 364 Science Party 2021. Shock-deformed zircon from the Chicxulub impact crater and implications for cratering process. *Geology* 49:755–760. https://doi.org/10.1130/G48278.1.

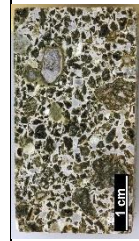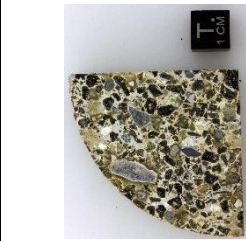# APPENDIX A: Petrographic descriptions of IODP-ICDP Expedition 364 drill core samples
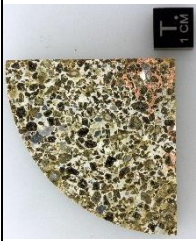
This table includes petrographic descriptions of the 194 thin sections prepared for this thesis work from the IODP-ICDP Expedition 364 drill core. Mbsf: meters below seafloor. PFs: planar fractures; FFs: feather features; PDFs: planar deformation features.
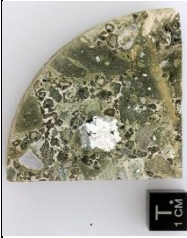
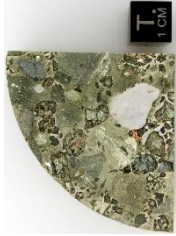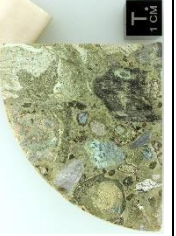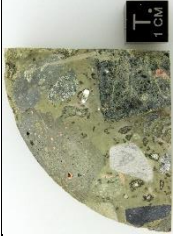| Sample name	Depth (mbsf)	Unit or *rock type*	Macrophotograph	Description
40R2_7–9	617.74	Bedded suevite		Polymict impact melt-bearing breccia (or suevite). Blue-green-gray in color. The suevite is clast-supported, fine-grained, with altered brown glassy clasts being the main component. Slight horizontal bedding is visible at the macroscopic scale on the side parallel to the vertical axis of the drill core. Other clasts include calcite/carbonate, rare quartz grains (occurring as ballen silica), and opaque minerals. The matrix is composed of micritic carbonate with fossils (including foraminifera).
40R2_107–109	618.74	Bedded suevite		Suevite (clast size generally below 1 mm) with the main component consisting of angular brown glassy shards. Carbonate clasts also occur with reaction rims. Matrix fine-grained, composed of micritic carbonate and fossils. Calcite veins crosscut the matrix but not the clasts. Alteration to phyllosilicates is also present. Opaque minerals are observed in the largest glass clasts.
41R1_106–108	620.35	Bedded suevite		Suevite, matrix with micritic carbonate, with bedding clearly visible. Clasts of relatively small size, i.e., millimeter to submillimeter-sized, mainly carbonates (fossils), rare quartz grains (ballen silica type V observed), and abundant angular altered glass brownish-greenish (alteration with clay minerals?). Quartz grains are toasted. One shocked quartz grains with two PDF sets are seen.

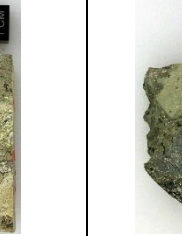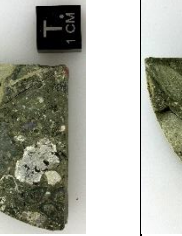| Sample	Type		Description
41R2_21–23.5	Graded suevite		Suevite with slightly larger clasts (~1–3 mm in size) than in previous samples (see above). Angular brown-green glassy clasts are the main component (~35–40 vol%) of the suevite. Carbonate clasts also occur as well as very rare quartz grains as clasts. The matrix is made of micritic carbonate containing also rounded fossils (foraminifera). Matrix appears slightly more brownish (possibly due to alteration?) in contrast to previous samples from the top of the core that display a gray-green-blue matrix.
41R2_50–54	Graded suevite		Suevite, poorly-sorted, with areas displaying ~1 mm-sized clasts, while others parts of the sample show clasts <1 mm (roughly ~0.5 mm in average). Clasts seem somewhat preferentially oriented (indicative of a flow direction?). Micritic carbonate matrix. Clasts are abundant, with shard-shaped glassy clasts as the main population, as well as carbonate clasts. Rare quartz grains occur.
41R2_131–133.5	Graded suevite		Suevite, clast-rich, with better sorting than 41R2_50–54. Similar in petrography to the previous samples (see above). Clast size generally ~1 mm, with rare larger clasts ~2–3 mm in size. Clast population dominated by angular/shard altered glassy clasts. Carbonate/calcite clasts also occur. Reaction rim visible around some rounded carbonate clasts. Matrix is composed of micritic carbonate.
42R2_86–88.5	Graded suevite		Suevite, clast-rich. Clast population and size is similar to the previous samples (i.e., dominated by altered brownish glassy clasts, and, to a lesser extent, carbonate clasts embedded in a micritic carbonate matrix). Rare clasts with ~0.5 cm in size (altered glass penetrated by matrix material). Rare angular quartz grains occur, and also opaque minerals (pyrite?).
43R1_104–106.5	Graded suevite		Suevite similar to the sample 42R2_86–88.5, with clast size in average ~1–2 mm. Altered angular glass clasts represents ~80–85 vol% of the clasts. Alteration of the glass to clay minerals has been observed. Few larger clasts (~0.5–0.6 mm in size) consisting of fine-grained carbonate material or altered melt particles. Vesicles are filled by sparry calcite. Rare quartz grains are seen (ballen silica type V were noted) and a few opaque minerals. Matrix consists of micritic carbonate, grayish in color.

Sample	Classification	Image	Description
44R2_51–53	Graded suevite		Suevite, matrix supported. Clast size ~1–2 mm in general with few clast up to ~7 mm in size. Glassy (vitric) altered clasts, subrounded to angular in shape, are the most abundant clasts. Other clast types include fine-grained carbonate, microcrystalline impact melt rock clasts, quartz (toasted, ballen silica type V with chert-like texture were seen). Matrix is composed of micritic carbonate and some fossils.
44R2_84–87	Graded suevite		Suevite similar to the previous sample from the same section (44R2_51–53). A nearly ~1 cm yellow–orange altered glassy clast was noted, with vesicles filled by calcite.
45R2_31–33.5	Graded suevite		Suevite, matrix supported (micritic carbonate matrix). Composed mainly of glassy (vitric) melt and microcrystalline impact melt rock clasts. Clast size is mainly ~2–3 mm, with few larger clasts (~0.5–1 cm in size). Fine-grained carbonate clasts are also observed. Some clasts are surrounded by reaction rims.
46R2_49–51.5	Graded suevite		Suevite with average clast size of ~1–2 mm. Clast population and matrix similar to previous samples. Ballen silica type V and toasted quartz are noted.
47R2_94–96.5	Graded suevite		Suevite with clast size generally below 5 mm. Main clasts are glassy (vitric) melt and microcrystalline impact melt rock. Fine-grained carbonate clasts also occur and show well defined reaction rims (brownish in color). A partially digested granitic basement clast (mainly quartz and feldspar) is observed in the macroscopic sample.
49R1_64–66.5	Graded suevite		Suevite with average clast size of ~2–3 mm, and up to ~7–8 mm in size. Clasts seem generally larger in size compared to previous sample 47R2_94–96.5. Altered glass clasts are greenish in color and the most abundant ones. Also are microcrystalline (clast-poor) impact melt rock clasts. Rounded fine-grained carbonate clasts are noted with reaction rims. Toasted quartz with PDFs (2 sets visible), and ballen silica type V were

Sample	Classification	Image	Description
			seen. Micritic carbonate matrix seems to have been extensively altered (clay minerals). Very rare opaque minerals also occur.
50R3_24–26.5	Graded suevite		Suevite displaying several clasts of more than 1 cm in size. Smaller clasts are generally ~4–5 mm in size. Also, clasts are generally subrounded. Vesicles in glassy clasts are largely filled with calcite. A brownish (altered?) microcrystalline impact melt rock clast is noted. Large clasts include vesicular, clast-poor, impact melt rock (with a ~1 cm gneiss clast), and also a granitic clast with shocked quartz (toasted with PDF, 1 set visible) and feldspar grains. Fine-grained carbonate clasts also occur. Ballen silica of type V are seen.
51R2_69–71.5	Graded suevite		Suevite with clast size above 5 mm. At the macroscopic scale, a dark ~2 cm-sized, rounded, dark microcrystalline impact melt rock is noted. Glassy clasts are altered and greenish to brownish in color (alteration with clay minerals). Matrix composed of micritic carbonate. A partially digested (and highly deformed) granitic basement clast is observed in thin section, mainly consisting of feldspar and quartz crystals.
52R1_37–39.5	Graded suevite		Suevite sample with similar grain size and clast population that the previous sample 51R2_69–71.5. A ~1.2 cm microcrystalline (mainly composed of acicular plagioclase) impact melt rock (clast poor (<500 μm in size) is noted, with the clasts being mainly undigested quartz and feldspar minerals. Ballen quartz type V also occurs. The clasts inside the impact melt rock clasts are slightly elongated, highlighting a flow texture. A quartzite clast (?) is also present in the suevite, and is mainly composed of small quartz gains (<100 μm in size) with no shock features visible under the microscope. Fine-grained carbonate clasts display different degrees of alteration (presence of clay minerals and/or calcite filling vesicles).
52R2_127–129.5	Graded suevite		Sample relatively similar to the previous one (see above). Matrix of micritic carbonate. The main clast population consists of more or less altered glassy (vitric) melt shards and impact melt rock clasts. Rare carbonate clasts with reaction rims and felsic basement clasts composed of quartz and feldspar are noted.

Sample	Depth		Image	Description
54R1_57–59	659.51	Graded suevite		Suevite sample with average clast size between ~2 and 3 mm. Large, centimeter-sized, clasts are rarer than in samples from core sections 50, 51, and 52 (see above). The sample appears brownish in color, probably due to the presence of an alteration band cutting the core at this depth.
54R1_66–68.5	659.60	Graded suevite		Suevite sample similar in term of clast size and population to the previous sample from the same section (54R1_57–59). The alteration band is absent in this sample. A carbonate clast, almost 1 cm in size, sub-rounded was noted. The micritic carbonate matrix appears dark grey in thin section, mainly due to the presence of clay minerals, suggesting a rather high degree of alteration. Glassy (vitric) melt clasts appear heavily altered with the presence of clay minerals and reaction rims. Carbonate fossils are also present.
55R1_87–89.5	662.86	Graded suevite		Poorly-sorted suevite with clast size ranging from ~2 mm to ~1 cm. Glass (vitric) melt clasts represent the main population (~40 vol% of the clasts) as in previous samples. Microcrystalline impact melt rock clasts also occur (with undigested quartz and feldspar grains, as well as basement clasts, both gneiss and granite). A partly digested basement clast with shocked quartz (multiple PDF sets) is also noted.
55R1_105–107	663.04	Graded suevite		Suevite similar to 55R1_87–89.5, with centimeter-sized impact melt rock clasts, containing undigested felsic basement clasts. Preserved fossil clasts with reaction rims are noted.
56R2_95–97.5	667.20	Graded suevite		Suevite with average clast size ~0.5 cm, including some larger clasts. In addition to altered vitric melt clasts and microcrystalline impact melt rock, mineral clasts, one shocked quartz grain (with undulose extinction and two PDF sets visible), another quartz grain is toasted, and one with ballen silica type V are noted. Clay minerals are abundant in the matrix, preventing good observation of the original micritic carbonate matrix. A mafic basement clast was also observed, i.e., a porphyritic dolerite composed of plagioclase laths, up to 1 mm in length, and also pyroxene crystals. A ~1 cm silica mineral clast (see macrophotograph) is also present, and consists
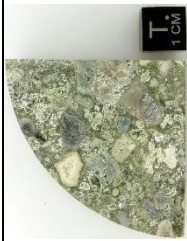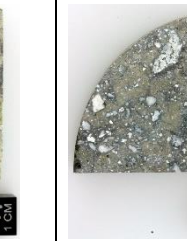
Sample	Depth	Type	Image	Description
				of fine-grained quartz (showing ballen silica type V, and possibly ballen quartz type IV).
57R1_27–29.5	668.36	Graded suevite		Suevite with clast size ~0.5–1 cm. Mainly composed of altered vitric melt clasts and impact melt rock clasts with undigested or partially digested quartz and feldspar crystals. A red-brownish altered melt clast was noted. Carbonate clasts show reaction rims. A fractured plagioclase mineral clast and fossils are also noted.
58R3_8–10.5	673.68	Graded suevite		Suevite, with clast size between ~0.5 an 1.5 cm. The matrix is clastic, with mainly quartz carbonate, and is hydrothermally altered (presence of opaque phases and clay minerals, brownish in color). Large centimeter-sized carbonate clasts, brownish glass clasts, altered and fractured, surrounded with reaction rims, and impact melt rock (clast-poor) clast occur. Rare quartz grains were noted (including ballen type V and toasted quartz). The impact melt rock clast, with a finely crystallized matrix (i.e., mainly microliths of plagioclase and likely pyroxene), contains quartz grains (shocked with PDFs and toasted), one plagioclase, and a larger carbonate clast with reaction rim.
59R2_76–78.5	675.93	Graded suevite		Suevite with a more or less bimodal distribution of clasts (i.e., ~2–5 mm and >1 cm). Similar matrix and clast population as in the previous samples. A large (~1 cm) granitic basement clast is noted, and is mainly composed of quartz (toasted and with PDFs) and feldspar.
59R3_90–92.5	677.06	Graded suevite		Suevite with similar bimodal distribution of clast size as in the previous sample. Mainly angular, altered vitric (glassy) brownish melt clasts, as well as impact melt rock clasts are noted. In some of the glassy melt clasts, mineral clasts are preserved (e.g., quartz). A ~5 mm rounded mafic clast (amphibolite) is composed of alternating bands consisting of finely crystallized plagioclases and amphiboles; iron oxide minerals are also present. Carbonate and quartz occur as clasts, with ballen silica type IV observed. Matrix is composed mainly of micritic carbonate, with also a few larger calcite grains.
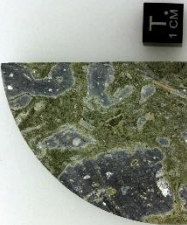
Sample	Image	Type	Description
59R3_95–97		Graded suevite	Suevite similar to 59R3_90–92.5 (same section). Large (~1 cm) impact melt rock clasts appear greenish in color. A highly-deformed granite basement clast (2 cm in size) is preserved in the suevite (composed of deformed shocked quartz with PDFs and feldspar). Carbonate clasts also occur, some showing reaction rims. A ~8 mm gneiss clast is noted (composed of oriented quartz (shock features not observed) and biotite grains). Toasted quartz, as well as ballen silica type V with reaction rim is noted. The matrix seems to have experienced a rather strong alteration.
61R1_9–11.5		Graded suevite	Suevite, poorly-sorted. A ~2.5 cm fine-grained carbonate clast is present. Impact melt rock clasts are greenish in color (and appear glassy in thin section), generally altered with phyllosilicates. Some undigested clasts (mainly mineral such as quartz and feldspar) are preserved in the impact melt. An angular ~1 cm sized granite basement clast is observed (see macroscopic photograph of the sample).
62R1_31–33.5		Graded suevite	Suevite, greenish in color and fractured at the macroscopic scale, indicating an extensive alteration. Several clasts, between ~1 and 2 cm in size. Altered impact melt rock (clast-poor) clasts as well as dark gray to greenish in color, microcrystalline or glassy clasts. Quartz-rich basement clasts and some carbonate clasts are also noted.
63R1_7–9.5		Graded suevite	Suevite, poorly-sorted. Matrix is more abundant than in previous samples located above in the core. Matrix is composed of micritic carbonate, grayish in color. Small clasts (<0.5 cm) are relatively rare, while clasts of ~1–2.5 cm are more common. Clast population includes mainly greenish (glassy) impact melt rock, mainly composed of calcite and clay minerals (alteration), and angular in shape clast-poor and microcrystalline black impact melt rock, with undigested mineral clasts (including shocked quartz and feldspar). A fine-grained carbonate clast is observed.
63R2_79–81.5		Graded suevite	Suevite sample similar to 63R1_7–9.5. Reddish alteration areas are observed. Preserved granite clast, deformed, mainly composed of quartz (shocked with two visible PDF sets), feldspar, and rare chloritized biotite. An angular gneiss clast is observed on the macroscopic sample. Carbonate clasts are also present.

Sample	Depth	Classification	Image	Description
65R1_38–40.5	688.29	Graded suevite		Suevite, poorly-sorted, with rare clasts of ~5 mm in size, embedded within the matrix. Other clasts are commonly ~2 cm or more in size. One large rounded carbonate clast, and also an angular dolerite clast (composed of plagioclase and pyroxene laths) is noted.
67R1_15–17.5	690.61	Graded suevite		Suevite similar to the previous sample 65R1_38–40.5. Matrix is generally hidden by phyllosilicates, indicating a high degree of hydrothermal alteration. Clast sizes are generally from ~1.5 to ~3 cm. Some smaller clasts (<0.5 cm) also occur. Clast population dominated by black and green (glassy) impact melt rock. Fracturing is common within green impact melt clasts (desiccation cracks?). Red-orange mineralization occurs within the matrix. Granitic basement clasts were identified (composed of shocked quartz toasted/with PDFs, and feldspar), as well as carbonate clasts.
72R1_94.5–99	698.04	Graded suevite		Suevite with a dark green matrix, highly fractured (desiccation cracks?) and altered (presence of phyllosilicates). Large clasts are generally more than 2 cm, while millimeter-sized clasts are rare. Sample dominated by green and black impact melt rock clasts. Reaction rims occur around some of the green impact melt clasts. A ~1.2 cm granite clast, with fractures filled by matrix, was observed in the macroscopic sample. A small (~6 mm) amphibolite clast is also noted.
73R1_20–23	699.29	Graded suevite		Suevite, poorly-sorted, similar to sample 72R1_94.5–99, with desiccation cracks occurring within the matrix and high level of alteration. Clast size generally of 1–3 cm, with rare millimeter-sized clasts. In addition to black and green impact melt rock clasts, a dolerite clast is observed (composed of plagioclase and pyroxene laths, equigranular), and also carbonate clasts.
73R2_102–104.5	700.94	Graded suevite		Suevite similar to sample 73R1_20–23. Green (glassy) impact melt rock clasts seem more abundant than black impact melt clasts. A ~1 cm clast composed of calcite is surrounded by a reddish reaction rim. Mostly calcite-filled vesicles.
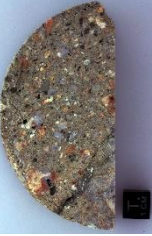
Sample	Depth (m)	Classification	Image	Description
76R1_117–119.5	703.56	Graded suevite		Suevite with large clasts (>1.5 cm). Matrix obscured by phyllosilicates and showing desiccation cracks. The thin section is dominated by a greenish impact melt rock clast; the matrix is altered (presence of phyllosilicates). An impact melt, clast-poor, contains mainly undigested quartz (including ballen silica type V) and feldspar grains. Calcite is also observed. Reddish alteration at the rim of the clasts is noted.
77R1_15–18	703.69	Graded suevite		Suevite, highly fractured and altered. A ~3 cm in size black impact melt (clast-poor) clast shows flow textures. Reddish alteration is relatively abundant. Felsic basement clasts (granite?) are noted. Carbonate clasts are rare.
80R2_61–63.5	706.57	Graded suevite (*Amphibolite* clast)		Amphibolite clast, ~40 cm in size, within a large impact melt rock clast (~70 cm in size) itself embedded in the graded suevite. Homogeneous sample, finely crystallized (mineral size between 100–400 µm), slightly foliated (?), with mainly plagioclase, amphibole, and pyroxene as well as rare quartz grains, shocked with one PDF set and showing undulatory extinction. Minerals are highly fractured (shock microstructures are noted).
81R1_8–10	707.42	Graded suevite		Suevite with fractured greenish matrix (altered with the presence of phyllosilicates and reddish recrystallization). Mainly composed of clasts larger than 2 cm in size and very rare clasts <0.5 cm. Gneiss and granite clasts are noted. The granite clast, only 3 cm in the sample is larger, having a total size of ~6 cm. Granite is composed of quartz (shocked with up to two visible PDF sets, toasted, and deformed), feldspar, and biotite commonly chloritized and kinked. Fractures are filled with matrix material. An angular, clast-poor, microcrystalline black impact melt rock clast is present.
81R1_67–69	708.01	Graded suevite		Suevite, relatively similar to the sample 81R1_8–10. A ~3 cm greenish impact melt rock clast, clast-poor occurs. In addition to felsic basement clasts (~2 cm granite clast observed), carbonate clasts also occur in this sample. Ballen quartz type II is noted.
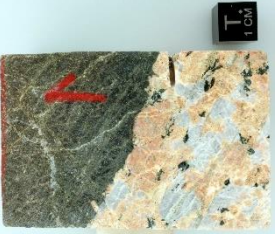
Sample	Depth	Type	Image	Description
81R3_32–34.5	710.31	Non-graded suevite		Suevite with clasts more abundant than matrix. Clasts between ~1–5 mm are relatively abundant (nearly similar to samples from sections 58 and 59), in addition to centimeter-sized clasts. Mainly black and green, clast-poor, angular impact melt rock clasts are noted. Rare carbonate and felsic basement clasts occur.
82R1_35–38.5	710.74	Non-graded suevite		Suevite, poorly-sorted, clast-supported. Matrix less abundant relative to clasts, and mainly composed of carbonate material. The lower part of the sample is composed of limestone, part of a ~40 cm carbonate clast. Flow-structure is observed.
83R1_22–24.5	712.30	Non-graded suevite		Strongly altered impact melt rock clast (in suevite) with 1-2 mm thick greenish veins filled with secondary clay minerals. Clast-poor, with carbonate clasts and quartz (ballen silica are noted), less than 0.5 cm in size. One clast of granitoid is noted and is composed of K-feldspar and quartz.
84R3_27–29.5	715.09	Non-graded suevite		Suevite, poorly sorted. The matrix is composed of calcite, and also isolated fossils (foraminifera) are noted. Clasts are mainly, green (glassy) and microcrystalline (black) impact melt rock clasts. Vesicles filled with calcite within the glassy impact melt rock. Black impact melt rock is clast-poor, with some undigested quartz grains (ballen silica type II). Millimeter-sized granitic clasts preserved (only seen in macroscopic sample).
85R1_30–31	716.79	Upper impact melt rock		Brecciated impact melt rock sample, with possible schlieren (but obscured by alteration). The matrix appears microcrystalline with red-orange bands. Microcrystalline calcite is also observed. Clast size is below 1 mm with a few ~5–10 mm in size clasts. A felsic basement clast, angular, and composed of small quartz grains is noted. Other clasts are mainly undigested quartz and feldspar grains. Quartz grains are shocked with the occurrence of PDFs, show undulatory extinction, and are toasted.

Sample	Unit	Image	Description
86R1_19–21.5	Upper impact melt rock		Green impact melt rock, relatively clast-rich. Clasts generally ~1–3 mm in size with rare larger clasts ~5–8 mm. Flow texture visible at thin section scale. Alteration by phyllosilicate is important. A carbonate clast, subangular in shape is noted. Quartz grains occur and are toasted, as well as ballen silica type V (possibly part of a partially digested granite clast).
88R1_12–14.5	Upper impact melt rock		Impact melt rock showing schlieren texture with black melt and green phase. Black melt: matrix is finely crystallized (microliths of plagioclase) but brownish in color, suggesting some alteration, clast-poor (mainly single mineral clasts, quartz dominant, less K-feldspar). Quartz grains are generally toasted; some ballen silica (type IV?) are also noted. Carbonate clasts are rare. Green phase: calcite/carbonate is the main phase, very fine-grained; strong alteration highlighted by clay minerals.
88R2_9–11.5	Upper impact melt rock		Impact melt rock relatively rich in undigested basement (granitic) clasts, with a ~2 cm, highly deformed granite clast noted in one part of the sample (not sampled in the thin section). The green schlieren is less visible than in the previous and next sample and appears more "patchy" (green patches). Quartz grains are shocked (toasted and with PDFs). A ~6 mm amphibolite clast is present.
88R3_45–47.5	Upper impact melt rock		Black melt dominant compared to green phase. Green phase is carbonate-rich, and strongly altered. Contact between the two phases is rather sharp. Black melt is clast-poor, with some mineral oriented along the flow direction. Clasts are mainly quartz grains (both shocked and ballen silica present), as well as rare carbonate grains with reaction rims. Matrix is glassy and very finely crystallized (plagioclase microliths). Post-impact calcite vein crosscut both melt phases.
89R1_59–61.5	Upper impact melt rock		Sample showing schlieren (black melt and green phase). Black melt is clast-poor; one large gneiss clast (2-3 mm) is observed. Single mineral clasts are mainly quartz, carbonate, and one plagioclase. Green phase is similar to the previous sample (88R3_45–47.5). Quartz grains are shocked and toasted, ballen silica type V is also noticed. Open fractures are commonly observed, crosscutting the sample at the macroscopic scale.

Sample	Depth	Type	Image	Description
89R2_49–51.5	727.36	Upper impact melt rock		Impact melt rock with schlieren, similar to previous samples, clast-poor. A ~3-mm-sized angular gneiss clast (alternating bands of quartz and altered biotite) occurs.
91R1_102–104.5	732.76	Upper impact melt rock		Black impact melt rock sample, in contact with a centimeter-sized, partially digested granite clast (removed for geochemical investigations). No flow texture is visible. The impact melt rock is clast-poor with a microlithic matrix. Single mineral clast population includes quartz grains (some of them partially digested), carbonates, and felspars. Quartz grains are toasted; ballen silica type V are observed. Calcite veins are crosscutting the sample. Some greenish areas seem to indicate, to some extent, alteration.
92R2_74–77	736.95	Upper impact melt rock		Impact melt rock with schlieren of green phase and flow texture. Several centimeter-sized undigested, or partially digested, granite clasts occur in the sample. Quartz grains occurring as single mineral clasts are shocked and toasted.
92R2_89–91.5	737.10	Upper impact melt rock		Impact melt rock with schlieren of the green phase. A flow texture is visible in the black melt. Otherwise, similar to other samples with schlieren. Carbonate-rich green melt with clay mineral alteration. The black melt is clast-poor, with clast size generally below 1 mm. Clasts consist mainly of undigested quartz grains (shocked and toasted) and also of rare plagioclase.
92R3_39–41	737.78	Upper impact melt rock		Black impact melt rock sample. Zeolite alteration visible at the naked eye. Discrete flow texture is visible in the matrix. Clasts are relatively undeformed. Sample similar to other black melt rock samples.
93R1_121–123.5	739.05	Upper impact melt rock		Homogeneous black melt sample, clast-poor, exhibiting some diffuse greenish alteration of the matrix. Vesicles (empty) of 1-3 mm occurred. No flow texture is visible. However, at the macroscopic scale, the sample exhibits a "patchy" texture, with brownish-greenish patches and darker, black areas in between. Small brownish altered globules are observed.

Sample	Depth	Unit	Image	Description
				Carbonates are nearly absent. Some undigested quartz grains (toasted and shocked) are noted.
93R2_11–12.5	739.32	Upper impact melt rock		Black impact melt (clast-poor) with a granitoid clast (1-2 cm; removed for the geochemical investigations). The granitoid clast (mainly quartz and K-feldspar, maybe plagioclase) is not fully digested and is crosscut by cataclasite material and the impact melt with recrystallization of the plagioclase (acicular). Strong mineral deformation is noted. No carbonate clasts are observed; very similar to other black melt samples.
94R3_38–40	743.57	Upper impact melt rock		Sample mainly composed of granite (partly digested granite clast of ~5 cm in size) embedded in a clast-poor black impact melt rock. A diffuse greenish alteration is visible in the impact melt. Flow texture is observed within the impact melt. The matrix is composed of microcrystalline plagioclase and pyroxene, as well as quartz, K-feldspar, and plagioclase mineral clasts (ballen silica type V is observed). The granite is coarse-grained, composed of K-feldspar, quartz, and plagioclase (mineral size ~0.1–1.1 cm), while micas are completely decomposed. Accessory phases include apatite, titanite, and zircon grains. Quartz grains within the granite are shocked with multiple decorated PDF sets, PFs, and FFs, and also toasted and show strong undulatory extinction. The contact between the granite and the impact melt rock is composed of microbrecciated material. Calcite-filling of vesicles and fractures is noted.
95R1_18–20	744.12	Upper impact melt rock		Black impact melt rock in contact with a partially digested 3-cm-sized granitoid clast. Clast-poor. Clast seem relatively more abundant than in samples from the core section 93R1. Clasts are generally millimeter-sized, with quartz grains representing the main population and, to a lesser extent, feldspar. Diffuse, greenish alteration (phyllosilicate minerals) is also visible.
95R1_84–87	744.78	Upper impact melt rock		Black impact melt rock, clast-poor, displaying a "patchy" texture, with the patches being light gray in color. In term of microscopic observations, this sample is very similar to the previous sample (95R1_18–20).

Sample	Depth	Rock type	Image	Description
95R2_19–22	745.07	Upper impact melt rock (*granite* clast)		Sample of a coarse-grained granite clast (~45 cm total size in core) within the black impact melt rock. Pervasively fractured at the sample scale. Main mineral phases are K-feldspar, plagioclase, quartz (mineral size ~0.5–2.5 cm), and biotite (<0.5 cm). Accessory phases include titanite, apatite, and zircon grains. A ~0.2 cm vein of brecciated quartz and feldspar (cataclasite) crosscut the entire thin section. Quartz grains are fractured, and shocked (up to three PDF sets in one grain; occurrence of PFs). Kinkbanding is common in biotite, as well as shock microstructures in titanite (at least one set is noted).
96R2_50–52	748.70	*Brecciated granite*		Monomict granite breccia. The sample is composed of subrounded, ~0.5 mm mineral clasts (mainly quartz and K-feldspar) with rare occurrence (<2 vol%) of biotite. The matrix (~45 vol%) is made of brecciated quartz, K-feldspar, and, to a lesser extent, calcite. The clastic breccia shows no signs of melting. Quartz grains are shocked, with up to two PDF sets per grain.
97R3_10–12.5	752.54	*Granite*		Coarse-grained granite (uppermost thin section of the granite basement unit in the drill core). The subsequent granite samples show similar mineral assemblage, with only variations in abundances and degree of deformation. Grain size is ~0.2–1.5 cm. Composed of K-feldspar, quartz, and plagioclase. Biotite is rare and commonly chloritized. Accessory phases include muscovite, apatite (fluor-apatite), titanite, zircon, epidote (allanite), and magnetite. Quartz grains are shocked with multiple PDF sets, PFs, and FFs, undulatory extinction, and kinkbanding in some grains. Shock microstructures in plagioclase (microtwins?) are noted. Kinkbanding is common in biotite, while apatite and titanite display planar microstructures (one to two sets). Some minerals are also sheared. A thin (<1 mm) cataclasite vein is observed, composed of subrounded, microbrecciated quartz and feldspars. Plagioclase shows high level of sericitization, especially in the cores of the grains, and to a lesser degree at the rims. Some fractures are also filled with calcite.
101R1_88–90.5	760.07	*Granite*		Coarse-grained granite with grain size generally ~1–2.5 cm. K-feldspar, quartz, and rarer plagioclase are the main components. Biotite is very rare and chloritized. Other accessory phases are titanite, allanite, and apatite (very low abundance). K-feldspars are orange in color, and display one to

			two PF sets visible at the macroscopic scale. Quartz grains are fractured and shocked (PDFs, PFs, and FFs, as well as undulatory extinction).
105R2_83–89	772.83	*Granite / Felsite dike*	Felsite dike cross cutting a granite. The contact with granite is sharp. The felsite is slightly porphyritic (feldspar and pyroxene are the main porphyritic crysts). Finely crystallized, acicular plagioclase microliths are noted. Calcite, and, to a lesser extent, quartz (shocked with PDFs (two sets)) also occurs. The felsite seems heavily altered with several calcite veins crosscutting the sample and a relatively high abundance of brownish veins. The calcite seems to have replaced a former anhedral mineral. The granite is coarse-grained (grain size ~0.2–1.5 cm) and mainly composed of K-feldspar, plagioclase, quartz, and chloritized biotite. Mineral fracturing is common in the granite.
106R3_67–70	777.41	*Aplite*	Aplite sample, corresponding to an aplite dike crosscutting the granite. A shatter cone was observed at the macroscopic scale in this level of the drill core. It is fine-grained (average mineral size <1 mm), homogeneous, with an equigranular texture. On one part of the thin section, minerals seem oriented. The main mineral phases are K-feldspar, quartz, and plagioclase. Biotite is nearly absent (<1 vol%). Plagioclase commonly exhibits sericitization. Shock features in the form of PFs and up to two visible sets of PDFs are observed in quartz grains.
109R2_89–91	785.83	*Granite*	Moderately deformed, coarse-grained granite. K-feldspar, quartz, and plagioclase, with grain size ~0.2–2 cm. Cataclasite (~1 mm thick) cutting the sample, composed of microbrecciated quartz and feldspar. Biotite is relatively abundant in this sample in contrast to sample 97R3_10–12.5. Chloritization of biotite is common. Kinkbanding is common in biotite, and also, biotite grains look like if they were entrained within cataclasite material (strong deformation). Titanite and magnetite grains represent the main accessory phases. All quartz grains are shocked (PFs, FFs, and up to three PDF sets visible, and show undulatory extinction). Common sericitization of plagioclase. Possible PFs in K-feldspar.

Sample	Depth	Type	Image	Description
110R2_14–16	788.07	*Granite*		Coarse-grained granite (grain size ~0.1–1 cm; one K-feldspar ~3 cm in size). Composed of K-feldspar, quartz, plagioclase, and chloritized biotite (rare). Accessory phases include muscovite, titanite, magnetite, apatite, and zircon grains. Mineral fracturing is common. Thin (<1 mm thick) cataclasite vein cut across the sample, and is composed of microbrecciated shocked quartz and feldspar grains. Quartz grains show undulatory extinction and are shocked, with several sets of PFs (with associated FFs), and up to three visible PDF sets. Titanite is strongly fractured, while kinkbanding is common in chloritized biotite and muscovite. Rare calcite-filling of fractures, and variable degrees of sericitization of the plagioclase grains.
114R2_42–45	800.48	*Granite*		Coarse-grained granite similar to 110R2_14–16. K-feldspar, plagioclase, quartz, and biotite (commonly chloritized). Kinkbanding observed in one quartz grain. All quartz grains are shocked (PFs, FFs, and decorated PDFs). Rare accessory phases (titanite, epidote, apatite, and zircon grains) are noted.
116R1_105–109	805.99	*Granite*		Moderately deformed coarse-grained granite. Mainly composed of K-feldspar, plagioclase, quartz, and commonly chloritized biotite. Shearing is observed. Cataclasite areas (two ~1 mm thick veins) crosscut the sample and are filled with microbrecciated and altered (presence of secondary epidote, piemontite?) material (quartz, feldspar, and also calcite). Titanite, allanite, and magnetite grains are also observed. Quartz grains are shocked. K-feldspar are also partly altered. Common sericitization of plagioclase.
116R2_58–62	806.71	*Granite*		Coarse-grained granite (grain size ~0.2–3 cm) composed of K-feldspar (abundant, ~45 vol%), plagioclase, quartz, and biotite. Biotite is commonly chloritized. Accessory phases include titanite, apatite, and magnetite. A 0.5–1 mm thick cataclasite vein crosscut the sample, and is composed of microbrecciated rounded quartz and feldspar grains and some secondary epidote grains. Quartz is shocked with PFs, FFs, and PDFs (multiple sets).
121R1_22–24	814.31	*Granite*		Well-deformed coarse-grained granite (grain size ~0.2–2.5 cm). Sample is crosscut by several cataclasite veins (up to ~5 mm thick). Cataclasite mainly composed of brecciated quartz (shocked with PDFs) and feldspars grains. High level of alteration of plagioclase (sericitization) and K-feldspar

Sample	Depth	Rock type	Image	Description
				in the granite. Biotite is commonly chloritized and kinked. Titanite is also observed with possible shock microstructures.
125R1_40–42.5	826.69	*Granite*		Relatively undeformed coarse-grained granite. Grain size is ~0.1–1.5 cm. Composed of K-feldspar, quartz, plagioclase, and biotite (chloritized). Accessory phases include muscovite, apatite, titanite, magnetite, and zircon grains. Fracturing is common, with some fractures filled by calcite. Quartz is shocked with PFs, FFs, and multiple decorated PDF sets; quartz shows undulatory extinction. Plagioclase grains are more or less sheared and PFs and possible PDFs are noted. Planar microstructures are also observed in apatite grains, while kinkbanding is common in biotite.
132R1_54–57	838.76	*Granite*		Coarse-grained granite, relatively undeformed. Grain size is ~0.2–1.5 cm in general. Very similar to the sample 125R1_40–42.5.
132R2_105–109	840.48	*Granite*		Coarse-grained granite, moderately deformed (grain size ~0.1–1.0 cm). The sample is crosscut by a ~1 cm thick cataclasite vein showing a fluidal texture. Shearing occurs at the contact between granite and cataclasite. Mainly composed of brecciated granite material (i.e., shocked quartz and feldspar). Greenish alteration at the sample scale, taking the form of secondary epidote, and calcite is observed at the thin section scale. Strong sericitization of plagioclase.
134R2_69–73	845.94	*Granite*		Coarse-grained granite (grain size ~0.5–1.0 cm), composed of K-feldspar, quartz, plagioclase, and chloritized biotite. Main accessory phases are muscovite, apatite, titanite, epidote, zircon, and magnetite. Mineral fracturing is important, and fractures are generally filled with calcite. Plagioclase is sericitized. Quartz is shocked (PFs, FFs, and decorated PDFs). PFs are noted in feldspars. Shearing occurs in apatite and epidote grains (generally associated with fracturing). Common kinkbanding of micas.
134R3_75–79	846.93	*Granite / Dolerite dike*		Coarse-grained granite, moderately deformed, in contact with a dolerite dike. In the granite, strong sericitization of plagioclase grains, and common chloritization of biotite is noted. Shear fractures are also observed in the granite. The contact between granite and dolerite is marked by a brecciated and sheared area (with some small granite fragments that appear to be

Sample	Depth	Rock type	Image	Description
				"entrained" by the dolerite). The dolerite is porphyritic, and composed mainly of ~0.2–0.3 mm long subhedral to euhedral plagioclase laths (generally fractured, and presenting possible shock microstructures in some cases), pyroxene (clinopyroxene?, fractured), and possibly former olivine now serpentinized. These phenocrysts are embedded in a microlithic groundmass, with microliths being mainly plagioclase and pyroxene (?). The phenocrysts are oriented subparallel to the contact between the granite and the dolerite. Opaque minerals are also observed.
135R1_10–14	847.64	*Granite / Dolerite* dike		Coarse-grained granite in contact with a dolerite dike. This sample is similar to sample 134R3_75–79 (see detailed description above).
136R2_20–25	851.37	*Granite*		Coarse-grained granite (grain size up to 1 cm) displaying K-feldspar, quartz, plagioclase (often sericitized), chloritized biotite, apatite, titanite, and magnetite. Fracturing is quite abundant. Some fractures are filled with calcite and crosscut the sample. Quartz with PFs, FFs, and decorated PDFs. Kinkbanding is common in micas/chlorite.
140R2_5–8	854.59	*Dolerite* dike		Fine-grained porphyritic dolerite. Plagioclase and pyroxene are the main mineral phases. Relatively high abundance of opaque minerals is noted. Occurrence of calcite in veins as well as veins filled with finely crystallized plagioclase. Pyroxenes are highly fractured and plagioclases seem to have undergone some alteration. Olivine also occurs and is highly altered, generally replaced by sheet silicates (probable serpentinization).
140R2_102–105	855.56	*Granite*		Coarse-grained granite (grain size ~0.5–2 cm). Composed of K-feldspar, plagioclase, quartz, and very rare (<1 vol%) biotite. Accessory phases observed are allanite, apatite, and titanite. The sample is crosscut by a ~1 mm thick cataclasite composed of microbrecciated quartz and feldspar. Secondary epidote and calcite are also associated with the cataclasite (greenish in color at the macroscopic scale). Sericitization of plagioclase is noted. Quartz show undulatory extinction and is shocked with PFs, FFs, and PDFs.

Sample	Image	Rock type	Description
142R2_105–109		*Granite*	Coarse-grained granite with grain size of ~0.5–1.0 cm, K-feldspar, quartz, plagioclase, and chloritized biotite. Titanite, apatite, and magnetite are the main accessory phases. The quartz grains are all shocked, commonly displaying two to three sets of decorated PDFs, but also PFs (up to two sets), FFs, and they also show undulatory extinction. Planar microstructures were also observed in feldspars. The sericitization degree of plagioclase varies from grain to grain, and some fractures are filled with calcite.
142R3_48–50		*Granite*	Coarse-grained granite (grain size ~0.5–1.0 cm) composed mainly of K-feldspar (fractured), plagioclase, and quartz (shocked). Similar to sample 142R2_105–109, with only a higher biotite abundance of ~7 vol% in this case.
143R2_103–106		*Granite / Dolerite dike*	Coarse-grained granite, moderately deformed (grain size ~0.2–1.5 cm) in contact with a porphyritic dolerite dike. Close to the contact, a strong alteration zone of the granite is noted. Slight brecciation of the granite at the contact. Mineral fracturing is common in the granite; quartz grains are shocked. Possible planar microstructures in plagioclase are observed. In the dolerite, phenocrysts (plagioclase, altered pyroxene, and serpentinized olivine) seem less abundant than in the dolerite dike seen in sections 134 and 135 (see descriptions above). Microlithic plagioclase and pyroxene are noted in the groundmass. The phenocrysts are highly fractured and also relatively subparallel to the contact between the dolerite and the granite.
144R2_52–55		*Granite*	Coarse-grained granite, relatively similar to sample 142R3_48–50, except for the presence, at the macroscopic scale, of a large K-feldspar (2.5 x 2.5 cm in size) showing at least two sets of PFs. Biotite is moderately chloritized. Accessory minerals include titanite, apatite, and magnetite. Quartz is shocked (PFs, PDFs). Sericitization is noted mainly within the cores of the plagioclases.
147R2_0–3		*Aplite*	Aplite dike sample with a fine-grained (average mineral size <1 mm), homogeneous, equigranular texture. The main mineral phases are K-feldspar, quartz, and plagioclase. Biotite is nearly absent (<1 vol%). Plagioclase exhibit common sericitization and some calcite veins crosscut the sample. Shock features in the form of PFs and up to three sets of PDFs are observed in quartz grains.
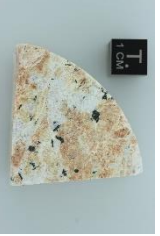
148R2_15–18	879.03	*Granite*		Coarse-grained granite, relatively undeformed. The grain size is ~0.2–1.0 cm. Composed of K-feldspar, plagioclase, quartz, and biotite (commonly chloritized, but some preserved biotite also occurs). Titanite, epidote (allanite), apatite, zircon, and magnetite grains are also observed. All quartz grains are shocked (PFs, FFs, and PDFs) and show undulatory extinction. Common sericitization of plagioclase is noted.
153R1_47–50.5	890.81	*Granite*		Coarse-grained granite, well deformed. Biotite is rare and strongly chloritized. Fracturing and shearing is common. The sample is cut by a ~1 cm wide cataclastic vein composed of brecciated granite material (mainly shocked quartz and feldspars). Mineralization of calcite and secondary epidote (piemontite?) indicates that the cataclasite was subsequently altered.
156R3_11–15	902.07	*Granite*		Coarse-grained granite (grain size up to 1 cm) composed of K-feldspar, plagioclase, quartz (shocked), and relatively abundant biotite relative to the other granite samples (~10 vol%, see also macrophotograph). Plagioclase is also abundant (~35 vol%). In term of accessory phases, titanite and apatite are relatively abundant, as well as zircon grain. Titanite and apatite display fracturing and shock microstructures. Biotite is commonly kinked.
157R2_0–2	903.75	*Granite*		Coarse-grained granite, weakly deformed. Composed mainly of K-feldspar, plagioclase, quartz, and biotite (commonly chloritized). Titanite, apatite, and allanite are also observed. The sample is crosscut by a ~2–3 mm thick fracture filled with fine-grained quartz (cataclasite or shear fracture?). A mineralization of secondary epidote (green in color, piemontite?) is noted. Quartz grains are fractured and shocked (PFs, FFs, and multiple PDF sets are visible). Important sericitization of the plagioclase.
160R1_37–44	911.96	*Granite*		Coarse-grained granite (grain size ~0.2–1.5 cm) with K-feldspar, quartz (shocked), plagioclase, and biotite (kinkbanding common, as well as chloritization). Similar to other previously described undeformed granites.
162R1_76–78	913.30	*Granite / Dolerite dike*		Well-deformed coarse-grained granite (grain size ~0.5–1.0 cm) in contact with a dolerite dike. The granite is highly fractured, and biotite is rare. Similarly to samples from sections 134, 135, and 143, the contact is marked by a brecciation of the granite, which seems to have been slightly entrained within the dolerite. Dolerite is porphyritic (phaneritic), with 2–3 mm sized plagioclase laths, as well as euhedral pyroxene and serpentinized olivine

Sample	Lithology	Image	Description
			grains. A microlithic texture of the groundmass with acicular plagioclase and pyroxene is noted. Some fractures occur within the dolerite, with calcite filling.
162R2_91.5–97	*Granite / Dolerite dike*		Highly deformed coarse-grained granite (grain size ~0.5–1.5 cm) with K-feldspar (orange and highly fractured, with two visible PF sets), quartz (shocked), plagioclase (one grain displays kinkbanding), and rare biotite, in contact with the dolerite dike. At least two shear fractures are visible, filled with brecciated granite material, and also calcite. Both dolerite and granite have been affected by shearing (deformation affecting similarly both lithologies). The dolerite texture is equigranular (aphanitic), with finely crystallized plagioclase and pyroxene (mainly, size up to ~5 mm).
163R1_76–77.5	*Granite*		Coarse-grained granite, undeformed, with grain size ~0.2–1.0 cm. K-feldspar, quartz, and biotite occur. Biotite is commonly chloritized. Accessory phases include titanite, magnetite, zircon, and monazite (?). All quartz grains are shocked (slightly decorated PDFs with up to three visible sets) and show undulatory extinction. Sericitization is common in plagioclase, and some fractures are filled with opaque minerals.
163R3_13–16	*Granite*		Coarse-grained granite, moderately deformed, with grain size ~0.5–2 cm. K-feldspar dominate the sample (~50 vol%), also quartz and rarer plagioclase and chloritized biotite are noted. The sample is cut by a greenish vein of ~4–5 mm thick, corresponding to a cataclasite, mainly composed of brecciated granite which was subsequently altered.
163R3_52–57	*Granite / Lower impact melt-bearing unit*		Strongly deformed coarse-grained granite with K-feldspar and plagioclase being strongly altered. The bottom part of the sample corresponds to an injection of impact melt rock (microcrystalline, with some millimeter-sized clasts of granite and single mineral clasts (quartz and feldspar), but also possibly rare dolerite clasts) within the granite. The contact between the granite and the impact melt rock is relatively sharp. In the granite, allanite and titanite grains were identified as accessory phases.

Sample	Depth	Lithology	Image	Description
164R1_48–50	918.27	*Granite*		Moderately deformed coarse-grained granite, with grain size ~0.2–1.0 cm. Composed of K-feldspar, plagioclase, quartz, and biotite often chloritized. Biotite seems slightly elongated according to the deformation direction. Titanite, apatite, and allanite are the main accessory phases. Quartz grains are shocked with the occurrence of PFs and PDFs, and they show undulatory extinction. Kinkbanding in biotite is noted. Thin (~1 mm) cataclasite vein crosscut the sample, and is composed of microbrecciated quartz and feldspar grains.
164R2_47–52	919.52	*Granite / Aplite*		Coarse-grained granite (grain size ~0.2–1.1 cm) in contact with an aplite dike, of similar composition and texture than sample 147R2_0–3. Granite is composed of K-feldspar, quartz, and plagioclase with minor biotite (commonly chloritized). K-feldspar is fractured (two PF sets) and show possible PDFs. Quartz is shocked (two visible PF sets and decorated PDFs) and shows undulatory extinction.
164R2_110–115	920.15	*Granite / Dacite dike*		Coarse-grained granite in contact with a dacite dike. Granite is relatively undeformed and mainly composed of K-feldspar, quartz, plagioclase, and biotite (generally chloritized). The thin section was prepared from the dacite area. The dacite is porphyritic, with millimeter-sized, zoned plagioclase crystals (dominating the lithology; commonly sericitized), as well as shocked quartz grains (two sets of PFs and up to three sets per grain visible), and rare biotite (<5 vol%, often chloritized, and showing kinkbands). Rare K-feldspar are noted. The matrix is composed of plagioclase, quartz, and biotite/chlorite. Accessory phases include apatite, titanite, allanite, and opaque minerals. A titanite with two (visible) sets of well-developed planar microstructures is observed.
164R3_19–21	920.41	*Dacite dike*		Porphyritic dacite dike, similar to sample 164R2_110–115. Only K-feldspar is slightly more abundant. Also, a euhedral hornblende crystal is observed within the thin section. Fracture occurs with calcite-filling or mineralization of secondary epidote (piemontite). Two sets of planar microstructures in an allanite grain are noted.

Sample	Lithology	Image	Description
168R1_56–58.5	*Granite*		Coarse-grained granite, slightly deformed, with grain size ~0.3–0.8 cm. Composed of K-feldspar, quartz, plagioclase, and biotite (~8 vol%). Biotite is commonly chloritized and kinked. Accessory phases include titanite, apatite, and opaque minerals. Common sericitization of plagioclase and alteration of K-feldspar is noted. Quartz grains are shocked.
168R1_82–84	*Granite*		Coarse-grained granite, very similar to the sample 1668R1_82–84. The granite is in contact with a dike of dark, highly deformed material comprising ~0.5–0.8 cm granitic clasts. Possibly a shearing fracture, or a dike of impact melt material (not within the thin section).
172R1_118–121	*Granite*		Typical coarse-grained granite (grain size ~0.3–1.0 cm), similar to other granite samples; mainly composed of K-feldspar, quartz, plagioclase, and rare chloritized biotite. Titanite, apatite, zircon, and magnetite are the main accessory phases. Shearing is observed, and mineral fracturing is common. Quartz grains are shocked (PF, FFs, and PDFs are noted) and show undulatory extinction. Shock microstructures are present in feldspars.
176R2_23.5–25	*Granite* / Lower impact melt-bearing unit		Coarse-grained granite (grain size ~0.3–1.3 cm), slightly deformed but highly altered. An impact melt rock dike occurs in the sample (area covered by the thin section). The impact melt rock is microcrystalline, relatively clast-poor, and highly altered, preventing a good observation of the matrix. Fluidal texture is noted. Some undigested mineral clasts, including shocked quartz with PDFs and feldspar are noted.
176R2_97–100	*Brecciated granite*		Brecciated granite, with a few crystals up to 0.5 cm in size. Mainly subrounded quartz, K-feldspar, and plagioclase grains, while biotite is nearly absent. Shearing occurs within the breccia. This sample may be interpreted as a cataclastic area. Quartz grains display generally shock metamorphic features in the form of PDFs.
176R2_112–116	*Granite*		Typical shocked, coarse-grained granite (grain size ~0.2–1.0 cm) crosscut by several shear fractures. A cataclasite area with microbrecciated quartz and feldspar occurs in the thin section. Biotite is chloritized and kinkbanding is common. Opaque minerals, titanite, apatite, and zircon grains are the main accessory phases.

Sample	Rock type	Image	Description
177R2_18–23	*Granite*		Coarse-grained granite crosscut by a ~1 cm thick cataclasite area composed of microbrecciated quartz and feldspars. Rare secondary epidote and calcite at the contact between the granite and the cataclasite. K-feldspar represents the main mineral component. Biotite is mostly chloritized and shows kinkbands. Quartz grains are shocked (with PFs and PDFs).
180R1_7.5–10	*Granite*		Typical shocked coarse-grained granite (grain size ~0.2–1.0 cm) similar to other investigated granite samples, but relatively undeformed. Biotite is commonly chloritized and is relatively abundant in some parts of the sample.
181R3_41–43	*Granite*		Strongly deformed coarse-grained granite with grain size generally no more than 1.5 cm. The sample is crosscut by several shear fractures that are crosscut by cataclastic material (as seen on macroscopic sample and in thin section). Biotite, generally chloritized, is elongated according to the deformation direction. Quartz grains are shocked (with PFs and PDFs).
183R1_20–23	*Granite / Dacite*		Coarse-grained granite (deformed) in contact with a dacite enclave. Grain size in the granite is ~0.3–1.5 cm. K-feldspar, quartz, plagioclase, and rare biotite (generally chloritized and elongated; some with kinkbanding) are noted. The dacite enclave is equigranular (no millimeter-sized phenocrysts) and composed of plagioclase, quartz, biotite, and opaque minerals. Quartz are commonly shocked (with PDFs). Contact between dacite and granite is relatively sharp.
188R2_11–13.5	*Granite*		Typical, relatively undeformed, shocked coarse-grained granite. Grain size is ~0.2–1.2 cm. Similar to the other undeformed coarse-grained granite samples.
198R1_68–71	*Granite / Dolerite dike*		Deformed and fractured coarse-grained granite in contact with a dolerite dike. Granite is composed of K-feldspar (altered and fractured), plagioclase (commonly sericitized; kinkbanding also observed), quartz (shocked with PFs, FFs, and PDFs), and biotite. Muscovite is also present. Common chloritization and kinkbanding observed in micas. Fractures in the granite are associated with shearing. A fracture is filled with secondary epidote (piemontite). In proximity of the granite, the dolerite appears relatively
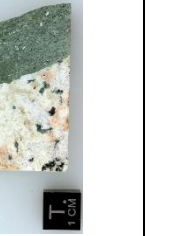
Sample	Lithology	Image	Description
			equigranular with mainly plagioclase and pyroxene grains no more than 1 mm in size. The contact area (not straight) is relatively brecciated, with fragments of granite and dolerite. Away from the contact, the dolerite appears porphyritic, with ~2–3 mm plagioclase laths, euhedral pyroxene and former olivine, now serpentinized, in a microlithic groundmass. In contrast to the previously described dolerite dikes (see above), the phenocrysts do not seem oriented parallel to the contact direction in this case.
199R2_50–54	*Granite / Dolerite dike*		Deformed coarse-grained granite (grain size ~0.5–3.0 cm) with K-feldspar, plagioclase, and rarer quartz and biotite. Biotite is generally chloritized. Titanite, apatite, and zircon grains are also observed but rare. The thin section is dominated by a K-feldspar mineral (2.5 cm width) which is fractured and displaying shocked planar microstructures; it is also crosscut by a shear fracture filled with calcite and secondary epidote (piemontite?). The dolerite (not represented in thin section) dike is ~2 cm thick, with an undulating, but relatively sharp contact with the granite, and displays a porphyritic texture with up to 5 mm plagioclase laths in a likely microlithic groundmass. The pyroxene and serpentinized olivine grains are not visible at the macroscopic scale.
200R3_12.5–15	*Granite*		Coarse-grained granite (grain size ~0.2–0.8 cm) with K-feldspar, quartz, plagioclase, biotite (rare and often chloritized), muscovite, apatite, titanite, zircon, epidote (allanite), and magnetite grains. Fracturing is observed. Thin (<1 mm) cataclastic areas with microbrecciated quartz and feldspar grains (subrounded). Quartz grains are shocked, showing PFs, FFs, and decorated PDFs; they also show slight undulatory extinction. Kinkbanding is common in micas/chlorite. Planar microstructures in apatite (two sets) and in titanite grains were also noted.
201R1_70–74	*Granite*		Coarse-grained granite (grain size ~0.2–1.2 cm) with K-feldspar, shocked quartz (with PF, FFs, and PDFs), plagioclase, and biotite (chloritized). The sample is crosscut by several parallel shear fractures, ~1–2 mm thick, filled with brecciated quartz and feldspar grains. Fractures filled with calcite are also noted.

Sample	Unit	Image	Description
202R2_48.5–53	*Granite* / Lower impact melt-bearing unit		Impact melt rock in contact with granite. Clast-poor close to the contact with the granite, and enriched in clasts with increasing distance to the granite, with a low melt abundance. Undigested quartz mineral clasts (shocked with PDF; some grains are toasted) are abundant in the impact melt. K-feldspar and calcite are also noticed. In proximity with the granite, the matrix is glassy, with no microliths visible. The granite is coarse-grained, fractured and deformed (sheared). Main phases are K-feldspar and plagioclase, and to a lesser extent, quartz (shocked with PFs and PDFs) and biotite (generally chloritized and kinked). Allanite and titanite grains are also observed.
204R2_46–48.5	*Granite*		Coarse-grained granite, with grain size up to ~1 cm, showing signs of slight deformation. K-feldspar, plagioclase, quartz, and biotite (common chloritization) are the main components. Strong sericitization of plagioclase is noted. Quartz grains are shocked (with multiple PFs and PDF sets). Kinkbanding is common in micas.
207R1_2–4	Lower impact melt-bearing unit		Impact melt rock, clast-rich, with flow texture, and undigested quartz (shocked), feldspar, and plagioclase clasts. Contact with granite is relatively sharp, with local microbrecciation of the granite.
212R1_129–131.5	*Granite*		Typical coarse-grained granite, very similar to the other granite samples. Grain size is ~0.5–2.0 cm. PFs in K-feldspar are visible at the macroscopic scale. A titanite grain with shock microstructures was observed.
219R1_105.5–108	*Granite* / *Aplite*		Typical, relatively undeformed, coarse-grained granite (grain size ~0.2–1.5 cm). Shearing is observed. Plagioclase grains are zoned and sericitized at cores. Several shocked titanite grains show planar microstructures (up to two visible sets). Quartz grains are shocked (with PFs and PDFs). The granite is in contact with an aplite dike, equigranular and homogeneous, with fine-grained K-feldspar, plagioclase, and quartz. Biotite is nearly absent. Some fractures are filled with calcite. Quartz grains are shocked with up to three PDF sets visible.

Sample	Depth	Lithology	Image	Description
220R2_20–22.5	1080.57	*Granite*		Coarse-grained granite, relatively undeformed (grain size up to ~2 cm) with a high abundance of biotite (~15 vol%). K-feldspar is altered and display possible shock microstructures. Plagioclases display PFs and possible PDFs(?). Quartz grains are shocked (with PFs and PDFs) and show undulatory extinction. Biotite is forming aggregates which are partially or fully chloritized, some of which show kinkbanding. Apatite, titanite, and opaque minerals also occur.
222R1_65–67.5	1085.23	*Granite / Dolerite dike*		Quartz-rich breccia, fractured, and altered. Quartz are shocked (with PDFs) and fractured, and show undulatory extinction. Rare plagioclase and biotite are noted. In contact with a porphyritic dolerite dike. The contact between the two lithologies is sharp. The dolerite is composed of plagioclase (~2–3 mm laths), pyroxene (fractured and altered), and possible serpentinized olivine phenocrysts in a microlithic groundmass (composed of finely crystallized plagioclase and pyroxene). The phenocrysts are subparallel to the contact between the two lithologies.
224R1_61–63.5	1091.39	*Granite*		Typical coarse-grained granite (grain size is ~0.5–2.5 cm). K-feldspar, plagioclase, quartz, and rare chloritized biotite. Mineral fracturing is important. Quartz grains are highly shocked with up to three PFs sets and three PDF sets visible; they also show a strong undulatory extinction. Fractures are filled with calcite and/or secondary epidote (piemontite). K-feldspar and plagioclase are altered (sericitization is noted in plagioclase).
225R2_53–56	1095.82	*Granite*		Fine-grained granite (grain size up to ~3 mm), composed of K-feldspar, plagioclase, and quartz. Biotite is absent. Fine dark "needles" ~1 cm long, identified as possible tourmaline(?). Some opaque minerals are noted. Most rock-forming minerals are shocked.
229R2_62–67	1107.19	*Granite / Aplite*		Coarse-grained granite (typical, undeformed, shocked, with grain size ~0.5–1.3 cm) in contact with an aplite dike, fine-grained, equigranular, with grain size <1 mm, and composed of K-feldspar, plagioclase, quartz, and very rare biotite. Biotite is commonly chloritized. Accessory phases are muscovite, apatite, titanite, epidote (allanite), magnetite, zircon, and monazite (?) grains. Open fractures occur; some are filled with calcite. Quartz grains are highly shocked (both in granite and aplite) with PFs, FFs, and multiple decorated PDF sets per grains. K-feldspar with PFs and other

Sample	Rock type	Image	Description
			planar microstructures (possible PDFs?). Planar microstructures (one to two sets) are also observed in titanite and apatite grains. Kinkbanding is common in micas. Shearing observed in feldspar and apatite grains. Sericitization of plagioclase is noted.
230R2_108–112	*Granite / Aplite*		Coarse-grained granite (grain size up to 2.5 cm), in contact with an aplite dike. The granite is composed mainly of K-feldspar and plagioclase, while quartz and biotite are nearly absent. Quartz are shocked and are brownish (slightly toasted?). Kinkbanding, PFs (up to three sets), and other planar shock microstructures (possible PDFs?) are observed in plagioclase. Some fractures are filled with calcite. The aplite is similar to the other aplite samples already described, with homogeneous, equigranular, and fine-grained (<1 mm) texture of K-feldspar, plagioclase, quartz, and very rare biotite. Highly deformed muscovite is also observed.
236R1_90–92.5	*Granite*		Typical coarse-grained granite (grain size ~0.3–2 cm), relatively undeformed, and composed of K-feldspar, plagioclase, quartz, and biotite. Accessory phases include titanite, apatite, zircon, and magnetite. Biotite is commonly chloritized and kinked. Mineral fracturing is common. Quartz grains are shocked (with PFs, FFs, and PDFs) and show undulatory extinction. PFs and other planar microstructures are noted in feldspars.
238R1_101–103.5	*Dacite* dike		Porphyritic dacite, with millimeter-sized plagioclase crystals in a microcrystalline matrix (composed of plagioclase and quartz). Quartz is shocked with occurrence of PDFs (up to three sets per grain visible). Less abundant K-feldspars are observed. Minor opaque minerals, biotite (often chloritized), apatite, and titanite grain are noted. Planar microstructures are observed in apatite (one set). Plagioclase is commonly sericitized.
238R2_16.5–20	*Dacite* dike		Porphyritic dacite dike (same dike as sample 238R1_101–103.5) similar to the previous sample. An open fracture visible at macroscopic scale crosscut the sample (induced during drilling?). The dacite is crosscut by a ~1 cm thick granite dike mainly composed of K-feldspar, quartz, and plagioclase, with no biotite. Quartz is shocked with PFs and PDFs. Also, in the dacite, K-feldspars display a reaction rim, which seem to indicate that they were derived from the granite and entrained within the dacite, and reacted with it.

239R1_121–124	1138.30	*Felsite* dike	Felsite sample from a dike which crosscut the granite basement. A nicely developed shatter cone is visible at the macroscopic scale. The texture of the sample is slightly porphyritic with some grains (feldspars and pyroxene) of ~1 mm in size, while the fine grains are ~100–300 µm in size. The phenocrysts consist mainly of former pyroxene altered to chlorite and/or amphibole. Feldspars (difficult to distinguish due to the small grain size) and quartz are also observed. Quartz grains show generally undulatory extinction; one grain shows a set of slightly decorated PDF but in general, shock features are hard to recognize due to the small size of the grains. Opaque minerals are relatively abundant, also, a possible tourmaline (?) is observed.
242R3_23–26	1149.01	*Aplite*	Aplite dike sample similar to the sample 147R2_0–3, with a fine-grained (average mineral size <1 mm), homogeneous, equigranular texture. The main mineral phases are K-feldspar, quartz, and plagioclase. Biotite is nearly absent (<1 vol%). Plagioclase exhibit common sericitization. Some calcite veins crosscut the sample. Shock features in the form of PFs and up to two sets of PDFs are observed in quartz grains. Planar shock microstructures are in some cases also observed in plagioclase.
246R3_38.5–42.5	1159.72	*Granite / Dacite* dike	Typical shocked coarse-grained granite, relatively undeformed (grain size ~0.5–2.0 cm) composed of K-feldspar, quartz, plagioclase, and biotite (only a few grains). Granite is in contact with a dacite dike, porphyritic, and similar to previously described dacite dikes (~0.3–1.0 cm plagioclase and quartz (shocked with multiple PDF sets) in a microcrystalline matrix with plagioclase, quartz, and commonly chloritized biotite). Titanite grains are also observed. Common sericitization/alteration of plagioclase is noted.
247R1_6.5–9	1160.06	*Dacite*	Dacite sample belonging to the same dike as the sample 246R3_38.5–42.5, similar in texture and in mineralogy. Rare K-feldspar are also observed with reaction rims. Titanite with two sets of planar microstructures, as well as allanite, is observed. Reddish alteration in some parts of the sample. Fractures are also observed to be filled with secondary epidote (piemontite?).
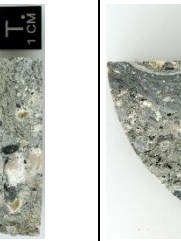
Sample	Depth	Rock type	Image	Description
248R1_5.5–7	1163.15	*Granite*		Coarse-grained granite, mainly composed of K-feldspar (up to two PF sets visible), quartz, and rarer plagioclase and biotite. The sample is crosscut by a network of greenish (alteration) veins (with a maximum thickness of ~0.8 cm) containing brecciated granitic material (cataclasite?). The veins are also filled with calcite and secondary epidote. Several titanite crystals are present in the thin section, displaying planar microstructures. Apatite and zircon grains are also observed.
248R3_22–25.5	1165.70	*Granite*		Typical coarse-grained granite (grain size of ~0.2–2.5 cm), with K-feldspar, plagioclase, quartz, and biotite (commonly chloritized). Quartz grains are shocked and mineral fracturing is common. Similar to previously described undeformed granite samples.
252R1_109–111.5	1176.58	*Granite*		Coarse-grained granite, similar to previous sample 248R3_22–25.5, slightly deformed. The alteration of K-feldspar and plagioclase (sericitization, and alteration to phyllosilicate) seem more pronounced in this sample than in the previous ones. Fractures are filled with calcite.
256R1_70–72.5	1188.57	*Granite*		Coarse-grained and shocked granite, slightly deformed (grain size generally ~0.2–0.6 cm). Similar to other typical coarse-grained granite. K-feldspar is less abundant relative to quartz and plagioclase. Biotite is commonly chloritized.
258R3_28–29	1196.78	*Granite*		Typical coarse-grained granite, relatively undeformed. Granite is composed of K-feldspar, plagioclase, quartz, and rare biotite. Quartz grains are shocked with PFs and PDFs. Common sericitization of plagioclase is noted. Biotite is chloritized and sometimes kinked. The granite is in contact with a brecciated vein of ~2.0 cm thick corresponding to a cataclasite, containing crushed granite material. Only rare K-feldspar and quartz (~1 mm in size) were preserved while the matrix consists of microbrecciated material. Greenish alteration is noted.
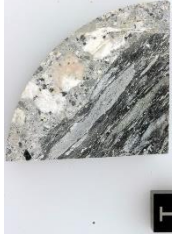
Sample	Lithology / Unit	Image	Description
264R1_75–77.5	*Granite*		Coarse-grained granite, moderately deformed (grain size ~0.2–1.5 cm). Very similar to previously described granite samples. Rock-forming minerals are shocked, especially quartz (with PFs, FFs, and PDFs); quartz grains also show undulatory extinction. K-feldspar is fractured. Large ~2 mm titanite crystal is noted. Biotite is commonly chloritized. Apatite, allanite, and zircon grains also occur.
265R2_9–11	*Granite* / Lower impact melt-bearing unit		Impact melt rock in contact with coarse-grained granite. Quite heterogeneous structure. In proximity with the granite, black to brownish impact melt rock, exhibiting flow structure at the macroscopic scale. Matrix is made of microliths (plagioclase and pyroxene?). Undigested shocked quartz (PDFs observed) and, to a lesser extent, pyroxene constitute the main clast population. Intercalation of crystallized material is also noticed. When going further away from the contact with the granite, the impact melt is crystallized with plagioclase and pyroxene laths, and the matrix is brown, with abundant microliths. The repartition is not homogeneous as recrystallized plagioclase and pyroxene are more abundant in some areas, while others have more microlithic melt. This may be a partially digested dolerite (or mafic basement clast?). Some altered olivine grains are also observed.
265R2_55.5–59	*Granite* / Lower impact melt-bearing unit		Strongly deformed coarse-grained granite, displaying a foliation further crosscut by shear fractures. K-feldspar display PF (one visible set), while chloritized biotite crystals are elongated following the foliation. The granite is in contact and pervasively intruded by an impact melt breccia, clast-rich, dark grey in color, with a fine-grained matrix (mainly composed of feldspars and quartz). Clasts consist of undigested granite, as well as single mineral clasts, including quartz and feldspar. No other lithology was identified among the clast population.
265R2_107.5–110.5	*Granite* / Lower impact melt-bearing unit		Gray impact melt-bearing breccia. The matrix is composed of fine-grained plagioclase and quartz grains with locally melted areas. Clasts are rounded and consist mainly of partially digested granite. Mineral clasts: K-feldspar with reaction rim, quartz (shocked with PDFs), and plagioclase. Flow structures are noted.
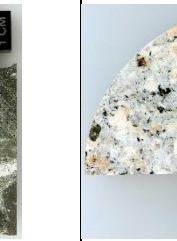
Sample	Unit	Image	Description
265R3_42–45	Lower impact melt-bearing unit		Impact melt rock, clast-rich, with schlieren texture. In contrast to the two previously described samples (265R2_55.5–59 and 265R2_107.5–110.5), the amount of melt is higher, appearing brown to black in parts of the thin section (devitrified?) with only some undigested quartz grains, while other parts of the matrix are composed of fine-grained quartz and feldspars. Partially digested, strongly deformed granite clasts, rounded to subangular, from ~0.8 to ~3 cm in size. Mainly composed of quartz and feldspars. Feldspars are altered (sericitization of plagioclase) and have PFs generally filled with opaque minerals. Quartz grains are shocked with PFs (and rare FFs) and PDFs (one to two visible sets), and sometimes toasted; they also show strong undulatory extinction. Biotite is nearly absent, with a few of them displaying kinkbanding.
266R1_9–12	Lower impact melt-bearing unit		Clast-rich impact melt rock, composed uniquely of granite clasts from millimeter-sized to centimeter-sized. Matrix appears brown (devitrified) to gray (containing fine-grained quartz and feldspar grains). Granite clasts are generally strongly deformed (foliation, shearing). Shock features are noted in quartz grains (PFs and PDFs). Quartz grains show strong undulatory extinction. Some biotite grains are also observed, and generally chloritized.
266R2_95.5–98.5	*Granite*		Coarse-grained granite, deformed, with grain size <0.8 cm. Mainly composed of K-feldspar, quartz, plagioclase, and biotite (relatively low chloritization in contrast to other granite samples). Accessory phases include muscovite, magnetite, apatite, epidote, and titanite. Fracturing is important, associated with shearing. A cataclasite area is observed, containing microbrecciated quartz, feldspar, and opaque minerals. Quartz grains are shocked with PFs, FFs, and decorated PDFs (one to two sets visible). Planar microstructures in feldspars are noted. Kinkbanding is common in biotite. Sericitization is also observed in plagioclase cores.
266R3_52–55	*Brecciated granite*		Strongly deformed (foliated and sheared) coarse-grained granite in contact with a brecciated dike (possibly an impact melt bearing breccia, as a small area containing brown, devitrified melt occurs). Matrix mainly composed of fine-grained, brecciated quartz and feldspar grains displaying a fluidal texture. Rare clasts more than 1 mm in size (K-feldspar and quartz). Shock features are difficult to detect or unrecognizable due to the small size of the

Sample	Unit	Image	Description
			grains; however, a PF set is noted in one K-feldspar clast. Biotite is nearly absent.
267R1_78–80.5	*Granite* / Lower impact melt-bearing unit		Strongly deformed (and shocked) coarse-grained granite in contact with an impact melt bearing breccia. The contact between the two lithologies is irregular, with parts of the granite which seem entrained within the impact melt breccia, which is composed mainly of brecciated granite material. Melt areas are of irregular shape and generally altered (possible microcrystalline texture?). The clasts are generally no more than 2 mm in size, and consist of undigested minerals forming the granite (K-feldspar, plagioclase, and quartz).
267R3_52.5–55.5	Lower impact melt-bearing unit		Black to grayish impact melt rock, clast-rich, with flow structure visible. Clast are submillimeter-sized, with quartz dominating the clast population. The impact melt is in contact with a highly deformed granite (clast?). The matrix is finely crystallized and also comprises microbrecciated material.
271R1_13.5–15.5	*Granite* / Lower impact melt-bearing unit		Strongly deformed coarse-grained granite, displaying foliation further crosscut by shearing fractures. Composed of K-feldspar, plagioclase, quartz, and very rare biotite, generally elongated according to the foliation. Quartz grains are shocked (PFs and PDFs) and show a strong undulatory extinction, while planar microstructures are present in feldspars. Common sericitization of plagioclase and alteration of K-feldspar is noted. The granite is in contact with a clast-rich impact melt rock. The impact melt rock is mainly composed of granite-derived clasts, as well as gneiss clasts.
272R1_28–30.5	*Granite*		Coarse-grained granite, moderately deformed, with grain size ~0.1–1.0 cm. Shear fractures crosscut the granite. Very similar to other previously described shocked granite samples.
276R2_62–64.5	*Granite*		Coarse-grained granite, strongly deformed (grain size ~0.2–1.1 cm). Composed of K-feldspar, plagioclase, quartz, and rare biotite (chloritization occurs). Deformation includes foliation and shear fractures. Thin (<1 mm) cataclasite veins, composed of microbrecciated quartz and feldspar grains, crosscut the sample. PFs and planar microstructures in K-feldspar are
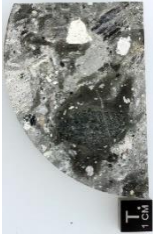
Sample	Unit	Image	Description
277R1_59.5–62	Lower impact melt-bearing unit		observed. Quartz grains are shocked, with PFs, FFs, and multiple PDF sets; Quartz grains show undulatory extinction. Impact melt rock, clast-rich. The clasts consist of angular basement clasts (gneiss and granite) from ~1–3 cm in size. Quartz is the main mineral clast within the melt. Clasts are also cross-cut by the impact melt rock. The melt is homogeneous, black in color, and no crystallization is visible.
277R1_88–92	Lower impact melt-bearing unit		Impact melt rock sample, clast-rich, with basement clasts embedded in a black, homogeneous melt, where microliths are absent in some place or, when present, seem to be altered. Areas exhibiting brownish color (alteration) are noted. A large 1.5 cm gneiss clast occurs. No carbonate clasts present.
277R2_25–27	Lower impact melt-bearing unit		Black impact melt rock with greenish areas, indicating that some alteration affected the sample. Parts of the impact melt rock exhibit clear flow structures with elongated minerals. Some altered brownish to orange glassy clasts are present. A 1 cm in size gneiss clast is also observed. In the gneiss clast, intercalations of finely crystallized plagioclase (like shards) veins. Recrystallization of plagioclase and maybe pyroxene (as shards) are also observed in the impact melt.
277R3_20–22.5	Lower impact melt-bearing unit		Impact melt-bearing breccia, composed mainly of brecciated granite material (undigested). Vitric melt is pervasively intruded within a strongly deformed, partially digested coarse-grained granite (composed mainly of K-feldspar, plagioclase, quartz, and rare biotite). A ~1 cm thick vein of microbrecciated quartz and feldspar crosscut the sample. Quartz grains are shocked. Sericitization of plagioclase is noted.
278R1_43–45	*Granite* / Brecciated granite		Brecciated granite sample, with ~50 vol% of matrix, strongly deformed with a mylonitic-like texture. The breccia is in contact with a large, 7 cm sized, coarse-grained granite which is relatively undeformed, and composed of K-Feldspar (up to ~1 cm), plagioclase (~0.5 cm), quartz (<0.2 cm), and biotite (generally chloritized).

Sample	Unit	Image	Description
278R3_6.5–8.5	Lower impact melt-bearing unit		Impact melt-bearing breccia, clast-rich. Mainly composed of brecciated granite material. Melt areas appear brownish and glassy. Fine-grained (microcrystalline) quartz and feldspars form the remaining parts of the matrix. Centimeter-sized undigested, strongly deformed and shocked granite clasts are noted. Biotite is poorly preserved.
279R1_37.5–40	Lower impact melt-bearing unit		Impact melt-bearing breccia, clast-rich, with centimeter-sized undigested clasts. The amount of vitric melt is relatively low, while fine-grained matrix dominates the sample. A part of the thin section is composed of greenish, altered melt rock, microcrystalline with undigested quartz and feldspars (<1 mm in size). A ~0.5 cm subangular equigranular dolerite clast is preserved, as well as a ~2 cm sized gneiss clast which is altered (chloritization of biotite within the gneiss). Undigested K-feldspar, plagioclase, and quartz grains (with shock features) also occur.
279R2_87.5–90	Lower impact melt-bearing unit		Impact melt rock, clast-rich. Microcrystalline dark gray, ~1 cm thick melt rock vein crosscut the sample, displaying well defined flow structures. Undigested mineral fragments (quartz and feldspars, up to ~1 mm in size), rounded to angular, occur. Larger (centimeter-sized) partially digested and brecciated granite and gneiss clasts are in contact with the melt vein. Rare biotite and titanite grains are preserved.
279R3_2–4.5	Lower impact melt-bearing unit		Impact melt rock, clast-rich, relatively similar to the previous sample, with a microcrystalline vein of melt rock (~1 cm thick) relatively rich in undigested quartz and feldspar clasts. The vein is in contact with a large (~4 cm) gneiss clast, with coating of melt (i.e., melt partially injected in the gneiss through open fractures). The melt rock vein is also surrounded by highly brecciated material (clast size <1 cm) with clast population including undigested and partially digested granite-forming minerals (shocked quartz with PDFs, plagioclase, titanite, and opaque minerals), and also equigranular dolerite.
280R1_47–49	*Granite*		Coarse-grained granite, with grain size up to ~1.0 cm. Appears brownish in color, mainly composed of K-feldspar, plagioclase, quartz, and very rare biotite (commonly chloritized). Titanite and apatite grains are also observed. The granite is moderately deformed, with the occurrence of shear fractures. Fractures are filled with calcite and also secondary epidote

Sample	Depth (m)	Unit		Description
280R2_51.5–53.5	1263.52	*Granite*		(piemontite?). Quartz is shocked with two visible sets of PFs and PDFs; Quartz grains show undulatory extinction. Common sericitization of plagioclase is noted. Coarse-grained granite similar to sample 280R1_47–49. A cataclasite vein, ~1 mm thick, crosscut the sample and is composed of microbrecciated quartz and feldspars grains.
280R3_9.5–12	1264.28	Lower impact melt-bearing unit		Impact melt rock, clast-rich. One part of the sample is composed of a partially digested granite clast composed of ~1 cm sized plagioclase and K-feldspar crystals, which are fractured and possibly shocked, embedded in a fine-grained brecciated matrix (mainly granite mineral components). This undigested granite clast is in contact with a melt rock displaying well-defined flow banding structures, with alternating gray and black bands. The gray areas are generally microcrystalline, while black areas are vitric, with few mineral clasts.
281R2_31–33	1266.25	Lower impact melt-bearing unit		Impact melt rock sample, composed of a large gneiss clast (~4 cm) embedded within a black, clast-rich impact melt. The gneiss is strongly altered (greenish in color) with chloritization of micas and sericitization of plagioclase. The black impact melt displays flow textures, and is composed mainly of undigested minerals, such as quartz and feldspars. The matrix is microcrystalline to vitric.
282R1_11–13.5	1268.05	Lower impact melt-bearing unit		Impact melt rock, clast-rich, composed of a gneiss clast occupying half of the thin section. The gneiss is similar to the previous sample 281R2_31–33, less altered, with alternating bands of quartz/feldspars and biotite (chloritized). The black impact melt, clast-rich, displays undigested mineral clasts (quartz and feldspar). A fine flow banding texture (?) with alternating bands composed of devitrified melt (black) and microcrystalline material (gray) is also noted. The contact between the two lithologies is marked by a ~3–4 mm thick "cataclasite"-like vein of microbrecciated quartz and feldspar, with also recrystallization of secondary epidote.

Sample	Depth	Unit	Image	Description
282R1_101.5–104	1268.96	Lower impact melt-bearing unit		Impact melt rock, clast-rich, composed of dark brown/black melt veins (microcrystalline with undigested mineral clasts to 1 mm in size), injected into a strongly deformed granite. The granite material is finely brecciated in some parts, while some rock-forming minerals (mainly quartz and plagioclase) are undigested. Some shock features in quartz (PFs and PDFs) and in plagioclase (planar microstructures) are noted.
282R2_82–84.5	1269.98	Lower impact melt-bearing unit		Impact melt rock, clast-rich, and strongly brecciated. The melt areas are very similar to previous samples of the same section. Flow texture is well-developed. In addition to granite-bearing minerals, an undigested dolerite clast (rounded, ~0.5 cm in size) is preserved.
284R2_10–12.5	1275.46	Lower impact melt-bearing unit		Clast-rich impact melt rock in contact with a large (~5 cm) equigranular dolerite clast. The impact melt matrix appears glassy, and clast-rich. The clasts consist mainly of undigested minerals (quartz, plagioclase, K-feldspar, with size up to ~2 mm). Shock features in quartz, including PFs (one set), PDFs (three sets), and kinkbanding are observed in the largest crystals. The equigranular dolerite is composed of plagioclase laths (nearly acicular), pyroxene, and former olivine (now serpentinized), with a grain size ~0.5 mm.
285R2_26–28.5	1278.70	*Granite*		Coarse-grained granite, strongly deformed (shear fractures), and partly brecciated. Composed of K-feldspar, quartz, plagioclase, and biotite. Grain size is ~0.2–1.0 cm for the non-brecciated granite, while the breccia is fine-grained. Quartz grains are shocked with PFs and PDFs in the larger grains.
286R1_127–130.5	1281.61	Lower impact melt-bearing unit		Impact melt rock, clast-rich. The sample is composed of dark gray melt rock surrounded by brecciated material and in contact with centimeter-sized undigested granite and gneiss clasts. The granite clast is coarse-grained, relatively undeformed (grain size ~0.5–1.0 cm) and composed of K-feldspar, quartz, plagioclase, and biotite (chloritization occurs). Quartz grains are shocked (with PFs, and up to three non-decorated PDF sets visible) and show undulatory extinction. Planar fractures in K-feldspar (filled with opaques minerals) and other planar microstructures (possible PDFs?) are observed. Variable sericitization of plagioclase is noted.

Sample	Unit	Description
		Titanite grains with two sets of planar microstructures are observed, as well as zircon grains. The gneiss clast is composed of alternating bands of plagioclase/quartz (rounded) and altered biotite (generally chloritized). The contact between the melt rock and the granite is marked by a brecciated area, ~1 cm in thickness, with a mineralogy similar to that of granite (probably brecciated granite, sharp contact with the granite clast). Clasts are millimeter-sized in a microcrystalline matrix. The contact between the melt rock and the gneiss is sharp. The melt is microcrystalline, and contains undigested mineral clasts no more than ~1.0 mm in size.
288R1_61–64	*Granite*	Coarse-grained granite, shocked, and slightly deformed (grain size ~0.3–1.5 cm). Sample similar to previously described granite samples, with shock features occurring in quartz and in feldspar grains. Some shear fractures are observed.
290R1_66–68	Lower impact melt-bearing unit	Impact melt rock, clast-rich. One part of the sample is made of black impact melt rock with partially digested and undigested basement clasts (gneiss and granite). The matrix is made of black melt (microliths are barely visible). Some greenish alteration veins are noted. Quartz is the main mineral clast (shocked, with PDFs, rarely toasted). The other half of the sample consists of a porphyritic dolerite clast with large plagioclase and pyroxene laths (generally 0.5 cm long). Minerals are heavily fractured. An intercalation of finely crystallized plagioclase and pyroxene veins occurs.
292R2_66–68.5	Lower impact melt-bearing unit	Black impact melt rock, homogeneous. Large clasts are less abundant than in samples from the section 277R, and smaller in size (no more than 1 cm size). However, the impact melt is clast-rich, with abundant clasts <1 mm, consisting generally of shocked quartz, plagioclase, and K-feldspar. Rare undigested pyroxenes are also noted.
294R1_67.5–70	Lower impact melt-bearing unit	Grayish, clast-rich impact melt rock with a strong flow-banding texture (mineral well elongated in the direction of the flow). In contact with a large 2-3 cm gneiss clast. A feldspar vein crosscuts the impact melt.

Sample	Unit	Image	Description
295R2_51–53	*Granite*		Coarse-grained granite, strongly deformed with mineral ductile deformation and shear fractures. Appears brownish in color. Grain size is no more than 1.0 cm. K-feldspar are abundant relative to plagioclase, quartz, and biotite. Biotite is generally elongated according to the deformation. Accessory phases include titanite, apatite, and zircon grains. Quartz grains are shocked with occurrence of PDFs; they also show undulatory extinction. Planar fractures in K-feldspar are noted. Sericitization of plagioclase is common.
295R3_48–50	Lower impact melt-bearing unit		Clast-rich impact melt rock displaying a large variety of clasts. Clast size varies from micrometer-sized to ~2.0 cm. Areas of black melt are microcrystalline with the presence of undigested mineral clasts (quartz, feldspar, and pyroxene(?)). Clast population includes gneiss, equigranular dolerite, possible mica schist(?), and partially digested granite. Shock features in the form of PDFs and PFs in quartz grains are observed.
296R1_62–65	Lower impact melt-bearing unit		Impact melt-bearing breccia, in contact with granite unit. The granite is coarse-grained, moderately deformed, and composed of K-feldspar, quartz, plagioclase, and biotite (locally more abundant). Fracturing is common, with some fractures filled with calcite. Quartz grains are shocked with PFs and PDFs; they also show undulatory extinction. PFs are observed in feldspars. Biotite is commonly chloritized. Rare titanite, apatite, allanite and zircon grains are noted. The granite is in contact with an impact melt breccia, with some impact melt clasts (~0.3 cm in size, microcrystalline) embedded in brecciated granite (very fine-grained).
296R1_116–118	*Granite*		Coarse-grained granite, moderately deformed (grain size ~0.5–1.5 cm). In contrast to granite samples located above in the drill core, K-feldspar grains appear more orange/brown in color. Quartz and plagioclase are the other main components, while biotite is nearly absent, and often chloritized. A low abundance of accessory minerals is noted, including muscovite, apatite, magnetite, and zircon grains. A thin (<1 mm thick) cataclasite vein with microbrecciated (and shocked) quartz and feldspar is observed. Fracturing is common with also partial calcite-filling of fractures. Shearing occurs in minerals. Quartz grains are shocked with PFs, FFs, and decorated PDFs sets (at least two sets visible); they also commonly show undulatory extinction. Planar fractures (up to two–three sets) are visible at the macroscopic scale in K-feldspar grains. Kinkbanding is observed in plagioclase, and also,

Sample	Depth	Unit	Image	Description
				rarely, in quartz grains. Calcite filling PFs in quartz is noted. Moderate sericitization of plagioclase is observed.
296R2_10–12	1311.37	*Granite*		Coarse-grained granite, slightly more deformed (common fracturing and shearing) than the granite sample 296R1_116–118. Mineralogical composition and features are similar to this latter sample.
297R1_36–38	1313.35	*Granite*		Coarse-grained granite with common shearing and fracturing. Abundant K-feldspar are observed as well as quartz, plagioclase, and rare biotite. Sample similar to samples already described in the section 296. The granite is in contact with a ~1 cm thick microbrecciated vein (cataclasite) composed of quartz and feldspar grains (rounded). The cataclasite shows a fluidal texture.
297R2_90.5–93	1315.09	Lower impact melt-bearing unit		Impact melt-bearing breccia, clast-rich. Impact melt rock is nearly absent (only rare occurrence of millimeter-sized black, microcrystalline impact melt rock). Clast-size varies from millimeter-sized to ~3 cm. Gneiss clasts seems to be the main component, followed by single mineral clasts, possibly originating from the basement (such as quartz or feldspars grains). A possible rounded, ~0.8 cm-sized, equigranular dolerite clast is visible in the macroscopic sample. Shock-induced features are generally preserved in the largest mineral (such as PFs and PDFs in quartz).
298R1_4.5–6.5	1316.14	*Granite*		Coarse-grained granite, strongly deformed, and in contact with brecciated material (granite-forming minerals) filling shear fractures. Large K-feldspar grain (~2 cm) in thin section with PFs and planar microstructures (possible PDFs?).
298R1_41–43	1316.50	*Granite*		Coarse-grained granite, moderately deformed (grain size ~0.2–3.0 cm). Abundant K-feldspar, and cataclasite veins filled with microbrecciated quartz and feldspars. Biotite is relatively rare, as well as other accessory phases (including titanite, apatite, and zircon grains). Planar microstructures in feldspars are noted. Quartz grains (rare) are shocked with PFs and PDFs.

Sample	Lithology	Image	Description
298R3_1.5–3.5			Coarse-grained granite, similar to the previous sample (298R1_41–43).
299R1_52.5–55	*Granite*		Coarse-grained granite with orange/brown K-feldspar, plagioclase, quartz, and rare biotite. Biotite is commonly chloritized and seems elongated according to a slight deformation direction. Mineral fracturing is important, with up to two PF sets in quartz. K-feldspar is generally altered. Titanite (in part brecciated) and allanite were also noted. Quartz grains are shocked with several PDF sets.
300R1_78–79.5	*Granite / Aplite*		Coarse-grained granite (grain size ~0.3–3.0 cm) with red/brownish K-feldspar, quartz, plagioclase, and rare biotite. Several shear fractures crosscut the granite, and are filled with microbrecciated quartz and feldspar and/or microcrystalline calcite. Quartz grains show undulatory extinction and are shocked; PFs, FFs, decorated PDFs, and rare kinkbanding are noted. Fractures in sericitized plagioclase grains are filled with opaque minerals. The granite is in contact with an aplite dike, which is fine-grained (grain size <1 mm), equigranular, and mainly composed of K-feldspar, plagioclase, rare quartz, and biotite. Fractures filled with calcite crosscut the aplite.
303R2_82–84.5	*Granite*		Coarse-grained granite, strongly deformed, with the occurrence of centimeter-sized cataclasite veins composed of microbrecciated K-feldspar and quartz. Biotite is nearly absent. Reddish alteration in some areas of the cataclasite is noted. K-feldspar grains are altered, and plagioclase is commonly sericitized. Quartz grains are relatively rare and shocked (PFs and PDFs).
303R3_22.5–25	Lower impact melt-bearing unit		Impact melt rock (black to brownish in color). It is "mingled" with more brecciated material (mainly granitic material consisting of quartz and feldspars). Melt seems to have a rather low abundance of microliths. Quartz grains are shocked and some toasted. A highly deformed, partially digested, brownish clast is also noted, possibly the remnant of a mafic lithology (amphibolite?).

APPENDIX B: Major element compositions of IODP-ICDP Expedition 364 drill core samples

This table presents the major element concentrations (in wt.%) measured using bulk XRF analysis of 112 powdered samples from the IODP-ICDP Expedition 364 drill core recovered within the Chicxulub impact structure peak ring. The samples are classified according to the lithological unit to which they belong. Iron oxide is reported as total ferrous Fe (Fe_2O_3*). LOI: loss on ignition; b.d.l.: below detection limit; mbsf: meters below seafloor; UIM: upper impact melt rock unit; LIMB: lower impact melt-bearing unit.

Sample	Depth (mbsf)	SiO_2	TiO_2	Al_2O_3	Fe_2O_3*	MnO	MgO	CaO	Na_2O	K_2O	P_2O_5	LOI	Total
Suevites													
40R2_107–109	618.7	31.6	0.32	7.48	2.85	0.15	3.06	26.0	2.20	1.75	0.09	21.5	97.07
41R1_106–108	620.4	36.0	0.35	8.37	3.23	0.17	3.50	22.5	3.01	1.57	0.09	18.2	96.89
41R2_21–23.5	621.0	39.4	0.38	8.89	2.77	0.12	3.55	20.3	2.85	1.99	0.10	18.4	98.68
42R3_46–48.5	625.3	46.5	0.41	9.58	2.88	0.11	2.56	15.9	3.21	2.41	0.10	15.4	99.09
43R2_54–56.5	627.4	49.8	0.44	10.3	3.47	0.09	2.91	13.1	3.43	2.55	0.11	12.9	98.98
44R2_51–53	630.2	49.4	0.44	10.4	3.68	0.10	3.12	13.3	3.43	2.33	0.10	13.3	99.58
46R2_49–51.5	636.5	50.1	0.43	10.6	3.67	0.09	3.33	13.2	3.51	2.32	0.10	12.3	99.56
48R2_54–56.5	642.0	47.8	0.47	10.8	4.44	0.08	4.21	12.7	2.95	2.65	0.10	12.4	98.59
49R1_64–66.5	644.3	46.1	0.50	11.0	5.11	0.10	4.87	13.1	2.88	2.62	0.12	12.8	99.24
50R1_94–96.5	647.7	47.4	0.42	10.4	3.73	0.09	3.84	14.2	2.64	3.01	0.10	13.1	98.90
51R2_69–71.5	651.1	47.8	0.49	11.2	4.57	0.10	4.15	13.2	3.05	2.87	0.11	11.4	98.90
52R1_37–39.5	653.2	49.3	0.43	10.7	4.07	0.09	4.02	13.2	2.92	2.83	0.10	12.2	99.81
54R1_57–59	659.5	48.7	0.47	11.2	3.69	0.08	3.34	12.7	3.40	2.67	0.11	12.6	98.93
56R1_97–99.5	666.0	47.3	0.57	11.5	5.50	0.10	5.10	11.5	3.62	2.25	0.13	11.8	99.36
57R1_27–29.5	668.4	48.2	0.48	11.0	4.37	0.10	4.17	12.4	2.82	3.22	0.11	12.2	99.01
58R3_8–10.5	673.7	46.6	0.45	10.8	4.00	0.10	4.28	15.1	2.81	2.61	0.10	12.8	99.63
59R2_76–78.5	675.9	44.4	0.44	10.5	3.96	0.14	4.23	16.3	2.70	2.45	0.10	14.0	99.11
62R1_31–33.5	681.9	48.1	0.43	10.3	3.81	0.12	4.34	14.4	2.51	2.52	0.09	12.5	99.10
63R1_7.5–9	683.4	47.8	0.46	10.5	3.98	0.10	4.67	13.5	2.41	2.82	0.10	12.7	98.99
63R1_68–70	684.0	52.9	0.44	11.1	3.75	0.08	4.11	11.5	2.91	2.39	0.10	10.6	99.88
75R1_13–16	702.2	45.2	0.45	10.7	3.64	0.08	4.81	15.7	1.74	1.32	0.11	14.7	98.37
78R1_12–16	704.9	46.2	0.45	10.4	4.08	0.09	6.15	15.1	1.75	1.07	0.09	14.1	99.51
82R1_35.5–38.5	710.7	30.6	0.34	6.49	2.61	0.14	3.19	28.5	2.11	0.29	0.09	24.2	98.66
84R2_19–21.5	713.7	28.0	0.34	6.66	2.60	0.11	4.18	29.2	1.90	1.05	0.09	24.3	98.45
Impact melt rocks (UIM)													
80R2_126–128	707.2	63.5	0.54	15.1	4.33	0.10	3.18	3.06	3.80	2.00	0.11	3.06	98.74
83R1_22–24.5	712.3	56.1	0.74	15.5	5.45	0.07	3.96	7.24	4.01	2.54	0.16	3.14	98.87
86R1_19–21.5	717.8	37.3	0.49	9.13	4.41	0.12	5.89	20.4	2.52	1.59	0.10	17.0	98.94
88R1_12–14.5	722.7	45.4	0.58	12.3	3.64	0.11	2.94	16.8	3.35	2.59	0.13	11.5	99.35
88R3_45–47.5	724.9	57.7	0.84	17.0	5.00	0.08	2.55	6.28	4.41	3.22	0.16	1.89	99.10
89R1_59–61.5	726.2	51.6	0.57	13.2	4.52	0.10	3.96	12.4	3.39	3.28	0.13	6.70	99.83
91R1_102–104.5	732.8	56.4	0.74	15.3	5.19	0.13	2.94	6.71	3.97	4.53	0.16	2.83	98.93

Appendix B. *(Continued)*

Sample	Depth (mbsf)	SiO$_2$	TiO$_2$	Al$_2$O$_3$	Fe$_2$O$_3$*	MnO	MgO	CaO	Na$_2$O	K$_2$O	P$_2$O$_5$	LOI	Total
91R2_89–91.5	733.8	57.4	0.67	15.4	4.45	0.14	2.03	7.31	3.89	5.03	0.15	3.27	99.73
92R2_89–91.5	737.1	44.6	0.50	10.7	5.45	0.13	5.98	15.6	2.97	2.20	0.12	10.1	98.29
92R3_39–41	737.8	60.5	0.62	16.2	4.86	0.09	3.11	4.03	4.12	4.68	0.14	2.04	100.36
93R1_21–23.5	738.1	60.3	0.59	15.3	4.70	0.09	3.12	4.52	4.26	4.01	0.14	2.03	99.03
93R1_121–123.5	739.1	58.1	0.64	16.1	5.52	0.07	3.95	5.04	3.90	3.59	0.14	1.51	98.62
93R2_11–12.5	739.3	58.9	0.66	16.2	5.43	0.07	3.41	4.98	4.33	3.39	0.15	1.47	98.95
95R1_18–20	744.1	58.8	0.61	16.9	4.78	0.06	2.83	5.27	4.26	3.72	0.14	2.37	99.73
95R1_84–87	744.8	60.3	0.63	17.8	3.52	0.05	1.18	5.2	4.14	4.58	0.14	1.87	99.37
95R2_45–47.5	745.3	60.2	0.62	16.3	4.26	0.05	2.54	4.60	4.42	3.75	0.14	1.97	98.88

Impact melt rocks (LIMB)

Sample	Depth (mbsf)	SiO$_2$	TiO$_2$	Al$_2$O$_3$	Fe$_2$O$_3$*	MnO	MgO	CaO	Na$_2$O	K$_2$O	P$_2$O$_5$	LOI	Total
191R2_18–20	995.4	64.0	0.44	14.0	4.12	0.06	3.80	2.39	4.24	3.25	0.09	3.52	99.93
192R1_47–49.5	997.6	62.9	0.46	13.3	4.77	0.07	4.32	2.69	3.96	2.78	0.10	3.77	99.09
202R2_48.5–53	1026.3	57.9	0.57	13.7	5.79	0.10	5.60	2.85	3.61	3.44	0.11	4.51	98.22
214R3_10–13	1063.2	70.6	0.18	12.9	1.87	0.03	1.70	2.02	3.80	4.62	0.07	2.14	99.92
265R2_9–11	1216.5	45.3	0.97	14.2	12.4	0.20	13.2	2.80	3.52	0.30	0.12	5.29	98.21
267R3_52.5–55.5	1224.4	67.4	0.31	14.1	3.77	0.07	2.76	1.47	4.29	4.08	0.09	1.86	100.24
277R1_59.5–62	1253.0	53.1	0.77	15.9	8.57	0.13	8.01	1.86	5.02	2.43	0.17	3.51	99.43
277R1_88–92	1253.3	53.0	0.76	15.5	8.09	0.14	7.78	2.49	4.36	3.08	0.17	2.81	98.16
277R2_25–27	1253.9	52.2	0.86	16.1	8.93	0.21	7.38	2.74	4.71	2.42	0.21	2.97	98.71
280R3_9.5–12	1264.3	68.6	0.43	14.2	3.50	0.06	1.95	1.55	4.65	3.18	0.12	1.29	99.55
282R2_82–84.5	1270.0	60.2	0.65	14.7	6.94	0.11	5.65	1.90	4.91	1.83	0.14	2.86	99.94
286R2_81.5–84	1282.5	70.5	0.30	13.4	2.35	0.03	1.29	1.42	4.40	3.78	0.09	0.92	98.51
289R1_57–59.5	1290.2	60.4	0.67	14.3	6.40	0.13	5.12	1.85	4.45	2.60	0.15	2.63	98.65
290R1_66–68	1292.0	61.9	0.69	14.5	5.92	0.17	4.29	2.57	4.37	2.30	0.16	1.95	98.86
292R2_66–68.5	1299.4	62.1	0.78	15.6	6.41	0.20	4.33	3.30	4.25	2.31	0.17	1.68	101.14
294R1_67.5–70	1304.4	59.4	0.92	15.0	7.75	0.17	4.16	3.11	4.79	1.46	0.38	2.31	99.42
297R2_90.5–93	1315.1	53.1	0.85	16.8	8.89	0.12	5.50	4.01	3.56	1.49	0.19	3.93	98.38
297R3_72–76	1316.1	55.5	0.76	15.0	8.65	0.11	6.47	2.46	4.18	1.36	0.17	3.66	98.29
303R3_22.5–25	1334.4	64.8	0.60	14.1	5.75	0.11	3.85	1.94	4.31	2.65	0.16	1.93	100.17

Granitoids (granite, granite breccia, and aplite)

Sample	Depth (mbsf)	SiO$_2$	TiO$_2$	Al$_2$O$_3$	Fe$_2$O$_3$*	MnO	MgO	CaO	Na$_2$O	K$_2$O	P$_2$O$_5$	LOI	Total
95R2_19–22	745.1	75.8	0.19	12.7	0.94	b.d.l.	0.63	1.57	3.82	3.95	0.09	0.53	100.23
96R2_50–52	748.7	70.5	0.23	13.2	1.62	0.04	1.10	2.32	4.39	3.61	0.08	2.14	99.15
97R3_10–12.5	752.5	74.3	0.16	13.0	1.07	0.02	0.46	1.31	3.71	4.82	0.05	1.06	99.90
110R2_14–16	788.1	72.3	0.21	14.9	1.09	0.02	0.47	1.41	4.82	4.56	0.05	b.d.l.	99.76
116R2_58–62	806.7	69.7	0.21	16.1	1.28	0.02	0.61	1.68	4.75	4.88	0.07	1.34	100.63
125R1_40–42.5	826.7	74.7	0.14	13.7	0.90	0.01	0.36	1.36	4.36	4.27	0.04	0.52	100.31
134R3_75–79	846.9	70.4	0.26	12.6	1.60	0.04	1.32	3.04	4.52	2.91	0.08	2.28	99.10
136R2_20–25	851.4	74.5	0.12	13.5	0.67	0.01	0.33	1.53	4.67	3.38	0.03	1.08	99.85
142R2_105–109	861.9	71.4	0.20	15.1	1.50	0.02	0.62	1.73	5.05	3.64	0.07	0.01	99.32
142R3_48–50	862.6	72.2	0.38	13.2	2.55	0.04	0.94	1.73	4.23	3.48	0.20	0.70	99.60
147R2_0–3	875.7	74.4	0.05	14.3	0.55	0.01	0.07	0.96	5.12	4.17	0.02	0.54	100.17
153R1_47–50.5	890.8	75.9	0.24	13.0	1.04	0.01	0.56	1.21	5.38	2.27	0.10	1.04	100.81
156R3_11–15	902.1	66.7	0.48	15.0	3.76	0.06	1.35	2.19	4.93	4.04	0.34	0.49	99.32
163R1_76–77.5	915.5	70.4	0.22	15.6	1.47	0.02	0.61	1.72	5.41	3.37	0.09	0.62	99.47
163R3_52–57	917.3	74.8	0.19	13.7	0.94	0.01	0.61	0.81	4.11	4.73	0.06	0.71	100.70

Appendix B. *(Continued)*

Sample	Depth (mbsf)	SiO₂	TiO₂	Al₂O₃	Fe₂O₃*	MnO	MgO	CaO	Na₂O	K₂O	P₂O₅	LOI	Total
172R1_118–121	942.9	75.5	0.15	12.6	0.83	0.02	0.36	1.45	4.41	3.24	0.04	1.10	99.64
176R2_112–116	953.6	69.7	0.26	14.9	1.50	0.02	0.55	2.09	4.04	4.10	0.09	2.64	99.89
188R2_11–13.5	986.2	71.3	0.27	14.6	1.82	0.03	0.74	1.68	5.22	3.09	0.13	0.67	99.48
200R3_12.5–15	1021.0	73.9	0.24	13.6	1.23	0.02	0.49	1.27	4.28	3.89	0.05	1.05	100.10
212R1_129–131.5	1056.0	72.2	0.19	13.9	1.28	0.02	0.57	1.64	4.90	3.03	0.04	1.21	98.95
219R1_105.5–108	1077.0	72.2	0.21	14.2	1.48	0.04	0.62	1.43	5.24	3.17	0.06	0.64	99.34
229R2_62–67	1107.2	75.8	0.21	12.3	1.32	0.03	0.59	1.58	4.30	2.55	0.07	1.15	99.87
236R1_90–92.5	1128.8	73.7	0.20	13.8	1.29	0.02	0.56	1.38	3.89	4.55	0.06	0.60	100.05
242R3_23–26	1149.0	75.0	0.09	13.2	0.59	0.02	0.15	1.03	4.37	4.48	0.03	0.66	99.60
256R1_70–72.5	1188.6	73.1	0.20	14.5	1.57	0.02	0.66	1.71	5.08	3.06	0.07	0.60	100.51
266R2_95.5–98.5	1220.5	72.9	0.29	14.6	1.74	0.02	0.61	1.72	5.01	3.05	0.11	0.47	100.55
272R1_28–30.5	1237.2	74.8	0.26	13.5	1.58	0.02	0.56	1.58	5.01	2.94	0.09	0.77	101.10
276R2_62–64.5	1250.9	74.0	0.18	14.0	1.26	0.01	0.55	1.13	5.03	3.64	0.06	0.69	100.55
278R1_43–45	1256.0	71.8	0.22	14.1	1.69	0.02	0.67	1.17	4.90	4.21	0.10	0.53	99.43
280R1_47–49	1262.2	74.5	0.13	13.9	0.96	0.03	0.36	0.78	4.52	4.30	0.04	0.57	100.04
280R2_51.5–53.5	1263.5	75.7	0.13	12.2	0.87	0.01	0.33	0.70	3.80	4.91	0.06	0.46	99.15
285R2_26–28.5	1278.7	72.9	0.24	13.3	1.69	0.02	0.64	1.32	5.13	3.20	0.11	0.45	99.00
288R1_61–64	1287.2	73.0	0.19	13.7	1.14	0.02	0.51	1.09	5.42	3.22	0.07	0.44	98.80
295R2_51–53	1308.5	74.3	0.13	13.5	1.01	0.01	0.26	0.95	4.36	4.32	0.05	0.80	99.61
296R1_116–118	1311.1	73.0	0.16	13.7	1.28	0.03	0.30	1.51	4.50	4.00	0.07	1.29	99.78
297R1_36–38	1313.4	72.8	0.14	14.1	1.23	0.01	0.29	1.35	4.22	5.16	0.05	1.25	100.62
298R1_41–43	1316.5	72.6	0.23	13.7	1.25	0.02	0.48	1.23	4.66	4.29	0.09	1.04	99.56
298R3_1.5–3.5	1318.7	76.5	0.13	12.3	0.71	0.01	0.28	1.05	4.38	3.46	0.04	0.83	99.63
299R1_52.5–55	1319.7	77.5	0.16	11.6	1.22	0.02	0.56	0.88	4.01	2.92	0.08	1.04	99.89
300R1_78–79.5	1323.1	73.0	0.17	14.1	0.91	0.02	0.25	1.43	4.46	4.67	0.06	1.33	100.35
303R2_82–84.5	1333.7	73.3	0.16	12.7	0.59	0.01	0.14	2.37	4.11	4.13	0.08	1.93	99.49
Pre-impact lithologies (dike or clast)													
80R2_61–63.5 (amphibolite)	706.6	50.6	0.93	15.6	9.91	0.25	7.30	8.09	3.69	1.30	0.29	0.79	98.69
105R2_83–89 (felsite)	772.8	50.6	0.82	15.0	6.00	0.16	4.74	6.32	3.24	4.80	0.49	5.67	97.88
140R2_5–8 (dolerite)	854.6	44.4	1.12	14.6	11.8	0.27	11.4	7.68	2.32	0.52	0.11	3.89	98.11
143R2_103–106 (dolerite)	864.8	43.2	1.12	15.5	12.8	0.19	12.0	5.22	2.39	0.60	0.11	5.76	98.78
164R2_110-115 (dacite)	920.2	69.2	0.48	14.5	2.50	0.04	1.05	1.79	4.66	4.13	0.21	0.69	99.22
164R3_19–21 (dacite)	920.4	67.7	0.46	15.0	2.68	0.04	1.22	1.82	4.48	4.51	0.22	0.92	98.99
198R1_68–71 (dolerite)	1016.1	42.6	1.68	15.6	13.6	0.19	11.8	2.84	4.03	0.41	0.19	6.67	99.47
234R2_97–98 (felsite)	1124.1	51.9	0.85	15.4	6.77	0.09	5.78	4.17	3.48	3.81	0.52	5.58	98.37
238R1_101–103.5 (dacite)	1135.1	67.4	0.52	14.7	2.83	0.05	1.40	2.26	4.61	3.70	0.28	1.04	98.80
239R1_121–124 (felsite)	1138.3	54.5	0.67	14.2	5.58	0.08	4.55	5.72	3.60	3.57	0.45	5.55	98.50
247R1_6.5–9 (dacite)	1160.0	68.7	0.46	14.7	2.49	0.04	1.38	2.17	4.73	3.26	0.18	1.00	99.18
284R2_10–12.5 (dolerite)	1275.5	46.5	1.00	14.9	12.5	0.26	11.0	2.77	4.24	0.37	0.09	4.28	97.92

APPENDIX C: Trace element compositions of IODP-ICDP Expedition 364 drill core samples

This table presents the trace element concentrations (in ppm, unless specified otherwise) measured using bulk XRF and INAA of 117 powders of samples from the IODP-ICDP Expedition 364 drill core recovered within the Chicxulub impact structure peak ring, including also a few samples from the transitional unit (core section 40R1, only analyzed using INAA). The samples are classified according to the lithological unit to which they belong. mbsf: meters below seafloor; UIM: upper impact melt rock unit; LIMB: lower impact melt-bearing unit; *Element measured only using bulk XRF; n.a.: not analyzed; b.d.l.: below detection limit (see details in Son and Koeberl (2005), Mader and Koeberl (2009) for INAA, and Nagl and Mader (2019) for XRF).

References

Mader D. and Koeberl C. 2009. Using instrumental neutron activation analysis for geochemical analyses of terrestrial impact structures: Current analytical procedures at the University of Vienna Geochemistry Activation Analysis Laboratory. *Applied Radiation and Isotopes* 67:2100–2103. https://doi.org/10.1016/j.apradiso.2009.04.014.

Nagl P. and Mader D. 2019. X-ray fluorescence (XRF) and instrumental neutron activation analysis (INAA) for the geochemical analysis of rocks, presented on in-house control samples (abstract). *Mitteilungen der Österreichischen Mineralogischen Gesellschaft* 165:67.

Son T. H. and Koeberl C. 2005. Chemical variation within fragments of Australasian tektites. *Meteoritics & Planetary Science* 40:805–815. https://doi.org/10.1111/j.1945-5100.2005.tb00156.x.

Sample	40R1_35–36	40R1_36.5–39	40R1_107.5–108	40R1_108–109	40R1_109–110	40R2_107–109	41R1_106–108	41R2_21–23.5
Rock type	Upper transitional unit	Transitional unit	Lower transitional unit	Lower transitional unit	Lower transitional unit	Suevite	Suevite	Suevite
Depth (mbsf)	616.60	616.62	617.32	617.33	617.34	618.7	620.4	621.0
Na (wt.%)	0.16	0.10	0.69	1.04	0.89	1.65	2.33	2.23
K (wt.%)	0.16	0.01	0.61	1.24	1.22	1.61	1.37	1.77
Sc	2.93	1.64	7.80	6.30	13.3	8.72	10.6	11.0
V*	n.a.	n.a.	n.a.	n.a.	n.a.	77.5	85.8	107
Cr	58.9	17.0	37.9	29.3	40.6	32.9	38.1	39.8
Fe (wt.%)	1.49	0.54	3.98	2.71	1.77	1.85	2.33	1.93
Co	8.00	3.68	121	56.3	17.1	12.5	9.68	9.52
Ni	87.9	33.6	230	108	65.2	26.6	17.5	20.5
Cu*	n.a.	n.a.	n.a.	n.a.	n.a.	27.8	22.0	30.4
Zn	158	25.1	78.7	44.9	292	19.1	26.9	27.3
Ga	7.8	0.8	10.9	11.9	11.4	8.0	8.4	9.1
As	4.3	0.8	4.9	2.3	1.4	3.1	5.0	1.5
Br	5.66	4.84	11.5	11.6	11.0	13.6	23.6	22.3
Rb	12.7	b.d.l.	36.3	38.3	39.1	35.0	27.0	36.4
Sr	225	241	1150	1141	934	504	582	468
Y*	n.a.	n.a.	n.a.	n.a.	n.a.	13.6	15.7	15.8
Zr	b.d.l.	34.9	90.9	84.1	109	69.1	76.2	84.7
Nb*	n.a.	n.a.	n.a.	n.a.	n.a.	3.1	3.5	4.0
Sn*	n.a.	n.a.	n.a.	n.a.	n.a.	4.6	7.0	7.5
Cs	0.96	0.32	2.14	1.63	2.52	2.25	3.77	3.53
Ba	9.60	7.25	57.6	106	138	239	385	367
La	5.32	4.88	7.84	8.58	8.62	12.1	15.2	14.0
Ce	6.48	7.19	15.2	15.2	15.6	21.1	26.7	24.7
Nd	4.47	3.48	7.54	6.61	7.43	11.7	12.2	12.5
Sm	1.38	0.99	2.12	2.03	2.39	2.3	3.24	3.33
Eu	0.24	0.19	0.51	0.50	0.54	0.54	0.69	0.63
Gd	1.08	0.85	0.90	2.08	2.51	1.84	2.19	2.28
Tb	0.16	0.11	0.30	0.27	0.26	0.33	0.37	0.37
Yb	0.63	0.49	0.94	0.92	1.03	1.21	1.52	1.44
Lu	0.12	0.08	0.16	0.15	0.18	0.18	0.27	0.20
Hf	0.61	0.36	1.33	1.26	2.04	1.53	1.95	1.95
Ta	0.11	0.06	0.20	0.21	0.29	0.27	0.31	0.32
Ir (ppb)	0.7	0.6	b.d.l.	b.d.l.	b.d.l.	b.d.l.	b.d.l.	b.d.l.
Au (ppb)	3.9	2.2	b.d.l.	b.d.l.	b.d.l.	0.2	b.d.l.	b.d.l.
Pb*	n.a.	n.a.	n.a.	n.a.	n.a.	2.8	5.0	3.5
Th	1.38	0.77	3.12	3.13	3.66	3.46	4.39	4.21
U	2.24	2.01	2.59	2.50	4.08	2.07	2.53	2.20

Appendix C. *(Continued)*

Sample	42R3_46–48.5	43R2_54–56.5	44R2_51–53	46R2_49–51.5	48R2_54–56.5	49R1_64–66.5	50R1_94–96.5	51R2_69–71.5
Rock type	Suevite	Suevite	Suevite	Suevite	Suevite	Suevite	Suevite	Suevite
Depth (mbsf)	625.3	627.4	630.2	636.5	642.0	644.3	647.7	651.1
Na (wt.%)	2.44	2.73	2.76	2.84	2.27	2.10	1.80	2.09
K (wt.%)	2.08	2.05	2.09	2.18	2.32	2.14	2.71	2.46
Sc	12.1	13.7	13.4	12.2	13.6	14.6	8.31	13.2
V*	105	106	102	106	106	115	93.6	135
Cr	43.1	47.9	46.9	43.6	49.2	50.3	32.0	43.5
Fe (wt.%)	1.98	2.53	2.70	2.51	3.19	3.24	1.91	3.07
Co	10.8	13.3	11.6	10.3	12.8	11.9	7.59	11.5
Ni	18.3	21.5	19.7	18.2	20.7	21.4	18.2	21.0
Cu*	28.3	30.8	29.1	30.2	33.9	26.9	26.4	29.5
Zn	31.2	40.5	40.0	46.7	55.8	56.5	48.8	60.0
Ga	8.9	10.1	10.3	9.8	10.4	11.3	10.4	11.1
As	2.9	1.2	0.5	b.d.l.	b.d.l.	b.d.l.	0.4	b.d.l.
Br	23.5	17.5	23.1	24.7	22.5	17.7	13.8	20.6
Rb	39.1	39.6	39.4	38.1	52.1	57.4	59.7	53.6
Sr	338	414	354	389	359	412	306	341
Y*	17.3	17.6	17.6	17.9	18.2	18.7	17.3	21.1
Zr	89.0	94.4	95.9	90.8	96.2	98.4	90.0	97.2
Nb*	4.3	4.5	4.5	4.4	4.6	4.9	5.6	4.6
Sn*	6.8	6.3	7.3	5.9	5.3	7.4	5.9	5.4
Cs	5.58	7.17	6.15	6.67	3.08	2.24	1.48	2.23
Ba	363	381	355	378	350	329	319	384
La	14.7	15.6	16.0	16.1	16.1	15.7	13.6	16.9
Ce	26.3	30.5	29.3	29.1	29.2	29.8	22.8	30.1
Nd	10.2	13.1	13.4	13.5	13	13.7	10.7	13.9
Sm	2.70	3.03	3.14	3.69	3.07	3.04	2.46	3.66
Eu	0.70	0.84	0.79	0.82	0.79	0.78	0.60	0.82
Gd	2.81	3.06	2.42	2.70	2.86	2.67	2.50	0.90
Tb	0.39	0.51	0.44	0.45	0.46	0.47	0.36	0.45
Yb	1.62	1.75	1.92	1.81	1.68	1.81	1.30	1.90
Lu	0.20	0.28	0.21	0.29	0.21	0.31	0.16	0.31
Hf	2.20	2.47	2.33	2.33	2.43	2.54	2.06	2.25
Ta	0.31	0.38	0.34	0.35	0.36	0.37	0.35	0.31
Ir (ppb)	b.d.l.	b.d.l.	b.d.l.	b.d.l.	b.d.l.	b.d.l.	b.d.l.	b.d.l.
Au (ppb)	b.d.l.	b.d.l.	b.d.l.	b.d.l.	b.d.l.	b.d.l.	b.d.l.	b.d.l.
Pb*	5.7	7.8	6.0	6.4	4.0	4.1	4.6	4.1
Th	4.30	5.33	4.99	4.97	5.00	5.63	4.31	4.71
U	1.84	1.82	1.46	1.83	1.48	1.77	1.56	1.92

Appendix C. *(Continued)*

Sample	52R1_37–39.5	54R1_57–59	56R1_97–99.5	57R1_27–29.5	58R3_8–10.5	59R2_76–78.5	62R1_31–33.5	63R1_7.5–9
Rock type	Suevite	Suevite	Suevite	Suevite	Suevite	Suevite	Suevite	Suevite
Depth (mbsf)	653.2	659.5	666.0	668.4	673.7	675.9	681.9	683.4
Na (wt.%)	2.26	2.67	2.69	2.25	2.28	2.04	1.65	1.62
K (wt.%)	2.18	2.25	2.28	2.38	2.39	2.12	1.78	2.14
Sc	12.6	13.3	15.5	16.5	13.6	12.8	10.6	12.7
V*	111	128	138	117	90.3	92.1	81.2	96.2
Cr	43.6	48.8	54.7	59.1	52.5	45.7	44.0	45.3
Fe (wt.%)	2.99	2.58	3.24	3.70	3.03	2.80	2.45	2.65
Co	11.6	10.4	12.7	14.1	11.5	10.5	8.92	9.84
Ni	21.7	19.3	25.2	23.3	18.1	18.6	18.9	19.6
Cu*	30.0	55.7	39.2	24.0	22.6	29.0	30.9	26.3
Zn	57.6	48.8	63.1	56.4	57.4	47.4	54.1	49.9
Ga	10.7	10.4	11.9	11.2	10.0	10.1	9.8	10.7
As	b.d.l.	b.d.l.	b.d.l.	b.d.l.	b.d.l.	0.4	b.d.l.	0.9
Br	16.3	15.4	16.9	19.8	13.0	16.4	12.9	13.6
Rb	52.7	48.8	43.3	57.5	50.6	52.2	52.1	61.5
Sr	466	417	406	471	404	436	301	333
Y*	18.8	21.4	22.8	18.6	18.5	19.7	16.8	18.2
Zr	97.3	97.8	112	99.1	92.8	92.4	96.8	100
Nb*	5.3	4.7	5.4	4.9	4.5	4.4	5.3	4.9
Sn*	6.5	6.9	6.7	6.5	5.7	6.0	6.5	5.0
Cs	2.39	4.18	5.32	3.38	2.52	1.88	0.73	1.25
Ba	351	349	342	310	313	321	410	265
La	15.2	18.6	17.8	17.7	16.1	16.4	12.6	13.8
Ce	28.0	33.1	35.3	33.0	30.7	30.4	23.8	26.1
Nd	13.1	13.8	16.0	15.5	13.5	13.0	10.9	13.1
Sm	3.12	3.14	2.94	3.75	3.29	4.00	2.46	3.02
Eu	0.76	0.86	0.97	0.89	0.87	0.85	0.65	0.72
Gd	2.99	2.83	3.35	3.31	3.16	0.90	2.11	2.85
Tb	0.50	0.55	0.62	0.57	0.51	0.49	0.36	0.41
Yb	1.64	2.10	2.00	2.13	1.80	1.86	1.45	1.58
Lu	0.29	0.34	0.35	0.35	0.29	0.31	0.19	0.21
Hf	2.57	2.47	3.07	2.86	2.57	2.43	2.25	2.51
Ta	0.43	0.39	0.43	0.52	0.39	0.38	0.39	0.34
Ir (ppb)	b.d.l.	b.d.l.	b.d.l.	b.d.l.	b.d.l.	b.d.l.	b.d.l.	b.d.l.
Au (ppb)	b.d.l.	b.d.l.	b.d.l.	b.d.l.	b.d.l.	b.d.l.	b.d.l.	b.d.l.
Pb*	4.3	4.4	4.5	4.6	6.2	5.6	5.5	8.9
Th	5.46	5.23	6.84	6.45	5.46	5.22	5.07	4.75
U	1.92	1.85	2.21	2.50	1.72	1.90	1.56	1.78

Appendix C. *(Continued)*

Sample	63R1_68–70	75R1_13–16	78R1_12–16	82R1_35.5–38.5	84R2_19–21.5	80R2_126–128	83R1_22–24.5	86R1_19-21.5
Rock type	Suevite	Suevite	Suevite	Suevite	Suevite	Impact melt rock (UIM)	Impact melt rock (UIM)	Impact melt rock (UIM)
Depth (mbsf)	684.0	702.2	704.9	710.7	713.7	707.2	712.3	717.8
Na (wt.%)	2.07	1.23	1.26	1.79	1.36	2.60	2.75	1.69
K (wt.%)	1.96	0.98	0.93	b.d.l.	0.87	1.47	1.72	1.09
Sc	11.4	13.1	13.8	9.38	8.89	15.4	18.9	12.7
V*	87.9	83.9	90.7	71.9	68.4	92.5	134	15.8
Cr	40.3	41.9	48.8	37.3	35.4	10.9	72.2	52.7
Fe (wt.%)	2.62	2.57	3.01	1.89	1.77	2.88	3.57	2.95
Co	9.12	10.3	10.2	7.97	7.46	7.48	12.8	12.1
Ni	17.6	16.5	19.8	15.3	17.9	4.20	27.2	28.9
Cu*	27.7	28.6	34.7	29.4	23.3	10.4	11.5	9.10
Zn	46.8	45.2	56.4	41.8	47.9	68.2	74.2	68.4
Ga	11.2	10.5	10.4	7.3	7.5	11.3	17.1	12.2
As	b.d.l.	0.7	0.7	1.3	0.9	b.d.l.	b.d.l.	2.5
Br	15.7	12.7	8.8	11.6	7.7	2.5	7.5	11.3
Rb	53.9	30.2	27.2	7.40	24.3	39.7	53.4	33.1
Sr	346	492	569	464	681	393	467	425
Y*	17.9	20.8	18.5	15.4	15.1	23.7	24.9	15.8
Zr	110	101	97.2	66.5	71.5	139	151	86.4
Nb*	4.4	4.2	4.6	2.8	3.0	5.2	6.8	3.4
Sn*	6.9	6.3	5.7	5.9	7.3	8.0	8.0	5.7
Cs	1.60	0.96	0.83	0.66	0.32	1.83	0.18	0.24
Ba	262	219	139	98.8	242	441	450	195
La	14.2	21.5	19.3	15.8	14.3	25.0	33.1	26.0
Ce	26.8	38.1	37.6	27.2	25.0	50.6	54.9	43.7
Nd	14.5	18.7	18.0	11.8	11.5	22.4	23.8	15.5
Sm	4.10	3.75	4.43	2.58	2.80	5.38	4.86	3.26
Eu	0.76	0.89	0.95	0.66	0.64	1.07	1.23	0.76
Gd	3.02	3.06	4.44	2.29	2.56	b.d.l.	4.53	3.09
Tb	0.43	0.53	0.65	0.41	0.43	0.71	0.63	0.41
Yb	1.71	1.84	2.25	1.39	1.38	2.23	2.34	1.38
Lu	0.23	0.26	0.37	0.23	0.22	0.38	0.37	0.17
Hf	2.70	2.56	2.69	1.80	1.79	3.63	3.57	1.95
Ta	0.36	0.36	0.39	0.25	0.30	0.33	0.43	0.29
Ir (ppb)	b.d.l.	b.d.l.	b.d.l.	b.d.l.	b.d.l.	b.d.l.	b.d.l.	b.d.l.
Au (ppb)	b.d.l.	b.d.l.	b.d.l.	b.d.l.	b.d.l.	b.d.l.	b.d.l.	b.d.l.
Pb*	6.60	9.00	6.10	2.60	3.50	4.40	19.4	6.00
Th	4.81	5.15	5.89	3.24	2.96	6.27	6.17	3.43
U	2.17	2.23	4.22	2.10	2.06	0.94	2.94	1.52

Appendix C. *(Continued)*

Sample	88R1_12–14.5	88R3_45–47.5	89R1_59–61.5	91R1_102–104.5	91R2_89–91.5	92R2_89–91.5	92R3_39–41	93R1_21–23.5
Rock type	Impact melt rock (UIM)	Impact melt rock (UIM)	Impact melt rock (UIM)	Impact melt rock (UIM)	Impact melt rock (UIM)	Impact melt rock (UIM)	Impact melt rock (UIM)	Impact melt rock (UIM)
Depth (mbsf)	722.7	724.9	726.2	732.8	733.8	737.1	737.8	738.1
Na (wt.%)	2.48	3.35	2.56	2.98	2.82	2.08	3.35	3.27
K (wt.%)	2.50	2.89	2.69	3.70	3.21	1.47	4.47	3.29
Sc	16.2	23.2	16.4	21.0	18.5	13.3	19.3	16.5
V*	90.4	131	92.5	126	114	82.6	109	101
Cr	58.8	94.9	67.1	82.3	62.7	52.3	69.6	57.8
Fe (wt.%)	2.49	3.73	3.26	3.93	3.11	3.78	3.70	3.45
Co	18.5	12.7	12.8	15.6	11.9	12.8	15.6	15.1
Ni	32.2	25.0	26.2	29.2	21.4	25.5	26.2	26.0
Cu*	12.1	9.00	28.3	15.6	14.0	22.6	42.6	42.1
Zn	197	300	91.1	111	99.8	119	85.0	86.5
Ga	14.6	18.5	15.9	16.5	15.9	14.7	16.7	16.0
As	6.9	4.4	3.4	12.1	3.1	2.9	3.5	2.1
Br	8.78	9.04	6.57	8.32	9.65	4.86	8.31	11.4
Rb	50.0	54.0	69.3	79.6	92.4	48.7	91.1	83.3
Sr	552	532	431	316	337	526	318	367
Y*	22.3	22.7	21.1	22.8	21.2	19.5	21.6	23.1
Zr	119	164	125	149	141	102	146	140
Nb*	5.4	7.5	6.3	7.1	7.1	4.8	7.5	7.5
Sn*	6.4	7.6	6.6	6.9	7.4	6.6	7.5	8.3
Cs	0.21	0.25	0.31	0.40	0.38	0.41	0.43	0.21
Ba	393	684	385	420	504	257	546	548
La	21.3	27.1	21.4	27.8	25.9	17.6	30.5	32.4
Ce	39.8	48.7	40.8	53.5	47.8	33.4	51.0	51.6
Nd	20.0	20.1	17.8	20.9	18.8	15.3	22.7	20.0
Sm	3.87	4.31	3.64	4.42	3.89	3.51	4.86	4.22
Eu	1.08	1.22	1.06	1.21	0.99	0.88	1.05	1.10
Gd	3.11	3.33	3.46	4.61	3.71	3.17	4.24	4.51
Tb	0.47	0.56	0.56	0.68	0.56	0.56	0.63	0.64
Yb	1.75	2.47	1.96	2.37	2.07	1.99	2.52	2.57
Lu	0.30	0.42	0.33	0.40	0.34	0.34	0.41	0.41
Hf	2.99	4.33	3.17	3.98	3.56	2.49	4.09	3.75
Ta	0.39	0.57	0.48	0.58	0.54	0.42	0.62	0.57
Ir (ppb)	b.d.l.	b.d.l.	b.d.l.	b.d.l.	b.d.l.	b.d.l.	b.d.l.	b.d.l.
Au (ppb)	b.d.l.	0.67	b.d.l.	b.d.l.	b.d.l.	b.d.l.	1.16	b.d.l.
Pb*	9.30	18.0	10.1	13.6	14.1	6.50	17.8	19.7
Th	5.60	6.95	6.96	7.45	7.49	5.32	9.59	8.88
U	1.94	4.07	2.06	2.52	2.28	2.32	3.13	2.02

Appendix C. *(Continued)*

Sample	93R1_121–123.5	93R2_11–12.5	95R1_18–20	95R1_84–87	95R2_45–47.5	191R2_18–20	192R1_47–49.5	202R2_48.5–53
Rock type	Impact melt rock (UIM)	Impact melt rock (UIM)	Impact melt rock (UIM)	Impact melt rock (UIM)	Impact melt rock (UIM)	Impact melt rock (LIMB)	Impact melt rock (LIMB)	Impact melt rock (LIMB)
Depth (mbsf)	739.1	739.3	744.1	744.8	745.3	995.4	997.6	1026.3
Na (wt.%)	2.67	3.17	3.19	3.21	3.24	2.86	2.97	2.78
K (wt.%)	2.59	2.54	3.06	4.14	2.80	2.51	2.42	2.63
Sc	17.1	19.6	16.2	16.6	18.3	8.42	9.37	11.1
V*	114	116	106	98.2	92.0	69.9	72.3	86.5
Cr	58.1	65.4	55.3	57.6	58.3	97.2	120	155
Fe (wt.%)	3.66	4.06	3.37	2.56	3.03	2.74	3.63	4.42
Co	13.7	14.3	12.5	11.1	13.8	14.4	18.6	25.2
Ni	29.0	24.8	22.5	15.7	25.8	54.8	63.2	83.7
Cu*	40.6	49.3	36.8	56.1	36.7	19.0	11.1	28.7
Zn	82.0	79.1	118	164	201	59.7	67.2	101
Ga	18.7	17.8	18.8	17.8	19.7	23.4	23.5	29.7
As	b.d.l.	b.d.l.	0.9	5.2	7.0	b.d.l.	4.4	b.d.l.
Br	11.1	13.4	16.8	18.5	11.6	16.9	15.4	21.0
Rb	68.1	77.4	79.6	90.6	80.9	101	86.0	91.0
Sr	451	448	450	425	414	287	280	266
Y*	26.0	26.9	24.8	20.2	19.7	9.8	10.8	13.3
Zr	152	154	153	161	151	101	100	120
Nb*	7.7	7.9	8.3	8.8	8.3	6.5	7.0	8.5
Sn*	9.2	7.0	8.3	5.8	7.5	7.0	6.3	6.0
Cs	0.21	0.26	0.17	0.21	0.25	1.15	1.24	0.96
Ba	569	573	712	638	608	417	426	506
La	36.8	42.4	42.2	44.6	39.9	14.8	16.7	18.7
Ce	56.9	67.0	65.5	70.4	62.0	28.3	31.6	36.3
Nd	22.0	23.4	24.5	27.6	20.3	15.1	16.4	15.2
Sm	4.61	4.73	5.92	6.26	4.04	2.63	3.09	4.01
Eu	1.14	1.29	1.24	1.27	1.08	0.75	0.81	1.10
Gd	4.27	4.10	b.d.l.	4.13	2.85	2.20	2.33	3.84
Tb	0.69	0.72	0.79	0.54	0.49	0.28	0.34	0.51
Yb	2.51	2.53	2.65	2.32	2.21	0.65	0.90	1.10
Lu	0.44	0.52	0.43	0.40	0.38	0.11	0.11	0.17
Hf	3.68	4.22	3.81	4.17	4.00	2.64	2.80	3.53
Ta	0.59	0.63	0.63	0.74	0.62	0.49	0.64	0.81
Ir (ppb)	b.d.l.	b.d.l.	b.d.l.	b.d.l.	b.d.l.	b.d.l.	b.d.l.	b.d.l.
Au (ppb)	b.d.l.	b.d.l.	b.d.l.	b.d.l.	b.d.l.	b.d.l.	b.d.l.	b.d.l.
Pb*	21.6	24.4	25.9	24.6	28.6	13.7	14.3	23.0
Th	9.16	10.5	11.6	11.3	9.86	8.74	9.19	12.8
U	2.56	2.10	3.21	8.72	4.17	2.73	3.45	4.78

Appendix C. *(Continued)*

Sample	214R3_10–13	265R2_9–11	267R3_52.5–55.5	277R1_59.5–62	277R1_88–92	277R2_25–27	280R3_9.5–12	282R2_82–84.5
Rock type	Impact melt rock (LIMB)	Impact melt rock (LIMB)	Impact melt rock (LIMB)	Impact melt rock (LIMB)	Impact melt rock (LIMB)	Impact melt rock (LIMB)	Impact melt rock (LIMB)	Impact melt rock (LIMB)
Depth (mbsf)	1063.2	1216.5	1224.4	1253.0	1253.3	1253.9	1264.3	1270.0
Na (wt.%)	2.57	2.56	2.95	3.42	2.96	3.44	3.29	3.41
K (wt.%)	3.64	b.d.l.	2.85	1.81	1.84	1.78	2.67	1.44
Sc	2.54	48.2	6.87	18.4	20.3	23.2	9.93	17.1
V*	28.8	260	49.0	115	123	144	71.5	95.2
Cr	9.94	299	59.1	31.8	41.7	37.5	19.7	28.5
Fe (wt.%)	1.26	9.30	2.55	5.45	5.59	6.26	2.29	4.52
Co	4.36	58.2	9.88	17.8	20.0	18.1	8.60	11.7
Ni	9.10	180	31.7	22.5	26.0	20.6	18.0	19.0
Cu*	27.0	62.9	60.6	43.3	44.4	43.8	26.8	59.8
Zn	37.0	176	48.0	124	103	106	29.3	91.4
Ga	14.7	22.0	20.0	23.6	23.9	24.3	16.9	20.6
As	b.d.l.	b.d.l.	b.d.l.	1.6	3.0	b.d.l.	1.8	0.6
Br	8.81	8.49	11.4	12.4	5.22	6.42	10.3	14.6
Rb*	136	11.4	108	70.6	77.0	64.3	96.6	54.4
Sr	314	247	359	238	233	247	290	256
Y*	4.70	23.8	8.00	22.8	19.8	21.2	12.6	20.8
Zr	88.7	90.9	119	147	143	138	117	130
Nb*	5.2	4.0	6.1	5.6	5.5	5.5	5.2	5.5
Sn*	5.8	5.0	7.9	7.0	5.4	7.3	6.6	6.6
Cs	0.93	0.71	0.64	0.63	0.71	0.66	1.42	0.67
Ba	698	51.1	585	234	247	236	383	179
La	13.7	10.0	26.3	16.8	14.4	21.9	21.0	22.0
Ce	25.6	23.5	45.5	31.9	31.5	41.9	37.9	37.6
Nd	11.1	13.0	16.6	15.0	14.1	18.6	14.8	15.7
Sm	2.05	3.05	2.71	4.33	3.34	4.06	3.77	4.45
Eu	0.41	0.88	0.59	0.81	0.85	1.09	0.72	0.94
Gd	3.27	3.02	2.26	3.76	5.00	3.25	2.55	3.81
Tb	b.d.l.	0.66	0.21	0.52	0.53	0.57	0.33	0.61
Yb	0.45	2.42	0.55	2.55	1.78	2.02	1.23	2.32
Lu	0.06	0.42	0.10	0.42	0.31	0.34	0.23	0.40
Hf	2.37	2.35	2.98	3.46	3.57	3.49	2.93	3.24
Ta	0.50	0.25	0.45	0.42	0.38	0.38	0.45	0.47
Ir (ppb)	b.d.l.	b.d.l.	b.d.l.	b.d.l.	b.d.l.	b.d.l.	b.d.l.	b.d.l.
Au (ppb)	b.d.l.	b.d.l.	b.d.l.	b.d.l.	b.d.l.	b.d.l.	b.d.l.	b.d.l.
Pb*	17.6	17.4	22.7	22.3	16.0	12.5	16.4	21.1
Th	20.7	1.36	12.1	6.66	6.38	5.45	12.2	5.56
U	4.58	1.26	3.33	3.47	1.70	1.66	4.12	5.11

Appendix C. *(Continued)*

Sample	286R2_81.5–84	289R1_57–59.5	290R1_66–68	292R2_66–68.5	294R1_67.5–70	297R2_90.5–93	297R3_72–76	303R3_22.5–25
Rock type	Impact melt rock (LIMB)	Impact melt rock (LIMB)	Impact melt rock (LIMB)	Impact melt rock (LIMB)	Impact melt rock (LIMB)	Impact melt rock (LIMB)	Impact melt rock (LIMB)	Impact melt rock (LIMB)
Depth (mbsf)	1282.5	1290.2	1292.0	1299.4	1304.4	1315.1	1316.1	1334.4
Na (wt.%)	2.85	3.24	3.03	3.33	3.55	2.67	3.07	2.97
K (wt.%)	2.78	2.19	1.16	1.42	1.00	1.33	1.03	1.66
Sc	6.14	16.3	18.0	23.2	23.5	24.8	23.6	16.7
V*	52.3	100	109	137	87.6	174	139	108
Cr	20.7	66.8	39.2	53.9	17.0	93.5	151	45.0
Fe (wt.%)	1.55	4.55	4.30	4.96	5.33	6.27	6.22	4.01
Co	5.33	14.7	14.0	18.1	7.76	20.8	25.8	17.8
Ni	11.9	26.4	20.2	23.7	17.0	36.1	45.5	19.2
Cu*	20.9	30.9	47.4	51.2	17.3	53.7	31.9	13.0
Zn	23.4	66.7	100	173	94.2	158	119	45.9
Ga	16.4	18.8	17.6	19.0	17.6	22.9	24.0	19.2
As	1.1	1.4	1.7	2.3	0.9	3.2	2.2	b.d.l.
Br	7.29	11.4	4.63	3.90	9.76	18.2	14.2	6.36
Rb	113	82.0	72.6	72.5	32.6	46.2	42.1	80.1
Sr	326	255	233	283	215	275	228	211
Y*	8.80	18.2	21.5	17.6	32.8	22.6	24.0	19.8
Zr	106	112	136	133	107	110	126	121
Nb*	5.5	6.3	5.6	6.1	4.2	3.7	4.6	5.9
Sn*	6.6	7.1	6.9	9.6	6.6	5.8	6.7	6.1
Cs	1.13	1.12	1.11	1.29	1.80	1.45	1.06	0.87
Ba	370	257	283	375	311	248	207	308
La	17.6	27.7	17.4	18.1	15.0	30.0	20.9	16.1
Ce	29.4	46.4	34.0	37.3	28.8	54.6	38.5	32.2
Nd	12.8	18.5	16.0	16.7	17.8	21.8	18.0	16.1
Sm	2.16	3.31	3.65	3.80	5.65	5.27	5.28	3.23
Eu	0.52	0.95	1.12	1.23	1.59	1.27	1.16	0.84
Gd	2.20	3.42	4.02	3.70	5.70	3.97	4.46	2.91
Tb	b.d.l.	0.48	0.60	0.55	0.82	0.66	0.63	0.50
Yb	0.74	1.77	2.21	1.89	3.15	2.27	2.36	1.70
Lu	0.10	0.22	0.38	0.32	0.50	0.36	0.28	0.30
Hf	2.61	2.95	3.52	3.70	2.67	2.73	3.05	3.04
Ta	0.33	0.46	0.45	0.50	0.28	0.27	0.29	0.47
Ir (ppb)	b.d.l.	b.d.l.	b.d.l.	b.d.l.	b.d.l.	b.d.l.	b.d.l.	b.d.l.
Au (ppb)	b.d.l.	b.d.l.	b.d.l.	b.d.l.	b.d.l.	b.d.l.	b.d.l.	b.d.l.
Pb*	18.9	13.8	16.4	16.4	9.20	30.9	16.1	12.8
Th	9.24	6.75	6.55	6.41	3.90	3.18	3.95	7.70
U	2.92	2.37	1.80	2.24	0.72	0.94	1.29	3.03

Appendix C. *(Continued)*

Sample	95R2_19–22	96R2_50–52	97R3_10–12.5	110R2_14–16	116R2_58–62	125R1_40–42.5	134R3_75–79	136R2_20–25
Rock type	Granite clast	Granite breccia	Granite	Granite	Granite	Granite	Granite	Granite
Depth (mbsf)	745.1	748.7	752.5	788.1	806.7	826.7	846.9	851.4
Na (wt.%)	3.04	3.51	2.84	3.47	3.65	3.07	3.65	3.23
K (wt.%)	3.55	2.94	4.10	3.98	4.39	3.33	2.12	2.65
Sc	3.17	4.49	2.52	2.22	2.98	1.83	3.76	1.57
V*	30.1	48.7	23.4	20.4	26.5	16.8	47.8	12.5
Cr	11.8	30.9	10.4	10.3	11.1	9.06	13.1	7.27
Fe (wt.%)	0.74	1.27	0.80	0.73	0.91	0.64	1.36	0.45
Co	6.45	5.62	2.51	2.42	3.20	1.97	6.98	1.90
Ni	7.1	14.2	2.7	2.8	4.0	2.4	8.8	2.1
Cu*	19.0	12.2	25.5	24.5	9.8	12.6	21.2	13.6
Zn	25.6	29.0	17.3	25.8	31.3	19.5	15.0	12.2
Ga	13.0	17.4	16.5	17.5	19.0	15.5	15.5	15.5
As	2.6	4.2	0.9	0.3	2.6	1.4	b.d.l.	1.9
Br	4.94	6.46	3.65	3.40	5.66	1.72	3.42	1.53
Rb	101	122	143	135	148	132	87.1	114
Sr	450	352	333	437	487	374	491	447
Y*	7.5	6.8	4.5	6.4	4.8	4.6	10.9	4.5
Zr	92.5	97.3	78.1	105	103	95.5	133	81.1
Nb*	5.6	5.6	5.2	6.8	5.2	3.7	8.8	3.2
Sn*	8.1	7.3	6.7	8.3	5.1	6.7	8.4	6.5
Cs	0.57	1.30	1.19	0.94	1.02	0.93	0.88	0.77
Ba	491	420	847	742	636	576	461	441
La	4.60	20.7	17.1	28.8	13.9	8.30	18.2	2.10
Ce	10.1	28.3	30.1	52.4	33.6	14.3	34.2	9.70
Nd	8.4	15.0	10.0	17.2	9.1	8.0	16.4	4.1
Sm	2.97	2.54	1.73	3.36	1.89	1.67	5.96	1.09
Eu	0.58	0.60	0.40	0.64	0.46	0.35	0.85	0.32
Gd	1.41	1.32	1.88	1.67	1.67	1.64	3.89	1.26
Tb	0.20	0.19	0.16	0.19	0.14	0.13	0.36	0.07
Yb	0.67	0.48	0.40	0.49	0.60	0.23	0.95	0.50
Lu	0.10	0.08	0.06	0.08	0.06	0.06	0.14	0.05
Hf	2.57	3.06	2.34	2.56	2.76	2.38	4.23	2.03
Ta	0.66	0.52	0.60	0.91	0.46	0.30	0.95	0.33
Ir (ppb)	b.d.l.	b.d.l.	b.d.l.	b.d.l.	b.d.l.	b.d.l.	b.d.l.	b.d.l.
Au (ppb)	b.d.l.	b.d.l.	b.d.l.	b.d.l.	b.d.l.	b.d.l.	b.d.l.	b.d.l.
Pb*	33.3	280	24.3	34.1	21.8	24.0	25.0	23.0
Th	13.5	8.84	10.3	19.1	7.29	7.71	13.1	5.57
U	3.45	4.30	8.86	4.61	4.12	2.91	16.3	3.12

Appendix C. *(Continued)*

Sample	142R2_105–109	142R3_48–50	147R2_0–3	153R1_47–50.5	156R3_11–15	163R1_76–77.5	163R3_52–57	172R1_118–121
Rock type	Granite	Granite	Aplite	Granite	Granite	Granite	Granite clast	Granite
Depth (mbsf)	861.9	862.6	875.7	890.8	902.1	915.5	917.3	942.9
Na (wt.%)	4.14	3.25	4.00	3.86	3.70	4.04	3.07	3.46
K (wt.%)	2.98	2.21	3.46	2.09	3.08	2.80	3.88	2.92
Sc	3.62	5.25	3.46	3.62	7.82	3.37	2.85	2.09
V*	29.8	50.3	6.7	38.4	76.0	32.2	29.2	18.3
Cr	12.4	15.3	7.10	10.5	21.2	11.1	9.67	9.53
Fe (wt.%)	1.17	1.91	0.42	0.83	2.97	1.04	0.66	0.60
Co	3.51	5.96	0.52	2.45	8.49	3.39	2.43	1.80
Ni	4.4	6.8	0.5	4.4	10.2	4.4	4.3	2.0
Cu*	36.0	123	11.0	12.6	9.70	47.7	9.90	9.50
Zn	31.5	47.8	7.30	28.4	89.8	33.4	17.4	17.8
Ga	18.8	19.0	21.1	16.9	23.8	20.0	14.5	15.2
As	1.3	0.5	1.7	0.5	1.1	0.6	b.d.l.	0.7
Br	1.68	2.53	3.15	2.95	2.22	2.44	2.95	3.34
Rb	113	124	175	125	171	117	145	104
Sr	456	384	179	269	404	459	323	313
Y*	3.7	9.9	8.2	5.7	10.5	5.7	5.6	4.8
Zr	114	138	52.6	98.0	204	109	91.5	90.8
Nb*	4.0	10.2	13.2	7.1	12.2	6.4	5.5	4.4
Sn*	6.2	6.9	5.8	6.3	6.1	5.9	7.4	7.0
Cs	0.90	1.49	1.67	2.87	4.87	1.25	1.22	1.33
Ba	514	514	182	338	568	467	532	477
La	9.70	30.5	4.50	15.4	18.4	9.80	13.3	15.9
Ce	20.8	56.2	10.6	30.7	45.7	29.8	30.2	31.2
Nd	7.6	23.0	8.3	10.0	19.0	5.1	11.0	9.5
Sm	1.43	4.09	2.29	2.04	1.21	1.61	1.74	2.12
Eu	0.42	0.81	0.40	0.45	0.79	0.43	0.45	0.39
Gd	1.26	4.56	2.46	1.59	1.23	1.03	1.24	1.15
Tb	0.08	0.30	0.24	0.16	0.29	0.11	0.12	0.11
Yb	0.90	0.90	0.90	0.43	0.79	0.90	0.35	0.34
Lu	0.06	0.11	0.10	0.06	0.14	0.08	0.06	0.06
Hf	3.72	3.93	2.86	2.92	5.91	3.27	2.58	2.74
Ta	0.30	0.90	1.14	0.69	0.92	0.57	0.46	0.46
Ir (ppb)	b.d.l.	b.d.l.	b.d.l.	b.d.l.	b.d.l.	b.d.l.	b.d.l.	b.d.l.
Au (ppb)	b.d.l.	b.d.l.	b.d.l.	b.d.l.	b.d.l.	b.d.l.	b.d.l.	b.d.l.
Pb*	22.4	45.4	26.2	98.5	21.8	40.8	18.9	19.4
Th	6.88	16.2	15.0	4.63	18.8	6.46	7.57	11.2
U	3.05	6.02	5.95	4.10	10.3	5.44	1.73	5.15

Appendix C. *(Continued)*

Sample	176R2_112–116	188R2_11–13.5	200R3_12.5–15	212R1_129–131.5	219R1_105.5–108	229R2_62–67	236R1_90–92.5	242R3_23–26
Rock type	Granite	Granite	Granite	Granite	Granite	Granite	Granite	Aplite
Depth (mbsf)	953.6	986.2	1021.0	1056.0	1077.0	1107.2	1128.8	1149.0
Na (wt.%)	2.79	4.33	3.44	3.72	4.10	3.24	3.07	3.32
K (wt.%)	3.16	2.77	3.18	2.32	2.54	1.97	3.78	3.78
Sc	3.50	4.12	2.66	3.01	3.96	3.41	3.10	1.98
V*	34.8	36.5	25.6	26.6	27.6	25.7	37.3	14.8
Cr	9.84	13.3	10.9	10.8	10.3	9.76	10.2	5.41
Fe (wt.%)	0.97	1.44	0.97	1.00	1.10	0.94	1.02	0.46
Co	2.69	4.34	2.69	3.27	3.45	3.20	3.19	0.92
Ni	4.4	4.9	2.8	3.4	3.8	3.7	5.2	0.9
Cu*	21.0	15.1	10.2	11.9	12.6	10.7	11.4	16.5
Zn	30.0	38.1	24.8	32.8	39.6	35.7	37.9	13.8
Ga	19.6	19.4	16.0	18.2	20.4	16.9	15.9	21.2
As	1.2	1.0	1.6	b.d.l.	0.3	1.6	2.5	1.8
Br	6.74	4.82	5.11	4.89	2.93	3.85	3.38	4.00
Rb	159	104	109	94.9	127	88.5	122	187
Sr	231	486	368	412	366	319	409	192
Y*	5.5	6.9	5.7	4.6	7.1	6.1	5.1	6.2
Zr	116	127	94.1	106	103	110	102	52.8
Nb*	6.7	6.7	7.8	4.9	8.9	8.6	4.9	11.8
Sn*	6.0	7.5	6.6	7.1	5.9	7.1	7.2	6.6
Cs	1.76	1.22	1.08	0.95	2.07	0.94	1.64	1.38
Ba	647	478	580	421	394	308	611	170
La	22.4	9.10	28.8	19.4	12.7	14.6	17.0	10.4
Ce	40.0	26.0	53.4	38.1	21.7	32.9	20.5	16.5
Nd	14.0	8.6	13.9	11.7	8.8	14.0	12.5	5.8
Sm	1.94	3.64	2.47	2.40	2.03	2.03	1.70	2.66
Eu	0.49	0.60	0.56	0.43	0.47	0.43	0.43	0.40
Gd	1.86	2.70	2.34	1.88	1.43	2.63	1.40	1.54
Tb	0.11	0.19	0.13	0.11	0.20	0.19	0.13	0.20
Yb	0.80	0.55	0.90	0.35	0.47	1.04	0.28	0.61
Lu	0.06	0.09	0.07	0.06	0.09	0.08	0.05	0.10
Hf	3.73	4.00	2.93	2.99	3.46	3.78	2.78	2.63
Ta	0.50	0.52	0.77	0.42	0.80	0.78	0.39	1.97
Ir (ppb)	b.d.l.	b.d.l.	b.d.l.	b.d.l.	b.d.l.	b.d.l.	b.d.l.	b.d.l.
Au (ppb)	b.d.l.	b.d.l.	b.d.l.	b.d.l.	b.d.l.	b.d.l.	b.d.l.	b.d.l.
Pb*	17.7	18.0	20.9	21.1	26.9	23.1	24.8	39.2
Th	10.0	21.8	12.4	10.6	8.28	12.1	5.25	20.3
U	2.84	7.83	3.98	5.09	6.43	7.19	2.05	12.5

Appendix C. *(Continued)*

Sample	256R1_70–72.5	266R2_95.5–98.5	272R1_28–30.5	276R2_62–64.5	278R1_43–45	280R1_47–49	280R2_51.5–53.5	285R2_26–28.5
Rock type	Granite	Granite	Granite	Granite	Granite breccia	Granite	Granite	Granite clast
Depth (mbsf)	1188.6	1220.5	1237.2	1250.9	1256.0	1262.2	1263.5	1278.7
Na (wt.%)	3.60	3.72	3.42	3.62	3.60	3.42	2.93	3.90
K (wt.%)	2.49	2.29	2.08	3.21	3.05	3.70	4.86	2.83
Sc	2.99	3.61	3.86	2.96	3.84	2.46	2.36	4.06
V*	30.7	34.3	35.1	27.2	36.4	23.1	23.6	28.5
Cr	17.2	12.4	11.2	10.7	10.9	11.4	10.0	11.4
Fe (wt.%)	1.11	1.36	1.10	0.97	1.32	0.73	0.73	1.22
Co	3.12	3.65	3.95	2.63	3.42	1.82	1.98	3.02
Ni	3.7	3.8	4.3	3.2	4.6	3.3	2.8	3.7
Cu*	12.6	14.5	12.2	12.2	21.9	15.6	12.5	12.2
Zn	31.4	37.1	33.6	13.4	11.9	10.9	5.2	20.1
Ga	19.0	19.2	19.1	16.2	19.3	13.7	15.0	16.7
As	2.6	3.1	2.6	b.d.l.	0.7	2.2	0.2	2.1
Br	4.91	4.02	5.55	11.3	5.65	4.61	4.63	8.06
Rb	96.4	106	96.4	111	122	165	163	113
Sr	437	444	351	334	270	252	220	317
Y*	4.6	5.8	6.5	5.3	9.3	6.1	5.9	6.1
Zr	106	137	135	99.6	123	85.2	70.0	117
Nb*	5.0	5.7	6.9	4.6	8.5	6.0	6.2	7.0
Sn*	7.0	6.2	7.9	6.8	7.2	7.7	7.2	6.7
Cs	0.75	2.01	1.48	1.24	1.07	2.04	1.61	1.41
Ba	419	482	303	396	266	343	315	331
La	8.60	26.1	6.8	10.2	12.7	16.5	9.20	13.0
Ce	29.6	31.5	36.2	30.1	26.3	24.8	11.5	30.9
Nd	9.2	16.1	11.9	11.8	15.3	9.4	10.4	12.6
Sm	2.24	2.16	3.16	2.56	3.07	1.78	2.80	3.06
Eu	0.42	0.56	0.52	0.38	0.46	0.28	0.36	0.45
Gd	1.64	2.33	1.61	2.14	2.60	2.20	b.d.l.	2.31
Tb	0.14	0.17	0.24	0.11	0.22	0.13	0.16	0.16
Yb	0.31	1.00	0.52	0.29	0.76	0.51	0.58	0.47
Lu	0.05	0.06	0.09	0.06	0.14	0.10	0.10	0.10
Hf	2.62	3.82	4.56	2.69	3.97	2.73	2.25	3.38
Ta	0.42	0.43	0.49	0.34	0.79	0.54	0.82	0.50
Ir (ppb)	b.d.l.	b.d.l.	b.d.l.	b.d.l.	b.d.l.	b.d.l.	b.d.l.	b.d.l.
Au (ppb)	b.d.l.	b.d.l.	b.d.l.	b.d.l.	b.d.l.	b.d.l.	b.d.l.	b.d.l.
Pb*	20.0	19.2	19.0	16.2	24.1	13.4	23.3	17.5
Th	9.30	14.7	12.7	10.8	11.8	12.5	20.0	10.2
U	2.54	3.98	5.84	4.17	5.11	6.09	8.70	7.07

Appendix C. *(Continued)*

Sample	288R1_61–64	295R2_51–53	296R1_116–118	297R1_36–38	298R1_41–43	298R3_1.5–3.5	299R1_52.5–55	300R1_78–79.5
Rock type	Granite	Granite clast	Granite	Granite	Granite	Granite	Granite	Granite
Depth (mbsf)	1287.2	1308.5	1311.1	1313.4	1316.5	1318.7	1319.7	1323.1
Na (wt.%)	4.03	3.03	3.15	3.26	3.39	3.29	3.13	3.37
K (wt.%)	2.71	3.28	2.95	4.28	3.24	3.27	3.06	4.28
Sc	2.78	2.72	2.25	1.86	2.46	2.54	2.76	2.39
V*	21.6	18.4	22.4	18.6	26.2	22.8	16.6	18.7
Cr	9.70	10.4	8.41	11.7	9.82	9.86	16.8	9.92
Fe (wt.%)	0.90	0.68	0.87	0.92	0.87	0.61	0.91	0.65
Co	3.27	1.91	2.52	1.82	2.36	1.73	2.34	1.22
Ni	2.6	2.7	4.0	2.0	4.6	3.6	4.0	2.1
Cu*	15.9	11.2	13.5	9.00	15.2	9.00	8.40	8.70
Zn	15.4	6.3	15.4	17.1	20.2	15.8	22.3	13.5
Ga	15.8	15.5	16.5	13.8	18.0	15.6	14.3	16.5
As	0.5	0.1	b.d.l.	0.9	0.4	b.d.l.	0.4	b.d.l.
Br	6.73	7.35	5.90	5.45	7.44	6.63	3.76	6.39
Rb	109	159	144	167	133	116	118	162
Sr	328	195	225	265	301	246	200	291
Y*	5.3	6.6	5.8	5.2	7.2	4.8	4.6	6.3
Zr	102	78.4	77.2	69.2	105	74.5	82.7	73.0
Nb*	4.9	6.4	7.3	5.8	10.1	5.3	5.7	8.1
Sn*	5.1	6.7	5.7	7.1	7.0	7.4	5.9	5.5
Cs	1.42	1.50	1.59	2.06	1.50	1.41	1.99	1.39
Ba	428	211	292	762	381	260	229	509
La	12.6	14.4	15.6	6.00	11.4	14.4	12.6	11.1
Ce	24.9	34.0	27.1	12.7	22.1	21.0	20.1	27.8
Nd	10.3	13.0	11.7	4.0	10.6	10.1	9.0	11.8
Sm	2.31	1.82	1.84	1.36	4.95	1.63	1.39	3.25
Eu	0.39	0.34	0.32	0.27	0.40	0.30	0.29	0.36
Gd	1.75	2.52	3.08	1.87	b.d.l.	1.10	2.42	3.26
Tb	0.14	0.15	0.13	0.12	0.20	0.11	0.11	0.13
Yb	0.34	0.70	0.90	0.47	0.76	0.37	0.52	0.90
Lu	0.06	0.10	0.08	0.08	0.14	0.07	0.07	0.10
Hf	2.77	2.42	2.51	2.04	3.40	2.12	2.48	2.24
Ta	0.41	0.76	0.61	0.60	0.94	0.61	0.53	0.69
Ir (ppb)	b.d.l.	b.d.l.	b.d.l.	b.d.l.	b.d.l.	b.d.l.	b.d.l.	b.d.l.
Au (ppb)	b.d.l.	b.d.l.	b.d.l.	b.d.l.	b.d.l.	b.d.l.	b.d.l.	b.d.l.
Pb*	33.9	20.5	13.4	20.8	20.3	22.7	16.6	23.5
Th	8.30	26.3	21.9	14.4	31.2	10.9	10.2	12.7
U	4.14	7.05	7.68	6.55	29.2	3.32	4.16	24.9

Appendix C. *(Continued)*

Sample	303R2_82–84.5	80R2_61–63.5	105R2_83–89	140R2_5–8	143R2_103–106	164R2_110–115	164R3_19–21	198R1_68–71
Rock type	Granite	Amphibolite (clast)	Felsite	Dolerite	Dolerite	Dacite	Dacite	Dolerite
Depth (mbsf)	1333.7	706.6	772.8	854.6	864.8	920.15	920.41	1016.07
Na (wt.%)	3.30	1.30	2.54	1.82	1.80	3.51	3.37	3.02
K (wt.%)	3.81	0.91	3.45	b.d.l.	0.54	3.56	3.98	b.d.l.
Sc	2.30	33.7	22.0	40.7	43.0	4.94	4.81	32.6
V*	22.4	274	193	233	261	56.3	59.5	211
Cr	10.7	181	105	542	480	13.8	12.8	512
Fe (wt.%)	0.46	7.14	4.65	9.39	9.09	1.94	1.89	9.66
Co	10.1	32.4	26.2	68.3	51.0	6.68	6.62	60.4
Ni	1.8	81.0	103	266	208	7.5	8.7	318
Cu*	8.80	21.2	28.9	110	107	36.0	66.1	107
Zn	4.0	108	107	99.9	118	50.2	53.9	138
Ga	13.9	15.5	18.4	16.2	21.1	18.9	19.5	21.6
As	0.5	1.4	30.8	1.6	1.4	2.3	1.1	0.6
Br	9.61	7.31	5.75	1.42	6.81	2.46	3.01	7.17
Rb	138	31.6	168	21.5	23.6	143	134	20.9
Sr	241	370	1177	303	298	493	587	261
Y*	6.6	19.4	39.7	19.5	16.2	11.6	10.0	21.9
Zr	83.2	73.3	234	72.1	72.1	155	148	123
Nb*	6.8	8.0	6.5	7.9	8.1	12.4	10.6	14.0
Sn*	6.9	5.5	11.4	3.6	4.0	7.5	8.5	6.7
Cs	1.37	0.64	2.42	1.47	1.27	2.09	1.03	11.7
Ba*	311	210	2406	119	93.0	488	673	88.0
La	22.0	13.7	126	6.38	21.4	25.9	30.9	17.7
Ce	35.9	33.8	236	14.1	37.6	56.7	59.2	36.5
Nd	10.6	13.6	79.2	8.8	15.7	26.0	20.6	21.5
Sm	2.62	2.85	16.8	2.62	3.32	4.72	3.31	4.34
Eu	0.42	1.06	3.73	1.12	1.03	0.99	0.89	1.45
Gd	2.61	2.92	11.1	2.27	1.74	3.23	2.27	3.44
Tb	0.10	0.53	1.32	0.55	0.39	0.38	0.27	0.63
Yb	0.57	1.84	3.21	1.87	1.65	0.83	0.80	1.76
Lu	0.10	0.33	0.55	0.30	0.22	0.14	0.12	0.23
Hf	2.87	1.72	6.13	2.12	1.95	4.32	3.86	3.18
Ta	0.71	0.42	0.60	0.69	0.70	0.83	0.58	1.05
Ir (ppb)	b.d.l.	b.d.l.	b.d.l.	b.d.l.	b.d.l.	b.d.l.	b.d.l.	b.d.l.
Au (ppb)	b.d.l.	b.d.l.	b.d.l.	b.d.l.	b.d.l.	b.d.l.	b.d.l.	b.d.l.
Pb*	20.5	9.8	16.2	11.6	19.1	22.1	21.8	56.8
Th	15.1	3.51	50.6	0.55	0.69	10.0	12.1	0.64
U	5.66	1.96	11.5	2.30	1.13	8.51	4.14	1.20

Appendix C. *(Continued)*

Sample	234R2_97–98	238R1_101–103.5	239R1_121–124	247R1_6.5–9	284R2_10–12.5
Rock type	Felsite	Dacite	Felsite	Dacite	Dolerite (clast)
Depth (mbsf)	1124.1	1135.05	1138.3	1160.01	1275.46
Na (wt.%)	2.60	3.59	2.88	3.11	3.34
K (wt.%)	3.10	2.34	2.81	2.65	b.d.l.
Sc	23.3	5.44	19.1	5.78	46.7
V*	173	56.2	142	59.4	248
Cr	108	13.7	90.3	13.4	203
Fe (wt.%)	5.08	2.27	4.31	1.92	9.69
Co	27.4	8.22	22.0	6.76	72.7
Ni	106	9.6	86.0	10.0	102
Cu*	41.2	105	13.0	39.2	129
Zn	82.1	54.1	80.0	51.4	148
Ga	20.4	19.8	17.2	19.5	23.3
As	0.2	2.0	3.1	1.1	4.9
Br	8.46	4.08	3.87	3.06	8.32
Rb	113	118	97.8	101	11.7
Sr	769	806	1178	677	189
Y*	38.1	10.9	41.3	9.2	20.6
Zr	237	154	236	137	55.8
Nb*	6.7	11.5	6.1	8.6	0.9
Sn*	9.7	7.6	8.7	7.3	4.9
Cs	1.90	0.92	1.24	0.64	1.23
Ba	1468	604	2001	588	32.7
La	92.8	32.9	122	27.7	3.69
Ce	181	62.3	235	52.0	8.3
Nd	85.5	26.1	102	22.0	12.3
Sm	14.4	4.42	18.8	3.56	2.22
Eu	3.04	1.17	4.11	0.91	0.75
Gd	9.23	2.77	20.5	2.16	2.64
Tb	1.17	0.36	1.40	0.30	0.53
Yb	3.27	0.84	3.48	0.66	1.82
Lu	0.51	0.14	0.50	0.12	0.29
Hf	5.95	4.07	5.90	3.75	1.85
Ta	0.55	0.71	0.53	0.58	0.12
Ir (ppb)	b.d.l.	b.d.l.	b.d.l.	b.d.l.	b.d.l.
Au (ppb)	b.d.l.	b.d.l.	b.d.l.	b.d.l.	b.d.l.
Pb*	58.4	30.7	62.2	21.1	5.8
Th	49.7	7.58	51.8	8.91	0.34
U	10.5	2.17	12.0	3.17	0.70

APPENDIX D: Highly siderophile element concentrations and Re-Os isotopic compositions

This table presents the highly siderophile element concentrations (Re, Os, Ir, and Pt, in ppb) and the Re–Os isotopic compositions of 19 selected samples from the IODP-ICDP Expedition 364 drill core recovered within the Chicxulub impact structure peak ring. The composition of seven samples of the transitional unit were added here compared to the table presented in the publication Chapter 7. mbsf: meters below seafloor; n.a.: not analyzed; UIM: upper impact melt rock unit; LIMB: lower impact melt-bearing unit. The $(^{187}Os/^{188}Os)_i$ ratio is calculated at the impact age (~66.05 Ma).

Sample	Depth (mbsf)	Re (ppb)	Os (ppb)	Ir (ppb)	Pt (ppb)	$^{187}Os/^{188}Os$	2σ	$^{187}Re/^{188}Os$	2σ	$(^{187}Os/^{188}Os)_i$
Transitional unit (TU)										
40R1_28–30 (Paleogene limestone)	616.53	0.231	0.190	0.493	0.793	0.2052	0.0044	n.a.		
40R1_33–35 (gray-green marlstone)	616.58	0.320	0.824	1.27	3.870	0.2261	0.0042	n.a.		
40R1_35–36 (upper TU)	616.60	0.571	0.500	0.855	3.813	0.2563	0.0004	n.a.		
40R1_36.5–39 (TU)	616.62	0.684	0.460	0.355	5.785	0.2259	0.0022	n.a.		
40R1_107.5–108 (lower TU)	617.32	2.889	0.717	0.101	2.303	0.3226	0.0028	n.a.		
40R1_108–109 (lower TU)	617.33	2.620	0.246	0.105	2.365	0.3391	0.0008	n.a.		
40R1_109–110 (lower TU)	617.34	34.54	1.321	0.110	4.220	0.5122	0.0004	n.a.		
Impact melt rocks (UIM)										
83R1_22–24.5	712.3	0.387	n.a.	0.027	0.086	n.a.		n.a.		
88R3_45–47.5	724.9	1.528	0.084	0.025	0.111	0.6374	0.0090	92.545	2.776	0.5355
89R1_59–61.5	726.2	2.828	0.045	0.033	0.079	1.0900	0.0300	341.210	10.240	0.7143
91R1_102–104.5	732.8	1.290	0.125	0.250	0.103	0.4154	0.0240	51.029	1.531	0.3592
93R1_21–23.5	738.1	0.883	0.096	0.023	0.149	0.4363	0.0095	45.555	1.367	0.3861
93R2_11–12.5	739.3	0.573	0.410	0.022	0.083	0.2025	0.0028	6.722	0.202	0.1951
95R2_45–47.5	745.3	0.511	0.068	0.031	0.077	0.3189	0.0035	36.835	1.105	0.2783
Impact melt rocks (LIMB)										
202R2_48.5–53	1026.3	0.145	0.062	0.039	0.040	0.203	0.001	11.277	0.338	0.1905
265R2_9–11	1216.5	0.915	0.344	0.324	0.352	0.184	0.002	12.760	0.383	0.1704
277R1_88–92	1253.3	1.524	0.077	0.017	0.136	1.061	0.024	105.910	3.180	0.9444
292R2_66–68.5	1299.4	n.a.	0.075	n.a.	n.a.	0.585	0.030	n.a.		
303R3_22.5–25	1334.4	1.014	0.015	0.018	0.088	2.086	0.016	309.600	9.290	1.7451
Suevites										
41R1_106–108	620.4	5.800	0.134	0.010	0.094	0.6163	0.0017	201.67		0.3943
58R3_8–10.5	673.7	2.003	0.027	0.002	0.073	1.1390	0.0170	350.31		0.7533
Pre-impact lithologies										
80R2_61–63.5	706.6	0.424	0.025	0.028	0.210	2.4740		79.790		2.3862
140R2_5–8 (dolerite)	854.6	0.710	0.245	0.156	0.346	0.1700	0.0040	13.547		0.1551
238R1_101–103.5 (dacite)	1135.1	0.237	0.105	0.003	0.037	0.2015	0.0069	10.600		0.1899
Granites										
136R2_20–25	851.4	0.698	0.026	0.008	0.106	0.1569	0.0098	124.56		0.0198
200R3_12.5–15	1021.0	0.335	0.022	0.001	0.077	0.1609	0.0081	72.710		0.0808

APPENDIX E: Rb-Sr and Sm-Nd isotopic composition of granites and other pre-impact lithologies

This table, also presented in the publication in Chapter 6, presents the Rb–Sr and Sm–Nd isotopic compositions of 16 granites, as well as of seven pre-impact lithologies occurring either as dike cross-cutting the granite basement, or as clast in impact melt rock (i.e., three dolerite, two dacite, and two felsite samples). Additionally, the impact melt rock sample 265R2_9–11 (1216.5 mbsf), likely representing a melted dolerite, was also investigated and is reported here. All these samples were recovered from the IODP-ICDP Expedition 364 drill core within the Chicxulub impact structure peak ring. mbsf: meters below seafloor.

Table E.1. Rb–Sr isotopic compositions measured using TIMS (see details in Chapter 4) of selected granite, dolerite, felsite, dacite, and impact melt rock samples. Isotopic ratios are calculated at t=66.05 Ma (impact age), and t=326 Ma in the case of the granite samples (i.e., age determined by U–Pb dating of zircon grains (Zhao et al., 2020)). The Rb and Sr abundances were taken from bulk XRF and INAA analysis (see Chapter 7, and Appendix C).

Sample	Depth (mbsf)	Rb (ppm)	Sr (ppm)	$^{87}Rb/^{86}Sr^a$	$^{87}Sr/^{86}Sr^b$	$(^{87}Sr/^{86}Sr)$ t=66.05Ma	$(^{87}Sr/^{86}Sr)$ t=326Ma
Granites							
97R3_10–12.5	752.5	143	333	1.2431	0.709614	0.70844	0.70385
125R1_40–42.5	826.7	132	374	1.0217	0.708963	0.70800	0.70422
136R2_20–25	851.4	114	447	0.7382	0.707975	0.70783	0.70455
142R3_48–50	862.6	124	384	0.9347	0.708807	0.70793	0.70447
153R1_47–50.5	890.8	125	269	1.3452	0.709801	0.70854	0.70356
156R3_11–15	902.1	171	404	1.2254	0.710231	0.70908	0.70454
176R2_112–116	953.6	159	231	1.9933	0.713210	0.71134	0.70396
200R3_12.5–15	1021.0	109	368	0.8573	0.708447	0.70764	0.70447
229R2_62–67	1107.2	89	319	0.8075	0.708159	0.70740	0.70441
266R2_95.5–98.5	1220.5	106	444	0.6910	0.707981	0.70733	0.70477
280R2_51.5–53.5	1263.5	163	220	2.1457	0.713705	0.71169	0.70375
297R1_36–38	1313.4	167	265	1.8248	0.712105	0.71039	0.70364
299R1_52.5–55.5	1319.7	118	200	1.7083	0.711652	0.71004	0.70373
300R1_78–79.5	1323.1	162	291	1.6118	0.711322	0.70981	0.70384
Granite clasts							
285R2_26–28.5	1278.7	113	317	1.0319	0.709111	0.70814	0.70432
295R2_51–53	1308.5	159	195	2.3614	0.713686	0.71147	0.70273
Dolerites							
143R2_103–106	864.8	24	298	0.2331	0.706992	0.70677	
198R1_68–71	1016.1	21	261	0.2329	0.706927	0.70671	
284R2_10–12.5 (clast)	1275.5	12	189	0.1838	0.707439	0.70727	

Felsites

234R2_97–98	1124.1	113	769	0.4252	0.706295	0.70590
239R1_121–124	1138.3	98	1178	0.2407	0.705555	0.70533

Dacites

164R2_110–115	920.2	143	493	0.8396	0.708217	0.70743
247R1_6.5–9	1160.1	101	677	0.4317	0.706401	0.70600

Impact melt rock (LIMB)

265R2_9–11	1216.5	11	247	0.1289	0.707567	0.70745

[a]The uncertainty on ^{87}Rb/^{86}Sr is ± 1.0%.
[b]The uncertainty on ^{87}Sr/^{86}Sr ratio is ± 2σ = 0.000004.

Table E.2. Sm–Nd isotopic compositions measured by TIMS (see details in Chapter 4) of selected granite, dolerite, felsite, dacite, and impact melt rock samples. Isotopic ratios are calculated at t=66.05 Ma (impact age), and t=326 Ma in the case of the granite samples (i.e., age determined by U–Pb dating of zircon gains(Zhao et al., 2020)). The Sm and Nd abundances were taken from bulk XRF and INAA analysis (see Chapter 7, and Appendix C).

Sample	Depth (mbsf)	Sm (ppm)	Nd (ppm)	^{147}Sm/^{144}Nd[a]	^{143}Nd/^{144}Nd[b]	ε_{Nd}[c]	(ε_{Nd}) t=66.05Ma	(ε_{Nd}) t=326Ma	$T^{Nd}_{DM(326Ma)}$ (Ga)[d]
Granites									
97R3_10–12.5	752.5	1.73	10.0	0.1025	0.512410	-4.4	-3.7	-0.5	1.1
125R1_40–42.5	826.7	1.70	8.0	0.1285	0.512470	-3.3	-2.7	-0.4	1.1
136R2_20–25	851.4	1.09	4.1	0.1607	0.512484	-3.0	-2.7	-1.5	1.2
142R3_48–50	862.6	4.09	23.0	0.1075	0.512424	-4.2	-3.4	-0.5	1.1
153R1_47–50.5	890.8	2.00	10.0	0.1209	0.512449	-3.7	-3.0	-0.5	1.2
156R3_11–15	902.1	1.20	19.0	0.0382	0.512464	-3.4	-2.1	3.2	0.8
176R2_112–116	953.6	1.94	14.0	0.0838	0.512433	-4.0	-3.0	0.7	1.0
200R3_12.5–15	1021.0	2.47	13.9	0.1074	0.512439	-3.9	-3.1	-0.2	1.1
229R2_62–67	1107.2	2.02	14.0	0.0872	0.512467	-3.3	-2.4	1.2	0.9
266R2_95.5–98.5	1220.5	2.16	16.0	0.0816	0.512436	-3.9	-3.0	0.8	1.0
280R2_51.5–53.5	1263.5	2.80	10.4	0.1628	0.512477	-3.1	-2.9	-1.7	1.2
297R1_36–38	1313.4	1.36	4.0	0.2055	0.512454	-3.6	-3.7	-4.0	1.4
299R1_52.5–55.5	1319.7	1.39	9.0	0.0934	0.512447	-3.7	-2.8	0.6	1.0
300R1_78–79.5	1323.1	3.25	11.8	0.1659	0.512449	-3.7	-3.4	-2.4	1.2
Granite clasts									
285R2_26–28.5	1278.7	3.10	12.6	0.1487	0.512447	-3.7	-3.3	-1.7	1.2
295R2_51–53	1308.5	1.82	13.0	0.0846	0.512440	-3.9	-2.9	0.8	1.0
Dolerites									
143R2_103–106	864.8	3.30	15.7	0.1271	0.512571	-1.3	-0.7		
198R1_68–71	1016.1	4.30	21.5	0.1209	0.512665	0.5	1.2		
284R2_10–12.5 (clast)	1275.5	2.2	12.0	0.1108	0.512757	2.3	3.1		

Felsites

234R2_97–98	1124.1	14.4	85.5	0.1024	0.512472	-3.2	-2.4
239R1_121–124	1138.3	18.8	102	0.1118	0.512481	-3.1	-2.4

Dacites

164R2_110–115	920.2	4.70	26.0	0.1093	0.512478	-3.1	-2.4
247R1_6.5–9	1160.1	3.60	22.0	0.0989	0.512458	-3.5	-2.7

Impact melt rock (LIMB)

265R2_9–11	1216.5	3.10	13.0	0.1442	0.512490	-2.9	-2.4

[a]The uncertainty on $^{147}Sm/^{144}Nd$ is ± 5.0%.

[b]The uncertainty on $^{143}Nd/^{144}Nd$ ratio is ± 2σ = 0.000004.

[c]Calculated using $^{143}Nd/^{144}Nd_{CHUR}$ = 0.512638 (DePaolo and Wasserburg, 1976). CHUR: chondritic uniform reservoir.

[d]Two-stage Nd model age calculated for granitoids following the method of Liew and Hofmann (1988) with $^{143}Nd/^{144}Nd_{DM}$ = 0.513151, $^{147}Sm/^{144}Nd_{DM}$ = 0.219, and $^{147}Sm/^{144}Nd_{CC}$ = 0.12. DM: depleted mantle; CC: continental crust.

Reference

Zhao J., Xiao L., Gulick S. P. S., Morgan J. V., Kring D. A., Urrutia-Fucugauchi J., Schmieder M., de Graaff S. J., Wittmann A., Ross C. H., Claeys P., Pickersgill A., Kaskes P., Goderis S., Rasmussen C., Vajda V., Ferrière L., Feignon J.-G., Chenot E., Perez-Cruz L., Sato H., Yamaguchi K., and IODP-ICDP Expedition 364 Scientists. 2020. Geochemistry, geochronology and petrogenesis of Maya Block granitoids and dykes from the Chicxulub impact crater, Gulf of Mexico: Implications for the assembly of Pangea. *Gondwana Research* 82:128–150. https://doi.org/10.1016/j.gr.2019.12.003.

<u>Curriculum vitae</u>

Name: Jean-Guillaume FEIGNON
Nationality: France
E-mail: jean-guillaume.feignon@univie.ac.at

Education and Research experience

2017–2022: PhD Student, Department of Lithospheric Research, University of Vienna, Austria

- PhD project: Petrography, shock metamorphism, and geochemistry of the impactites from the Chicxulub impact crater peak ring IODP-ICDP Expedition 364 drill core.
- Supervisors: Prof. Dr. Christian Koeberl and Dr. Ludovic Ferrière.
- Optical microscopy, universal stage, SEM, micro-XRF, sample preparation for chemical analysis, INAA, bulk XRF analysis, Re–Os and Sr–Nd isotope analysis (TIMS).

December 2015–September 2017: Invited student at Laboratoire Magmas et Volcans, Blaise Pascal University, Clermont-Ferrand, France

- Complementary analysis of melt inclusions from 1750 BP eruption of the Mocho-Choshuenco volcano (Chile).
- Raman 3D mapping, LA-ICPMS analysis, magmatic processes modelling using Petrolog.

September–December 2015: Four-months internship at Liège University, Belgium

- Preliminary work on a PhD project titled: Deciphering the Magmatic system under Osorno volcano, Chile.
- Supervisor: Prof. Dr. Jacqueline Vander Auwera.

2013–2015 Master in Earth Sciences at Laboratoire Magmas et Volcans, Blaise Pascal University, Clermont-Ferrand, France

- 2014-2015 → 6 month research project: Characterization and analysis of pyroclastic deposits and melt inclusions of an eruption of the Mocho-Choshuenco volcano, Chile.

  - Supervisors: Prof. O. Roche, Prof. P. Schiano, Dr. S. Moune, and Dr. N. Cluzel.

  - Optical microscopy, magnetic separation of minerals, microprobe, SIMS, estimation of pre-eruptive volatile contents.

- 2013-2014 → 2 month research project: Analysis of volcanic glass contained in MD11-3349 core sampled offshore La Réunion Island and datation.
  - Supervisor: Prof. P. Bachèlery.
  - Electron microprobe, LA-ICPMS, $\delta^{18}O$ datation technique.
- Teaching: 2 hours courses (Basic elements of geology) per week for first year BSc Earth Sciences students.

2010–2013 Bachelor's degree in Earth Sciences at the University Blaise Pascal, Clermont-Ferrand, France

Award

2019

- Barringer Family Fund for Meteorite Impact Research for field work in order to explore the possible Bateke impact structure in Gabon.

Field experience

2021

- Observation and imagery of the Fagradallsfjall volcanic eruption (Iceland).
- Observation and sampling of the La Palma volcanic eruption (Canary Islands, Spain).

2020

- Field work campaign in Gabon/Republic of the Congo (with an award from the Barringer Family Fund for Meteorite Impact Research).

2018

- Two day field trip at the Chicxulub impact structure proximal ejecta deposits at El Ramonal and at Bacalar (Mexico), within the framework of the Expedition 364 post-cruise meeting that took place in Merida.

2015

- One week observation and sampling of pyroclastics flow deposits from the Sinabung volcano (Indonesia).

2014

- Two-week field work on active volcanoes in Italy (Vesuvius, Campi Flegrei, Stromboli, and Vulcano) and ophiolite massifs in the Alps (Chamrousse, Chenaillet, Queyras, Viso, and Lanzo).

2013

- Mapping project in volcanic terrains (Massif du Mont Dore, Auvergne, France).
- Mapping project in metamorphic terrains (Massif de l'Agly, Pyrénées, France).
- Mapping project in sedimentary terrains and thrust zone (Corbières, France).
- Field trip to study the volcanism of Mauritius and Réunion islands.

2012

- Mapping project in metamorphic terrains (Cap Creus, Spain).
- Mapping project using GPS methods and MapInfo software in order to create a geological map (Pic-Saint-Loup, France).
- Field trip on the Cascade Range volcanoes (in western North America).

2011

- Mapping project in the Alps (Alpe d'Huez, France).
- Field work (Montagne Noire massif, France).
- Observation of volcanism in Vanuatu (Ambrym, Yasur, and Ambae).

2010

- Observation of the partial dome collapse (11th February) at the Soufriere Hills, Montserrat (West Indies).

2007

- One week internship with mountain guide specialized in volcanology, Auvergne, France.

Public outreach

October 16th, 2021

- Interview for Le Parisien French newspaper regarding the ongoing eruption at La Palma   (https://www.leparisien.fr/societe/on-se-senta-sa-merci-aux-iles-canaries-la-fureur-sans-fin-duvolcan-cumbre-vieja-16-10-2021-MANHKVFZVFHQ5GWPVZF3MUNJZA.php).

July 4th, 2019

- Interview for France Info radio channel on the strong explosive eruption which occurred at Stromboli   (https://www.francetvinfo.fr/monde/italie/italiepourquoi-la-derniere-eruption-du-volcan-strombolisort-de-l-ordinaire_3520805.html).

Since 2010

- Regular lectures for the general public and guided field trips in the framework of the French non-profit organization: the European Volcanological Association (L.A.V.E.).
- Board member (and former President) of the European Volcanological Association (L.A.V.E.) and administrator of the L.A.V.E. grant.

List of publications

Papers published in refereed journals

Zhao J., Xiao L., Gulick S. P. S., Morgan J. V., Kring D., Urrutia Fucugauchi J., Schmieder M., de Graaff S. J., Wittmann A., Ross C. H., Claeys Ph., Pickersgill A., Kaskes P., Goderis S., Rasmussen C., Vajda V., Ferrière L., **Feignon J.-G.**, Chenot E., Perez-Cruz L., Sato H., Yamaguchi K., and IODP–ICDP Expedition 364 scientists* 2020. Geochemistry, geochronology and petrogenesis of Maya Block granitoids and dykes from Chicxulub Impact Crater, Gulf of México: Implications for the assembly of Pangea. *Gondwana Research* 82:128–150, https://doi.org/10.1016/j.gr.2019.12.003.

Pittarello L., Ferrière L., **Feignon J.-G.**, Osinski G. R., and Koeberl C. 2020. Preferred orientation distribution of shock-induced planar microstructures in quartz and feldspar. *Meteoritics and Planetary Science* 55(5):1082–1092, https://doi.org/10.1111/maps.13490.

Feignon J.-G., Ferrière L., Leroux H., and Koeberl C. 2020. Characterization of shocked quartz grains from Chicxulub peak ring granites and shock pressure estimates. *Meteoritics and Planetary Science* 55(10):2206–2223, https://doi.org/10.1111/maps.13570.

Goderis S., Sato H., Ferrière L., Schmitz B., Burney D., Kaskes P., Vellekoop J., Wittmann A., Schulz T., Chernonozhkin S., Claeys Ph., de Graaff S.J., Déhais T., de Winter N.J., Elfman M., **Feignon J.-G.**, Ishikawa A., Koeberl C., Kristiansson P., Neal C.R., Owens J.D., Schmieder M., Sinnesael M., Vanhaecke F., Van Malderen S.J.M., Bralower T.J., Gulick S.P.S., Kring D.A., Lowery C.M., Morgan J.V., Smit J., Whalen M.T., and the IODP-ICDP Expedition 364 Scientists 2021. Globally distributed iridium layer preserved within the Chicxulub impact structure. *Science Advances* 7(9):eabe3647, https://doi.org/10.1126/sciadv.abe3647.

Feignon J.-G., de Graaff S. J., Ferrière L., Kaskes P., Déhais T., Goderis S., Claeys Ph., and Koeberl C. 2021. Chicxulub impact structure, IODP-ICDP Expedition 364 drill core: Geochemistry of the granite basement. *Meteoritics and Planetary Science* 56(7):1243–1273, https://doi.org/10.1111/maps.13705.

de Graaff S. J., Kaskes P., Déhais T., Goderis S., Debaillle V., Ross C. H., Gulick S. P. S., **Feignon J.-G.**, Ferrière L., Koeberl C., Smit J., Mattielli N., and Claeys Ph. 2022. New insights into the formation and emplacement of impact melt rocks within the Chicxulub impact structure, following the 2016 IODP-ICDP Expedition 364. *GSA Bulletin* 134(1–2):293–315, https://doi.org/10.1130/B35795.1.

Kaskes P., de Graaff S. J., **Feignon J.-G.**, Déhais T., Goderis S., Ferrière L., Koeberl C., Smit J., Wittmann A., Gulick S. P. S., Debaillle V., Mattielli N., and Claeys Ph. 2022. Formation of the crater suevite sequence from the Chicxulub peak ring: A petrographic, geochemical, and sedimentological characterization. *GSA Bulletin* 134(3–4):895–927, https://doi.org/10.1130/B36020.1.

Feignon J.-G., Schulz T., Ferrière L., Goderis S., de Graaff S. J., Kaskes P., Déhais T., Claeys Ph., and Koeberl C. 2022. Search for a meteoritic component within the impact melt rocks of the Chicxulub impact structure peak ring, Mexico. *Geochimica et Cosmochimica Acta* 323:74–101, https://doi.org/10.1016/j.gca.2022.02.006.

Feignon J.-G., Cluzel N., Schiavi F., Moune S., Roche O., Clavero J., Schiano P., and Auxerre M. 2022. High CO_2 content in magmas of the explosive andesitic Enco eruption of Mocho-Choshuenco volcano (Chile). *Bulletin of Volcanology* 84, Article #40, 20 p. https://doi.org/10.1007/s00445-022-01550-y.

de Graaff S. J., Ross. C. H., **Feignon J.-G.**, Kaskes P., Gulick S. P. S., Goderis S., Déhais T., Debaillle V., Ferrière L., Koeberl C., Mattielli N., Stockli D., and Claeys Ph. 2022. The Chicxulub impact structure reveals the first in-situ Jurassic-aged magmatic intrusions of the Yucatán Peninsula, Mexico. *Lithos* (*Submitted 2022-06-12*).

Abstracts published

Ferrière L., **Feignon J.-G.**, Leroux H., and Koeberl C. 2018. What do shocked quartz grains in impactites from the IODP Expedition 364 drill core tell us about the Chicxulub impact event? (abstract #2238). 49th Lunar and Planetary Science Conference.

Feignon J.-G., Ferrière L., and Koeberl C. 2018. Petrography and shock metamorphism of granitoid samples from the Chicxulub peak-ring IODP-ICDP expedition 364 drill core (abstract #10750). *Geophysical Research Abstracts* 20.

Feignon J.-G. 2018. The European Volcanological Association (L.A.V.E.): a French-speaking non-profit organization dedicated to general public communications, activities, and meeting of volcanology enthusiasts. *Abstracts Volume of the International meeting "Cities on Volcanoes 10"*, pp. 1266.

Gulick S., Morgan J. V., Bralower T., E. Chenot E., Christeson G. L., Claeys Ph., Cockell C., Coolen M. J. L., Ferrière L., Gebhardt C., Goto K., Green S., Jones H., Kring D. A., Lofi J., Lowery C., Ocampo-Torres R., Perez-Cruz L., Pickersgill A., Poelchau M. H., Rae A. S. P., Rasmussen C., Rebolledo-Vieyra M., Riller U., Sato H., Schmitt D., Smit J., Tikoo S., Urrutia-Fucugauchi J., Wittmann A., Xiao L., Yamaguchi K. E., Vellekoop J., Neal C. R., Grice K., Ormö J., Melosh J., Collins G. S., Rodriguez-Tovar F., Osinski G. R., Stockli D. F., Schmieder M., Snedden J., Freeman K. H., Hall B., Smith V., Grieve R. A. F., Koeberl C., Goderis S., Nixon C., Vajda V., Warny S., Schulte F., Artemieva N., Sluijs A., McCall N., Schaefer B.,

Diaw A., Lyons S., O'Malley K., Gattacceca J., Quesnel Y., Ross C., and **Feignon J.-G.** 2018. Insights into impact processes and extinction mechanisms from IODP-ICDP Chicxulub crater drilling (paper no. 319280). Geological Society of America *Abstracts with Programs* 50(6), doi: 10.1130/abs/2018AM-319280.

Feignon J.-G., Ferrière L., Koeberl C., de Graaff S. J., Kaskes P., Goderis S., Déhais T., and Claeys Ph. 2019. Geochemistry and petrography of granitoid basement from the Chicxulub peak-ring (abstract #10791). *Geophysical Research Abstracts* 21.

Feignon J.-G., Roche O., Moune S., Cluzel N., Schiavi F., Clavero J., Schiano P., and Auxerre M. 2019. High CO_2 content in magmas at an arc volcano: the andesitic Enco eruption of Mocho-Choshuenco volcano (Chile) (abstract #16065). *Geophysical Research Abstracts* 21.

Feignon J.-G., Ferrière L., and Koeberl C. 2019. Petrography, shock metamorphism, and geochemistry of the main lithologies from the Chicxulub impact structure peak-ring IODP-ICDP Expedition 364 drill core (abstract). Impacts and their role in the Evolution of Life, 10–13rd June, 2019, Tällberg, Siljan area, Sweden, Schedule & Abstract volume, pp. 44–45.

Pittarello L., Ferrière L., **Feignon J.-G.**, and Osinski G. R. 2019. Study of the preferential orientation distribution of shock-induced planar microstructures in quartz and feldspar. In *Large Meteorite Impacts and Planetary Evolution VI,* Abstract #5053. LPI Contribution No. 2136, Lunar and Planetary Institute, Houston.

Goderis S., Sato H., L. Ferrière L., Schmitz B., Burney D., Bralower T. J., de Graaff S. J., Déhais T., de Winter N. J., Elfman M., **Feignon J.-G.**, Gulick S. P. S., Ishikawa A., Kaskes P., Koeberl C., Kristiansson P., Lowery C. M., Morgan J., Neal C. R., Owens J. D., Schulz T., Sinnesael M., Smit J., Vellekoop J., Whalen M. T., Wittmann A., Vanhaecke F., Van Malderen S., and Claeys Ph. 2019. The final settling of meteoritic matter on the peak-ring of the Chicxulub impact structure at site M0077A of IODP-ICDP expedition 364. In *Large Meteorite Impacts and Planetary Evolution VI,* Abstract #5068. LPI Contribution No. 2136, Lunar and Planetary Institute, Houston.

de Graaff S. J., Kaskes P., Déhais T., Goderis S., Debaille V., **Feignon J.-G.**, Ferrière L., Koeberl C., Ross C. H., and Claeys Ph. 2019. Making (more) sense of destruction – A comprehensive geochemical investigation of Chicxulub impactites recovered during IODP-ICDP expedition 364. In *Large Meteorite Impacts and Planetary Evolution VI,* Abstract #5079. LPI Contribution No. 2136, Lunar and Planetary Institute, Houston.

Kaskes P., De Graaff S. J., Déhais T., Goderis S., **Feignon J.-G.**, Ferrière L., Koeberl C., Smit J., and Ph. Claeys Ph. 2019. Geochemical and petrographic characterization of the suevite sequence within the IODP-ICDP exp. 364 core of the Chicxulub peak ring. In *Large Meteorite Impacts and Planetary Evolution VI,* Abstract #5085. LPI Contribution No. 2136, Lunar and Planetary Institute, Houston.

Feignon J-G., Ferrière L., and Koeberl C. 2019. Shocked quartz grains in granitoids from the Chicxulub impact structure peak-ring IODP-ICDP Expedition 364 drill core: Characterization and shock pressure estimations. In *Large Meteorite Impacts and Planetary Evolution VI,* Abstract #5098. LPI Contribution No. 2136, Lunar and Planetary Institute, Houston.

Feignon J.-G., Ferrière L., and Koeberl C. 2020. Characterization of shocked quartz grains and shock pressure estimations in the Chicxulub impact structure peak-ring granites from IODP-ICDP Expedition 364 drill core (abstract #1388). 51st Lunar and Planetary Science Conference.

Feignon J.-G., de Graaff S. J., Ferrière L., Kaskes P., Déhais T., Goderis S., Claeys P., and Koeberl C. 2021. Petrological and geochemical investigations of the granite basement in the Chicxulub peak ring: Implications for the Yucatán target rock (abstract #1557). 52nd Lunar and Planetary Science Conference.

Feignon J.-G., Schulz T., Ferrière L., Goderis S., de Graaff S. J., Kaskes P., Déhais T., Claeys P., and Koeberl C. 2021. Examining the (potential) presence of a preserved impactor signature in the impact melt rocks of the Chicxulub impact structure peak ring. 84th Annual Meeting of The Meteoritical Society, 15–21 August, 2021, Chicago, USA. LPI Contribution No. 2609, Abstract #6238.

Feignon J.-G., Schulz T., Ferrière L., Goderis S., de Graaff S. J., Kaskes P., Déhais T., Claeys P., and Koeberl C. 2021. Do the impact melt rocks within the Chicxulub impact structure peak ring (Yucatán peninsula, Mexico) preserve an impactor signature? *Geological Society of America Abstracts with Programs*. Vol 53, No. 6, https://doi.org/10.1130/abs/2021AM-367071.

de Graaff S. J., Kaskes P., Déhais T., Goderis S., Debaille V., Ross C. H., Gulick S. P. S., **Feignon J.-G.**, Ferrière L., Koeberl C., Smit T., Mattielli N., and Claeys P. 2021. New insights into the formation and emplacement of impact melt rocks within the Chicxulub impact structure, following the 2016 IODP-ICDP Expedition 364. *Geological Society of America Abstracts with Programs*. Vol 53, No. 6, https://doi.org/10.1130/abs/2021AM-369141.

Kaskes P., de Graaff S. J., **Feignon J.-G.**, Déhais T., Goderis S., Ferrière L., Koeberl C., Smit T., Wittmann A., Gulick S. P. S., Debaille V., Mattielli N., and Claeys P. 2021. Suevite emplacement within the Chicxulub impact structure: new insights from the 2016 IODP-ICDP Expedition 364 drilling. *Geological Society of America Abstracts with Programs*. Vol 53, No. 6, https://doi.org/10.1130/abs/2021AM-369033.

Kaskes P., de Graaff S. J., **Feignon J.-G.**, Déhais T., Goderis S., Ferrière L., Koeberl C., Smit T., Wittmann A., Gulick S. P. S., Debaille V., Mattielli N., and Claeys Ph. 2022. The drill core diary: Unravelling the rapid emplacement of suevite and impact melt phases within the Chicxulub impact structure (abstract #2656). 53rd Lunar and Planetary Science Conference.

Feignon J.-G., Schulz T., Ferrière L., Goderis S., de Graaff S. J., Kaskes P., Déhais T., Claeys Ph., and Koeberl C. 2022. Search for a meteoritic component within the Chicxulub impact structure peak ring impact melt rocks: Implications for the fate of the projectile (abstract #S2T4). International Congress-Festival – CIRIR 2022, June 28th – July 3rd, 2022, Rochechouart, France.

Kaskes P., Ferrière L., Chernonozhkin S., Goderis S., de Graaff S. J., Déhais T., **Feignon J.-G.**, Koeberl C., Vanhaecke F., and Claeys Ph. 2022. Mode of emplacement of suevite and impact melt particles within the Chicxulub peak ring (abstract #S2T3). International Congress-Festival – CIRIR 2022, June 28th – July 3rd, 2022, Rochechouart, France.

Ferrière L., **Feignon J.-G.**, Baratoux D., and Koeberl C. 2022. Prison break and the tentative exploration of the Bateke Plateau structure, a possible meteorite impact crater located in either Gabon or Congo (abstract #6154). 85th Annual Meeting of The Meteoritical Society, 14–19 August, 2022, Glasgow, Scotland.

Feignon J.-G., Schulz T., Ferrière L., Goderis S., de Graaff S. J., Kaskes P., Déhais T., Claeys Ph., and Koeberl C. 2022. Lack of ubiquitous impactor component in the Chicxulub peak ring impact melt rocks: Implications for the fate of the projectile (abstract #6200). 85th Annual Meeting of The Meteoritical Society, 14–19 August, 2022, Glasgow, Scotland.